Consiglio Nazionale
delle Ricerche

GEOMORPHOMETRY 2025

THE 8TH CONFERENCE OF THE INTERNATIONAL SOCIETY FOR GEOMORPHOMETRY

Perugia, June 9-13 2025

editors
Massimiliano Alvioli
Laura Melelli
Ivan Marchesini

PROCEEDINGS

GEOMORPHOMETRY 2025

THE 8TH CONFERENCE OF THE INTERNATIONAL SOCIETY FOR GEOMORPHOMETRY

Perugia, June 9-13 2025

editors
Massimiliano Alvioli
Laura Melelli
Ivan Marchesini

edizioni
Consiglio Nazionale delle Ricerche

Supporting institutions

Commercial partners

Cite this book as: M. Alvioli, L. Melelli, I. Marchesini, (2026). Proceedings of Geomorphometry 2025, 9-13 June, Perugia, Italy. CNR Edizioni, Rome. ISBN 978 88 8080 765 0. DOI: https://doi.org/10.30437/gmft25pg

Supported by project "URGERE: URban Geodiversity for a Resilient Environment" 2022M7EP3M_PE10_PRIN2022 - PNRR M4.C2.1.1 Funded by the European Union - Next Generation EU CUP: B53D23007260006

Consiglio Nazionale delle Ricerche
Istituto di ricerca per la protezione idrogeologica

ISBN (electronic edition) 978 88 8080 765 0
https://doi.org/10.30437/gmft25pg

The digital version is published in Open Access on www.edizioni.cnr.it

Sviluppo grafico a cura di Fulvia Ciurlia, Cnr-Unità editoria
Impaginazione a cura di Patrizia Andronico, Iit / Cnr-Unità editoria

Piazzale Aldo Moro, 7
00185 Roma
www.edizioni.cnr.it

GEOMORPHOMETRY 2025

THE 8TH CONFERENCE OF THE INTERNATIONAL SOCIETY FOR GEOMORPHOMETRY

Scientific Commitee

Alexander Brenning Germany
A-Xing Zhu USA
Carlos Grohman Brazil
Cheng-Zhi Qin China
Giuseppe Amatulli USA
Hannes I. Reuter EU
Helena Mitasova USA
Ian Evans UK
Jaroslav Hofierka Slovakia
John Gallant Australia
John Lindsay Canada
Jozef Minár Slovakia
Laurence Hawker UK
Lucian Dragut Romania
Massimiliano Alvioli Italy
Mihai Niculita Romania
Peter L. Guth USA
Qiming Zhou China
Samantha Arundel USA
Scott D. Peckham USA
Sebastiano Trevisani Italy
Steve Kopp USA
Tomislav Hengl Netherlands
Vincent Lecours Canada

Organizing Commitee

Massimiliano Alvioli CNR IRPI Perugia
Ivan Marchesini CNR IRPI Perugia
Laura Melelli University of Perugia
Giulia Sofia Consorzio LEB
Mihai Niculita University Al. I. Cuza

Index

1.1 - Digital elevation models 17

Update on MICRODEM in DEMIX 18

Activities of the DEMIX Subgroup 3 "Platforms and Processing" 22

A qualitative comparison of corrected global DEMs 26

High-Resolution Digital Terrain Model on a sample area of the Italian national territory 30

DEM Generalization Tool Using Grid-Based Quadric Error Metric 34

Towards implementation of segmentation into Physical geomorphometry tools: Case of generalization 38

Enriching LiDAR data with partial derivatives and its uncertainty estimates 42

Global Ensemble Digital Terrain model and parametrization at 1 arc-second resolution 46

Innovative Terrain Mapping: A Comparison of Drone and iPhone + viDoc Techniques 50

Machine Learning Model Transferability for Urban Point Cloud Classification: 54

A Study of Random Forest and XGBoost across Datasets 54

Geomorphometry in the Cloud: New Capabilities and Future Directions of ArcGIS 58

1.2 - Topographic Attributes 62

Roughness who? 63

Formal weaknesses of some definitions of roughness, and a solution proposal 67

Derivation and Applications of Fuzzy Slope Position Information 71

Time to Revamp the Slope Algorithm and KISS? 75

Elevation residual analysis with scale mosaics 79

Profile Integral, a robust and unified metric for measuring profile concavity 83

New Tool for Calculating Land Surface Parameters 87

1.3 - Stream and slope applications 91

Reflections on Geomorphometry and Hydrology 92

Automatic optimization and delineation of nested slope units with r.slopeunits v2.0 96

A minimal dispersion flow algorithm 100

Computing Channel Slope from a DEM: A Review of Issues and Two Algorithms 104

The role of spatial resolution and vertical accuracy of global DEMs in delineating stream networks 108

Probabilistic surface change detection with a 2-d array of robust adaptive Kalman filters 112

Automatic delineation of river centerline using high density topographic LiDAR point cloud 116

Spatio-temporal monitoring of bankfull geometry using a semi-automated tool on high-resolution Digital Terrain Models 120

2 - Landforms and Processes 124

2.1 - Landslides 125

Global Landslide Susceptibility Mapping Using Multi-Model Machine Learning Approaches on Geospatial Satellite Data 126

Influence of Data Resolution on Logistic Regression Models for Landslide Susceptibility in Tropical Environments 130

Rockfall susceptibility along communication routes and in urban areas in Italy based on physical and statistical models 134

On two implicit issues in prediction modeling of landslide susceptibility 138

Forest cover controls on debris flow sediment connectivity in the Stolla Basin, Italy 142

Regional-Scale Debris-Flow Susceptibility Modelling.
A case study in the Rocky Mountains 146

Automatic Landslide Detection Using Google Earth Engine, a case study for Quang Nam Province, Vietnam 150

Assessing the morphological changes of a large landslide using high-resolution UASand airborne LiDAR data 154

A new perspective on geohazards assessment: leveraging gigapixel imaging technique 158

A comparative study of mass movement morphometry in two adjacent watersheds of southern Italy 162

Comparing hybrid and machine learning models for rainfall-induced shallow l andslide susceptibility 165

Regional landslide prediction: comparing open-access Digital Elevation Models to delineate slope units 168

2.2 - Fluvial processes 172

Soil Erosion And Intensive Agriculture (Lessini Veronesi, NE Italy):
Multi-Temporal Modelling On DEMs From Photogrammetry And Lidar 173

Gully erosion potential by hypsometric curve and morphometric analysis 177

An open-source tool for modelling reservoir bottom gully head erosion volume 181

Monitoring Badlands Features through TLS and UAV Technology 185

2.3 - Glacial processes 189

Geomorphic evolution of the Miage Lake: a morphometric evaluation of the changes from 2018 to 2024 190

Rocks from the ice: DEMs of subglacial concretions through photogrammetry 194

2.4 - Tectonic processes 198

Coupling UAV-derived Lidar and geophysical data for the reconstruction of high-resolution 3D model of active faults: an example from the Piano di Pecore intramontane basin (Mt. Marzano, southern Italy) 199

The Central Italy's 1997-2009-2016 Seismic Sequences: a comparison of surface deformation from a review of DinSAR results 203

Airborne LiDAR survey for Monte Cefalone Fault structural analysis 207

2.5 - Landform classification 211

Multidisciplinary Application of Geomorphometry for the Characterization of the Northern Gulf of Mexico Seafloor, United States 212

Introducing the Geomorphometric Atlas of Romania: A Publicly Available Database of Landform Classifications and Land-Surface Variables based on FABDEM 216

Geomorphic Distribution Modeling of Desert Pavements: Towards a Global Assessment 219

Application of Physical Geomorphometry in Digital Geomorphological Mapping 223

2.6 - Physical and other surface processes **227**

Advances in theory of physical geomorphometry 228

Extending Physical Geomorphometry into 3D: A Case Study on Domica Cave, Slovakia 232

Photogrammetry for morphometric analysis of anhydrite-gypsum weathering zones 236

Retrieval of Digital Elevation Models from optical sensors data in a Coastal Dune Systems:
geomorphometric analysis for environmental monitoring 239

The role of elevation in the spatial distribution of sub-daily rainfall extremes 243

3 - GEORESOURCES 246

Geodiversity and Geomorphometry: Methods and Applications in Landscape Assessment 247

Geomorphodiversity index of Switzerland for multiscale analysis 253

Integrating Geosystem Services classifications: a preliminary framework from the piedmont area of the Sesia Val Grande UNESCO Global Geopark 257

Modeling Pre-Anthropogenic Topography: A Reconstruction in the Perugia Center Using Subsoil Data 261

Global Assessment of Mining Activities Using TanDEM-X Digital Elevation Change Maps 265

The use of historical cartographic materials and contemporary lidar models to determine changes in terrain relief in hard coal mining area (Bytomka Catchment, Southern Poland) 269

Program

Sunday, June 8	
19:00 - 20:30	Icebreaker: let's meet for a drink

Monday, June 9		
08:30 - 08:45	Opening Ceremony	
08:45 - 09:00	Greetings	
09:00 - 09:45	Keynote: Sebastiano Trevisani	Roughness who?
09:45 - 10:00	Peter Guth	Time to Revamp the Slope Algorithm and KISS?
10;00 - 10:15	Scott Peckham	Computing Channel Slope from a DEM: A Review of Issues and Two Algorithms
10:15 - 10:30	John Lindsay	A minimal dispersion flow algorithm
10:30 - 10:45	Daniel Newman and Yuichi Hayakawa	Probabilistic surface change detection with a 2-d array of robust adaptive Kalman filters
10:45 - 11:15	**Coffee**	
11:15 - 11:30	Richard Feciskanin and Jozef Minár	DEM Generalization Tool Using Grid-Based Quadric Error metric
11:38 (short)	Carlos López-Vázquez, Francisco-Javier Ariza-López and Juan-Francisco Reinoso-Gordo	Enriching LiDAR data with partial derivatives and its uncertainty estimates
11:46 (short)	Antonella Marsico, Rosa Colacicco, Marco La Salandra, Rodolfo Roseto, Teresa Scolamacchia and Domenico Capolongo	Monitoring Badlands Features through TLS and UAV Technology
11:54 (short)	Francesco Parizia, Walter Alberto, Marco Giardino and Luigi Perotti	Geomorphic evolution of the Miage Lake: a morphometric evaluation of the changes from 2018 to 2024
12:02 (short)	Adrian Jarzyna, Maciej Bąbel and Firouz Vladi	Photogrammetry for morphometric analysis of anhydrite-gypsum weathering zones
12:10 (short)	Veronika Hajdúchová, Hana Bobáľová, Alexandra Benová and Jozef Minár	Towards implementation of segmentation into Physical geomorphometry tools: Case of generalization
12:18 (short)	Michal Gallay, Jozef Šupinský, Michaela Nováková and Jozef Minár	Extending Physical Geomorphometry into 3D: A Case Study on Domica Cave, Slovakia
12:26 (short)	Muhammad Muneeb, Andrea Ermini, Riccardo Salvini, Stefano Pucci, Riccardo Civico and Paolo Marco De Martini	Airborne LiDAR survey for Monte Cefalone Fault structural analysis
12:34 (short)	Mihai Niculita and Nicusor Necula	A critical evaluation of global forest height data for DTM creation
12:45 - 14:30	**Lunch + Posters**	
14:30 - 14:45	Cheng-Zhi Qin, Liang-Jun Zhu and A-Xing Zhu	Derivation and Applications of Fuzzy Slope Position Information
14:45 - 15:00	John Lindsay, Yannan Wang and Marina Coric	Elevation residual analysis with scale mosaics
15:00 - 15:15	Yingkui Li, Ian S. Evans and Jonathan M. Harbor	Profile Integral, a robust and unified metric for measuring profile concavity
15:15 - 15:30	Jozef Minár, Richard Feciskanin, Michal Gallay and Jozef Šupinský	Advances in theory of physical geomorphometry
15:30 - 15:45	Maarten Pronk, Hugo Ledoux and Marieke Eleveld	A qualitative comparison of corrected global DEMs
15:45 - 16:15	Book Presentation: Chair: Peter Guth Speakers: Carlos Grohmann, Vincent Lecours, Hannes Reuter (book editors)	Geomorphometry book: new edition
16:15 - 16:30	**Coffee**	
16:30 - 16:45	Yu-Feng Ho, Leandro Parente, John Lindsay, Carlos Henrique Grohmann, Hannes Isaak Reuter and Tomislav Hengl	Global Ensemble Digital Terrain model and land relief parameterization at 1 arc-second resolution: a community-based open data service to support regional and global modeling
16:45 - 17:00	Alexandre Rétat, Nathalie Thommeret, Frederic Gob, Jean-Stéphane Bailly, Laurent Lespez and Karl Kreutzenberger	Automatic delineation of river centerline using high density topographic LiDAR point cloud.
17:00 - 17:15	Marina Muto, Mario Panza, Giulio Iovine, Ivan Marchesini, Mauro Rossi and Massimiliano Alvioli	High-Resolution Digital Terrain Model on a sample area of the Italian national territory

17:15 - 17:30	Massimiliano Alvioli and Ivan Marchesini	Automatic optimization and multi-scale delineation of nested slope units with r.slopeunits v2.0
17:30 - 17:45	Petr Basta, Jana Maresova and Vitezslav Moudry	The role of spatial resolution and vertical accuracy of global DEMs in delineating stream networks

Tuesday, June 10	
08:00 - 18:00	Field trip to Civita di Bagnoregio

Wednesday, June 11		
09:00 - 09:45	Keynote: Zbigniew Zwoliński	The fascinating fusion of geomorphometry and geodiversity
09:45 - 10:00	Vincent Lecours, Riccardo Arosio, Benjamin Misiuk, Rachel Barrett and Margaret Dolan	Multidisciplinary application of geomorphometry for the characterization of the Northern Gulf of Mexico, United States
10:00 - 10:15	Haoyu Cao, Liyang Xiong and Hongen Wang	Landform Classification Using Hydrological Knowledge derived from Digital Elevation Models
10:15 - 10:30	Andrea G Fabbri	On two implicit issues in prediction modeling of landslide susceptibility
10:30 - 10:45	Manuel Stark, Annalisa Sannino and Francesca Vergari	Assessing the morphological changes of a large landslide using high-resolution UAS and airborne LiDAR data
10:45 - 11:00	**Coffee**	
11:00 - 11:15	Nawajish Noman, Steve Kopp and Tania Lopez-Cantu	Geomorphometry in the Cloud: New Capabilities and Future Directions of ArcGIS
11:15 - 11:30	Richard Feciskanin and Veronika Hajdúchová	New Tool for Calculating Land Surface Parameters
11:30 (short)	Paola Mazzoglio, Ilaria Butera and Pierluigi Claps	The role of elevation in the spatial distribution of sub-daily rainfall extremes
11:38 (short)	Tra My Nguyen, Kervyn Matthieu, Smets Benoît, Quoc Dinh Nguyen, Thanh Long Nguyen and Luu Chinh	Automatic Landslide Detection Using Google Earth Engine, a case study for Quang Nam Province, Vietnam
11:46 (short)	Jason Goetz, Stefan Steger and Vittoria Scorpio	Calibrating Regional Debris Flow Runout Simulations for Connectivity: Forest Controls on Sediment Transport in the Stolla Basin, Italy
12:54 (short)	Chinh Luu, Quynh Bui, Dang Do and Matthieu Kervyn	Quantitative assessment of landslide impacts using satellite imagery: A case study of Phuoc Son district, Quang Nam province, Vietnam
12:02 (short)	Margherita Bufalini, Marco Materazzi, Ugo Ciccolini and Francesco Dramis	Gully erosion potential by hypsometric curve and morphometric analysis
12:10 (short)	Alex-Andrei Cuvuliuc, Denisa-Elena Ursu and Mihai Niculiță	An open-source tool for modelling reservoir bottom gully head erosion volume
12:18 (short)	Mahnoor Ahmed, Giacomo Titti, Sebastiano Trevisani, Lisa Borgatti and Mirko Francioni	Regional landslide prediction: comparing open-access Digital Elevation Models to delineate slope units
12:26 (short)	Nabanita Sarkar and Massimiliano Alvioli	Rockfall susceptibility along communication routes and in urban areas in Italy based on physical and statistical models
12:45 - 14:30	**Lunch + Posters**	
14:30 - 14:45	Giacomo Titti, Liwei Hu, Pietro Festi, Letizia Elia, Lisa Borgatti and Luigi Lombardo	SZ-plugin: a space-time data-driven modeler in QGIS
14:45 - 15:00	Saverio Mancino, Francesco Paolo Lovergine, Capolongo Domenico and Giuseppe Amatulli	Global Landslide Susceptibility Mapping Using Multi-Model Machine Learning Approaches on Geospatial Satellite Data
15:00 - 15:15	Florian Strohmaier and Alexander Brenning	Comparing hybrid and machine learning models for rainfall-induced shallow landslide susceptibility.
15:15 - 15:30	Txomin Bornaetxea Estela, Ivan Marchesini and Andrée Blais-Stevens	Regional-Scale Debris-Flow Susceptibility Modelling. A case study in the Rocky Mountains
15:30 - 15:45	Rebeca Durso Coelho, Camila Duelis Viana, John Lindsay and Carlos Henrique Grohmann	Influence of Data Resolution on Logistic Regression Models for Landslide Susceptibility in Tropical Environments
15:45 - 16:00	Saverio Romeo, Alessandro Fraccica and Valerio Vitale	A new perspective on geohazards assessment: leveraging gigapixel imaging technique
16:00 - 16:15	**Coffee**	
16:15 - 16:30	Martina Burnelli, Laura Melelli, Emmanuel Reynard and Massimiliano Alvioli	Geomorphodiversity index of Switzerland for multiscale analysis

16:30 - 16:45	Pedro Alberto Pereira Zamboni, Hanne Hendrickx and Anette Eltner	Machine Learning Model Transferability for Urban Point Cloud Classification: A Study of Random Forest and XGBoost across Datasets
16:45 - 17:00	Carlo Alberto Brunori, Massimiliano Barchi, Vincenzo De Novellis, Diego Reale, Eugenio Sansosti, Massimiliano Porreca and Laura Melelli	The Central Italy's 1997-2009-2016 Seismic Sequences: a comparison of surface deformation from a review of DinSAR results.
17:00 - 17:15	Alessandra Vinci, Raffaella Brigante, Laura Marconi and Sara Zollini	Innovative Terrain Mapping: A Comparison of Drone and iPhone + ViDoc Techniques

Thursday, June 12		
09:00 - 09:45	Keynote - Lifetime Achievement Award: David Tarboton	Reflections on Geomorphometry and Hydrology
09:45 - 10:00	Michele Delchiaro, Valeria Ruscitto, Davide Torre, Wolfgang Schwanghart, Daniela Piacentini, Francesco Ballio and Francesco Troiani	Spatio-temporal monitoring of bankfull geometry using a semi-automated tool on high-resolution Digital Terrain Models
10:00 - 10:15	Vitezslav Moudry, Katerina Gdulova and Kamila Svobodova	Global Assessment of Mining Activities Using TanDEM-X Digital Elevation Change Maps
10:15 - 10:30	Alexander Brenning, Lucca Güldner, Kerstin Schepanski, Michael Dietze and Markus Fuchs	Geomorphic Distribution Modeling of Desert Pavements: Towards a Global Assessment
10:30 - 10:45	Veronica Chiarini, Stefano Castelli and Alessandro Fontana	Rocks from the ice: DEMs of subglacial concretions through photogrammetry
10:45 - 11:15	**Coffee**	
11:15 - 11:30	Anton Popov and Jozef Minár	Application of Physical Geomorphometry in Digital Geomorphological Mapping
11:30 (short)	Barbara Rigon, Sandro Rossato, Giacomo Vinci, Paolo Mozzi and Stefano Castelli	Soil Erosion And Intensive Agriculture (Lessini Veronesi, NE Italy): Multi-Temporal Modelling On DEMs From Photogrammetry And Lidar
11:38 (short)	Lucia Contillo, Giusy Dimola, Giuseppe Corrado and Marcello Schiattarella	A comparative study of mass movement morphometry in two adjacent watersheds of southern Italy
11:46 (short)	Laura Paola Calderon Cucunuba, Laura Melelli, Fabio Silvani, Luca Domenico Venanti and Massimiliano Alvioli	Modeling Pre-Anthropogenic Topography: A Reconstruction in the Perugia Center Using Subsoil Data
11:54 (short)	Maksymilian Solarski, Mariusz Rzętała, Robert Machowski and Martyna A. Rzętała	The use of historical cartographic materials and contemporary lidar models to determine changes in terrain relief in hard coal mining area (Bytomka Catchment, Southern Poland)
12:02 (short)	Arianna Negri and Marco Giardino	Integrating Geosystem Services classifications: a preliminary framework from the piedmont area of the Sesia Val Grande UNESCO Global Geopark
12:10 (short)	Alfonso Valerio Ragazzo, Giuliano Fontinovo, Giorgio Pennazza and Alessandro Mei	Digital Elevation Models retrieval from optical/LiDAR sensor data in a Coastal Dune Systems: geospatial analysis for environmental monitoring
12:18 (short)	Dario Gioia, A. M. Amodio, N. Abate, A. Ascione, P. P. C. Aucelli, M. Buonasera, C. Cerrone, L. Contillo, R. Colacicco, G. Corrado, M. Delchiaro, M. Della Seta, G. Di Paola, G. Fubelli, A. Gionta, F. Matano, F. Pavano, V. Ruscitto, M. Schiattarella, C. Scirocco, F. Silvani, E. Valente	Coupling UAV-derived Lidar and geophysical data for the reconstruction of high-resolution 3D model of active faults: an example from the Piano di Pecore intramontane basin (Mt. Marzano, southern Italy)
12:26 (short)	Andrei Ioniță and Lucian Drăguț	Introducing the Geomorphometric Atlas of Romania: A Publicly Available Database of Landform Classifications and Land-Surface Variables based on FABDEM
12:30 - 14:30	**Lunch + Posters**	
14:30 - 14:45	Axel Corseaux, Kévin Gross and Serge Riazanoff	Activities of the DEMIX Subgroup 3 "Platforms and Processing"
14:45 - 15:00	Peter Guth and Virginia Herrera-Cruz	Developing Methodologies to Extend DEMIX to 5m (0.15 arc second) Global DEMs
15:00 - 15:15	Carlos López-Vázquez	Formal weaknesses of some definitions of roughness, and a solution proposal

15:15 - 15:45	Additional DEMIX presentations (more info about DEMIX here) Conrad Bielski: A short review of the DEMIX report Peter Guth: Update on MICRODEM in DEMIX (PDF) Carlos López-Vázquez: Update on some accuracy and uncertainty topics in DEMIX (PDF)	
15:45 - 16:00	**Coffee**	
16:00 - 17:00	ISG PLENARY MEETING	
17:00 - 17:30	Paper & poster awards	
17:30 - 19:00	Side event: AIGeo Working Group meeting	
20:00	Social Dinner	

Friday, June 13 (workshops)	
09:00 - 10:50	Corey White, Caitlin Haedrich: Propagating DEM Uncertainty to Stream Extraction using GRASS GIS
10:50 - 11:10	**Break**
11:10 - 13:00	Giuseppe Amatulli: Generating hydrographic products with GRASS GIS: A hands-on workshop on the Hydrography90m methodology
13:00 - 14:00	**Break**
14:00 - 15:50	Nawajish Noman (Esri): Geomorphometry with ArcGIS Pro and ArcGIS Online
15:50 - 16:10	**Break**
16:10 - 18:00	Axel Corseaux: DEMIX Operations Platform
10:00 - 13:00	Side event: DEMIX / CEOS-TMSG meeting (sala Dessau)

Introduction

This volume collects the Proceedings of Geomorphometry 2025, the 8th conference of the International Society for Geomorphometry (ISG)[1]. The conference continues a well-established series of geomorphometry meetings, started in 2009 (Zurich, CH), and followed by meetings in Redlands (2011, US), Nanjing (2013, CN), Poznań (2015, PL), Boulder (2018, US), Perugia/online (2020/21, IT), and Iași (2023, RO). Other geomorphometry appointments that are held at regular intervals are the annual EGU in Vienna.

Geomorphometry, broadly defined as the quantitative description and analysis of landforms and related processes, has progressively evolved from a collection of numerical descriptors into a mature scientific framework that integrates theory, data, and software tools. The increasing availability of digital terrain data, advances in data collection technologies, including ground stations and remote sensing technologies, in parallel with the development of sophisticated numerical methods and conceptual approaches linking surface landforms to land surface processes, all contributed to the evolution of the field.

As a result, geomorphometry today encompasses a wide spectrum of research activities, ranging from foundational questions on the definition and meaning of terrain metrics to applied studies addressing landscape dynamics, natural hazards, geomorphology, hydrology, and management of georesources and geoheritage.

As in previous editions, the 2025 event in Perugia, Italy, aimed at providing a forum for researchers working on different aspects of quantitative terrain analysis, fostering dialogue between methodological developments and applied studies. This volume reflects both continuity and innovation within the field, bringing together contributions that address long-standing conceptual issues as well as emerging challenges associated with new data sources, computational paradigms, and application across diverse environments and spatial scales.

We have identified three groups of contributions for this volume: 1) data and methods, 2) Landform and processes, and 3) georesources and geoheritage. Papers in group 1) and 2) are further split into subgroups, while group 3) collects contributions about georesources, geoheritage, and geodiversity.

The latter group, with the keynote talk by Prof. Zwolinski, represented the project "URban Geodiversity for a Resilient Environment, URGERE", sponsoring the conference. Moreover, during the conference, the upcoming new edition of the book "Geomorphometry: concepts, software, applications" edited by H. I. Reuter, C. H. Grohmann, and V. Lecours was presented. Additional side events took place. First, the DEMIX (DEM Intercomparison eXercise) collaboration, a CEOS / WGCV / TMSG initiative supported by ESA as part of the EDAP+ project and by USGS, presented several contributions, culminating with the final DEMIX CEOS-TMSG meeting. Second, the AIGeo Working Group "Sistemi e tecnologie integrate per l'analisi morfotettonica, SISTEC" presented their contributions and held their side meeting during the event. The last full day of the conference was devoted to four hand-on workshops, held in a computer lab, in which participants were invited to experiment with different practical applications of Geomorphometry.

During the conference, the International Society for Geomorphometry council awarded the customary Lifetime Achievement Award to Prof. David Tarboton, for his outstanding contributions to Geomorphometry: the 2011-2023

1 http://www.geomorphometry.org

hall of fame of the award is listed on the conference website. Moreover, the conference attendees voted for a few additional awards: the best student papers/presentations were awarded to joint winners Andrei Ionita and Arianna Negri, and the best paper/presentation was awarded to Massimiliano Alvioli.
Here follows a short description of all the contributions to the conference, including keynote talks by Sebastiano Trevisani, David Tarboton, and Zbigniew Zwoliński.

Group 1.1, Data and methods: Digital elevation models.

A substantial number of contributions focus on digital elevation models and on the methods used for their generation, processing, and evaluation. Several studies address global and regional DEM products and examine the implications of their characteristics for geomorphometric analysis. Guth discusses recent developments related to DEMIX activities, emphasizing data integration and consistency, while Corseaux et al. present complementary contributions on DEMIX platform development, addressing harmonization of processing workflows and interoperability. Pronk et al. provide a qualitative comparison of corrected global DEMs, highlighting their suitability and limitations for geomorphometric applications, and Panza et al. analyze high-resolution DTMs over selected areas, discussing the effects of data quality on derived terrain attributes. Issues related to scale and abstraction are addressed by Feciskanin et al. and Hajduchová et al., who investigate DEM generalization techniques and their ability to preserve geomorphological information. The potential of high-resolution remote sensing is further explored by López-Vázquez et al., who examine the enrichment of LiDAR datasets through partial derivatives, by Ho et al., who analyze global DEM products from a comparative perspective, and by Vinci et al. and Zamboni et al., who present UAV- and drone-based surveys for detailed terrain mapping. Noman et al. complement these contributions by discussing cloud-based environments for DEM processing, reflecting the increasing importance of scalable computational infrastructures.

Group 1.2, Data and methods: Land surface analysis.

Several papers address land-surface analysis and the definition, computation, and interpretation of geomorphometric parameters. The concept of surface roughness, widely used but often ambiguously defined, is revisited in the keynote talk by Trevisani, who critically examines its geomorphological meaning, and by López-Vázquez et al., who analyze formal inconsistencies in commonly adopted roughness metrics. Qin et al. propose fuzzy slope position indices as an alternative framework for land-surface characterization. Guth revisits slope algorithms, arguing for robust and parsimonious formulations, while Lindsay explores elevation residuals using scale mosaics to investigate terrain structure across spatial scales. Evans introduces a concavity-related metric based on the profile integral, contributing to long-standing discussions on slope and curvature descriptors. Feciskanin et al. present a software tool for calculating land-surface parameters, explicitly addressing issues of scale dependency and parameter stability.

Group 1.3, Data and methods: Hydro-Geomorphological features

Hydro-geomorphological features and terrain representations relevant to hydrological analysis are examined in several contributions. Tarboton presented his keynote talk about reflections on the conceptual links between geomorphometry and hydrology, emphasizing terrain controls on flow processes. Alvioli et al. present an automated

approach for delineating nested slope units, supporting objective terrain partitioning. Lindsay introduces a minimal-dispersion flow algorithm aimed at improving flow-routing accuracy, while Peckham et al. review methods for computing channel slope from DEMs, highlighting unresolved methodological issues. The influence of DEM characteristics on river network extraction is analyzed by Basta et al., while Newman et al. propose a probabilistic framework for surface change detection that explicitly accounts for uncertainty. Retat et al. focus on river centerline extraction, and Delchiaro et al. analyze bankfull geometry variations, illustrating how geomorphometric tools can support fluvial studies.

Group 2.1, Landform and Processes: Landslides.

A large portion of the volume is devoted to landforms and geomorphological processes, with landslide-related studies representing a particularly prominent theme. Mancino et al. present a global landslide susceptibility analysis based on ensemble machine-learning approaches, while Grohmann et al. investigate the influence of data resolution on susceptibility modelling. Sarkar et al. focus on rockfall susceptibility along transportation corridors, and Fabbri et al. discuss landslide susceptibility modelling with particular attention to curve interpretation and uncertainty. Debris-flow processes are examined by Goetz et al. and Bornaetxea et al., who address detection and susceptibility at different spatial scales. Nguyen et al. explore landslide detection using Google Earth imagery, Stark et al. analyze landslides using LiDAR data, Romeo et al. provide a geohazard assessment perspective based on gigapixel imagery, Contillo et al. investigate landslide morphometry, Strohmaier et al. analyze rainfall–landslide relationships, and Ahmed et al. contribute additional insights into landslide processes.

Group 2.2, Landform and Processes: Fluvial processes.

Fluvial and erosional processes are addressed through studies of soil erosion, gully development, and badlands morphology. Rigon et al. analyze soil erosion using multi-temporal DEMs, Bufalini et al. and Cuvuliuc et al. focus on gully erosion processes, and Marsico et al. investigate badlands morphology using combined terrestrial laser scanning and UAV data.

Group 2.3, Landform and Processes: Glacial processes.

Glacial environments are represented by Parizia et al., who analyze glacial landforms and their evolution, and by Chiarini et al., who focus on subglacial features derived from DEM analysis.

Group 2.4, Landform and Processes: Tectonic processes.

Geomorphometry is also applied to tectonic and morpho-structural analysis. Contillo et al. investigate fault-related landforms, while Brunori et al. analyze surface expressions associated with recent seismic sequences. Muneeb et al. integrate high-resolution airborne LiDAR with geomorphometric and structural analyses to characterize the Monte Cefalone Fault, demonstrating how detailed DEMs support fault scarp identification, throw measurement, and tectonic interpretation.

Group 2.5, Landform and Processes: Landform classification.

Several contributions address landform classification and the broader application of physical geomorphometry. Lecours et al. focus on landform characterization in marine and terrestrial settings, Ionita et al. present a national-

scale landform classification, Brenning et al. apply geomorphic distribution modelling to desert environments, and Popov et al. discuss applications of physical geomorphometry in classification workflows.

Group 2.6, Landform and Processes: Physical and other surface processes.

Advances in physical geomorphometry are further discussed by Minár et al., while Supiński et al. extend geomorphometric analysis to cave environments. Jarzyna et al. investigate weathering processes using geomorphometric approaches, Ragazzo et al. focus on marine environments, and Mazzoglio et al. analyze the role of elevation in rainfall extremes, linking geomorphometry and hydro-climatology.

Group 3, Georesources and Geoheritage.

The final set of contributions highlights applications related to georesources and geoheritage. Zwoliński et al. address in his keynote talk geodiversity assessment, Burnelli et al. propose a geomorphodiversity index at national scale, Negri et al. discuss geomorphometry in the context of geoparks, Calderón et al. focus on mapping and reconstruction of pre-anthropogenic topography, Moudrý et al. present a global assessment of mining activities, and Solarski et al. analyze mining-related landscape changes using historical cartography.

M. Alvioli, L. Melelli, I. Marchesini

1 - Data and Methods

1.1 - Digital elevation models
1.2 - Topographic Attributes
1.3 - Stream and slope applications

1.1 - Digital elevation models

Update on MICRODEM in DEMIX

Peter L. Guth, Professor Emeritus
Annapolis, Maryland, USA
prof.pguth@gmail.com

Cite as: Guth, P. L. (2025). Update on MICRODEM in DEMIX. In: Proceedings of Geomorphometry 2025, 9-13 June, Perugia, Italy. M. Alvioli, L. Melelli, I. Marchesini eds. CNR Edizioni, Rome. ISBN 978-88-8080-765-0. DOI: 10.5281/zenodo.15381174

Abstract—**MICRODEM has been used for almost all the data manipulation and statistical computations in DEMIX. Continued work seeks to improve and extend the computations, and compare DEMs. The original landmark DEMs: SRTM, ASTER, and NASADEM should now be retired since Copernicus DEM now clearly outperforms them .**

I. Introduction

While the JRC Technical Report (Bielski and others, in press) was in preparation (group work ended at the end of summer 2023), multiple preprint versions of the paper on the DEMIX wine contest were posted. The JRC Technical Report will contain significant coverage of the paper published in February 2024 with 12 authors [1]. In September 2024 6 of that paper's authors, including 5 of the 10 authors of the JRC technical report, published a follow-on paper [2] which was started after preparation of the JRC report and final writing of the earlier paper [1]. This paper discusses work in MICRODEM since work on the JRC Technical Paper was completed. Essentially all of the analysis for the DEMIX comparisons in both papers was done in MICRODEM [3,4].

II. Enhanced DEMIX Data and Methodology

The second paper [2] significantly improved the methodology of the first [1]. Figure 1, the paper's abstract, highlights the changes:

- Included 124 test areas and 3462 DEMIX tiles, an order of magnitude increase. Of most interest, this allows creation of figures like those in section 4 of this paper.
- Considered 4 additional global DEMs: DSM TanDEM-X, and DTMs CoastalDEM, DiluviumDEM, and DeltaDTM. Of the total of 10 test DEMs considered, 4 are edited DTMs.
- Used 16 different derived land surface parameters (LSPs) in addition to elevation to compare grids. This compares to 2 LSPs plus elevation used in [1], where the 5 criteria for each LSP are highly correlated and not independent. The new DEMIX GIS database [5] includes the original 15 criteria for anyone who still wants to use them.
- Introduced fraction of unexplained variance (FUV), ranging from 0 (best) to 1 (worst), as a better criterion than the statistics of the difference distribution. This allows directly comparing different criteria, and compares the criteria in terms of correspondence with the reference DEMs. The evaluations from the difference distributions [1] have different ranges in different test areas and for the different criteria, making comparisons difficult.
- Used 2 geomorphometric classifications of every pixel, also with a range from 0 to 1.
- Expanded the channel network criterion to the entire data set, also with a range from 0 to 1.
- Used evaluations rather than rankings as a better way to show differences among global DEMs, decreasing the effects of having to set a tolerance for ties.
- Due to the severe challenges of applying subjective criteria at scale to hundreds or thousands of test tiles, the rationale for the wine contest statistics becomes murky. This was not explicitly stated, but is clear from the modified methodology adopted which does not have to deal with the complexity added with subjective criteria.

Based on their limited utility, [2] did not do some of the analysis in the first paper [1]:

- Compare to reference DSMs, which are available only for a limited number of test areas. Because the test DEMs are in many cases perform better than the edited DTMs, even when compared with a reference DTM, this is not a significant limitation.
- Compute per-pixel land type statistics. Breaking down the results by characteristics of the tile proves more useful, as shown in the diagram in the lower right corner of Figure

1. This only becomes feasible with the much larger number of tiles.
- Publish any Friedman statistics which they found less useful than other metrics and graphics.

III. New published DEMIX results

Key results from [2]:

- CopDEM generally remains the best DEM, even when compared to a reference DTM or the edited derivatives of CopDEM to produce a DTM.
- ALOS DEM (AW3D30) is slightly better than CopDEM in very steep terrain.
- Edited DTMs (FABDEM, CoastalDEM, DiluviumDEM, and DeltaDTM generally improve slightly on elevation metrics compared to CopDEM, but are worse for many derived LSPs because they were only trained for elevation to remove vegetation and they can hallucinate.
- None of the global DEMs, even the edited ones designed for low elevation coastal areas, perform well in areas with average slopes under 5%.
- Strongly implied that NASADEM makes few changes to SRTM, and that NASADEM, SRTM, and ASTER should be retired. Results for these were included in the new data base [5], but excluded from much of the analysis to concentrate of the DEMs that are reasonable choices to use.
- LSPs can be ranked in terms of their FUV and the sensitivity of the LSPs to DEM quality; curvature measures are hardest for global DEMs to match to the reference.
- Edited DTMs can hallucinate,

IV. Work in Progress with New 1 arcsec DTMs

Several new one second global DEMs have appeared (FathomDEM, EDTM, and GEDTM), and the MICRODEM DEMIX analysis has been adapted to them (Figure 2). Preliminary work suggests very high quality for FathomDEM.

V. Work in Progress with New 0.15 arcsec DTMs

Guth and Herrera-Cruz have a paper at Geomorphometry 2025 on developing a methodology to compare commercial 5 m DEMs to reference high resolution lidar DTMs. Particularly in urban areas, it is very hard to replace the buildings with a realistic ground surface. What the lidar cannot see, but the national mapping agency fills in to create the DTM, is not what the radar or optical sensors see from space (it's in fact not really there, but some approximation), and the comparison is problematical. The 5 m scale also proves very sensitive to slight variations in elevation within the window used for computing LSPs: relative accuracy can be more important than absolute elevation accuracy for many computations.

VI. Importance of the pixel geometry model

Previous DEMIX papers [1,6] stressed the importance GeoTIFF GTRasterTypeGeoKey (#1025). The addition of more DEMs requires a more nuanced pixel origin/geometry model, which is unambiguously encoded in GeoTIFF files in two tags, GTRasterTypeGeoKey (#1025) and ModelTiepointTag (#33922). The GTRasterTypeGeoKey has two values, pixel-is-point and pixel-is-area, but only defines how to interpret the area of the pixel, and does not refer to the sampling strategy for the pixel (even Landsat is coded by USGS as pixel-is-point). The two models were defined as SRTM and ALOS, for the first global DEMs to use each (Table 1).

Some software changes the GTRasterTypeGeoKey (#1025). When operating on a pixel-is-point DEM, Whitebox did not change tag #1025 when creating a slope map, GDAL changed the tag when creating a slope map, SAGA changed the tag when creating an aspect map, and QGIS changed the tag when rewriting the DEM. Those programs that changed tag #1025 also changed ModelTiepointTag (#33922) with a ½ pixel shift, so that all the grids retain the SRTM geometric model. I have talked to the author of another geomorphometry program and programmers for a commercial GIS, and we agree that internally the programs need to adopt a single model (if needed change tag #1025 and shift the coordinates in #33922 by ½ pixel), and that the pixel-is-point makes computations simplest; obviously other programs make a different choice.

1

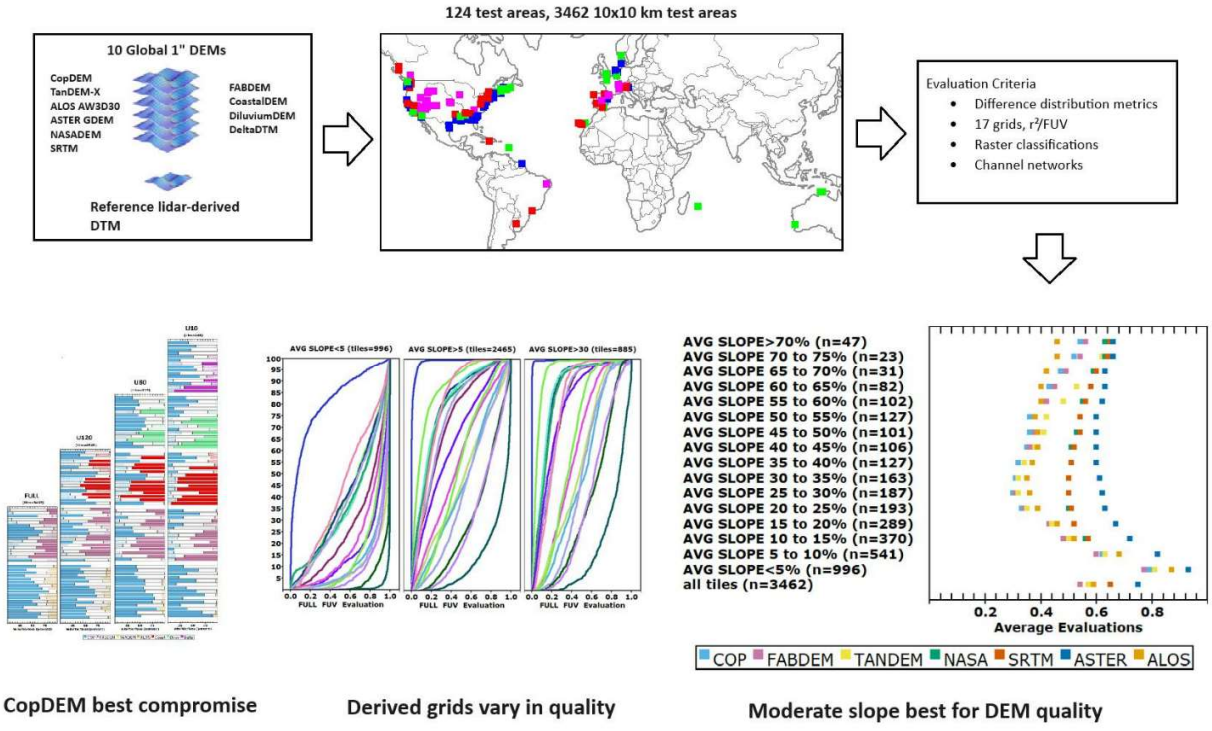

Figure 1. Graphical abstract [2]. Top row shows the data and methodology, and bottom row highlights the key results.

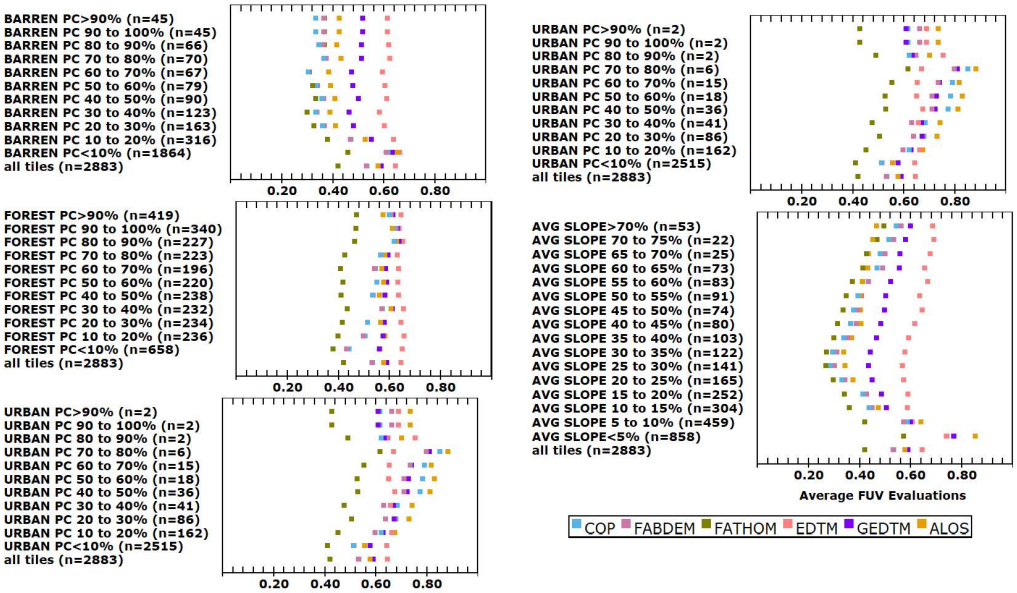

Figure 2. Comparing 6 global DEMs, 4 DTMs and 2 DSMs. This averages 9 criteria: elevation, hillshade, curvatures (plan, profile, and tangential), roughness, slope, and topographic position index.

Table 1. Pixel origin or geometric model for global 1” DEMs

DEMs	Geotiff Pixel is (tag #1025)	Model tie point (tag #33922)	DEM nominal corner contains	Pixel origin model
CopDEM, FABDEM, FathomDEM, SRTM, and NASADEM	Point	DEM nominal corner	Pixel centroid	SRTM
ASTER	Area	½ pixel offset from nominal corner	Pixel centroid	SRTM
ALOS, USGS 3DEP, Diluvium DEM, EDTM, GEDTM, Coastal DEM	Area	DEM nominal corner	Pixel corner	ALOS

If GTRasterTypeGeoKey (#1025) were to be defined to reflect the sampling underlying the data in the Geotiff (whether the elevations represent a point, or a pixel average), advocated by some workers, there are several significant issues that need to be resolved:

- Many legacy data sets did not use it that way, and they will be around for a long time, so that interpretations will be questionable. All global 1” sample a large area, and not the exact elevation at the point.
- Many software programs will have to be rewritten to avoid changing the tag.
- Having only two choices for the sampling for the grid is probably too simplistic. Which choice is appropriate for a slope grid? A filtered DEM? A drainage contributing area? A map algebra grid, say from shifting vertical datums?
- If the grid value is really from a point, but had to be assigned to the nearest grid node because the sampled points were not on the grid, how should tag #1025 be coded?
- Should there be a clean break, with a Geotiff tag for the sampling strategy, and if so, how many choices should be present?

Some workers complain about the duplication of one row and column with the adjacent tile, but this is just an implementation decision that adds minimally to the size of the DEM and is handled transparently by software. They also complain that the contributing area for edge pixels lies “outside the DEM”, but this is only a matter of interpreting the file name (which only includes a corner by convention) or the metadata. Equally valid would be to consider the pixel centroids, which many software programs use for all computations.

VII. Acknowledgments

This work would not have been possible without countless contributions from my DEMIX colleagues. This paper underwent minor additions after the Perugia conference to reflect discussions there.

References

[1] Bielski, C., and 11 others, 2024. Novel approach for ranking DEMs: Copernicus DEM improves one arc second open global topography. IEEE Transactions on Geoscience & Remote Sensing. vol. 62, pp. 1-22, 2024, Art no. 4503922, https://doi.org/10.1109/TGRS.2024.3368015

[2] Guth, P.L.; and 6 others, 2024,. Ranking of 10 Global One-Arc-Second DEMs Reveals Limitations in Terrain Morphology Representation. Remote Sensing. 16, 3273. https://doi.org/10.3390/rs16173273

[3] Guth, P.L., 2025a. GIT-MICRODEM [Delphi source code, archived installation versions]. URL: https://github.com/prof-pguth/git_microdem

[4] Guth, P.L., 2025b, MICRODEM: Open-source GIS with a focus on Geomorphometry [Win64 executable and help file]: https://microdem.org/

[5] Guth, P., 2024, DEMIX GIS Database Version 3 [Data set]. Zenodo. https://doi.org/10.5281/zenodo.13331458

[6] Guth, P.L., and 14 others, Digital Elevation Models: Terminology and Definitions. Remote Sens. 2021, 13, 3581. https://doi.org/10.3390/rs13183581

Activities of the DEMIX Subgroup 3 "Platforms and Processing"

Axel Corseaux[1], Kévin Gross[2], Serge Riazanoff[3]
VisioTerra, 14 rue Albert Einstein, 77420 Champs-sur-Marne
[1] axel.corseaux@visioterra.fr, [2] kevin.gross@visioterra.fr, [3] serge.riazanoff@visioterra.fr

Cite as: Corseaux, A., Gross, K., Riazanoff, S. (2025). Activities of the DEMIX Subgroup 3 "Platforms and Processing". In: Proceedings of Geomorphometry 2025, 9-13 June, Perugia, Italy. M. Alvioli, L. Melelli, I. Marchesini eds. CNR Edizioni, Rome. ISBN 978-88-8080-765-0. DOI: 10.5281/zenodo.15213919

Abstract—**In recent years, an important number of global Digital Elevation Models (DEMs) have been released publicly, with very permissive licenses. Although beneficial to the scientific field, this profusion of data makes it difficult to choose the most adequate DEM for a given field of application. Since 2020, DEM assessment and comparison methodologies have been standardised under the frameworks of the Earthnet Data Assessment Project (EDAP / EDAP+) led by the European Space Agency (ESA), and the DEM Intercomparison eXercise (DEMIX) initiated by the Committee on Earth Observation Satellites (CEOS). EDAP evaluation guidelines provide a comprehensive set of criteria to assess Earth Observation (EO) missions and products based on their documentation. While initially conceived for missions, these standard guidelines were adapted to the case of DEM products. On the other hand, the DEMIX methodology, based on the Randomized Complete Block Design (RCBD), allows users to rank DEMs according to user-defined areas of interest and criteria. Jointly used, these frameworks give scientists a complete analysis of DEM products, from overall assessments to very specific user criteria. While these evaluation standards are mature, fundamental DEM activities are still performed under EDAP and DEMIX. Most of these works are carried-out and discussed in the DEMIX Subgroup 3 (SG3) called "Platforms and processing". Since the beginning of DEMIX, this subgroup carried out global DEM quality assessments using spaceborne LiDAR data, DEM planimetric misregistration assessments, extended DEM transformation studies including resampling methods, reprojections and datum changes, and analyses of open local VHR DEMs. The knowledge gained from these studies has been used to develop free DEM visualisation and processing web applications, including VtWeb, QGIS tools, a DEMIX Jupyter Notebook, the DEMIX Operations Platform and DEM4Sentinels-1-2. Thanks to these free tools, public users are now able to visualise and process DEMs in an easy interactive way.**

I. Introduction

A Digital Elevation Model (DEM) is a digital representation of elevations (or height) of a topographic surface in form of a georectified point-based or area-based grid, covering the Earth or other solid celestial bodies [1]. Numerous of these models are now publicly available, with various spatial coverages (city, state, country; continental or global) and temporal extents (several days to more than a decade). The most popular public DEMs are global and generated at a Ground Sampling Distance (GSD) of 1'' arcsecond (e.g., ALOS World 3D, ASTER GDEM, Copernicus DEM GLO-30, SRTM). These models are the result of a complex processing chain, usually involving a main (or primary) source of elevations processed from Earth Observation (EO) acquisitions (radar interferometry, optical photogrammetry or LiDAR aggregation). Due to instrument limitations or to insufficient qualified observations, DEM products may present voids, be edited (interpolations, lake flattening…) or filled with external sources of elevations. These characteristics complicate the choice of the "best" DEM for a given application, as it is dependent on a wide variety of parameters and criteria. Fortunately, two complementary frameworks allow the evaluation of DEM products: the EDAP project, led by ESA, and DEMIX, initiated by the CEOS. These two frameworks respectively allow to perform overall product maturity assessments and user-defined tests specific to the field(s) of study and area(s) of interest. Both projects have benefited from each other and are still jointly evolving thanks to the financing of the DEMIX Subgroup 3 (SG3) "Platform and Processing" activities through EDAP. The current paper aims to summarize the main achievements and future works of DEMIX SG3, from the contributions to EDAP quality assessment guidelines to the DEM transformation studies (resampling, datum and projection changes) and the development of free DEM processing and visualisation tools (VtWeb, the DEMIX Operations Platform, the DEMIX Jupyter Notebook and DEM4Sentinels-1-2). Section II presents the EDAP project and quality assessment guidelines. Section III presents DEMIX and its subgroups. Section IV focuses on the works of DEMIX Subgroup 3 (SG3), dedicated to platforms and processing.

II. The Earthnet Data Assessment Project (EDAP)

The EDAP project (2018-2021) and its successor EDAP+ (since 2022) are responsible for assessing the quality and

suitability of candidate missions being considered for ESA's Earthnet Programme as Third-Party Missions (TPM) [2]. This includes optical, Synthetic-aperture radar (SAR), atmospheric, Automatic Identification System (AIS) and Radio Frequency (RF) missions, multi-mission studies and DEM assessments. EDAP assessments are performed with regards to evaluation guidelines available in generic and mission (or product) specific versions [3]. These guidelines cover the entire chain of processing, from the instrument calibrations to the generation of EO products. Following these guidelines, the overall maturity of an EO mission and its derived product(s) can be precisely assessed. Naturally, users can also be interested by the "fitness for purpose" of a given product to their specific application. For the case of DEMs, quality assessment and ranking methodologies developed by the DEMIX community are perfectly suitable for this purpose.

III. The Digital Elevation Model Intercomparison eXercise (DEMIX)

The DEMIX working group is a CEOS initiative aiming at "providing harmonised terminology and methods, as well as practical guidelines and results allowing the intercomparison of continental or global Digital Elevation Models (DEM)" [4]. DEMIX has been divided into three subgroups, focused on the "Terminology and analytical basis" (subgroup 1, or SG1), "Algorithms and software" (SG2) and "Platforms and processing" (SG3). A fundamental work of DEMIX SG1 has provided a terminology and definitions for DEM products [1]. Works of DEMIX SG2 resulted in the creation of a DEM ranking framework, based on the Randomized Complete Block Design (RCBD) methodology [5]. Given a set of DEMIX tiles [6] (≈10x10km areas), DEMs and criteria (defined and/or implemented by the user), this methodology allows to rank the DEMs with potential ties. Finally, works of DEMIX SG3 focused on DEM quality assessments (LiDAR or VHR DEM reference data) [7] and transformation studies (resampling methods, projections, datum changes), DEM planimetric misregistration assessment methodology [8] and the development of free DEM processing and visualisation platforms [9].

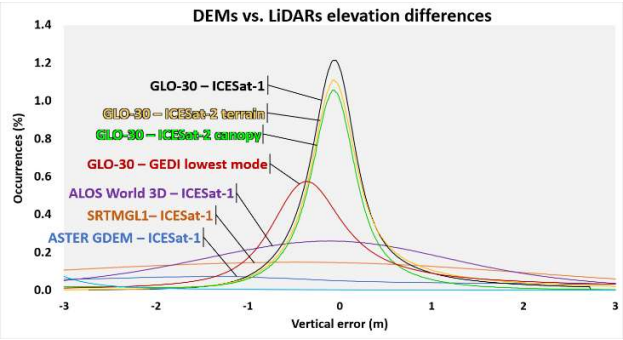

Figure 1. DEMs vs. LiDAR elevation difference histograms (-3m to +3m).

IV. DEMIX SG3 – Platforms and Processing

The works performed in DEMIX SG3 are primarily meant to open the DEMIX methodology (defined by SG2) to a wider audience, through the development of dedicated free tools and web applications. These developments would not be possible without the support of preliminary studies focused on DEM validation and transformation methods, which are presented hereafter.

A. Global DEMs vs. LiDAR datasets

Since 2020, the DEMIX SG3 working group has carried out several DEM studies, beginning with the assessment of global DEMs (ASTER GDEM, ALOS World 3D, Copernicus DEM GLO-30 and SRTMGL1) from global reference LiDAR datasets (ICESat-1, ICESat-2 and GEDI) [10]. The assessments have shown the superiority of Copernicus DEM GLO-30 over the three other global DEMs, either in terms of product quality (with regards to the EDAP guidelines) or in a quasi-global statistical comparison from 59 319 279 ICESat-1 elevation measurements (see Fig.1 for histograms). With regards to this reference data, Copernicus DEM GLO-30 has shown an elevation difference RMSE of 0.628 m, followed by ALOS World 3D (1.660 m), SRTMGL1 (2.554 m) and finally ASTER GDEM (7.911 m). In a subsequent study, Copernicus DEMs (EEA-10, GLO-30 and GLO-90) were compared to the ICESat-2 and GEDI LiDAR products. Copernicus DEM GLO-30 has shown low elevation errors with regards to ICESat-2 terrain (0.999 m), followed by the top of canopy (2.907 m). Higher errors were found with GEDI lowest mode (3.431 m) and highest return (6.603 m) measurements. While Copernicus DEM GLO-30 is statistically better than other DEMs at a global scale, thematic applications can still benefit from other DEMs, such as ALOS World 3D showcasing more roughness than Copernicus DEMs in the Afar Triangle (Mount Musa Ali Terara and region of Balho, west of Randa). The spaceborne LiDAR datasets used in this study are adequate for global assessments, but may be too sparse for very specific study areas. Local LiDAR campaigns and their derived Very High-Resolution (VHR) DEMs perfectly fit this purpose.

B. VHR DEMs studies

In recent years, many airborne LiDAR campaigns were carried out, resulting in Very High-Resolution (VHR) DEMs of cities, regions and countries of the world. Many of these DEMs are now public, with very permissive licenses. Several of these VHR DEMs were integrated into VtWeb [11] and the DEMIX Operations Platform [12], free web applications allowing the

visualisation and processing of DEMs (further discussed in section E). These integrations required to find crucial DEM metadata (licenses and access rights, resolution, spatial and temporal extent, horizontal and vertical datums, projection with associated coordinates systems, point or area pixel type…) to bring these models into the WGS84 datum and EGM2008 geoid. In most cases, this information is either difficult to find or poorly documented. This problem motivated the creation of a continuously maintained DEM metadata table [13], gathering all the information required to use and intercompare DEMs. Despite this fundamental work, the transformations required to express these DEMs in international datums and common projections can still be difficult to perform for end users. Consequently, further SG3 studies have been carried out on this issue, with the goal of creating free automatic tools to perform this task.

C. *Datums, projection changes and resampling*

Most global DEMs are referenced to international horizontal datums (e.g, WGS84 or ITRS) and vertical datums (e.g., EGM96 or EGM2008), in an equirectangular projection (or "geographic" CRS). In these cases, DEM comparisons are relatively simple, consisting of resampling one DEM to be superimposable with the second one, and, if necessary, performing a vertical reference system change by using geoid height grids. However, most of the local VHR DEMs have a proper datum and projection showing non-negligible differences with these international systems. Studies performed to resample VHR DEMs to these international datums highlighted the most important metadata to be retrieved, which are the horizontal datum (including name and realization), the projection (and associated coordinate reference system), and the vertical datum (usually, a geoid model which is released as a grid of heights, often above WGS84). Additionally, a transformation method (and potentially parameters) is necessary to convert coordinates from a local datum to a continental or international one. Most datum transformations operate on geocentric coordinates (e.g., NAD83 to ITRS realizations [14]), but transformations on geodetic or projected coordinates also exist (e.g., the OSTN15 model of UK and Ireland [15]). The accurate superimposition of DEMs also depends on the resampling methods. For DEMs, interpolation methods (e.g., nearest neighbour, bilinear, bicubic) are typically used to increase the number of elevation samples (smaller GSD), whereas aggregation methods (e.g., mean or gaussian weighted) are used to lower the number of samples (higher GSD). Studies carried out by SG3 highlighted the impact of interpolation methods on DEM elevations and derived layers. These studies show that the bicubic interpolation is the most suitable for the resampling of DEMs, as its "edge enhancement" can be parameterized to preserve features of interest (elevations, slopes, curvatures). Consequently, this interpolation has been chosen for studies regarding the assessment of planimetric shifts between DEMs.

D. *Planimetric Misregistration Assessment*

Planimetric displacements of features (e.g., crests, thalwegs, shores, trees, buildings) can be observed from one DEM to another. These misalignments are an important source of biases in DEM comparison studies, as they have a direct impact on the elevation differences (see Fig.2). Members of the DEMIX SG3 have defined a new methodology allowing to estimate sub-pixel displacement between two DEMs sharing the same geometry [8] (i.e., on the same grid of pixels) based on the disparity analysis algorithm. Using this method, a displacement vector field is retrieved, allowing to visualise systematic errors (vectors of same direction and length) or local anomalies. The methodology has shown to retrieve artificial planimetric displacements at a sub pixel level, with an error ranging from 12 to 20% of the pixel size. These accuracies can be further improved by increasing the "context" of the algorithm (precisely, the correlation window size) with an additional computation cost. As many comparison methods, the algorithm requires both input DEMs to be sampled over the same grid. Further studies have been performed to retrieve the best resampling method for this purpose, based on several bicubic interpolations with different slope values (increasing or decreasing the sharpness of the output image). The study shows that the best bicubic (BBC) slope parameter is dependent on the study area, and shows a logarithmic correlation coefficient of 0.717 with regards to terrain roughness.

E. *DEM visualisation and processing tools*

The knowledge acquired from these studies allowed to develop and maintain free and easy to use DEM visualisation and processing tools. The VtWeb [11] platform allows the multi-scale

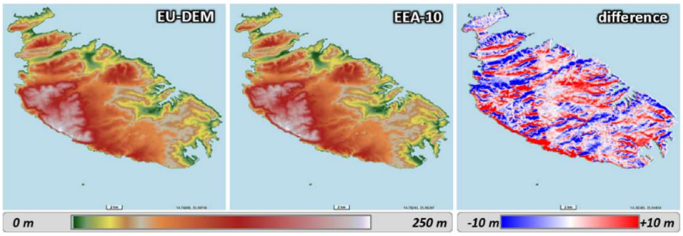

Figure 2. Effects of planimetric shifts - EU-DEM vs. EEA-10 over Malta.

on-the-fly processing and visualisation of EO data. Several global DEMs and VHR local DEMs of Brazil, England, France, Italy, Uruguay and Wales have been integrated into VtWeb. Using the Processing On-the-Fly Macro-Language (POF-ML), users are able to display elevations in a chosen range, apply colormaps, compute DEM elevation differences or derived layers such as slope norms,

slope azimuths and curvatures. DEM integrations are generally followed by the edition of hyperlook documents reporting the main features and defects of the integrated DEM, to display the differences between two DEMs [16] or to highlight the difference between the successive versions of a same DEM [17]. These documents are enriched with "hyperlook" links, allowing to retrieve interactive views of DEMs on the VtWeb platform. Additionally, two plugins have been developed to interpolate profiles on DEM elevations and to visualise VtWeb layers directly into QGIS. In parallel of these developments, the DEMIX Jupyter Notebook [18] and the DEMIX Operations Platform [12] were developed to download VHR and global DEMIX tiles, and to ease the access to the DEMIX methodology and DEM processing. The DEMIX Jupyter Notebook is oriented toward scientists, allowing to retrieve DEM elevations and compute criteria over user defined DEMIX tiles (areas of approximately 10x10km) by writing a few lines of Python code. Complementarily, the DEMIX Operations Platform provides access to these functions with a simpler user interface and easy-to-use functionalities (DEM ranking and GeoTIFF exports).

V. Conclusion

In continuation of the fundamental works of DEMIX SG1 and SG2, the studies performed by SG3 tackled important aspects of DEM comparisons, from transformations (resampling, projections and datum changes) to validation methods (assessments from LiDAR datasets, planimetric misregistrations assessment). Results of these studies were applied to the development of free tools allowing the access to DEMs and the DEMIX methodology to a wide audience. Additionally, the extensive work on VHR DEMs allowed the definition of EDAP standard guidelines dedicated to DEM products. With the increasing availability of these local DEMs expressed in various geometries, the work of DEMIX SG3 remains crucial up to this date. Ongoing works on aggregation methods, future works on cross-border merging algorithms and future DEM integrations could pave the way to a future multi-scale and multi-source DEMs, created from the seamless and dynamic processing of a wide variety of local and global DEMs.

VI. Acknowledgments

The authors thank the EDAP+ project for funding the works of DEMIX SG3, including the present article, as well as members of the DEMIX working groups for their support throughout the studies and development of DEM processing tools.

References

[1] Guth, P. L., et al. (2021). *Digital Elevation Models: Terminology and Definitions*. Remote Sensing. 2021; 13(18):3581. https://doi.org/10.3390/rs13183581

[2] European Space Agency (ESA). (n.d.). *Earthnet Data Assessment Project (EDAP)*. https://earth.esa.int/eogateway/activities/edap

[3] European Space Agency (ESA). (n.d.). *EDAP Best Practice Guidelines*. https://earth.esa.int/eogateway/activities/edap/edap-best-practice-guidelines

[4] Strobl, P. A., et al. (2021). *THE DIGITAL ELEVATION MODEL INTERCOMPARISON EXPERIMENT DEMIX, A COMMUNITY-BASED APPROACH AT GLOBAL DEM BENCHMARKING*. Int. Arch. Photogramm. Remote Sens. Spatial Inf. Sci., XLIII-B4-2021, 395–400, https://doi.org/10.5194/isprs-archives-XLIII-B4-2021-395-2021

[5] Bielski, C., et al. (2024). *Novel Approach for Ranking DEMs: Copernicus DEM Improves One Arc Second Open Global Topography*. IEEE Transactions on Geoscience and Remote Sensing, vol. 62, pp. 1-22, 2024, Art no. 4503922. https://doi.org/10.1109/TGRS.2024.3368015

[6] Guth, P. L., et al. (2023). *DEMIX 10k Tile Data Set (1.0)*. Zenodo. https://doi.org/10.5281/zenodo.7504791

[7] Riazanoff, S. (2023). *DEMIX SG3 – "Platforms and processing" - Presentation of studies*, Geomorphometry 2023, Iasi, Romania. http://www-igm.univ-mlv.fr/~riazano/publications/VT-A003-SLD-109-E-01-00_VisioTerra_DEMIX_SG3_Geomorphometry_2023_Iasi_20230712.pdf

[8] Riazanoff, S., et al. (2024). *Best BiCubic Method to Compute the Planimetric Misregistration between Images with Sub-Pixel Accuracy: Application to Digital Elevation Models*. ISPRS International Journal of Geo-Information, 13(3), 96. https://doi.org/10.3390/ijgi13030096

[9] Riazanoff, S. (2023). *Interactive presentation of Web platforms: -VtWeb, -DEMIX operations platform, -DEM4S2*, Geomorphometry 2023, Iasi, Romania. http://www-igm.univ-mlv.fr/~riazano/publications/VT-A003-SLD-110-E-01-00_Presentation_VtWeb_DEMIX-operations-platform_DEM4S2_Geomorpho-2023_Iasi_Romania_20230714.pdf

[10] ESA. (2021). Technical Note on Quality Assessment for Copernicus DEM. https://earth.esa.int/eogateway/documents/20142/37627/Technical+Note+on+Quality+Assessment+for+Copernicus+DEM.pdf

[11] VisioTerra. (2024). *VtWeb*. https://visioterra.org/VtWeb/

[12] VisioTerra. (2024). *DEMIX Operations Platform*. https://visioterra.org/DemixOperationsPlatform/

[13] VisioTerra. (2024). *DEM metadata table*, issue 15. https://visioterra.fr/telechargement/P317_DEMIX/VT-P317-TAB-001-E-01-15_DEM_metadata_table.xls

[14] National Geodetic Survey. (n.d.). *Historical Helmert Transformation*. https://www.ngs.noaa.gov/CORS/news/historical_helmert.shtml

[15] Ordnance Survey. (n.d.). *National Grid Transformation OSTN15/ETRS89/OSGB36.* https://docs.os.uk/more-than-maps/deep-dive/a-guide-to-coordinate-systems-in-great-britain/from-one-coordinate-system-to-another-geodetic-transformations/national-grid-transformation-ostn15-etrs89-osgb36

[16] VisioTerra. (2023). *COP-DEM and EU-DEM Comparison*. https://visioterra.fr/telechargement/A003_VISIOTERRA_COMMUNICATION/HYP-098-VtWeb-E_COP-DEM_EU-DEM_comparison.pdf

[17] VisioTerra. (2023). *Comparison of Copernicus DEM v2022 vs v2021*. https://visioterra.fr/telechargement/A003_VISIOTERRA_COMMUNICATION/HYP-107-VtWeb-E_Comparison_of_Copernicus_DEM_releases_2022_vs_2021.pdf

[18] VisioTerra. (2022). *Releases of the DEMIX Jupyter Notebook.* https://visioterra.fr/telechargement/P317_DEMIX/notebook/releases/

A qualitative comparison of corrected global DEMs

Maarten Pronk
Hydrology Software
Deltares
Delft, the Netherlands
maarten.pronk@deltares.nl

Hugo Ledoux
Urban Data Science
Delft University of Technology
Delft, the Netherlands
h.ledoux@tudelft.nl

Marieke Eleveld
Data Science, Water quality
Deltares
Delft, the Netherlands
marieke.eleveld@deltares.n

Cite as: Pronk, M., Ledoux, H., & Eleveld, M. A. A qualitative comparison of corrected global DEMs. In: Proceedings of Geomorphometry 2025, 9-13 June, Perugia, Italy. M. Alvioli, L. Melelli, I. Marchesini eds. CNR Edizioni, Rome. ISBN 978-88-8080-765-0. DOI: 10.5281/zenodo.15277544

Abstract— **Over the past few years, several attempts have been made to derive a bare-earth model from the CopernicusDEM GLO-30 dataset, yielding FABDEM, DiluviumDEM, CoastalDEM (from version 3 onwards), and DeltaDTM (by the authors). These "urban and vegetation corrected" datasets have been quantitively compared with auxiliary datasets, demonstrating differences in the order of decimeters in terms of vertical accuracy. More recently, the accuracy of the parameters derived from these DEMs has also been evaluated. However, despite being based on the same source dataset and using similar secondary datasets—such as ICESat-2 and GEDI—the derived datasets differ in their applied methods and resulting formats. In this study, we qualitatively investigate these differences between datasets. We assess whether new artefacts are introduced in the corrected datasets, assess whether original CopernicusDEM artefacts have been corrected, and examine the tile size, compression method, license, source code, and distribution method of the corrected datasets. We find that datasets using machine learning have uncorrected patch sized artefacts, while DeltaDTM exhibits "bomb-craters" within individual tiles due to unfiltered outliers in ICESat-2 data. In all datasets, most of the original CopernicusDEM artefacts remain uncorrected. Additionally, all datasets use slightly different file formats and often resample CopernicusDEM to different tiling schemes. None of these methodological choices or datasets can be deemed the "best," although some are less optimal. We conclude that all datasets have room for improvement, and future versions will likely benefit from adopting strategies used in creation of the other datasets.**

I. Introduction

Over the past few years, several attempts have been made to derive a bare-earth model from the CopernicusDEM GLO-30 [1] dataset. These include FABDEM [2], DiluviumDEM [3], CoastalDEM (from version 3 onwards) [4, 5], and DeltaDTM [6, 7]. All datasets attempt to remove urban and vegetation biases present in the CopernicusDEM source dataset—itself a surface model (DSM)—to arrive at a terrain model (DTM). Of these "corrected" datasets, only FABDEM is available globally, the others are *coastal* datasets, only available up to some meters above sea-level.

Most datasets (Table 1) make use of machine learning to regress the elevations of CopernicusDEM, with two opting for a Random Forest (RF) models. Only CoastalDEM uses a Neural Network, moving to a Convolutional Neural Network (CNN) in v3.0. DeltaDTM is the odd one out, with applying a custom heuristic scheme of bias correction, filtering and interpolation. DiluviumDEM and DeltaDTM share an open CC-BY license, whereas FABDEM and CoastalDEM have a restricted license, with free use only for research purposes.

More recent datasets (or version updates thereof) tend to be more vertically accurate by their own metrics. Third party comparisons have shown that these datasets improve on the elevation accuracy of CopernicusDEM, but less so on derived metrics, such as slope or flow accumulation [8].

Qualitative differences, such as the details on distribution of the datasets, or the effect the different methodologies have on elevation (corrections), have been studied less. In this study we aim to improve that, as these qualities are not only essential for ease of use and adoption for end users, but also for the developers of these datasets. We want to be upfront about our involvement as authors of DeltaDTM and emphasize our impartiality in this reproduceable comparison. Our goal is to improve current and future global terrain models.

TABLE I. OVERVIEW OF DATASETS

Name	***Year of release***	***Current version***	***Scope***	***Method***	***License***
FABDEM	2022	1.2	Global	RF	Restricted
CoastalDEM	2018	3.0	Coastal, up to 120 m	CNN	Restricted
DiluviumDEM	2023	1.0	Coastal, up to 80 m	RF	Open
DeltaDTM	2024	1.1.1	Coastal, up to 30 m (initially up to 10 m)	Heuristic	Open

II. RESULTS

A. Elevation inconsistencies

Several artefacts exist in CopernicusDEM itself, often from the underlying radar processing, such as radar shadows. Each new release of CopernicusDEM (currently at the 9th release of 2024_1, © DLR e.V. 2010–2014 and © Airbus Defence and Space GmbH 2014–2018 provided under COPERNICUS by the European Union and ESA; all rights reserved) improves on this, but several artefacts on smaller scales—such as diagonal "walls" and pits—are persistent (Fig. 1). None of the datasets improve such diagonal patterns, and only some fix the presence of pits (FABDEM, CoastalDEM, and DeltaDTM to an extent). FABDEM and CoastalDEM might have made these fixes accidentally by smoothing and resampling, respectively.

Depending on how one improves the elevations of CopernicusDEM, different terrains emerge. On larger scales these landscapes have been validated by deriving parameters such as slope or roughness, but details related to the method used to correct the elevation emerge on smaller scales. In Fig. 2, we can identify the different methods (and datasets) by the artifacts created by each of them. FABDEM introduces square artefacts of 3x3 pixels, sometimes creating larger patterns in dense tropical forests. Similarly, CoastalDEM—using a CNN—has patch-sized artefacts of 64x64 pixels where little or no correction has been applied. We assume that no ICESat-2 or GEDI data was available for such a patch. DiluviumDEM, by regressing a single pixel at a time, creates a very rough surface, as pixels in a striped pattern are much lower than the surrounding surface. Unlike FABDEM, the resulting surface was not smoothed. Finally, DeltaDTM has so called "bomb-craters" caused by low outliers in ICESat-2, which were not filtered everywhere. This pattern is sometimes also seen in airborne-lidar processing.

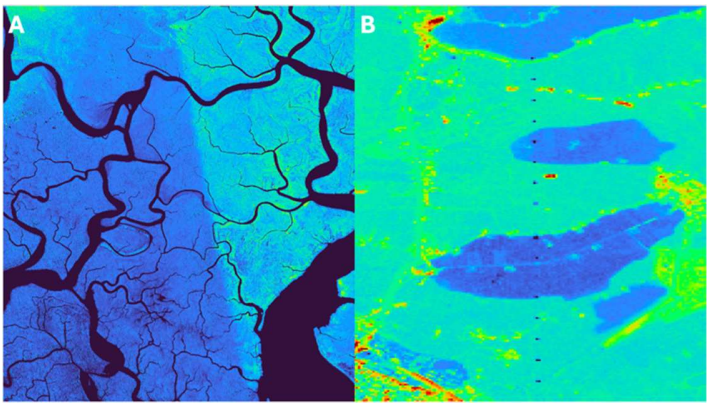

Figure 1. Artefacts in CopernicusDEM. A) Diagonal "wall" of 1.5m in an otherwise flat delta. B) Pits caused by electricity poles (multiple reflections)

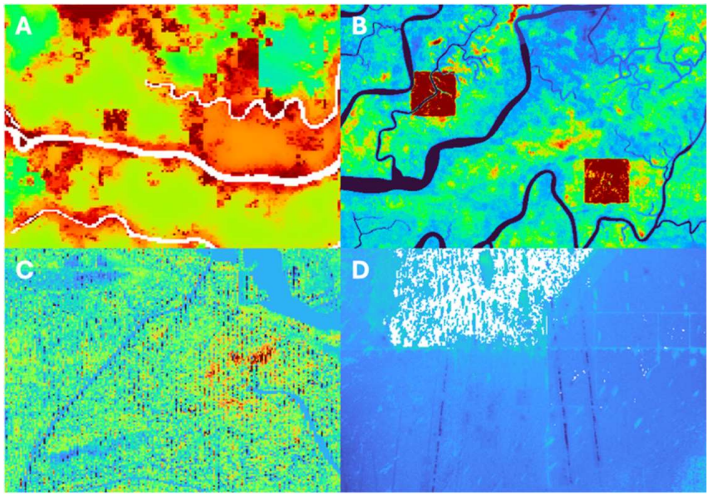

Figure 2. Artefacts introduced by each method: A) Square artefacts in FABDEM, starting at 3x3 pixels. B) Patch-sized 64x64 pixel artefacts in CoastalDEM. C) Very low individual pixels in a striped pattern (high roughness) in DiluviumDEM and D) Stripes (ICESat-2 tracks) of low outlier craters in DeltaDTM.

B. Formats and distribution

All datasets, like CopernicusDEM itself, distribute their files as geotiffs in 1 by 1-degree tiles. The comparisons end there however, as all datasets change the format (Table II). Indeed, most opt for a single tile size everywhere, instead of the DGED specification (different tile sizes per latitude range, with Copernicus being 3601x3601 pixels at the equator).

Except for CoastalDEM (at least the 90 m research version), all datasets cut off the single pixel row/column that overlaps with other tiles. FABDEM and DeltaDTM distribute the data as Cloud Optimized Geotiffs (COG), which includes sub-tiling and adding overviews to each tile, which requires an even tile size.

TABLE II. DISTRIBUTION FORMATS

Name	*File Format*	*Compression*	*Water*	*Mask supplied*	*Tile size*	*Single tile size*
FABDEM	COG	Deflate	Original	No	3600	Yes
CoastalDEM	Geotiff	Deflate	Original	No	1201 (90 m resolution)	Yes
DiluviumDEM	Geotiff	LZW	Original	No	3600	Yes
DeltaDTM	COG	ZSTD	Nodata	Yes	3600	No

FABDEM, DiluviumDEM and DeltaDTM can be downloaded from public data repositories without user registration. FABDEM distributes zip files containing all tiles in a 10 by 10-degree area, and DiluviumDEM does so for a 5 by 5-degree area. DeltaDTM provides zip files per continent, and CoastalDEM provides a single large zip file after registration and manual approval.

Compression options vary for the datasets, with FABDEM and CoastalDEM choosing the widely available Deflate algorithm. DiluviumDEM and DeltaDTM opt for the LZW and ZSTD algorithms respectively, to save more storage space.

Most datasets keep the elevation values for water (e.g. 0 for sea and ocean, and elevations in rivers increasing with steps of 0.5 m) in CopernicusDEM intact, with only DeltaDTM opting to replace them with nodata values. DeltaDTM is also the only dataset to distribute the original mask tiles of CopernicusDEM next to the dataset.

III. DISCUSSION

While all datasets start with the same CopernicusDEM dataset, they differ considerably in their outcomes. While no single dataset (decision) can be defined as best, common patterns between datasets emerge that we would qualify as optimal here.

None of the datasets correct larger artefacts present in CopernicusDEM, but some fix the presence of pits. All datasets could be further improved by checking for artefacts introduced by their methods. DeltaDTM could reconsider using raw ICESat-2 values directly. All other datasets—based on ML—could be improved by not using the raw ML output (whether individual pixels or patches) directly, or using outputs that overlap, to prevent square-like artefacts common to these datasets.

In terms of file format, using Cloud Optimized Geotiff, but with a common algorithm such as Deflate, would optimize for (future) cloud-based workflows, and still be useable by most GISes. All datasets strip the single pixel column/row overlap of CopernicusDEM, which is required for COG. Most datasets also resample to a fixed tile size, foregoing the DGED spacing per latitude zone. While easier to handle, there is some data loss involved with resampling, and common derivatives like slope operations require awareness of the resulting non-square pixels at higher latitudes.

Masking out water values as done by DeltaDTM seems suboptimal, but we suggest that providing CopernicusDEM (water)masks (but resampled) is optimal, as users cannot otherwise identify or mask water values.

Distribution of the datasets is best done on a publicly accessible website, and in zip files spanning several degrees (tiles). It seems distribution by continent, let alone all data in a single zip, is suboptimal. We note that while FABDEM and DeltaDTM store their data as COG, a (public) cloud location where individual tiles (i.e. no zip files) can be accessed has not been advertised.

IV. ACKNOWLEDGMENTS

We would like to thank the authors of FABDEM, CoastalDEM, DiluviumDEM and DeltaDTM for their work and enabling this research by providing the datasets for research purposes.

REFERENCES

[1] European Space Agency; Airbus. (2022). Copernicus DEM, European Space Agency. doi:10.5270/ESA-c5d3d65

[2] Hawker, L.; Uhe, P.; Paulo, L.; Sosa, J.; Savage, J.; Sampson, C.; Neal, J. (2022). A 30 m global map of elevation with forests and buildings removed, *Environmental Research Letters*, Vol. 17, No. 2, 024016. doi:10.1088/1748-9326/ac4d4f

[3] Dusseau, D.; Zobel, Z.; Schwalm, C. R. (2023). DiluviumDEM: Enhanced accuracy in global coastal digital elevation models, *Remote Sensing of Environment*, Vol. 298, 113812. doi:10.1016/j.rse.2023.113812

[4] Kulp, S. A.; Strauss, B. H. (2018). CoastalDEM: A global coastal digital elevation model improved from SRTM using a neural network, *Remote Sensing of Environment*, Vol. 206, 231–239. doi:10/gc9n4s

[5] Kulp, S. A.; Strauss, B. H. (2024). *CoastalDEM v3.0: Improving fully global coastal elevation predictions through a convolutional neural network and multi-source DEM fusion* Climate Central

[6] Pronk, M.; Hooijer, A.; Eilander, D.; Haag, A.; de Jong, T.; Vousdoukas, M.; Vernimmen, R.; Ledoux, H.; Eleveld, M. (2024). DeltaDTM: A global coastal digital terrain model, *Scientific Data*, Vol. 11, No. 1, 273. doi:10.1038/s41597-024-03091-9

[7] Pronk, M. (2024, December 12). DeltaDTM: A global coastal digital terrain model, 4TU.ResearchData. doi:10.4121/21997565

[8] Guth, P. L.; Trevisani, S.; Grohmann, C. H.; Lindsay, J.; Gesch, D.; Hawker, L.; Bielski, C. (2024). Ranking of 10 Global One-Arc-Second DEMs Reveals Limitations in Terrain Morphology Representation, *Remote Sensing*, Vol. 16, No. 17, 3273. doi:10.3390/rs16173273

High-Resolution Digital Terrain Model on a sample area of the Italian national territory

Marina Muto[1]
University of Calabria – Department of Biology, Ecology and Earth Sciences (DiBEST), Rende, Cosenza, Italy

Giulio Iovine
Istituto di Ricerca per la Protezione Idrogeologica, Consiglio Nazionale delle Ricerche, via Cavour 4-6, I-87036 Rende, Cosenza, Italy

Mario Panza[2], Mauro Rossi, Massimiliano Alvioli, Ivan Marchesini
Istituto di Ricerca per la Protezione Idrogeologica, Consiglio Nazionale delle Ricerche, via Madonna Alta 126, I-06128 Perugia, Italy

[1] marinamuto@cnr.it, [2] mariopanza@cnr.it

Cite as: Muto, M., Panza, M., Iovine, G., Rossi, M., Alvioli, M., Marchesini, M. High-Resolution Digital Terrain Model on a sample area of the Italian national territory. In: Proceedings of Geomorphometry 2025, 9-13 June, Perugia, Italy. M. Alvioli, L. Melelli, I. Marchesini eds. CNR Edizioni, Rome. ISBN 978-88-8080-765-0. DOI: 10.5281/zenodo.15277544

Abstract— **This study presents the development of a high-resolution (5 m) digital terrain model (DTM) for Italy, prepared within the PNRR project "*National Centre for HPC, Big Data and Quantum Computing*". The goal is to enhance the accuracy of national-scale elevation data, improving upon the existing dataset TINITALY, originally at 10 m spatial resolution across Italy, by integrating sparse but extensive multi-source LiDAR data.**

A key challenge is the heterogeneous and fragmented distribution of LiDAR datasets, acquired by different institutions at different times, with varying resolutions, and different coordinate reference systems (CRS). To address this, a structured database has been designed to allow efficient updates as new LiDAR data become available. The methodology combines high-performance computing infrastructure with open-source software, leveraging GRASS GIS, Linux shell scripts, and data-parallel workflows to process large-scale datasets.

The data processing pipeline includes automated data processing, including CRS harmonization and mosaicking, ensuring a seamless and homogeneous national DTM. TINITALY data were interpolated to 5 m to bridge LiDAR gaps, prioritizing data recency and resolution in overlapping areas. The workflow was tested on a sample area with complex topography, validating the feasibility of the approach and ensuring data consistency across diverse terrains.

The final product is a high-accuracy DTM, suitable for hydrological and slope stability modeling, natural hazard assessment, and environmental management. This methodology, scalable and updatable, will provide a nationally consistent dataset, enabling analyses that were previously constrained by data fragmentation and resolution limitations.

I. INTRODUCTION

The increasing availability of high-resolution digital elevation models (DEMs) has revolutionized geomorphological, hydrological, and environmental analyses, enabling accurate terrain modeling [1]. However, merging data from different sources – such as airborne LiDAR, photogrammetric data, and satellite-based DEMs, with medium-resolution models like TINITALY [2], [3], [4]– introduces significant challenges, including managing data discontinuities and ensuring smooth transitions between elevation models with different characteristics [5].

Several studies proposed advanced fusion methods to improve DEM consistency and accuracy [6], highlighting how variable-weighted approaches can significantly reduce vertical errors and enhance topographic representation. A systematic review by Ref. [5] identified key fusion techniques, including weighted averaging based on vertical errors and adaptive interpolation to reduce discontinuities between DEMs of different origins.

According to Ref. [7], in the Italian context, the availability of LiDAR data is limited to approximately 63% of the national territory, with many regions showing gaps in spatial coverage. This limitation presents a challenge in creating complete and accurate high-resolution DEMs.

The present study, developed within the frame of the PNRR project "*National Centre for HPC, Big Data and Quantum Computing*", builds upon these findings and proposes an advanced methodology for high-resolution DEM fusion in Italy, by integrating LiDAR data from various sources and using the TINITALY elevation model to fill areas lacking high-resolution data.

The proposed approach consists of three main phases: data collection and pre-processing, DEM fusion using variable-weighted algorithms, and validation of the resulting elevation model. The effectiveness of this method was tested in a sample area in Emilia-Romagna (Northern Italy).

The final goal is to develop a coherent and accurate DEM, which is essential for environmental, hydrological, and land management applications. In fact, TINITALY is currently the highest-resolution DEM covering the whole of Italy, and is widely used by Italian researchers and practitioners, for a variety of applications [3]. The existence of such relatively high-resolution

DEM allows the consistent use across Italy of physically based models. For example, Refs.[8], [9] are example applications of a 3D rockfall model, Ref. [10] of a conceptual model for rapid-flow landslides, and Ref. [11] of an infinite slope stability model, though in a smaller area. We expect that the new DTM presented here will represent a great opportunity for improving similar applications in Italy.

II. Data and Methods

A. Data description

The objective of this work is to establish a procedure for generating a high-resolution (HR) digital terrain model (DTM) for the Italian territory. This HR model was designed to enhance the resolution of TINITALY and ensure greater accuracy in elevation measurements through the integration of multiple LiDAR sources.

To achieve this, three primary types of digital elevation data were considered. The first consists of LiDAR data provided by the Ministry of the Environment and Energy Security (MEES), which covers the entire national territory and is available at 1m and 2m resolutions. These datasets are distributed directly from the MEES (https://sim.mase.gov.it/portalediaccesso/mappe/#/viewer/new) The second category includes LiDAR data from other institutions, such as regional administrations, municipalities, and Civil Protection agencies, which have the same resolution as the MEES data but may overlap or leave coverage gaps. The third dataset is TINITALY, a national-scale DEM with 10 m resolution , which is used to fill in gaps where LiDAR data are unavailable.

B. Merging procedure

The process of constructing the HR DTM consists of three phases: i) data collection and pre-processing, ii) data processing and merging, and iii) preliminary quality control.

1) Data collection and pre-processing

The first step involved collecting and cataloging LiDAR datasets from official sources. Metadata analysis was performed to categorize the data based on resolution, acquisition date, and geographic reference system. A structured database was created to store all relevant information, facilitating organized data management. To automate and expedite the acquisition process, customized scripts were developed and run in a Linux environment, allowing downloading the data directly from official websites, extracting the compressed files, and identifying the corresponding reference systems. The most common geographic reference systems encountered were WGS84 (EPSG 4326) and ETRS89 (EPSG 4258). Figure 1 shows the number of tiles and the corresponding EPSG for the MEES data. Note that, typically, a LiDAR tile at 1 m resolution contains 1,000,000 grid cells. Knowledge of the reference system of each piece of data allows assigning EPSG codes, and setting up corresponding GRASS GIS [12], [13] locations and mapset to collect and process them. A test area within the Emilia-Romagna region was selected as a representative sample, due to its varied topography and widespread LiDAR coverage. This region featured a mix of MEES and regionally acquired LiDAR data, making it an ideal environment for validating the merging procedure.

2) Data processing and merging

The next phase focused on merging and standardizing the collected data. The first step involved projecting the data into a common reference system. Since various datasets had different geographic reference systems, all data were projected into Italy Zone EPSG:6875 [14]. A new GRASS GIS location was set up for this purpose, and separate map sets were generated for each region to store the projected LiDAR data. A few GRASS GIS scripts were

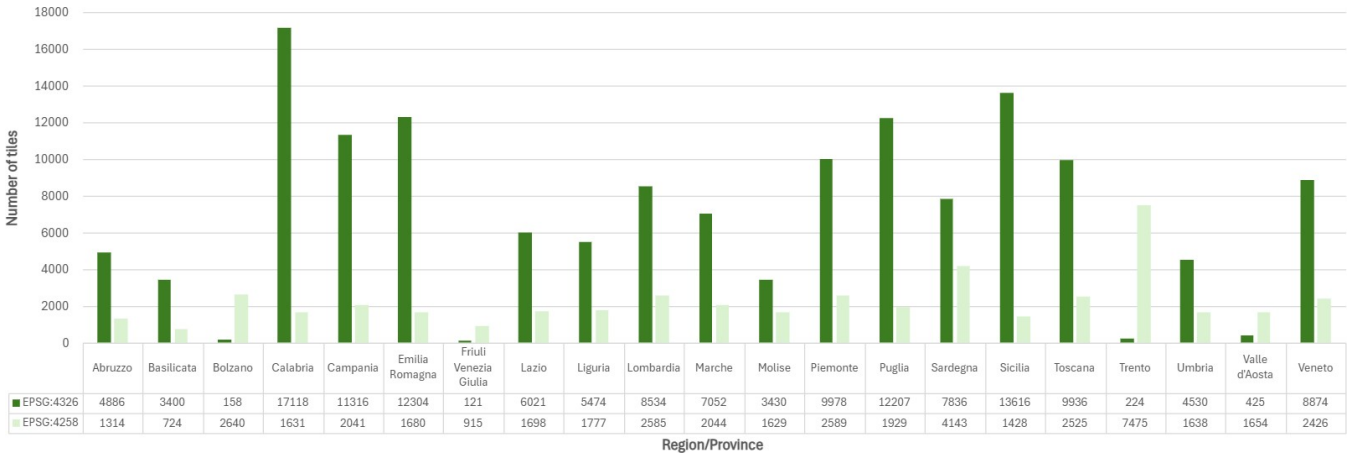

	Abruzzo	Basilicata	Bolzano	Calabria	Campania	Emilia Romagna	Friuli Venezia Giulia	Lazio	Liguria	Lombardia	Marche	Molise	Piemonte	Puglia	Sardegna	Sicilia	Toscana	Trento	Umbria	Valle d'Aosta	Veneto
EPSG:4326	4886	3400	158	17118	11316	12304	121	6021	5474	8534	7052	3430	9978	12207	7836	13616	9936	224	4530	425	8874
EPSG:4258	1314	724	2640	1631	2041	1680	915	1698	1777	2585	2044	1629	2589	1929	4143	1428	2525	7475	1638	1654	2426

Figure 1. LiDAR tiles available for this study, with the corresponding EPSG reference system codes. Data split by administrative region or province.

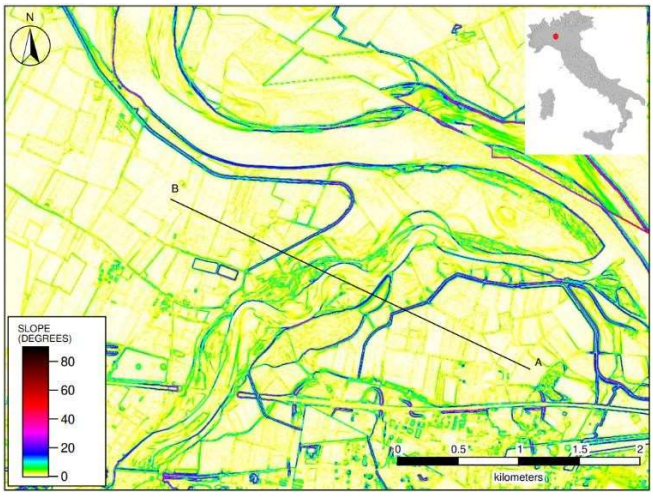

Figure 2. Spatial analysis of a sample area in Emilia Romagna (Northern Italy): slope map from the DTM at 5-meter resolution. The black segment refers to the topographic profile of Figure 4.

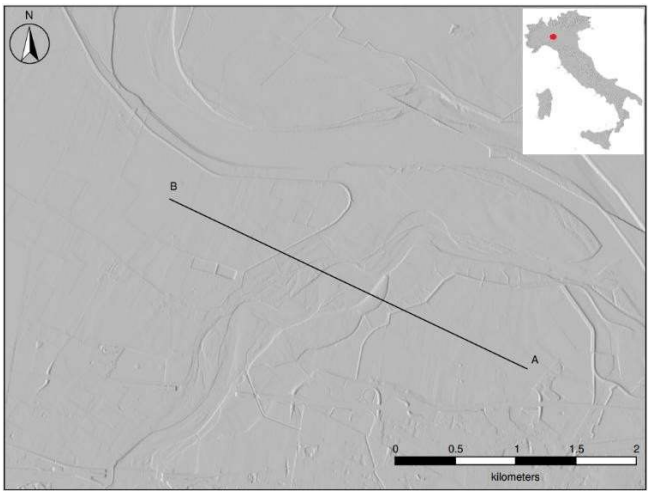

Figure 3. Spatial analysis of a sample area in Emilia Romagna (Northern Italy): hill-shade. The black segment refers to the topographic profile of Figure 4.

developed to parallelize the processing of individual LiDAR tiles, expediting the merging process. In case of overlapping LiDAR datasets, the following prioritization strategy was implemented that favored the most recent dataset, between datasets with same resolution. Gaps in LiDAR coverage were filled with TINITALY data. To further improve data consistency, smoothing algorithms [1] were applied to reduce abrupt elevation changes between overlapping datasets. Additionally, TINITALY was interpolated to a 5 m resolution to match the high-resolution LiDAR mosaic. A crucial step in the merging process involved

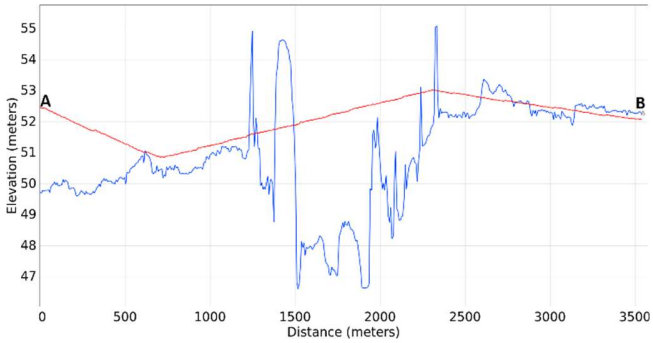

Figure 4. Topographic profile. Key: elevation data from TINITALY (red line), and HR-DTM (blue line). For profile location, cf. Figures 2 and 3.

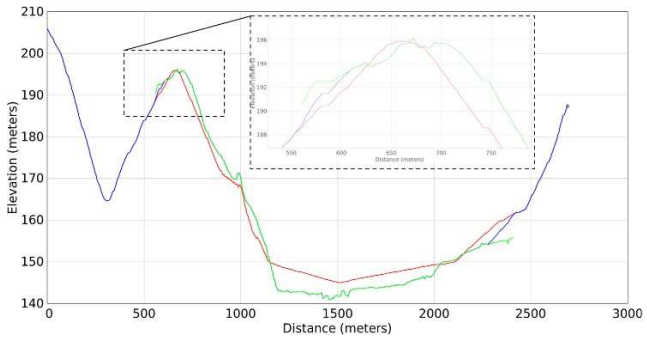

Figure 5. Topographic profile. Key: elevation data from TINITALY (red line); HR-DTM (blue line); LiDAR data (green line). The inset zooms on the transition zone between LiDAR and TINITALY data, showing the smoothing effect in the HR-DTM, with respect to the original datasets.

adjusting elevation discrepancies. The mean elevation difference between TINITALY and the LiDAR-derived mosaic were computed, and the LiDAR mosaic was accordingly adjusted to align with TINITALY's baseline elevation. This correction was necessary to ensure seamless integration between the datasets. The final high-resolution DTM was obtained by merging the corrected LiDAR mosaic with the resampled TINITALY DEM at a 5 m resolution.

3) Preliminary quality control

The final step of the procedure consists of a thorough validation and quality control process to assess the accuracy and coherence of the merged dataset. Spatial analysis tools helped verifying discrepancies and discontinuities were reduced to a minimum. Preliminary quality control checks confirmed that the merging procedure significantly reduced inconsistencies in elevation data, as shown for a sample area in Figures 2, 3, and 4. More in detail, the *slope* of the sample area obtained from the DTM at 5 m resolution is shown in Figure 2, with gentle slopes

prevailing in a hilly river-plain sector. In Figure 3, the *hill shade* of the same area allows to appreciate the meandering pattern of the water courses, and the borders of terraced sectors. Figure 4 shows the topographic profiles obtained from the TINITALY DTM at 10 m resolution, and the HR DTM at 5 m resolution.

Figure 5 shows an example of a topographic profile for a transition zone between LiDAR data and TINITALY data is shown. The figure 5 illustrates that the HR DTM coincides with the TINITALY data in the areas without LiDAR data (ends of the profile). In the middle part, both data types are available, and in HR DTM priority is given to LiDAR data. Smoothing techniques are applied in the transition zones. In the inset, the detail of the profiles for the different data types (TINITALY, LiDAR, HR DTM) in the transition zone indicated by the dashed box can be appreciated.

III. Discussion and Conclusions

The proposed methodology relies on a computing infrastructure based on open-source software. The use of Linux-based environments, GRASS GIS, and Bash scripting allows for a full exploitation of servers equipped with four CPUs with a total 96 computing cores, and 530 gigabytes of RAM, ensuring efficient parallel processing and automation. The adopted setup significantly reduces computational time, with respect to a serial code, and enhances scalability, potentially allowing for progressive integration of new LiDAR data.

A major challenge in creating a high-resolution DTM for Italy is the fragmentation and uneven distribution of LiDAR datasets. Unlike centralized repositories, multiple regional and national institutions manage Italian LiDAR data, characterized by different acquisition times, formats, and coverages, hindering data integration. Nevertheless, the structured database presented here was designed for efficient updates, allowing seamless incorporation of new LiDAR datasets, and ensuring the DTM remains current and comprehensive.

The choice of 5-meter resolution represents a compromise between available high-resolution LiDAR (1-2 m) and coarser TINITALY (10 m) datasets. Whereas resampling TINITALY is not a conventional approach, it resulted in a limited impact, according to random sample tests. Most areas where LiDAR is not available are, in fact, in steep mountainous regions, where interpolation errors are acceptable. Therefore, the result is a spatially homogeneous DTM, enabling large-scale applications at high resolution.

The methodology outlined here ensures obtaining an accurate and comprehensive HR DTM, by leveraging high-resolution LiDAR data and compensating gaps with TINITALY data. The results demonstrated the effectiveness of the adopted approach in producing a seamless, high-resolution DTM for the Italian territory. By integrating cutting-edge computational resources, a scalable database, and a balanced resolution strategy, the obtained DTM is flexible, updatable, and accurate, and may be employed in diverse fields of application, from hydrological and slope stability modeling to environmental planning.

IV. Acknowledgments

Work supported by the PNRR project "National Centre for HPC, Big Data and Quantum Computing - HPC" – CN00000013 – CUP B93C22000620006, Spoke 5 – Environment & Natural Disasters, Task 1.1 & Task 1.2.

References

[1] A. Petrasova, H. Mitasova, V. Petras, e J. Jeziorska, «Fusion of high-resolution DEMs for water flow modeling», Open geospatial data, softw. stand., vol. 2, fasc. 1, p. 6, mar. 2017, doi: 10.1186/s40965-017-0019-2.

[2] S. Tarquini et al., «TINITALY/01: a new Triangular Irregular Network of Italy», Annals of Geophysics, vol. 50, fasc. 3, dic. 2009, doi: 10.4401/ag-4424.

[3] S. Tarquini e L. Nannipieri, «The 10 m-resolution TINITALY DEM as a trans-disciplinary basis for the analysis of the Italian territory: Current trends and new perspectives», Geomorphology, vol. 281, pp. 108–115, mar. 2017, doi: 10.1016/j.geomorph.2016.12.022.

[4] S. Tarquini, I. Isola, M. Favalli, A. Battistini, e G. Dotta, «TINITALY, a digital elevation model of Italy with a 10 meters cell size (Version 1.1)». Istituto Nazionale di Geofisica e Vulcanologia (INGV), 2023. doi: 10.13127/TINITALY/1.1.

[5] C. J. Okolie e J. L. Smit, «A systematic review and meta-analysis of Digital elevation model (DEM) fusion: pre-processing, methods and applications», ISPRS Journal of Photogrammetry and Remote Sensing, vol. 188, pp. 1–29, giu. 2022, doi: 10.1016/j.isprsjprs.2022.03.016.

[6] S. Zhao, J. Liu, W. Cheng, e C. Zhou, «Fusion Scheme and Implementation Based on SRTM1, ASTER GDEM V3, and AW3D30», IJGI, vol. 11, fasc. 3, p. 207, mar. 2022, doi: 10.3390/ijgi11030207.

[7] G. D'Amico et al., «Are we ready for a National Forest Information System? State of the art of forest maps and airborne laser scanning data availability in Italy», iForest, vol. 14, fasc. 2, pp. 144–154, apr. 2021, doi: 10.3832/ifor3648-014.

[8] M. Alvioli et al., «Rockfall susceptibility and network-ranked susceptibility along the Italian railway», Engineering Geology, vol. 293, p. 106301, nov. 2021, doi: 10.1016/j.enggeo.2021.106301.

[9] M. Alvioli et al., «Seismically induced rockfall hazard from a physically based model and ground motion scenarios in Italy», Geomorphology, vol. 429, p. 108652, mag. 2023, doi: 10.1016/j.geomorph.2023.108652.

[10] I. Marchesini et al., «National-scale assessment of railways exposure to rapid flow-like landslides», Engineering Geology, vol. 332, p. 107474, apr. 2024, doi: 10.1016/j.enggeo.2024.107474.

[11] M. Alvioli et al., «Implications of climate change on landslide hazard in Central Italy», Science of The Total Environment, vol. 630, pp. 1528–1543, lug. 2018, doi: 10.1016/j.scitotenv.2018.02.315.

[12] M. Neteler, M. H. Bowman, M. Landa, e M. Metz, «GRASS GIS: A multi-purpose open source GIS», Environmental Modelling & Software, vol. 31, pp. 124–130, mag. 2012, doi: 10.1016/j.envsoft.2011.11.014.

[13] I. Marchesini, M. Neteler, alessandro furieri, A. Frigeri, P. Cavallini, e L. Casagrande, GIS Open Source. GRASS GIS, Quantum GIS e Spatialite. 2012.

[14] V. Cima, M. Carroccio, e R. Maseroli, «Corretto utilizzo dei Sistemi Geodetici di Riferimento», 2014.

DEM Generalization Tool Using Grid-Based Quadric Error Metric

Richard Feciskanin, Jozef Minár
Dept. of Physical Geography and Geoinformatics
Faculty of Natural Sciences, Comenius University
Bratislava, Slovakia
richard.feciskanin@uniba.sk

Cite as: Fesickanin, R., Minár, J. (2025). DEM Generalization Tool Using Grid-Based Quadric Error Metric. In: Proceedings of Geomorphometry 2025, 9-13 June, Perugia, Italy. M. Alvioli, L. Melelli, I. Marchesini eds. CNR Edizioni, Rome. ISBN 978-88-8080-765-0. DOI: 10.5281/zenodo.15024141

Abstract—**We introduce a novel tool for generalizing Digital Elevation Models (DEMs) using the Quadric Error Metric (QEM), specifically adapted for raster grids. While traditional QEM methods have been used for polygonal simplification, our approach applies QEM directly to raster DEMs, providing a robust solution for land surface generalization. This method enables progressive generalization through an iterative process that smooths out subtle details while preserving key landforms and geomorphic structures. The tool incorporates a sharpness parameter that allows users to fine-tune the generalization process by balancing edge preservation (or even accentuation) and simplification. The tool avoids the typical peak-clipping and valley-filling effects associated with simpler smoothing techniques, effectively maintaining the depth and height of non-generalized forms. Additionally, the approach ensures that significant surface features are preserved even at high levels of generalization. Implemented in Rust, this command-line tool provides an efficient, open-source solution for processing DEMs in geomorphometric and other geoscientific applications.**

I. Introduction

Modern mapping technologies, primarily LiDAR, enable the creation of high-precision Digital Elevation Models (DEMs) capable of capturing subtle topographic variations. While these high-resolution DEMs inherently include surface roughness and small landforms, preserving such detail is unnecessary—and often undesirable—for analyses focused on larger geomorphic structures. According [1], neither the highest resolution nor the initial data scale ensures optimal representation, emphasizing the need for scale optimization. Additionally, calculating derivatives amplifies high-frequency noise, with higher-order derivatives being nearly unusable without DEM smoothing [2]. Thus, small-scale noise is often suppressed through techniques like grid resampling, low-pass filtering, or polynomial smoothing, although these methods do not effectively preserve critical features such as ridges and valleys [3, 4]. Efforts to minimize excessive feature smoothing have involved the implementation of variable-size filters [5] and the utilization of restricted neighborhoods [6].

Advanced methods aim to preserve key land surface features while reducing noise. Wavelet transformations, morphological operations, and drainage-preserving approaches target specific applications, but they have their own limitations [7] and require subjective parameter tuning, limiting their broader use. These methods often fail to support the high-level generalization needed to identify and analyze the major geomorphic structures bounded by distinct edges. For such cases, Triangulated Irregular Networks (TIN) based generalization methods are more effective. Various techniques, such as those by [8, 9], have been developed to generalize and reconstruct land surfaces using TINs, which involve extracting 3D points and triangulation. In other fields, numerous procedures have been developed, with the Quadric Error Metric (QEM), introduced by [10], excelling in polygonal model simplification by producing near-optimal triangles for surface representation [11].

While QEM-based TIN models perform well, their lack of smoothness complicates the calculation of some land surface parameters (LSPs) [12], and the conversion back to grids adds complexity [13]. This limitation motivated us to adapt the QEM framework for raster DEMs, offering a novel approach to land surface simplification. Unlike previous work [14], which, as known, only used QEM for grids (in basic form and not solely on the grid), our method operates directly on raster grids, utilizing the full potential of the QEM method, similar to its original application. By leveraging QEM's strengths within a grid structure, our approach introduces a new methodology for generalized DEMs that retains essential land surface features,

while the spatial structure meets the requirements for many subsequent analyses. The resulting generalized gridded DEM is primarily intended for analyzing the noise-free surface of larger landforms but can also be used, for instance, to detect the filtered signal component representing residual topography.

II. Methods

A. Original Quadric Error Metric Approach

QEM, first introduced by [10], is a widely used method for polygonal surface simplification. It reduces mesh complexity while preserving the overall shape by quantifying the geometric error introduced during simplification. Each vertex is associated with a set of planes derived from the triangles surrounding it, capturing local surface curvature. The quadric error for a vertex is calculated as the sum of squared distances from the vertex to the planes of adjacent triangles. Vertices on the original surface have zero error. Simplification involves collapsing edges, merging incident planes, and displacing vertices, which increases the error.

QEM is compactly represented by a 4×4 symmetric matrix Q, known as the quadric matrix

$$Q = \begin{bmatrix} a & b & c & d \\ b & e & f & g \\ c & f & h & i \\ d & g & i & j \end{bmatrix} \quad (1)$$

The matrix Q encodes the surface characteristics and enables the calculation of vertex error and the optimal vertex position. The Q matrix can be visualized as an ellipsoidal level surface. When two vertices are contracted, their quadric matrices Q_1 and Q_2 are summed such that $Q = Q_1 + Q_2$. The resulting matrix encodes the combined surface properties, allowing efficient determination of the optimal new vertex position to minimize distortion. This approach ensures a balance between simplification and geometric fidelity.

B. Grid-Based Adjustments to the Quadric Error Metric

QEM can also be adapted for raster grid simplification, although significant modifications are necessary compared to its application to polygonal surfaces. In this adaptation, grid nodes act as vertices, with their associated planes calculated using the eight triangles formed by the node and its eight neighbors. Each node is assigned a quadric matrix Q, representing the local surface characteristics. Combining the node Q matrix with the Q matrices of neighboring nodes and calculating the new elevation constitute a generalization step.

Unlike polygonal surfaces, where vertices can be repositioned, raster grids fix the x and y coordinates, requiring only the elevation z to be optimized. The optimal z value minimizes the error function derived from Q:

$$z = -\frac{cx + fy + i}{h} \quad (2)$$

where the coefficients are derived from Q matrix (1).

Incorporating neighboring nodes' Q matrices into the calculation introduces a smoothing effect, as noted by [14]. However, they did not use the key strength of QEM, which lies in its ability to evaluate errors after simplification steps, enabling changes that minimize distortion and preserve significant features, even at high levels of generalization.

For raster grids, an effective approach involves including neighbors whose errors, relative to their ideal positions based on Q, fall below a set threshold (Fig. 1). This ensures that nodes contributing to the new Q-values belong to a similar surface shape. Nodes beyond landform edges, which are associated with higher errors, are excluded, preserving critical surface features. When iteratively repeated with progressively increasing error thresholds, this process mirrors the original QEM procedure.

III. Results

A. Algorithm Implementation

Implementation of presented algorithm for grid-based QEM generalization needs to solve problem of setting suitable error threshold. Rather than using a fixed threshold, we dynamically set the threshold for each iteration based on the errors from the previous step, selecting a chosen percentile that increases from its initial value to 100 by the final iteration. This approach introduces a *sharpness* parameter (ranging from 0 to 9) to balance generalization between less complex areas (with smaller deviations) and regions with significant shape changes (with larger deviations). The initial percentile is calculated as $1 - (0.1 \times sharpness)$. Higher *sharpness* values preserve edges and pronounce shape changes but require more iterations to

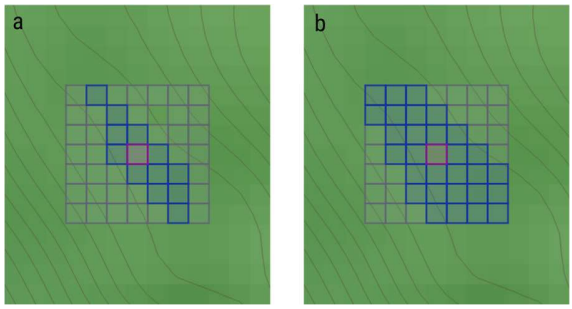

achieve the same level of generalization.

Figure 1. Pixel selection for QEM-based simplification. a) Low threshold: selects pixels (blue) with most similar shapes to the central pixel (purple). b) High threshold: includes more contributing pixels.

We implemented the described iterative generalization algorithm and developed the QEM Generalization, a command-line tool written in the Rust programming language. It relies on

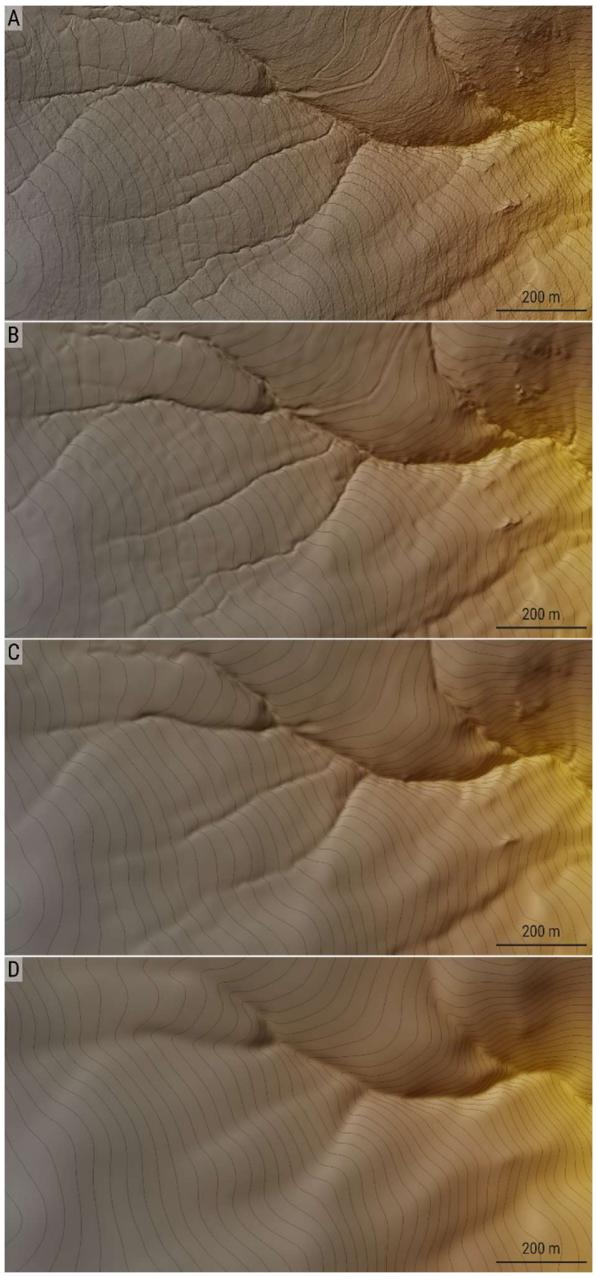

Figure 2. Generalization levels: A – Input DEM, B – 20 iterations, C – 100 iterations, D – 500 iterations. Contour interval: 10 m. Site: Mlynská dolina, Lúčanská Fatra, Slovakia.

GDAL for raster handling and requires a Rust development environment for building from source. The source code, along with detailed instructions for building and usage, is available on GitHub [15]. This tool is part of the broader Physical Geomorphometry Tools project, which focuses on physically based methods for detecting and analyzing land surface structures and land surface dynamics. Its goal is to provide useful tools for processing DEMs within this framework.

B. Using the QEM Generalization Tool

One of the advantages of generalization using QEM is that it does not require advanced settings. The input to the algorithm comprises a DEM raster, the desired level of generalization (specified as the number of iterations), and a *sharpness* parameter (defaulting to 5). The output is a generalized DEM raster. Raster traversal for value calculations is parallelized, and number of used cores can be selected. Given our focus on high levels of generalization where preserving the original resolution is not critical, users have an option for resampling the data to a lower resolution.

The main generalization parameter is the number of iterations, with a higher number naturally leading to a greater level of generalization. Fig. 2 shows the incremental generalization of a detailed LiDAR DEM with increasing iterations. The algorithm progressively generalizes the surface, smoothing out subtle features while retaining essential structures. Notably, the algorithm avoids the peak-clipping and valley-filling effects typical of simple smoothing methods. It effectively preserves the depth or height of small non-generalized forms, addressing a challenge faced by many other methods. Edges are preserved based on their significance through QEM's advanced surface shape handling in the surrounding area of each pixel.

The *sharpness* parameter can be used to fine-tune the generalization. Increasing the sharpness value not only improves edge retention but can even accentuate edges. This compensates for the implicit edge smoothing caused by downsampling when it is used. On the other hand, a *sharpness* value of zero removes the use of QEM error for selecting neighbors with similar surface shapes, resulting in the uniform use of all neighboring points. The difference between the extreme values of sharpness is shown in Fig. 3.

IV. CONCLUSION

The developed tool introduces an innovative approach to generalizing DEMs by adapting the QEM for direct use with

raster grids. This method effectively integrates the capabilities of

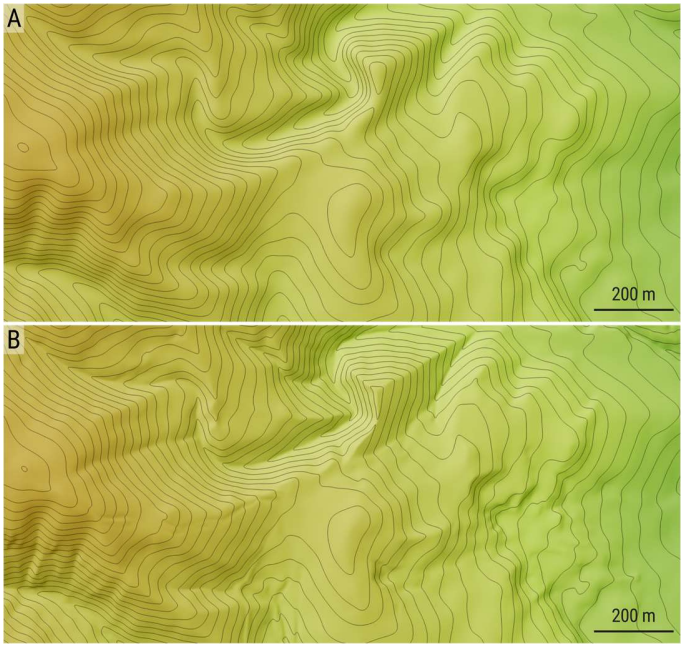

QEM with the benefits of the most common grid-based structure.

Figure 3. Different *sharpness* settings: A – *sharpness* = 0, B – *sharpness* = 9. Generalized with 100 iterations. Contour interval: 10 m. Site: Piatrová, Lúčanská Fatra, Slovakia.

A major strength of the tool is its ability to retain edges, significant landforms, and maintain the depth and height of small terrain features. Moreover, its simplicity makes it highly user-friendly, not requiring advanced input parameters for effective operation. However, the inclusion of a sharpness parameter allows users to fine-tune generalization, balancing edge preservation and the enhancement of important surface features. This versatility makes it well-suited for diverse needs, ensuring the preservation of critical structural details even under significant generalization. It provides a robust and efficient solution for processing high-resolution DEMs, serving as a valuable tool for land surface analysis, especially for the physically based digital geomorphological mapping where such generalization has a key role [16].

V. Acknowlegments

This work was supported by the Slovak Research and Development Agency under the contract No. APVV-22-0024.

References

[1] Newman, D.R., Cockburn, J.M.H., Drăguţ, L., and Lindsay, J. B., 2022. "Local scale optimization of geomorphometric land surface parameters using scale-standardized Gaussian scale-space", Computers & Geosciences, 165, 105144. https://doi.org/10.1016/J.CAGEO.2022.105144.

[2] Florinsky, I. V. (2012). "Digital Terrain Analysis in Soil Science and Geology", Elsevier Inc. https://doi.org/10.1016/C2010-0-65718-X.

[3] Chen, Y., Wilson, J.P., Zhu, Q., and Zhou, Q., 2012. "Comparison of drainage-constrained methods for DEM generalization", Computers and Geosciences, 48, 41–49. https://doi.org/10.1016/j.cageo.2012.05.002.

[4] Popov, A.B., Minár, J. and Gallay, M.,2021. "Multiresolution land surface segmentation and generalization of DEM: Tentative searching for the optimal settings of detecting elementary forms", Transactions in GIS, 25(5), 2376–2393. https://doi.org/10.1111/tgis.12842.

[5] Gallant, J., Land, C., Canberra, W., 2011. "Adaptive smoothing for noisy DEMs", Geomorphometry 2011 (Redlands, CA, USA, 7. – 11. 9. 2011).

[6] Lindsay, J.B., Francioni, A., & Cockburn, J.M.H., 2019. LiDAR DEM Smoothing and the Preservation of Drainage Features. Remote Sensing, 11(16), 1926. https://doi.org/10.3390/rs11161926.

[7] Wu, Q., Chen, Y., Wilson, J.P., Liu, X., & Li, H., 2019. "An effective parallelization algorithm for DEM generalization based on CUDA", Environmental Modelling and Software, 114, 64–74. https://doi.org/10.1016/j.envsoft.2019.01.002.

[8] Zakšek, K., and Podobnikar, T., 2005. "An effective DEM generalization with basic GIS operations", 8th ICA WORKSHOP on Generalisation and Multiple Representation.

[9] Chen, Y., Ma, T., Chen, X., Chen, Z., Yang, C., Lin, C., and Shan, L., 2016. "A new DEM generalization method based on watershed and tree structure", PloS ONE, 11(8). https://doi.org/10.1371/journal.pone.0159798.

[10] Garland, M., and Heckbert, P.S., 1997. "Surface simplification using quadric error metrics", Proceedings of the 24th Annual Conference on Computer Graphics and Interactive Techniques, SIGGRAPH 1997, 209–216. https://doi.org/10.1145/258734.258849.

[11] Feciskanin, R., and Minár, J., 2021. "Polygonal simplification and its use in DEM generalization for land surface segmentation", Transactions in GIS 25, 2361–2375. https://doi.org/10.1111/TGIS.12796.

[12] Hu, G., Xiong, L., Lu, S., Chen, J., Li, S., Tang, G., and Strobl, J., 2022. "Mathematical vector framework for gravity-specific land surface curvatures calculation from triangulated irregular networks", GIScience & Remote Sensing, 59(1), 590–608. https://doi.org/10.1080/15481603.2022.2044149.

[13] Feciskanin, R., 2023. "DEM generalization using polygonal simplification", Geomorphometry 2023 (Iași, Romania, 10. – 14. 7. 2023). https://doi.org/10.5281/zenodo.7861927

[14] Löffler, F., and Schumann, H., 2010. "QEM-filtering: A new technique for feature-sensitive terrain mesh simplification", Vision, Modeling and Visualization 2010, 1–8. https://doi.org/10.2312/PE/VMV/VMV10/001-008.

[15] Feciskanin, R., 2024. "QEM Generalization – Land Surface Generalization Tool", Available online: https://github.com/xiceph/physical-geomorphometry-tools/tree/main/generalize.

[16] Minár, J., Drăguţ, L., Evans, I. S., Feciskanin, R., Gallay, M., Jenčo, M., and Popov, A., 2024. "Physical geomorphometry for elementary land surface segmentation and digital geomorphological mapping", Earth-Science Reviews, 248, 104631. https://doi.org/10.1016/J.EARSCIREV.2023.104631.

Towards implementation of segmentation into Physical geomorphometry tools: Case of generalization

Veronika Hajdúchová [1], Hana Bobáľová, Alexandra Benová, Jozef Minár
Dept. of Physical Geography and Geoinformatics
Faculty of Natural Sciences, Comenius University
Bratislava, Slovakia
[1] veronika.hajduchova@uniba.sk

Cite as: Hajdúchová, V., Bobáľová, A., Benová, A., Minár, J. (2025). Towards implementation of segmentation into Physical geomorphometry tools: Case of generalization. In: Proceedings of Geomorphometry 2025, 9-13 June, Perugia, Italy. M. Alvioli, L. Melelli, I. Marchesini eds. CNR Edizioni, Rome. ISBN 978-88-8080-765-0. DOI: 10.5281/zenodo.15275419

Abstract— **The Physical Geomorphometry Tools project aims to develop a segmentation tool for physically based land surface segmentation, integrating with the new generalization and land surface parameters (LSP) calculator tools. This study evaluates the segmentation process across a complex, geomorphologically diverse area in western Slovakia, characterized by various landforms. The generalization of the digital elevation model (DEM) was conducted using a Quadric Error Metric (QEM) based method, preserving essential land surface features even at high generalization levels, and the K_0 index, the measure of kurtosis of curvature changes, was employed to determine optimal generalization levels, followed by segmentation using multiresolution segmentation (MRS). The study also assessed the Local Variance (LV) of geomorphometric variables within segments across different generalization levels. Results indicate that resampling the DEM at peak K_0 values enhances segmentation accuracy while maintaining an appropriate balance between terrain simplification and detail retention.**

I. Introduction

Physical geomorphometry tools is a set of programs created within the project "Physical Geomorphometry for Physical Geographical Research" available on the website https://xiceph.github.io/physical-geomorphometry-tools/. We are working on the creation of a "segmentation" tool, which should provide elementary physically-based land surface segmentation in conjunction with the use of the other two tools "generalization" and "lsp-calculator".

Algorithm and applications of the elementary segmentation has recently been presented in [1] and [2]. The original algorithm [1] is more complex, its application in [2] is simplified. In both cases, very small areas were segmented, in the case of [2] also genetically and morphostructurally homogeneous. Creating a universal segmentation tool requires a thorough examination of all segmentation steps over a much larger and more heterogeneous area, in connection with the main purpose of segmentation - digital geomorphological mapping.

The chosen area is situated in western Slovakia, within the Záhorie region, near the village of Plavecký Mikuláš at the

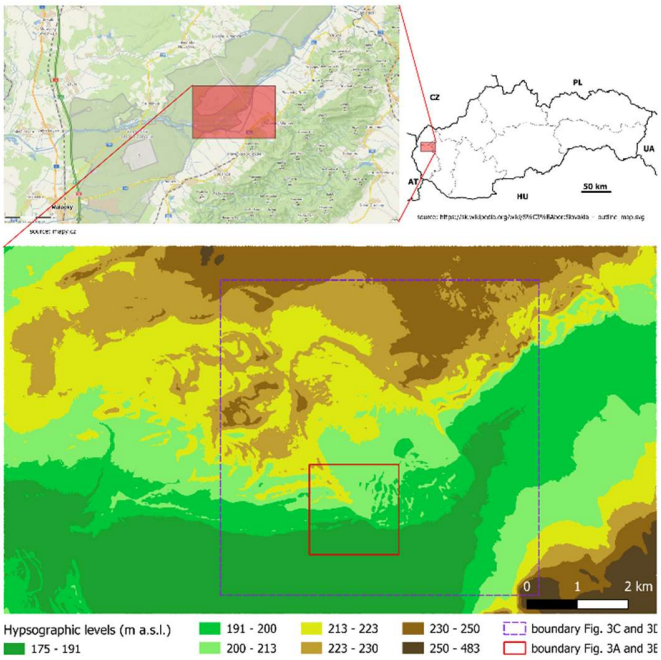

Figure 1. Selected study area (94 m2) with a hypsographic level.

junction of the Carpathians and the Vienna Basin with an extremely varied and enigmatic genesis (Fig.1). In its center there is a half-graben structure probably filled at the end of the Pleistocene with a paleolake, partially enclosed by a dune. The lake was probably catastrophically drained during a strong earthquake in the direction of today's flow of the Rudava River, which formed the unique features of its valley and very specific landslides occurred on the shore of the former lake, which were previously considered dune fields. This created an enigmatic set of aeolian, lacustrine, fluvial, tectonic and gravitational forms, which should be distinguished and aptly characterized by a good segmentation tool. The base DEM of the area was derived from Slovakia's Airborne Laser Scanning (ALS) data, provided by the Geodesy, Cartography, and Cadastre Authority of the Slovak Republic with resolution 1×1 m and vertical accuracy less than 7 cm.

Although the key role of generalization was emphasized in [1] and [2], only a simple smoothing of the surface by approximation by a polynomial in an increasing computational window was used. Therefore, as a first step in building our tool, we tested the use of our much more sophisticated "generalization" tool [3].

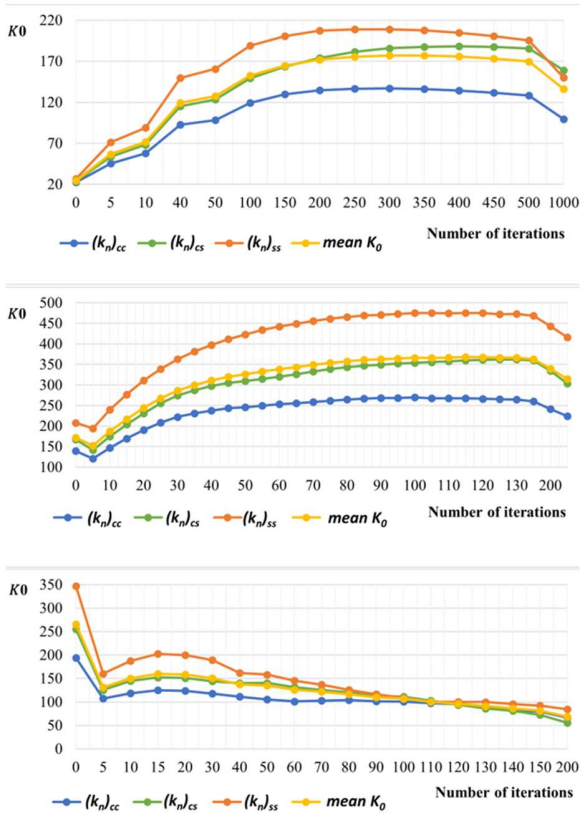

Figure 2. Values of K_0 derived from the third-order parameters and their average across different resolution. A – original 1×1 m resolution data, B – resampled 5×5 m resolution data, C – resampled 25×25 m resolution data

II. EXPERIMENT DESIGN

A. Research questions

We were looking for answers to the following questions:

1. Can the new generalization method simplify the DEM so that the elementary forms of the different hierarchical levels are gradually emphasized in it?
2. Can the maximum of the K_0 index, recommended in [2], be used to select appropriate generalization levels?
3. How can the scale parameter be set for segmentation at a selected level of generalization? Can the Estimation of Scale Parameter (ESP) tool be used?
4. Does the simplified form of the algorithm [2] work well in even in more complex areas?

B. Generalization

The main task for land surface segmentation using high resolution DEMs involves creating a generalized model and computation of land surface parameters. The generalization of DEM was performed using method with QEM (Quadric Error Metric) approach, which even under high level of generalization is able to preserve significant land surface features [4]. The generalization process was repeated multiple times with varying numbers of iterations ranging from 0 to 1000, with a general increase in steps (e.g., increments of 5, 10, 50, 100, etc.). During this process, while keeping the resolution constant at 1×1 meter and the sharpness parameter set to its default value (5), several new DEMs were generated.

To determine most suitable generalization level for segmentation, we used quantile-based measure of kurtosis (K_0) of concentration of data around zero. This measure was calculated from the third-order parameters (changes of plan and profile curvatures $(k_n)_{cc}$, $(k_n)_{cs}$, $(k_n)_{ss}$, and their average) across all generalized models at different levels of generalization [5].

$$K_0 = \frac{\tilde{x}_{95} - \tilde{x}_5}{\tilde{x}_{0+5} - \tilde{x}_{0-5}}$$

where $\tilde{x}_{95}$ and $\tilde{x}_5$ are percentiles representing the spread of the set disregarding extreme values and $\tilde{x}_{0+5}$ and $\tilde{x}_{0-5}$ represent the fifth percentiles on the right and on the left from the zero value [6]. The generalization process was first applied to the original 1×1 m resolution DEM, where 300 iterations resulted in the most stable K_0 values. Based on this optimal level, the dataset was resampled to a 5×5 m resolution, followed by a second generalization process. The optimal K_0 at this stage was found at 115 iterations, after which a final resampling to 25×25 m was performed. The graphs (Fig. 2) indicate that generalization effectively enhances terrain representation up to a certain number of iterations, beyond which additional iterations no longer significantly improve segmentation. This suggests that an optimal K_0 should be

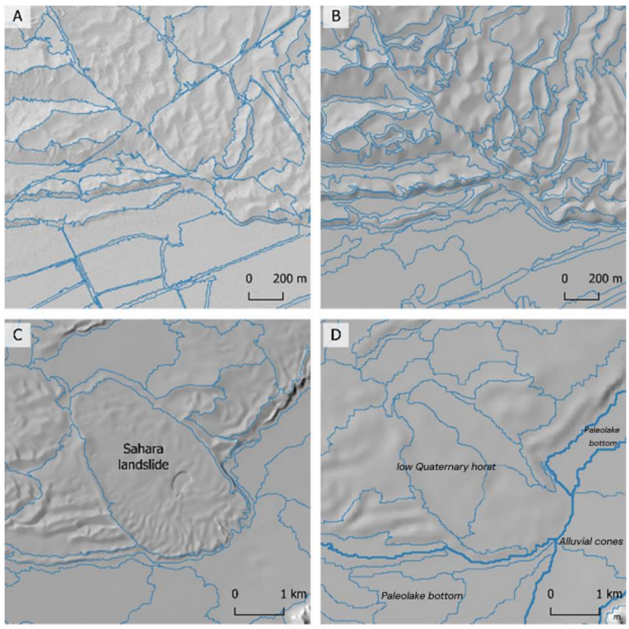

Figure 3. Elevation on generalized data with segmentation on a hillshade: A – original data (1×1 m), 998 seg., B – 300 iterations (1×1 m), 998 seg., C – 115 iterations (5×5 m), 49 seg., D – 15 iterations (25×25 m), 53 seg., thicker lines 7 seg. The progression across the images illustrates the effect of the generalization process on the land surface, with increasing smoothness and simplification of terrain features.

determined before resampling to maintain an appropriate balance between terrain simplification and detail retention.

C. LSP calculation

After the generalization process, we calculated geomorphometric variables – derivatives using the LSP calculator with the *for segmentation* flag and default polynomial degree of 3 [7]. These variables serve as inputs for the segmentation process. The calculated parameters include first-order: sine of slope, sine and cosine of aspect; second-order: normal slope line and contour curvature ($(k_n)_s$, $(k_n)_c$) and contour torsion (τ_c); third-order: contour change of normal contour curvature ($(k_n)_{cc}$), slope line change of normal contour curvature ($(k_n)_{cs}$) and slope line change of normal slope line curvature ($(k_n)_{ss}$). Curvatures and their changes were normalized [8] and all layers were clipped and rescaled to value range of 0 – 255.

D. Segmentation

Multiresolution segmentation (MRS) was performed at selected generalization levels based on the K_0 curve in the original 1-m resolution, specifically at levels 0 (non-generalized DEM), 5, 10, 40, 70, 100, 200, 300, 400, 500, and 1000. Segmentation was performed using the eCognition Developer 9 software. At the reference generalization level of 300, corresponding to the maximum K0 value, we applied the ESP2 tool [9] to determine the optimal scale parameter (SP). Due to computational complexity, the analysis was applied only to a section from the

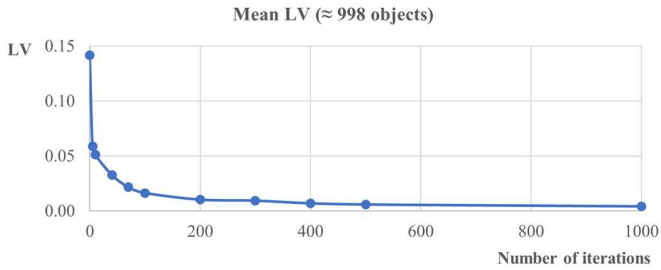

Figure 4. Mean local variance (LV) of image objects on different generalization levels, calculated from original 2nd and 3rd order LSPs in 1-m resolution.

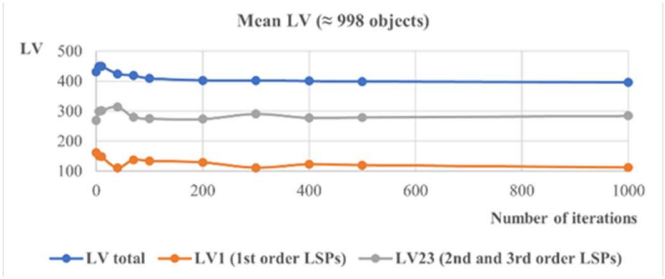

Figure 5. Mean local variance (LV) of image objects on different generalization levels, calculated from normalized and scaled LSPs in 1-m resolution.

central part of the study area containing the landslide, with steps of 5, 10, and 100 at three hierarchical levels. Instead of relying solely on the values recommended by the ESP2 tool, we selected the local minimum of the rate of change curve, signaling a decrease in local variance (LV) of image segments at scale parameter 440.

For the MRS applied to the entire study area, we assigned weights of 0.5 to the sine and cosine of aspect, and the weights of slope and $(k_n)_{cs}$ were doubled, following recommendations of [1] and [2]. The default values for the shape and compactness parameters (0.1 and 0.5, respectively) were retained. With a SP of 440, a total of 998 segments were generated at the generalization level 300. We aim to maintain a similar number of segments across other generalization levels to enable a comparison of local variance (LV) between the segmentations. In addition to calculating total LV, we separately computed the LV of the first-order variables (referred to as LV1), and the LV of the second- and third-order variables (referred to as LV23). Such distinction was made to assess the impact of normalizing the values of the curvatures and their changes on the resulting LV.

For the second sequence of generalizations with a 5×5 m resolution, we considered the generalization level 115 as the reference. At this level, the segmentation with the selected SP 400 and default weights for shape and compactness resulted in 50 image objects.

III. Results

On a non-generalized DEM, many segment boundaries follow artificial lines, such as roads or pipelines (Fig.3A). Even a slight

generalization allows for the creation of geomorphologically more meaningful segments. At higher levels of generalization, increasing the weight of the shape and compactness parameters (to 0.4 and 0.6, respectively) led to delineation of genetically homogeneous segments, such as the Sahara landslide (Fig.3C). The highly generalized DEM (Fig. 3D) is oversegmented using 53 segments. Segmentation with 7 segments, highlighting the main landforms, is more adequate.

Since normalization of second- and third-order LSPs emphasizes fluctuations of values around zero, the LV patterns for original and transformed curvature values differ. The LV curve calculated from the original curvature values (Fig.4) exhibits a sharp initial decline at the lowest generalization level (5), followed by a gradual decrease until it stabilizes around generalization level 200. This trend aligns with the behaviour of K_0, which also flattens out around the same level (Fig. 2).

A different pattern is observed in the LV23 curve derived from normalized and rescaled curvature values (Fig.5), where two local maxima were detected at generalization levels 40 and 300, with corresponding local minima on the LV1 curve (Fig.5). We assume that at these generalization levels, the segmentation isolates objects that are homogeneous in terms of elevation, slope, and aspect, while allowing for slight fluctuations in curvatures and their changes. Since these generalization levels are also reflected in the K_0 curve (with a sudden change in K_0 at level 40 and a maximum of K_0 at level 300 – Fig. 2), we consider the K_0 curve a suitable indicator to identify the optimal level of generalization when creating homogeneous segments.

IV. Discussion and Conclusion

The QEM-based generalization algorithm demonstrates strong performance, however as the number of iterations increases without adjusting the resolution, the effectiveness of generalization diminishes beyond the optimal K_0. A key challenge is identifying the appropriate timing for resampling. Initial results indicate that resampling at the peak K_0 value may be the most effective strategy.

The local variance of normalized curvatures and changes of curvatures values behaves differently compared to the LV of the original values, which directly express geomorphic energy. This discrepancy would be problematic if we were strictly following the equilibrium paradigm as applied in [10], where only equilibrium elementary forms are considered. However, within a shift towards a non-equilibrium paradigm [1], this property becomes advantageous. By emphasizing low curvature values and changes in curvature while reducing the weight of high values, the method enhances the acceptance of highly non-equilibrium segments in the final segmentation results.

The ESP tool appears insufficient for identifying the most suitable SP, instead, it may be necessary to search for minima beneath the trend line and the dependency of the local variance and average object size.

If the processed area contains highly contrasting morphostructures—such as a flat lake bottom, an aeolian hill, and a mountain foothill, as in our case—maximizing the K_0 index results in a generalization that is only suitable for segmenting the largest of these features. Therefore, generalization and subsequent segmentation should be conducted independently within the morphostructurally homogeneous areas, either based on expert-defined geomorphological units or regions identified through prior physically based morphostructural segmentation [11].

V. Acknowledgments

This work was supported by the Slovak Research and Development Agency under the contract No. APVV-22-0024.

References

[1] Minár, J., Drăguţ, L., Evans, I., Feciskanin, R., Gallay, M., Jenčo, M., and Popov, A., 2024. "Physical geomorphometry for elementary land surface segmentation and digital geomorphological mapping", Earth-Science Reviews, 248, 104631. https://doi.org/10.1016/j.earscirev.2023.104631

[2] Popov, A.B., Minár, J., and Drăguţ, L., 2025. "Physically based digital geomorphological mapping: Case study of glacial and karst topography", Geomorphology, Volume 470, 109539, ISSN 0169-555X, https://doi.org/10.1016/j.geomorph.2024.109539.

[3] Feciskanin, R., Minár, J., 2025. "Advancing Raster DEM Generalization with a Quadric Error Metric Approach", Computers and Geosciences, in review.

[4] Feciskanin, R., 2024. "DEM Generalization - Land Surface Generalization Tool", Available online: https://github.com/xiceph/physical-geomorphometry-tools/tree/main/generalization

[5] Feciskanin, R., Minár, J., 2020. "An optimization of triangular network and its use in DEM generalization for the land surface segmentation", 10.30437/GEOMORPHOMETRY2020_2. https://www.researchgate.net/publication/346778965

[6] Minár, J. et al. "Third-order geomorphometric variables (derivatives): Definition, computation and utilization of changes of curvatures". Int. J. Geogr. Inf. Sci. 27, pp. 1381–1402

[7] Feciskanin, R., Hajdúchova, V., 2024. "Land Surface Parameters Calculator", Available online: https://github.com/xiceph/physical-geomorphometry-tools/tree/main/lsp-calculator

[8] Csillik, O., Evans, I. S., & Drăguţ, L. 2015. "Transformation (normalization) of slope gradient and surface curvatures, automated for statistical analyses from DEMs", Geomorphology, 232, 65–77. https://doi.org/10.1016/j.geomorph.2014.12.038

[9] Drăguţ, L., Csillik, O., Eisank, C., Tiede, D., 2014, "Automated parameterisation for multi-scale image segmentation on multiple layers", ISPRS Journal of Photogrammetry and Remote Sensing, Volume 88, Pages 119-127, ISSN 0924-2716, https://doi.org/10.1016/j.isprsjprs.2013.11.018.

[10] Minár, J., and I.S. Evans, 2008. "Elementary forms for land surface segmentation: the theoretical basis of terrain analysis and geomorphological mapping", Geomorphology 95, 236–259. https://doi.org/10.1016/j.geomorph.2007.06.003.

[11] Bandura, P., Minár, J., and Bielik, M., 2021. "Physically based morphostructural land surface segmentation: Case of the Alps and Western Carpathians", Trans. GIS 25, 2394–2418. https://doi.org/10.1111/tgis.12847.

Enriching LiDAR data with partial derivatives and its uncertainty estimates

Carlos López-Vázquez
LatinGEO Lab IGM+ORT
Universidad ORT Uruguay
Montevideo, URUGUAY
carlos.lopez@pedeciba.edu.uy,
carloslopez@fi365.ort.edu.uy

F. J. Ariza-López
Dpto. Ingeniería Cartográfica, Geodésica y Fotogrametría.
Universidad de Jaén
Jaén, España
fjariza@ujaen.es

J. F. Reinoso-Gordo
Dpto. Expresión Gráfica Arquitectónica y en la Ingeniería
Universidad de Granada
Granada, España
jreinoso@ugr.es

Cite as: López-Vázquez, C., Ariza-López, F. J., Reinoso-Gordo, J. F. (2025). Enriching LiDAR data with partial derivatives and its uncertainty estimates. In: Proceedings of Geomorphometry 2025, 9-13 June, Perugia, Italy. M. Alvioli, L. Melelli, I. Marchesini eds. CNR Edizioni, Rome. ISBN 978-88-8080-765-0. DOI: 10.5281/zenodo.15161376

Abstract— **After some manipulations, raw LiDAR data can be filtered so as to describe the terrain surface or bare ground. The resulting set is composed of (x,y,z) triplets, with some uncertainty in all three dimensions. We want to describe a procedure able to enrich this 3D cloud adding also estimates of partial derivatives with its uncertainty, thus becoming a 7D point. Our theoretical framework assumes that the point cloud is itself error free, and that the uncertainty in the partial derivatives estimate will arise because of the finite spacing between points. Computing the enriched cloud will be a one-time operation. The resulting dataset could be used in many ways, including improving elevation estimates by using higher order Hermite interpolants intended to exploit the derivative values. The uncertainty information might be propagated to the interpolated elevation. The envisioned procedure has contacts with numerical methods for solving partial differential equations. Finite Difference methods rely on a regular grid like the one provided by standard DEMs to produce estimates of the partial derivatives which are functions of the grid size. Finite element methods use a non-regular grid, and its derivative estimates can also be related to some norm of the elements, defined through elaborated topological relationships. Meshless methods use cloud of points not linked in elements, an approach which offers enough flexibility to deal with selected problems in fluid mechanics, where moving boundaries and free surface precludes using rigid meshes. Tools already developed to estimate partial derivatives and its uncertainties can be conveniently reused with the LiDAR cloud dataset, even without a partial differential equation problem involved.**

I. INTRODUCTION

Slope information is used extensively for a wide range of applications, from terrain analysis and hydrological modeling to urban planning, agriculture, engineering, environmental protection, and recreation. By understanding how steep or flat the terrain is, professionals can make more informed decisions about land use, risk management, and infrastructure design. Additionally, slope is often combined with other spatial data to provide a more comprehensive understanding of the landscape. Aspect is also a critical terrain attribute of the terrain and has a wide range of applications across various domains. It is used to model and analyze solar exposure, climate variation, vegetation, agriculture, erosion, hydrology, landslide risk, wildlife habitats, and more. Aspect, in combination with other environmental factors, helps in decision-making processes for resource management, environmental conservation, urban planning, infrastructure design, and outdoor recreation.

Both slope and aspect are examples of functions defined from the first partial derivatives of the terrain surface, which in turn depends on a model of the terrain. The description of the terrain surface (in all its variants: surface, terrain, bathymetry, etc.) has become instrumental in many application fields. The dominant format is the Digital Elevation Model (DEM), which can be loosely defined as a set of elevation values defined over a regular grid. Other possibilities certainly exist: contour lines, triangular irregular networks (TIN), spectral models, etc. All of them have advantages and disadvantages. LiDAR point clouds and TIN data sets have some formal similarities, but we will focus in the LiDAR case. In traditional TIN models each point was measured

and selected carefully in the terrain, reflecting the choices of the surveyor. On the other hand, LiDAR data were produced by fully automated means, with little or no chances to select the point location. Thus, there is room for a more refined treatment. The popularity of LiDAR datasets is growing [1]. Lower instrument costs, affordable and better tools to process the huge number of points, use of UAV and steady increase in computer performance paved the way for this.

There are a number of options to estimate the partial derivatives, but its uncertainty is not very well known. When slope or aspect values are involved in a decision, their uncertainty might need to be known to ascertain their impact on the uncertainty of the decision. The procedure is named sensitivity analysis, and can lead to a non reliable decision if the uncertainty is too high.

Let's assume that the filtered LiDAR data define a cloud of points located over the terrain, while any other early hits for vegetation, power lines, bridges and so were removed. In addition we can restrict ourselves to the case where such points have themselves no positional error. Some interpolation procedure will be required in order to estimate the elevation in other locations. A number of options exist. They are more or less sophisticated, leading to different accuracy estimates for the surface. The simplest one is the nearest neighbor, only exact for constant (horizontal) terrain. A second possibility is the bilinear, which exactly matches elevation and slope provided the terrain is planar. They are examples of first and second order methods (p=1 and p=2), because they are exact interpolators of surfaces defined by polynomials up to degree p-1 but not degree p.

There exist many other methods (bicubic, radial base functions, inverse distance weighting, splines, natural neighbors, kriging, etc.) where the concept of order is not meaningful. The Hermite family is a particular one, and has the property to interpolate not just elevation values but also partial derivatives when they are available. The Shepard method (also known as IDW) is one of them, but there exist also bivariate Hermite, cubic Hermite, Hermite splines, Hermite Radial Base Functions, etc. They produce more accurate estimates of the elevation and slope at the price of using more data and computing time. Once established that there are interest in this we will describe how we plan to enrich a given LiDAR cloud with two first partial derivative estimates and its uncertainty. They comprise 4 extra attributes attached to a 3D point cloud adding up to a 7D point dataset, which might have other attributes as well.

II. CONNECTION TO PARTIAL DERIVATIVE EQUATIONS

All numerical methods for solving Partial Derivative Equations (PDE) follow a similar procedure. Given a set of (x_i,y_i), i=1,...,N locations where the solution value is requested, the first step is to assume that the z_i values are known. Then, some expressions relate the (x_j,y_j,z_j) values of points in the neighborhood of the i-th one to estimates of the partial derivatives at the i-th point. Given such partial derivative estimates, if we impose that they should satisfy the PDE then a set of (usually nonlinear) equations in z_i, i=1,...,N can be established, and the problem turns out to be an algebraic one. All the procedure is well established, carefully analyzed and documented in books [2]. There exist many computer libraries tailored to solving general problems, as well as others devoted to specific PDE e.g. OpenFOAM (https://github.com/OpenFOAM/OpenFOAM-dev), SU2 (https://github.com/su2code/SU2) or deal.II (https://github.com/dealii/dealii). One mandatory requirement for any estimate of the partial derivatives is that their uncertainty can be computed, and can be adjusted to a given tolerance. In a PDE context, this can be achieved by refining the grid, or adding extra locations. The uncertainty estimate of the partial derivative is thus integral part of the procedure, and it is not connected with the specific PDE to solve.

In our case we do not have a PDE to solve, but on the other hand we have no unknowns because we already have the elevation values. So, the partial derivatives estimates can be obtained straightforwardly using such routines. Following common practice, such values come jointly with its (deterministic) uncertainty estimate. In general such values are not deemed to be an error bound, but just a reasonable estimate of its size.

A. Case of regular grids (DEM)

This is the best known case. We are used to Finite Difference approaches, where (for example) a polynomial of second degree is fitted to elevations of points located over a 3x3 window. Depending on which of the 9 points we want to use, we can recover the Evans-Young formula [3], the Horn's one [4], or others intended for estimate first and second partial derivatives. If we need first, second and third partial derivatives we need to use at least a 5x5 window to use the formulae proposed by [5]. The location of the elevations is always over a regular grid, a situation far from the LiDAR case.

Recently [6] show that in this case it is possible to extract not only partial derivative estimates but also its uncertainty. To achieve so he proposed as an option to estimate it following standard practice ([7], [8]) by using two methods of different order. For example this can be done for first partial derivatives with the pair {Evans-Young, Florinsky}, which are examples of methods of order 2 and 4. The uncertainty of the higher accuracy Florinsky's method can be estimated as the absolute value of the difference of the Evans-Young's and Florinsky's values. Similar results hold for the second partial derivatives despite not considered in [9]. However, since Evans-Young's cannot produce estimate of the third partial derivatives, to estimate its uncertainty Florinsky's method needs to be used jointly with an even higher order method when available.

Despite not widely considered in geosciences, it is possible to use the uncertainty value to further refine the method. If at the j-th point the pair {Evans-Young, Florinsky} produces an uncertainty estimate which is too large, it is is possible to switch locally to an even higher order method pair to reduce it at the price of involving a larger neighborhood and more sophisticated methods. This will be explained in the following section.

B. Case of irregularly placed points (LiDAR and TIN)

Neither Florinsky nor Evans-Young can be used with irregularly placed points. None of them produces uncertainty estimates, which is the novelty here. Thus, we propose to reformulate the problem from the beginning. Instead of using Finite Difference methods, we will resort to another less known PDE approach named Meshless methods. They are almost the single alternative to certain PDE problems. For example, problems in fluid mechanics with moving boundaries like free surface flows, or crack propagation in solids. They are very difficult to tackle with rigid meshes, so Meshless methods were designed.

Among other alternatives, we will sketch a basic one denoted strong p-version. Given a neighborhood $J=\{i, j_2, ..., j_k\}$ of the i-th point, for k=3 (k = number of points in the neighborhood including the i-th) we can use points in J to fit a plane that goes to the three points. Then, an estimate of both first partial derivatives are at hand so we have an estimate with p=2. We can then request k=6. With the set J we can estimate a second order polynomial that goes to the six points. New estimates of the first partial derivatives are available, now with p=3. If the absolute difference between $f_{x,(p=2)}$ and $f_{x,(p=3)}$ are below a given tolerance tol we are done. Otherwise, we can request k=9, discard the estimate of p=2 and analyze the difference between $f_{x,(p=3)}$ and $f_{x,(p=4)}$. In general, to attain degree p we will need $k=(p+1)(p+2)/2$ points in the J set. After specifying a tolerance tol, the method increases the smallest p until the uncertainty is below tolerance.

As described the process is very straightforward, and we omit some practical details here. The set J must be unisolvent, i.e. the corresponding Vandermonde matrix should be invertible. Otherwise, a point can be discarded and substituted by another neighbor. The use of polynomials is indeed not the single option, and Radial Basis Functions are also an alternative [8]. Many of these possibilities are considered, however, in mathematical libraries e.g. SciPy, NumPy, Scikit-Learn for the Phyton environment include specific modules for interpolation interpolations and fitting, and we need not to describe it further here. The overall procedure is denoted as the strong form of the p-version of the Meshless methods. Describing other alternatives (weak form, h-version and r-version, etc.) are outside our goal here.

III. ILLUSTRATING THE OPERATION

Fig.1 illustrates the Meshless approach, using a PDE solver of the heat equation. Points are located irregularly in the domain, and its color denotes the order of the approximation locally used to estimate the partial derivatives. At the beginning the approximation is of 2nd order everywhere. The presence of a heat source (red cross in the figure) introduces an irregularity in the problem. This is conceptually similar to a pit in the terrain, or a sharp mountain. Our goal here is to illustrate the procedure by looking at the final solution in Fig. 2. Notice that most of the points, far from the heat source, remain of 2nd order approximation.

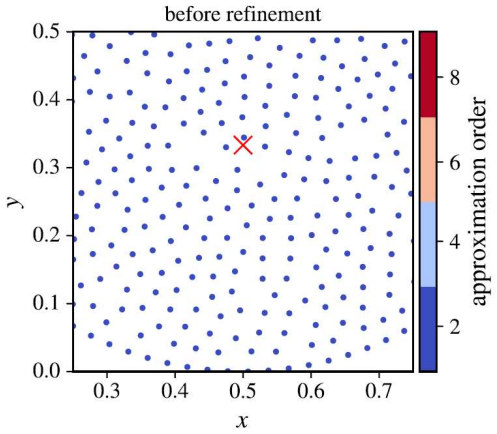

Figure 1. Example of a derivative approximation of variable order. The red cross denotes an irregularity (a heat source) while solving a PDE. Notice that all points are initially blue, corresponding to a derivative approximation with p=2. (from [10])

However, in the vicinity of the source the approximation order was increased attaining even p=8, in order to keep uncertainty below a given tolerance.

The sketched procedure is a simplified version of what needs to be implemented. Many details are omitted, and future works will offer a throughout description. Presently we are considering the use of the MEDUSA package [10] which has libraries suited for the purpose. It implements the strong form of the Meshless method.

The abovementioned procedure can be extended even to DEM. Present day procedures are of fixed order for the whole domain, typically p=2. There is nothing between the choice of the 9 points of a 3x3 window and 25 points of a 5x5 window. Such limitation does not apply to a Meshless method, which can add one point at a time thus using more compact schema. As described, we considered only explicit schemas; there are also implicit ones, able to attain (over regular grids) substantially larger values for p (of the order of p=100).

IV. CONCLUSIONS

Despite we present here work in progress, we feel that the connection with well developed numerical procedures for solving PDE equations is already an interesting contribution. For a PDE is mandatory to keep the partially derivative error estimates under control, so there are provisions to alter either the grid size (for the case of Finite Difference methods over regular grids), or the order of the approximation for the Finite Element method. The former is known as the h-version while the latter is known as the p-version. For the case of LiDAR data sets, the geometry can be appropriately handled through the so-called Meshless method, which is itself an even more flexible approach than the Finite

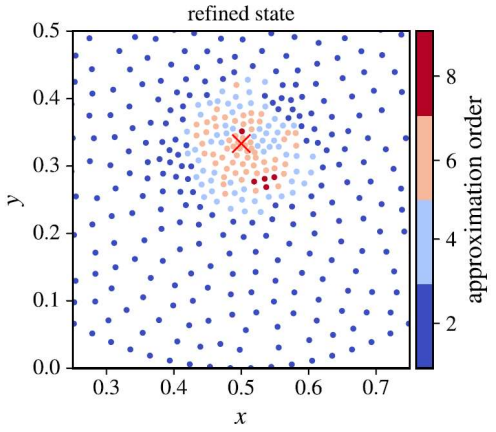

Figure 2. Same set of points than in Fig. 1, but now its color illustrates the local approximation order used in order to keep the uncertainty below a prescribed tolerance. In the neighborhood of the irregularity the order increases up to p=8. (from [10])

Element method. Our assumptions are that the filtered LiDAR data representing base ground is free from positional errors, thus attaching the entire uncertainty estimate to the effect of finite distances between points. Two reasons prevent using the h-version. The first one is that we assume that the LiDAR information is already captured. The second one is that adjusting for the density might introduce scale effects, because closer points describe information not available at other scale. So we plan to compute the partial derivatives using as many as necessary points in the neighborhood chosen to be separated at least a prescribed h distance. The approach is fully deterministic, establishing an interval for the estimates independent of any stochastic assumption of the elevation error surface. On the other hand, it does not provide any cue of the distribution of the likely random error of the derived variables. We plan to use the MEDUSA package [10] on a LiDAR dataset of Andalusia as a case test.

V. ACKNOWLEDGMENTS

This research has been partially funded by the Project: "Point-to-point quality in LiDAR data for Digital Terrain Elevation Models in Engineering" (PID2022-138835NB-I00) funded by MICIU/AEI/10.13039/501100011033/ and FEDER, UE. More information is available online: https://coello.ujaen.es/investigacion/web_giic/P2PQuaLiDEN/ (accessed on 8 January 2025).

REFERENCES

[1] Guth, P. L., and T.M. Geoffroy, 2021. LiDAR point cloud and ICESat-2 evaluation of 1 second global digital elevation models: Copernicus wins. Transactions in GIS, 25, 2245–2261. https://doi.org/10.1111/tgis.12825

[2] Pinder, G. F., 2019. Numerical Methods for Solving Partial Differential Equations: A Comprehensive Introduction for Scientists and Engineers. Wiley. ISBN: 978-1-119-31611-4

[3] Young, M. and Evans, I.S., 1978. Statistical characterization of altitude matrices. Report No. 5, Grant DA-ERO-591-73-G0040. Dept. of Geography, University of Durham, England, 26 pp.

[4] Horn, B.K., 1981. Hill shading and the reflectance map. Proceedings of the IEEE, 69(1), pp.14-47. https://doi.org/10.1109/PROC.1981.11918

[5] Florinsky, I. V., 2009. Computation of the third-order partial derivatives from a digital elevation model. International Journal of Geographical Information Science, 23 (2), 213–231. https://doi.org/10.1080/13658810802527499

[6] López-Vázquez, C., 2022. Uncertainty interval estimates for computing slope and aspect from a gridded digital elevation model. International Journal of Geographical Information Science, 36(8), pp.1601-1628. https://doi.org/10.1080/13658816.2022.2063294

[7] Zienkiewicz, O.C. and Zhu, J.Z., 1987. A simple error estimator and adaptive procedure for practical engineerng analysis. International journal for numerical methods in engineering, 24(2), pp.337-357. https://doi.org/10.1002/nme.1620240206

[8] Jančič, M., Strniša, F. and Kosec, G., 2022, July. Implicit-explicit error indicator based on approximation order. In 2022 7th International Conference on Smart and Sustainable Technologies (SpliTech) (pp. 01-04). IEEE. https://doi.org/10.23919/SpliTech55088.2022.9854342

[9] Jančič, M. and Kosec, G., 2024. Strong form mesh-free hp-adaptive solution of linear elasticity problem. Engineering with Computers, 40(2), pp.1027-1047. https://doi.org/10.1007/s00366-023-01843-6

[10] Slak, J. and Kosec, G., 2021. Medusa: A C++ library for solving PDEs using strong form mesh-free methods. ACM Transactions on Mathematical Software (TOMS), 47(3), pp.1-25. https://doi.org/10.1145/3450966

Global Ensemble Digital Terrain model and parametrization at 1 arc-second resolution

Yu-Feng Ho [1,a], Leandro Parente [1,b], Carlos Henrique Grohmann [2,c], Hannes Isaak Reuter [3,d], John Lindsay [4,e], Tomislav Hengl [1,f]

[1] OpenGeoHub, Doorwerth, the Netherlands

[2] Institute of Astronomy, Geophysics and Atmospheric Sciences, Universidade de São Paulo, São Paulo, Brazil

[3] gisxperts, Trier, Germany

[4] Department of Geography, Environment & Geomatics, University of Guelph, Guelph, Canada

[a] yu-feng.ho@opengeohub.org, [b] leandro.parente@opengeohub.org, [c] guano@usp.br, [d] hannes@gisxperts.de, [e] jlindsay@uoguelph.ca, [f] tom.hengl@opengeohub.org

Cite as: Ho, Y.F., Parente, L., Grohmann, C. H., Reuter, H. I., Lindsay, J., Hengl, T. (2025). Global Ensemble Digital Terrain model and parametrization at 1 arc-second resolution. In: Proceedings of Geomorphometry 2025, 9-13 June, Perugia, Italy. M. Alvioli, L. Melelli, I. Marchesini eds. CNR Edizioni, Rome. ISBN 978-88-8080-765-0. DOI: 10.5281/zenodo.15178621

***Abstract*—This paper describes the first publicly available 1 arc-second global ensemble digital terrain model based on multi-source digital elevation models and its derivative parameters in multiscale (GEDTM30). A machine learning model was built from two global LiDAR datasets (GEDI02 and ICESat-2 ATL08) and two digital surface models (GLO30 and AW3D30). The model was trained by a global parent model using stratified global samples, followed by local child models to adapt diverse landforms. GEDTM30 reaches RMSE 2.74m in built-up area, 6.77m in forest, 3.36m in dense short vegetation. Furthermore, an automated pipeline was built to process the DTM into various land surface parameters, adopting the Equi7 tiling system, and implemented tile overlapping to mitigate border effects. Whitebox Workflows was used for parametrization and for hydrological correction on a large scale. The optimized pipeline allows the data to be updated within 48 hours.**

I. Introduction

In geography, topography or relief are best represented by Digital Elevation Models [1,2]. DEMs are often used to measure the spatial variability in hydrological, geomorphological, and biological processes [3,4]. The need for a global DTM arises from the increasing demand for consistent and seamless terrain. Moreover, the wider user community, most likely requires a single best (ensemble) reference estimate of world elevations and is less interested in the complexity of ellipsoid, noise effects and artifacts. Besides, the facing challenge of land relief parametrization follows the higher resolution DTM product [5,6]. An optimized, scalable automation of parametrization is required to provide the wide user community of environmental research with an up-to-date ensemble DTM product and its parametrization.

This paper aims to bridge the gap of lacking a single consistent, open-source and complete estimation of world topography at 1 arc second and produces two main products: (1) the DTM product based on multi-source high quality world elevation data, and (2) the automated global DTM parametrization process and products from the novel ensemble DTM.

II. Result

A. Production of ensemble DTM

We implemented a direct modeling of the terrain from DSMs to a DTM, fusing DSMs (GLO30 and AW3D30), vegetation object models, artificial object models, optical remote sensing indices and coarser DTM slope. In addition, we adopted a framework to train a "*global-to-local*" model in order to address the global diversity of land covers and landforms. "*Global-to-local*" modeling is a two-step transfer learning training framework: the global model with representative, globally stratified sampling, and the local model inherits the global samples with additional locally stratified sampling (Fig. 1).

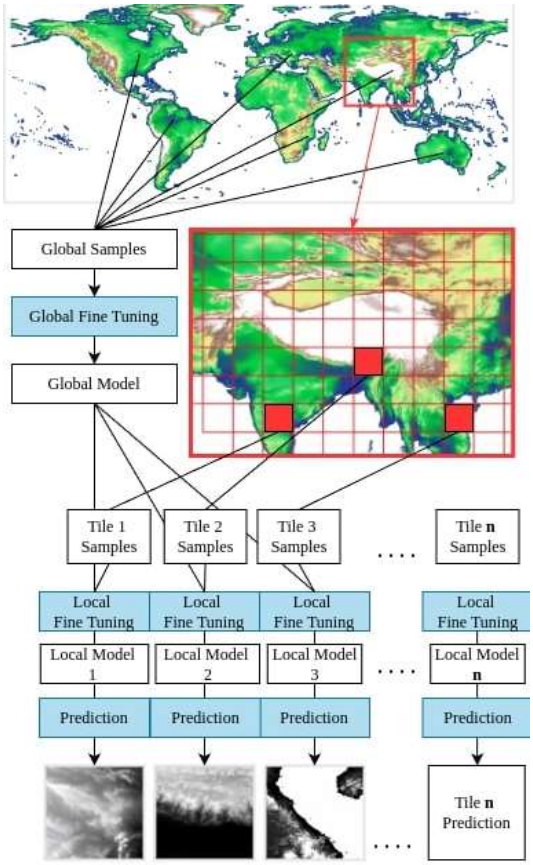

Figure 1. Visual explanation of the "global-to-local" transfer learning modeling. The system consists of M models where M corresponds to the number of tiles: M + 1 global model.

The "*global-to-local*" model preserves the generalization of the global model, but also reinforces the local features to achieve better performance. Figure 2 shows the visual comparison of the global versus "*global-to-local*" model. That additional local training data improves prediction producing a lower difference between the reference model and GEDTM30.

GEDTM30, is compared with the previous EDTM presented in Geomorphometry 2023 [7,8]. We aggregated the pixels from all the reference DTM sites [9] and group them by stable land use and land cover through GLAD Global LULC Change [10]. Table 1 summarizes RMSE, MAE and ME across the land cover. GEDTM30 performs better in all metrics (RMSE, MAE, and ME), notably, ME shows a drop to maximal 1m across in all land covers. These results suggest that GEDTM30 improves the accuracy in diverse land cover types from EDTM, making it a more reliable model for terrain mapping.

B. DTM parametrization Result

We implemented a pyramid-representative DTM parametrization to create multi-scale parameters at 30, 60, 120, 240, 480, 960m resolution. The multiscale process comprises two steps: (1) the DTM is down-scaled to coarse resolution, and (2) the original layer and the down-scaled DTM layers run the DTM parametrization independently (Fig. 3).

Table 1 Accuracy comparison between GEDTM30 and EDTM across different land cover types.

Dataset	Corine	Corine %	RMSE	MAE	ME
EDTM	Cropland, stable	11.3	2.08	1.39	1.03
GEDTM30			1.54	0.93	0.38
EDTM	Built-up, stable built-up	12.5	3.78	2.27	0.57
GEDTM30			2.74	1.74	0.03
EDTM	Terra firma, true desert	5.3	5.31	2.97	1.89
GEDTM30			2.65	1.55	-0.09
EDTM	Terra firma, stable tree cover	15.0	9.90	7.01	2.07
GEDTM30			6.77	4.43	1.02
EDTM	Terra firma, semi-arid	20.3	6.38	3.89	2.44
GEDTM30			3.41	1.98	0.65
EDTM	Terra firma, dense short vegetation	15.9	5.65	3.44	2.27
GEDTM30			3.36	1.91	1.10

To optimize the parametrization, a test was carried out by running the 60m resolution parametrization for all tiles. The processing time for each tile was recorded. Figure 5 illustrates the average individual and cumulative processing time of DTM parametrization in 60m resolution. According to Fig. 4, breaching depression takes the longest average processing time at 194 seconds per tile and the topographic wetness index takes the shortest to complete at the average processing time of 5 seconds. The complete computational workflow averages 742 seconds per 600 km by 600 km Equi7 tile at 60 m resolution. Extrapolating

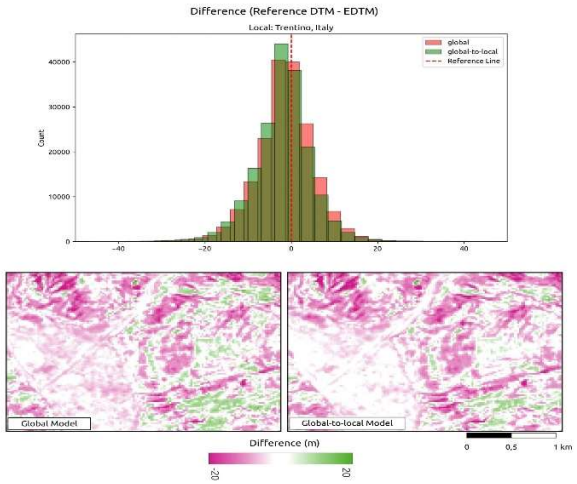

Figure 2. Improvement of terrain modeling by a "*global-to-local*" model. Location shown: Trentino, Italy.

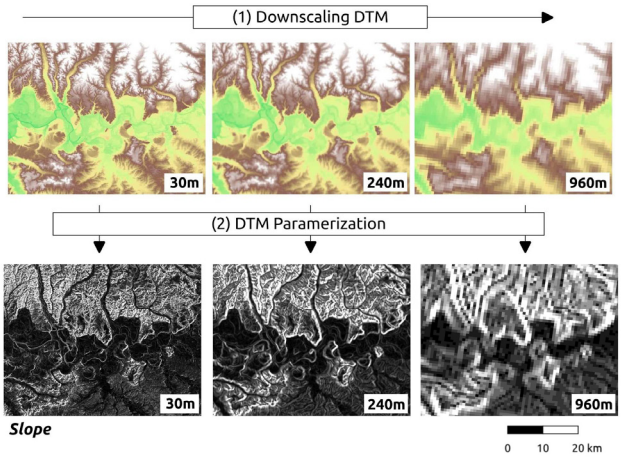

Figure 3. Pyramid representation of DTM parametrization. Above: GEDTM30 at three scales; below: corresponding slope maps generated using WhiteboxTools.

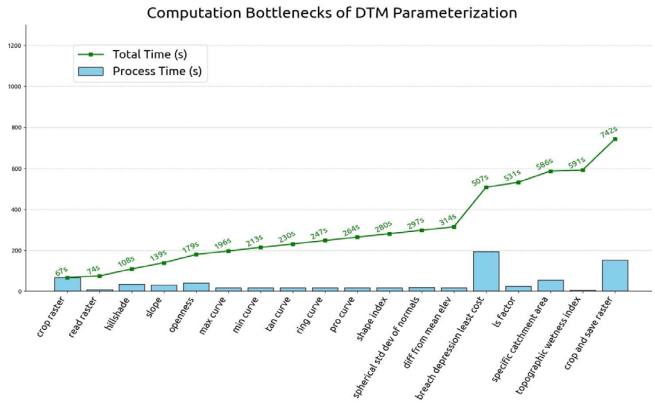

Figure 4. Individual and cumulative processing times for DTM parametrization at 60 m resolution, averaged across all tiles.

from this, a 30 m resolution parametrization is estimated to complete within a day, using 1,344 CPUs on 14 servers equipped with 1 TB of RAM each and connected to S3 storage servers with InfiniBand. Using this infrastructure, the possible update for the multi-resolution parameters can be completed in less than 48 hours.

A total of 15 land surface parameters (LSPs) from GEDTM30 are produced, including hillshade, slope in degree, negative openness, positive openness, profile curvature, minimal curvature, maximal curvature, tangential curvature, ring curvature, shape index, ls factor, difference from mean elevation, spherical standard deviation of normals, specific catchment area and topographic wetness index. Figure 5 is the example of all of the parameters in 1 arc sec resolution at Volcano National Park, the border of Rwanda, Uganda and Democratic Republic of the Congo (DRC).

Figure 6 additionally illustrates the pyramid representation of the topographic wetness index (TWI) at different resolutions (30 m, 60 m, 120 m, 240 m, 480 m, and 960 m) in the Jhuoshuei River Basin, central Taiwan. The representation of the TWI pyramid in the alluvial plain highlights how the channel size and the distinctiveness of the cells evolve with increasing resolution. In the flat plain region shown in Fig. 6, the 30m resolution TWI clearly differentiates between wet and dry pixels. As the size of the grid increases, the primary channel becomes more prominent and by the coarsest resolution (960m), the flat plain exhibits a nearly uniform wetness distribution. This multiscale TWI representation effectively captures a gradient spatial variability of wetness.

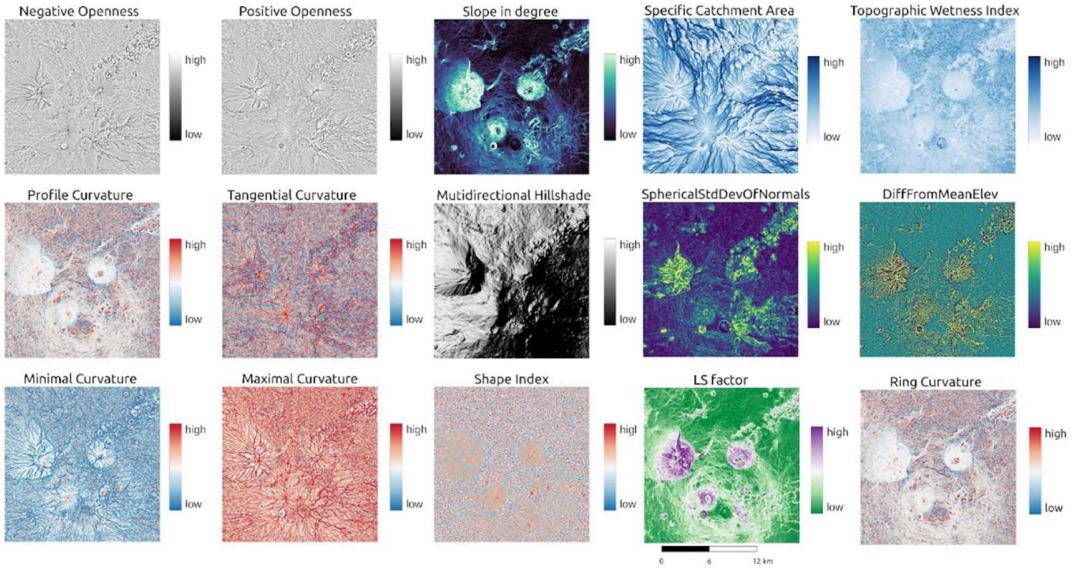

Figure 5. 15 land surface parameters derived from GEDTM30 in Volcano National Park, Uganda, Rwanda, and DRC

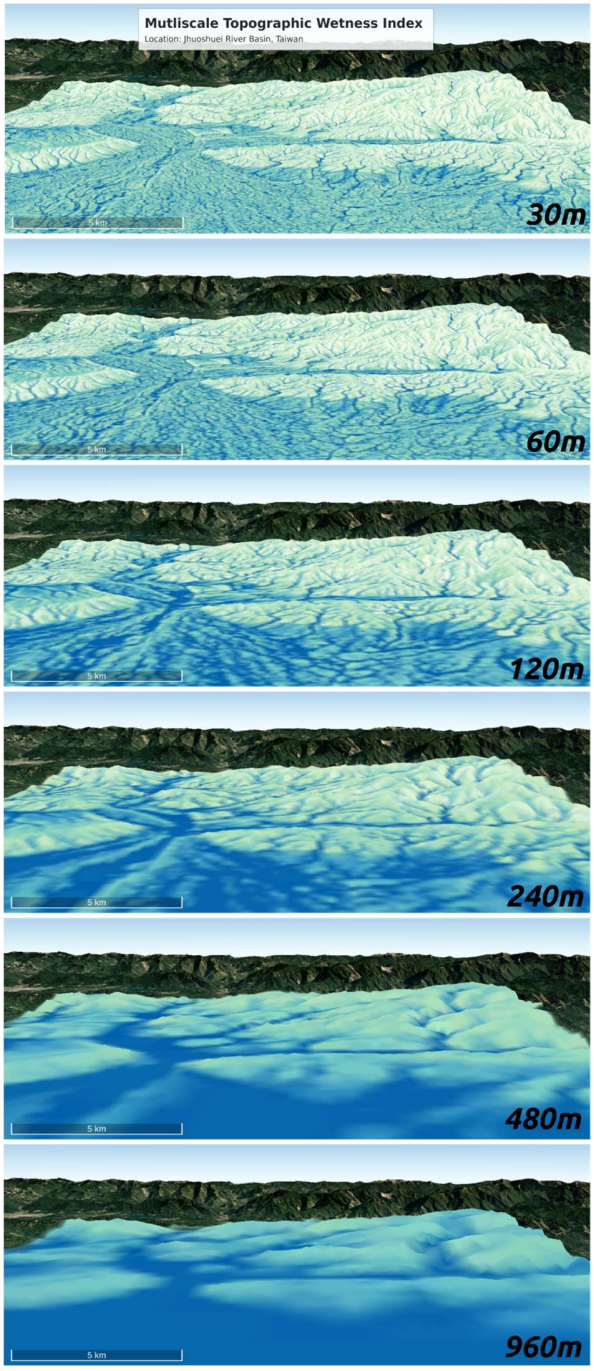

Figure 6. Mutli-scale topographic wetness index in Jhuoshuei River Basin at centre Taiwan

Ultimately, GEDTM and multi-scale LSPs results are produced in single files for each parameters in Cloud Optimized GeoTIFF (COG) and published under permissive license CC-BY 4.0 in Zenodo [11] and registered in OpenLandMap STAC (https://stac.openlandmap.org). Code and documentation to support reproducibility is distributed at GitHub (https://github.com/openlandmap/GEDTM30).

ACKNOWLEDGMENTS

The authors first met in Geomorphometry 2023 in Iași, Romania (Thanks for The International Society for Geomorphometry). Back in the time, the demand of a single open-source global digital terrain model was raised and emphasized. From then on, we kicked off the project of mapping global terrain models and parameters. The work is mainly supported by The Open-Earth-Monitor Cyberinfrastructure project, which has received funding from the European Union's Horizon Europe research and innovation programme under grant agreement No. 101059548, and CHG supported by FAPESP grant #2023/1197-1 and CNPq grant #311209/2021-1.

REFERENCES

[1] Hengl, T., & Reuter, H. I. (2008). Geomorphometry: Concepts, Software, Applications (Vol. 33; T. Hengl & H. I. Reuter, Eds.). Amsterdam: Elsevier.

[2] Guth, P. L., Van Niekerk, A., Grohmann, C. H., Muller, J.-P., Hawker, L., Florinsky, I. V., . . . others (2021b). Digital elevation models: Terminology and definitions. Remote Sensing, 13(18), 3581.

[3] Moore, I. D., Grayson, R., & Ladson, A. (1991). Digital terrain modelling: a review of hydrological,geomorphological, and biological applications. Hydrological processes, 5(1), 3–30. doi: 10.1002/hyp.3360050103

[4] Pike, R. J., Evans, I. S., & Hengl, T. (2009). Chapter 1. Geomorphometry: a brief guide. In T. Hengl & H. I. Reuter (Eds.), Geomorphometry: Concepts, software, applications (Vol. 33, pp. 3–30). Amsterdam: Elsevier. doi: 10.1016/S0166-2481(08)00001-9

[5] Amatulli, G., McInerney, D., Sethi, T., Strobl, P., & Domisch, S. (2020). Geomorpho90m, empirical evaluation and accuracy assessment of global high-resolution geomorphometric layers. Scientific Data, 7(1), 162. doi: 10.1038/s41597-020-0479-6

[6] Amatulli, G., Garcia Marquez, J., Sethi, T., Kiesel, J., Grigoropoulou, A., ¨Ublacker, M. M., . . . Domisch, S. (2022). Hydrography90m: A new high-resolution global hydrographic dataset. Earth System Science Data, 14(10), 4525–4550. doi: 10.5194/essd-14-4525-2022

[7] Yu-Feng HO, Tomislav Hengl, & Leandro Parente. (2023, April 28). A Simply Updatable Cloud-based Ensemble Digital Terrain Model. doi: 10.5281/zenodo.7877509

[8] Yu Feng HO, Tomislav Hengl, & Leandro Parente. (2023). Ensemble Digital Terrain Model (EDTM) of the world (1.1) [Data set]. Zenodo. doi: 10.5281/zenodo.7634678

[9] Guth, P. L., Riazanoff, S., Corseaux, A., Grohmann, C., Trevisani, S., & López-Vázquez, C. (2023, June). Demix 1" reference dems version 2.0. Zenodo. doi: 10.5281/zenodo.80868

[10] Potapov, P., Hansen, M. C., Kommareddy, I., Kommareddy, A., Turubanova, S., Pickens, A., . . . Ying, Q. (2020). Landsat analysis ready data for global land cover and land cover change mapping. Remote Sensing, 12(3), 426. doi: doi.org/10.3390/rs12030426.

[11] Ho, Y., & Hengl, T. (2025). Global Ensemble Digital Terrain Model 30m (GEDTM30) (Version v20250130) [Data set]. Zenodo. doi: 10.5281/zenodo.14900180

Innovative Terrain Mapping: A Comparison of Drone and iPhone + viDoc Techniques

Alessandra Vinci
Department of Agricultural, Food and Environmental Science
University of Perugia
Perugia, Italy
alessandra.vinci@unipg.it

Raffaella Brigante
Department of Engineering
University of Perugia
Perugia, Italy
raffaella.brigante@unipg.it

Laura Marconi
Department of Engineering
University of Perugia
Perugia, Italy
laura.marconi@unipg.it

Sara Zollini
Dept. of Civil, Construction-Architectural & Environmental Engineering
University of L'Aquila
L'Aquila, Italy
sara.zollini@univaq.it

Cite as: Vinci, A., Brigante, R., Marconi, L., Zollini, S. (2025). Innovative Terrain Mapping: A Comparison of Drone and iPhone + viDoc Techniques. In: Proceedings of Geomorphometry 2025, 9-13 June, Perugia, Italy. M. Alvioli, L. Melelli, I. Marchesini eds. CNR Edizioni, Rome. ISBN 978-88-8080-765-0. DOI: https://doi.org/10.5281/zenodo.15172921

Abstract—**This study presents a comparison of two different surveying methodologies aimed at terrain modeling. The first approach involved a drone equipped with multispectral sensors, while the second utilized an iPhone combined with the viDoc RTK Rover for data acquisition, which enables the creation of high-accuracy 3D models by generating geo-referenced images in real time. The comparison was possible thanks to precise georeferencing, achieved by performing NRTK (Network Real Time Kinematic) surveys of control points placed near the area of interest and visible in both drone and iPhone-acquired images. The difference between the two-point clouds was evaluated by performing point-to-point distance comparisons, while digital elevation models (DEMs) were compared in a GIS environment using pixel-by-pixel subtraction. The analysis revealed that the differences in point positions between the two surveys were within a few centimeters, with variations primarily attributed to sensor and environmental factors. Similarly, the elevation differences between the DEMs were also in the centimeter range, indicating high precision in both methods. These findings demonstrate that both technologies can provide accurate terrain models, with minor differences that are typically within the acceptable range for many precision agriculture and land management applications. The results underscore the strengths and limitations of each technology, offering insights into their practical applicability for field surveying.**

I. Introduction

Terrain modeling is a crucial aspect for the monitoring of environmental changes due to natural (such as soil erosion) and anthropic causes (such as tillage). Recently, [1] compared the capability of a drone equipped with a multispectral sensor to that of Terrestrial Laser Scanning (TLS) for assessing interrill soil erosion in agricultural plots under different soil management practices, leveraging the multispectral sensor's ability to distinguish vegetation within the plots. The first results showed a good performance of multispectral drone. Therefore, [2] tested the effects of the vegetation on the morphological reconstruction of the surface. The study showed that the presence of a crop could negatively affect the terrain model.

Other studies, instead, have compared UAV photogrammetry surveys with airborne and terrestrial laser scanning surveys to obtain high-resolution elevation data for monitoring terrain changes. [3, 4].

This paper aims to test a new rapid and low-cost method for terrain surveying, comparing it with the commonly used approach of UAV photogrammetry for this type of investigation. A viDoc RTK rover by Pix4D, integrated with an Apple iPhone 15 Pro Max, was used to model the survey area and was compared to a UAV-based method. Currently, the main applications of this system are in the field of cultural heritage [5, 6]. Only a few

studies have been conducted in other sectors, such as road mapping [7, 8], environmental surveying [9], and to test the accuracy of the instruments [10]. The goal of this work is to assess the use of the viDoc RTK rover in terrain mapping for small-scale agricultural and hydraulic applications, as an alternative to UAV-based methods.

II. Materials and Methods

A. Study area

The study was conducted at SERLAB, the experimental site of the University of Perugia's Department of Agricultural, Food, and Environmental Sciences, located 20 km south of Perugia in Umbria, central Italy. The site includes ten plots (dimensions: 8 × 22 m, 4 × 22 m, 4 × 11 m, and 2 × 11 m) aligned with the 16% maximum slope. The soil, classified as Calcaric Cambisol with a silty-clay-loam texture, is monitored for runoff and soil loss after erosive events (events producing measurable runoff). Hydraulic boundaries, made of galvanized steel sheets embedded 0.25 m into the soil and reinforced with metal stakes, direct runoff into storage tanks for measurement. Precipitation data are recorded at 5-minute intervals. For this study, six plots were surveyed using UAV photogrammetric techniques and an integrated iPhone + viDoc approach, both conducted simultaneously in November 2024 (Figure 1). The land had been previously prepared, and at the time of the survey, it exhibited scattered vegetation. To georeference the surveys, 14 checkerboard targets (GCPs – Ground Control Points) positioned around the plots were surveyed using GNSS technique in NRTK mode with a Topcon Hiper HR receiver.

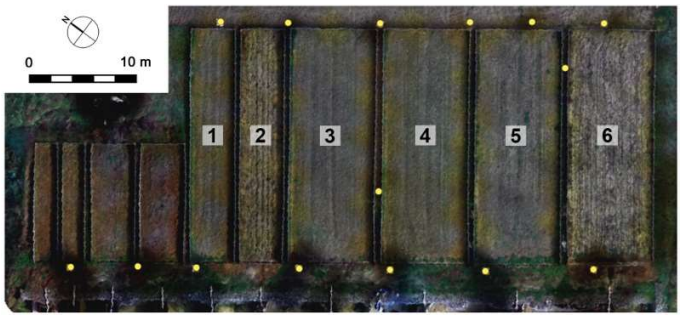

Figure 1. Study area and GCPs position (yellow points)

B. Photogrammetric UAV survey

Image acquisition was performed using a DJI Phantom 4 RTK Multispectral UAV (including six ½.9-inch CMOS sensors: one for RGB imaging and five covering spectral bands blue, green, red, red edge, and near-infrared) (Figure 2a). A sunlight sensor on the UAV adjusts for real-time irradiance, enhancing data accuracy. An integrated D-RTK GNSS receiver ensures centimeter-level camera positioning accuracy. Flight planning, executed via DJI GSPro on an Apple iPad, used a polygon grid at 10 m altitude, with 75% image overlap and a speed of 2 m/s in "Hover & Capture" mode. A total of 425 images were acquired with a GSD (Ground Sample Distance) of 0.5 cm/pixel. The DJI D-RTK2 GNSS receiver provided additional accuracy, supporting multiple satellite systems (GPS, BEIDOU, GLONASS, and Galileo) for stable performance in diverse conditions.

C. Iphone + viDoc survey

The survey was also conducted using an Apple iPhone 15 Pro Max equipped with the viDoc RTK Rover (Figure 2b). The viDoc RTK Rover is a German-designed GNSS rover that includes an RTK antenna and is specifically designed to be compatible with Apple devices equipped with LIDAR sensors. When combined with the Pix4Dcatch app, it enables the creation of high-accuracy 3D models by generating RTK-accurate, geo-referenced images in real time. Each plot was surveyed individually by manually moving the equipment around it in a full loop. For every plot, an average of 398 images were acquired.

a b

Figure 2. DJI Phantom4 Multispectral (a) and Apple iPhone 15 Pro Max with viDoc RTK Rover (b)

D. Point clouds and DEMs generation

The 425 UAV-acquired images were processed using Agisoft Metashape Professional (v.1.7.5) with the Structure from Motion (SfM) photogrammetric method. Of the 14 targets surveyed, 10 were used as Ground Control Points (GCPs), while the remaining 4 served as Check Points (CPs). The resulting point clouds contained approximately 200 million points, with an average of around 135000 points per m^2. The average error was 0.030 m on the GCPs and 0.046 m on the CPs positions. The reconstruction of data acquired with iPhone + viDoc was performed using Pix4Dmatic software. A dense point cloud can be generated from the RGB images, while the depth map can be obtained from the LiDAR data. The two datasets were then unified into a single fused point cloud obtaining an average of approximately 235000 points per m^2. For consistency with the point cloud generated from the UAV survey, the same 14 targets were used to georeference the cloud obtained from the iPhone data, with an average error of 0.024 m on the GCPs and 0.038 m on the CPs positions. Both point clouds generated from the two surveys were subjected to a noise reduction filter, which was particularly necessary due to the presence of grass in the plots, a likely contributor to the noise,

especially in the iPhone-derived clouds. For subsequent analysis, the plots were aligned and clipped to the same shape, removing the edges where the weeds were most dense (Figure 3).

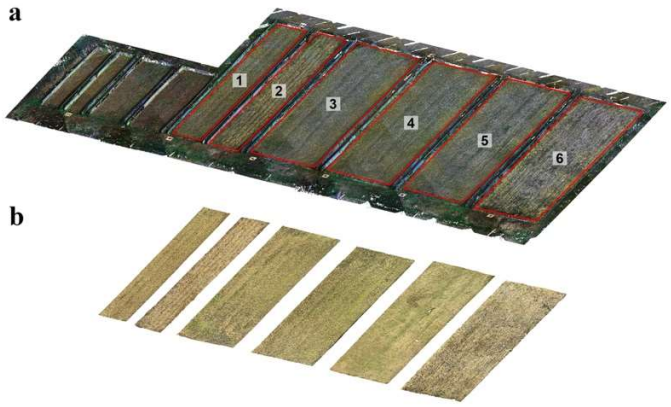

Figure 3. Point clouds with RGB values obtained by UAV (a) and iPhone+viDoc (b)

Both point clouds obtained from UAV and iPhone + viDoc surveys were processed with Cloud Compare (v.2.13) to generate raster-based Digital Elevation Models (DEMs) with 1 cm of resolution.

E. Comparison between point clouds and DEMs

To evaluate the differences between the two surveys (drone-based and iPhone + viDoc), point cloud comparisons were performed using Cyclone 3DR software, leveraging the "cloud-to-cloud" inspection tool to assess spatial discrepancies and quantify variations between the datasets. The comparison considered both the three-dimensional positions of the points and their discrepancy along the three axes (N, E, H). In addition, Digital Elevation Models (DEMs) derived from both methods were compared through a pixel-by-pixel subtraction performed in QGIS. This method allowed for the identification of localized variations and overall trends in terrain representation between the two survey techniques.

III. RESULTS AND DISCUSSIONS

Figures 4 and 5 show the results of the comparison between the two point clouds and the two DEMs, derived from UAV and viDoc data, respectively. In the first case, since the evaluation was based on the distance to the nearest points between the two point clouds, only positive differences are observed. In contrast, the DEMs comparison was performed through pixel-by-pixel subtraction, resulting in both positive and negative values.

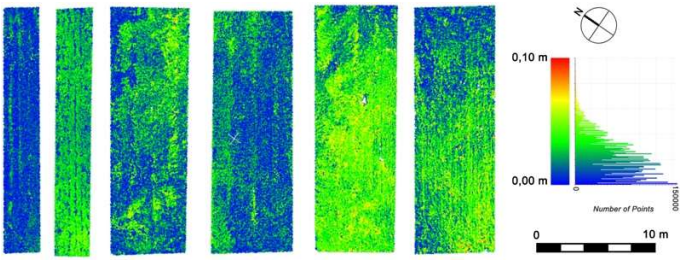

Figure 4. Comparison between UAV and iPhone+viDoc point clouds (3D)

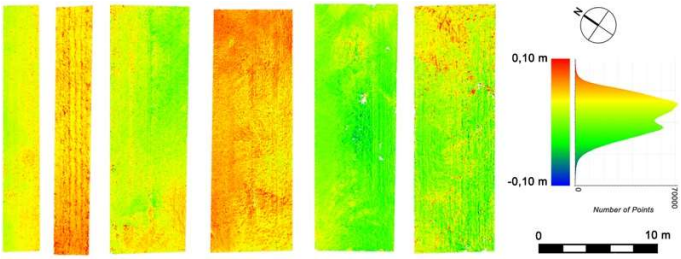

Figure 5. Difference between DEMs obtained by UAV and Iphone+viDoc

In Table I the differences (m) obtained from the "cloud-to-cloud" comparison between the point clouds derived from UAV and iPhone+viDoc surveys, considering the 3D points position, are reported. The monitored plots result coupled, i.e. the plot 4 could be considered the replicated of the plot 1 (same dimension, same slope and the same soil management), so the results can be analyzed considering the similar plots (plot 6 vs plot 2, plot 1 vs plot 4 and plot 5 vs plot 3). The statistical parameters of the differences showed a good accordance between the plot 6 and 2 and the plot 5 and 3. For the plot 1 and 4 more differences are found.

TABLE I. STATISTICAL DIFFERENCES (M) (MEAN, 10TH PERCENTILE AND 90TH PERCENTILE) DERIVED FROM THE COMPARISON CLOUDS TO CLOUDS BETWEEN UAV AND IPHONE+VIDOC POINT CLOUDS

Cloud to cloud (3D positions)	**3D points position Differences (m)**					
	Plot 1	***Plot 2***	***Plot 3***	***Plot 4***	***Plot 5***	***Plot 6***
Mean	0.018	0.019	0.016	0.033	0.019	0.020
10th percentile	0.005	0.003	0.002	0.010	0.003	0.003
90th percentile	0.031	0.034	0.033	0.054	0.041	0.041

In Table II the differences (m) obtained from the Z-axis (elevation) comparison between the point cloud derived from UAV and iPhone+viDoc surveys were reported. This comparison was reported to evaluate the effect of the DEM interpolation on the elevation differences.

In Table III the differences (m) obtained from the DEMs derived from UAV and iPhone+viDoc surveys are reported.

TABLE II. STATISTICAL DIFFERENCES (M) (MEAN, 10TH PERCENTILE AND 90TH PERCENTILE) DERIVED FROM THE COMPARISON CLOUD TO CLOUD ALONG THE Z-AXIS (ELEVATION) BETWEEN UAV AND IPHONE+VIDOC POINT CLOUDS

Cloud to cloud (Z-axis)	Points positions Differences (m) along Z-axis					
	Plot 1	*Plot 2*	*Plot 3*	*Plot 4*	*Plot 5*	*Plot 6*
Mean	0.017	0.031	0.004	0.032	-0.014	-0.001
10th percentile	0.001	0.008	-0.022	0.007	-0.040	-0.032
90th percentile	0.031	0.051	0.030	0.054	0.011	0.031

TABLE III. STATISTICAL DIFFERENCES (M) (MEAN, 10TH PERCENTILE AND 90TH PERCENTILE) DERIVED FROM THE COMPARISON DEMS OBTAINED BY UAV AND IPHONE+VIDOC

DEMs	Elevation Differences (m)					
	Plot 1	*Plot 2*	*Plot 3*	*Plot 4*	*Plot 5*	*Plot 6*
Mean	0.021	0.039	0.007	0.040	-0.017	-0.003
10th percentile	0.009	0.025	-0.016	0.021	-0.039	-0.033
90th percentile	0.032	0.055	0.030	0.057	0.005	0.026

Comparing Tables II and III, it is demonstrated that considering DEMs or Z-axis differences have no influence on the final result as the obtained values are comparable. The mean values are around 2 centimeters for all plots when considering the 3D positions, while the DEM differences reach a maximum of 4 centimeters. Even if higher, both comparisons show mean values comparable to measurement errors.

IV. CONCLUSIONS

In conclusion, the tested methodology proved to be a valid tool for agricultural applications, especially those involving terrain modeling or, for example, the definition of geometric characteristics of vegetation. The 3D models obtained through viDoc survey are characterized by high accuracy and resolution and are already metrically corrected, with proper scale and orientation. In particular, the use of NRTK corrections enables the creation of a model that is directly georeferenced in a global reference system with centimeter-level accuracy. Apart from being less expensive compared to traditional ground measuring equipment, the main advantage of using the viDoc RTK rover integrated with an Apple smartphone is the ability to combine RGB and LiDAR data in a single, small, handheld, and lightweight device, thus optimizing both data acquisition and processing time. Therefore, for small areas, as demonstrated in the presented case study, the use of the viDoc RTK rover can be particularly valuable for fast surveys. Additionally, unlike drone flights, it is not subject to regulatory constraints related to operator permits and specific areas. However, it should be noted that for larger areas, a traditional UAV survey is always recommended. The first important result showed that the presence of vegetation influences the quality of the point clouds by introducing higher level of noise. This situation can be worsened due to the wind effect. What was also noticed is that the presence of metal around the plots generates multiple reflections especially when it comes to Lidar reconstruction. This is why a good practice is removing a small buffer around metal objects. The different sizes of the analyzed plots seem not to have any impact on the results. In fact, the differences are around a few centimeters, in accordance with the measurement errors.

V. ACKNOWLEGMENTS

The study was financed by European Union-Next-GenerationEU-National Recovery and Resilience Plan (NRRP)–MISSION 4 COMPONENT 2, INVESTIMENT N. 1.1, CALL PRIN 2022 D.D. 104 02-02-2022–(Soil Conservation for sustainable AgricuLture in the framework of the European green deal-SCALE) CUP N. J53D23010340006.

REFERENCES

[1] Vinci, A., Brigante, R., Vergni, L., Tosti, G., Marconi, L. Innovative technologies for monitoring interrill erosion, in L. Sartori et al. (Eds.): MID-TERM AIIA 2024, Lecture Notes in Civil Engineering, 586, pp. 1-9, 2025. https://doi.org/10.1007/978-3-031-84212-2_1

[2] Vinci, A., Brigante, R., Vergni, L. in press. Soil loss estimation under different soil management using a multispectral UAV, 2024 IEEE Workshop on Metrology for Agriculture and Forestry (MetroAgriFor), Padova, Italy.

[3] Grohmann,C. H., Garcia, G. P. B., Affonso, A. A., Albuquerque, R. W., 2020. Dune migration and volume change from airborne LiDAR, terrestrial LiDAR and Structure from Motion-Multi View Stereo, Computers & Geoscience, Volume 143, 104569, ISSN 0098-3004, https://doi.org/10.1016/j.cageo.2020.104569.

[4] Guisado-Pintado, E., Jackson, D. W. T., Rogers, D. 2018. 3D mapping efficacy of a drone and terrestrial laser scanning over a temperate beach-dune zone. Geomorphology, Volume 328, pp. 157-172, ISSN 0169-555X, https://doi.org/10.1016/j.geomorph.2018.12.013.

[5] Rapuca A. and Matoušková E, 2023. Testing of close-range photogrammetry and laser scanning for easy documentation of historical objects and buildings parts. Stavební Obzor - Civil Engineering Journal, 32(4), 504-518. https://doi.org/10.14311/CEJ.2023.04.0038

[6] Aksoy, E., 2025. Determining the usability of the viDoc device, which integrates with smart phones, in documenting historical structures. Measurement, 242, Part D, 116156, ISSN 0263-2241. https://doi.org/10.1016/j.measurement.2024.116156

[7] Suleymanoglu, B., Tamimi, R., Yilmaz, Y., Soycan, M., and Toth, C., 2023. Road infrastructure mapping by using iPhone 14 pro: an accuracy assessment. Int. Arch. Photogramm. Remote Sens. Spatial Inf. Sci., XLVIII-M-1-2023, 347–353. https://doi.org/10.5194/isprs-archives-XLVIII-M-1-2023-347-2023

[8] Tamimi, R. and Toth, C., 2023. Performance assessment of a mini mobile mapping system: iPhone 14 Pro installed on a e-scooter. Int. Arch. Photogramm. Remote Sens. Spatial Inf. Sci., XLVIII-M-3-2023, 307–315, https://doi.org/10.5194/isprs-archives-XLVIII-M-3-2023-307-2023

[9] Chauvin, S., 2023. Water Table Height and Microtopography in Swamps of Southeastern Michigan as Influences of Black Ash Tree Establishment and Survival in the Presence of Emerald Ash Borer. Honors College Theses. 80. https://digitalcommons.wayne.edu/honorstheses/80

[10] Tamimi, R., Relative accuracy found within iPhone data collection, 2022. Int. Arch. Photogramm. Remote Sens. Spatial Inf. Sci., XLIII-B2-2022, 303–308. https://doi.org/10.5194/isprs-archives-XLIII-B2-2022-303-2022

Machine Learning Model Transferability for Urban Point Cloud Classification: A Study of Random Forest and XGBoost across Datasets

Pedro Alberto Pereira Zamboni [1], Hanne Hendrickx [2], and Anette Eltener [3]

Institute of Photogrammetry and Remote Sensing
Dresden University of Technology
Dresden, Germany

[1] pedro.zamboni@tu-dresden.de, [2] hanne.hendrickx@tu-dresden.de, [3] anette.eltner@tu-dresden.de

Cite as: Zamboni, P. A. P., Hendrickx, H., Eltener, A. (2025). Machine Learning Model Transferability for Urban Point Cloud Classification: A Study of Random Forest and XGBoost across Datasets. In: Proceedings of Geomorphometry 2025, 9-13 June, Perugia, Italy. M. Alvioli, L. Melelli, I. Marchesini eds. CNR Edizioni, Rome. ISBN 978-88-8080-765-0. DOI: 10.5281/zenodo.15275413

Abstract— **The increasing availability of point cloud data from platforms such as Uncrewed Aerial Vehicles (UAVs) has facilitated urban mapping and analysis. However, the transferability of machine learning models trained on different point cloud datasets remains an open challenge. This study evaluates the transferability of two random forest and XGBoost, for urban point cloud classification across different datasets. Two datasets were used, a photogrammetry and a LiDAR dataset. The LiDAR dataset was used for training and the photogrammetry to assess model transferability. XGBoost outperformed random forest in both benchmark and unseen photogrammetric datasets, with facades and roofs showing the best transferability. The study highlights the need for larger annotated datasets and improved model generalization for robust urban point cloud classification.**

I. Introduction

Urban centers and cities are characterized by their complexity and constant evolution, driven by human activity. Mapping these environments is essential for various applications, such as flood modeling (Zamboni et al., 2024). Point clouds play a pivotal role in understanding urban environments, serving as a valuable tool for detecting, delineating, and mitigating issues associated with urbanization (Stilla and Xu, 2023). The increasing accessibility of data collection platforms, such as Uncrewed Aerial Vehicles (UAVs), has led to a significant reduction in the cost and time required for acquiring raw point cloud data. However, to generate meaningful data, it is essential to incorporate semantic information into the raw point cloud.

Machine learning has been extensively employed in a range of data processing tasks. In the context of 3D point cloud semantic segmentation, supervised machine learning and deep learning approaches have garnered significant attention. Within a vast array of models, decision tree-based methods, such as random forest and XGBoost, have demonstrated competitive performance in comparison to deep learning approaches for urban point cloud segmentation (e.g. Kölle et al., 2021), while exhibiting a comparatively uncomplicated structure and reduced computational demands. However, the scarcity of large-scale labeled datasets has posed a significant challenge in the adoption of supervised machine learning methods.

Compared to image annotations, 3D labelling is more difficult and demanding. Thus, benchmark point cloud datasets usually cover only small areas. Moreover, across available open datasets, there is a high discrepancy between hand annotated classes. This discrepancy can render such datasets domain-specific, thereby limiting the generalizability of models trained on these datasets.

The objective of this study is to assess the transferability of random forest and XGBoost machine learning models across diverse datasets. We trained both machine learning models using the H3D benchmark dataset (Kölle et al., 2021). Subsequently, the performance of these models on the semantic segmentation task in a novel and unseen test dataset was assessed.

II. Material and Methods

A. Study area and photogrammetry dataset

We conducted UAV flights in a small urban area in the southern region of Germany using a DJI Matrice 300RTK with a P1 full-frame camera (35 mm focal length and 4.4 µm pixel pitch). The flight height was set at 120 meters, which resulted in a ground sampling distance (GSD) of 1.47 centimeters. A total of 341

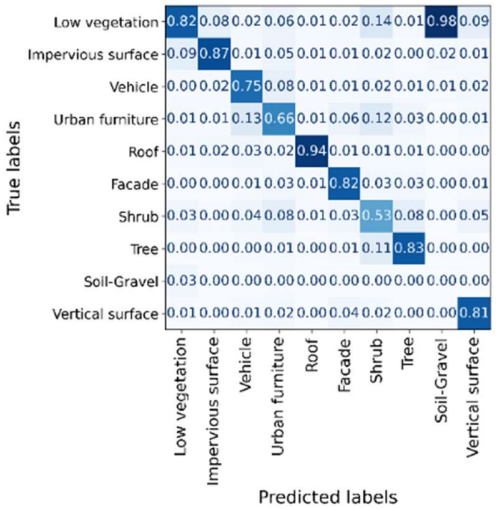

Figure 1. Confusion matrix (normalized by column) for the random forest model on the H3D dataset.

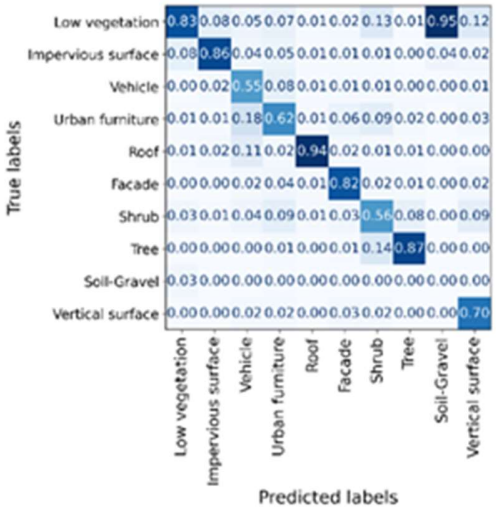

Figure 2. Confusion matrix (normalized by column) for the XGBoost model on the H3D dataset.

images were collected, with a side and forward overlap of 70%. The generation of the photogrammetry point cloud was achieved through the implementation of Structure from Motion and Multi-View Stereo techniques. The generation of the point cloud was facilitated by the utilization of nine ground control points (GCP) and twelve permanent structures (e.g., manholes) that served as checkpoints (CP), yielding a root mean square error (RMSE) of 2 cm. A segment of the comprehensive point cloud was manually labeled encompassing about 30 million points (about 31% of the total number of points). For the labelling, we considered the same classes as in the H3D dataset (Kölle et al., 2021), except for the chimney class. Hereinafter referred to as a photogrammetry dataset.

B. H3D benchmark dataset

The H3D dataset was proposed by Kölle et al. (2021). The data was collected using an UAV equipped with LiDAR, in conjunction with two oblique-looking cameras. The flight height was set at 50 meters, which resulted in a GSD of 1.5 to 3 centimeters. The resulting dataset offers a high-dense point cloud, with 800 points per square meter. In addition to the XYZ coordinates, the dataset encompasses LiDAR features, including echo number and reflectance. Additionally, the RGB color information was made available. The March 2019 Epoch was selected for analysis due to its comprehensive coverage of the area and the capture of data under close-to-optimal flight conditions. The dataset contains eleven classes: low vegetation, impervious surface, vehicle, urban furniture, roof, facade, shrub, tree, soil/gravel, vertical surface, and chimney. Different from the photogrammetry dataset, the H3D dataset was captured with a LIDaR, therefore, presenting different intrinsic characteristics. We selected a subset of points from the train and validation sets of the March 2019 epoch of the H3D dataset. A random grid subsampling technique was employed to extract a subset of points from the original, high-density point cloud. The train set was divided into two subsets: one used for model training and the other to assess the training performance. The validation set from the H3D dataset was utilized to evaluate the models.

C. Random forest and XGBoost

Random forest and XGBoost are tree-based ensemble machine learning algorithms. However, they present key architecture differences. Random forest employs a bagging technique, where individual trees are trained in parallel, using a subset of the training dataset. This method takes the prediction of each tree and based on the majority vote of predictions, makes the final predictions. On the other hand, XGBoost applies a bosting technique, where trees are built sequentially to correct errors of previous trees. It builds multiple decision trees sequentially, correcting errors at each step to improve accuracy while incorporating regularization to prevent overfitting. The number of trees and their depth are key hyperparameters for both Random Forest and XGBoost, directly affecting model complexity and performance. Number of trees controls how many decision trees are used, while depth determines how many splits each tree can make, influencing how well the model captures patterns or overfits.

D. Experimental setup

The training of classification models was achieved through the integration of geometric and radiometric features. The geometric features of all points in the train and validation sets from the benchmark dataset, as well as the photogrammetry dataset, were computed in accordance with the methodology proposed by Weinmann et al. (2015) and Chehata et al. (2009). A multi-search radius approach was employed to analyze features at various levels. The search radiation was set to 0.125, 0.25, 0.5, 0.75, 1, 2,

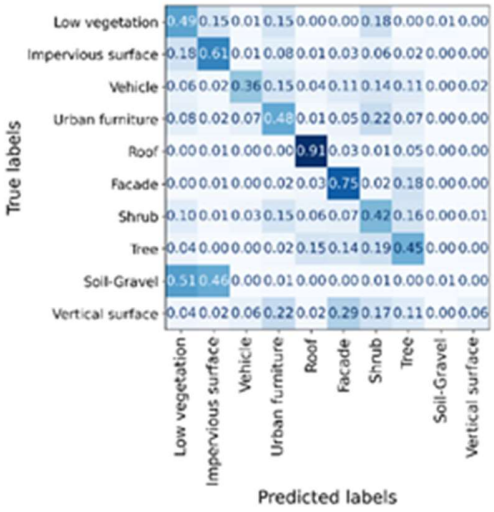

Figure 3. Confusion matrix (normalized by row) for the random forest model on the photogrammetry dataset dataset.

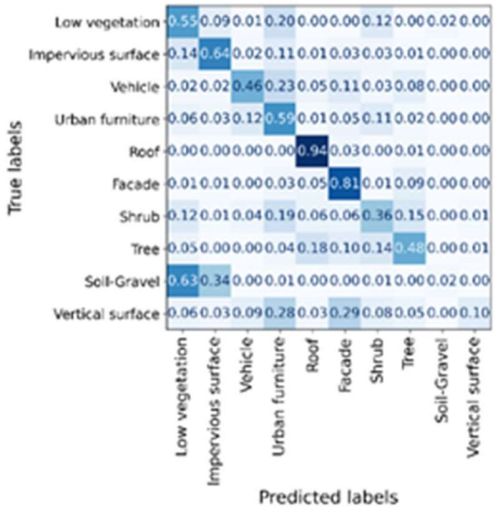

Figure 4. Confusion matrix (normalized by row) for the XGBoost model on the photogrammetry dataset dataset.

3, and 5 meters, and spherical neighborhoods were utilized. For each search radius, the following metrics were calculated: the sum of eigenvalues, omni-variance, eigen-entropy, anisotropy, planarity, linearity, surface variation, sphericity, verticality, the first and second largest eigenvalues from the principal component analysis (PCA), and the number of neighbors. In addition, point density and height above ground were incorporated as geometric features. In addition, radiometric characteristics were taken into account, with the calculated HSV (hue, saturation, value) colors being utilized in conjunction with RGB (red, green, blue) values.

Subsequent to the initial testing phase, the number of trees was set to 18 and tree depth to 100 for the random forest model. In the context of XGBoost, a configuration of 25 trees with a depth of 100 was implemented.

E. Evaluation metrics

To evaluate and compare different models across different datasets, the weighted precision, recall, and F1-score are assessed. Precision is defined as the accuracy of positive predictions made by the model. Precision is calculated as the ratio of true positives to the sum of true positives and false positives. Values close to 1 indicate that most positive predictions were accurate, i.e., almost no wrong predictions were made. Recall, on the other hand, signifies the proportion of all positive values that were accurately classified as positive, and it is defined as the ratio of true positives and the sum of true positives and false negatives. Values approaching 1 suggest that most actual positive cases were identified, i.e., not many were missing. The F1-score is a harmonic mean between precision and recall, synthesizing both into a single value. Due to the high imbalance present in the dataset, a weighted strategy was employed to calculate all metrics. Weights were calculated based on the proportion of each class on the dataset. Furthermore, a confusion matrix was utilized to assess the performance of each model across various classes.

III. Results and Discussion

A. Model performance on the H3D dataset

The random forest model demonstrated an average weighted precision of 0.83, a recall of 0.844, and an F1-score of 0.833 on the validation set. In comparison, XGBoost demonstrated a marginally superior overall performance, with an average precision of 0.836, a recall of 0.850, and an F1-score of 0.841.

As demonstrated in Figures 1 and 2, XGBoost exhibited superior performance across all classes, with a notable decline in performance for classes with a smaller number of points, such as vehicle and vertical surface. For classes with more representative features, such as roof and facade, both models demonstrated comparable performance. Additionally, the XGBoost model exhibited slightly higher performance in vegetation classes.

B. Model transferability assessment

In this study, trained machine learning models were utilized to generate semantic segmentation for each point also on the photogrammetry dataset. The XGBoost model demonstrated a marginal superiority over the random forest model in terms of the photogrammetry dataset's F1-score, which was recorded at 0.60. In contrast, the random forest model attained an F1-score of 0.55 for the same evaluation metric. As demonstrated in Tables 1 and 2, both models generally exhibited comparable precision and recall values.

It was observed that XGBoost exhibited superior precision for classes with a greater number of points and a higher recall for classes with a smaller number of points. In terms of precision, XGBoost demonstrated a substantial enhancement, with

TABLE I. PRECISION, RECALL, F1-SCORE, AND NUMBER OF POINTS OF EACH CLASS OF THE PHOTOGRAMMETRY DATASET USING THE RANDOM FOREST MODEL.

Class	Metrics			
	Precision	*Recall*	*F1-Score*	*Number of points*
Low vegetation	0.80	0.49	0.61	5291449
Impervious surface	0.41	0.61	0.49	1226356
Vehicle	0.29	0.36	0.32	87539
Urban furniture	0.01	0.48	0.02	27577
Roof	0.71	0.91	0.79	819837
Facade	0.66	0.75	0.71	897068
Shrub	0.09	0.42	0.15	336267
Tree	0.70	0.45	0.54	1570103
Soil-Gravel	0.06	0.01	0.01	604228
Vertical Surface	0.23	0.06	0.10	89717
Weighted average	0.65	0.52	0.55	10950141

TABLE II. PRECISION, RECALL, F1-SCORE, AND NUMBER OF POINTS OF EACH CLASS OF THE PHOTOGRAMMETRY DATASET USING THE XGBOOST MODEL

Class	Metrics			
	Precision	*Recall*	*F1-Score*	*Number of points*
Low vegetation	0.81	0.55	0.66	5291449
Impervious surface	0.53	0.64	0.58	1226356
Vehicle	0.26	0.46	0.33	87539
Urban furniture	0.01	0.59	0.02	27577
Roof	0.68	0.94	0.79	819837
Facade	0.72	0.81	0.76	897068
Shrub	0.12	0.36	0.18	336267
Tree	0.81	0.48	0.60	1570103
Soil-Gravel	0.08	0.02	0.03	604228
Vertical Surface	0.24	0.10	0.14	89717
Weighted average	0.69	0.56	0.60	10950141

increase in precision values of approximately 0.1 for classes designated as impervious surface and tree. A similar increase in recall values was observed for classes vehicles and urban furniture. This behavior might indicate that XGBoost can better handle an imbalanced dataset, giving more weight to minority classes, with the gradient boosting technique adjusting weights iteratively.

As illustrated in Figures 3 and 4, the confusion matrix for both models on the photogrammetry dataset is presented. It is evident that XGBoost demonstrated a superior overall performance. Roof and facades exhibited higher degrees of transferability among the classes. This observation may be indicative of a certain degree of similarity between the classes across the two datasets, given their common origin in urban environments within Germany. The class of vertical surfaces, which exhibited the lowest score, was found to be highly misclassified as urban furniture and facades. The misclassification of these three classes, which share similar geometric characteristics, is likely the primary cause of the observed discrepancies. The soil-gravel class exhibited the poorest performance across both datasets, demonstrating a high degree of misclassification as low vegetation.

IV. CONCLUSION

The XGBoost model demonstrated a marginal superiority in its performance on the laser scanning benchmark dataset, and exhibiting enhanced transferability to the unseen, photogrammetric dataset. Among all ten classes, facades and roof demonstrated the highest performance across both datasets, while soil–gravel exhibited the lowest performance. The findings of this study demonstrate the capacity of machine learning models to generate satisfactory outcomes on unseen, cross-platform data; nevertheless, their implementation necessitates meticulous consideration. Our findings underscore the necessity of enhancing the accessibility of large-scale annotated point cloud datasets, increasing data variability, and facilitating the development of models with a higher degree of generalization.

V. ACKNOWLEGMENTS

This work is part of the project 'Automated fusion and classification of ALS and UAV data for the creation of heavy rain hazard maps' funded by the ZIM programme (Zentrales Innovationsprogramm Mittelstand, grant number KK5549901PR3), Germany's largest innovation programme for small and medium- sized enterprises. Furthermore, we would like to thank Eveline Bezerra for annotating the UAV-photogrammetry based point cloud.

REFERENCES

[1] Chehata, N., Guo, L., and Mallet, C. 2009. Airborne LiDAR feature selection for urban classification using random forests. XXXVIII-3/W8 ISPRS Archives (2009), pp. 207-212

[2] Kölle, M., Laupheimer, D., Schmohl, S., Haala, N., Rottensteiner, F., Wegner, J. D., and Ledoux, H. 2021. The Hessigheim 3D (H3D) benchmark on semantic segmentation of high-resolution 3D point clouds and textured meshes from UAV LiDAR and Multi-View-Stereo, mISPRS Open Journal of Photogrammetry and Remote Sensing, Volume 1, https://doi.org/10.1016/j.ophoto.2021.100001.

[3] Stilla, U. and Xu, Y. 2023. Change detection of urban objects using 3D point clouds: A review, ISPRS Journal of Photogrammetry and Remote Sensing, Volume 197, https://doi.org/10.1016/j.isprsjprs.2023.01.010.

[4] Zamboni, P. A. P., Hendrickx, H., Sprute, D., Flatt, H., Rushdi, M. I., Brodrecht, F., and Eltner, A. 2024. Synergistic image and point cloud processing of UAV data for urban flood modeling: point cloud smart thinning and curb mapping, Int. Arch. Photogramm. Remote Sens. Spatial Inf. Sci., XLVIII-2/W8-2024, 483–490, https://doi.org/10.5194/isprs-archives-XLVIII-2-W8-2024-483-2024

[5] Weinmann, M., Jutzi, B., Hinz, S. and Mallet, C. 2015. Semantic point cloud interpretation based on optimal neighborhoods, relevant features and efficient classifiers ISPRS J., 105, pp. 286-304

Geomorphometry in the Cloud:

New Capabilities and Future Directions of ArcGIS

Nawajish Noman[1], Steve Kopp[2], Tania Lopez-Cantu[3]
Esri – Spatial Analyst Team
Redlands, CA, USA
[1] nnoman@esri.com, [2] skopp@esri.com, [3] tlopezcantu@esri.com

Cite as: Noman, N., Kopp, S., Lopez-Cantu, T. (2025). Geomorphometry in the Cloud: New Capabilities and Future Directions of ArcGIS. In: Proceedings of Geomorphometry 2025, 9-13 June, Perugia, Italy. M. Alvioli, L. Melelli, I. Marchesini eds. CNR Edizioni, Rome. ISBN 978-88-8080-765-0. DOI: 10.5281/zenodo.15391104

Abstract— **Over the last decade, the geospatial user community and Esri have moved toward increasing use of cloud hosted data and analysis provided as web services. Most GIS usage now relies to some extent on web services. ArcGIS provides an integrated system of desktop and cloud-hosted software and services. The desktop application was designed from inception with web services integration in mind, to provide a comprehensive yet simple experience to publish and consume web services. It is now possible to perform a complete GIS analysis project in the cloud, and we anticipate increasing use of fully cloud-hosted research and applications. This paper provides a brief overview of the components of that system and their use. Esri is an active partner in the geomorphometry community and here additionally provides an update on relevant recent developments, focusing on new and improved algorithms, and computational performance.**

I. GEOMORPHOMETRY IN THE CLOUD

Esri provides a fully cloud hosted geomorphometry platform in ArcGIS Online, a complete Software as a Service (SaaS) platform to collect, explore, analyze, visualize, and share spatial data services, and develop web map applications. It includes a rich collection of open global terrain data, online processing to collect and build terrain data, geomorphometry analysis services, and terrain visualization. ArcGIS Online provides a place for users to publish their data as web services to share with others, from within ArcGIS Online or from ArcGIS Pro. No knowledge of web services or cloud hosting is required. Analogous to how people share videos by uploading to YouTube and other video hosting services, ArcGIS users share data and analysis through ArcGIS Online as web services. The SaaS infrastructure relies upon leading global hosting partners to provide performance, data residency, and redundancy. The system is used by over 650,000 organizations with several million users, supporting over 3 billion requests per day.

A. Terrain Data Services

ArcGIS Online hosts over 20 million data layers, including a curated collection of open and community contributed elevation from more than 60 organizations. This is nearly 150 Tb of lossless compressed gridded elevation data at multiple resolutions, including global coverage (minus a few restricted countries) of the Airbus 24-meter WorldDEM4Ortho, and over 27 million km^2 of 50-centimeter resolution Maxar Precision 3D. The terrain data is available as web services for visualization and analysis in a variety of ArcGIS client applications including ArcGIS Pro and can also be downloaded for offline analysis. Users can upload their elevation to ArcGIS Online and publish as web services for their use, grant access to others in their organization, or provide fully open access.

B. ArcGIS Online Raster Analytics

The full suite of GIS and image analysis capabilities, including terrain analysis are available in ArcGIS Online, providing hosted compute in a secure environment. The user has access to scalable server setups where they can run raster analysis tools and functions [Fig.1]. Analysis outputs are hosted in the users' ArcGIS Online account and immediately available as image services.

In contrast to ArcGIS Enterprise - which also allows for scalability in a secure environment, in ArcGIS Online, Esri provides the infrastructure including setup and maintenance, as

well as data hosting. Available tools and functions include terrain and hydrologic analysis tools to characterize terrain, define viewsheds and extract hydrologic information from surface rasters.

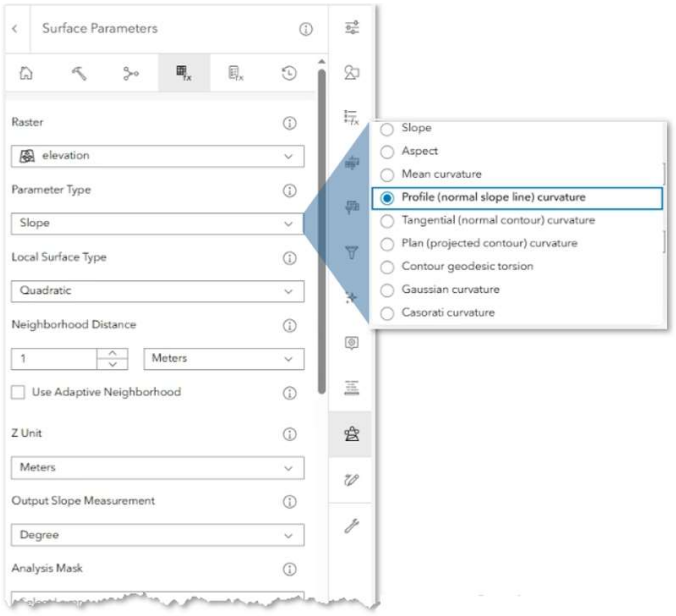

Figure 1. The Surface Parameters raster function dialog in ArcGIS Online provides access to slope, aspect, and 7 geometric curvatures.

C. *Ready to Use Services*

For common analysis tasks on widely used datasets, ArcGIS provides a collection of Ready to Use services, combining source data and cloud-optimized analysis. They are accessible in ArcGIS Pro, ArcGIS Online, and via REST API. For hydrologic analysis these include watershed delineation and downstream tracing where the user provides only the initiation location [1]. The source data is built from 90m SRTM globally and 30m NHD in the United States, which have been further hydroconditioned, and optimized for fast compute. The user provides only the starting locations points, and result polygons or lines are returned in 15-30 seconds as hosted feature services. Visibility analysis, elevation summary statistics, and elevation profile services are also provided for a wide range of elevation sources and resolutions. These services simplify the user experience, save ArcGIS users thousands of hours of processing, and are provided at no cost.

D. *Scalable Analytics*

In recent years Esri has put considerable effort into keeping algorithms up to date leveraging rapidly advancing computing architectures. This work includes parallel algorithms for multicore desktops and single nodes, GPU-specific implementations, optimizations for distributed computation across many nodes, and a cloud-native Kubernetes version. Kubernetes is an open-source technology for managing and scaling containerized applications in the cloud. ArcGIS on Kubernetes testing included raster data of nearly 4 trillion pixels and 400 CPUs.

More than 300 analysis tools in ArcGIS run parallel, and 40 of those have GPU specific implementations. This includes the frequently used land-surface parameter tools and hydrology tools. For example, running hydrologic analysis tools on the full global 30m DEM, over 540 billion cells, in Kubernetes with 40 nodes / 200 pods completes FlowDirection in 4.4 hours, where a single processor machine would require 14 days. The ArcGIS geoprocessing analysis environment provides options for the user to control how many processors to use and when to use CPU or GPU computation. New analysis tools are designed for parallel distributed computation from inception and also evaluated for their GPU suitability and benefit.

II. NEW CAPABILITIES AND FUTURE DIRECTIONS

A. *Geodesic Algorithms*

Many geomorphometry indices use distances and angles as part of their computation, e.g. slope, curvature. A significant percentage of DEMs and other geospatial data are provided in spherical coordinates (latitude / longitude) where there is a difference in the length of a degree in X and Y. To accommodate measuring distances and angles, softwares used a conversion factor to compensate for this difference or required reprojection to a planar coordinate system. We agree with Guth and Kane [2] this approach is outdated and introduces unacceptable bias. To remove problems of planar algorithms applied to spherical data, more than 40 ArcGIS tools were rewritten using spherical math, including calculations of slope, aspect, curvatures, visibility, solar radiation, and more. Future analysis tools computing distance are designed for both planar and geodesic implementations.

The new curvature implementation expanded the list of available curvatures types to include 7 geometric curvatures following the math and clarity of naming conventions of Minár et al [3, 4].

B. *Landscape Scale*

Terrain processes occur at a range of scales and terrain data is available at a range of spatial resolutions. Deriving terrain metrics from high resolution data over large areas drove the earlier mentioned efforts improving algorithm performance and scalability. Traditional geomorphometric moving window algorithms typically used only the immediate 3x3 neighborhood of values. This worked well for modeling common landform processes with commonly available data of 10m to 90m resolution. However higher resolution data of 1 meter and finer require different consideration. For a land planning application, is the slope at 1 meter resolution important or is the slope at *10-meter*

resolution more useful? To accommodate such applications ArcGIS now allows the user to specify a desired window size for their calculations. An auto-adaptive window size is also provided which uses local terrain variance to determine an appropriate window size.

The adaptive window is particularly useful when there are widely varying sizes of terrain features of interest, such as small gullies and large plateaus in the study area.

ArcGIS Pro 3.4 also includes several multiscale tools developed in collaboration with John Lindsay of Whitebox GeoSpatial Inc. The new multiscale tools characterize terrain in terms of elevation difference and percentile values [Fig.2], measuring how they respond to changes in scale. Scales are identified using neighborhood distances. The user can specify a minimum and a maximum, and an increment to control the increase in neighborhood distance. Analyzing different scales allows to find the most extreme values and identify prominent landscape features.

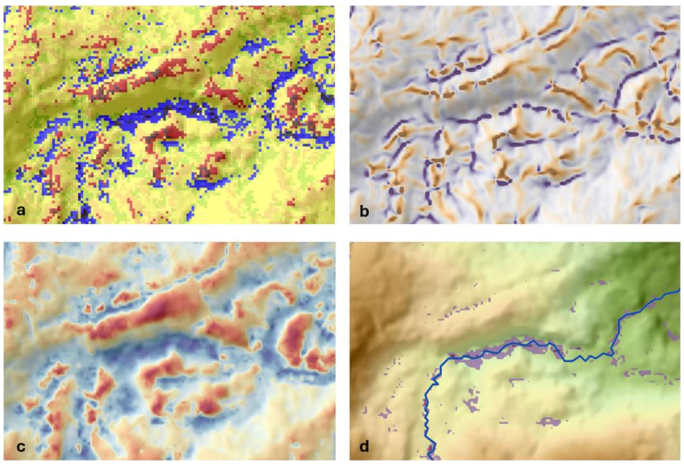

Figure 2. Inputs and output (d) of a streamline index model for identifying most likely stream paths. In addition to flow accumulation the model uses (a) Geomorphons, (b) Planform (projected contour) curvature, and (c) Multiscale elevation percentile.

C. *Hydrology*

ArcGIS hydrologic analysis capabilities cover a wide range: from fundamental tools (ArcGIS Spatial Analyst) to application-oriented (Arc Hydro) and decision-support tools (flood simulation).

ArcGIS Spatial Analyst includes foundational tools to address fundamental problems. These include preparing a DEM for hydrologic analysis, extracting hydrologic information such as watersheds, streams or storage capacity, and characterizing stream information in terms of connectivity and order. More recent tools allow for hydrologic information extraction with minimal DEM modification [5] considering higher resolution DEMs which may contain a more realistic representation of terrain. For working with noisy high resolution terrains Feature Preserving Smoothing [6] was included at ArcGIS Pro 3.4.

Arc Hydro [7] is no-cost collection of more than 200 terrain and hydrologic analysis tools, and hydrologic data production and modeling workflows. It is used to build foundational datasets for use in water resource analyses and for integration with water resource models. The underlying Arc Hydro data model standardizes water data structures so that data can be used consistently and efficiently to solve a wide range of water resource problems at any scale—regional, national, or international.

Flood simulation modeling was recently added to ArcGIS Pro. The simulation uses shallow water equations within a defined area of interest to model how water moves and accumulates on the landscape [8]. It is used in disaster scenario planning, and interactive visualization of flood impacts from changes in the landscape, urban development, or flood mitigation efforts. Typical use is to analyze the flooding impact through different scenarios created by changing relevant variables interactively. The process starts with creating one or more flood simulation layers in a scene, run the scenario, and review the visual results. Then create another scenario with parameter adjustments or changes to the landscape, such as increasing the rainfall or adding a dike or flood wall and visualize the change of impact.

D. *Artificial Intelligence Integration*

The use of geospatial artificial intelligence (GeoAI) modeling techniques has seen rapid growth in the geomorphometry community. Esri and its customers are using GeoAI for terrain hydroconditioning, wetland mapping [9], landslide risk [10], and a wide range of image feature extraction and spatial modeling tasks. To ease the learning curve and empower more people to use these capabilities, Esri provides direct integration with a large collection of deep learning models and toolkits. Additionally, Esri provides a collection of pretrained models [11] for common spatial tasks such as landcover mapping, change detection, disaster damage assessment, and a variety of other object detection.

Beyond analytic methods, Esri uses knowledge of its software best practices in customizing and training its own AI models to improve users' ability to find appropriate tools, compose workflows, and to assist in writing code.

E. *Solar and Planetary Enhancements*

Since the last Geomorphometry meeting Esri has replaced its solar radiation modeling tools. The new implementation computes in geodesic space, has both GPU and distributed CPU capabilities, and in collaboration with NASA was adapted to use the Moon's coordinate systems and planetary ephemeris to enable

solar energy calculations for use in Moon rover route planning and Moon base site suitability modeling.

F. Partnering

Esri is an engaged collaborator in the geomorphometry community, following and promoting emerging research as well as contributing. Work described above on geodesic calculations, curvatures, and adaptive window size are available as a standalone, open-source Jupyter notebook [12] for others to leverage in implementing new methods. For example if someone wanted to create a new moving window metric but lacked the time or skills to implement the geodesic math or adaptive window, those pieces are all available in the notebook.

Our recent collaboration with John Lindsay incorporates some of the novel work of Whitebox into ArcGIS as native tools (Feature Preserving Smoothing and the multiscale tools mentioned above). Implementing them as native tools in ArcGIS enables them to read and write all supported formats in ArcGIS, support the full analysis environment, and take advantage of our performance and scalability software framework.

III. Extending ArcGIS

The geomorphometry research community is quite active in developing new methods, and applying them to relevant societal problems. To support this and other communities Esri provides an open, extensible system with numerous APIs and examples. Python is the primary scripting language of the geospatial community and has been the scripting language of ArcGIS for over 20 years. Python has been used by many developers to implement new algorithms, build solution-oriented toolboxes [13] or integrate entire software packages. In recent years use of R with ArcGIS has also increased with projects such as the FluvialGeomorph toolbox [14] leveraging Esri's R [15] and Python integration. In addition to approaches to integrate new tools and toolboxes, ArcGIS also includes APIs and templates for web mapping, web app development, mobile app development, game engine integration, and more.

REFERENCES

[1] Kopp, Steve; Djokic, Dean; and Noman, Nawajish, "Global Multiscale Hydrologic Web Services", 2012. *International Congress on Environmental Modelling and Software*. 383.

[2] Guth, P. L., and Kane, M, 2021. Slope, aspect, and hillshade algorithms for non-square digital elevation models. Transactions in GIS, 25, 2309-2332. https://doi.org/10.1111/tgis.12852

[3] Minár, J., Evans, I. S., & Jenčo, M, 2020. A comprehensive system of definitions of land surface (topographic) curvatures, with implications for their application in geoscience modelling and prediction. Earth-Science Reviews, 103414. https://doi.org/10.1016/j.earscirev.2020.103414

[4] *How surface parameters works*. (2025) ArcGIS Pro 3.4 Online help. Accessed April 30, 2025, from https://pro.arcgis.com/en/pro-app/latest/tool-reference/spatial-analyst/how-surface-parameters-works.htm

[5] Metz, M., Mitasova, H., & Harmon, R. S. 2011. "Efficient extraction of drainage networks from massive, radar-based elevation models with least cost path search." *Hydrology and Earth System Sciences* 15(2): 667-678.

[6] Lindsay JB, Francioni A, Cockburn JMH. 2019. LiDAR DEM smoothing and the preservation of drainage features. Remote Sensing, 11(16), 1926; DOI: 10.3390/rs11161926.

[7] Arc Hydro Docs. (2025) Esri Online help. Accessed April 30, 2025, from https://esrips.github.io/ah-docs/

[8] Flood simulation in ArcGIS Pro 3.4; An Esri technical paper, (2024). Retrieved April 30, 2025, from https://www.esri.com/content/dam/esrisites/en-us/media/technical-papers/flood-simulation-arcgis-pro.pdf

[9] O'Neil, G. L., Goodall, J. L., Behl, M., & Saby, L. 2020. Deep learning using physically-informed input data for wetland identification. Environmental Modelling & Software, 2020.

[10] Azarafza, M., Azarafza, M., Akgün, H. *et al.* 2021. Deep learning-based landslide susceptibility mapping. *Scientific Reports* 11, Article no. 24112 https://doi.org/10.1038/s41598-021-03585-1

[11] Deep learning models in ArcGIS models (2025) ArcGIS Pro 3.4 Online help. Accessed April 30, 2025, from https://livingatlas.arcgis.com/en/browse/?q=dlpk%20detection#d=2&q=dlpk+detection

[12] Holderman, C., Kopp, S., Noman, N., & Lopez-Cantu, T. (2021, August 27). A New Analytic Framework and Notebook for Terrain Analysis. https://doi.org/10.5281/zenodo.5297224

[13] Bravard, Emma E., Emily Zimmerman, John C. Tyndall, and David James. 2022. *The agricultural conservation planning framework financial and nutrient reduction tool: A planning tool for cost effective conservation*. Journal of Environmental Quality, Vol. 51, no. 4. 2022. DOI: 10.1002/jeq2.20345

[14] Haring, C. P., and Dougherty, M. P., 2023. Geomorphic metrics used in FluvialGeomorph. Accessed April 30, 2025, from https://apps.dtic.mil/sti/trecms/pdf/AD1208937.pdf

[15] Aydin, O, Pavlushko, D., Walbridge, S., Kopp, S., and Janikas, M. V. 2024 arcgisbinding: An R package for integrating R and ArcGIS. Environmental Modelling & Software 172 (2024): 105904.

1.2 - Topographic Attributes

Roughness who?

Sebastiano Trevisani
Dept. Culture del Progetto
University Iuav of Venice,
Venice, Italy
strevisani@iuav.it

Cite as: Trevisani, S. (2025). Roughness who? In: Proceedings of Geomorphometry 2025, 9-13 June, Perugia, Italy. M. Alvioli, L. Melelli, I. Marchesini eds. CNR Edizioni, Rome. ISBN 978-88-8080-765-0. DOI: 10.5281/zenodo.15024572

Abstract—**This abstract presents some of the topics of the author's keynote at the Geomorphometry 2025 conference. Some intricacies, ephemerality and controversial concepts concerning the characterization of surface texture are discussed. Surface texture in earth sciences and ecology is most often referred to as surface roughness or surface ruggedness, even if many other related terms are adopted. Starting from ambiguities in the concepts and terminology other key aspects are discussed. One central theme, sometime forgotten despite self-evidence, is that the conventional raster representation of topography provides a representation of apparent roughness. Another key point is related to the generalization or smoothing of digital elevation models, and more in general to the decomposition of the topographic signal in different components of spatial variability. Then a crucial and difficult aspect is related to the need to create a repository of benchmark surface textures, fundamental to describe, compare and test surface roughness metrics. Unlike surface metrology and image texture analysis, the creation of collections of reference textures is a difficult task given the complex spatial-statistical characteristics of analyzed morphologies. Some key aspects of surface texture characterization are pointed out by means of the analysis of different landscapes. The purpose of the talk is not to propose the "right" terminology or the best recipes for roughness characterization. The main objective is to highlight the complexity of the topic, the variety of purposes and applications concerning surface roughness, and the many cross-contaminations with other disciplines, such as surface metrology and image analysis.**

I. Introduction

Surface roughness (SR) is a key concept in multiple fields of sciences and engineering, including earth sciences and ecology, showing an increasing interest in the last decades [1–8]. Surface "roughness", similarly to "ruggedness", is one of those buzzwords in earth sciences and ecology that many researchers use and compute with some related metric, generally having an intuitive idea of its meaning but without having or providing a clear definition of it. Even though the analysis of SR related metrics returns relevant information concerning the geoenvironmental factors and processes being studied or modelled, there are evident ambiguities in SR definition, computation and application among different disciplines and scholars. These ambiguities, even if unavoidable to some extent, should be mitigated or at least the controversial aspects should be pointed out. In geomorphometry there is a lack of consensus [1,2,9] on a definition of SR. Multiple related terms are adopted, such as "fabric", "ruggedness", "rugosity", "texture", "waviness" and others (e.g., [10–12]). Some authors describe SR as a metric related to surface (or "topographic", "terrain", etc.) "complexity", inheriting all the fuzziness (and complexity!) related to term "complexity". Is a horizontal surface with some fine-grain roughness more complex than a smooth folded quadratic surface? Most of the popular computed SR indexes are relatively simple measures of surface spatial variability and are not capable of providing real information on complexity. Complexity of topography is not just variability in general terms; an expression of complexity can be for example the coalescence of morphological features with multiple wavelengths or the presence of complex curvilinear spatial patterns. From a geostatistical perspective [13], SR indexes are related to the spatial statistical variability structure of surfaces, so a wide range of indexes related to the morphological spatial patterns can be envisioned. Probably, referring to "surface texture" (ST) is more intuitive even if still with some fuzziness. But at least ST permits to use an intuitive concept related to human perception (visual and tactile) and also to analogous approaches adopted in metrology and computer vision [14–17]. Intuitively, ST may imply the presence of some repetitive pattern; however, this implication is not mandatory and sometime singular and not repetitive patterns are very distinctive elements of topographic signature [10]. Hereinafter, the term SR is intended as a synonym of ST and hence something referring to the overall spatial variability structure of

surfaces. Accordingly, SR is intended differently from the surface metrology discipline, where roughness is considered a short-range aspect of ST. However, also in surface metrology there is an unavoidable ambiguity related to the scale of analysis with respect to the scale of morphological features analyzed (e.g., when does roughness become waviness?). The use in this talk of SR as synonym of ST is related to the fact that many works using the keywords surface "roughness" or surface "ruggedness" are referring to the wider concept of surface texture more than to "surface roughness" as intended in surface metrology.

II. SOME KEY POINTS

A. Signal decomposition

The concept of signal decomposition in different components of spatial variability is a key step in geomorphometric analysis, including ST analysis. This step underlays many algorithms for the computation of basic land surface parameters (LSPs), such as slope and curvatures [18]. Every time a quadratic surface is fitted to the data to compute a LSP, this implies the smoothing of the DEM via local polynomial of order 2. Even when computing LSPs parameters without fitting quadratic functions, just using discrete partial derivatives, many authors smooth the DEM before computation. Another example is represented by the generalization of DEM required for calculating LSPs from the perspective of physical based geomorphometry and landscape segmentation [19]. The generalization or regularization of the surface is a well-known concept in geostatistics [20], where the signal is generally decomposed in two components, the trend, the deterministic/structured component, and the random part, generally representing fine-scale morphology (from which the roughness is generally evaluated). Both components are interesting and serve different purposes. Unfortunately, the decomposition between the two is not univocal and contributes to the complexity of many DEM preprocessing steps. This is the case of "residual topographies" derived subtracting from the original DEM a generalized/regularized/smoothed version of it. In the "residual topographies" we find a wide range of terms such as topographic position index (TPI), relative position, residual DEM, residual relief, detrended surface, etc. [21,22] Apart from very simple situations, there is no best way to split the signal in the two components; moreover we are not limited to a dual representation. This is because of the complexity of real surfaces and also in relation to the different approaches that can be used for generalization. In fact, in addition to the selection of the level of generalization, there are many approaches, essentially convolutions, that can be adopted to generalize the DEM, such as: single pass moving averages, multi-pass moving averages, moving medians, gaussian kernels, local polynomials, and others. The decomposition of the signal is relatively simple if one has in mind the range of wavelengths of the features to be highlighted (e.g., the granulometry of the gravel of a riverbed) and if this range does not change too much from place to place. But in general, given the characteristics of real topographies, it is better to adopt multiscale approaches considering different levels of generalization. At the end it is a matter of dispersion variance [20]. Considering for simplicity a smoothing based on moving average (i.e., a local polynomial of order 0 or a convolution with a square wave), the bigger the window is more spatial variability is filtered out, leaving features with longer wavelengths in the smoothed DEM. Conversely, the complementary part of the signal is represented in the residual topography. In addition, analogously to what is performed with wavelets analysis, differentiating different levels of DEM generalization is possible to isolate specific wavelengths (or frequencies in the frequency domain).

B. Overtreatment?

There are various efforts toward the creation of improved SR indexes and the comparison of the existing ones. However, for a variety of reasons, the way forward isn't smooth and there are open questions to be addressed. Some questions are the typical ones related to the standardization and benchmarking of metrics: according to which cost function the metrics should be evaluated? With respect to which benchmark data sets? And, more importantly, better according to which purpose? These are central questions for comparing existent ST indexes and for creating new ones. However, on top of this, we need also to consider how real surfaces are represented digitally. The way in which we sample/measure a real surface and represent it digitally affects the fidelity in surface spatial variability reproduction. Dealing with measures of spatial variability, two key aspects need special care: 1) sampling spatial density and 2) measurement spatial support. The two interlinked aspects affect spatial variability, both from the perspective of Nyquist-Shannon sampling theorem and from the perspective of dispersion variance [20]. Let's focus on the widespread representation of surfaces on a regular grid, i.e. a raster DEM, which is essentially a 2D representation obtained projecting a 3D surface onto a horizontal (at least locally) surface. This kind of representation has some characteristics to consider when computing spatial variability indexes. For example, for a DEM with a projected coordinate system the maximum sampling density is along the cardinal directions and the lowest along the diagonals. This should be clearly considered when computing lag dependent indexes such as topographic ruggedness index (TRI), radial roughness index (RRI) and other geostatiscal approaches [9,23]. This aspect is more challenging when dealing with DEMs in geographical coordinates, given the latitude dependent spacing along longitude [24]. A key aspect is that we are dealing with an apparent roughness and in general to a morphology as seen "from above"; the true surface morphology is lost and cannot be retrieved, except without formulating restrictive assumptions on its characteristics. Given this biased representation on topography, one should always ask to which extent push forward the efforts for improving SR metrics. For example, is it worth extending the RRI to increments of order 3 or more to filter out more complex local trends, when at the end what we want to describe is inherently flawed?

On another perspective, it is difficult to state what makes a metric a proper measure of SR, especially when this is intended in the general sense of ST (e.g., [25]). Considering the definition of SR limited to fine-grain spatial variability, the characteristics of a proper index are relatively easy to be defined: it should be positive, independent from the structural component of spatial variability (local slope for sure, but what about curvature?), it should measure the variability of the surface considering small distances between pixels, it should use enough samples and based on a robust estimator (if you don't want to highlight outliers). Considering the wider concept of ST, the definition of metric properties can be trickier; for example, it could not be mandatory to assure the positiveness of a ST index.

C. Reference datasets

A compact plain language definition of texture is: "the way that something feels when you touch it" (Britannica dictionary). Accordingly, texture (of a surface or of an image) is something related to the object but also to the observer. For example, the ST is perceived differently if we are touching a surface with a finger or with the palm of the hand, or if one person has tiny or big fingers. The fact that surface and image texture are a perceptive property implies some observer subjectivity. If we ask people to segment an hillshade or a residual topography according to ST, different individuals will perform different segmentations, at least if we don't consider very simple topographies with very distinct domains of ST. In fact, the presence of coalescent multiscale morphological spatial patterns creates many difficulties in creating benchmarking/references datasets such as labelled subdomains with specific surface textures.

In surface metrology the surfaces have often rhythmic spatial structures, and the textures are relatively simple in terms of spatial patterns, in addition to a well-defined genesis. For example, the standard sets for comparing roughness instruments are relatively simple. Also, in the context of image analysis generally the textures analyzed are relatively simple and repetitive. However, earth and planetary morphologies are often much more complex, with coalescent multiscale structures, sometimes multifractal, and nonstationary in the spatial-statistical sense. One specific aspect of nonstationarity is represented by spatial discontinuity, manifested by abrupt morphological transitions like hot spots, lineaments and sharp variations from one textural domain to another. Sometime these are present in repetitive spatial patterns and sometimes are just singular distinctive features in the landscape. These discontinuous features have a special significance both for interpretation as well as for the impact on the calculation of spatial variability indexes, especially when using non-robust estimators. Accordingly, to create collections of "archetypes" of surface textures for benchmarking purposes, like in surface metrology and image analysis, we need to isolate specific patterns of ST (e.g., Fig. 1). This makes sense intuitively; however, which kind of rules should we follow to create this collection of surface textures?

A complementary solution is also the creation of synthetic surfaces, because these permit to control the properties of surfaces, isolate specific aspects and mimic also the impact of the different digital representations.

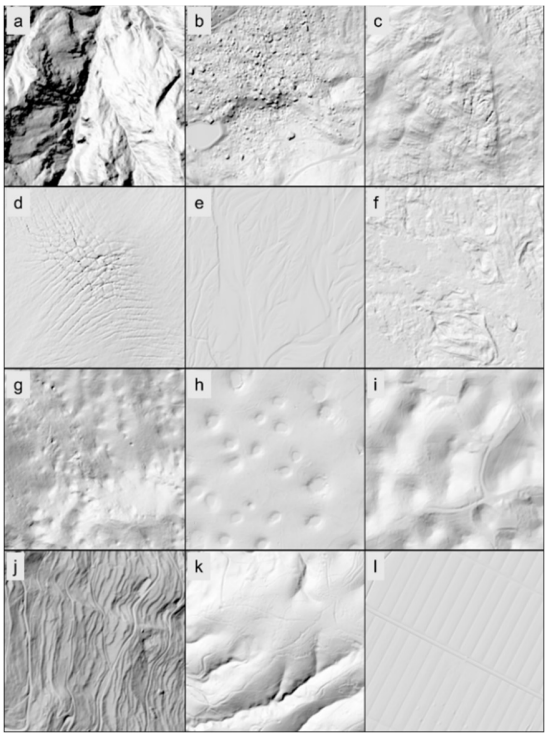

Figure 1. Example of a mosaic of different real surface textures, represented with a hillshade (512 x 512 pixels, resolution 2 m)

D. Complex morphological patterns

Even if there are important differences in the main conventional and less conventional SR indexes some of these can be highly correlated especially when considering small search windows. In fact, most of the popular indexes convey similar information, being relatively simple measures of variability of local morphology. The point is that, thinking to the complexity of surface textures (Fig. 2) and to the different purposes of "roughness analysis", there is the need of indexes capable to detect specific aspects at specific scales. For example, anisotropy in short range-roughness is one of them, but other interesting indexes to be developed could highlight asymmetric and curvilinear features. In addition, the metrics should be designed in relation to the application (e.g., analysis of ecological connectivity, impedance to flow, etc.). Accordingly, in most morphological settings to describe ST just one index isn't enough (or at least a single scalar property) and multiscale approaches should be adopted.

III. CONCLUSIONS

There is still a lot of work to be done on many fronts: a) perseverate in exploiting the cross-contaminations with other related fields, e.g., surface metrology and image analysis, including pattern recognition [16,17]; b) try to find a consensus on terminology and definitions; c) Create benchmark datasets of surface textures (real and synthetic) for testing, comparing and benchmarking algorithms; d) develop indexes tailored to highlight specific patterns and to specific tasks; e) clarify interconnections between different approaches and with the morphogenetic processes.

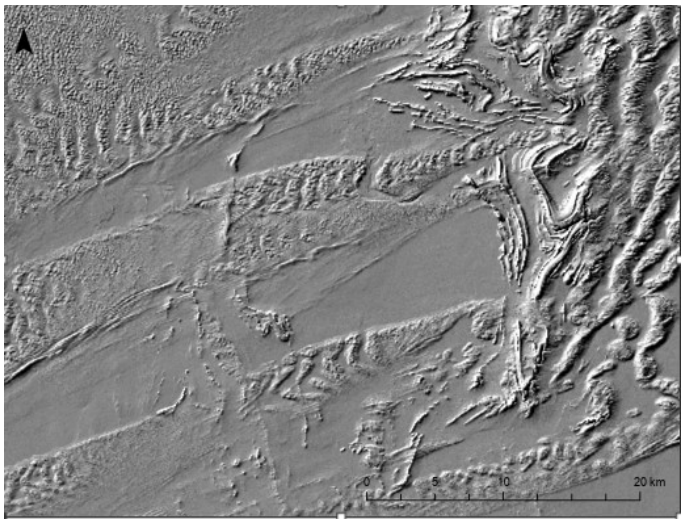

Figure 2. Example of a complex landscape from the perspective of surface texture (projected Copernicus DEM, 30 m, UTM zone 38N, Mauritania desert)

IV. ACKNOWLEDGMENTS

The author is grateful to the reviewers for their suggestions

REFERENCES

[1] Shepard, M.K.; Campbell, B.A.; Bulmer, M.H.; Farr, T.G.; Gaddis, L.R.; Plaut, J.J. The Roughness of Natural Terrain: A Planetary and Remote Sensing Perspective. *Journal of Geophysical Research: Planets* **2001**, *106*, 32777–32795, doi:10.1029/2000JE001429.

[2] Smith, M.W. Roughness in the Earth Sciences. *Earth-Science Reviews* **2014**, *136*, 202–225, doi:10.1016/j.earscirev.2014.05.016.

[3] Herzfeld, U.C. Vario Functions of Higher Order - Definition and Application to Characterization of Snow Surface Roughness. *Computers and Geosciences* 2002, *28*, 641–660.

[4] Grohmann, C.H.; Smith, M.J.; Riccomini, C. Multiscale Analysis of Topographic Surface Roughness in the Midland Valley, Scotland. *IEEE Transactions on Geoscience and Remote Sensing* **2011**, *49*, 1200–1213.

[5] Trevisani, S.; Rocca, M. MAD: Robust Image Texture Analysis for Applications in High Resolution Geomorphometry. *Computers and Geosciences* **2015**, *81*, 78–92.

[6] Lindsay, J.B.; Newman, D.R.; Francioni, A. Scale-Optimized Surface Roughness for Topographic Analysis. *Geosciences (Switzerland)* **2019**, *9*, doi:10.3390/geosciences9070322.

[7] Trevisani, S.; Teza, G.; Guth, P. A Simplified Geostatistical Approach for Characterizing Key Aspects of Short-Range Roughness. *CATENA* **2023**, *223*, doi:10.1016/j.catena.2023.106927.

[8] Doane, T.H.; Gearon, J.H.; Martin, H.K.; Yanites, B.J.; Edmonds, D.A. Topographic Roughness as an Emergent Property of Geomorphic Processes and Events. *AGU Advances* **2024**, *5*, doi:10.1029/2024AV001264.

[9] Trevisani, S.; Teza, G.; Guth, P.L. Hacking the Topographic Ruggedness Index. *GEOMORPHOLOGY* **2023**, *439*, doi:10.1016/j.geomorph.2023.108838.

[10] Pike, R.J. The Geometric Signature: Quantifying Landslide-Terrain Types from Digital Elevation Models. *Mathematical Geology* **1988**, *20*, 491–511, doi:10.1007/BF00890333.

[11] Guth, P.L. Quantifying Terrain Fabric in Digital Elevation Models. *GSA Reviews in Engineering Geology* **2001**, *14*, 13–25.

[12] Du Preez, C. A New Arc–Chord Ratio (ACR) Rugosity Index for Quantifying Three-Dimensional Landscape Structural Complexity. *Landscape Ecology* **2015**, *30*, 181–192, doi:10.1007/s10980-014-0118-8.

[13] Hristopulos, D.T. Random Fields for Spatial Data Modeling: A Primer for Scientists and Engineers. *Advances in Geographic Information Science* 2020, 1–867.

[14] Haralick, R.M.; Dinstein, I.; Shanmugam, K. Textural Features for Image Classification. *IEEE Transactions on Systems, Man and Cybernetics* **1973**, *SMC-3*, 610–621, doi:10.1109/TSMC.1973.4309314.

[15] Lucieer, A.; Stein, A. Texture-Based Landform Segmentation of LiDAR Imagery. *International Journal of Applied Earth Observation and Geoinformation* **2005**, *6*, 261–270, doi:10.1016/j.jag.2004.10.008.

[16] Ojala, T.; Pietikainen, M.; Maenpaa, T. Multiresolution Gray-Scale and Rotation Invariant Texture Classification with Local Binary Patterns. *IEEE Transactions on Pattern Analysis and Machine Intelligence* **2002**, *24*, 971–987, doi:10.1109/TPAMI.2002.1017623.

[17] Jasiewicz, J.; Stepinski, T.F. Geomorphons a Pattern Recognition Approach to Classification and Mapping of Landforms. *Geomorphology* **2013**, *182*, 147–156, doi:10.1016/j.geomorph.2012.11.005.

[18] Florinsky, I.V. An Illustrated Introduction to General Geomorphometry. *Progress in Physical Geography* **2017**, *41*, 723–752.

[19] Minár, J.; Drăguţ, L.; Evans, I.S.; Feciskanin, R.; Gallay, M.; Jenčo, M.; Popov, A. Physical Geomorphometry for Elementary Land Surface Segmentation and Digital Geomorphological Mapping. *Earth-Science Reviews* **2024**, *248*, doi:10.1016/j.earscirev.2023.104631.

[20] Isaaks, E.H.; Srivastava, R.M. *An Introduction to Applied Geostatistics* 1989.

[21] Trevisani, S.; Cavalli, M.; Marchi, L. Variogram Maps from LiDAR Data as Fingerprints of Surface Morphology on Scree Slopes. *Natural Hazards and Earth System Science* **2009**, *9*, 129–133.

[22] Hiller, J.K.; Smith, M. Residual Relief Separation: Digital Elevation Model Enhancement for Geomorphological Mapping. *Earth Surface Processes and Landforms* **2008**, *33*, 2266–2276, doi:10.1002/esp.1659.

[23] Riley, S.J.; DeGloria, S.D.; Elliot, R. A Terrain Ruggedness Index That Quantifies Topographic Heterogeneity. *Intermountain Journal of Sciences* 1999, *5*, 23–27.

[24] Guth, P.; Kane, M. Slope, Aspect, and Hillshade Algorithms for Non-Square Digital Elevation Models. *Transactions in GIS* **2021**, *25*, 2309–2332.

[25] Kreslavsky, M.A.; Head, J.W.; Neumann, G.A.; Rosenburg, M.A.; Aharonson, O.; Smith, D.E.; Zuber, M.T. Lunar Topographic Roughness Maps from Lunar Orbiter Laser Altimeter (LOLA) Data: Scale Dependence and Correlation with Geologic Features and Units. *Icarus* 2013, *226*, 52–66.

Formal weaknesses of some definitions of roughness, and a solution proposal

Carlos López-Vázquez
LatinGEO Lab IGM+ORT, Universidad ORT Uruguay, Montevideo, URUGUAY
carlos.lopez@pedeciba.edu.uy, carloslopez@fi365.ort.edu.uy

Cite as: López-Vázquez , C. (2025). Formal weaknesses of some definitions of roughness, and a solution proposal. In: Proceedings of Geomorphometry 2025, 9-13 June, Perugia, Italy. M. Alvioli, L. Melelli, I. Marchesini eds. CNR Edizioni, Rome. ISBN 978-88-8080-765-0. DOI: 10.5281/zenodo.15161390

Abstract— **We have analyzed from a formal point of view two definitions of roughness. Both are applicable only for elevations modeled through a DEM. One (named α) states that roughness is computed as the standard deviation of the slope at the 9 grid points of a 3x3 window. Another similar one (named β), computes the same over a detrended version of the elevation surface. As defined, we prove that both roughness values vanish at the limit of the cell size going down to zero, irrespective of any other characteristic of the terrain. Despite both metrics attempt to compute a property of the topographical surface through the use of a regular sample of elevations (i.e. DEM) we can show that the value is still a function of the cell size. Thus, a seemingly intrinsic property of the topographic surface is dependent of one arbitrary characteristic of the sample: the DEM cell size. Through a cumbersome but otherwise straightforward formal manipulation we can prove that the squared standard deviation of the slope over a 3x3 window is directly proportional to the cell size h raised to a power 1 or 2. If we consider instead the slightly modified definition β where the surface is first detrended, then the power is always 2. The proposed adjusted definition of roughness requires using the standard deviation of the detrended slope over a 3x3 window divided by the squared cell size h. We will show the relationship of such magnitude to the set of partial derivatives of the topographic surface, thus offering a mathematical counterpart of the so defined roughness. In addition, a procedure to estimate its uncertainty under the assumption that the elevation values are error free is also provided.**

I. INTRODUCTION

The DEMIX initiative [1] conducted a comparison exercise between global DEM of 1 arc second resolution. Among other criteria, it was proposed to compare the accuracy of the roughness obtained from the candidate vs. what is deemed as a reference value. Since the reference could be computed from a local DEM of higher resolution, it was questioned if the computation should be carried out at high resolution and later coarsened, or first coarsened and then computed. It was argued that the roughness derived from high resolution DEM was systematically different from the candidate one. Also, no cue about its accuracy was offered, since as defined the roughness is not easily measurable in the field. According to [2] there are a number of possible definitions for roughness. Following some authors, ([3], [4]) and within DEMIX interim report [5], roughness was defined for every grid point in terms of the standard deviation of the slope computed at the points of a 3x3 window centered in the point. Such definition (denoted hereinafter as α) was used throughout this paper despite that, according to [6], the final chosen window for DEMIX was 7x7. If we denote as S_i, i={1,2,...,9} the slope value computed at the i-th point, the mean slope M and the roughness R will be

$$M = \frac{1}{9}\sum_{1}^{9} S_i ; R = \sqrt{\frac{1}{8}\sum_{1}^{9}(S_i - M)^2} \quad (1)$$

For convenience we will work with the squared roughness R^2 hereinafter. It is clear that, provided a 3x3 window is used to compute the slope, all points of the 5x5 window will be involved in the computation of R^2 (see Fig. 1).

Irrespective of the windows size within DEMIX most of the comparison was done resorting to an independent reference dataset. In order to declare that some value could be considered as a reference one, we should be able to confirm that its accuracy is significantly better than the value under analysis. That was offered at [7] for the computation of the slope and aspect. Unlike slope, for roughness we have not resorted to a mathematical definition but just to the computation procedure. So, our first goal will be to find an expression showing the relationship between the roughness and the local properties of the topographical surface at point 1. To the best of our knowledge this has never been done before. Once we have such relationship, we will be able to consider similar tricks as used by [7] in order to estimate its uncertainty. The formulae are strictly valid only for the stated roughness definition, but illustrate the procedure for other ones.

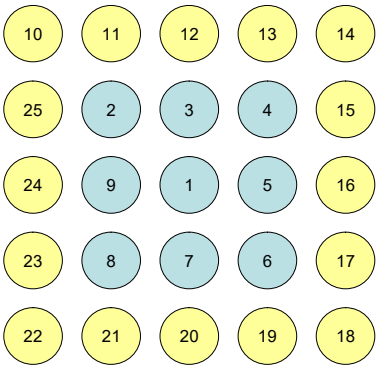

Figure 1. 3x3 (light blue) and 5x5 (light blue and yellow) computation window. Roughness is to be defined at point 1, but definitions α and β involve all points in the 5x5 window (from [7])

In this paper we will not discuss the representativeness of so defined roughness for the intended purpose neither its interpretability. We will just argue around some basic formal properties, using as a starting point not a mathematical but an algorithmic definition. Some authors even questioned the status of the roughness as a significant parameter. For example, [8] states that it is not a morphometric variable. We refer the reader to traditional references as [9] for further analysis.

We will show that both considered definitions of roughness could not describe an intrinsic property of the terrain surface. In particular, both are dependent on the cell size h and vanish when h goes down to zero. If we remove the dependency w.r.t. h, then different grids will have different roughness as now, but the dependence with h will be removed. The roughness will be a function of the point value of some partial derivatives. For finite h they will be just an estimate of the limit value, which does not automatically goes down to 0.0 everywhere if h decreases. We will suggest a slight modification that addresses or solves the issue. With such modification an uncertainty estimate could be formally derived, which in turn could be used to compute roughness reference values from other sources.

II. WHAT IS INDEED ESTIMATED

Computing the slope of points of a 3x3 window using a 3x3 rule spans over a 5x5 window. All the elevation values at the nodes of the 5x5 window can be expressed in terms of the Taylor expansion of the topographical surface function around the point 1 and the cell size (Δ_x, Δ_y). It is immediate that all the slope values, derived from them will also be a function of the same variables. As a conclusion, the so-defined roughness will also be a function of the partial derivatives at point 1, as well as the cell size.

A. Establishing the relationship between roughness and partial derivatives for the first definition

There is no mathematical definition of the roughness at hand but just a computation algorithm. The procedure to compute the squared roughness R^2 is as follows:

1. For every point i, i={1,...,9} compute the slope S_i using (for example) the Evans-Young formula [10]
2. Compute M, the mean slope S_i, i={1,...,9}
3. Compute the squared standard deviation of the slope S_i, i={1,...,9}

The exact expression for the roughness in terms of point value elevation is very long, but otherwise tractable. It can be shown that it differs depending if the local slope vanishes or not. If we collect all the terms and use just the partial derivatives at point 1 we obtain (Eq. 2):

$$R_\alpha^2 = \begin{cases} \dfrac{3}{4}\dfrac{\left[P_x^2\left(f_x f_{xx}+f_y f_{xy}\right)^2+P_y^2\left(f_y f_{yy}+f_x f_{xy}\right)^2\right]}{f_x^2+f_y^2}h+O\left(h^3\right) & \text{if} \quad f_x^2+f_y^2\neq 0 \\ \left\{-\dfrac{1}{9}\left[(P+Q)\left(UP_x+VP_y\right)+UVP_xP_y+PQ\right]+\right. & \\ \left.\dfrac{7}{24}\left(P^2+Q^2\right)\right\}h^2+O\left(h^3\right) & \text{if} \quad f_x^2+f_y^2=0 \end{cases} \tag{2}$$

being

$$U=\sqrt{f_{xx}^2+f_{xy}^2};V=\sqrt{f_{yy}^2+f_{xy}^2};W=f_{xy}\left(f_{xx}+f_{yy}\right)$$
$$P=\sqrt{U^2P_x^2-2WP_yP_x+V^2P_y^2};Q=\sqrt{U^2P_x^2+2WP_yP_x+V^2P_y^2} \tag{3}$$
$$h=\max\left(\Delta_x,\Delta_y\right);\ P_x=\Delta_x/h;\ P_y=\Delta_y/h$$

Some comments regarding this expression:

- The partial derivatives are a property of the topographic surface function, while h, P_x and P_y are a property of its sampling strategy (i.e. the DEM)
- Ideally, the roughness value should be invariant after rotation of the reference frame [11].
- If we neglect the numerical importance of P_x and P_y (both will be 1.0 if the grid is square), in the general case the squared roughness can be interpreted as the product of a property of the terrain and the grid size h. The key conclusion is that its value will go down to zero when h goes to zero, irrespective of the characteristics of the terrain.
- If the center point has zero slope the limit value for the roughness is also zero but now at least quadratic with h.
- As defined, the first terms of the Taylor expansion of the squared roughness are a function of the first and second order derivatives, not involving higher order ones.

In order to make the squared roughness α independent on the DEM design, in the general case its value should be divided by the largest grid dimension h raised to the power 1 or 2 depending on the local slope. The fact that the exponent is not constant is an issue which complicates further manipulations [2]. In any case, we uncovered the limit value for the so-defined roughness in terms of local partial derivatives, which is one main result of this paper.

B. Establishing the relationship between roughness and partial derivatives for the β definition

It is interesting to notice that some authors proposed to compute the roughness using not the DEM elevations but its difference with those of a best fit plane [12]. Such plane through point 1 will be selected with the same exact slope as the topographical surface. Its difference will have, by consequence, a zero slope in the center, leading to the particular case already studied. Despite not very popular in the literature, such detrended surface option has been informally considered at earlier stages within DEMIX. To the best of our knowledge such definition (named β hereinafter) has never been published. To be strict the exact slope at point 1 is not known in advance. Because a 5x5 window is already involved, it is fit to use a better schema for estimating it than the lower order one due to Evans-Young [10].

It has been shown [7] that with a 5x5 window the first partial derivatives p and q can be computed with 4th order accuracy using the schema proposed by [13]. Using our point numbering definition, the formula for each component of the first partial derivative is

$$\begin{aligned} p = \frac{1}{420h}\{&44(f_{13}-f_{11}+f_{19}-f_{21})+31[f_{10}-f_{14}+f_{22}-f_{18}+2(f_4-f_2+f_6-f_8)]+\\ &17[f_{16}-f_{24}+4(f_5-f_9)]+5(f_{15}-f_{25}+f_{17}-f_{23})\}+\\ &h^4\left(\frac{1}{30}f_{xxxxx}+\frac{17}{30}f_{xxxyy}+\frac{3}{35}f_{xyyyy}\right)+O(h^6) \end{aligned} \quad (4)$$

$$\begin{aligned} q = \frac{1}{420h}\{&44(f_{25}-f_{23}+f_{15}-f_{17})+31[f_{22}-f_{10}+f_{18}-f_{14}+2(f_2-f_8+f_4-f_6)]+\\ &17[f_{12}-f_{20}+4(f_3-f_7)]+5(f_{11}-f_{21}+f_{13}-f_{19})\}+\\ &h^4\left(\frac{1}{30}f_{yyyyy}+\frac{17}{30}f_{xxyyy}+\frac{3}{35}f_{xxxxy}\right)+O(h^6) \end{aligned} \quad (5)$$

where f_i stands for the elevation a the i-th point (following Fig. 1) and the suffix x and y denote partial derivatives of the surface. After a rather involved formal manipulation, the squared roughness from the detrended surface can be presented as a multiple of the grid size squared, being the multiple a function of the second order derivatives. The particular case already considered of zero slope at point 1 is still valid, provided the fourth order estimate due to [13] for the 5x5 window is used for detrending. This result could not be anticipated, and if we use instead a lower order estimate it can be different.

$$\frac{R_\beta^2}{h^2} = \frac{7}{24}\left(P^2+U^2\right)-\frac{1}{9}\left[(P+Q)\left(UP_x+VP_y\right)+UVP_xP_y+PQ\right]+O(h) \quad (6)$$

Regarding this second expression, the limit for small h links the scaled squared roughness from the detrended surface to a rather convoluted function of the second derivatives of the topographic surface. No higher order derivatives are involved in such limit value. We can conclude that the traditional roughness divided by the cell size h will now have a limit when it goes to zero. Let's denote as r_h^2 the detrended scaled squared roughness.

C. Estimating the uncertainty of the roughness value

If the β definition is adopted, then the detrended scaled squared roughness can be computed with second order accuracy in general, irrespective of the local slope. In both definitions we are interested in estimating an uncertainty value. We will assume that the elevations are without error, and the only source of uncertainty is due to the finite cell size h. Given that the exponent is known, one possibility to estimate an uncertainty value is to use the Richardson Extrapolation [14] as [7] did. The approach is simple but has two weaknesses. First, for the α definition the order might vary between 1 and 2. Second, and more important, it mixes estimates with different scales. An alternative option (not fully researched yet) is to compute the slope at the 9 points but using for each a 5x5 window. The overall window will be thus 7x7. The higher order formulae for slope will produce a higher order estimate of roughness, even using the β definition. With two estimates of the same roughness value each with different order we can compute its uncertainty as the absolute value of its difference. This alternative was presented also in [7] for the slope and aspect. The main advantage w.r.t. the Richardson Extrapolation option is that it only involves a grid of cell size h, thus assuring that scale is fully comparable between high and low order estimates. The computational effort is anyway modest.

The mixing of two different order estimates will work properly either for α or β roughness definition. On the other hand, the Richardson Extrapolation option does not hold for the α definition because the remainder has different power of h depending whether the local slope vanishes or not.

III. DISCUSSION

- We have found the analytical, exact expression, relating roughness definitions α and β to local partial derivatives.
- The β definition leads to a limit value that only involves second order derivatives of the topographic surface. Unlike the α definition, its order is also constant.
- We offer two different uncertainty estimates. One might be poisoned with scale issues, because for the Richardson extrapolation we use terms from cell size h and 2h. This is a problem. The second one uses the higher order formula

by [13] involving a local 5x5 window to compute the slope. Following this workaround the cell size will be always h, so no scale issues will affect the estimate. For the sake of completeness in future works we should establish the order of the leading term of the Taylor expansion, which certainly will be larger than 2.

- Comparable roughness values are important only while dealing with DEMs of different cell size. Within DEMIX all of them were 1" DEMs (same h) so the roughness estimate with one DEM is indeed comparable with the one from another. However, the reference values used to measure the accuracy are questionable.
- Obtaining reference values for roughness are not easy feat. High resolution datasets can produce estimates for a given h through a moving window. The resulting high resolution dataset of h-resolution roughness values could then safely be processed, and an uncertainty value could be derived provided we have a Taylor expansion analysis like the one offered here. Merely using higher accuracy elevations need not to be enough in order to satisfy the requirements to produce a suitable reference roughness dataset.

IV. CONCLUSIONS

- We have found the analytical, exact expression, relating two different definitions of roughness (α and β) to local partial derivatives and the cell size h.
- It has been shown that the limit value of the roughness for the β definition only involves second order derivatives.
- Future works might complete the analysis of uncertainty estimates which properly deal with scale issues. However, the solution will not be complete unless we can consider the effect of the uncertain elevations. Such activity has been done for the case of elevation and for the case of slope (but still unpublished) and needs to be developed from scratch in the case of roughness.
- In order to gather a roughness reference value, the rule is "compute first, resample later", but using a DEM of sufficiently higher resolution.
- Other algorithmic definitions of roughness (standard deviation of the elevation over a 3x3 window, for example) are waiting for a detailed analysis as illustrated here producing its mathematical counterpart.

V. ACKNOWLEGMENTS

This research was motivated by the DEMIX initiative. I am grateful for the opportunity to have participated in the discussions, exchanges and even mild controversies that arose there. I gratefully acknowledge the comments raised by the reviewers, which helped improve this contribution.

REFERENCES

[1] Strobl, P.A., Bielski, C., Guth, P.L., Grohmann, C.H., Muller, J.P., López-Vázquez, C., Gesch, D.B., Amatulli, G., Riazanoff, S. and Carabajal, C., 2021. The Digital Elevation Model Intercomparison eXperiment DEMIX, a community-based approach at global DEM benchmarking. The International Archives of the Photogrammetry, Remote Sensing and Spatial Information Sciences, 43(B4), pp.395-400. https://doi.org/10.5194/isprs-archives-xliii-b4-2021-395-2021

[2] Shepard, M.K., Campbell, B.A., Bulmer, M.H., Farr, T.G., Gaddis, L.R., Plaut, J.J., 2001. The roughness of natural terrain: A planetary and remote sensing perspective. J. Geophys. Res. Planets 106 (E12), 32777–32795. https://doi.org/10.1029/2000JE001429

[3] Frankel, K.L. and Dolan, J.F., 2007. Characterizing arid region alluvial fan surface roughness with airborne laser swath mapping digital topographic data. Journal of Geophysical Research: Earth Surface, 112(F2). https://doi.org/10.1029/2006JF000644

[4] Grohmann, C.H., Smith, M.J. and Riccomini, C., 2010. Multiscale analysis of topographic surface roughness in the Midland Valley, Scotland. IEEE Transactions on geoscience and Remote Sensing, 49(4), pp.1200-1213. https://doi.org/10.1109/TGRS.2010.2053546

[5] Bielski, C.; López-Vázquez, C.; Guth. P.L.; Grohmann, C.H. and the TMSG DEMIX Working Group, 2023. DEMIX Wine Contest Method Ranks ALOS AW3D30, COPDEM, and FABDEM as Top 1" Global DEMs. https://arxiv.org/pdf/2302.08425v1

[6] Bielski, C., López-Vázquez, C., Grohmann, C.H., Guth, P.L., Hawker, L., Gesch, D., Trevisani, S., Herrera-Cruz, V., Riazanoff, S., Corseaux, A. and Reuter, H.I. 2024. Novel approach for ranking DEMs: Copernicus DEM improves one arc second open global topography. IEEE Transactions on Geoscience and Remote Sensing, 62, pp.1-22. https://doi.org/10.1109/TGRS.2024.3368015

[7] López-Vázquez, C., 2022. Uncertainty interval estimates for computing slope and aspect from a gridded digital elevation model. International Journal of Geographical Information Science, 36(8), pp.1601-1628. https://doi.org/10.1080/13658816.2022.2063294

[8] Florinsky, I.V., 2017. An illustrated introduction to general geomorphometry. Progress in Physical Geography, 41(6), pp.723-752. https://doi.org/10.1177/0309133317733667

[9] Hobson, R. D. 1972. Surface roughness in topography: quantitative approach. Pages 221–245 in R. J. Chorley, editor. Spatial analysis in geomorphology. Harper and Row, New York, New York, USA

[10] Young, M. and Evans, I.S., 1978. Statistical characterization of altitude matrices. Report No. 5, Grant DA-ERO-591-73-G0040. Dept. of Geography, University of Durham, England, 26 pp.

[11] Hoffman, R. and Krotkov, E., 1990. Terrain roughness measurement from elevation maps. In Mobile Robots IV (Vol. 1195, pp. 104-114). SPIE. https://doi.org/10.1117/12.969874

[12] Sakude, M.T., Schiavone, G.A., Morelos-Borja, H., Martin, G. and Cortes, A., 1998. Recent advances on terrain database correlation testing. Enabling Technology for Simulation Science II, 3369, pp.364-376. https://doi.org/10.1117/12.319353

[13] Florinsky, I. V., 2009. Computation of the third-order partial derivatives from a digital elevation model. International Journal of Geographical Information Science, 23 (2), 213–231. https://doi.org/10.1080/13658810802527499

[14] Zlatev, Z., Dimov, I., Faragó, I. and Havasi, Á., 2017. Richardson extrapolation: Practical aspects and applications (Vol. 2). Walter de Gruyter GmbH & Co KG.

Derivation and Applications of Fuzzy Slope Position Information

Cheng-Zhi Qin
State Key Laboratory of Resources and Environmental Information System, Institute of Geographic Sciences and Natural Resources Research, CAS
Beijing, China
qincz@lreis.ac.cn

Liang-Jun Zhu
State Key Laboratory of Resources and Environmental Information System, Institute of Geographic Sciences and Natural Resources Research, CAS
Beijing, China
zlj@lreis.ac.cn

A-Xing Zhu
Department of Geography, University of Wisconsin-Madison
Madison, USA
azhu@wisc.edu

Cite as: Qin, C.-Z., Zhu, L.-J., Zhu, A.-X. (2025). Derivation and Applications of Fuzzy Slope Position Information. In: Proceedings of Geomorphometry 2025, 9-13 June, Perugia, Italy. M. Alvioli, L. Melelli, I. Marchesini eds. CNR Edizioni, Rome. ISBN 978-88-8080-765-0. DOI: 10.5281/zenodo.14994521

Abstract—**This extended abstract presents systematic research originated from quantifying the spatial gradation of slope positions (such as ridge, shoulder slope, backslope, foot slope, and valley) as fuzzy slope positions information, which were conducted by the authors in the past decade. We designed new methods for solving a series of scientific questions, including not only deriving the fuzzy slope positions information from DEMs, but also applying such a comparatively new type of terrain information to geographical analysis and optimization tasks. Specifically, for deriving fuzzy slope position information considering both parameter space and spatial context, a prototype-based method was developed to derive the fuzzy slope positions information through using those typical locations of slope positions. Then, to fix the practicality issue, an automated method as well as an open-sourced tool were developed to make the above method automated through data mining in a high-efficiency way. To explore the usability of such a new type of terrain information, a digital soil mapping method was developed to apply the fuzzy slope position information to not only purposive soil sampling but also soil spatial prediction. Further exploration was made on the potential of applying the fuzzy slope position information to best management practices (BMPs) scenario optimization based on watershed simulation. The recently proposed methods can innovatively use the fuzzy slope position information to dynamically adjust the boundaries of the slope position units for configuring BMPs during spatial or spatiotemporal optimization of BMPs scenarios, which may support watershed management decision with more practical and optimal solutions resulted from such optimization.**

I. INTRODUCTION

Spatial gradation (or transitions) between slope positions (such as ridge, shoulder slope, backslope, foot slope, and valley) is common terrain phenomena, which is often related to analyzing the spatial distribution of other terrain-related geographical phenomena such as soil and vegetation [1-3]. It had been proposed to quantify the spatial gradation of each slope position type across an interest area as fuzzy membership values (or similarities), or saying, fuzzy slope position information, for analyzing terrain-related geographical phenomena [2,3] (Fig. 1). This is a typical example of bridging the topographic attributes often presented as spatial continuous field recorded with gridded terrain model and the terrain features often presented as spatial discrete objects (i.e., according to crisp classes).

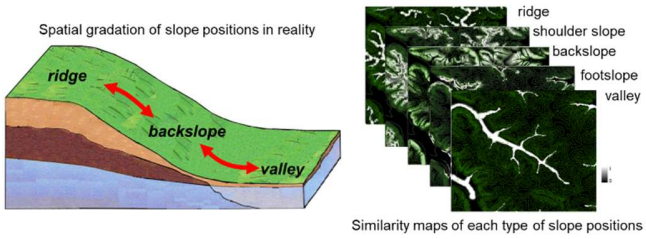

Figure 1. Spatial gradation of slope positions

This extended abstract presents systematic research originated from quantifying the spatial gradation of slope positions as fuzzy slope positions information, which were conducted by the authors and their collaborators in the past decade. We designed new methods for solving a series of scientific questions, including not only deriving the fuzzy slope positions information from DEMs, but also applying such a comparatively new type of terrain information to geographical analysis and optimization tasks. In this extended abstract, we do not plan to describe the details of each individual method which had been documented in published papers. Instead, here we hope to bring these methodological

studies together to present a systematic geomorphometric research, which may show the value and potential of new geomorphometric method design for not only terrain analysis but also those terrain-related geographic modeling domains.

II. Derivation of Fuzzy Slope Position Information

A. How to reasonably derive fuzzy slope position information

Those former methods of deriving fuzzy slope positions based on gridded DEM were based on fuzzy clustering in topographic attributes (or parameter space) [2,4,5], or expert-specified fuzzy classification rules within parameter space [3,6,7]. They ignore the spatial context across diverse terrain conditions, thus are unreasonable.

For deriving fuzzy slope position information considering both parameter space and spatial context, Qin et al. [8] proposed a method of deriving the fuzzy slope positions information through using those typical locations as prototypes of slope positions within an interest area, which contain tacit knowledge on spatial transitions between slope positions within the area and also consider both attribute and spatial domains (Fig. 2).

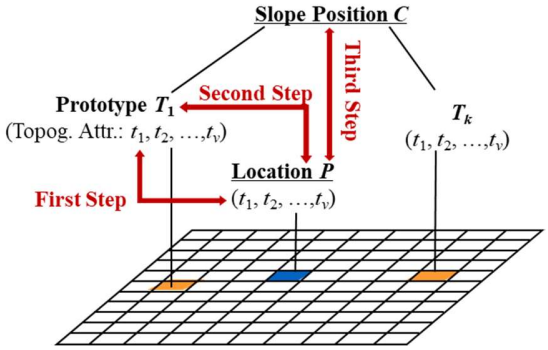

Figure 2. Schema of deriving fuzzy slope position information with typical locations as prototypes of slope positions in an interest area [8]

B. How to automatically derive fuzzy slope position information

However, the method proposed by [8] is not easy to implement in real applications, because it needs tedious processes (such as preparing topographic attributes, extracting typical locations as prototypes, and determining parameters of fuzzy inference) which are also time consuming with the traditional serial computing implementation. To fix such practicality issue, an automated method [9] as well as an open-sourced tool (https://github.com/lreis2415/AutoFuzSlpPos) were developed to make the above method automated through data mining with gridded DEM in a high-efficiency parallel-computing way (Fig. 3).

III. How to Apply Fuzzy Slope Position Information to Geographic Modeling

For such a comparatively new type of terrain information, there was bare of direct applications in geographic modeling. Therefore,

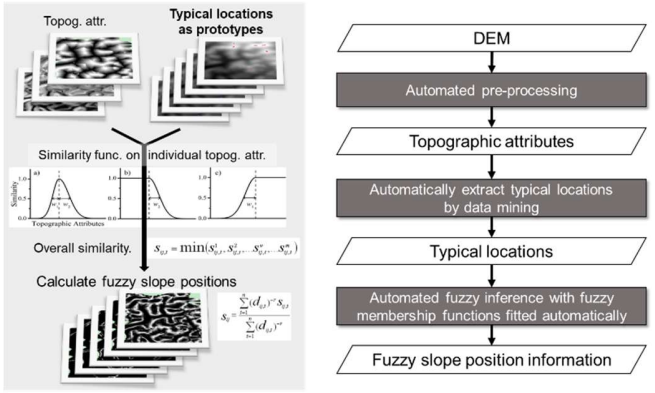

Figure 3. Schema of automatically deriving fuzzy slope position information [9]

we further explored new methods of applying fuzzy slope position information to geographical analysis and optimization tasks, specifically, digital soil mapping and watershed best management practices (BMPs) scenario optimization.

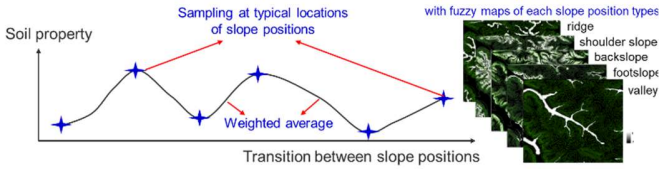

Figure 4. Schema of applying the fuzzy slope position information to not only purposive soil sampling but also soil spatial prediction [10]

A. New method of applying fuzzy slope position information to digital soil mapping

A new digital soil mapping method based on fuzzy slope position information was developed [10]. It applies the fuzzy slope position information to two procedures in digital soil mapping:

1) Purposive soil sampling, that is, using the fuzzy slope position information to suggest those potential sampling locations for measuring the typical soil property value for each slope position type within an interest area;

2) Spatial prediction of soil properties, that is, using the fuzzy slope position information as weight in a weighted-average model (FSPW for short) to predict the soil property values at each unvisited locations (Fig. 4).

The case study within a small (~4 km^2) and low-relief farm in northeastern China showed that fuzzy slope position information on a system of five slope positions (i.e., ridge, shoulder slope, back

slope, foot slope, and channel) can direct purposive sampling to collect a few samples of soil organic matter (SOM) content (first-layer: 10~15 cm; second-layer: 35~40 cm) as modeling points (Fig. 5a). In the model-development area, the proposed model can achieve soil spatial prediction result comparable with that from a traditional multiple linear regression (MLR) model with much more modeling points (Fig. 5b; Table 1) [10]. In the model-extrapolation area with similar environmental conditions to the model-development area, the evaluation results of first-layer SOM prediction based on 102 validation points (Fig. 5c) showed that the proposed model was much more portable (with RMSE=1.31) than MLR (RMSE=1.49) [10].

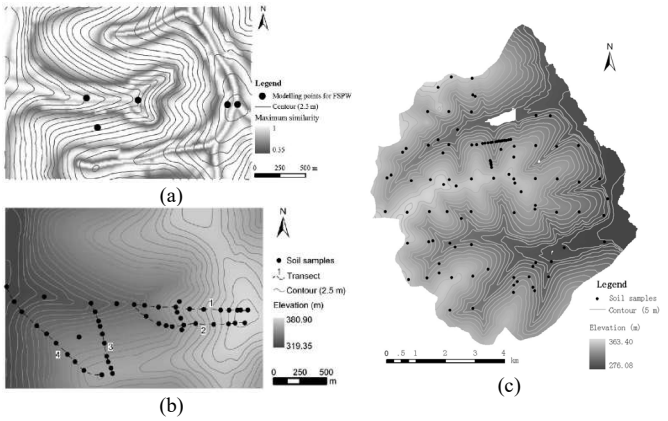

Figure 5. (a) The five purposive sampling points collected at accessible typical locations identified by fuzzy slope position information at 10-m resolution in the case study area in northeastern China (the base map shows the maximum similarity to five slope positions; only one sampling point collected for one slope position type); (b) 48 points for evaluation on the proposed weighted-average model with fuzzy slope positions, meanwhile for modeling of multiple linear regression (MLR) for comparison; (c) 102 validation samples (first-layer organic matter) in the model-extrapolation area (~60 km^2, within 10 km distance to the model-development area and with similar environmental conditions) [10].

TABLE I. EVALUATION RESULTS OF SOM PREDICTED IN THE MODEL-DEVELOPMENT AREA [10]

Predictive model	Evaluation points	RMSE of SOM (10-15 cm)	RMSE of SOM (35-40 cm)
FSPW (with 5 modelling points)	43 (independent with modelling points)	1.40	1.30
MLR (with 48 modelling points)	48 (same as modelling points)	0.98	0.94
	cross-validation	1.24	1.16

B. New method of applying fuzzy slope position information to watershed BMP scenario optimization

Further exploration was made on the potential of applying the fuzzy slope position information to a methodologic framework of best management practices (BMPs) scenario optimization based on watershed simulation (or a simulation-optimization framework for short; Fig. 6) [11].

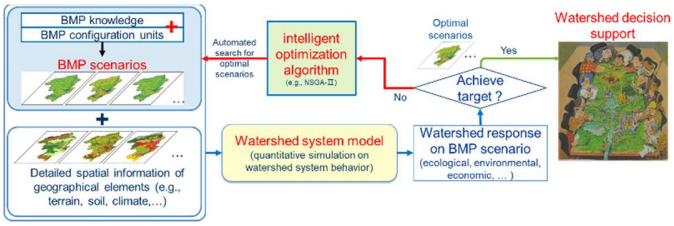

Figure 6. Framework of BMPs scenario optimization based on watershed system simulation

When slope positions were proposed to be used as spatial units for configuring BMPs with more effectively representing the spatial relationships between BMPs and considering the corresponding empirical knowledge [12], more reasonable and practical optimization results could be achieved than using traditional BMPs configuration units such as hydrologic response units (HRUs), farms, and fields [12,13].

Extended from the above method, also with the adaption of a modular and parallelized watershed modeling framework (SEIMS) [14] and an intelligent optimization algorithm (NSGA-II), new proposed methods can innovatively use the fuzzy slope position information to adjust the boundaries of the slope position units as spatial units for configuring BMPs during spatial optimization of BMPs scenarios (Fig. 7) [11].

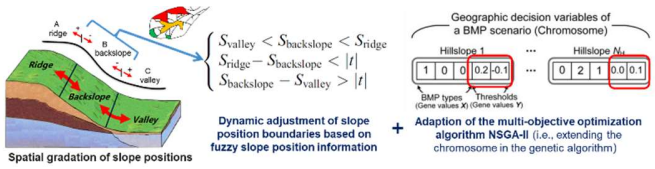

Figure 7. Schema of applying the fuzzy slope position information to adjusting the boundaries of the slope position units for configuring BMPs during BMPs scenarios optimization [11]

A case study was conducted in a small, typical red-soil hilly watershed (~5.4 km^2) in Southeastern China. Four BMPs (i.e., closing measures, arbor-bush-herb mixed plantation, low-quality forest improvement, and orchard improvement) were considered for the watershed management goal of maximizing the soil erosion reduction rate and minimizing the investment. The results showed that using such boundary-adaptive BMP configuration units with fuzzy information at 10-m resolution on three slope position types (i.e., ridge, backslope, and valley; Fig. 8a) in the case study area can enlarge the search space and thus achieve optimal BMP scenarios with better cost effectiveness (i.e., better near-optimal Pareto solutions) than the traditional way of using boundary-fixed units (Fig. 8b) [11].

The adoption of fuzzy slope position information for boundary-adaptive configuration units can further support spatiotemporal

optimization for optimal BMPs scenarios [15],

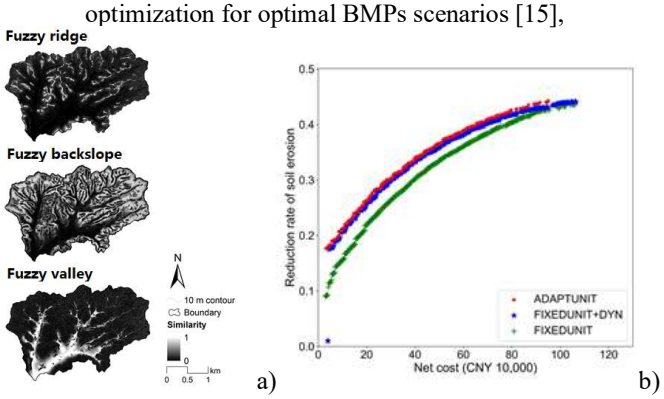

Figure 8. (a) Fuzzy slope positions maps in the case study area in southeastern China; and (b) Near-optimal Pareto solutions of BMP scenario optimization with three ways respectively (ADAPUNIT: the proposed boundary-adaptive BMP configuration units with fuzzy slope position information; FIXEDUNIT: the traditional way of using boundary-fixed units; FIXEDUNIT+DYN: first using boundary-fixed units and then further using the proposed boundary-adaptive optimization) [11]

which may support watershed management decision with more practical solutions [15,16].

IV. CONCLUSION AND DISCUSSIONS

This extended abstract presents systematic research originated from quantifying the spatial transitions between slope positions to be fuzzy slope positions information, which were conducted by the authors and their collaborators in past decade. We designed new methods for solving a series of scientific questions on not only deriving the fuzzy slope positions information from gridded DEM, but also applying such a comparatively new type of terrain information to geographical analysis and optimization tasks. We hope such a systematic presentation on these researches may show the values and potential of new geomorphometric method design for not only terrain analysis but also those terrain-related geographic modeling domains.

Future research may include method research on how to effectively combine fuzzy slope position information (as a typical multiple-layer dataset with interplayed semantics) with other often used topographic attributes for terrain-related geographic analysis and modeling, such as detailedly geomorphic unit identification or classification, and large-area spatial prediction on geographic phenomena (soil variation, vegetation distribution, landslide susceptibility, etc.) for spatial decision-making support.

V. ACKNOWLEGMENTS

We thank the support from National Natural Science Foundation of China [42471499 and 42101480], State Key Laboratory of Resources and Environmental Information System [YPI005], and Shaanxi Normal University [2023-148].

REFERENCES

[1] Deng, Y., 2007. "New trends in digital terrain analysis: landform definition, representation, and classification." Progress in Physical Geography, 31, 405–419.

[2] Irvin, B., S. Ventura, and B. Slater, 1997. "Fuzzy and isodata classification of landform elements from digital terrain data in Pleasant Valley, Wisconsin." Geoderma, 77, 137–154.

[3] MacMillan, R., W. Pettapiece, S. Nolan, and T. Goddard, 2000. "A generic procedure for automatically segmenting landforms into landform elements using DEMs, heuristic rules and fuzzy logic." Fuzzy Sets and Systems, 113, 81–109.

[4] de Bruin, S., and A. Stein, 1998. "Soil-landscape modeling using fuzzy c-means clustering of attribute data derived from a Digital Elevation Model (DEM)." Geoderma, 83, 17–33.

[5] Burrough, P., P. van Gaans, and R. MacMillan, 2000. "High-resolution landform classification using fuzzy k-means." Fuzzy Sets and Systems, 113, 37–52.

[6] Schmidt, J., and A. Hewitt, 2004. "Fuzzy land element classification from DTMs based on geometry and terrain position." Geoderma, 121, 243–256.

[7] Fisher, P., J. Wood, T. Cheng, 2004. "Where is Helvellyn? Fuzziness of multi-scale landscape morphometry." Transactions of the Institute of British Geographers, 29, 106-128.

[8] Qin, C.-Z., A-X. Zhu, X. Shi, B.-L. Li, T. Pei, and C. Zhou, 2009. "Quantification of spatial gradation of slope positions." Geomorphology, 110, 152-161.

[9] Zhu, L.-J., A-X. Zhu, C.-Z. Qin, and J.-Z. Liu, 2018. "Automatic approach to deriving fuzzy slope positions." Geomorphology, 304, 173-183.

[10] Qin, C.-Z., A-X. Zhu, W.-L. Qiu, Y.-J. Lu, B.-L. Li, and T. Pei, 2012. "Mapping soil organic matter in small low-relief catchments using fuzzy slope position information." Geoderma, 171-172, 64-74.

[11] Zhu, L.-J., C.-Z. Qin, and A-X. Zhu, 2021. "Spatial optimization of watershed best management practice scenarios based on boundary-adaptive configuration units." Progress in Physical Geography: Earth and Environment, 45(2), 207-227.

[12] Qin, C.-Z., H.-R. Gao, L.-J. Zhu, A-X. Zhu, J.-Z. Liu, and H. Wu, 2018. "Spatial optimization of watershed best management practices based on slope position units." Journal of Soil and Water Conservation, 73(5), 504-517.

[13] Zhu, L.-J., C.-Z. Qin, A-X. Zhu, J.-Z. Liu, and H. Wu, 2019. "Effects of different spatial configuration units for spatial optimization of watershed beneficial management practices scenarios." Water, 11(2), 262.

[14] Zhu, L.-J., J.-Z. Liu, C.-Z. Qin, and A-X. Zhu, 2019. "A modular and parallelized watershed modeling framework." Environmental Modelling & Software, 122, 104526.

[15] Shen, S., C.-Z. Qin, L.-J. Zhu, and A-X. Zhu, 2023. "Optimizing implementation orders of watershed best management practices with time-varying effectiveness under stepwise investment." Water Resources Research, e2022WR032986.

[16] Shen, S., C.-Z. Qin, L.-J. Zhu, and A-X. Zhu, 2023. "From scenario to roadmap: Design and evaluation of a web-based participatory watershed planning system for optimizing multistage implementation plans of management practices under stepwise investment." Journal of Environmental Management, 342, 118280.

Time to Revamp the Slope Algorithm and KISS?

Peter L. Guth, Professor Emeritus
Annapolis, Maryland, USA
prof.pguth@gmail.com

Cite as: Guth, P. L. (2025). Time to Revamp the Slope Algorithm and KISS? In: Proceedings of Geomorphometry 2025, 9-13 June, Perugia, Italy. M. Alvioli, L. Melelli, I. Marchesini eds. CNR Edizioni, Rome. ISBN 978-88-8080-765-0. DOI: 10.5281/zenodo.15163237

Abstract—**The slope and aspect algorithm, crucial for many applications of digital elevation models suffers from a number of variants that produce very similar results. While some early implementations used other approaches, most current algorithms use least squares to fit a surface to the analysis window, and then derive two partial derivatives to estimate the slope and aspect. Simplification of the least squares solution leads to the common Evans methods. It is time to standardize on a single slope algorithm, with four parameters that can be adjusted: the order of the polynomial, the size of the window, whether the computation can proceed with voids, and if it uses all available points in the window. Pre-filtering of the DEM should not be needed with current DEMs, but selection of a larger analysis window can smooth and generalize the slope and aspect grids and have the same effect as pre-filtering.**

I. Introduction

Slope is perhaps the most pervasive and important land surface parameter (LSP) derived from digital elevation models (DEMs), used in a multitude of applications. A true value for the slope at a point does not exist; even when a geomorphologist measures slope in the field, the value depends on the region over which the measurement takes place. Aspect follows directly from slope; more derived parameters like curvature require additional partial derivatives.

The choices for slope computation involve several distinct aspects:

1. The actual algorithm. The traditional and most common terminologies use the originator's name (e.g. Evans [1], Horn [2], Zevenberger and Thorne [3], or Shary [4]), but some recent descriptions refer to the mathematical basis, such as quadratic [5] or least squares.
2. The window size used in the computations, most commonly 3x3. The higher order partial derivatives for curvature often require a larger window.
3. Use of all the points in the window, or only the required points at the outer edge of the window. Typical implementations use only 8 elevations, even when a window larger than 3x3 has many more points. Third or higher order polynomials require more than 8 points and must use all points in a 5x5 window.
4. Allow the window to have missing data. This allows computations at the edge of the DEM and over some data gaps, with the drawback that the fitted surface could be an extrapolation with perhaps unfortunate effects.
5. The need for pre-filtering of the DEM. This suggestion [6, 7] dates to a time when overall DEM quality and resolution differed greatly from current products derived from lidar or later generation radar sensors.

The suggested computation uses least squares to fit a polynomial trend surface to all points within the window [8] centered on each pixel in the DEM, which introduces some smoothing. The user can select the order of the polynomial, which determines the terms in the equation and the minimum number of points required (Table I). The quadratic equation below shows the coefficients as components of the vector b returned by the least squares solution, with higher order solutions merely adding more terms to the equation. Previous authors have been inconsistent about nomenclature for the coefficients, using different letters, starting the sequence with the lowest or highest order terms, or including the constants from the partial derivatives.

```
z = b[1] + b[2]*x + b[3]*y +
      b[4]*x^2 + b[5]*x*y + b[6]*y^2 +
      b[7]*x^3 + b[8]*x^2*y + b[9]*x*y^2 + b[10]*y^3 +
      b[11]*x^4 + b[12]*x^3*y + b[13]*x^2*y^2 +
      b[14]*x*y^3 + b[15]*y^4
```

Slope and aspect require first order partial derivative z_x and z_y, Curvature requires three second order partial derivatives, z_{xx}, z_{xy}, and z_{yy}.

TABLE I. POLYNOMIAL ORDER REQUIREMENTS

Polynomial order	Terms in equation	Minimum window	Required elevations in window
1 (plane)	3	3x3	3 / 9
2	6	3x3	6 / 9
3	10	5x5	10 / 25
4	15	5x5	15 / 25

The central point has coordinates (0,0), with surrounding points in terms of DEM grid spacings dx and dy in meters, which can be efficiently computed even for DEMs with arc second spacing [9]. When evaluating the partial derivatives at the central point, all terms with x or y disappear. For slope or aspect, the first or second order polynomials have the same b[2] and b[3] coefficients and produce the same results as the Evans [1] or Shary methods [4]. The third and fourth order polynomials produce identical slope and aspect values, which differ from the lower order polynomials because their b[2] and b[3] differ.

All slopes in this paper are reported in percent, and the aspects are in degrees with respect to true north.

II. DATA USED

We merged 4 USGS DTMs at 1 m UTM grid spacing, each 10km x 10 km, covering part of Glacier National Park in Montana. We created a 30 m DEM by mean aggregation, and then extracted a 500 x 500 subset (the largest we can display for the figures in this paper). We also created a 500 x 500 subset of the 1 m DEM, which covers a tiny fraction (1/900th) of the 30 m DEM.

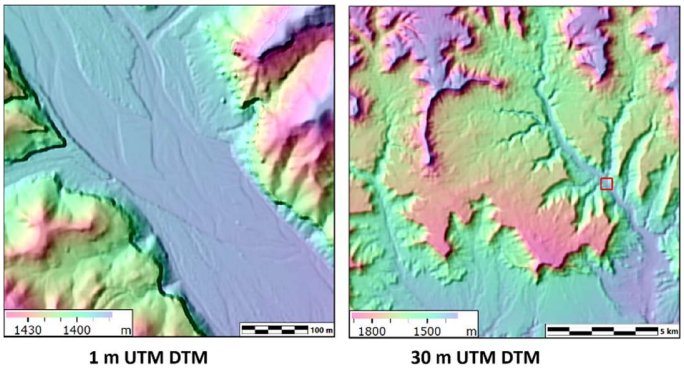

Figure 1. Montana test areas. Outline of 1 m DTM shown on the 30 m DTM.

III. RESULTS

Figures 2 and 3 shows the effect of changing the window size for the order 1 or 2 polynomial, using all points in the window for the least squares solution. Increasing the window size smooths the resulting grids, but neither of these DTMs has appreciable noise and smoothing would only be needed if the user wanted generalization to remove some fine detail. Figure 4 shows that for both these DTMs, the parametric isotropic filtering recommended [6,7] has negligible effect on the slope grids.

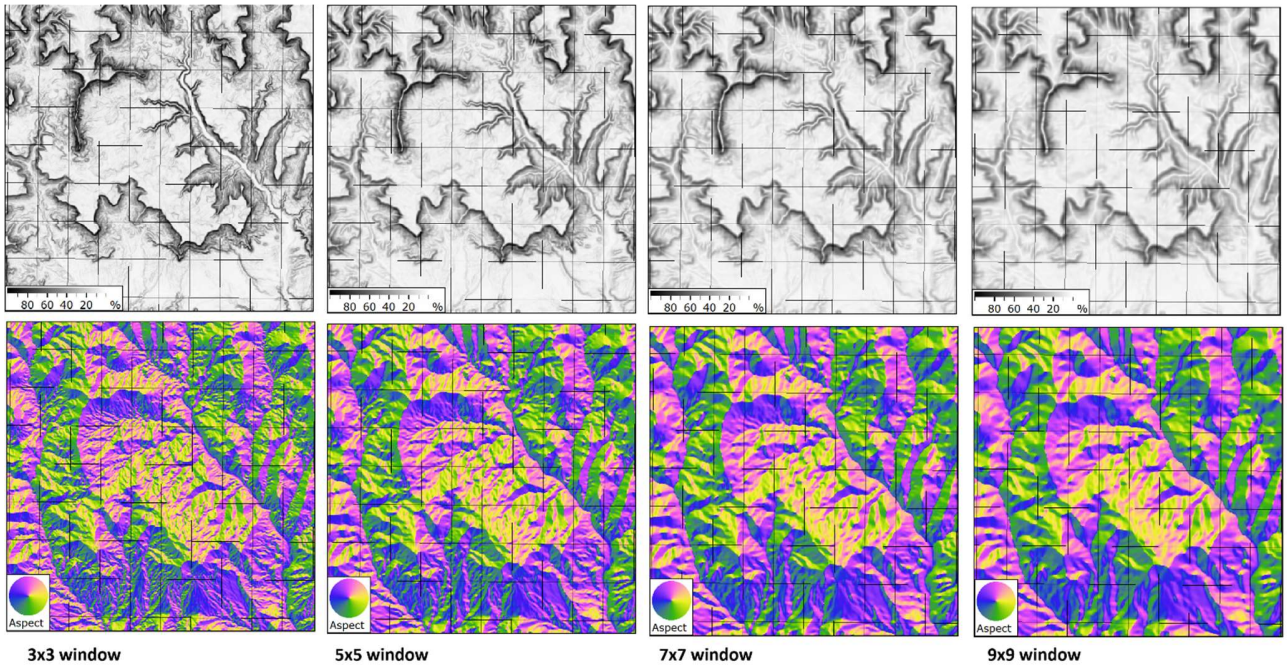

Figure 2. Effect of changing the computation window for the order 1 or 2 polynomial for the 30 m DTM, for slope (top row) and aspect (bottom row).

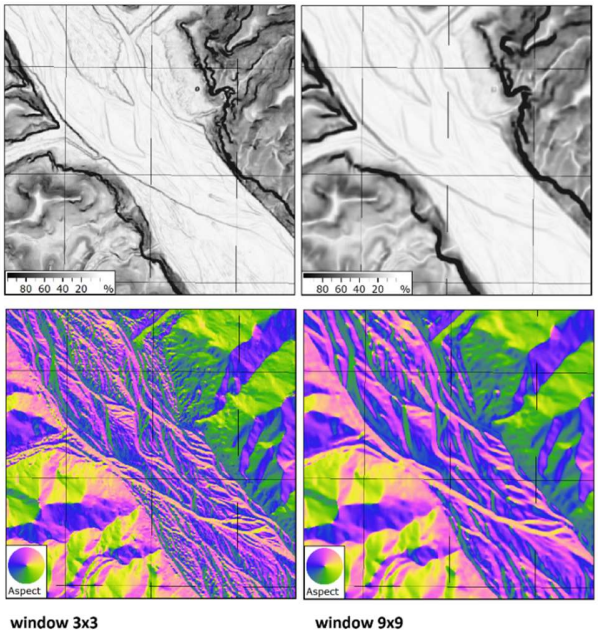

Figure 3. Effect of changing computation window for order 1 or 2 polynomial for the 1 m DTM, for slope (top row) and aspect (bottom row).

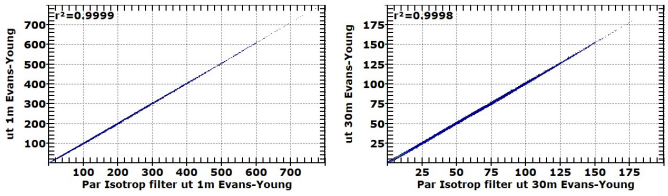

Figure 4. Negligible effects of parametric isotropic filtering before slope computation on the 1 m and 30 m DTMs. The r^2 value is shown in the upper left corner of the graphs.

While a higher order polynomial is required for the higher order partial derivatives needed to compute curvature, it makes little difference for slope computations. Figure 5 compares the slopes from the first/second order polynomial with the third/fourth order polynomial. In simple surfaces all of the polynomials will be equally good and most differences are very small. Moderate differences only occur at the breaks in steep slopes on the cliff edges and canyon bottoms.

Figure 6 shows a correlation matrix for the 4 most common traditional slope algorithms, and the two least squares polynomials with different window sizes. The figure on the right shows the mean absolute differences; by taking the absolute values, high and low differences cannot cancel out. The least squares polynomial with a 3x3 window correlates extremely highly with the traditional algorithms, and has very small mean absolute differences.

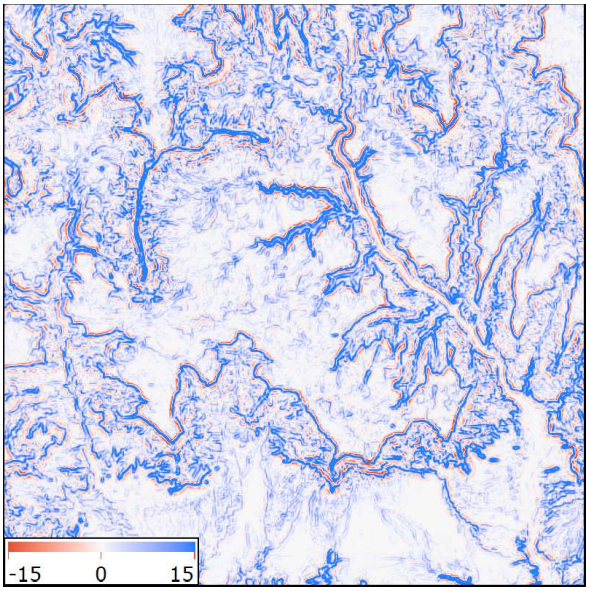

Figure 5. Difference between slope maps for the 30 m DTM computed with an order 1 or 2 polynomial and an order 3 or 4 polynomial. Red colors for the lower order polynomial yielding steeper slopes, and blue when the higher order polynomial is steeper.

IV. Conclusions

Prefiltering the DEM before slope computations: with current DEMs there may be no need for this (Figure 4). If the analysis would benefit from smoothing and generalization beyond that introduced by the polynomial, use of a larger computation window could achieve the same result without creation of a filtered DEM (Figures 2 and 3). The story might be different with integer resolution DEMs, but those have passed their expiration date and should be retired. High resolution lidar DEMs might benefit from smoothing, or alternatively aggregation to a coarser resolution which better matches the scale of interest.

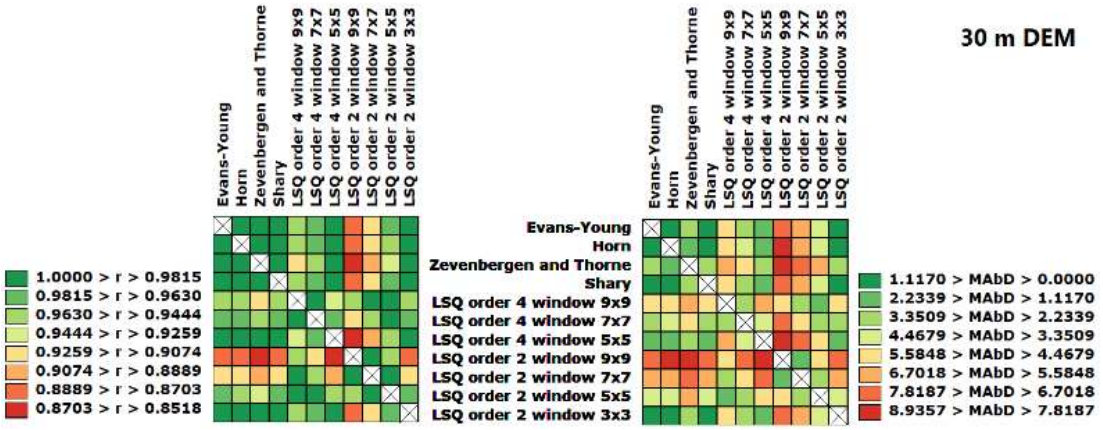

Figure 6. Correlation (left) and mean absolute differences (right) among slope algorithms for a 30 m DEM.

Use of a higher order polynomial: for slope and aspect, order 3 or 4 polynomials (which produce identical results) have results that are substantially different from the traditional estimates of slope and should not be used for slope and aspect. Future work might attempt to determine what the "true" slope should be.

Window size: all points in the 3x3 window should be used, and only computed when the window contains no missing data [10]. Larger windows should be used only when generalization and smoothing are required.

Choosing the best algorithm for curvature is beyond the scope of this paper. Curvatures are among the LSPs with the greatest variability when comparing the current one arc second global DEMs to reference data [11], and geomorphometry programs show much bigger differences in their computations for curvature compared to slope or aspect. If the requirements for the higher order partial derivatives to compute curvature require a more complex estimate for the local terrain surface, perhaps the computation for slope should use a simpler formulation, and users of curvature should understand their metrics could have significant uncertainties.

V. ACKNOWLEDGMENTS

The suggested algorithm is implemented in MICRODEM [12, 13], with options to rapidly compare the effect of varying parameters. While MICRODEM is primarily a GUI program, it can be invoked from the command line to create slope and aspect maps using the methodology described in this paper. MICRODEM created all the figures in this paper. A preprint [10] contains additional figures and analysis.

References

[1] Evans, I.S., 1980, An integrated system of terrain analysis and slope mapping: Zeitschrift für Geomorphologie. Supplementband 36, p. 274-295.

[2] Horn, B.K.P., 1981, Hill shading and the reflectance map: Proceedings of the IEEE, vol.69, no.1, pp.14-47.

[3] Zevenbergen, L.W., and Thorne, C.R., 1987, Quantitative analysis of land surface topography: Earth Surface Processed and Landforms, vol.12, p.47-56. https://doi.org/10.1002/esp.3290120107

[4] Shary, P. A. (1995). Land surface in gravity points classification by a complete system of curvatures. Mathematical geology, 27, 373-390. https://doi.org/10.1007/BF02084608

[5] ESRI, no date, Surface Parameters (Spatial Analyst): https://pro.arcgis.com/en/pro-app/latest/tool-reference/spatial-analyst/surface-parameters.htm, last viewed 12 January 2025.

[6] Shary, P.A., Sharaya, L.S. and Mitusov, A.V., 2002. Fundamental quantitative methods of land surface analysis. Geoderma, 107(1-2), pp.1-32. https://doi.org/10.1016/S0016-7061(01)00136-7

[7] Reuter, H.I., Hengl, T., Gessler, P. and Soille, P., 2009. Preparation of DEMs for geomorphometric analysis. Developments in Soil Science, 33, pp.87-120. https://doi.org/10.1016/S0166-2481(08)00004-4

[8] Davis, J.C., 1973, Statistics and data analysis in geology: New York, Wiley, 1st edition, 550 p. [contains FORTRAN code not present in second edition]

[9] Guth, P., & Kane, M. (2021). Slope, aspect, and hillshade algorithms for non-square digital elevation models. Transactions in GIS, 25, 2309–2332.https://doi.org/10.1111/tgis.12852

[10] Guth, P. (2025). Using MICRODEM to Compare Slope Algorithms. Zenodo preprint. https://doi.org/10.5281/zenodo.15156208

[11] Guth, P.L, and 6 others, C. Ranking of 10 Global One-Arc-Second DEMs Reveals Limitations in Terrain Morphology Representation. Remote Sens. 2024, 16, 3273. https://doi.org/10.3390/rs16173273

[12] Guth, P.L., 2025. GIT-MICRODEM [Delphi source code, archived installation versions]. URL: https://github.com/prof-pguth/git_microdem

[13] Guth, P.L., 2025, MICRODEM: Open-source GIS with a focus on Geomorphometry [download latest Win64 executable and CHM help file] URL: https://microdem.org/

Elevation residual analysis with scale mosaics

John B. Lindsay [1], Yannan Wang, and Marina Coric
Dept. of Geography, Environment and Geomatics
University of Guelph,
Guelph, Canada
[1] jlindsay@uogueph.ca

Cite as: Lindsay, J., Wang, Y., Coric, M. (2025). Elevation residual analysis with scale mosaics. In: Proceedings of Geomorphometry 2025, 9-13 June, Perugia, Italy. M. Alvioli, L. Melelli, I. Marchesini eds. CNR Edizioni, Rome. ISBN 978-88-8080-765-0. DOI: 10.5281/zenodo.15310299

Abstract—**This paper introduces two elevation residual indices, the multiscale low-lying index (MsLLI) and the multiscale elevated index (MsEI), for mapping landforms associated with bottomland and upland positions respectively. These indices use a scale mosaicking approach to represent index values at spatially varying characteristic scales indicative of the local topographic variability in the neighborhood surrounding each grid cell in the input digital elevation model (DEM). The indices were extracted from two study DEMs, one in a complex landscape dominated by past continental glaciation, and the other in a relatively simpler fluvial landscape. Examination of the scale mosaics and key-scale maps allowed for a topographic analysis of the study sites.**

INTRODUCTION

Elevation residual analysis characterizes the relationship between a point on Earth's surface and the surrounding landscape [1] and is generally used to map local topographic position [2] and surface roughness or complexity [3]. These land-surface parameters (LSPs) are frequently used as predictors in a range environmental modelling applications, including soils, vegetation, landform, and geological mapping. Selection of an appropriate modelling scale, or neighborhood size, is one of the key challenges in performing elevation residual analysis [1]. Gallant and Wilson [4] argue that scale selection should be based on matching the length scale of the process under study and suggested that the process scale will be equivalent to the hillslope length in fluvial landscapes. However, in complex landscapes and/or at larger spatial extents, scale selection is complicated by the fact that process scale is likely to vary. Many landscapes are shaped by superimposed processes operating at vastly different spatial scales.

Lindsay et al. [5] demonstrated how locally adaptive scale selection criteria (scale mosaicking) can be used to calculate deviation from mean elevation (DEV), a common elevation residual LSP. Scale mosaicking is a multiscale analysis technique that allows for the representation of a LSP at a range of spatial scales within a single raster map [3]. A scale mosaic is a map of a single parameter (e.g., slope, curvature, topographic position, roughness, etc.), where the parameter is measured at varying spatial scales in different locations [6]. Each grid cell in a scale mosaic represents the parameter at a *characteristic scale*, or *key scale*, that accounts for the unique topographic setting of the site [3,5]. Characteristic scales are identified for a grid cell by finding minima/maxima in the *scale signature* associated with the site. A scale signature is the function that relates an LSP for a site to spatial scales across a range of tested scales [6]. Therefore, a scale mosaic can be conceptualized as a way of collapsing a stack of scaled LSP rasters into a single raster, where each cell takes a maximal (or minimal) LSP value from the stack.

Scale mosaicking has several attractive qualities. Scale mosaics can represent topographic properties associated with landforms of widely varying spatial scales in a single map. This makes them well suited to mapping in complex landscapes that have been shaped by multiple geomorphic processes operating at widely ranging spatial/temporal scales. Because topography is the expression of landscape process, selecting characteristic scales based on topographic settings is more likely to result in a match between the process and modelling scales compared with non-spatially varying scale selection methods. Having the ability to represent local and broad scale features in the same map also implies that scale mosaics have a higher information density than any single uniform scale LSP map sampled from a scale stack. Every LSP scale mosaic also has an accompanying key-scale

raster, which maps the spatial pattern of selected characteristic scales. These key-scale rasters have the potential to provide additional insights into fundamental landscape properties (e.g., where are topographic properties dominated by local versus broad scale processes?). These properties of scale mosaicking led Lindsay [7] to propose the scale mosaic hypothesis, which states: *LSP scale mosaics based on locally optimized scale selection criteria can provide model predictors with denser information, that are better representative of landscape process scales and thereby can improve modelling performance.*

Newman et al. [8] demonstrated that any LSP can be calculated using a scale mosaicking approach. For LSPs that characterize surface shape at a point, e.g., slope and curvatures, scaling can be achieved by measuring the LSP across a series of scaled digital elevation models (DEMs) using a Gaussian scale space approach [9] to suppress topographic detail at shorter scale ranges. Compared with other LSPs, however, those associated with elevation residuals are particularly well suited to scale mosaicking because they are based on neighborhood analysis, i.e. they are measured using roving kernels, or windows, of varying size. That is, their scale dependency is inherent in their definition and how they are measured. In this paper we introduce two new multiscale elevation residual indices based on the scale mosaicking approach, the multiscale low-lying index (MsLLI) and the multiscale elevated index (MsEI). These indices can be used to characterize the extent to which a location occupies an anomalously low-lying or elevated position across a range of spatial scales.

I. The Multiscale Low-Lying and Elevated Indices

Local topographic position (LTP) is the general topographic property that describes how elevated or low-lying a site is relative to its surroundings. Measures of LTP either situate each grid cell in a DEM within the context of benchmark elevations (e.g., height above the nearest drainage, or percent elevation between peak and outlet) or by comparing a grid cell's elevation to that of a local neighborhood of a specified size. The latter definition of LTP takes the form of elevation residual analysis, and common examples include difference from mean elevation (DIFF), DEV, and elevation percentile (EP) [1]. Each of these LTP measures can be represented using a scale mosaic approach [2, 5]. These scale mosaic versions of LTP measures have generally defined characteristic scales by identifying the scale at which the LSP value is either minimal (a trough) or maximal (a peak) in the scale signature. For example, DEV can be positive (indicating a location is more elevated than its surrounding) or negative (indicating that it is lower than its surroundings). The scale mosaic version of DEV, known as DEV_{max} [5], defines the characteristic scale for a cell as the scale at which the *absolute value* of DEV, measured across a range of scales, is maximal. The scale mosaic version of EP, which varies from 0-100%, identifies characteristic scales that are most deviated from a medial landscape position, i.e., the scale at which the scale signature is farthest from 50%, either above or below the medial reference point.

The property of representing both elevated and low-lying positions in the same map is somewhat problematic because a site can be low-lying at one scale and elevated at another. This can result in sharp discontinuities in some scale mosaics, particularly when they are derived from very wide scale ranges (Fig. 1). It is for this reason that Lindsay et al. [5] recommended breaking wide scale ranges into smaller local, intermediate, broad scale ranges, allowing sites that flip from low-lying to elevated, or vice versa, to be represented in the set of smaller-range scale mosaics and reducing the prevalence of discontinuities.

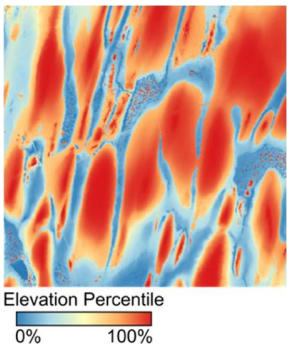

Figure 1. An elevation percentile scale mosaic for a 10-m DEM of a site near Peterborough, Canada, derived from a scale range of 5-250 grid cells.

As an alternative, we propose separating scale signature minimum and maximum functions, creating a separate multiscale low-lying index (MsLLI) and multiscale elevated index (MsEI). To calculate these two scale mosaics, we must first specify a test scale range, defined by a starting scale (in grid cells) and scale sampling density (e.g. the interval between tested scales). While the test scale range can theoretically increase to the global extent, in practice, the upper bound occurs when scales approach the full extent of the DEM and no further increase in window size will yield meaningful variation. Even smaller upper bounds are likely appropriate. The measure of LTP used for MsLLI and MsEI is the difference from a Gaussian-weighted mean elevation ($DIFF_{Gaussian}$), effectively a high-pass Gaussian filter. For each tested scale in the scale range the original DEM is differenced from a smoothed DEM resulting from Gaussian filtering with a kernel size corresponding to the tested scale. The 2D Gaussian filter function is symmetrical and circular, even when measured using square kernels, which is an advantage of this approach, resulting in fewer windowing artifacts. The efficiency of the smoothing function is important for scale mosaicking methods because it limits the practicality of sampling scale space densely. Thus, our implementation of MsLLI and MsEI uses Kovesi's [10] fast almost-Gaussian filter based on constant-time (i.e., performance is independent of kernel size) integral image transform calculations.

Average $DIFF_{Gaussian}$ values derived from a DEM over a range of tested scales will increase monotonically. This is because average relief increases predicably with scale and this function is

in itself uninteresting for our purposes. Instead, we wish to identify scales at which a site is *anomalously* elevated/low-lying across the range of tested scales. Therefore, the high-pass Gaussian rasters derived from each tested scale is standardized by dividing $DIFF_{Gaussian}$ values by the standard deviation of the entire high-pass Gaussian raster. These rescaled $DIFF_{Gaussian}$ values are therefore z-scores and are unitless.

MsEI can then be calculated by identifying the highest rescaled $DIFF_{Gaussian}$ values for each grid cell and each tested scale. Sites that are not elevated across all the tested scales have a MsEI value of 0.0. Similarly, MsLLI is calculated by identifying the lowest rescaled $DIFF_{Gaussian}$ values; once found, however, this value is sign-reversed so that the index increases the more low-lying a site is relative to its surroundings. In addition to the scale mosaics, it is possible to track at which scale the maximum (MsEI) and minimum (MsLLI) values were identified for each grid cell, i.e., the key-scale map.

Our MsLLI and MsEI implementations are available for use in Whitebox Workflows as the `multiscale_low_lying_index` and `multiscale_elevated_index` functions.

II. Case Studies

The first case study data set was a 30-m lidar DEM of a 68×54 km^2 area near Peterborough, Canada. The site is bounded by Lake Ontario in the south. The southernmost section of the site is the former lakebed of the once larger Lake Ontario and exhibits organized dendritic drainage patterns, including the Ganaraska River. The site has been largely shaped by the processes of past continental glaciation. The Oak Ridges moraine dominates the southern half of the site and large bedrock outcrops are present in the north. The central region of the site contains several lakes, the largest of which is Rice Lake. Numerous tightly spaced drumlins cover the southern and central regions.

None of the scale mosaics in Fig. 2 exhibit any of the sharp discontinuities observed in Fig. 1, which is apparent upon closer inspection. Instead, index values were found to vary gradually. MsLLI (Fig. 2A), calculated at a broad scale range of 250 grid cells to 978 cells, was highest for the former lakebed (south) and its superimposed river systems, the lakes (mid-section), and lowlands between bedrock outcrops (north). The corresponding key-scale raster (Fig. 2B) shows that characteristic scales at or near the upper bound of the tested range were prevalent in the former lakebed and modern lake areas, and that the narrower lowlands between rocky outcrops were associated with shorter characteristic scales. However, all tested scales were present in the key-scale raster (Fig. 2B) and are represented in the low-lying index scale mosaic (Fig. 2A). We calculated MsEI for two separate scale ranges, 0.03-3.0 km (1-100 grid cells) and 7.5-29.44 km (250-978 grid cells) (Fig. 2), to illustrate how the technique can be used to separate landforms of widely varying spatial scale. The scale mosaic derived from the shorter scale range is dominated by the numerous drumlins (Fig. 2C) while the moraine dominates the broad-range scale mosaic (Fig. 2E). Smaller bedrock outcrops are present in Fig. 2C and larger outcrops are mapped in the northern sections of Fig. 2E. The outcrops, which occupy an intermediate scale range between the relatively smaller drumlins and larger morainal ridges, can be seen to occupy the upper scale bounds of the smaller scale range map (Fig. 2D) and the lower scale bounds of the broader scale range map (Fig. 2F).

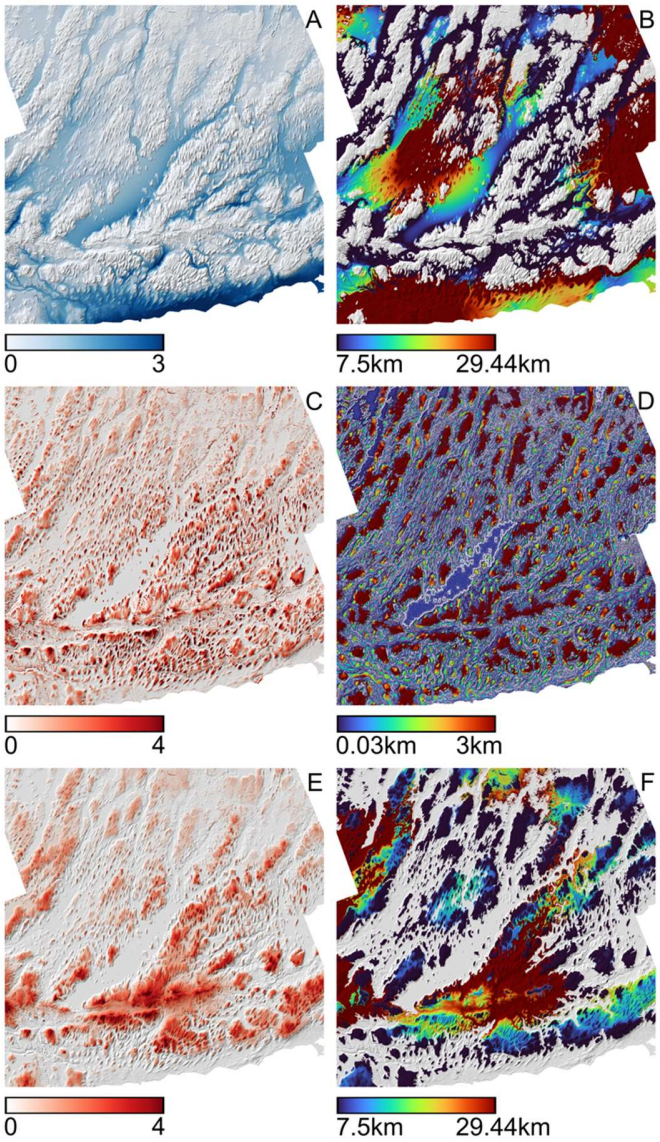

Figure 2. Peterborough site A) MsLLI for the scale range 7.5-29.44 km, B) the corresponding key-scale raster, C) MsEI for the scale range 0.03-3.0 km, D) the corresponding key-scale raster, E) MsEI for the scale range 7.5-29.44 km, and F) the corresponding key-scale raster. Grey areas in the key scale rasters (B, D, F)

correspond to sites with no index value because it is not low lying (MsLLI) or elevated (MsEI) at any tested scale.

The second case study data set is a 1-m lidar DEM of an approximately 5×8 km^2 area located 65 km northeast of Grand Junction, Colorado. The site contains two wide and deeply incised canyons, with East Fork Parachute Creek in the south and East Middle Fork Parachute Creek in the north; both are tributaries of the Colorado River. Cliffs line the walls of the two canyons. Outside of the canyons, topography is also dominated by fluvial processes, with a high drainage density and abundant small, incised headwater valleys. Fig. 3 shows the patterns of MsLLI and MsEI derived from the DEM. Unsurprisingly, the canyon bottoms dominate the low-lying index map (Fig. 3A). The corresponding key-scale raster (Fig. 3B) shows how the scale mosaic approach adapts the selected characteristic scales to the varying hillslope length, from the widest canyons to the narrowest headwater valleys. The elevated index scale mosaic map (Fig. 3D) is dominated by the ridges between incised river valleys and the upper cliff walls.

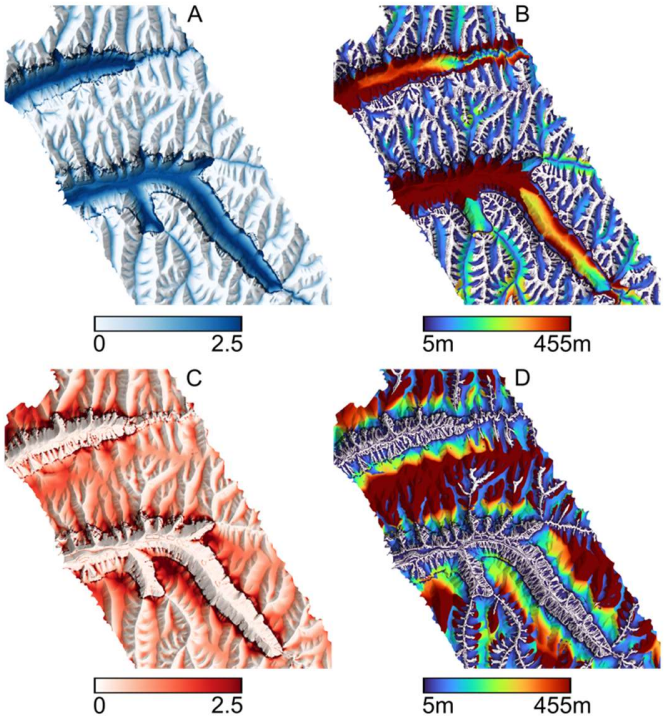

Figure 3. Grand Junction site A) MsLLI for the scale range 5-455 (grid cells), B) the corresponding key-scale raster, C) MsEI for the scale range 5-455 (grid cells), and D) the corresponding key-scale raster.

III. Conclusions

This paper introduces two scale-mosaic derived LSPs for multiscale mapping of landforms associated with bottomland and upland topographic positions. These indices allow for elevation residual analysis across wide scale ranges in a way that is unaffected by the discontinuities that can sometimes impact other scale mosaic measures of LTP. By applying the indices to two test sites, it was shown that the indices can map landforms that occupy widely varying spatial scales within complex landscapes shaped by diverse geomorphic processes; furthermore, even in relatively simpler fluvial landscapes the scale mosaic method is able to automatically adapt measurement scales to varying hillslope lengths. Further work should explore whether the high information density of MsLLI and MsEI rasters can improve the performance of predictive mapping applications that rely on LSPs as predictors.

IV. Acknowlegments

Funding for this research has been provided by the Natural Sciences and Engineering Research Council of Canada (NSERC), grant number 401107.

References

[1] Wilson, J.P., 2018. “Environmental applications of digital terrain modeling”. John Wiley & Sons.

[2] Newman, D.R., Lindsay, J.B., and Cockburn, J.M.H., 2018. Evaluating metrics of local topographic position for multiscale geomorphometric analysis. Geomorphology, 312, 40-50.

[3] Lindsay, J.B., Newman, D.R., and Francioni, A., 2019. Scale-optimized surface roughness for topographic analysis. Geosciences, 9(7), 322.

[4] Gallant, J.C. and J.P. Wilson, 2000. “Primary topographic attributes”, Terrain analysis: Principles and applications, 87-131.

[5] Lindsay, J.B., Cockburn, J.M.H., and Russell, H.A.J., 2015. An integral image approach to performing multi-scale topographic position analysis. Geomorphology, 245, 51-61.

[6] Wood, J., 2009. Geomorphometry in LandSerf. in T. Hengl and H.I. Reuter, Geomorphometry: a brief guide. Developments in Soil Science, 33, , 333-349. https://doi.org/10.1016/S0166-2481(08)00014-7.

[7] Lindsay, J.B., 2023. “The case for locally scale optimized land-surface parameters”. Keynote presentation at Geomorphometry 2023, Iasi, Romania; July 10-14.

[8] Newman, D.R., Cockburn, J.M., Drăguţ, L., and Lindsay, J.B., 2022. Local scale optimization of geomorphometric land surface parameters using scale-standardized Gaussian scale-space. Computers & Geosciences, 165, 105144.

[9] Lindeberg, T., 1994. Scale-Space Theory in Computer Vision. doi:10.1007/978-1-4757-6465-9. ISBN 978-1-4419-5139-7.

[10] Kovesi, P., 2010. Fast Almost-Gaussian Filtering, Digital Image Computing: Techniques and Applications (DICTA), 2010 International Conference on Digital Image Computing: Techniques and Applications (pp. 121-125). IEEE.

Profile Integral, a robust and unified metric for measuring profile concavity

Li, Yingkui
Dept. of Geography & Sustainability, U. of Tennessee, Knoxville, USA
yli32@utk.edu

Evans, Ian S.*
Dept. of Geography, Durham U.
Durham, U.K.
i.s.evans@durham.ac.uk

Harbor, Jonathan M.
Dept. of Earth, Atmos. & Planet. Scis., Purdue U.
W. Lafayette, U.S.A.

Cite as: Li, Y., Evans, I. S., Harbor, J. M. (2025). Profile Integral, a robust and unified metric for measuring profile concavity. In: Proceedings of Geomorphometry 2025, 9-13 June, Perugia, Italy. M. Alvioli, L. Melelli, I. Marchesini eds. CNR Edizioni, Rome. ISBN 978-88-8080-765-0. DOI: 10.5281/zenodo.15106525

Abstract— **To measure the shape of topographic profiles in two dimensions (height v. distance), we propose a new metric (and develop its related toolbox) based on integrating the area under the profile. It is applicable to any cross-valley profile, slope profile, long profile or arbitrary profile. By analogy with the Hypsometric Integral, we term the metric the Profile Integral. It is a normalized value between 0 and 1 with the value of 0.5 representing either a straight-line long profile or a V-shaped cross-profile and values of > 0.5 for convex profiles and <0.5 for concave profiles. Correlations with the V-index, the VWDR, the K-curve, the power curve and the quadratic polynomial are analyzed. The advantages of the Profile Integral are (1) its flexibility in providing a metric with similar interpretations for long profiles, slope profiles and valley cross-profiles and (2) its applicability to asymmetric cross-profiles in full, including those close to the confluence of tributary valleys (asymmetric cross-profiles, reaching different heights on each side, are common yet are excluded from most analyses of valleys and troughs). Our toolbox generates smoothed streamlines (thalwegs) to provide starting points for a series of cross-profiles. Applications to glaciated valleys in the Tian Shan (Daxi) and northern Iceland (Eyjafjarðardalur) are illustrated.**

I. Introduction

Measures of concavity are used, for example, to characterize slope profiles and river long profiles, to express the degree of cirque development (Çılğın et al., 2024[1]) and the degree of glacial modification of valleys from V to U-shaped cross-profiles (Harbor, 1995[2]; Harbor and Wheeler, 1996[3]). Methods include fitting exponential, power and quadratic functions, and indices based on width and depth. It is not clear which methods provide the most valuable results.

Here we propose a new metric, the Profile Integral (PI), and develop its related toolbox based on integrating the area under the profile. We then compare it with a range of indices of concavity measures fitted to two-sided valley cross-profiles and to one-sided long or slope profiles. We present correlations between the various indices and exponents and find that our proposed metric, PI, with a simple expression has numerous advantages as a single-index measure of concavity. We advocate its use for a broad range of profiles.

II. PREVIOUS INDICES

Indices applicable to two-sided valley cross-profiles have included: the coefficients 'a' and 'b' of a power law function to the relationship between the width/depth ratios at different depths of the valley - the VWDR (Valley Width-Depth Ratio) model (Li et al., 2001a[4]);

$$y = ax^b \quad (1);$$

'c' in the quadratic equation

$$y = a + bx + cx^2 \quad (2)$$

(James, 1996[5]; Li et al., 2001a[6]); and the

$$V\text{-index} = (Ax/Av) - 1 \quad (3)$$

(Zimmer and Gabet, 2018[7]), where Ax is the valley cross-sectional area above the profile, up to a fixed height, and Av is the V-shaped area with the same height and width. Finally, as the difference in height on the two sides of a valley is of some importance, the degree of deviation from equality in height can be expressed as:

$$HHratio = hmin/hmax \quad (4),$$

where hmin and hmax relate to the heights of left and right valley sides, hl and hr in Fig.1c.

Indices for one-sided (slope or long) profiles include 'a' and 'b' for the power law fit to altitude values, as in equation (1) (there are complications in applying it to a full cross-profile, Harbor and Wheeler, 1992[3]); 'a' and 'b' of the exponential fit

$$y = ae^{bx} \quad (5);$$

the coefficient ‘c’ of Kcurve (Krause et al., 2022[8]):

$$y = (1-x)e^{cx} \quad (6);$$

Profile Closure, the difference between maximum and minimum slope gradient along an axial profile (Li et al., 2024[9]: cf. Evans and Cox, 1995[10]); and the Stream length – Gradient index for river long profiles,

$$SL = dH/dL * L \quad (7),$$

where L is the cumulative length from the start point of the stream profile; dH and dL are the differences respectively in elevation and length of a short segment along the stream profile.

III. PROFILE INTEGRAL AND SAMPLING

The newly proposed Profile Integral (PI) is defined as:

$$PI = h\_mean/H = (E\_mean – E\_min)/(E\_max – E\_min) \quad (8),$$

where h_mean is the average of the heights along the profile, H is the height/depth of the profile, E_mean, E_min, and E_max are the average, minimum, and maximum elevations above sea level of all equally spaced points along the profile. PI represents the ratio of the area under the profile to the area (L * H) of the

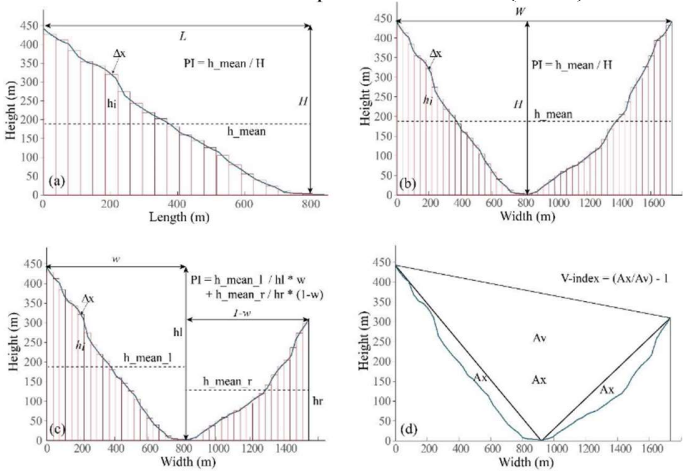

Figure 1. Definition of the profile integral (PI) for a one-sided topographic profile (a), a two-sided valley cross-sectional profile with the same height at both sides (b), and a two-sided asymmetric valley cross-sectional profile with different heights at either side (c): l = left and r = right. (d) extends the definition of the V-index proposed by Zimmer and Gabet (2018), to apply more generally to a two-sided valley cross-sectional profile which is asymmetric, with different heights on the two sides. Av is the triangle area of the two end points and the lowest point of the profile. Ax is the area above the topographic profile, up to the top line of Av.

profile’s rectangular envelope, or the area under the standardized topography profile if both y (height) and x (width or length) are standardized to [0, 1], which is similar to the definition of the hypsometric integral (HI). Fig 1 illustrates its application in different situations, and how the definition of V-index can be adapted to the general situation of each valley side having a different height.

We develop a GIS toolbox to delineate the streamlines (thalwegs), generate cross-sectional profiles along streamlines, and derive PI and other related metrics for both two-sided cross-sectional profiles and one-sided profiles, like stream long profiles. We demonstrate how to use this toolbox for topographic profile analysis in two test areas: one in the Daxi Valley area, eastern Tian Shan, China, and the other in the Eyjafjarðardalur area, Northern Iceland. Fig. 2 shows how valley cross-profiles can be defined automatically, starting from the streamline (thalweg) network. Some profile lines are deleted manually because bends in a streamline produced obliquity to the valley-side.

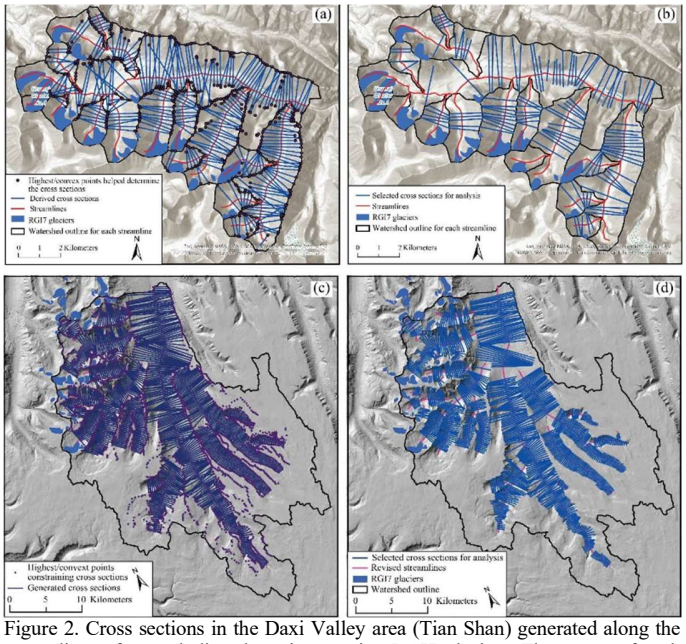

Figure 2. Cross sections in the Daxi Valley area (Tian Shan) generated along the streamlines after excluding those intersecting RGI7 glaciers. The extent of each cross-section is constrained by the lowest (above threshold) convex point on each side of the cross-section. (b) Selected cross sections after visual checks and revisions for valley morphological analysis in the Daxi Valley area. (c) Cross-sections in the Eyjafjarðardalur area (Iceand) generated along the streamlines after excluding the cross sections intersecting RGI7 glaciers. (d) 484 cross-sections selected for further analysis after visual checks and revisions based on valley morphological analysis in the Eyjafjarðardalur area.

IV. RESULTS

Table I shows strong correlation between PI and the V-index in the Daxi valley area. They both correlate moderately with ‘m’ and ‘n’ coefficients of VWDR, which correlate strongly with each other.

TABLE I. PEARSON CORRELATIONS OF CONCAVITY METRICS IN THE DAXI VALLEY AREA FOR CROSS-PROFILES, n = 123.

	PI	Ln(V_index+1)	Ln(Quad_c)	Ln(VWDR_m)	VWDR_n
PI	1.00				
Ln(V_index+1)	-0.88	1.00			
Ln(Quad_c)	-0.04	-0.18	1.00		
Ln(VWDR)_m	-0.59	0.40	0.03	1.00	
VWDR_n	0.49	-0.27	-0.27	-0.95	1.00

Fig. 3 shows the greater concavity (lower PI) of the trunk glacial trough in the Eyjafjarðardalur area (heading north toward Akureyri) compared with tributary troughs. Only a few cross-profiles, mainly near headwaters in the east, show net-convex valley-sides (red). While the frequency distribution of PI values is close to symmetrical, some other indices are highly skewed (Csillik et al., 2015[11]). Thus, to calculate correlation coefficients, a logarithmic scale is needed for both the quadratic 'c' and the VWDR 'm' coefficient; and the logarithm of V-index is taken after adding 1 to avoid negative values.

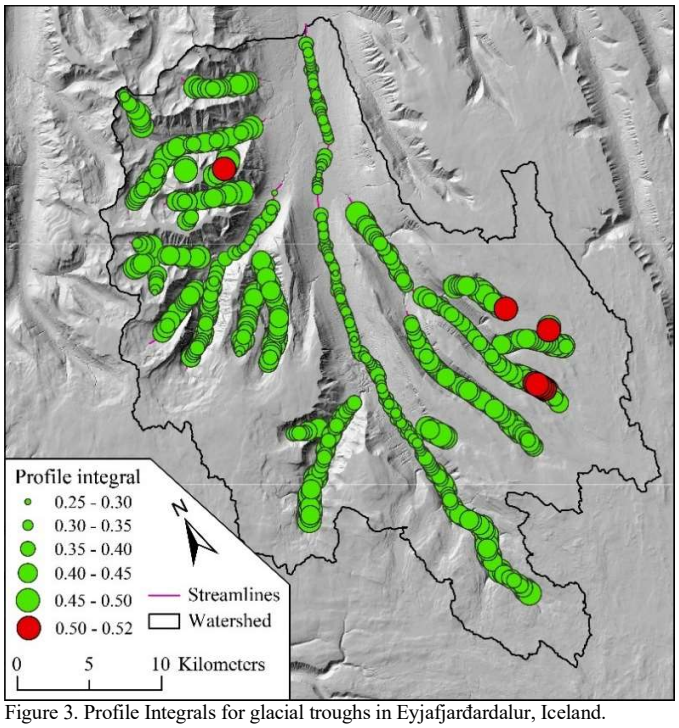

Figure 3. Profile Integrals for glacial troughs in Eyjafjarðardalur, Iceland.

Table II gives correlations both for the whole set of cross-profiles and (in brackets) for the subset with asymmetry limited to HHratio > 0.7, in the Eyjafjarðardalur area. The latter mainly provides slightly stronger correlations, especially for V-index, because the V-index is a special case of PI for valleys with two sides of equal height, while its calculation for asymmetric cross-profiles differs, as illustrated in Fig. 1 (c) and (d). All correlations for Quad_c are weak for Daxi, but higher for Eyjafjarðardalur.

Table III gives indices for the 1490 valley-sides with profiles over 100 m long in the Eyjafjarðardalur area. Kcurve_c was formulated explicitly to express concavity of cirque profiles (Krause et al., 2022[8]): its very strong correlation (0.97) with PI shows that both are good indicators of concavity. Although the exponent 'b' of the power fit has been used widely to indicate the degree of glacial erosion giving U-shaped valleys, its correlation with PI is only -0.51, whereas that of power exponent 'a' is stronger (0.67). It seems that both a and b are required for a power fit to express concavity. The logarithms of both the coefficients of exponential fits have stronger correlations with PI and with Kcurve_c, but 'a' has stronger correlations than 'b'. The stream length - gradient index, SL, has weak correlations, the strongest being only -0.36 with PI.

TABLE II. PEARSON CORRELATIONS OF CONCAVITY METRICS IN EYJAFJARÐARDALUR AREA FOR CROSS-PROFILES

	PI	Ln(V-index+1)	Ln(Quad_c)	Ln(VWDR_m)
PI	1			
Ln (V-index+1)	-0.85 (-0.99)	1.00		
Ln (Quad_c)	0.65 (0.67)	-0.60 (-0.67)	1.00	
Ln (VWDR_m)	-0.88 (-0.88)	0.78 (0.88)	-0.71 (-0.69)	1.00
VWDR_n	0.76 (0.78)	-0.66 (-0.77)	0.38 (0.37)	-0.91 (-0.92)

The values outside of ( ) are for the whole dataset (n = 747); inside of ( ) are for cross sections with HHratio > 0.70 (n = 446).

TABLE III. PEARSON CORRELATIONS FOR HALF-VALLEY METRICS IN EYJAFJARÐARDALUR AREA. N = 1490. Values >|0.5| are in bold.

	PI	Closure	Kcurve_c	SL	(Pow_a)	Ln(Pow_b)	Ln (Exp_a)
PI	1						
Closure	-0.25	1					
Kcurve_c	**0.97**	-0.27	1				
SL	-0.36	0.33	-0.37	1			
Pow_a)	**0.67**	0.13	**0.65**	-0.15	1		
Ln(Pow_b)	**-0.51**	0.34	-0.45	0.24	0.19	1	
Ln(Exp_a)	**0.77**	-0.20	**0.68**	-0.31	0.28	**-0.87**	1
Ln(Exp_b)	**-0.69**	0.25	**-0.62**	0.34	-0.11	**0.94**	**-0.97**

V. CONCLUSIONS

We conclude that PI is a robust and flexible descriptor of the overall convexity or concavity of any profile. It is applicable to long profiles, transects and valley cross-profiles including those for valleys with one side higher than the other. It is closely related to the V-index (which can be regarded as a special case of PI) and to Kcurve_c, and is well correlated with VWDR at least for symmetrical valleys. The quadratic 'c' has moderate correlations with PI.

For one-sided profiles, both Profile Closure and Stream Length-Gradient have weak correlations with the other indices, presumably because neither fits the whole profile. There is no space here, however, to illustrate application to river long

profiles. Coefficients of exponential and power fits are only moderately correlated with PI because two-parameter models are not good at providing a single index for concavity. Logarithms of 'b' of the power fit and of 'a' and 'b' of the exponential fit, correlate strongly (r >|0.85|) with each other.

Our toolbox provides the option of saving all profiles to a folder for detailed analysis of their validity, their particular features and the reasons for variations between indices.

We advocate PI as the preferred index for measuring convexity or concavity of any topographic profiles, including cross-valley, slope, stream long profiles.

REFERENCES

[1] Çılğın, Z., Evans, I.S., Keserci, F., Canpolat, E., Bayrakdar, C., 2024. Morphometric characteristics of glacial cirques and former glaciers in the Geyik Mountains, Western Taurus, Türkiye. Geomorphology 467, 109474. https://doi.org/10.1016/j.geomorph.2024.109474

[2] Harbor, J.M., 1995. Development of glacial-valley cross sections under conditions of spatially variable resistance to erosion. Geomorphology 14, 99–107. https://doi.org/10.1016/0169-555X(95)00051-1.

[3] Harbor, J.M., Wheeler, D.A., 1992. On the mathematical description of glaciated valley cross-sections. Earth Surf. Processes Landforms 17, 477–485.

[4] Li, Y., Liu, G., Cui, Z., 2001a. Longitudinal variations in cross-section morphology along a glacial valley: a case-study from the Tien Shan, China. Journal of Glaciology 47, 243–250. https://doi.org/10.3189/172756501781832278

[5] James, L.A., 1996. Polynomial and power functions for glacial valley cross-section morphology. Earth Surf. Processes Landforms 21, 413–432.

[6] Li, Y., Liu, G., Cui, Z., 2001b. Glacial valley cross-profile morphology, Tian Shan Mountains, China. Geomorphology 38, 153–166. https://doi.org/10.1016/S0169-555X(00)00078-7.

[7] Zimmer, P.D., Gabet, E.J., 2018. Assessing glacial modification of bedrock valleys using a novel approach. Geomorphology 318, 336–347. https://doi.org/10.1016/j.geomorph.2018.06.021

[8] Krause, D., Fišer, J., Křížek, M., 2022. Morphological differences of longitudinal profiles between glacial cirques and non-glacial valley heads, described by mathematical fitting. Geomorphology 404, 108183. https://doi.org/10.1016/j.geomorph.2022.108183

[9] Li, Y., Evans, I.S., Spagnolo, M., Pellitero, R., Barr, I.D., Ely, J.C., 2024. ACME2: An extended toolbox for automated cirque metrics extraction. Geomorphology 445, 108982. https://doi.org/10.1016/j.geomorph.2023.108982

[10] Evans, I.S., Cox, N J., 1995. The form of glacial cirques in the English Lake District, Cumbria. Zeits.f. Geomorph., N.F. 39 (2), 175-202 doi: 10.1127/zfg/39/1995/175.

[11] Csillik, O., Evans, I.S., Drăguţ, L., 2015. Transformation (normalization) of slope gradient and surface curvatures, automated for statistical analyses from DEMs. Geomorphology 232, 65-77. DOI:10.1016/j.geomorph.2014.12.038.

DEM Generalization Tool Using Grid-Based Quadric Error Metric

Richard Feciskanin, Jozef Minár
Dept. of Physical Geography and Geoinformatics
Faculty of Natural Sciences, Comenius University
Bratislava, Slovakia
richard.feciskanin@uniba.sk

Cite as: Fesickanin, R., Minár, J. (2025). DEM Generalization Tool Using Grid-Based Quadric Error Metric. In: Proceedings of Geomorphometry 2025, 9-13 June, Perugia, Italy. M. Alvioli, L. Melelli, I. Marchesini eds. CNR Edizioni, Rome. ISBN 978-88-8080-765-0. DOI: 10.5281/zenodo.15024141

Abstract—**We introduce a novel tool for generalizing Digital Elevation Models (DEMs) using the Quadric Error Metric (QEM), specifically adapted for raster grids. While traditional QEM methods have been used for polygonal simplification, our approach applies QEM directly to raster DEMs, providing a robust solution for land surface generalization. This method enables progressive generalization through an iterative process that smooths out subtle details while preserving key landforms and geomorphic structures. The tool incorporates a sharpness parameter that allows users to fine-tune the generalization process by balancing edge preservation (or even accentuation) and simplification. The tool avoids the typical peak-clipping and valley-filling effects associated with simpler smoothing techniques, effectively maintaining the depth and height of non-generalized forms. Additionally, the approach ensures that significant surface features are preserved even at high levels of generalization. Implemented in Rust, this command-line tool provides an efficient, open-source solution for processing DEMs in geomorphometric and other geoscientific applications.**

I. Introduction

Modern mapping technologies, primarily LiDAR, enable the creation of high-precision Digital Elevation Models (DEMs) capable of capturing subtle topographic variations. While these high-resolution DEMs inherently include surface roughness and small landforms, preserving such detail is unnecessary—and often undesirable—for analyses focused on larger geomorphic structures. According [1], neither the highest resolution nor the initial data scale ensures optimal representation, emphasizing the need for scale optimization. Additionally, calculating derivatives amplifies high-frequency noise, with higher-order derivatives being nearly unusable without DEM smoothing [2]. Thus, small-scale noise is often suppressed through techniques like grid resampling, low-pass filtering, or polynomial smoothing, although these methods do not effectively preserve critical features such as ridges and valleys [3, 4]. Efforts to minimize excessive feature smoothing have involved the implementation of variable-size filters [5] and the utilization of restricted neighborhoods [6].

Advanced methods aim to preserve key land surface features while reducing noise. Wavelet transformations, morphological operations, and drainage-preserving approaches target specific applications, but they have their own limitations [7] and require subjective parameter tuning, limiting their broader use. These methods often fail to support the high-level generalization needed to identify and analyze the major geomorphic structures bounded by distinct edges. For such cases, Triangulated Irregular Networks (TIN) based generalization methods are more effective. Various techniques, such as those by [8, 9], have been developed to generalize and reconstruct land surfaces using TINs, which involve extracting 3D points and triangulation. In other fields, numerous procedures have been developed, with the Quadric Error Metric (QEM), introduced by [10], excelling in polygonal model simplification by producing near-optimal triangles for surface representation [11].

While QEM-based TIN models perform well, their lack of smoothness complicates the calculation of some land surface parameters (LSPs) [12], and the conversion back to grids adds complexity [13]. This limitation motivated us to adapt the QEM framework for raster DEMs, offering a novel approach to land surface simplification. Unlike previous work [14], which, as known, only used QEM for grids (in basic form and not solely on the grid), our method operates directly on raster grids, utilizing the full potential of the QEM method, similar to its original application. By leveraging QEM's strengths within a grid structure, our approach introduces a new methodology for generalized DEMs that retains essential land surface features,

grid as is common in geomorphometry, but general mathematical matrix-based formulas, similar to [9]. This approach offers several advantages: straightforward application to polynomials of various degrees, support for grids with different spacing along the individual axes (essential for input in geographic coordinates), and the ability to handle incomplete 5×5 windows (at the edges of a study area), as further detailed below. With appropriate optimization, the computation is not significantly more demanding than analogous computations using the classical approach. Moreover, the purpose-built tool allows for the calculation of all supported LSPs in a single run, making it far more efficient than other existing tools.

II. Methods

The main task in calculating LSPs involves computing the partial derivatives of elevation z (up to the required order for specific LSPs). This is based on the concept of the land surface being defined by a general bivariate function $z = f(x, y)$. A common approach involves fitting a bivariate polynomial, as presented above. To compute LSPs up to the third order, the minimum required polynomial degree is three. Shary [10] suggested that third-order LSPs for land surface description seems to be not feasible because of their excessive sensitivity to "noise". However, polynomial fitting using the least squares method mitigates data errors [2] (which [10] referred to as noise). Furthermore, advancements in DEM quality, driven by the LiDAR revolution, have seemingly reduced the prominence of data errors [11]. This improvement has opened the possibility of using higher-order polynomials, which may have a lesser impact on reducing data error. On the other hand, higher-order polynomials pose the risk of introducing artifacts, such as Runge's phenomenon. Therefore, for calculating third-order LSPs, polynomials of degree three or four are considered to be the most feasible options.

The total number of coefficients n in bivariate polynomials is calculated as

$$n = \frac{(d+1)(d+2)}{2} \tag{1}$$

where d is the degree of the polynomial. Thus, there are 10 and 15 coefficients for degrees 3 and 4, respectively. Using a 5×5 moving window provides sufficient data for the calculations, along with additional values for least squares fitting. This process creates an approximating surface with slight implicit smoothing.

In general, a bivariate polynomial $P(x, y)$ of total degree d, used for fitting to data points (x_i, y_i, z_i), where z_i represents the elevation at (x_i, y_i), is expressed as

$$P(x, y) = \sum_{j=0}^{n} c_j \cdot B_j(x, y) \tag{2}$$

where c represents the unknown coefficients to be determined, and B are the basis functions forming the basis function matrix A

$$A_{ij} = B_j(x_i, y_i) = x_i^{p_j} \cdot y_i^{q_j} \tag{3}$$

The members are the n combinations of exponents p, q such that $p + q \leq d$. A is a matrix of size (*num_points*×n). For example, for a third-degree polynomial and a full 5×5 moving window, A has a size of 25×10.

The solution for least squares fitting is obtained by solving the normal equations

$$M \cdot c = v \tag{4}$$

where M is the matrix

$$M = A^T \cdot A \tag{5}$$

and v is the right-hand side vector

$$v = A^T \cdot z \tag{6}$$

The coefficients c are computed as

$$c = M^{-1} \cdot v \tag{7}$$

The partial derivatives of a bivariate polynomial $P(x, y)$ are computed by differentiating each term of the polynomial individually. The partial derivative of the j-th basis function with respect to $x^p y^q$ is calculated as

$$\frac{\partial^{p+q} B_j}{\partial x^p \partial y^q} = \binom{p_j}{p} \cdot \binom{q_j}{q} \cdot x^{p_j - p} \cdot y^{q_j - q} \tag{8}$$

or derivative is zero, if $p > p_j$ or $q > q_j$. The contribution to the partial derivative of $P(x, y)$ is obtained by multiplying the derivative of the basis function by its corresponding coefficient c_j

$$\frac{\partial^{p+q} P}{\partial x^p \partial y^q} = \sum_{j=0}^{n} c_j \cdot \frac{\partial^{p+q} B_j}{\partial x^p \partial y^q} \tag{9}$$

Even though a fourth-order polynomial allows the calculation of fourth partial derivatives, only the first three orders are needed for LSP calculations, so $p + q \leq 3$ in (8) and (9).

III. Results

A. Polynomial Fitting in a Grid

The described general method for polynomial least-squares fitting can approximate a surface based on any set of elevation points, provided the minimum required number of points for the selected polynomial degree (1) is met. However, when applied to a regular grid, as implemented in the presented tool, the uniform spacing allows for the use of relative x, y coordinates (with fixed step sizes dx, dy), enabling optimization of the calculations. This optimization involves precomputing the basis function matrix A and the M matrix. Consequently, calculations that would otherwise need to be repeated for each new point are accelerated by using these precomputed matrices.

With different values of dx and dy, it is straightforward to implement direct calculation of LSPs from geographic coordinates. For each grid row, the values of dx and dy in meters are computed using ellipsoidal calculations as recommend in [12]. This approach means that matrices A and M are not precomputed once per grid but rather once per grid row.

In special cases where not all input data are available in a 5×5 moving window, derivatives can still be calculated if there are enough points for the selected polynomial degree (Fig. 1 A). This provides an advantage over traditional approaches, which require a full moving window. The absence of a full moving window in some tools either prevents calculation (Fig. 1 D) or results in the addition of fictitious elevation values (e.g., duplicating the central pixel elevation), leading to inaccuracies (Fig. 1 B,C). In this case, only part of the optimization can be used: a subset of the relevant rows in the precomputed A matrix, based on the available grid nodes, is employed, while the M matrix must be recalculated.

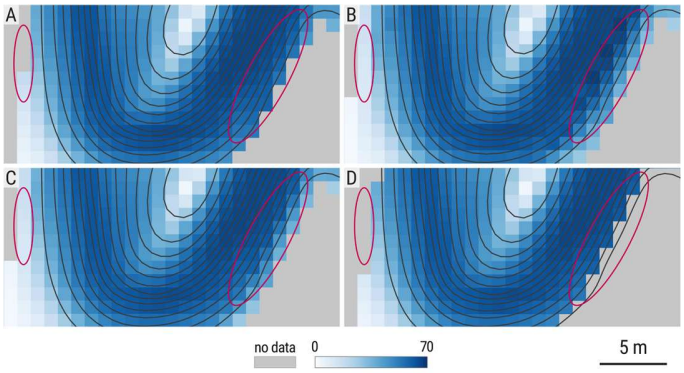

Figure 1. Slope calculation [°] at the area edge (bordering no-data pixels): A – LSP Calculator (our tool), correct where sufficient data is available; B – WhiteBoxTools, unnaturally low edge slopes with visible artifacts; C – GRASS GIS (-e flag for edge computation), unnaturally low edge slopes; D – GRASS GIS, correct but with missing data at the edge.

B. Calculated Land Surface Parameters

Our tool calculates partial derivatives to compute a wide range of local LSPs up to the third order. From the set of first-order LSPs, slope gradient S and aspect A can be derived, along with variants such as $\sin S$, $\sin A$, and $\cos A$ for direct input into specific algorithms. A comprehensive set of curvatures (Fig. 2), representing second-order LSPs, can also be calculated. Unlike other software, which often provides only the most common curvatures, our tool is capable of calculating all the curvatures presented here. For third-order LSPs, which describe changes in curvatures, the tool supports the calculation of contour change of normal contour curvature $(k_n)_{cc}$, slope line change of normal contour curvature $(k_n)_{cs}$, and slope line change of normal slope line curvature $(k_n)_{ss}$. These curvature changes have been shown to be suitable for physically based land surface segmentation [13]. Examples of less common LSPs are shown in Fig. 3 and 4.

All supported LSPs can be computed in a single run of the tool. This approach is computationally efficient, as the calculated partial derivatives are reused in the LSP calculations. It is also user-friendly, allowing users to obtain a set of requested LSPs calculated at once. For clarity, all the equations for the calculated LSPs are provided in the documentation in the repository [14].

C. Algorithm Implementation

We implemented the described algorithms and developed the Land Surface Parameters Calculator, a command-line tool written in the Rust programming language. This tool is part of the broader Physical Geomorphometry Tools project, which focuses on physically based methods for analyzing landforms and land surface dynamics. Its goal is to provide useful tools for processing DEMs within this framework.

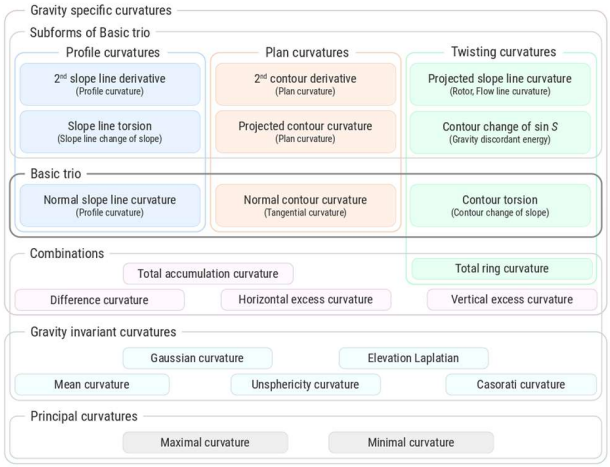

Figure 2. Set of land surface curvatures: schema, based on [3], later revised.

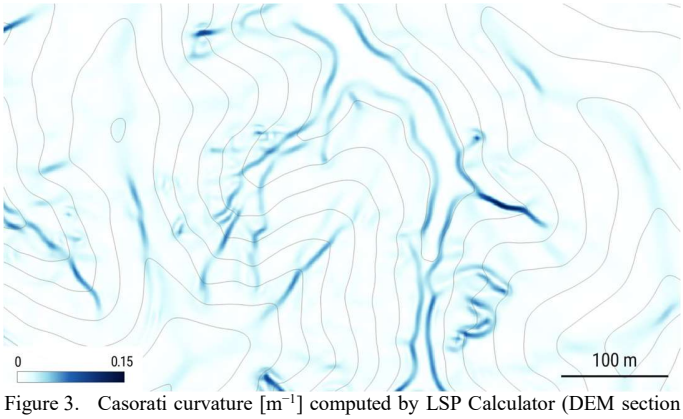

Figure 3. Casorati curvature [m^{-1}] computed by LSP Calculator (DEM section from Ponui Island, New Zealand).

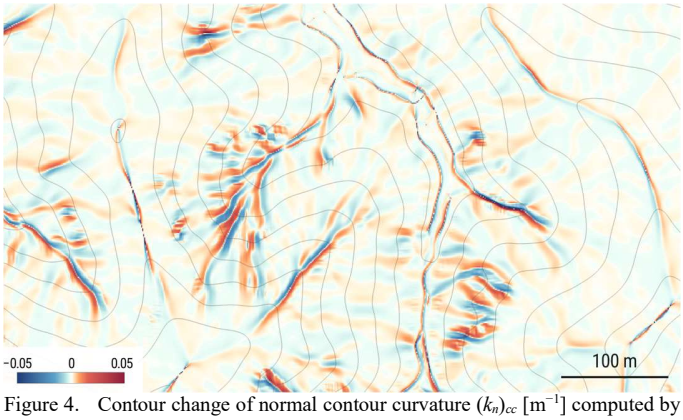

Figure 4. Contour change of normal contour curvature (k_n)$_{cc}$ [m^{-1}] computed by LSP Calculator (DEM section from Ponui Island, New Zealand).

The command-line interface allows users to specify an input DEM file (in GeoTIFF format) and an output prefix for the results. Users can compute a full suite of LSPs or select specific parameters or groups of parameters based on their research needs. The output consists of parameter-specific GeoTIFF files, systematically named using the provided output prefix.

The tool supports parallel processing, utilizing multiple CPU cores for improved performance. It relies on GDAL for raster handling and requires a Rust development environment for building from source. The source code, along with detailed instructions for building and usage, is available on GitHub [14].

IV. Conclusion

The newly developed tool introduces the capability to compute LSPs from DEMs up to the third order, which were previously underutilized due to computational challenges and limited tool support. By enabling the calculation of a wide range of LSPs, it makes less common second-order and third-order LSPs more accessible for broader applications, unlocking new possibilities for land surface analysis and geomorphological research. The tool is implemented in a modern programming language, incorporates various optimizations, and supports parallel processing for efficient calculations. Future efforts aim to improve its usability, provide a web service, and integration into advanced software.

V. Acknowlegments

This work was supported by the Slovak Research and Development Agency under the contract No. APVV-22-0024.

References

[1] Evans, I., and Minár, J., 2011. “A classification of geomorphometric variables”, Geomorphometry 2011 (Redlands, CA, USA, 7. – 11. 9. 2011). Eds. T. Hengl, I. S. Evans, J. P. Wilson, M. Gould, 105-107.

[2] Minár, J., Jenčo, M., Evans, I.S., Minár, J., Kadlec, M., Krcho, J., Pacina, J., Burian, L., and Benová, A., 2013. “Third-order geomorphometric variables (derivatives): Definition, computation and utilization of changes of curvatures”, International Journal of Geographical Information Science, 27(7), 1381–1402. https://doi.org/10.1080/13658816.2013.792113

[3] Minár, J., Evans, I.S., and Jenčo, M., 2020. “A comprehensive system of definitions of land surface (topographic) curvatures, with implications for their application in geoscience modelling and prediction”, Earth-Science Reviews, 211, 103414. https://doi.org/10.1016/j.earscirev.2020.103414

[4] Evans, I.S., 1972. “General geomorphometry: Derivatives of altitude, and the descriptive statistics”. In: Chorley, R. (ed.), Spatial Analysis in Geomorphology, London: Methuen & Co. Ltd, 17–90.

[5] Young, A., 1972. “Slopes.” Oliver & Boyd, Edinburgh. 288 pp.

[6] Zevenbergen, L.W. and Thorne, C.R., 1987. “Quantitative analysis of land surface topography”, Earth Surface Processes and Landforms, 12:47–56.

[7] Shary, P.A., 1995. “Land surface in gravity points classification by a complete system of curvatures”, Mathematical Geology 27(3): 373–390.

[8] Florinsky, I.V., 2009. “Computation of the third-order partial derivatives and derivation function from a digital elevation model”, International Journal of Geographical Information Science 23 (2): 213–231.

[9] Pacina, J., 2010. “Comparison of approximation methods for partial derivatives of surfaces on regular grids”, Geomorphologia Slovaca et Bohemica, Volume I, 25–32.

[10] Shary, P.A., Sharaya, L.S., and Mitusov, A.V., 2002. “Fundamental quantitative methods of land surface analysis.” Geoderma 107 (1), 1-32.

[11] Evans, I. S., Minár, J., Feciskanin, R., in review. Models of the land surface; Conceptual, Mathematical & Digital. In: Reuter, H.I., Grohmann, C.H., and Lecours, V. (eds.), Geomorphometry: Concepts | Software | Applications, 2nd ed.

[12] Guth, P., and Kane, M., 2021. “Slope, aspect, and hillshade algorithms for non-square digital elevation models”, Transactions in GIS, 25(5), 2309–2332. https://doi.org/10.1111/TGIS.12852

[13] Minár, J., Drăguţ, L., Evans, I. S., Feciskanin, R., Gallay, M., Jenčo, M., and Popov, A., 2024. “Physical geomorphometry for elementary land surface segmentation and digital geomorphological mapping”, Earth-Science Reviews, 248, 104631. https://doi.org/10.1016/J.EARSCIREV.2023. 104631.

[14] https://github.com/xiceph/physical-geomorphometry-tools/tree/main/lsp-calculator

1.3 - Stream and slope applications

Reflections on Geomorphometry and Hydrology

David G. Tarboton
Utah Water Research Laboratory
Utah State University
8200 Old Main Hill, Logan, Utah, USA, 84322
david.tarboton@usu.edu

Cite as: Tarboton, D. G. (2025). Reflections on Geomorphometry and Hydrology. In: Proceedings of Geomorphometry 2025, 9-13 June, Perugia, Italy. M. Alvioli, L. Melelli, I. Marchesini eds. CNR Edizioni, Rome. ISBN 978-88-8080-765-0.

Abstract—**Watershed and stream network delineation, along with the extraction of hydrologic information from digital elevation models (DEMs), are fundamental concepts that bridge hydrology and geomorphometry. Terrain analysis methods transform a simple grid of elevation values into richly structured datasets of hydrologically useful quantities derived from the terrain flow field. These methods are now widespread and support numerous hydrologic modeling and analysis efforts. This presentation will reflect on the ideas, concepts, algorithms, and code for hydrologic terrain analysis, providing examples of achievements and discussing future challenges and opportunities. It will begin with a description of watershed and channel network delineation, focusing on identifying topographic scale and objectively setting thresholds for channel initiation. Next, the presentation will review the D-infinity multiple flow direction model, which addresses limitations associated with single flow direction models. Following this, generalized terrain-based flow analysis will be presented as an approach to developing a broad class of terrain quantities derived from a non-circulating flow field. Examples and code logic to achieve this will be provided. Height Above Nearest Drainage (HAND), that has become popular in flood inundation modeling, will be discussed as a special case of distance downslope from generalized flow analysis. The computation of HAND using D-infinity flow directions and its application in determining channel hydraulic properties for flood mapping will be described. The open-source Terrain Analysis Using Digital Elevation Models (TauDEM) software, which performs many of the computations illustrated, will be highlighted.**

I. Introduction

A terrain flow data model that represents flow processes at and near the Earth's surface underpins much hydrologic terrain analysis and the computation of the rich set of terrain derivatives used in hydrology (Fig. 1). The input is a raw digital elevation model (DEM), comprising elevation values on a grid. This basic information is used to derive further hydrology-related spatial fields that enrich the information content of this basic data. The first step is to remove spurious sinks, commonly by filling [1, 2], but, where possible, using carving [3] or optimization [4] approaches that are less altering of the input data. Then, a flow field is defined. Flow directions based on topographic slope are computed from each grid cell to one or more neighboring grid cells, serving as a numerical representation of the flow field. This enables the calculation of a rich set of highly structured flow-related terrain information, including flow accumulation and other quantities based on the propagation of information up or downslope along flow directions, as well as logically linked catchments, watersheds, and channel networks.

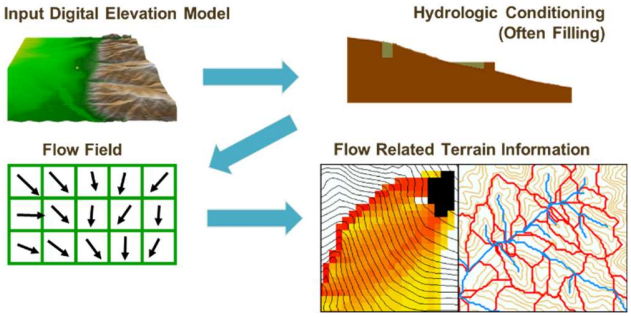

Figure 1. General Terrain Flow Data Model used to enrich the information content of a digital elevation model (DEM). Starting from a simple grid DEM, a rich set of data structures and information useful for hydrologic analysis is derived.

II. Objective Channel Network Delineation

Where do channels begin? The drainage network is an important topographic feature commonly extracted and mapped from digital elevation model (DEM) data. Hydrologic processes differ on hillslopes and in channels, and it is important to recognize and account for this in DEM-based channel network delineation. The scale of the channel network used controls the scale of hillslope and channel model elements in a hydrologic model. Topographic texture and drainage density vary across different

landscapes, necessitating methods to objectively map channels that account for this variability.

TauDEM (https://hydrology.usu.edu/taudem) implements methods [5-7] that use curvature-related quantities as weights in flow accumulation, with a threshold based on a t-test to identify a statistically significant break in the constant stream drop property [8] as the stream delineation threshold is reduced. This method adapts to spatial variability in drainage density. The result is a weighted support area threshold, selected objectively using the t-test, that maps the highest resolution drainage network with a mean drop of first-order streams not significantly different from the mean drop of higher-order streams. In this way, a channel network consistent with empirical geomorphological properties is delineated.

III. D-Infinity

Tarboton [9] introduced the D-infinity (D∞) multiple flow direction method, which determines flow direction as the steepest downward slope on eight triangular facets formed in a 3x3 cell window centered on the cell of interest. The most common procedure for routing flow over a terrain surface represented by a grid DEM is the eight-directional (D8) method [10]. In this model, the direction of steepest descent towards one of the eight (cardinal and diagonal) neighboring grid cells is used to represent the flow field [10]. However, the D8 approach is limited because it can assign flow to only one of eight possible directions, each separated by 45° in a square grid [9, 11]. Multiple flow direction methods [9, 12, 13] have been suggested to address the limitations of D8. These methods proportion the outflow from each element between one or more downslope elements, introducing dispersion (spreading out) into the flow while representing downslope flow in an average sense. The D∞ multiple flow direction model [9] was designed to balance consideration of grid bias and numerical dispersion by routing flow on average along a path perpendicular to the contours (Fig. 2).

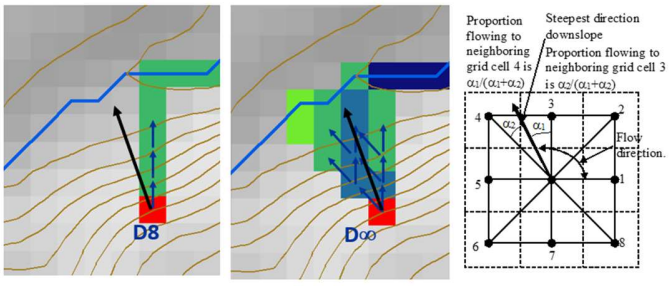

Figure 2. Single and Multiple Direction Representation of Terrain Flow Field.

IV. Generalized Terrain-Based Flow Analysis

Tarboton and Baker [14] introduced a general method for flow analysis that exploits flow field information for the calculation of a rich set of flow-based derivative surfaces, named flow algebra. The formalism developed applies to any non-circulating (non-looping) flow field, and flow directions used in flow algebra can be derived from any potential surface. The principles of flow algebra have been used to develop a number of specialized terrain-flow related quantities and proximity measures in TauDEM, including upslope and downslope distance proximity measures [15], transport-limited accumulation for modeling sediment erosion and transport, decaying accumulation useful for tracking a substance subject to decay or attenuation, and retention-limited runoff generation with run-on (Fig. 3). Generalized terrain-based analysis tools are framed as functions that capture terrain-flow effects in a general way, giving users the flexibility to use them with other inputs to meet their needs.

Global P, (r,c), q
FlowAlgebra(i)
for all k neighbors of i
  if $P_{ki}>0$
    FlowAlgebra(k)
next k

$$q_i = \max\left(\sum_{\{k:P_{ki}>0\}} P_{ki}q_k + r_i - c_i, 0\right)$$

return

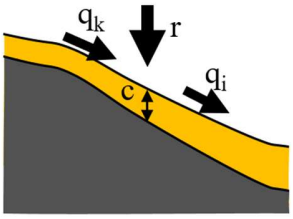

Figure 3. Flow algebra formulation for retention-limited runoff generation with run-on.

V. Height Above Nearest Drainage (HAND) and Flood Inundation Mapping

Height Above Nearest Drainage (HAND) is a special case of distance down proximity measure to an arbitrary target, with the target being a stream and distance measured vertically (Fig. 4).

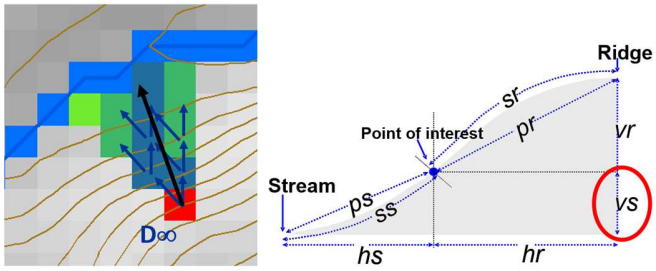

Figure 4. HAND evaluated using TauDEM D∞ Vertical Distance Down function [15]. Vertical distance to stream is evaluated as weighted average over multiple flow paths resulting in a "smooth" height above nearest drainage layer.

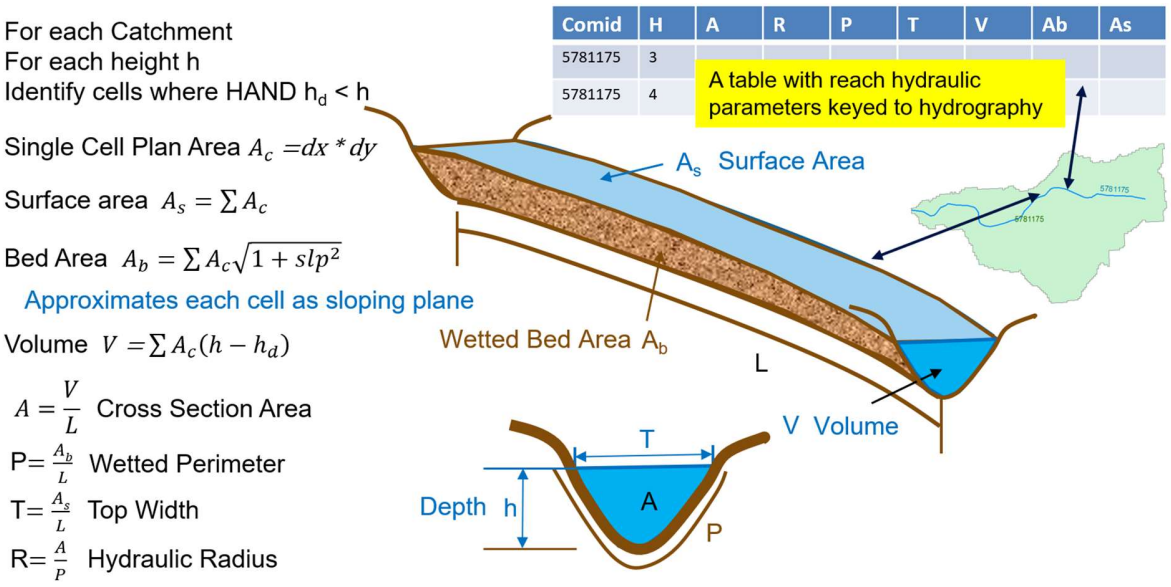

Figure 5. HAND-based derivation of "reach scale" hydraulic properties. Note that DEM topography should represent riverbed elevations [16].

HAND supports flood inundation mapping. Once the depth of flow in a stream is determined, the area and depth of flood inundation can be mapped. By dividing streams into reaches or segments, the area draining to each reach can be isolated, and a series of threshold depths applied to the grid of HAND values in that isolated reach catchment to determine inundation volume, surface area, and wetted bed area. Dividing these by length yields reach average cross-section area, width, and wetted perimeter, information useful for hydraulic routing and stage-discharge rating calculations in hydrologic modeling (Fig. 5) [16].

VI. Conclusions and Future Challenges

The DEM-based terrain flow data model enables the representation of flow processes at and near the Earth's surface and the derivation of a wide variety of information useful for the study of hydrologic processes. Starting from a simple DEM, one can compute slope, flow direction, drainage area, catchments, watersheds, channel networks, and multiple other flow-related quantities useful in hydrologic modeling and analysis. Much of this capability has been implemented in the freely available open-source TauDEM software, which includes both D8 and D∞ options for representing the flow field. It includes a number of functions derived using flow algebra, which generalizes the recursive flow accumulation methodology using both downslope and upslope logic. Queue-based approaches have been used to develop parallel methods that implement flow algebra logic.

Future challenges and opportunities include leveraging increasingly high-resolution data, such as from LiDAR, and integrating datasets from various sources and resolutions, including both vector and raster data. High-resolution DEMs present computational challenges, necessitating the use of emerging cloud and high-performance computing capabilities, as well as advancements in data structures and formats. DEMs with resolutions finer than approximately 5 meters introduce topographic details at scales smaller than typical topographic flow, requiring new methods to effectively utilize such data. Additionally, the objective channel network mapping problem is not fully solved, presenting opportunities to employ object detection approaches that blend remote sensing and high-resolution LiDAR data with traditional terrain analysis techniques.

VII. Acknowledgments

Thank you to the International Society for Geomorphometry for inviting me to present a keynote at its 2025 conference (https://www.geomorphometry2025.org/). Over the years TauDEM has been developed with funding from the US Army Research and Development Center (awards W912HZ-11-P-0338, W9124Z-08-P-0420), NOAA (Grant NA06NOS4190167), NASA (award NAG5-7521) and the US National Science Foundation (EAR-9318977). I appreciate this support. Numerous colleagues have collaborated in this work including Dan Ames, Matt Baker, Kiran Chinnayakanahalli, Pabitra Dash, Yan Liu, David Maidment, Irene Garousi-Nejad, Bob Pack, Ajay Prasad, Kim

Schreuders, Paolo Tarolli, Teklu Tesfa, Rob Wallace, Shaowen Wang, Dan Watson, Ahmet Yildirim, Xing Zheng.

REFERENCES

[1] Jenson, S.K. and J.O. Domingue, (1988), *Extracting Topographic Structure from Digital Elevation Data for Geographic Information System Analysis.* Photogrammetric Engineering and Remote Sensing. **54**(11): p. 1593-1600.

[2] Planchon, O. and F. Darboux, (2001), *A fast, simple and versatile algorithm to fill the depressions of digital elevation models.* Catena. **46**: p. 159-176. http://dx.doi.org/10.1016/S0341-8162(01)00164-3.

[3] Soille, P., J. Vogt, and R. Colombo, (2003), *Carving and adaptive drainage enforcement of grid digital elevation models.* Water Resources Research. **39**(12): p. 1366. http://doi.org/10.1029/2002WR001879.

[4] Soille, P., (2004), *Optimal removal of spurious pits in grid digital elevation models.* Water Resources Research. **40**(12): p. W12509. http://doi.org/10.1029/2004WR003060.

[5] Tarboton, D.G. and D.P. Ames. (2001), *Advances in the mapping of flow networks from digital elevation data*. in *World Water and Environmental Resources Congress*. Orlando, Florida: ASCE. May 20-24. http://dx.doi.org/10.1061/40569(2001)166.

[6] Tarboton, D.G., R.L. Bras, and I. Rodriguez-Iturbe, (1991), *On the Extraction of Channel Networks from Digital Elevation Data.* Hydrologic Processes. **5**(1): p. 81-100. http://dx.doi.org/10.1002/hyp.3360050107.

[7] Tarboton, D.G., R.L. Bras, and I. Rodriguez-Iturbe, (1992), *A Physical Basis for Drainage Density.* Geomorphology. **5**(1/2): p. 59-76. http://dx.doi.org/10.1016/0169-555X(92)90058-V.

[8] Broscoe, A.J., (1959), *Quantitative analysis of longitudinal stream profiles of small watersheds*, Department of Geology, Columbia University, New York.

[9] Tarboton, D.G., (1997), *A New Method for the Determination of Flow Directions and Contributing Areas in Grid Digital Elevation Models.* Water Resources Research. **33**(2): p. 309-319. http://dx.doi.org/10.1029/96WR03137.

[10] O'Callaghan, J.F. and D.M. Mark, (1984), *The Extraction of Drainage Networks From Digital Elevation Data.* Computer Vision, Graphics and Image Processing. **28**: p. 328-344.

[11] Fairfield, J. and P. Leymarie, (1991), *Drainage Networks from Grid Digital Elevation Models.* Water Resources Research. **27**(5): p. 709-717. http://dx.doi.org/10.1029/90WR02658.

[12] Quinn, P., K. Beven, P. Chevallier, and O. Planchon, (1991), *The Prediction of Hillslope Flow Paths for Distributed Hydrological Modeling Using Digital Terrain Models.* Hydrological Processes. **5**: p. 59-80. https://doi.org/10.1002/hyp.3360050106.

[13] Freeman, T.G., (1991), *Calculating Catchment Area with Divergent Flow Based on a Regular Grid.* Computers & Geosciences. **17**(3): p. 413-422.

[14] Tarboton, D.G. and M.E. Baker, (2008), *Towards an Algebra for Terrain-Based Flow Analysis*, in *Representing, Modeling and Visualizing the Natural Environment: Innovations in GIS*, N.J. Mount, G.L. Harvey, P. Aplin, and G. Priestnall, Editors, CRC Press: Florida. p. 496. http://dx.doi.org/10.1201/9781420055504.

[15] Tesfa, T.K., D.G. Tarboton, D.W. Watson, K.A.T. Schreuders, M.E. Baker, and R.M. Wallace, (2011), *Extraction of hydrological proximity measures from DEMs using parallel processing.* Environmental Modelling & Software. **26**(12): p. 1696-1709. http://dx.doi.org/10.1016/j.envsoft.2011.07.018.

[16] Zheng, X., D.G. Tarboton, D.R. Maidment, Y.Y. Liu, and P. Passalacqua, (2018), *River Channel Geometry and Rating Curve Estimation Using Height above the Nearest Drainage.* JAWRA Journal of the American Water Resources Association. **54**(4): p. 785-806. http://doi.org/10.1111/1752-1688.12661.

Automatic optimization and delineation of nested slope units with r.slopeunits v2.0

Massimiliano Alvioli, Ivan Marchesini
Istituto di Ricerca per la Protezione Idrogeologica, Consiglio Nazionale delle Ricerche,
Via Madonna Alta 126, I-06128, Perugia, Italy
{massimiliano.alvioli, ivan.marchesini}@irpi.cnr.it

Cite as: Alvioli, M., Marchesini, I. (2025). Automatic optimization and delineation of nested slope units with r.slopeunits v2.0. In: Proceedings of Geomorphometry 2025, 9-13 June, Perugia, Italy. M. Alvioli, L. Melelli, I. Marchesini eds. CNR Edizioni, Rome. ISBN 978-88-8080-765-0. DOI: 10.5281/zenodo.15274445

Abstract— **Slope unit delineation falls under the wider domain of geomorphological surface classification, with a few peculiarities. Surface classification is mostly achievable with variations of segmentation methods, requiring data of different nature, while (automatic) slope unit delineation only depend on the information in a digital elevation model. In particular, slope units strongly relate to the stream network in an area, which requires an extra bit of knowledge with respect to simple segmentation of the surface into areas with similar local properties. A slope unit encompasses a region of the surface of size typically ranging from a fraction to a few square kilometers, and is recognizable in the field as a hillslope. For automatic slope unit delineation, we rely on specialized software. This work introduces an updated version of the r.slopeunits software. The previous version of r.slopeunits, a GRASS GIS module published in 2016, represented a common choice for slope unit delineation in the literature. The new software introduces new features, especially the optimization of input parameters and multi-layer delineation capabilities. We briefly describe the new software, and describe preliminary results for a multi-layer slope unit map of Italy.**

I. Introduction

Slope units (SUs) are an alternative to grid cells, for selected applications. Slope units and grid cells are fundamentally different mapping units, as SUs have a strong relationship with topography, absent in the square grid representation. Drainage and divide lines define SU boundaries, so that they have meaningful hydrological properties and fulfil well-defined geomorphological constraints. That gives advantages for the description of slope-related phenomena, such as landslides, using SU-aggregated quantities.

Examples of specific advantages given by SUs are the possibility of using heterogeneous data for landslide susceptibility mapping, including point or polygonal landslide inventories, and considering data-scarce areas for landslide susceptibility with statistical methods [1]. Slope unit polygons, in this case, represent geographical domains to aggregate surface descriptors representing the predictors for landslide presence. Reducing the dimensionality of the problem from billions, independently described grid cells, to a few hundred thousands, homogeneous slope units, also renders manageable the study of very large areas in a consistent way.

Examples of different applications involve the use of SUs in conjunction with models of different nature, for example physically based methods [2-4]. In the latter case, SUs may still act as a-posterior aggregation units of model results originally obtained on grid cells [3], in difference with the use of SUs within statistical or machine learning models. Slope units may also serve as local reference boundaries for expert landslide mapping [5], or in combination with remote sensing data [6].

The continued interest in using SUs for landslide studies is supported by the recent introduction of various pieces of software designed for their automatic delineation, either using aspect homogeneity measures [7], stream order classification [8], clustering algorithms [9], or terrain topology considerations [10]. Typically, a software can produce SU maps independently of landslide susceptibility (LS) models. Examples are the SU maps of Italy [11] and of a large portion of the Himalayas [12]. The SU map of Italy was useful in a national zonation of LS for different landslide types [13]. A select subset of the map constitutes a benchmark dataset, established with the consensus of authors from several different institutions, for comparing different LS methods and developing a workflow as standardized as possible [14].

Here, we describe an update of the r.slopeunits software, designed to delineate slope units uniquely information from a digital elevation model (DEM). The original implementation, v1.0 [7], produced SU maps in a parametric way, using an adaptive algorithm to obtain half-basins of different granularity in different regions of the study area. The need to choose optimal values of

input parameters hindered applicability of the software for some users. Version 2.0 includes a built-in optimization function that returns values of optimal input parameters, based on an aspect segmentation function. As in the original implementation, SU delineation and optimization only depend on the input DEM, and requires no additional data.

The second novelty of r.slopeunits v2.0 is the possibility of producing several maps of nested SUs. We refer to each map as an individual layer, with the number (size) of SU polygons decreasing (increasing) with increasing layer, with the base layer represented by the map produced by the built-in optimization procedure. This feature entails producing coarser SU layers with increasing values of the *cvmin* input parameter, which controls the homogeneity of aspect within each SU. Larger *cvmin* values produce larger SUs, on average. We suggest such multi-layer, hierarchical SU map as an additional tool for a multi-scale description of landslide susceptibility in large areas.

II. Materials and Methods

The r.slopeunits software v2.0 is available as a regular add-on in GRASS GIS [11] (use the tool g.extension to install the module from a web repository). The new implementation consists of a toolset with five sub-modules:

1. r.slopeunits.create, the main tool for slope unit delineation, corresponding to v1.0 of the software, as in Ref. [7].
2. r.slopeunits.clean, providing several options to clean small areas resulting from r.slopeunits.create; also included in v1.0.
3. r.slopeunits.optimize, which selects optimal values for input parameters of r.slopeunits.create, for a given area and DEM. It represents the first major novelty of v2.0 of the software.
4. r.slopeunits.metrics, mostly used for the optimization procedure, called by r.slopeunits.optimize, used in Ref. [11] but never published before.
5. r.slopeunits.nested, which delineates several nested layers of slopeunits. It represents the second major novelty of v2.0 of the software.

The tools no. 1-4 were ported to GRASS GIS modules, in Python language, from hybrid Python code and bash scripts, with support from URGERE project of CNR IRPI (see Section V), while porting of tool no. 5 is underway, with support from the HySTC project of CNR IRPI (see Section V).

We applied the new software, in particular tool no. 5, to the European EU-DEM at 25 m spatial resolution in Italy, as in the previous single-layered version of the SU map of Ref. [11].

The software r.slopeunits.create identifies slope units as half-basins with a minimum aspect homogeneity *or/and* a minimum surface area thresholds set by the user. It works iteratively: it decreases the value of an initial (user-supplied) upslope contributing area threshold at each iteration, and stops the iterations at different stages depending on the local surface. The number of iterations is not predetermined, but it is adaptive, depending on local aspect homogeneity and on the minimum surface area required by the user. In the process, the software does not explicitly keep track of the basin/stream order hierarchy, and it only collects half-basins fulfilling the homogeneity and minimum area criteria requested by the user, by means of two input parameters *cvmin* and *areamin*.

The tool r.slopeunits.nested helps delineating different SU layers by running r.slopeunits.create, in the same area, with increasing values of the *cvmin* input parameter. In fact, the numerical values of the input parameters of the software, mainly by the *areamin* and *cvmin* parameters, control the size and shape of the output layers. Different combinations of the two parameters result in an output with a different number of slope units, with deterministic but not easily predictable shape and size. Increasing the value of *cvmin* results in SU polygons with a decreasing degree of aspect homogeneity, which corresponds to SUs of increasing size. A larger value of the *cvmin* parameter selects half-basins as slope units later in the iterative procedure than a lower value of the parameter would do. The benefit of r.slopeunits.nested is to produce different slope unit layers with nested edges, which is impossible to achieve with any parameter combination of the previous version of the software.

The optimized SU map of Italy introduced in Ref. [11] resulted partly from application of the algorithm implemented in r.slopeunits.optimize, and partly with a simple parameter scan. Use of the two options was peculiar of the method described in the quoted reference. Evaluation of the aspect segmentation metric (objective function) implemented in r.slopeunits.metrics, for different combination of parameters, allows selection of the optimal parameters as those corresponding to the maximum of the objective function. The process runs in parallel in each of the 439 watersheds defined for Italy in Ref. [11]. Here, the software runs separately in the same set of watersheds, keeping all input parameters fixed but *cvmin*, thus generating higher-order SU layers. Each additional SU layer was obtained selecting five different values of *cvmin*=0.3, 0.4, 0.5, 0.6, 0.7. Instead, the optimized values for *areamin* were the same obtained in Ref. [11], for each watershed. The final five new national SU maps result from merging the individual results, in each watershed.

III. Results and Discussion

We show preliminary results for several layers of nested slope units, obtained as a multi-scale extension of the national SU map described in Ref. [11] and published at the main slope unit-project webpage, https://geomorphology.irpi.cnr.it/tools/slope-units.

The new layers are such that SU polygons in each lower-order layer exactly nest inside the polygons of the higher-order layer, hierarchically from layer 0 to layer 5. Layer 0 correspond to the existing, optimized result of Ref. [11]. Layers 1-5 contain a decreasing number of SU polygons, as specified in Table I. The Table also shows that minimum area of polygons remains practically the same across all the layers, while the maximum area

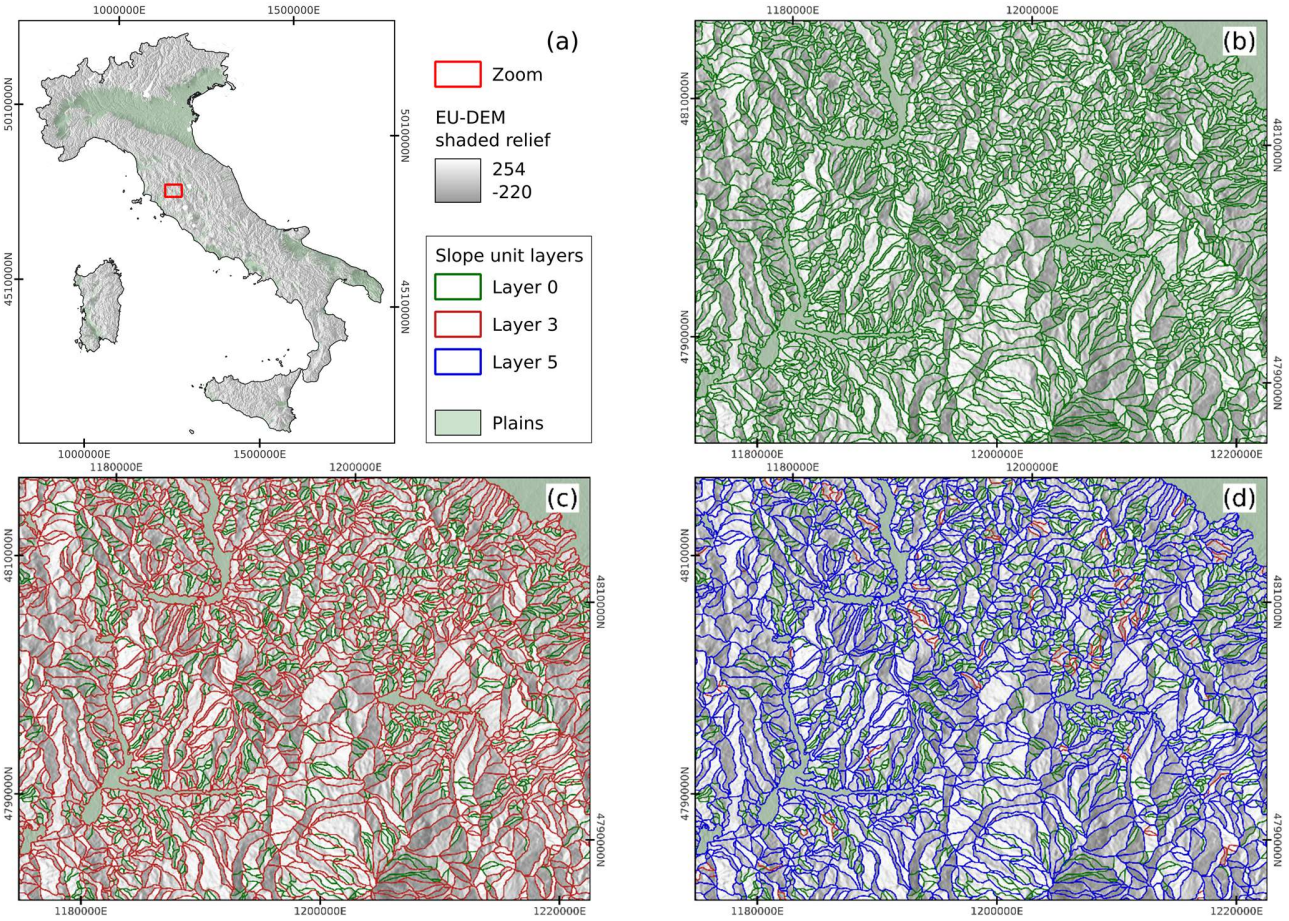

Figure 1. Three of the six nested slope unit layers obtained in this work. (a) General setting; (b) layer 0, as in Ref. [11]; (c) layer 3 superimposed to layer 0; (d) layer 5 superimposed to layers 0 and 3. See Table I for numerical figures of the different layers.

increases significantly, with the largest percent difference between layer 0 and layer 1. As shown in Ref. [11], the size distribution of optimized SUs in an area is a skewed towards small areas, with a long tail towards large areas, and with several outliers. The last column in Table I is intended to check whether this feature remains in higher-order layer. One can appreciate that the percent of polygons with sizes larger than the average size increases monotonically from 30 % to 37 %, denoting distributions less and less skewed. One can understand this feature noting that optimized SUs (layer 0) provide a better segmentation of the topography in terms of homogenous areas. Deviating from the optimal SU set, we necessarily start merging the smaller polygons, dense in highly dissected regions, mostly leaving untouched the larger ones, located in regions with a smoother surface.

Figure 1 shows details, in Central Italy, of a subset of the new layers. We only show details of layers 0, 3 and 5, for illustration. Showing the full six layers would be very difficult in a short contribution, and we encourage interested readers to download the vector layers at the main SU project page, to appreciate fully the nested feature of the polygons at the different scales.

IV. Conclusions

We introduced version 2.0 of the software r.slopeunits, whose previous version represented a common choice for slope unit delineation in the recent literature. We expect that the new features of the software, especially the optimization and multi-layer delineation capabilities, will make the software even more useful and user-friendly for a wider user base.

V. Acknowledgments

Implementation of modules no. 1-4 of the software supported by MUR PRIN Project “URGERE: URban Geodiversity for a Resilient Environment” 2022M7EP3M_PE10_PRIN2022 - PNRR M4.C2.1.1 - Funded by the European Union – Next

Table I. Numerical figures representing the number and size distributions of the slope unit polygons in the six different nested SU layers described in this work. Layers 0, 3 and 5 are shown Figure 1.

Layer no.	Input *cvmin* value	Minimum area [km^2]	Average area [km^2]	Maximum area [km^2]	Number of polygons	% units with area > average
0	*Optimized (Ref. [11])*	0.092	0.69	15.51	325,578	29.9
1	0.3	0.096	1.02	147.73	220,308	31.2
2	0.4	0.096	1.32	267.46	170,240	34.3
3	0.5	0.096	1.55	277.20	144,430	36.5
4	0.6	0.096	1.67	277.20	133,928	37.1
5	0.7	0.096	1.72	287.81	129,961	37.3

Generation EU - CUP: B53D23007260006. Development and implementation of module no. 5 of the software supported by project HySTC/RETURN "Hydrology and Stability of slopes along Transport Corridors" CODSOG_001744 - Funded by the European Union – Next Generation EU - CUP C99J24000390008.

The Mundialis team, based in Germany, performed porting of all modules from the original Python/bash scripts developed by IRPI CNR to modern code standards, and implemented the code as an official GRASS GIS add-on.

REFERENCES

[1] Jacobs, L., M. Kervyn, P. Reichenbach, M. Rossi, I. Marchesini, M. Alvioli, O. Dewitte (2020). Regional susceptibility assessments with heterogeneous landslide information: Slope unit- vs. pixel-based approach. Geomorphology, 356, 107084. https://doi.org/10.1016/j.geomorph.2020.107084

[2] Domènech, G., M. Alvioli, J. Corominas (2020). Preparing first-time slope failures hazard maps: from pixel-based to slope unit-based. Landslides, 17, 249–265. https://doi.org/10.1007/s10346-019-01279-4

[3] Alvioli, M., G. Falcone, A. Mendicelli, F. Mori, F. Fiorucci, F. Ardizzone, M. Moscatelli (2023). Seismically induced rockfall hazard from a physically based model and ground motion scenarios in Italy. Geomorphology 429, 108652. https://doi.org/10.1016/j.geomorph.2023.108652

[4] Lopez-Vinielles, J., J.A. Fernández-Merodo, P. Ezquerro, J.C. García-Davalillo, R. Sarro, C. Reyes-Carmona, A. Barra, J.A. Navarro, V. Krishnakumar, M. Alvioli, G. Herrera (2021). Combining Satellite InSAR, Slope Units and Finite Element Modeling for Stability Analysis in Mining Waste Disposal Areas. Remote Sensing, 13, 2008. https://doi.org/10.3390/rs13102008

[5] Alvioli, M., M. Santangelo, F. Fiorucci, M. Cardinali, I. Marchesini, P. Reichenbach, M. Rossi, F. Guzzetti, S. Peruccacci (2021). Rockfall susceptibility and network-ranked susceptibility along the Italian railway. Engineering Geology, 293, 106301. https://doi.org/10.1016/j.enggeo.2021.106301

[6] Alvioli, M., A.C. Mondini, F. Fiorucci, M. Cardinali, I. Marchesini (2018). Topography-driven satellite imagery analysis for landslide mapping. Geomatics, Natural Hazards and Risk, 9, 544-567. https://doi.org/10.1080/19475705.2018.1458050

[7] Alvioli, M., I. Marchesini, P. Reichenbach, M. Rossi, F. Ardizzone, F. Fiorucci, F. Guzzetti (2016). Automatic delineation of geomorphological slope units with r.slopeunits v1.0 and their optimization for landslide susceptibility modeling. Geoscientific Model Development, 9, 3975–3991. https://doi.org/10.5194/gmd-9-3975-2016

[8] Woodard, J.B., B.B. Mirus, N.J. Wood, K.E. Allstadt, B.A. Leshchinsky, M.M. Crawford (2024). Slope Unit Maker (SUMak): an efficient and parameter-free algorithm for delineating slope units to improve landslide modeling. Natural Hazards and Earth System Sciences, 24(1), 1-12. https://doi.org/10.5194/nhess-24-1-2024

[9] Li, Y., B. Fu, Z. Han, Z. Fang, N. Chen, G. Hu, W. Wang, G. Chen (2024). PSO-SLIC algorithm: A novel automated method for the generation of high-homogeneity slope units using DEM data. Geomorphology, 463, 109367. https://doi.org/10.1016/j.geomorph.2024.109367

[10] Zhang, L., D. Ming, Y. Li, J. Cai, Z. Zhang (2024). A new slope unit extraction method based on terrain topology searching and vector similarity constraint for landslide analysis. Catena, 246, 108355. https://doi.org/10.1016/j.catena.2024.108355

[11] Alvioli, M., F. Guzzetti, I. Marchesini (2020). Parameter-free delineation of slope units and terrain subdivision of Italy. Geomorphology, 358, 107124. https://doi.org/10.1016/j.geomorph.2020.107124

[12] Alvioli, M., Marchesini, I., B. Pokharel, K. Gnyawali, S. Lim (2024). Geomorphological slope units of the Himalayas. Journal of Maps, 18, 300-313. https://doi.org/10.1080/17445647.2022.2052768

[13] Loche, M., M. Alvioli, I. Marchesini, H. Bakka, L. Lombardo (2022). Landslide susceptibility maps of Italy: Lesson learnt from dealing with multiple landslide types and the uneven spatial distribution of the national inventory. Earth-Science Reviews, 232, 104125. https://doi.org/10.1016/j.earscirev.2022.104125

[14] Alvioli, M., M. Loche, L. Jacobs, C.H. Grohmann, M.T. Abraham, K. Gupta, N. Satyam, G. Scaringi, T. Bornaetxea, M. Rossi, I. Marchesini, L. Lombardo, M. Moreno, S. Steger, C.A.S. Camera, G. Bajni, G. Samodra, E.E. Wahyudi, N. Susyanto, M. Sinčić, S. Bernat Gazibara, F. Sirbu, J. Torizin, N. Schüßler, B.B. Mirus, J.B. Woodard, H. Aguilera, J. Rivera-Rivera (2024). A benchmark dataset and workflow for landslide susceptibility zonation. Earth-Science Reviews, 258, 104927. https://doi.org/10.1016/j.earscirev.2024.104927

[15] Neteler, M., H. Mitasova (2012). GRASS GIS: A multi-purpose open source GIS. Environmental Modelling & Software, 31, 124-130. https://doi.org/10.1016/j.envsoft.2011.11.014

A minimal dispersion flow algorithm

John B. Lindsay
Geography, Environment and Geomatics - University of Guelph, Guelph, Canada
jlindsay@uoguelph.ca

Cite as: Lindsay, J. B. (2025). A minimal dispersion flow algorithm. In: Proceedings of Geomorphometry 2025, 9-13 June, Perugia, Italy. M. Alvioli, L. Melelli, I. Marchesini eds. CNR Edizioni, Rome. ISBN 978-88-8080-765-0. DOI: 10.5281/zenodo.15306389

Abstract—**Over the past four decades numerous dispersive (multiple flow direction) flow algorithms have been proposed. Dispersive algorithms are often preferred for applications because they overcome the limitations of the main non-dispersive method, D8, specifically the unnatural appearing extensive straight/parallel flow patterns and the abundance of artifact source cells (ASCs). An ASC is a cell in a flow-direction (FD) raster that has no inflowing cells but is not situated at a summit within the digital elevation model. They represent locations where a flow line has been truncated in the upslope direction, disconnecting the flow line from its starting peak. Attempts to address the unnatural flow patterns of D8 using alternate non-dispersive flow algorithms have resulted in more abundant ASCs. Dispersive flow algorithms can yield more natural appearing flow patterns than D8 while reducing or eliminating ASCs. However, some researchers have argued that dispersion has little physical basis in the definition of upslope area and should be minimized in the formulation of these methods. It seems that a fundamental compromise in flow-path modelling exists between natural-looking flow patterns, the abundance of ASCs, and the need for dispersion. A new minimal dispersion flow algorithm (MDFA) is presented in this paper. MDFA restricts dispersion to locations where it is necessary to resolve ASCs in a non-dispersive path-corrected FD raster. A case study is presented, comparing flow algorithms for the prevalence of ASCs and the amount of dispersion in various non-dispersive and dispersive methods. Findings show that MDFA can produce the natural appearing flow patterns of a path-corrected non-dispersive flow algorithm, eliminates ASCs entirely, while requiring the least number of cells with multiple outflowing neighbors and the lowest average overall dispersion of any of the tested dispersive methods.**

I. Introduction

A flow line traces the route that a theoretical rain drop takes from a peak, downslope to the catchment outlet. If we assume that overland flow is controlled solely by gravity, flow lines follow paths of steepest descent, or slope lines, that are perpendicular to contour lines along their entire length [1]. Every point on the topographic surface belongs to one flow line, connecting that location to an upslope peak (summit) and a downslope outlet. Because there are infinite points on a surface, there are also infinite flow lines. Flow lines converge downslope in channels and upslope at ridges. The downslope direction of the flow line at a point is called the flow direction (FD) and is equivalent to aspect. Flow algorithms are used to derive FD rasters, which specify the upslope-downslope connections among grid cells and their neighbors, allowing for individual (approximated) flow lines, or flow paths, to be traced.

A source cell is a grid cell in an FD raster that has no inflowing neighbor. These cells are the starting points of flow lines. An artifact source cell (ASC) is a grid cell that has one or more higher neighbors in the digital elevation model (DEM), none of which flow into the cell in the FD raster. They are therefore non-summit flow line starting points. ASCs are somewhat analogous to artifact depressions, artificially truncating the path of a flow line, but in an upslope rather than downslope direction. They disconnect flow lines from their true starting points at summits. ASCs occur because FD rasters are necessarily finite representations of the infinite field of flow lines and because many flow algorithms crudely approximate flow directions, i.e., aspect.

FD rasters created using non-dispersive algorithms (single flow direction algorithms), such as D8 [2], possess more ASCs than those created using dispersive flow algorithms. D8 is the oldest, simplest, and most commonly applied method for routing surface flows based on DEMs. However, this algorithm is known to suffer many limitations, most notably it produces unnatural-appearing parallel flow patterns. This occurs because of the combination of crudely representing FD in intervals of 45° (8 directions), which causes a directional bias, and because of the algorithm's inability to represent flow divergence. While many researchers have discussed D8's unnatural flow patterns, far fewer have acknowledged the abundance of ASCs in D8 FD rasters as an issue [3]. ASCs are distributed throughout D8 FD rasters but are particularly common along ridges. That is, D8's approximated flow lines start at drainage divides, and do not continue along the divide upwards toward the summit. Because flow lines converge

upslope at divides (note, upslope convergence is equivalent to downslope divergence, which non-dispersive algorithms do not allow), D8 cannot represent flow divergence along ridges.

Several other non-dispersive algorithms have been developed to overcome the unnatural-looking flow patterns produced by D8. Fairfield and Leymarie [4] developed the Rho8 flow algorithm which reduces D8's directional bias, but suffers from the fact that it is stochastic, and thus produces a different result each time it is run on a data set. Gallant and Wilson [3] also recognized that Rho8 produces many times more ASCs than D8. Orlandini [5] proposed two non-dispersive flow algorithms, D8-LAD/LTD, that make path-based adjustments to individual FDs to better align with the overall path of flow lines, substantially reducing the directional bias of D8. However, this approach also produces abundant ASCs.

Why do attempts to correct D8's directional bias result in greater prevalence of ASCs? ASC are potentially introduced in flow pattern when an FD is deflected away from its D8 direction to a neighboring cell to better align with the flow-line aspect. The deflection causes the abandoned cell to be cut off from its upslope flow line. Unless another deflection redirects a neighboring parallel flow line toward the abandoned cell, it will become an ASC. Because these methods purposely reduce the occurrence of parallel flow patterns, this rectifying condition is unlikely to occur, and ASCs become abundant. This is an inherent property of nondispersive methods that break up parallel flow patterns and represents part of a *fundamental compromise of flow-path modelling*. We must either accept parallel non-dispersive flow patterns with fewer artifact source cells (D8), more-natural non-dispersive flow patterns with abundant artifact source cells (Rho8, D8-LAD/LTD), or dispersive flow.

Like the presence of parallel flow patterns, dispersion has the effect of reducing the occurrence of ASCs in FD rasters. In fact, not all flow algorithms produce ASCs. Fully dispersive flow algorithms that distribute flow to all downslope neighbors, such as Freeman's multiple-direction D8 (MD8) algorithm [6], and its many variants [7,8], do not create ASCs. However, these methods tend to be overly dispersive [9]. For example, with MD8, flow issuing from a point near the top of a conical surface will eventually flow to the opposite side of the cone. Increasing MD8's dispersion-dampening parameter cannot rectify this issue. Tarboton [10] argues that dispersion is inconsistent with the physical definition of upslope area, and that dispersion should be minimized to the extent possible in development of flow algorithms. If necessary, he states, physical dispersion can be modeled separately. Tarboton's D∞ method is an example of a dispersion-limiting flow algorithm, where flow is restricted to at most two adjacent downslope cells.

In this paper we describe a new flow algorithm that creates flow patterns with no ASCs and with minimal flow dispersion, by restricting dispersion to cells where it is necessary to resolve the ASCs in a non-dispersive FD raster.

II. MINIMAL DISPERSION FLOW ALGORITHM (MDFA)

The new minimal dispersion flow algorithm (MDFA) is conceptually simple. It begins by deriving a D8 FD raster from a depressionless DEM. Then, each flow path in this grid is traversed in the downslope direction, from longest to shortest, applying a path-based directional bias correction, somewhat similar to Orlandini's D8-LTD approach. All cells are identified in the FD raster that do not have inflowing cells but do have higher neighbors in their local 3×3 neighborhood. This is the set of ASCs. The highest neighbor of each ASC then has its FD altered to also point towards the downslope ASC. Because this cell would have already had an FD pointing towards a different downslope neighbor, this cell has now become dispersive. If there are more than one ASC in a cell's local neighborhood, it may have more than two outflowing neighbors, one for each ASC plus one for the original FD. Summit cells can shed flow to all eight neighbors.

FDs are stored using the same base-2 convention commonly used with MD8, allowing for pointers to multiple neighbors using a single value stored in each grid cell. For example, a cell flowing to its third and fourth neighbors (corresponding to the SE and S cells, if using the convention of ordering cells in a 3×3 starting from the NE and progressing clockwise) has an FD of $2^{3-1} + 2^{4-1} = 12$. A summit cell, flowing to all eight neighbors, would have an FD of $2^0 + 2^1 \ldots + 2^7 = 255$.

Finally, the FD raster is used as the input for a flow-accumulation operation to create the final MDFA total contributing area (TCA), or specific contributing area (SCA) grid. For any cell [r, c], the proportion of area (flow) directed towards neighboring cell, i, (F_i) is calculated as:

$$F_i = \begin{cases} p + (1-p)/N_{out}\,, & i = FD_{PC} \\ (1-p)/N_{out}\,, & i \neq FD_{PC} \end{cases} \qquad \text{[Eq. 1]}$$

where N_{out} is the number of outflowing neighbors of cell [r, c], FD_{PC} is the non-dispersive flow direction determined by the path-correcting algorithm, and p is the proportion of flow (0-1) that is given to FD_{PC} over and above any other secondary outflowing neighbors. This parameter preserves a preference toward the path-corrected direction in the flow accumulation grid. With p=0.0 (0%) there is no preference for any outflowing cell; with p=1.0 (100%) cells with multiple FDs will direct their flow entirely towards the original path-corrected direction and the algorithm behaves like a non-dispersive method. Therefore, MDFA has the flexibility of being either entirely non-dispersive (p=1.0) or partially dispersive (p<1.0). With p<1.0, it can be said that MDFA is minimally dispersive, since only the smallest possible subset of cells needed to eliminate ASCs will be dispersive.

III. CASE STUDY

The MDFA method was applied to a 19-million cell 1-m resolution lidar bare-earth DEM of Ponui Island, located approximately 35 km east of Aukland, New Zealand. The DEM

was filtered using the Whitebox Feature Preserving Smoothing tool to remove surface roughness and noise in the original DEM while preserving significant breaks-in-slope. Smoothing is an important preprocessing method for DEMs used in flow-path modelling because micro-topographic scale roughness and noise produce abundant <1 m relief "summits" that are hydrologically insignificant at the relevant modelling scale. Topographic depressions were also removed from the smoothed DEM using Whitebox's least-cost breaching method.

The resulting FD and SCA grids were compared with other common non-dispersive and dispersive flow algorithms in terms of their ASCs prevalence and their levels of dispersion (Table 1). Two measures of overall dispersion were used. The first measure was the percent of cells in the FD raster with multiple flow directions (%MFD), i.e., multiple outflowing neighbors. The second dispersion measure was related to the average percent of flow apportioned to secondary flow directions; a quantity referred to here as ϕ. The primary FD is the neighbor that receives the highest portion of flow, based on the flow algorithm's apportioning method and all other directions are secondary.

Fig. 1 shows the SCA patterns generated using a selection of common flow algorithms and MDFA, with p=0.75 (Fig. 1C) and p=0.0 (Fig. 1D), for a small catchment draining into Motunau Bay, Ponui Island. This allows for qualitative visual comparisons of the resulting SCA patterns. Although tests MDFA with p=0.5 and p=1.0 are reported in Table 1, their SCA patterns are not presented in Fig. 1 for brevity.

TABLE I. ASC ABUNDANCE AND FLOW DIVERGENCE CHARACTERISTICS OF VARIOUS FLOW ALGORITHMS

Algorithm	ASCs (%)	%MFD	ϕ (%)
Non-dispersive methods			
D8	4.7	0.0	0.0
Rho8	18.1	0.0	0.0
MDFA (p=1.0)	13.1	12.5	0.0
Dispersive methods			
MDFA (p=0.75)	0.0	12.5	1.6
MDFA (p=0.5)	0.0	12.5	3.2
MDFA (p=0.0)	0.0	12.5	6.3
D∞	0.8	95.3	24.4
MD8-Freeman	0.0	99.7	60.2

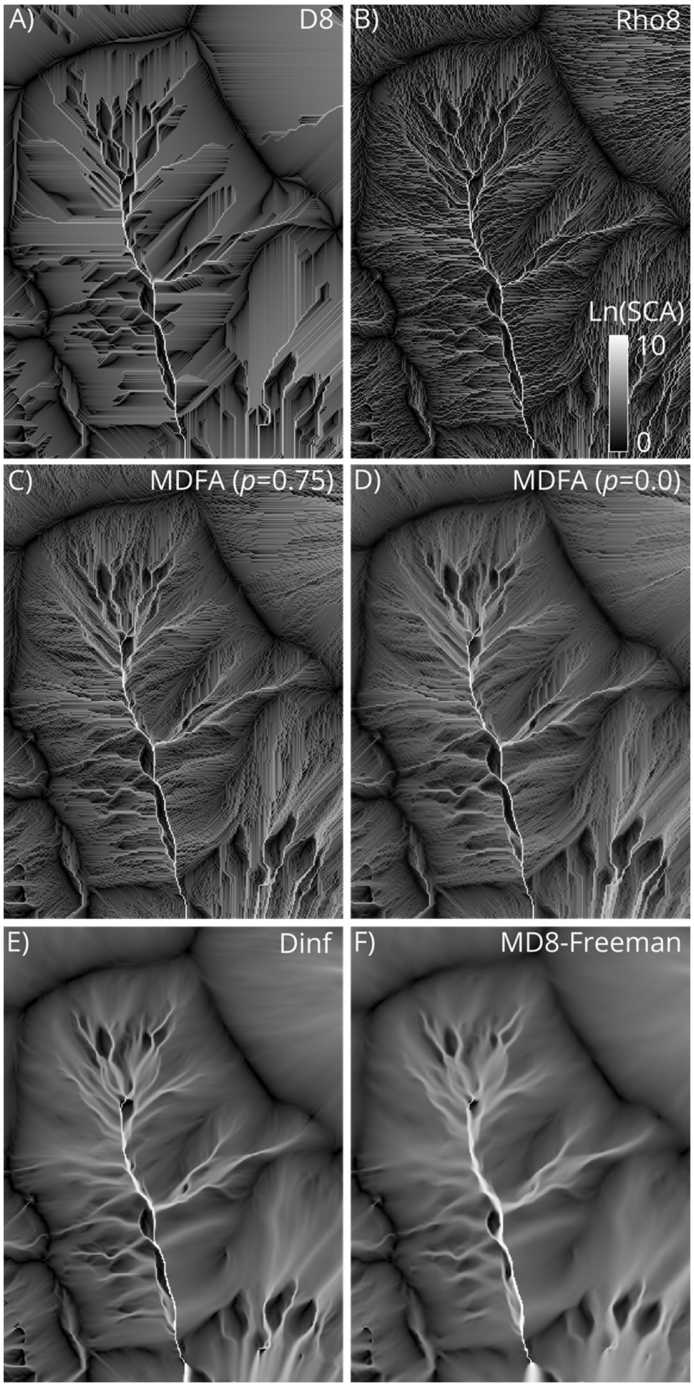

Figure 1. Comparison of SCA (m^2/m) patterns for a catchment draining into Motunau Bay, Ponui Island produced by D8 (A), Rho8 (B), MDFA with p=0.75 (C), MDFA with p=0.0 (D), D∞ (E), and MD8-Freeman (F).

IV. Discussion

As expected, MDFA FD rasters have no ASCs with p<1.0. When the algorithm is treated as a non-dispersive method (p=1.0), it was found to have an intermediate number of ASCs (13.1%) between D8 and Rho8 (Table 1). The reduced-dispersion algorithm D∞ was the only dispersive method tested that produced ASCs, albeit a small number of these artifacts were present in the test data (0.8% of the total grid cells) compared with non-dispersive methods. Inspection showed that the D∞ ASCs were largely associated with ridge positions, where D∞ is known to misrepresent divergent flow [11].

MDFA (with p<1.0) exhibited the least dispersion of any of the tested dispersive flow algorithms, by a significant margin (Table 1). Only 12.5% of the cells in the FD raster exhibited some level of dispersion, compared with >95% for D∞ and nearly 100% with MD8-Freeman. Similarly, even the most dispersive form of MDFA (p=0.0; no preference for the path-corrected FD at dispersive sites) demonstrated a 74% reduction in the average dispersion to secondary outflows (ϕ =6.3%) than the second least dispersive algorithm, Dϕ(∞ =24.3%). This was expected, given that MDFA limits flow dispersion to sites in the upslope neighborhoods of ASCs, and with 87.5% of cells therefore treated non-dispersively. While adjusting the p parameter does not impact the total number of dispersive cells, raising the value from 0.0 to 0.5 did decrease ϕ from 6.3% to 3.2%, an 87% decrease in dispersion compared with D∞. Similarly, setting p=0.75 lowered ϕ to 1.6%, a 93.5% decrease in dispersion compared with D∞. These findings indicate that p and ϕ are linearly and inversely related. The effects of varying p on the resulting SCA patterns were subtle (Fig. 1C and 1D) but discernable. It may be advisable for users to treat p as a mechanism for switching between dispersive (p=0.0) and non-dispersive (p=1.0) MDFA as required by the application, although more testing is required to find an optimal value.

The D8 SCA pattern showed extensive areas of unrealistically straight and parallel flow (Fig. 1A), that are not in the MDFA SCA rasters (Fig. 1C and 1D), even with p=0.0. The application of a path-correction method resulted in more natural flow patterns in the MDFA rasters than D8. In fact, MDFA SCA patterns appear to follow broadly similar trends to the corresponding D∞ and MD8-Freeman SCA patterns (Fig. 1E and 1F), although with visibly less overall dispersion. The level of dispersion in the SCA patterns increases from Fig. 1C (MDFA p=0.75) to Fig. 1F (MD8-Freeman). This is apparent throughout the catchment but is particularly obvious along the main valley bottom (highest SCA values) where MDFA creates a mostly single-cell wide flow line compared with the thicker, more heavily dispersed flow lines associated with the two other dispersive algorithms.

Further testing is needed to compare the accuracy of the new method in predicting SCA patterns on mathematically defined surfaces, with known SCA values. This exercise may provide better guidance on the setting of the p parameter. An implementation of the MDFA algorithm, developed using the Rust programming language, is available in the Whitebox Workflows (WbW-Pro) software.

V. Conclusions

This paper presents a new flow algorithm, MDFA, which aims to produce more natural flow patterns than D8, no ASCs, like fully dispersive algorithms (MD8), and substantially less overall dispersion than current dispersion-limiting methods (D∞). By limiting dispersion to cells where it is needed to ensure there are no ASCs, MDFA produces FD rasters where every grid cell is connected by a flow path to a downslope outlet cell and upslope to a summit, while most cells have a path-corrected (aspect aligned) single flow direction. MDFA occupies an optimal position in the fundamental flow-path modelling compromise between the needs for realistic flow patterns, no ASCs, and minimal use of dispersion.

VI. Acknowledgments

Funding for this research has been provided by the Natural Sciences and Engineering Research Council of Canada (NSERC), grant number 401107.

References

[1] Maxwell, J.C. 1870. “On hills and dales: To the editors of the philosophical magazine and journal”, The London, Edinburgh, and Dublin Philosophical Magazine and Journal of Science, 40(269), 421-427.

[2] O'Callaghan, J.F., and D.M Mark, (1984). “The extraction of drainage networks from digital elevation data”, Computer vision, graphics, and image processing, 28(3), 323-344.

[3] Gallant, J.C. and J.P. Wilson, 2000. “Primary topographic attributes”, Terrain analysis: Principles and applications, 87-131.

[4] Fairfield, J., and P. Leymarie, 1991. “Drainage networks from grid digital elevation models”, Water resources research, 27(5), 709-717.

[5] Orlandini, S., G. Moretti, M. Franchini, B. Aldighieri., and B. Testa, 2003. “Path-based methods for the determination of nondispersive drainage directions in grid‐based digital elevation models”, Water resources research, 39(6).

[6] Freeman, T.G. 1991. “Calculating catchment area with divergent flow based on a regular grid”, Computers and Geosciences, 17(3), 413-422.

[7] Quinn, P.F., K.J. Beven, and R. Lamb, 1995. “The in (a/tanβ) index: How to calculate it and how to use it within the topmodel framework”, Hydrological Processes 9(2): 161-182.

[8] Qin, C., A.X. Zhu, T. Pei, B. Li, C. Zhou, and L. Yang, 2007. “An adaptive approach to selecting a flow‐partition exponent for a multiple-flow-direction algorithm”, International Journal of Geographical Information Science, 21(4), 443-458.

[9] Gruber, S., and S. Peckham, 2009. “Land-surface parameters and objects in hydrology”, Developments in soil science, 33, 171-194.

[10] Tarboton, D.G. 1997. “A new method for the determination of flow directions and upslope areas in grid digital elevation models”, Water resources research, 33(2), 309-319.

[11] Seibert, J., and B.L. McGlynn, 2007. “A new triangular multiple flow direction algorithm for computing upslope areas from gridded digital elevation models”, Water resources research, 43(4).

Computing Channel Slope from a DEM: A Review of Issues and Two Algorithms

Scott D. Peckham
Rivix Software, LLC
Broomfield, Colorado USA
peckhams@rivix.com

Cite as: Peckham, S. (2025). Computing Channel Slope from a DEM: A Review of Issues and Two Algorithms. In: Proceedings of Geomorphometry 2025, 9-13 June, Perugia, Italy. M. Alvioli, L. Melelli, I. Marchesini eds. CNR Edizioni, Rome. ISBN 978-88-8080-765-0. DOI: 10.5281/zenodo.15395683

Abstract — **The problem of computing channel slope from a DEM is distinct from the problem of computing topographic slope in other parts of the landscape. This problem is important in the context of spatially distributed hydrologic modeling that starts with a DEM. Here, the challenge of computing good estimates of channel slope is explained, and then two different algorithms are described and compared. One of these, referred to here as the "slope-from-area algorithm", was published in a previous paper while the other is new and is referred to as the "zero-slope flow path algorithm". A MERIT DEM for Beaver Creek, Kentucky is used as a test case.**

I. Introduction

The problem of computing topographic slope from a raster DEM (Digital Elevation Model) has been well-studied. Evans (1972) proposed a method based on fitting a quadratic function (degree 2 polynomial) of x and y to the 9 elevations in the vicinity of a grid cell. Zevenbergen and Thorne (1987) proposed a method based on fitting a partial quartic (degree 4 polynomial) function of x and y, again using the elevation of a grid cell and its 8 neighbors. Since then, there have also been papers comparing the relative merits of these two well-known methods, with the latter method appearing to be more susceptible to DEM inaccuracies or noise. Methods for computing slope, aspect, and various types of curvature (plan, profile, and streamline) are described in Peckham (2011). However, the problem of obtaining accurate estimates of along-channel slope from a DEM has received less attention and turns out to be very important for spatial hydrologic models that are based on DEMs. The purpose of this paper is to first review the essence of the problem and then to describe and compare two different algorithms for addressing this problem. It will be seen that the problem persists even when using DEMs with high vertical and horizontal resolution.

II. Description of the Problem

Given a DEM with a vertical resolution of Δz and a horizontal resolution of Δx, the minimum, nonzero slope that is resolvable between a DEM grid cell and a nearest neighbor cell is: $\Delta z / \Delta x$. (It is slightly less than this between a grid cell and a diagonal neighbor.) So, for example, if Δz equals one meter and Δx equals 10 meters, slopes less than 0.1 will be unresolvable. This is a real problem because along-channel slopes in real rivers are often much smaller, typically between 10^{-4} and 10^{-6}. When channel slopes are too small to be resolved, one finds that along a channel flowline, the same elevation value occurs repeatedly many times (resulting in a slope of zero) before a lower elevation cell finally occurs. This can also result from filling pits in order to create a hydrologically sound DEM. Moving downstream, slope decreases and the number of repetitions before a drop in elevation tends to increase. At first glance, it may seem that increased vertical and horizontal resolution would resolve this issue. But decreasing Δz and Δx by the same factor does not change the minimum resolvable slope. Even if we decrease Δz to 0.01 meters (1 centimeter) but keep Δx to be 10 meters, slopes less than 0.001 will still be unresolvable and mapped to zero. Therefore, this problem is not addressed by using DEMs with higher vertical and horizontal resolution. Note that a slope of zero is not just wrong by some constant factor, it is completely unphysical, and even nonzero slopes can be off by factors of 100 to 1000 or more.

In a spatial hydrologic model, channel slope is an important variable because it determines the acceleration of the flow of water due to gravity. As a result, slope appears in Manning's formula for the flow velocity, v, given by:

$$v = (1/n)\, R_h^{2/3}\, S^{1/2} \qquad (1)$$

where S is the along-channel slope, R_h is the hydraulic radius, and n is Manning's bed roughness parameter. The flow velocity is one of the most important variables in a hydrologic model and is needed to compute the volumetric discharge. The widely used kinematic wave approximation relies on this formula. But notice that if a grid cell has a slope of zero, this gives a flow velocity of zero, resulting in a tower of water above that grid cell. If the slope is wrong by a factor of 100, then the computed velocity for that grid cell is wrong by a factor of 10.

III. The Slope-from-Area Algorithm

Peckham (2011) introduced an algorithm to address this problem that is based on an empirical law known as Flint's Law. Flint's Law (Flint, 1974) is an observed relationship given by:

$$S = c\, A^{\theta} \qquad (2)$$

that expresses the along-channel slope, S, at a basin's outlet as a power-law function of the basin's total contributing area, A. The exponent, θ, is negative (since slope decreases as area increases) and is between -1 and 0. It is sometimes called the concavity and is often close to -0.55 (Whipple, 2004).

To apply this algorithm, one first computes a grid of D8 flow directions and uses it to identify the grid cells that lie on the streamline of the main channel of the basin of interest. The main channel can be identified using a grid of total contributing area (computed by the D8 method) and repeatedly stepping upstream toward the D8 neighbor cell with the largest contributing area until a drainage divide is reached. According to Flint's Law, the predicted elevation for the k^{th} grid cell on the main channel is given by:

$$z_k(c,\theta) = z_0 + c \sum_{j=1,k} A_j^{\theta}\, \Delta L_j \qquad (3)$$

where z_0 is the elevation of the outlet grid cell, A_j is the total contributing area of the j^{th} grid cell on the main channel, and ΔL_j is the horizontal distance between adjacent main-channel grid cells. A nonlinear, least-squares regression is then used to estimate the parameters c and θ in equation (3) that give the best fit to the main channel elevation values extracted from the DEM. Next, we assume that the same parameters c and θ are approximately valid for every other elevation profile in the DEM. This allows us to compute a new grid of channel slopes from the values in the grid of contributing areas. This grid of channel slopes is guaranteed to decrease monotonically downstream since contributing areas computed by the D8 method always increase downstream. The final step is to create a new DEM from this new slope grid. This is done using an iterative procedure, starting with the grid cells that are furthest downstream and then computing and adding up the small, floating-point elevation changes that must be made to upstream neighbor cells in order to achieve the slope prescribed by the new slope grid. The iteration continues upstream until every grid cell has the prescribed slope.

While contributing areas computed using the D8 method will always be strictly increasing in the downstream direction, a plot of contributing area vs. distance downstream will exhibit numerous discontinuities or jumps (Figure 3), especially wherever a large tributary flows into the main channel. As a result, channel slopes computed using this algorithm will also exhibit discontinuities at the same locations, but slopes will be strictly decreasing in the downstream direction. These discontinuities are likely a real feature of river networks and not an artifact of the algorithm.

Note that Flint's Law is not expected to apply to the concave down portion of a longitudinal profile that always occurs near ridgetops where diffusive hillslope processes are known to dominate over fluvial processes. As a result, this algorithm tends to produce elevations near ridges that are considerably larger than those in the original DEM, and slopes that are considerably steeper. However, up to a point, the steeper slopes and narrower ridgelines it generates can be closer to the actual topography as resolved in higher-resolution DEMs. Over most of the new elevation profile (the lower portion), elevations differ from those in the original DEM by less than a few meters.

As already explained, slopes computed between adjacent grid cells in a DEM can be off by very large factors. However, contributing areas measured from a DEM have much smaller relative errors, as long as grid cell size is much smaller than the basin size. Near the basin outlet, errors in an area grid can't be wrong by more than a small percentage. So even if Flint's Law is a crude approximation, using it to compute channel slopes from contributing areas is likely to be more accurate than computing slope between adjacent grid cells directly. Notice that this same algorithm could be used with any other empirical relationship that allows channel slope to be computed from contributing area.

IV. The Zero-Slope Flow Path Algorithm

This innovative algorithm has the option to only change the channel slopes in a DEM that have a value of zero. The idea here is to first find all of the grid cells in the DEM that have (1) a nonzero D8 slope -- this means its elevation is higher than that of the cell just downstream (called its D8 parent), and (2) a D8 parent cell with a slope of zero. For each of these cells, follow the D8 channel profile downstream (stepping to D8 parents) until you reach a grid cell that has a lower elevation (the final cell). Excluding the initial and final cells on this flow path, all other cells have the same elevation, and all but the last one (before the final cell) have a D8 slope value of zero. (See Figure 1.) Compute the along-channel flow distance between the initial and final cells, which will typically be much larger than the distance between adjacent grid cells. Next, compute a slope value using this distance and the elevation drop between the initial and final cells. Finally, assign this same slope value to all of the grid cells that have a D8 slope of zero between the initial and final cell. It is actually reasonable to assign this new slope value to the initial cell and the

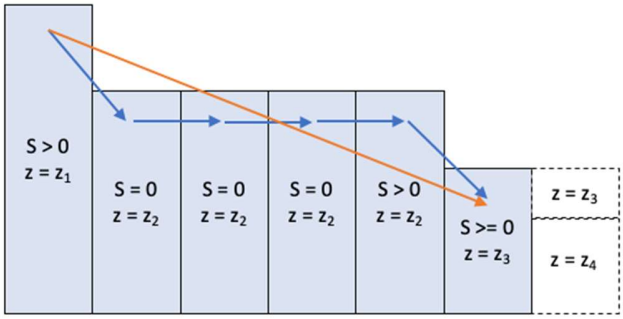

Figure 1. Diagram of a zero-slope flow path. The slope of the orange line is assigned to zero-slope cells and optionally to the first blue cell and the next-to-last blue cell, which have larger slopes.

next-to-last cell as well. This is optional but removes some unrealistic jumps in slope. Notice that it is possible for two (or more) such flow paths to merge, which leads to ambiguity as to which slope value to use downstream of their confluence. In this case, the lowest of the new slopes is used. Cells that initially had nonzero slopes are unaffected by this algorithm (unless the initial and next-to-last cell slopes are reassigned). If desired, a new DEM can be created from this new channel slope grid, as was done with the previous algorithm.

There are a few additional considerations when implementing this algorithm. One is that cells on the four edges of the DEM should be treated as having undefined (i.e., unreliable) D8 flow directions, and this can also be the case for other cells that flow to the edges. The algorithm does not assign slopes to these cells. Another issue is that there can be cells in flat areas that have a D8 slope of zero but no D8 children (upstream). Slopes can be assigned to these cells by allowing them to be the initial cell in a zero-slope flow path and allowing their slope to be changed. These cells have a contributing area of one grid cell and a slope of zero. This situation can be visualized by removing the first blue cell in Figure 1. Finally, notice that new slopes are assigned to short zero-slope paths before longer zero-slope paths. If saved to the same slope grid that is being used to follow paths, these can interfere with the proper assignment of slopes in the longer zero-slope paths. The solution is to use the original D8 slope grid for path-following and whenever a zero-slope cell lies on overlapping flow paths, smaller slope values overwrite larger ones.

V. Comparison of the Two Methods

A Jupyter notebook was created in order to analyze and compare these two algorithms and is available from the author. The figures in this section were created using a float-valued MERIT DEM for Beaver Creek, Kentucky, with a horizontal resolution of 3 arcseconds. Figure 2 shows the longitudinal profile of the main channel, extracted from the DEM, and the smooth profile computed using the slope-from-area algorithm. The best-fit Flint's Law parameters are c=0.1191 and θ= -0.886. Figure 4 shows the log of the slopes of the profile computed by this algorithm. The jumps in this plot correspond to jumps in the D8 areas for the main channel, caused by larger channels that flow into the main channel (Fig. 3). Figure 5 shows the profile of D8 slopes as measured from the DEM (many of which are zero), as well as the slopes computed from the slope-from-area algorithm. Figure 6 shows the profile of slopes computed using the slope-from-area algorithm, as well as those computed using the zero-slope flow path algorithm. While there are still jumps, the zero-slope flow path algorithm performs much better than the simple D8 slope algorithm. Further refinements to the algorithm are likely possible to eliminate some of these remaining jumps in slope.

VI. Conclusions

We have described and compared two algorithms for more accurately computing along-channel slopes from DEMs. This problem is distinct from the problem of computing slopes in more upland regions. The slope-from-area algorithm was previously described by Peckham (2011) while the zero-slope flow path algorithm is new. Both algorithms eliminate zero-slope grid cells and offer dramatic improvements over the simple D8 slope algorithm. Both have been implemented in a spatially distributed hydrologic model written in Python called TopoFlow (Peckham et al., 2017) and provide good results in this context. It is worth noting that the slope-from-area algorithm is based on an idealization that may only apply in more mature landscapes and it produces slopes that are everywhere significantly different from those in the original DEM. It also produces slopes and elevations that are too large if used near ridgelines. Except in the steepest parts of the basin, it produces new elevations that, while different, are within a few meters of the original values. The zero-slope flow path algorithm may be preferable in many situations since it preserves the original elevations and slopes except where they are

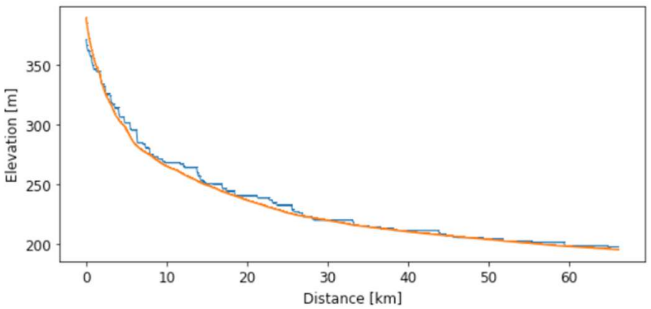

Figure 2. Main channel elevations of the Beaver Creek DEM (blue) and those from the slope-from-area algorithm. Best-fit Flint's Law parameters: c=0.1191 and q= -0.886. The uppermost portion of the profile has been excluded.

problematic.

While the zero-slope flow path algorithm only applies if there are zero-slope grid cells in the DEM, this can occur in several situations such as (1) after filling depressions in DEMs that aren't hydrologically sound, (2) after applying a flow-enforcement or "stream-burning" algorithm, (3) when using older, integer-valued DEMs, or (4) when using floating-point DEMs when only 1 to 3 digits after the decimal are considered significant or meaningful. By contrast, the slope-from-area algorithm can be applied to DEMs with no zero-slope cells. Note that D8 slopes in channels can still be inaccurate, even for hydrologically sound, float-valued DEMs, for the reasons explained in the Introduction. Moreover, algorithms to enforce hydrologic soundness can also introduce inaccuracies. For this short paper, a non-hydrologically-sound, float-valued MERIT DEM was used. Further refinements of these algorithms will be explored in future work.

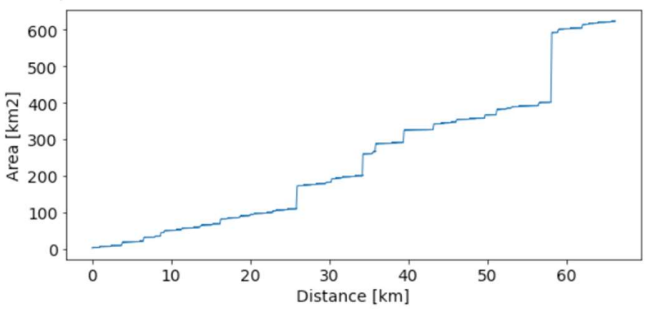

Figure 3. D8 total contributing area on main channel of Beaver Creek DEM, with jumps at major confluences.

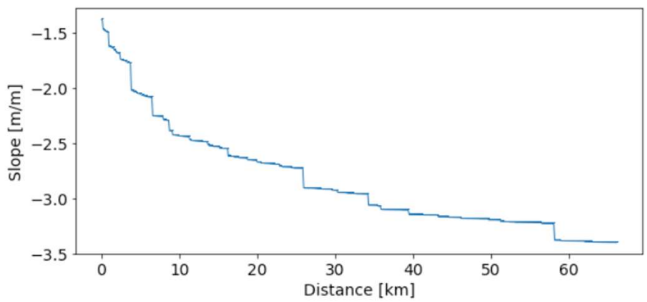

Figure 4. Base 10 log of slopes on main channel of Beaver Creek DEM computed with the slope-from-area algorithm.

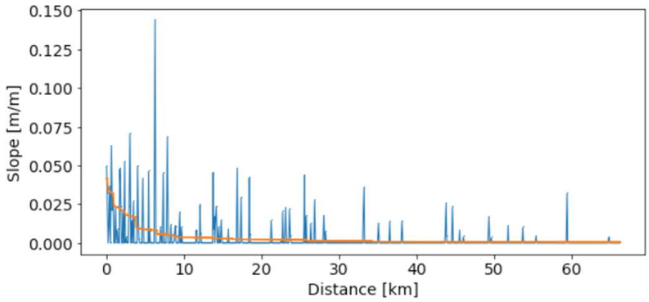

Figure 5. D8 slope on main channel of Beaver Creek DEM (blue) and slope from slope-from-area algorithm.

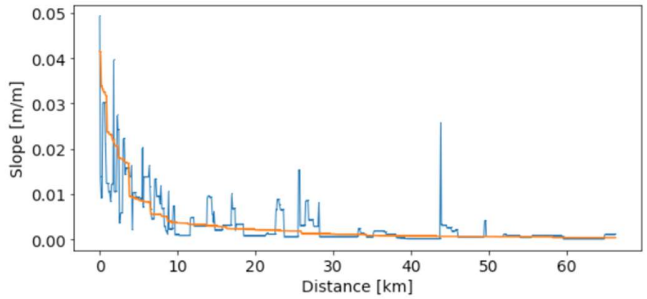

Figure 6. Slopes on main channel of Beaver Creek DEM computed using both the slope-from-area algorithm (orange) and the zero-slope flow path algorithm (blue).

REFERENCES

[1] Evans, I.S., 1972. "General geomorphometry, derivatives of altitude, and descriptive statistics", 17-90, In: Chorley, R.J. (Ed.) Spatial analysis in geomorphology, Methuen, London, 393pp.

[2] Flint J.J., 1974. "Stream gradient as a function of order, magnitude and discharge", *Water Resources Res*earch, 10(5), 969-973.

[3] Peckham, S.D., 2009. "A new algorithm for creating DEMs with smooth elevation profiles", *Proceedings of Geomorphometry 2009*, Zurich, Switzerland, pp. 34-37, http://geomorphometry.org/Peckham2009.

[4] Peckham, S.D., 2009. "Geomorphometry and spatial hydrologic modeling", In: Hengl, T. and Reuter, H.I. (Eds), *Geomorphometry: Concepts, Software and Applications*, Chapter 25, Developments in Soil Science, vol. 33, Elsevier, 579-602, http://dx.doi.org/10.1016/S0166-2481(08)00025-1. (TopoFlow)

[5] Peckham, S.D., 2011. "Profile, plan and streamline curvature: A simple derivation and applications", *Proceedings of Geomorphometry 2011*, Redlands, CA, pp. 27-30, http://geomorphometry.org/Peckham2011a.

[6] Peckham, S.D., M. Stoica, E.E. Jafarov, A. Endalamaw and W.R. Bolton, 2017. "Reproducible, component-based modeling with TopoFlow, a spatial hydrologic modeling toolkit", *Earth and Space Science,4(6), 377-394, special issue: Geoscience Papers of the Future*, American Geophysical Union, http://dx.doi.org/10.1002/2016EA000237.

[7] Whipple, K.X., 2004. "Bedrock rivers and the geomorphology of active orogens", *Annual Reviews of Earth and Planetary Sciences,* 32, 151-185.

[8] Zevenbergen, L.W. and C.R. Thorne, 1987. "Quantitative analysis of land surface topography", *Earth Surface Processes and Landforms*, 12, 47-56.

The role of spatial resolution and vertical accuracy of global DEMs in delineating stream networks

Petr Basta
Faculty of Environmental Sciences
Czech University of Life Sciences
Prague - Suchdol, 16500, Czechia
bastap@fzp.czu.cz

Jana Maresova
Faculty of Environmental Sciences
Czech University of Life Sciences
Prague - Suchdol, 16500, Czechia
maresovajana@fzp.czu.cz

Vitezslav Moudry
Faculty of Environmental Sciences
Czech University of Life Sciences
Prague - Suchdol, 16500, Czechia
moudry@fzp.czu.cz

Cite as: Basta, P., Maresova, J., Moudry, V. (2025). The role of spatial resolution and vertical accuracy of global DEMs in delineating stream networks. In: Proceedings of Geomorphometry 2025, 9-13 June, Perugia, Italy. M. Alvioli, L. Melelli, I. Marchesini eds. CNR Edizioni, Rome. ISBN 978-88-8080-765-0. DOI: 10.5281/zenodo.15285000

Abstract—**The efficacy of global digital elevation models (DEMs) derived from satellite observations is of paramount importance for hydrological applications, including stream network delineation. However, their effectiveness is constrained by spatial resolution and vertical biases introduced by vegetation and man-made structures. This study evaluates the performance of various global DEMs, including bare-earth models, in a Central European mountainous region. Utilizing lidar-derived digital terrain models (DTMs) and national stream networks as reference data, this study shows that bare-earth DEMs have higher vertical accuracy than conventional global DEMs across all land cover types. However, it is concluded that vertical accuracy alone is not a reliable indicator of a DEM's capacity to delineate stream networks. Instead, terrain slope and land cover exert a more significant influence on the accuracy of the delineated stream network. While the use of higher-resolution DEMs (e.g., 12 m TanDEM-X) has been shown to improve stream delineation, it has also been demonstrated to amplify errors related to vegetation bias. The study emphasizes that DEM selection should be based on their performance in delineating stream networks, rather than solely on vertical accuracy. The findings underscore the necessity of enhanced vegetation and building offset removal in high-resolution DEMs to optimize their applications in hydrology.**

I. INTRODUCTION

Digital Elevation Models (DEMs) are essential for hydrological applications, such as flood modelling [1] and stream network delineation [2]. However, their accuracy is often compromised by vertical biases and resolution limitations. DEMs derived from satellite radar or optical sensors frequently overestimate terrain heights due to their inability to penetrate dense vegetation or detect terrain beneath man-made structures [3, 4]. As a result, the effectiveness of DEMs for hydrological modelling depends not only on their vertical accuracy but also on their ability to reflect hydrologically relevant terrain features [5, 6, 7].

Our study evaluates eight global DEMs, including both original and bare-earth models, to assess their accuracy in stream network delineation. The study focuses on the area of Giant Mountains in Czech Republic (Fig. 1), a region with diverse topography and vegetation cover. Using lidar-derived Digital Terrain Models (DTMs) and national stream networks as reference datasets, we analyzed how land cover, terrain slope, and DEM resolution influence the accuracy of stream network delineation.

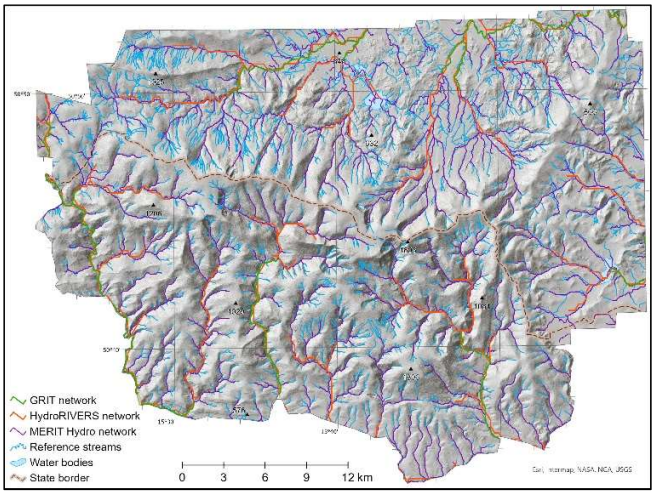

Figure 1. The reference stream network acquired from the Digital Database of Water Management Data (www.dibavod.cz; Czechia) and Polish National

Geoportal (geoportal.gov.pl; Poland) in comparison to global river networks data sets.

The study aims to address three key questions: (1) how does DEM vertical accuracy vary across different land cover types; (2) how do slope and land cover influence the accuracy of stream network delineation; (3) whether higher resolution (e.g., 12m TanDEM-X) or vegetation bias removal (e.g., FABDEM) is more important for improving stream network delineation. By answering these questions, the study seeks to determine which DEM provides the most reliable representation of stream networks for hydrological modelling.

II. Methods

The study evaluates eight DEMs categorised into two groups: (1) Original DEMs (digital surface models): SRTM (90m spatial resolution), TanDEM-X (12m and 90m), NASADEM (30m), and Copernicus DEM (COP; 30m), and (2) Bare-Earth DEMs: FABDEM (30m) [8], MERIT (90m) [9], and Continental Europe DEM (CON, 30m) [10], which have undergone processing to remove either vegetation offset (MERIT), or both vegetation and building offsets (FABDEM and CON, respectively). As a reference, we used a high resolution lidar-derived DTM (ALS) that was acquired in 2012 during the leaf-on period using a small-footprint airborne lidar system (RIEGL LMS Q - 680i). The ALS point cloud density was at least 4 points per m^2; we used the ground points to generate a digital terrain model (DTM) at a 2 m resolution. Accuracy assessment involved the following steps:

First of all, the vertical accuracy evaluation was assessed. Each DEM was compared against the reference ALS to determine errors in elevation representation. We calculated several validation metrics, but for simplicity, we only show the root mean square error (RMSE). Subsequently, we delineated stream networks and evaluated their accuracy using national hydrological dataset as a reference. Accuracy was measured based on intersection points, proximity to reference streams using eight buffer zones ranging from 0 and 200 m, and average distance. Finally, the accuracy of DEMs and delineated stream networks was evaluated with respect to terrain slope and land cover (forest, non-forest, and urban).

III. Results

Bare-earth DEMs performed better than original DEMs across all land cover types (Fig. 2) and slopes (Fig. 3). Non-forest areas showed the best DEM accuracy, followed by urban areas, with forests having the highest errors (Fig. 2). The RMSE increased with the slope in non-forest areas across all models. In forests, this relationship was less apparent, especially for very high slopes (Fig. 3).

DEMs with coarser resolution yielded a lower number of intersection points with reference streams (Table I), indicating more accurate stream network delineation. In addition, the higher was a particular DEM's spatial resolution, the greater was the proportion of vertices falling within the narrower buffer distance categories (Fig. 4). Stream networks extracted from bare-earth DEMs were more slightly accurate than those derived from original DEMs (Fig. 4).

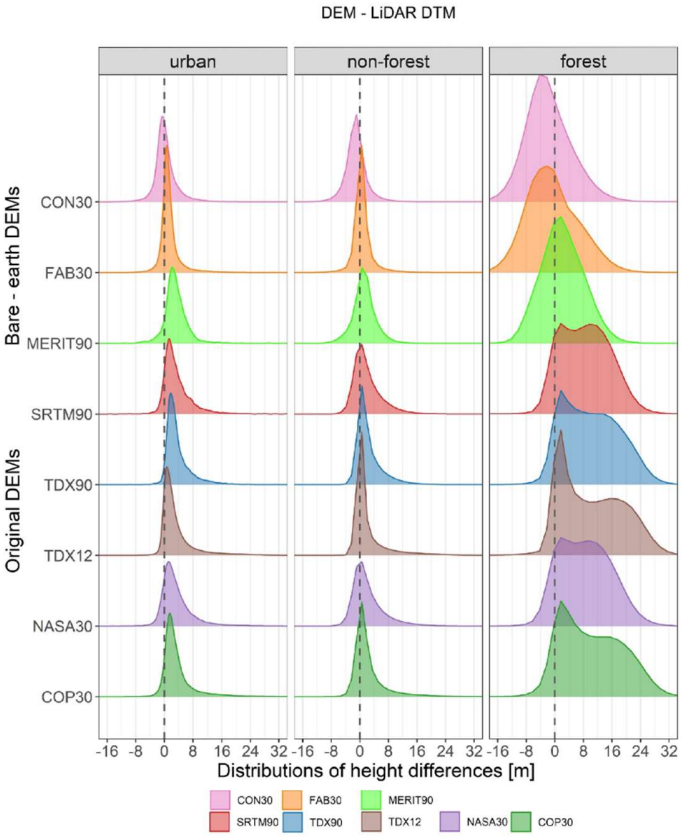

Figure 2. Distributions of height differences (compared to the lidar-derived DTM) for all evaluated DEMs for urban, non-forest, and forest areas. The vertical dashed line represents zero (perfect fit).

TABLE I. The number of intersect points

DEM	Number of points that intersect reference streams
SRTM	3,554
NASADEM	5,151
TanDEM-X (90m)	3,408
TanDEM-X (12m)	8,161
COP	5,484
MERIT	3,869
CON	5,167
FABDEM	5,447

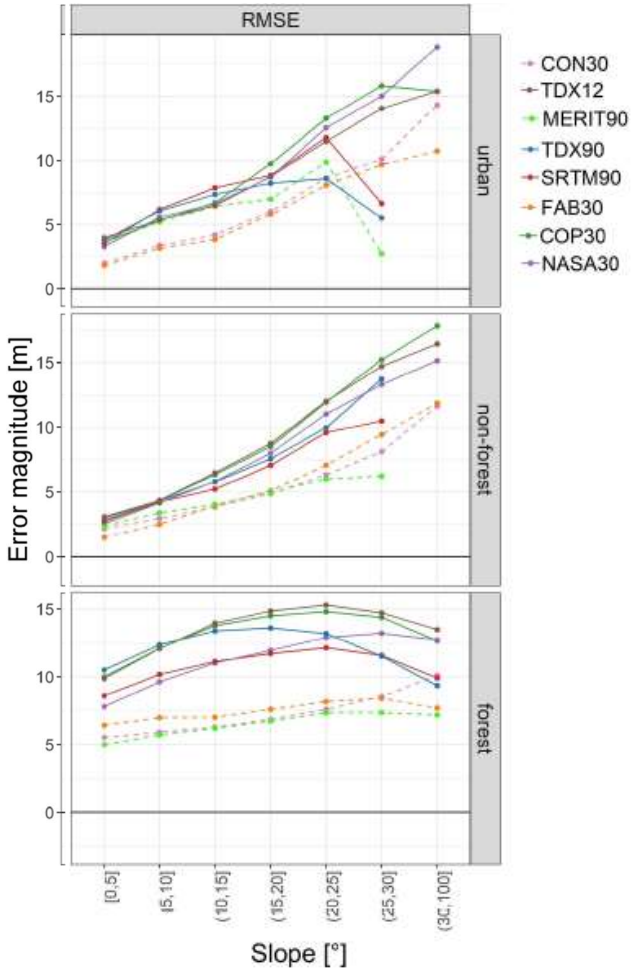

Figure 3. Effect of the slope on the accuracy (RMSE) of global DEMs.

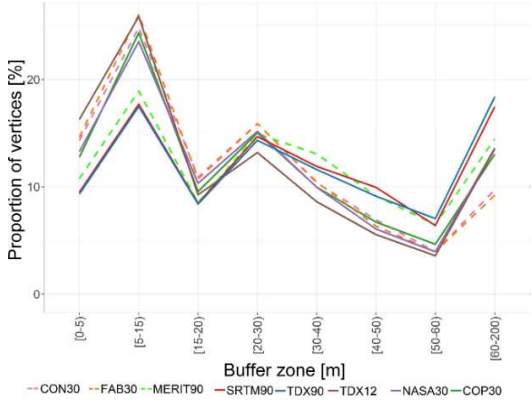

Figure 4. Percentages of vertices of DEM-derived streams falling within seven buffer zones from the reference stream network.

However, the accuracy of derived stream networks varied considerably across land cover and slope categories (Figure 5). In fact, land cover and slope affected the accuracy of the delineated stream networks more than the resolution and vertical bias of the adopted DEM. The slope had an inverse effect on DEM accuracy and stream delineation: (1) in DEM elevation accuracy, errors increased with steeper slopes, especially in non-forest areas; (2) in stream network delineation, accuracy improved with increasing slope, likely because steeper slopes facilitate more distinct drainage patterns. Furthermore, streams in forested areas were delineated with higher accuracy than in non-forest or urban areas, despite forests being the most challenging land cover for DEM vertical accuracy.

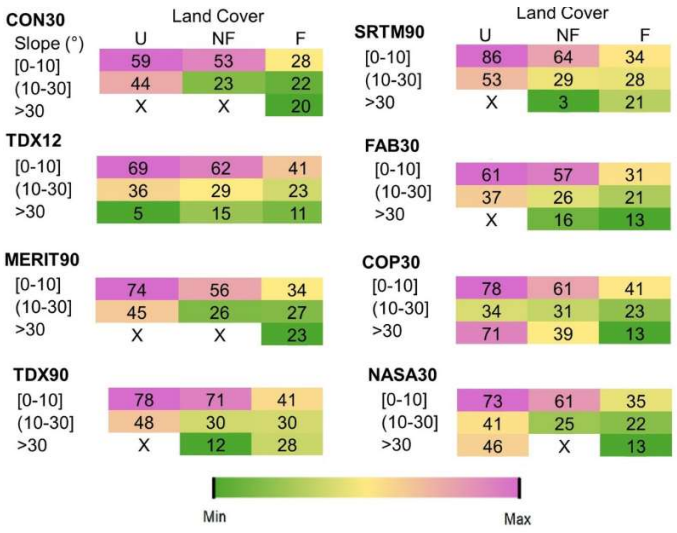

Figure 5. Average distance (in meters) of the evaluated DEM - derived streams from the reference stream network in three slope and land cover categories, respectively. Urban (U), non - forest (NF), and forest areas (F).

IV. Conclusion

Overall comparison of all assessed DEMs is shown in Table II. The study demonstrates that vertical accuracy alone is insufficient for evaluating DEMs for hydrological applications. This underscores the need to include stream network delineation in the quality assessment of global DEMs. While higher resolution improves spatial detail, removing vegetation and building-induced biases is equally important for accurate stream extraction. Among the evaluated DEMs, FABDEM performed the best overall, making it the most suitable choice for hydrological studies. As DEM technology continues to evolve, future models should focus on balancing high resolution with effective bias removal to optimize performance in diverse landscapes.

TABLE II. COMPARATIVE PERFORMANCE OF DEMS

DEM	Comparative Performance		
	Vegetation Bias Removed	*Vertical Accuracy*	*Stream Network Accuracy*
SRTM	No	Moderate	Low
NASADEM	No	Moderate	Low
TanDEM-X (90m)	No	Low	Moderate
TanDEM-X (12m)	No	Low	High
COP	No	Low	Moderate
MERIT	Yes	High	Moderate
CON	Yes	High	High
FABDEM	Yes	Highest	Highest

V. ACKNOWLEDGEMENTS

This work was funded by the Horizon Europe project EarthBridge (grant agreement No. 101079310). Funded by the European Union. Views and opinions expressed are, however, those of the author(s) only and do not necessarily reflect those of the European Union or the European Research Council Executive Agency. Neither the European Union nor the granting authority can be held responsible for them. JM, PB, were supported by the Internal Grant Agency of the Faculty of Environmental Sciences, Czech University of Life Sciences Prague (2022B0035). The TanDEM‑X DEM, with a 12 m resolution, was provided by the German Aerospace Agency (DLR) for the project "Comparison of Vegetation Height Derived from TanDEM‑X DEM with Reference Airborne Laser Scanning Data for Mountainous Areas in Czechia" (DEM_CALVAL1070).

REFERENCES

[1] Sanders, B. F., 2007. Evaluation of on-line DEMs for flood inundation modeling. Advances in Water Resources, 30(8), 1831–1843. https://doi.org/10.1016/j.advwatres.2007.02.005

[2] Yamazaki, D., Ikeshima, D., Sosa, J., Bates, P. D., Allen, G. H., & Pavelsky, T. M., 2019. MERIT Hydro: A High-Resolution Global Hydrography Map Based on Latest Topography Dataset. Water Resources Research, 55(6), 5053–5073. https://doi.org/10.1029/2019WR024873

[3] Bielski, C., López-Vázquez, C., Grohmann, C. H., Guth, P. L., Hawker, L., Gesch, D., Trevisani, S., Herrera-Cruz, V., Riazanoff, S., Corseaux, A., Reuter, H. I., & Strobl, P., 2024. Novel Approach for Ranking DEMs: Copernicus DEM Improves One Arc Second Open Global Topography. IEEE Transactions on Geoscience and Remote Sensing, 62, 1–22. https://doi.org/10.1109/TGRS.2024.3368015

[4] Gdulová, K., Marešová, J., & Moudrý, V., 2020. Accuracy assessment of the global TanDEM-X digital elevation model in a mountain environment. Remote Sensing of Environment, 241, 111724. https://doi.org/10.1016/j.rse.2020.111724

[5] Metz, M., Mitasova, H., & Harmon, R. S., 2011. Efficient extraction of drainage networks from massive, radar-based elevation models with least cost path search. Hydrology and Earth System Sciences, 15(2), 667–678. https://doi.org/10.5194/hess-15-667-2011

[6] Hawker, L., Bates, P., Neal, J., & Rougier, J., 2018. Perspectives on digital elevation model (DEM) simulation for flood modeling in the absence of a high‐accuracy open access global DEM. Frontiers in Earth Science, 6, 233. https://doi.org/10.3389/feart.2018.00233

[7] Mukherjee, S., Joshi, P. K., Mukherjee, S., Ghosh, A., Garg, R. D., & Mukhopadhyay, A., 2013. Evaluation of vertical accuracy of open source Digital Elevation Model (DEM). International Journal of Applied Earth Observation and Geoinformation, 21, 205–217. https://doi.org/10.1016/j.jag.2012.09.004

[8] Hawker, L., Uhe, P., Paulo, L., Sosa, J., Savage, J., Sampson, C., & Neal, J., 2022. A 30 m global map of elevation with forests and buildings removed. Environmental Research Letters, 17(2), 024016. https://doi.org/10.1088/1748-9326/ac4d4f

[9] Yamazaki, D., Ikeshima, D., Tawatari, R., Yamaguchi, T., O'Loughlin, F., Neal, J. C., Sampson, C. C., Kanae, S., & Bates, P. D., 2017. A high-accuracy map of global terrain elevations: Accurate Global Terrain Elevation map. *Geophysical Research Letters*, *44*(11), 5844–5853. https://doi.org/10.1002/2017GL072874

[10] Hengl, T., Leal Parente, L., Krizan, J., & Bonannella, C. (2020). Continental Europe Digital Terrain Model at 30 m resolution based on GEDI, ICESat-2, AW3D, GLO-30, EUDEM, MERIT DEM and background layers (v0.3). Zenodo. https://doi.org/10.5281/ZENODO.4724549

Probabilistic surface change detection with a 2-d array of robust adaptive Kalman filters

Daniel R. Newman
Faculty of Environmental Earth Science
Hokkaido University
Sapporo, Japan
daniel.newman@ees.hokudai.ac.jp

Yuichi S. Hayakawa
Faculty of Environmental Earth Science
Hokkaido University
Sapporo, Japan
hayakawa@eis.hokudai.ac.jp

***Cite as*:** Newman, D. R., Hayakawa, Y. S. (2025). Probabilistic surface change detection with a 2-d array of robust adaptive Kalman filters. In: Proceedings of Geomorphometry 2025, 9-13 June, Perugia, Italy. M. Alvioli, L. Melelli, I. Marchesini eds. CNR Edizioni, Rome. ISBN 978-88-8080-765-0. DOI: 10.5281/zenodo.15110492

Abstract—**The ability to collect high spatial and temporal resolution topographic data has increased interest in analyzing topographic changes resulting from dynamic surface processes. However comparing surveys directly compounds error and uncertainty from each source, prompting efforts to account for observation noise and other sources of uncertainty. The Kalman filter provides a solution to spatio-temporal modelling that has historically suffered from several challenges, notably the reliance on the accurate parameterization of noise statistics. This research presents the use of a 2-d array of robust adaptive Kalman filters to demonstrate the use of state-space models for probabilistic change detection. Four LiDAR surveys of a small basin affected by the 2018 Eastern Iburi landslide in Hokkaido, Japan were collected between October 2021 and June 2022. Rates of vertical displacement experienced by a bare-soil hillslope and were documented by the subtraction of survey DEMs and by estimation with the Kalman array. The spatial distributions of the probabilities associated with these estimates, along with model performance and uncertainty were shown to be useful tools for investigating surface change.**

I. Introduction

Low-cost surveying technology such as multi-sensor remotely piloted aerial systems (RPAS), have provided a platform for the collection of high spatial and temporal resolution topographic data. Data collected from RPAS mounted radar, photographic, or light detection and ranging (LiDAR) sensors are readily processed into digital elevation models (DEMs) [1]. While the specifications of the resulting elevation models are largely mission specific [2], vertical and horizontal accuracy of 1–20 cm and spatial resolutions of 5–50 cm are common [3,4]. These properties have made RPAS-derived topographic data ideal for monitoring dynamic systems such as natural hazards [5].

Multiple topographic surveys can form a spatio-temporal time-series of elevation observations from which many dynamic geomorphological phenomena can be examined. A common practice to introduce the temporal dimension to the data is to subtract elevation models, creating difference of DEMs (DoDs). These data quantify vertical displacement on a cell-by-cell basis, and are often used to derive volumetric change when investigating various dynamic processes [6]. However, comparing multiple DEMs propagates error and uncertainty from both sources into the results [7].

Probabilistic thresholding has been widely used to minimize erroneous elevation differences by restricting the analysis to high confidence estimates [7]. This is generally accomplished by estimating a local uncertainty field and deriving an associated probability using a statistical distribution. However, these analyses are highly dependent on the non-trivial task of accurately estimating local uncertainty [8]. Despite this challenge, accounting for noise when comparing multi-temporal elevation observations has proven to be a valuable endeavor for surface change detection and analysis [7,8].

Kalman filters are optimal estimators when noise statistics are known and Gaussian [9], and are widely employed to model discrete-time dynamic systems. The primary advantage offered by Kalman filters is the ability to account for multiple sources of noise and provide an internal estimate of uncertainty. However, filter performance is highly dependent on noise statistic parameters, resulting in the development of robust adaptive Kalman filters. This research will demonstrate the use of these filters to provide estimates of vertical displacement rates and the probability that the estimated vertical displacement rates are not zero given the uncertainty in each system.

II. Problem Formulation

The theory and governing equations of Kalman filters are well-documented, and will not be reiterated in the interest of

brevity. The equations behind the robust adaptive Kalman filter can be found in [10]. Robust adaptive Kalman filters differ from conventional Kalman filters by inflating uncertainty based on the accuracy of the model state relative to a robust estimate using current observations. The state vector (x) is defined by the coefficients of bivariate polynomial (β_1) concatenated with a companion vector representing the average rate of change for the polynomial coefficients (β_2). The state extrapolation matrix (A) follows a first-order kinematic model which extrapolates the rate of change vector over the time difference between surveys (Δ_t) to predict the next polynomial coefficients.

$$x = \begin{bmatrix}\beta_1\\ \beta_2\end{bmatrix}, \quad A = \begin{bmatrix}I & I\Delta_t\\ 0 & I\end{bmatrix}, \quad \mathrm{x_{t+1}} = A_t \mathrm{x_t}$$

where I is an identity matrix with dimensions equal to the number of coefficients in the polynomial.

The observation vector (y) is a vectorized local window of elevation observations (z) taken at a position and time.

$$y_{r,c} = \begin{bmatrix}z_0\\ \vdots\\ z_n\end{bmatrix} = vec\left(\begin{bmatrix}z_{r-w,c-w} & \cdots & z_{r-w,c+w}\\ \vdots & z_{r,c} & \vdots\\ z_{r+w,c-w} & \cdots & z_{r+w,c+w}\end{bmatrix}\right)$$

where r and c are row and column indices for a location and w is the half-length of the local window.

The observation model (C) projects the state into observation space as a vector of estimated elevation values ($\bar{y}$). The observation model is obtained by performing the basis expansion on the spatial positions of each observation (Φ) in the local window. Φ and C by extension are matrices of local spatial position monomials suitable for the task of estimating polynomial coefficients with least squares regression on y.

$$C = [\Phi \quad 0], \quad \bar{y_t} = Cx_t$$

Finally, the process uncertainty matrix (Q) is set to zero, assuming no process uncertainty in the state error. Instead, state error uncertainty is captured entirely by robust adaptive uncertainty inflation.

III. Methods

A. Study site

The study area is a small basin that drains into the Atsuma River and the reservoir formed by the Apporo Dam in Hokkaido, Japan (Fig. 1A). The area experienced many severe co-seismic landslides resulting from the 2018 Eastern Iburi earthquake. The study site focusses on a small, bare-soil hillslope with an area of approximately 0.024 km^2. The surface features relatively thick (1–3 m) and impermeable tephra layers from Shikotsu caldera volcanoes (9–20 ka), underlain by partially exposed Neogene sedimentary rocks. As a result, erosion and deposition processes dominate the surface dynamics of this area following the initial disturbance caused by the landslide.

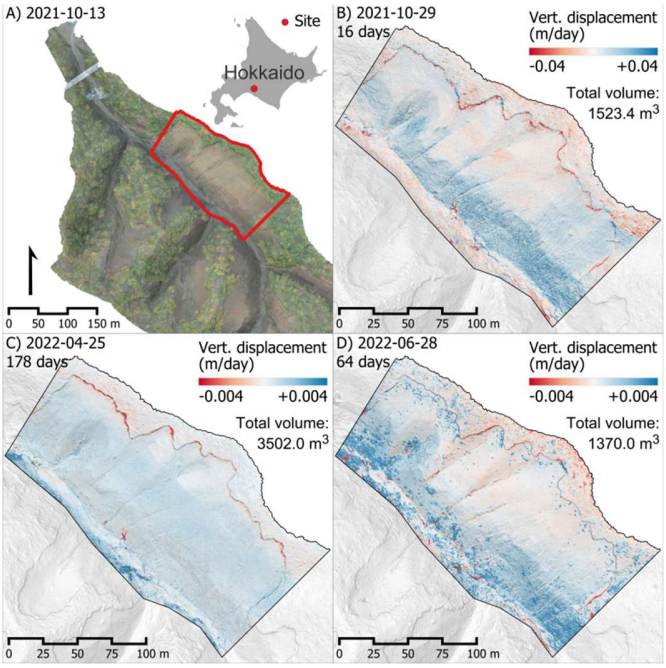

Figure 1. An air photograph and DoDs of the study site draped over the corresponding hillsahde images. Subfigure A shows a photograph collected during the 2021-10-13 survey, and subfigures B—D show the difference in elevation, expressed as a rate (m/day) between the date and the previous date for 2021-10-29, 2022-04-25, and 2021-06-28 respectively. The total volume of displaced material is annotated.

B. Data collection

Four surveys were conducted on the following dates: 2021-10-13, 2021-10-29, 2022-04-25, 2022-06-28 (YYYY-MM-DD) using a DJI Matrice 300 RTK RPAS equipped with a DJI Zenmuze L1 LiDAR sensor. While the study area is generally barren, some vegetation regrowth is observable as large positive vertical displacement in the western valley bottom of the 2022-06-28 survey (Fig. 1D), and was confirmed by aerial photography. A DJI D-RTK2 global navigation satellite system (GNSS) receiver was used as the local base station to perform real-time kinematic (RTK) correction of the aircraft positions. Based on this fixed base, a centimeter-level positional accuracy both in horizontal and vertical components was achieved. The LiDAR point clouds were post-processed and filtered using the equipped DJI Terra and ScanX online software (Locus Blue Co., Ltd., https://scanx.jp/). Interpolation into DEMs with a spatial resolution of 0.15 m was performed using natural neighbor interpolation in WhiteboxTools. All DEMs were clipped to 1465 rows and 1579 columns, sharing 1,070,251 coincident cells of data.

C. Analysis

A 2-d array of Kalman filters, each based on second-order bivariate polynomials, was initialized for all locations with the following parameter values:

$$P_0 = I \times 0.01, \quad R = I \times 0.01^2, \quad Q = 0$$

where I are identity matrices, P_0 is the initial estimate covariance matrix, referred to as uncertainty hereafter, and R is the measurement uncertainty matrix. The expression for R is based on the estimated measurement root mean squared error (RMSE) of 0.01 m, and is squared to represent a variance. All Kalman filters and the 2-d array were implemented in Python using the scientific computing package NumPy.

Observations were obtained with a local 3×3 window centered on the location of each Kalman filter (i.e., a roving window). The initial state vectors were estimated by weighted least squares (WLS) regression using C, weighted by R, and based on the observations from first and second DEMs available. Subsequent DEMs were processed sequentially using the Kalman filter predict-update functions on local windows of observations.

The normalized estimate error squared (NEES, denoted as ϵ) metric quantifies the squared error of the estimate normalized by the uncertainty covariance matrix. Here, error is defined as the difference between the state estimate and a null hypothesis of zero change (i.e., a zero vector). NEES is a chi-squared distributed variable with degrees of freedom equal to the dimensionality of the vector [11], so the conversion to probability is readily obtained by the chi-squared cumulative distribution function. Only the elements of the estimate uncertainty covariance matrix corresponding to the change coefficients ($P_{\beta 2}$) are used.

$$\epsilon = (\beta_2 - 0)^T P_{B_2}^{-1} (\beta_2 - 0)$$

While the entire change vector can be used for probabilistic change detection, inclusive or exclusive of change in position (i.e., polynomial intercept), only the rate of change in vertical position is examined in this research. Model error was evaluated using the RMSE of the posterior state estimate projected into measurement space ($\bar{y}$) relative to DEM observations.

IV. Results

The spatial distributions of posterior estimate of vertical displacement rate are shown in Fig. 2A1–C1, and can be compared to the corresponding DoDs (Fig. 1). In general, Kalman estimates were smaller and were less impacted by noise (e.g., Fig. 1D and Fig. 2C1). The survey Kalman filters disagreed with the DoD by estimating small, widespread negative vertical displacement with pronounced erosion in the gullies and both deposition and erosion in the valley (Fig. 2A1). The 2022-04-25 and 2022-06-28 Kalman filters maintained this pattern with negative vertical displacement occurring in the gullies and along the steep hillslope face. The spatial distributions of the non-zero vertical displacement probability (Fig. 2A2–C2) were generally correlated with high vertical displacement; however they also reflected the estimate uncertainty. All dates showed a high probability of vertical displacement in the valley bottom (Fig. 2), which corresponded to deposition areas in Fig. 2A2–C1. Relatively large negative vertical displacements from erosion were observed in the gullies, although the low probabilities suggest that the models had low confidence in these estimates (Fig. 2). Vegetation regrowth was observed as large positive displacement in 2022-06-28 with low probability (Fig. 2C1 and C2). Alternatively, the steep hillslope face experienced consistent negative vertical displacement with relatively high probability.

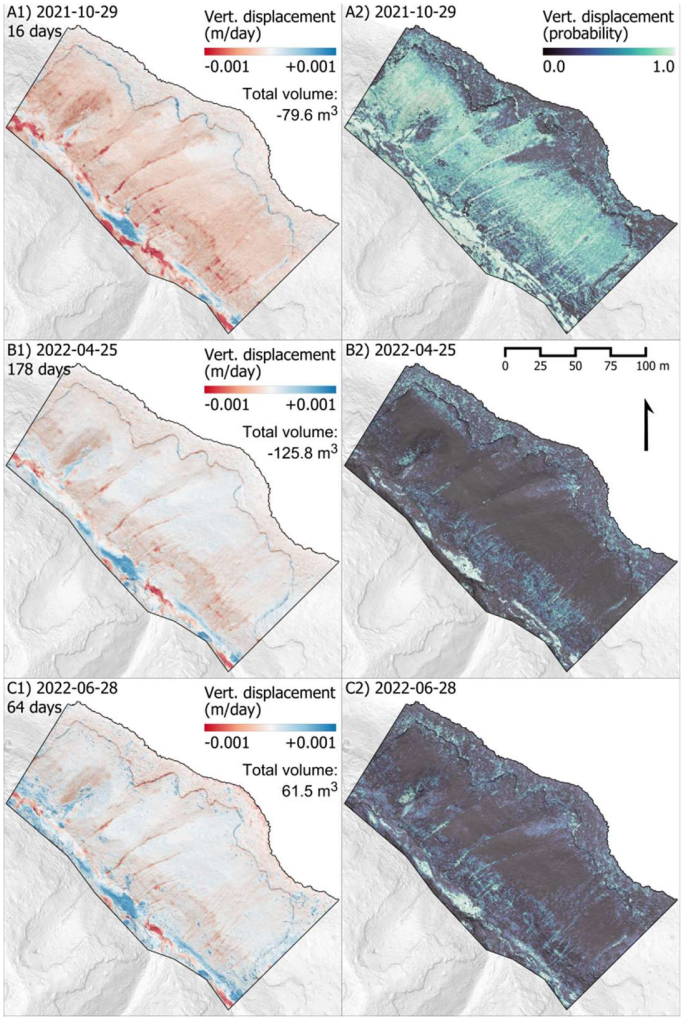

Figure 2. Kalman estimates of the rate of vertical displacement (m/day) are shown on the left column (subfigures A1, B1, and C1) and the associated probabilities on the right column (subfigures A2, B2, and C2). The total volume of displaced material is annotated.

Large predicted changes may be indicative of poor model performance rather than true change, and low probabilities may be indicative of high uncertainty. The spatial distributions of Kalman filter model RMSE and uncertainty are shown in Fig. 3A and B respectively. Centimeter scale model error was achieved, with the largest errors occurring along the rough, steep section of the hillslope (Fig. 3A). Uncertainty was generally correlated with the gullies, valley, and the upper hillslope (Fig. 3B).

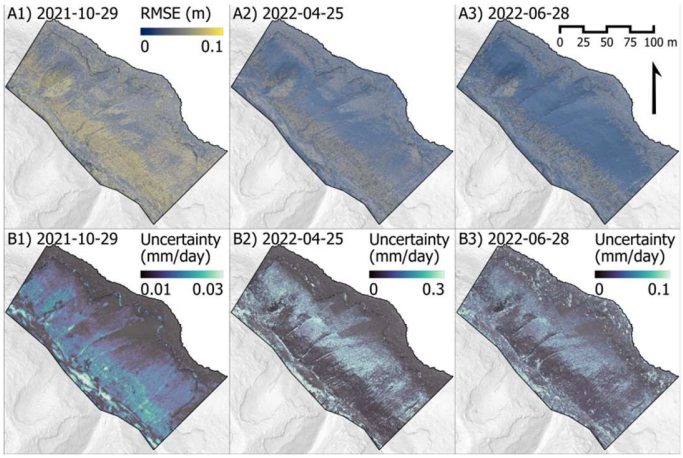

Figure 3. Spatial distributions of elevation error for the predicted 3×3 neighbourhood are shown in subfigures A1–A3. Spatial distributions of uncertainty are expressed as the square root of the posterior estimate error variance and are shown in subfigures B1–B3.

V. Discussion and Conclusions

Data from the hidden state may be analyzed with the assumption that uncertainty is minimized if model error is sufficiently low and models are considered reliable. The predicted vertical displacements disagreed with the DoD estimates, favoring erosive processes over depositional processes. The volume of displaced material for the DoD estimates are likely overestimated, especially for 2021-10-29 given the short 16 day time window. In general, the Kalman filters estimated more reasonable displacement volumes with low uncertainty, suggesting that the Kalman filters were more reliable estimators than DoDs. The robust adaptive Kalman filters remained performant without calibrating the initial uncertainty statistics, addressing a key weakness of conventional Kalman filters. The results suggest that the 2-d array of robust adaptive Kalman filters are an improvement over DoDs for analyzing surface dynamics such as vertical displacement while also providing spatially distributed estimates of uncertainty for probabilistic thresholding. The analysis can be readily extended to all change vector coefficients, and polynomial coefficients. Therefore, the Kalman array represents a novel and robust approach to interrogating the spatial relationships of surfaces, including dynamics, along with the associated geomorphological processes.

To the authors' best knowledge, this was the first time state-space modelling has been implemented in an array for multi-temporal local topographic analysis. The presentation of the concept with this simple case study revealed important considerations involving data preprocessing and parameterizing Q. Applying vertical alignment prior to filtering or restricting models to be exact predictors could help represent vertical processes such as erosion and deposition. Q was removed in this research to eliminate potentially erroneous parameterization and limit uncertainty inflation at the risk of creating overconfident models. This may underestimate uncertainty of known processes (e.g., seasonal processes), and may not always be appropriate. Further experimentation is required to identify the optimal strategy for Q estimation over a variety of surface dynamics.

Acknowledgments

This study was supported by JSPS KAKENHI Grant Numbers JP23KF0180 and JP23K20541.

References

[1] Nex, F., & Remondino, F. (2014). UAV for 3D mapping applications: a review. Applied Geomatics, 6, 1–15.

[2] Mueller, M. M., Dietenberger, S., Nestler, M., Hese, S., Ziemer, J., Bachmann, F., Leiber, J., Dubois, C., & Thiel, C. (2023). Novel UAV Flight Designs for Accuracy Optimization of Structure from Motion Data Products. Remote Sensing, 15(17).

[3] Fuad, N. A., Ismail, Z., Majid, Z., Darwin, N., Ariff, M. F. M., Idris, K. M., & Yusoff, A. R. (2018). Accuracy evaluation of digital terrain model based on different flying altitudes and conditional of terrain using UAV LiDAR technology. IOP Conference Series: Earth and Environmental Science, 169(1), 12100.

[4] Hashemi-Beni, L., Jones, J., Thompson, G., Johnson, C., & Gebrehiwot, A. (2018). Challenges and opportunities for UAV-based digital elevation model generation for flood-risk management: A case of Princeville, North Carolina. Sensors (Switzerland), 18(11).

[5] Giordan, D., Hayakawa, Y., Nex, F., Remondino, F., & Tarolli, P. (2018). Review article: The use of remotely piloted aircraft systems (RPASs) for natural hazards monitoring and management. Natural Hazards and Earth System Sciences, 18, 1079–1096.

[6] de Sousa, A. M., Viana, C. D., Garcia, G. P. B., & Grohmann, C. H. (2023). Monitoring Geological Risk Areas in the City of São Paulo Based on Multi-Temporal High-Resolution 3D Models. Remote Sensing, 15(12).

[7] Wheaton, J. M., Brasington, J., Darby, S. E., & Sear, D. A. (2010). Accounting for uncertainty in DEMs from repeat topographic surveys: Improved sediment budgets. Earth Surface Processes and Landforms, 35(2), 136–156.

[8] Schaffrath, K. R., Belmont, P., & Wheaton, J. M. (2015). Landscape-scale geomorphic change detection: Quantifying spatially variable uncertainty and circumventing legacy data issues. Geomorphology, 250, 334–348.

[9] Humpherys, J., Redd, P., & West, J. (2012). A Fresh Look at the Kalman Filter. SIAM Review, 54(4), 801–823.

[10] Yang, Y., He, H., & Xu, G. (2001). Adaptively robust filtering for kinematic geodetic positioning. Journal of Geodesy, 75, 109–116.

[11] Chen, Z., Heckman, C., Julier, S., & Ahmed, N. (2018). Weak in the NEES?: Auto-Tuning Kalman Filters with Bayesian Optimization. 2018 21st International Conference on Information Fusion (FUSION), 1072–1079.

Automatic delineation of river centerline using high density topographic LiDAR point cloud

Alexandre Rétat [1,a], Nathalie Thommeret [1,b], Frederic Gob [2,c], Jean-Stéphane Bailly [3,d], Laurent Lespez [1,e], Karl Kreutzenberger [5,f]

[1] Laboratoire de Géographie Physique (CNRS UMR 8591), Université Paris-Est Créteil, Thiais, France

[2] Laboratoire de Géographie Physique (CNRS UMR 8591), Université Paris 1 Panthéon-Sorbonne, Thiais, France

[3] LISAH, AgroParisTech, INRAE, Institut Agro, IRD, Université Montpellier, Montpellier, France

[4] Office français de la biodiversité, Direction générale, Service Eau et Milieux Aquatiques, Rennes, France

[a] alexandre.retat@cnrs.fr, [b] nathalie.thommeret@u-pec.fr, [c] frederic.gob@univ-paris1.fr, [d] bailly@agroparistech.fr, [e] laurent.lespez@u-pec.fr and laurent.lespez@cnrs.fr, [f] karl.kreutzenberger@ofb.gouv.fr

Cite as: Rétat, A., Thommeret, N., Gob, F., Bailly, J.-S., Lespez, L., Kreutzenberger, K. (2025). Automatic delineation of river centerline using high density topographic LiDAR point cloud. In: Proceedings of Geomorphometry 2025, 9-13 June, Perugia, Italy. M. Alvioli, L. Melelli, I. Marchesini eds. CNR Edizioni, Rome. ISBN 978-88-8080-765-0. DOI: 10.5281/zenodo.15274636

***Abstract*— LiDAR topographic data are more and more used in fluvial geomorphology where the delineation of the river water surface remains problematic. Indeed, the random absorption of infrared rays by water and by dense vegetation complicates the task of deterministic algorithms when working at a very large scale. Theses algorithms mainly use intensity and density of points to separate water from land but their threshold can vary depending on the transmitter and the study site characteristics. This work aims to delineate the centerline of rivers using a progressive research along the river path using only scatter of topographic LiDAR 3D points. We used the high point density, accuracy and classification of the newly created French IGN LiDAR HD to create a model calculating flow direction helping in river centerline delineation. The issues involved by the heterogeneity of the data are therefore limited thanks to the use of 8 different indicators instead of only the density and/or intensity factor. Results on 32 river reaches show a mean error of 23.65% and a median error of 8.5% of the river width coming from LiDAR automated river centerlines compared to references centerlines.**

I. Introduction

The precise location of the centerline of a watercourse is often one of the first needs of fluvial geomorphologists, hydrologists and hydrobiologists. When it is not measured in the field [1,2] or drawn manually [3], the centerline of fluvial channels is often calculated from the polygon corresponding to the water surface, itself identified using various methods, on DTMs, satellite images or orthophotographs. Unlike the location of the top of the banks, which is assumed to be relatively stable through time, the water surface of a river is an object whose shape and size highly change over time. They are intrinsically linked to the hydrological conditions of the river at the time of acquisition and to the cross-section shape of the river. Over the past 30 years, the development of high-resolution aerial and satellite topography techniques has led to the creation of numerous semi-automatic or fully automatic methods for identifying the water surface, which are still widely used nowadays. Methods based on satellite data (imagery, GNSS reflectometry, RaDAR) are developing strongly thanks to global space missions such as Landsat, SWOT or Sentinel, but are mostly limited to large rivers (~50m wide).

On a smaller scale, aerial or drone imagery and Canny filters give good results, but are rapidly limited when vegetation covers a substantial part of the water surface [4,5,6,7], which is mainly the case for narrower rivers. To limit the difficulties associated with the presence of vegetation and improve the data density and the geometric accuracy, others methods use LiDAR data to extract elevation DTMs and information such as point density and intensity, in order to distinguish ground from water [8,9,10,11,12]. In France, a high-resolution LiDAR coverage is carried out nationwide by the French Geographic National Institute (IGN). At that scale, the LiDAR data provided by IGN are inevitably not homogeneous in terms of density and intensity, making it difficult to use a deterministic method to delineate the centerline of very long river reaches. The aim of this work is to propose a direct method for determining the centerline of rivers for which the full water surface is unknown, and which can be better adapted to the characteristics of the river channel (river morphology, riparian vegetation) and the LiDAR data (density).

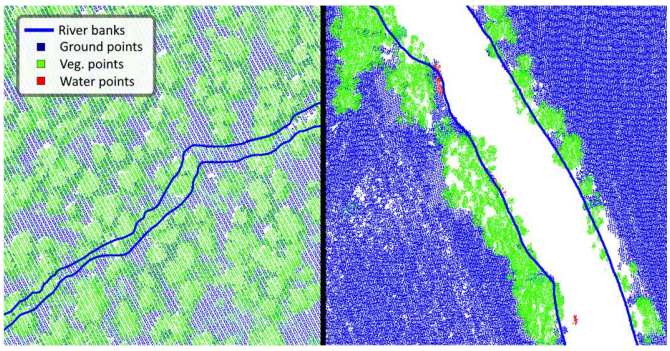

Figure 1. Aude reach (left) with points on water classified as "ground" and no "ground" point under vegetation, Hers-mort reach (right) with almost no points on water.

Three issues are therefore addressed: i) consideration of data heterogeneity (density, intensity), ii) consideration of study site heterogeneity (hydromorphological characteristics), iii) computer time and resources optimization.

II. Opportunities and Limitations of the LiDAR Data

The airborne HD LiDAR data provided by the IGN is characterized by a very high density of points (10 pulses per m², i.e. around 30M points per km² on average with multi-echo) with a guaranteed relative accuracy of $EMQ_{EN} \leq 25cm$, $EMQ_H \leq 5cm$ and absolute accuracy $EMQ_{EN} \leq 50cm$, $EMQ_H \leq 10cm$ [13] respectively. In addition, the point clouds obtained are classified by a hybrid method using deterministic algorithms, probabilistic methods relying on external data and a final manual control [14].

The intensity of the return signal is a specific property of LiDAR data which is sometimes used for water surface characterization due to low reflectivity of water. Theoretically, the near-infrared wavelength used by topographic LiDARs, classically λ=1064nm or λ=1550nm, allows the sensor to obtain very little return signal from a water surface [10]. In addition, intensity is however also very dependent on atmospheric transmittance and other LiDAR characteristics [15] : transmitted power; gain of the transmitter/receiving antenna; radar cross section; distance between the transmitter/receiver and the object.

Höfle [16] has shown that intensity coupled to elevation can be a good indicator for water surface identification when considering the atmospheric parameters. Deshpande [11] and Zheng [17], have rather chosen to ignore the intensity and work with the density instead because those LiDAR characteristics and atmospheric parameters were too difficult to describe. For these reasons, the intensity of the returned signal has not been used in this study to characterize the water surface.

For scanning transmitters, the near-absence of point on water (i.e., low return signal density) is primarily due to the signal absorption by water. Some part of the signal is also refracted in

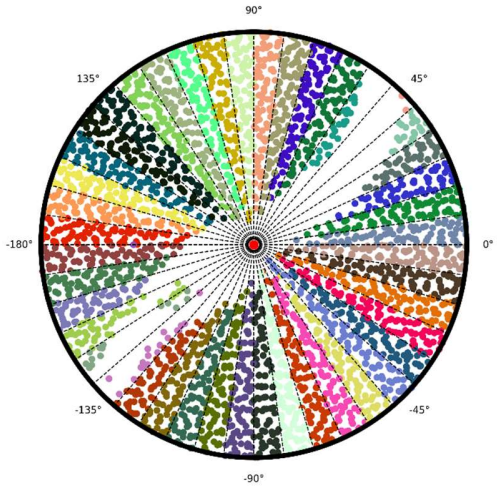

Figure 2. Cloud points sectorization around the origin point (8° sectors for this representation)

the water column, while the rest is reflected, a phenomenon further accentuated by the beam's incidence angle. Therefore, to register a returned a LiDAR infrared signal from the water, several conditions must be met, including the angle of incidence, water turbidity and surface conditions and the characteristics of the transmitter. This lack of data has been exploited by various authors to detect water surface. For example, Worstell [10] showed that the use of sliding windows with a radius of 5 meters on a 1 m LiDAR raster grid, containing fewer than 23 returns (i.e. 28% of the moving window), is sufficient to delineate water spaces. Deshpande [11] filled the voids by false points located much lower than the DTM and then calculated the intersection polygon between the resulting TIN DTM and a horizontal surface.

However, if the returned signal is not systematic at the water surface due to the refraction/reflection combination, the ground surface, particularly under forest cover, is also sometimes slightly affected by the LiDAR beam due to signal absorption by dense vegetation (Fig. 1). It is thus possible to not obtain any point on the water surface neither on the ground under the surrounding vegetation. This heterogeneity makes it difficult to develop a large-scale automatic method using only density and elevation to delineate water surfaces.

III. Method: Iterative River Centerline Delineation

The proposed method developed is based on a direct analysis of the point cloud to avoid raster interpolation and on an iterative downstream-upstream progression along vertices of the centerline. For any scene, the centerline delineation starts from a point (initial vertex) located in the river, which can be automatically obtained by correlating altitude and density data.

Delineation progresses upstream from the point of origin using a neighborhood analysis. The radius of neighborhood window is

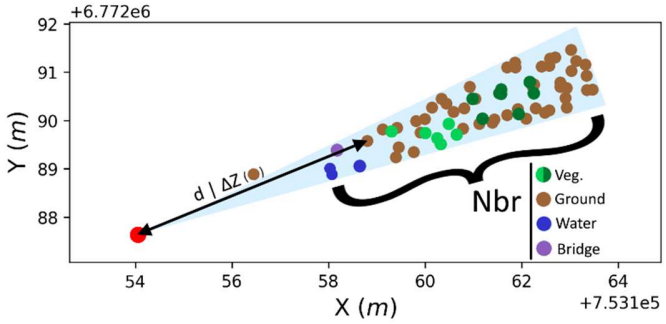

Figure 3. Criteria used in the research of flow direction in one sector (red dots: last centerline vertex; brown dots: ground points; blue dots: water points; green dots: vegetation points; purple dots: bridge points)

the main parameter. This radius has been determined thanks to a Bayesian optimization as 140 % of an estimated of the river width (+/-50%), taken in our case from the Carhyce hydromorphological database [18]. At each step, the next point on the centerline is searched among this surface cut in 0.5° sectors (Fig. 2 with 8° sectors for a legible representation).

The next centerline vertex identification process relies on the choice of the angular sector. This choice is based on several criteria calculated for each sector, including the point density in the sector, geometric criteria (altitude, mean distance) and semantic criteria from the point classification (presence of "Water" or "Bridge" points, presence of high vegetation) (Fig. 3). The range of values for these features has been determined so that they are minimal at the location of a theoretical water surface. These parameters are then modelled using a multi-variable linear combination where each criterion is assigned a coefficient. These coefficients were estimated by a 160-fold trained Bayesian optimization, as well as the neighborhood radius.

To find the sector angle that minimizes the combination of these variables, a 4-harmonic inverse Fourier transform is used to select the best candidates for stream direction (Fig. 4). The next vertex is calculated at a distance equal to one-fifth of the radius, in the direction of the best sector. Repeating the operation allows us to draw the streamline vectorially, limiting the search to a restricted radius in order to limit the mathematical constraints.

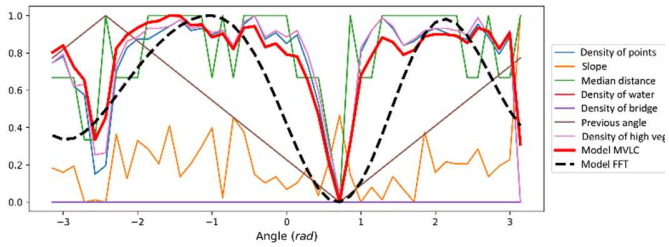

Figure 4. Modeling of the angular section criteria into a multi-variable linear combination (red) and his Fourier Transfom (black)

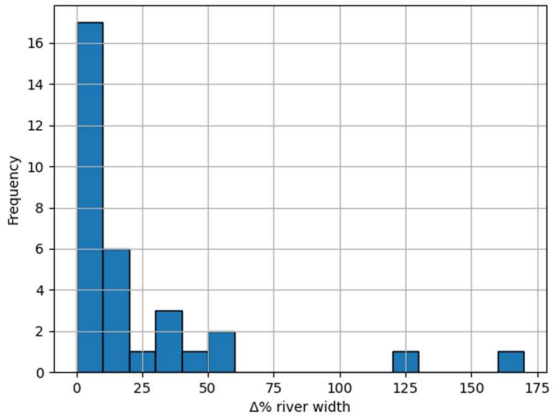

Figure 5. Error distribution in river width percentage (10% bins)

IV. Results

Can be used as a first step in the hydromorphological characterisation of rivers, the accuracy of the algorithm needs to be controlled. Indeed, if its resulting line is used as input for another automatic process, such as measuring width or slope along a river, it must, firstly, never leave the water surface polygon and, secondly, be as centered as possible within this polygon. Proven in a first study on a training set of 32 river reaches, this approach demonstrated relevant results for sites with varied characteristics (river size, sinuosity, etc.). We compared the central lines obtained with drawn reference lines. These references lines may include a bias due to manual tracing (5m to 10m edges). We segmented our lines into 100 equally-spaced points, then measured the absolute value of their distance from the reference line. The results are the average of these distances

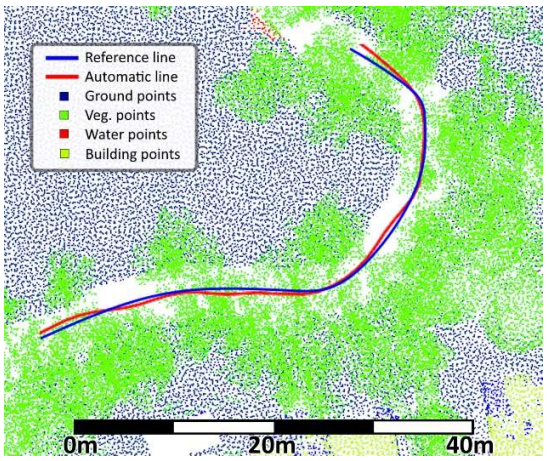

Figure 6. Choisille reach at Saint-Cyr-sur-Loire (blue line: centerline reference, red line: centerline calculated with our method, dots: LiDAR point cloud colorized according to classification)

as a percentage of the stream width (Fig. 5).

The automatically determined line remains very often close to our reference (Fig. 6), with a mean of 23.6% and a median of 8.5% of river width. Two of our cases fell victim to a drift phenomenon.

Even if it is limited, this problem is the main limitation of this methodology and is caused by a local difficulty, mainly for the smallest rivers, in differentiating the water zone from certain riparian zones, which are often low-lying and dense cover by vegetation (i.e. therefore with few return signal points). These areas may be difficult to detect even when the references lines are determined manually.

A study of 50 other stations is now underway to test our hyperparameters on sectors independent of the training set.

REFERENCES

[1] Luchi, R., J.M. Hooke, G. Zolezzi, and W. Bertoldi, 2010. Width variations and mid-channel bar inception in meanders: River Bollin (UK). Geomorphology, 119, 1-8p.

[2] De Milleville, L., F.Gob, N. Thommeret, L. Lespez, E. Tales, A. Zahm, and M. Girondin, 2023. The heterogeneity of the hydromorphological responses of a stream to the urbanization of its basin. Earth Surface Processing and Landforms, 48(4), 735-755p.

[3] Hooke, J.M., and L. Yorke, 2011. Channel bar dynamics on multi-decadal timescales in an active meandering river. Earth Surface Processes and Landforms, 36, 1910-1928p.

[4] Dillabaugh, C.R, K.O. Niemann, and D.E. Richardson, 2022. Semi-Automated Extraction of Rivers from Digital Imagery. GeoInformatica, 6(3), 263-284p.

[5] Zhao, J., H. Yu, X. Gu, S. Wang, 2010. The Edge Detection of River model Based on Self adaptive Canny Algorithm And Connected Domain Segmentation. 8th World Congress on Intelligent Control and Automation.

[6] Deshpande, S.S., 2024. Bank Line Extraction by Integration of Orthoimages and Lidar Digital Elevation Model Using Principal Component Analysis and Alpha Matting. Photogrammetric Engineering & Remote Sensing, 90(10), 631-638.

[7] Ye, S., R. Li, Z. Bai, A. Tuzikov, and C. Chen, (2024). Intelligent classification of water bodies with different turbidity levels based on Gaofen-1 multispectral imagery. Optics Express, 32(20).

[8] Korzeniowska, K., 2012. Modelling of water surface topography on the Digital Elevation Models using LiDAR data. AGILE 2012 International Conference on Geographic Information Science.

[9] Toscano, G.J., U.K. Gopalam, and V. Devarajan, 2014. Auto hydro break line generation using LiDAR elevation and intensity data. ASPRS 2014 Annual Conference.

[10] Worstell, B.B, S.K. Poppenga, G.A. Evans, and S.A. Prince, 2014, Lidar Point Density Analysis— Implications for Identifying Water Bodies. Scientific Investigations Report 2014–5191. U.S Department of the Interior, U.S. Geological Survey.

[11] Deshpande, S.S., and A. Yilmaz, 2017. A semi-automated method to create a lidar-based hydro-flattened DEM. International Journal of Remote Sensing, 38(5), 1365-1387p.

[12] Grau, J., K. Liang, J. Ogilvie, P. Arp, S. Li, B. Robertson, and F-R. Meng, 2021. Using Unmanned Aerial Vehicle and LiDAR-Derived DEMs to Estimate Channels of Small Tributary Streams. Remote Sensing, 13, 3380.

[13] Pauthonnier A., 2024. Le Programme Lidar HD de l'IGN. Forum de la Topographie 2024, Association Francophone de Topographie.

[14] Gaydon C., 2022. Myria3D: Deep Learning for the Semantic Segmentation of Aerial Lidar Point Clouds. IGN (French Mapping Agency).

[15] Darricau, J., 1981. Physique et théorie du radar. Edition Sopide, 2ème édition 1981.

[16] Höfle, B., M. Vetter, N. Pfeifer, G. Mandlburger, and J. Stötter, 2009. Water Surface Mapping From Airborne Laser Scanning Using Signal Intensity and Elevation Data. Earth Surface Processing and Landforms, 34(12), 1635-1649.

[17] Zheng, X., L. Godbout, J. Zheng, C. McCormick, and P. Passalacqua, 2019. An automatic and objective approach to hydro-flatten high resolution topographic data. Environmental Modelling & Software, 116, 72-86p.

[18] Office français de la biodiversité (OFB) et partenaires, programme de Caractérisation hydromorphologique des cours d'eau français [Application CARHYCE, en ligne], https://carhyce.eaufrance.fr/, données en date du 13/11/2023

Spatio-temporal monitoring of bankfull geometry using a semi-automated tool on high-resolution Digital Terrain Models

§ Michele Delchiaro [1], Valeria Ruscitto [1], Davide Torre [1], Wolfgang Schwanghart [2], Daniela Piacentini [1], Francesco Ballio[3], and Francesco Troiani [1]

[1] Department of Earth Sciences, Sapienza Università di Roma, Rome, Italy

[2] Institute of Earth and Environmental Science, Universität Potsdam, Potsdam, Germany

[3] Department of Civil and Environmental Engineering, Politecnico di Milano, Milan, Italy

§ michele.delchiaro@uniroma1.it

Cite as: Delchiaro, M., Ruscitto, V., Torre, D., Schwanghart, W., Piacentini, D., Ballio, F., Troiani, F. (2025). Spatio-temporal monitoring of bankfull geometry using a semi-automated tool on high-resolution Digital Terrain Models. In: Proceedings of Geomorphometry 2025, 9-13 June, Perugia, Italy. M. Alvioli, L. Melelli, I. Marchesini eds. CNR Edizioni, Rome. ISBN 978-88-8080-765-0. DOI: 10.5281/zenodo.15187690

Abstract— **Understanding river channel bankfull geometry is essential for fluvial monitoring and flood forecasting. The bankfull stage represents the point where water begins to spill onto the floodplain, typically recurring every 1–2 years. This stage and its corresponding discharge play a pivotal role in shaping channel morphology, making it critical for river management and hazard assessment. In this study, we test BankfullMapper, a specialized MATLAB tool designed to detect river channel bankfull levels. The method divides the river into evenly spaced sections and extracts bankfull geometry by computing a hydraulic depth function for each section. This function plots elevation above the river thalweg against the area-to-width ratio, identifying points that correspond to the bankfull stage. Key indicators include: (i) the lowest breakpoints from the thalweg or (ii) the most prominent breakpoints. Additionally, Manning's equation is applied to estimate bankfull discharge, enhancing the tool's utility for hydrological analysis. We validate the approach using the Marecchia River as a test site demonstrating its capability to capture spatio-temporal dynamics of bankfull geometry and discharge. The semi-automated detection method delivers reliable, high accuracy (>0.8) results across diverse river types, showing optimal performance when using the lowest breakpoints from the thalweg. By focusing on morphological break identification, our approach provides a detailed and precise representation of bankfull geometry, making it a valuable asset for hydrological studies and river management.**

I. INTRODUCTION

Detection of geomorphic features derived from Digital Terrain Models (DTMs) is critical for understanding the links between geo-hazards and human safety [1]. Improved availability and accuracy of digital topographic data allow detailed analysis of landforms and their connections to natural processes. Growing datasets highlight the need for tools linking geomorphometric measurements to geomorphological insights. These features serve as indicators of climate change impacts, aligning with the IPCC guidelines (2014, 2022) and the UN 2030 Agenda's goal to adapt to climate change. Identifying this link is also a goal within the framework of Italy's National Recovery and Resilience Plan (PNRR), funded by Next Generation EU, extended partnership RETURN (multi-Risk sciEnce for resilienT commUnities undeR a changiNg climate) aimed to strengthen research on environmental, natural, and anthropogenic risks associated with climate change. In this regard, semi-automatic detection methods provide extensive data for large-scale analyses. River channel geometry and its relationship with floodplains offer insights into landscape evolution driven by climate, tectonics, and lithology [2]. In particular, bankfull stage, often linked to incipient flooding, is a key parameter for studying channel formation and flood hazards [3]. Bankfull discharge, with a recurrence interval of ~1.5 years, shapes channel morphology, which is increasingly affected by climate-induced shifts in precipitation patterns. Methods for identifying bankfull geometry include: (i) qualitative field observations (e.g., floodplain breaks, inflection points), (ii) hydrological modeling using LiDAR data and software (HEC-RAS), and (iii) geometric terrain classification based on morphological breaks. Field methods, though accurate, are time-consuming and costly. Modeling requires advanced expertise, while terrain classification can be subjective. To address these

limitations, we test the BankfullMapper tool [4], developed in MATLAB. It uses high-resolution DTMs to identify bankfull geometry and estimate discharge, focusing on semi-confined channels. Tested on the Marecchia River, it analyzes spatio-temporal dynamics of bankfull features, leveraging methodology by [5]. This tool integrates Manning's equation for discharge estimation, offering a valuable resource for monitoring river systems and flood hazards.

II. MARECCHIA RIVER TEST SITE

The Marecchia River, stretching 70 km across northern Italy, drains 940 km² and flows into the Adriatic Sea. The study examines a 20 km segment affected by lithological heterogeneity and relevant anthropogenic modifications, including gravel mining and dam construction. Its humid subtropical climate (Cfa) averages 12.7 °C and 805.1 mm annual precipitation (1993–2022). Historical discharge records highlight several floods exceeding 200 m³/s, impacting sediment dynamics and channel morphology, particularly between 2009–2022.

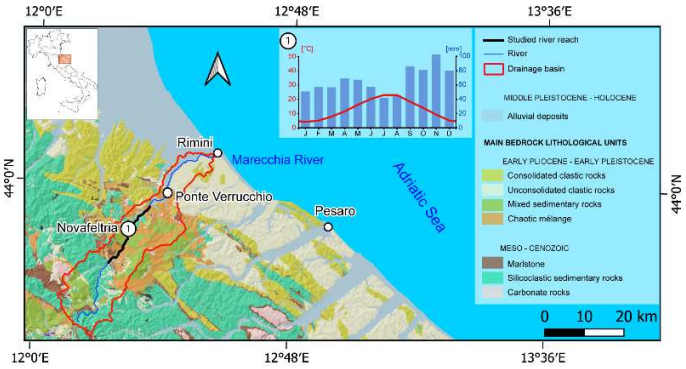

Figure 1. Lithological map of the central Apennines of Italy together with the location of the Marecchia River catchment and the study river reach. The climate chart related to the Novafeltria locality for the period 1993 - 2022 is also reported. Reference system is WGS84.

III. MATERIALS AND METHODS

BankfullMapper [4] is a MATLAB-based tool built on the TopoToolbox v2 package [6], the workflow requires a DTM, an Height Above River (HAR) model, and river course as inputs.

The test analysis performed on the Marecchia river course refers to the period 2008-2022. For 2008, the DTM derived from the LiDAR survey with density of points > 1.5 per m^2 (dataset available at http://www.pcn.minambiente.it/mattm/progetto-piano-straordinario-di-telerilevamento/) was considered. This 2008-DTM has a ground resolution of 1 m and presents an error accuracy lower than ± 15 cm in elevation and ± 30 cm in plane and has been acquired between 2008-2009. For the 2022, the DTM derived from the LiDAR survey with density points > 4 per m^2 (dataset available at https://geoportale.regione.emilia-romagna.it/approfondimenti/prodotti-lidar-e-ortofoto) was considered. This 2022-DTM has a ground resolution of 0.5 m and presents an error accuracy lower than ± 8 cm in elevation and ± 30 cm in plane and has been collected between February and March 2022. For the analysis, the 2022 dataset was resampled to the resolution and extent of the 2008-2009 DTM.

The algorithm workflow is articulated in the following list of functions:

1. Transverse Section Definition (PROF Function): This step defines river cross-sections using the DTM, HAR, and river course data. HAR is derived through a three-step process: sampling river elevations, interpolating values, and detrending the DTM to produce relative elevation data. Optional inputs allow customization of section width, cross-section spacing, and smoothing.
2. Hydraulic Depth Function (BANKFULL Function): Hydraulic depth, defined as the area-to-width ratio, is computed at 10 cm increments from the thalweg to a user-defined elevation (e.g., 6 m). Peaks in the profile indicate potential bankfull stages.
3. Peak Detection (DETECT_PEAK Function): Peaks are extracted to identify breakpoints in channel morphology. Users can select all peaks, the lowest peaks ("lowest" mode), or the most prominent peaks ("max" mode). Kernel density estimates further refine probable values for elevation, area, and perimeter.
4. Discharge Estimation (MANNINGEQ Function): Manning's equation estimates discharge based on hydraulic radius, slope, and roughness coefficients. This function is not currently tested in the present work. Slopes are calculated from section gradients or smoothed using TopoToolbox functions. Discharge values are computed for peak and probable elevations.
5. Mapping and Visualization (VISUAL Function): Bankfull elevation and discharge values are mapped for each section. Residuals between peak and probable values are also computed to highlight variations.

Bankfull extractions were then validated by comparing raster outputs with manually delineated active channel boundaries. Mappings considered low-flow channels, gravel bars, and sparse vegetation areas photointerpreted from orthophotos and prior study [7]. The model's performance was evaluated using the accuracy metric, calculated as the ratio of correctly classified pixels (true positives and true negatives) to the total number of pixels.

IV. RESULTS

The Marecchia River was analyzed for 405 sections in 2009 and 2022, using a 50 m step, 2500 m width, and 500 m planar smoothing (Figures 2 and 3). Results highlight differences in bankfull geometry and discharge over time. The "max" mode records higher elevations, with deviations between sections 255 and 350. The "lowest" mode in 2022 shows upstream elevation retreat, reflecting shifts from braided to wandering patterns.

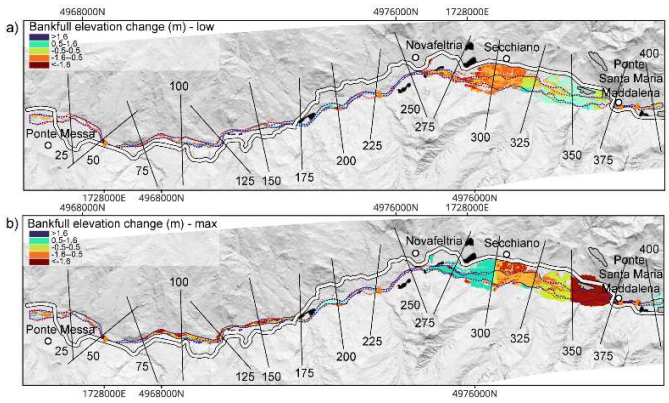

Figure 2. Map view of the bankfull elevation change during the period 2009-2022 in “lowest” (a) and “max” (b) modes. Reference system is WGS84 UTM33N.

Width narrows from 200–800 m to 100–500 m, with flow areas following similar trends. Slope oscillates around 0.01 but exceeds 0.02 near the Ponte Santa Maria Maddalena check dam. Discharge calculations correlate with elevation changes, suggesting aggradation and degradation processes. Changes near Novafeltria and downstream highlight anthropogenic impacts, such as quarries, influencing peak elevation identification.

Temporal comparisons reveal geomorphological changes over 13 years, impacting sediment transport and channel stability.

Finally, model validation results showed that the "lowest" mode achieved an accuracy of 0.81, while the "max" mode performed slightly lower at 0.78. In 2022, the "lowest" mode improved to an accuracy of 0.83, with the "max" mode yielding a comparable value of 0.80.

V. DISCUSSIONS

A. Method Evaluation

The tool works well in semi-confined channels but struggles in V-shaped valleys or terraces with ambiguous breaks. Combining modes offers complementary insights when validated by field data. The performance metrics suggest that the semi-automated detection method is generally effective, though its success varies with the selected mode and river course. Overall, both modes yield reliable results; however, the "lowest" mode consistently demonstrates higher accuracy, making it particularly well-suited for precise delineation of bankfull channels.

B. Interpretation and Limitations

The analysis of the Marecchia River reveals significant spatial and temporal variability driven by sedimentary processes and anthropogenic influences, underscoring the effectiveness of the method for dynamic river monitoring. Overall, bankfull elevation trends reflect a geomorphic transition from braided to single-thread and eventually to wandering reaches. From the river's headwaters to section 110, bankfull elevations range from approximately 1 m in the "lowest" mode to 2 m in the "max" mode. Between sections 110 and 255, the "lowest" mode shows a marked increase, approaching 2 m and aligning more closely with the "max" mode. In contrast, from sections 255 to 350—where the most pronounced temporal changes are observed—bankfull elevations in all modes decline to around 1 m.

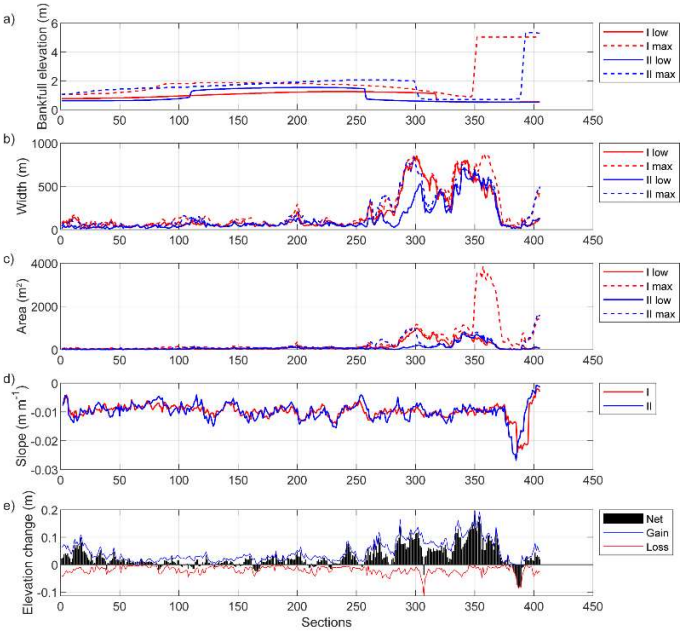

Figure 3. Plots along section number of the bankfull elevation (a), width (b), area (c), and channel slope (d). The average elevation changes for every section are also reported (e) (modified from [5]). “I” and “II” refer to the 2009 and 2022 respectively.

Complementary flow area calculations, which are closely linked to changes in topographic elevation, reveal that sections 255 to 365 experienced notable elevation gains. This increase corresponds with a reduction in flow area over time, suggesting a proportional decrease in discharge. These patterns reflect both aggradation and degradation processes, as variations in bankfull elevation and discharge align with topographic shifts caused by sediment deposition.

The spatial and temporal heterogeneity of these changes highlights the complexity of the river system. Particularly notable shifts in bankfull elevation and discharge occur between Novafeltria and the Ponte Santa Maria Maddalena check dam. In this stretch, the "lowest" mode indicates a sharp decline in bankfull elevation between sections 255 and 320. Meanwhile, the "max" mode initially shows a slight increase near Novafeltria before following a similar downward trend. The pronounced drop in elevation near the check dam is likely influenced by anthropogenic structures, which may interfere with accurate detection of peak elevations in the "max" mode.

Despite its strengths in scalability and resolution, the method has limitations—particularly in areas modified by human activity, where misclassifications can occur. Additionally, its reliance on assumptions inherent in Manning's equation introduces uncertainty. As such, field validation remains essential to refine and support interpretations drawn from the analysis.

VI. CONCLUSIONS

This study demonstrates the effectiveness of a semi-automated approach for extracting riverbank geometry, offering accurate, scalable, and adaptable insights into river morphology. The method's use of morphological break identification enables a detailed and precise representation of bankfull geometry, as supported by performance metrics when compared to traditional mapping techniques. However, caution is warranted in areas with anthropogenic alterations or complex topography, where accuracy may be reduced. Future improvements—such as enhanced field validation and parameter optimization—hold promise for further increasing the method's precision and broadening its applicability.

REFERENCES

[1] Tarolli, P., Sofia, G., & Dalla Fontana, G., 2012. "Geomorphic features extraction from high-resolution topography: landslide crowns and bank erosion". Natural Hazards, 61, 65-83. https://doi.org/10.1007/s11069-010-9695-2

[2] Lin, P., Pan, M., Allen, G. H., de Frasson, R. P., Zeng, Z., Yamazaki, D., & Wood, E. F., 2020. "Global estimates of reach‐level bankfull river width leveraging big data geospatial analysis". Geophysical Research Letters, 47(7), e2019GL086405. https://doi.org/10.1029/2019GL086405

[3] Phillips, C. B., Masteller, C. C., Slater, L. J., Dunne, K. B., Francalanci, S., Lanzoni, S., Merrits, D. J., Lajeuness, E., & Jerolmack, D. J., 2022. "Threshold constraints on the size, shape and stability of alluvial rivers". Nature Reviews Earth & Environment, 3(6), 406-419. https://doi.org/10.1038/s43017-022-00282-z

[4] Delchiaro, M., Ruscitto, V., Schwanghart, W., Brignone, E., Piacentini, D., and Troiani, F.. "BankfullMapper: a semi-automated MATLAB tool on high-resolution Digital Terrain Models for spatio-temporal monitoring of bankfull geometry and discharge". Computers and Geosciences (under review).

[5] Williams, G. P., 1978. "Bank‐full discharge of rivers". Water resources research, 14(6), 1141-1154. https://doi.org/10.1029/WR014i006p01141

[6] Schwanghart, W., & Scherler, D., 2014. "TopoToolbox 2–MATLAB-based software for topographic analysis and modeling in Earth surface sciences". Earth Surface Dynamics, 2(1), 1-7. https://doi.org/10.5194/esurf-2-1-2014

[7] Llena, M., Simonelli, T., & Brardinoni, F., 2024. "Inherited anthropogenic disturbance and decadal sediment dynamics in a mountain fluvial system: the case of the Marecchia River canyon, Northern Apennines". GSA Bulletin, 136(1-2), 741-764. https://doi.org/10.1130/B36720.1

2 - Landforms and Processes

2.1 - Landslides
2.2 - Fluvial processes
2.3 - Glacial processes
2.4 - Tectonic processes
2.5 - Landform classification
2.6 - Physical and other surface processes

2.1 - Landslides

Global Landslide Susceptibility Mapping Using Multi-Model Machine Learning Approaches on Geospatial Satellite Data

Saverio Mancino [1], Domenico Capolongo
Department of Earth and Geoenviromental Sciences,
University of Bari Aldo Moro,
Bari, Italy

Lovergine Francesco Paolo,
Institute for Electromagnetic Sensing of the Environment,
National Research Council of Italy,
Bari, Italy

Amatulli Giuseppe,
School of the Environment,
Yale University,
New Haven, CT, USA

[1] saverio.mancino@uniba.it

Cite as: Mancino, S., Lovergine, F. P. Capolongo, D., Amatulli, G. (2025). Global Landslide Susceptibility Mapping Using Multi-Model Machine Learning Approaches on Geospatial Satellite Data. In: Proceedings of Geomorphometry 2025, 9-13 June, Perugia, Italy. M. Alvioli, L. Melelli, I. Marchesini eds. CNR Edizioni, Rome. ISBN 978-88-8080-765-0. DOI: 10.5281/zenodo.15263708

Abstract—**Landslides globally represent a big threat to society and people, making accurate susceptibility models increasingly necessary in risk mitigation. We present a high-resolution, global-scale landslide susceptibility model that integrates several machine learning (ML) methodologies into a multi-model framework. Our approach aims to improve on the one used by NASA in 2016, to create a more reliable model through the use of a new rich global landslide catalog for training (UGLC), more accurate through the use of a global DEM at 90m (MERIT DEM) along with over 100 global predictive variables tracing the topographic, geological and environmental asset. Model development is done on high performance computing (HPC) for the required operational performance and to ensure model scalability with the injection of new data. In order to create a reliable and interpretable model that can support future dynamic early warning systems, linking baseline susceptibility mapping with phenomenon monitoring, enabling real-time disaster response, marking a milestone in global landslide risk assessment.**

I. Introduction

Landslides represent a significant natural hazard with global implications, impacting human settlements and infrastructure. Traditional landslide susceptibility mapping (LSM) efforts have been constrained by data integration challenges and computational limitations [15]. Understanding landslide susceptibility is critical for effective hazard mitigation and risk assessment, especially in densely populated areas [8]. Recent advancements in HPC and the availability of global data enable the development of large-scale models that improve predictive capabilities and generalizability [17]. This study introduces a global scale 90m resolution landslide susceptibility model leveraging a multi-model approach, incorporating machine learning (ML) techniques to enhance landslide susceptibility predictions by using high-resolution satellite data and robust computational methods [3, 8]. Traditionally, LSMs have been constrained to highly detailed sub-continental scale models due to the computational demands and complexities associated with large-scale data integration and model generalization [9, 15]. However, advances in high-performance computing (HPC) and the expanded availability of global satellite data now enable the development of LSM at a global level [17]. By leveraging HPC, we address the diverse global complexities of landslides, including variability in topography, geology, climate, and triggering mechanisms [16, 17]. The model harmonizes datasets across multiple spatial resolutions, ensuring a scalable, interpretable, and flexible solution for worldwide landslide monitoring [14, 21].

II. Method

The project builds upon NASA's 2016 landslide susceptibility model [17], incorporating substantial enhancements. Notable model advancements include a richer training dataset based on the Unified Global Landslide Catalog (UGLC). UGLC is a new global landslide catalogue created in the framework of this project, which combines 27 global datasets standardized at various scales, contributing over one million points and polygons (fig. 1) [10, 11].

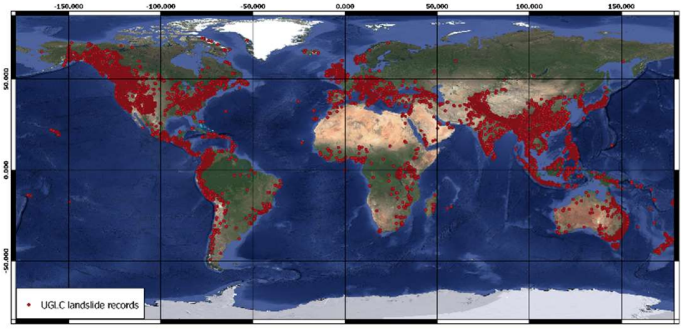

Figure 1. Unified Global Landslide Catalog (UGLC) point data distribution across the globe.

This catalogue provides more carefully categorized landslide records along with non-landslide data derived from a pixel-wise thresholding combined with dynamic buffers to minimize spatial autocorrelation and reduce overfitting risks [15, 21]. This is complemented by the MERIT DEM, a 90-meter resolution elevation [20] model that replaces NASA's 1 km SRTM DEM, enhancing spatial accuracy [17]. Additionally, the predictor features have been expanded from 4 to over 100, spanning terrain morphology, hydrology, soil characteristics, seismic activity, and geological indicators [1, 2, 5, 6, 7, 13, 19, 20]. This approach provides a more robust framework for susceptibility mapping and supports the integration of real-time trigger data [8, 14, 16]. Methodologically, this project employs a multi-model strategy that combines ensemble-based ML techniques (Random Forest) [4, 9, 18] and Multi-Layer Perceptron (MLP) for spatial pattern recognition [3,21]. Ensemble learning methods capitalize on the strengths of each individual model to ensure model interpretability and transferability across regions, allowing a dynamic adjustment to region-specific conditions, especially improving generalization in regions with limited landslide data [21]. To validate the robustness of the model across diverse geographical settings, k-fold and block cross-validation is employed. This validation considers subsets of training points grouped by trigger type, landslide type, and date range, ensuring relevance across temporal and spatial domains [15]. Due to the computational demands of the massive processing of satellite datasets and executing ML algorithms, the use of HPC resources is necessitated [16]. Our framework utilizes parallel processing across HPC nodes and distributed learning on GPU clusters, enabling efficient handling of high-dimensional data and accelerating model training [8]. This setup facilitates spatially detailed analysis and shortens computational time, making it feasible to deploy a large-scale global LSM model [17].

III. Preliminary Results

In this preliminary testing phase, we evaluated the main 49 out of over 100 proposed predictors, focusing on highly informative global raster from sources like MERIT DEM90m [19], SOILGRIDv1. [7], Geomorpho90m [2] and Hydrography90m (1) using a subsample of 50K train/test points (25K presence randomly picked from the UGLC, and 25K absence randomly picked using a morpho-topographic thresholding retaining only locations with a minimum slope of 5°). Although this approach will be refined in our final model, it has been shown in the literature [12] to be both straightforward and highly effective at identifying non-landslide areas.

A. MLP test on a 50K subsampled Dataset

A limited preliminary test was carried out on a simple 2 hidden layer MLP architecture using a subsample of only 25000 presence and 25000 absence points (Tab.1).

TABLE I. Multi-Layer Perceptron Test

Setting					
Hidden Layers/Nodes	Epochs	Learning Rate	Optimizer	Criterion	Test size
1°/16 (ReLU) 2°/32 (ReLU)	100	0.01	ADAM	Cross Entropy Loss	0.2

The model achieved a rapid convergence (fig.2) and high performances but highlighting some overfitting issues (Tab.2).

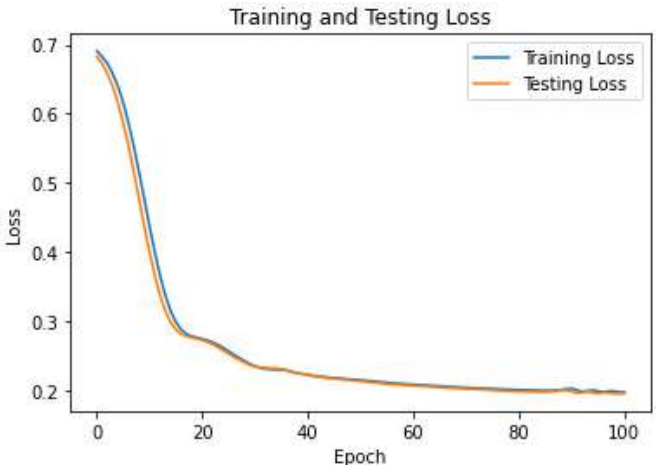

Figure 2. Performance diagram of MLP test on 25k UGLC landslide points.

TABLE II. Multi-Layer Perceptron Performances

Evaluation index	***Value***
Precision	93.16
Recall	94.57
F1 score	93.86
Confusion Matrix	

Evaluation index			*Value*
True Label	0	10899	915
	1	716	12470
		0	1
		Predicted Label	

B. RF test on a 50K subsampled Dataset

Subsequent model tests were carried out on HPC with the same subsample of 25000 presence and 25000 absence points on a Random Forest (RF) architecture (Tab.3).

TABLE III. RANDOM FOREST TEST

Setting		
Number of estimators	Observation samples	Test size
300	5	0.2

This model showed a high performance, with even greater accuracy scores (Tab.4). Also in this test, as with the MLP, high levels of performance seem coupled with high misclassification rates, highlighting some shared issues likely related to the training sample (Tab.4).

TABLE IV. RANDOM FOREST PERFORMANCES

Evaluation index			*Value*
Precision			0.9565
Recall			0.9670
F1 score			0.9628
Confusion Matrix			
True Label	0	23900	1100
	1	825	24175
		0	1
		Predicted Label	

C. Joint Model Features Analysis

A more in-depth comparative analysis of the two tested models was carried out by employing a SHAP analysis on the MLP to capture local and directional effects in a non-linear model (Fig.3) and a Permutation Feature Importance Analysis (PFIA) on the RF model (Fig.4). Both MLP-SHAP and RF-PFIA consistently rank topographic and soil predictors (e.g. rough-magnitude_90M, ELEV, CLYPPT) as most influential, reflecting robust underlying patterns. RF-PFIA concentrates on terrain-derived metrics used in high-level splits, whereas SHAP yields a more diffuse attribution profile that captures non-linear interactions. SHAP uniquely provides directional impact and per-observation variability of feature effects. Thus, MLP-SHAP and RF-PFIA are coherent in ranking but quantitatively slightly diverge due to model architecture and ranking methodology.

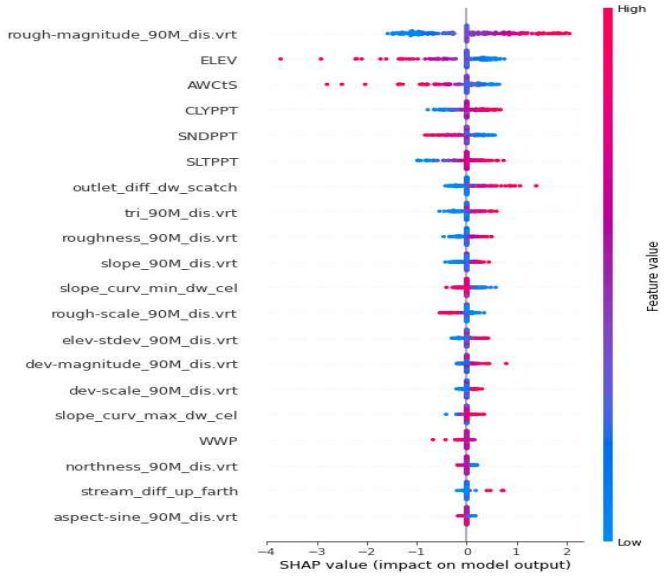

Figure 3. SHAP Analysis on MLP test with 25K presence and 25K absence points.

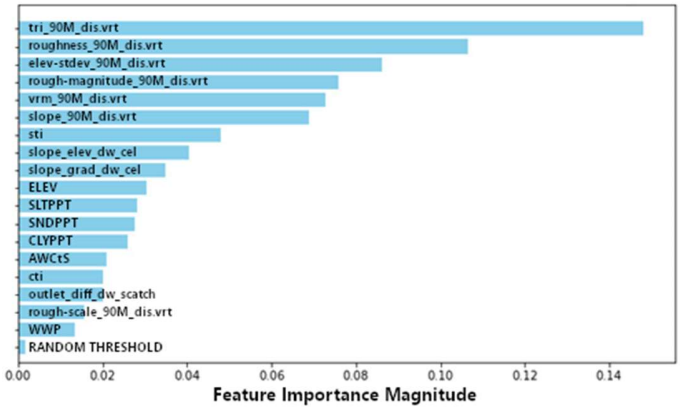

Figure 4. Feature Importance Analysis on RF test with all 1M presence and 1M absence points.

IV. FUTURE IMPROVEMENTS

Preliminary tests revealed consequences related to spatial and temporal inhomogeneity in the distribution of points in the dataset, thus leading to the need to develop a data balancing system. This system to be introduced in the forthcoming tests will be based on

point density and thematic subdivision of the tests by climate, event date and landslide type (thanks to the standardized information available in UGLC records), in order to improve model generalizability and error mapping. Moreover, different methods of morpho-topographic thresholding or buffering for a more precise sampling of non-landslide points [12] will also be tested, in order to pick non-landslide points as reliable as those present in the UGLC. Finally, in addition to the already planned validation with the polygons of the UGLC, we want to introduce a spatial-temporal cross-validation methodologies for thematic blocks (geographic, time, typology and climatic areas), and a final comparison phase with traditional detailed landslide susceptibility maps, obtained at a smaller scale. All this is highly necessary in order to model such a complex phenomenon, with heterogeneous and not always complete data, on a global scale [9].

V. Conclusion

In conclusion, this scalable global landslide susceptibility model, exploiting ML with a multi-model approach due to computation on HPC, opens new horizons on global-scale modeling of landslide susceptibility; highlighting how multi-model methods not only improve prediction accuracy, but also offer enhanced interpretability, which is essential for informed decision making. Thus, providing a concrete basis for future global early warning systems through dynamic integration of up-to-date or real-time data, moving from susceptibility mapping to an operational early warning tool that aids global disaster preparedness and response.

References

[1] Amatulli, G., Domisch, S., Tuanmu, M. N., Parmentier, B., Ranipeta, A., Malczyk, J., & Jetz, W. (2022). Hydrography90m: A new high-resolution global hydrographic dataset. Earth System Science Data Discussions, 1-29. https://doi.org/10.5194/essd-2022-9.

[2] Amatulli, G., McInerney, D., Sethi, T., Strobl, P., & Domisch, S. (2020). Geomorpho90m - Global High-Resolution Geomorphometry Layers. Distributed by OpenTopography. https://doi.org/10.5069/G91R6NPX.

[3] Azarafza, M., Azarafza, M., Akgün, H., et al. (2021). Deep learning-based landslide susceptibility mapping. Scientific Reports, 11, 24112. https://doi.org/10.1038/s41598-021-03585-1.

[4] Breiman, L. (2001). Random Forests. Machine Learning, 45, 5-32.

[5] Global Volcanism Program, Smithsonian Institution. (2013). Volcanoes of the World, v. 4.10.0. https://doi.org/10.5479/si.GVP.VOTW4-2013.

[6] Hasterok, D., Gard, M., & Webb, J. (2022). New maps of global geological provinces and tectonic plates. Earth-Science Reviews, 237, 104194. https://doi.org/10.1016/j.earscirev.2022.104194.

[7] Hengl, T., de Jesus, J. M., Heuvelink, G. B. M., Ruiperez Gonzalez, M., Kilibarda, M., Blagotić, A., ... & Kempen, B. (2017). SoilGrids250m: Global gridded soil information based on machine learning. PLoS One, 12(2), e0169748. https://doi.org/10.1371/journal.pone.0169748.

[8] Hussain, M. A., Chen, Z., Zheng, Y., Zhou, Y., & Daud, H. (2023). Deep Learning and Machine Learning Models for Landslide Susceptibility Mapping with Remote Sensing Data. Remote Sensing, 15(4703). https://doi.org/10.3390/rs15194703.

[9] Kirschbaum, D., Stanley, T., & Zhou, Y. (2015). Spatial and temporal analysis of a global landslide catalog. Geomorphology, 249. https://doi.org/10.1016/j.geomorph.2015.03.016.

[10] Mancino. S, Sblano A., Lovergine F.P., Sethi T., Capolongo D., Amatulli G. (2024), UGLC_point, v1, GitHub. https://github.com/UnibaGEO/UGLC_point,

[11] Mancino. S, Sblano A., Lovergine F.P., Sethi T., Capolongo D., Amatulli G. (2024), UGLC_polygonal, v1, GitHub. https://github.com/UnibaGEO/UGLC_polygonal,

[12] Marchesini, I., Ardizzone, F., Alvioli, M., Rossi, M., & Guzzetti, F. (2014). Non-susceptible landslide areas in Italy and in the Mediterranean region. Natural Hazards and Earth System Sciences, 14, 2215-2231. https://doi.org/10.5194/nhess-14-2215-2014.

[13] Pagani, M., Garcia-Pelaez, J., Gee, R., Johnson, K., Poggi, V., Styron, R., ... & Danciu, L. (2020). Global Earthquake Model (GEM) Seismic Hazard Map (version 2019.1). Geophysical Journal International, 222(3), 1734-1745. https://doi.org/10.1093/gji/ggaa287.

[14] Qiu, H., Xu, Y., Tang, B., et al. (2024). Interpretable Landslide Susceptibility Evaluation Based on Model Optimization. Land, 13(639). https://doi.org/10.3390/land13050639.

[15] Reichenbach, P., Rossi, M., Malamud, B. D., Mihir, M., & Guzzetti, F. (2018). A review of statistically-based landslide susceptibility models. Earth-Science Reviews, 180, 60-91. https://doi.org/10.1016/j.earscirev.2018.03.001.

[16] Rosi, A., Frodella, W., Nocentini, N., et al. (2023). Comprehensive landslide susceptibility map of Central Asia. Natural Hazards and Earth System Sciences, 23, 2229-2250. https://doi.org/10.5194/nhess-23-2229-2023.

[17] Stanley, T., & Kirschbaum, D. B. (2017). A heuristic approach to global landslide susceptibility mapping. Natural Hazards, 87(1), 145-164. https://doi.org/10.1007/s11069-017-2757-y.

[18] Xing, Y., Yue, J., Guo, Z., Chen, Y., Hu, J., & Travé, A. (2021). Large-Scale Landslide Susceptibility Mapping Using an Integrated Machine Learning Model: A Case Study in the Lvliang Mountains of China. Frontiers in Earth Science, 9. https://doi.org/10.3389/feart.2021.722491.

[19] Yamazaki, D., et al. (2017). MERIT DEM: A new high-accuracy global digital elevation model. AGU Fall Meeting Abstracts, 2017, H12C-04.

[20] Yamazaki, D., Ikeshima, D., Sosa, J., Bates, P. D., Allen, G. H., & Pavelsky, T. M. (2019). MERIT Hydro: A high-resolution global hydrography map based on latest topography dataset. Water Resources Research, 55(6), 5053-5073. https://doi.org/10.1029/2019WR024873.

[21] Youssef, K., Shao, K., Moon, S., et al. (2023). Landslide susceptibility modeling by interpretable neural network. Communications Earth & Environment, 4(162). https://doi.org/10.1038/s43247-023-00806-5.

Influence of Data Resolution on Logistic Regression Models for Landslide Susceptibility in Tropical Environments

Rebeca Durço Coelho
Institute of Geosciences,
Universidade de São Paulo,
São Paulo, Brazil
rebeca.coelho@alumni.usp.br

Camila Duelis Viana
Institute of Geosciences,
Universidade de São Paulo,
São Paulo, Brazil
camila.viana@usp.br

John B. Lindsay
Department of Geography,
Environment & Geomatics
The University of Guelph,
Guelph, Canada
jlindsay@uoguelph.ca

Carlos H. Grohmann
Institute of Astronomy,
Geophysics and Atmospheric
Sciences, Universidade de São
Paulo, São Paulo, Brazil
guano@usp.br

Cite as: Coelho, R. D., Viana, C. D., Lindsay, J. B., Grohmann, C. H. (2025). Influence of Data Resolution on Logistic Regression Models for Landslide Susceptibility in Tropical Environments. In: Proceedings of Geomorphometry 2025, 9-13 June, Perugia, Italy. M. Alvioli, L. Melelli, I. Marchesini eds. CNR Edizioni, Rome. ISBN 978-88-8080-765-0. DOI: 10.5281/zenodo.15078571

Abstract - **In February 2023, an extreme rainfall event on the northern coast of São Sebastião, southeastern Brazil, delivered over 450 mm of rainfall within 24 hours, triggering widespread landslides with severe social and environmental impacts. This study evaluates landslide susceptibility using Logistic Regression (LR) across three model configurations: M1 (trained and tested on 5 m data from a high-resolution Digital Surface Model), M2 (trained and tested on 30 m Copernicus DEM data), and M3 (trained on 5 m data and tested on 30 m data). Morphometric parameters (slope, aspect, curvatures, and Topographic Position Index) were derived using WhiteboxTools. M2 demonstrated superior performance, achieving the highest ROC AUC (78.40%) and accuracy (70.67%), underscoring its suitability for regional-scale analyses. In contrast, M1 captured finer spatial details but showed lower AUC (71.01%) and accuracy (66.30%), reflecting challenges in balancing resolution and generalization. M3 exhibited a notable trade-off: high sensitivity (recall = 80.34%) for landslide detection but reduced precision (67.19%), emphasizing the complexities of applying high-resolution models to coarser data. These results highlight the critical role of data resolution in landslide susceptibility modeling. While high-resolution data (M1) excels in local-scale precision, lower-resolution data (M2) offers robust regional insights. M3 bridges these scales but reveals inherent limitations, such as increased false positives. The generated maps provide actionable tools for disaster risk mitigation, particularly in data-scarce regions. This work underscores the need to align model resolution with application goals, balancing detail and generalizability for effective landslide risk management.**

I. INTRODUCTION

Landslides are among the most destructive natural hazards, causing significant social, economic, and environmental impacts worldwide. These events are often triggered by a combination of factors, such as intense rainfall, steep terrain, and geological and soil characteristics, frequently exacerbated by human activities. In this context, landslide susceptibility mapping plays a critical role in disaster risk reduction, providing essential support for land-use planning and the development of early warning systems.

In recent years, machine learning (ML) and classical statistical methods have become indispensable for landslide susceptibility modeling. Logistic Regression (LR), a statistical approach widely integrated into ML workflows, has proven particularly valuable due to its computational efficiency, interpretability, and capacity to handle diverse spatial datasets. While complex ML models (e.g., neural networks, decision trees) may excel in capturing non-linear relationships, recent research highlights that simpler, interpretable methods like LR remain competitive in geospatial applications [1], especially when balancing predictive performance with operational practicality. This versatility positions LR as a pragmatic choice for multi-scale landslide risk assessments, where transparency and adaptability to varying data resolutions are critical.

The Serra do Mar mountain range, located along the southeastern coast of Brazil, is characterized by steep slopes,

dense vegetation, and frequent landslides. These natural processes are intensified by the region's geomorphological conditions and high rainfall levels, which have historically contributed to catastrophic events resulting in significant social and economic losses [2][3]. Despite this history, the development of accurate susceptibility models in the region faces challenges related to the limited availability of high-resolution data, the absence of comprehensive landslide inventories, and the scarcity of detailed historical records.

Although machine learning techniques have proven effective in other regions, their application to the Serra do Mar remains largely unexplored. Addressing these gaps is essential for improving susceptibility models and strengthening risk mitigation strategies in the region. In this context, this study conducts a comparative analysis of two digital elevation models: a high-resolution 5 m Digital Surface Model (DSM) and a global 30 m Digital Elevation Model (DEM). The main objective is to evaluate the performance of models trained with high-resolution data when applied to lower-resolution datasets. The analysis focuses on the São Sebastião region, aiming to assess the scalability of the models and identify the limitations and potential benefits associated with using data at different spatial resolutions.

II. STUDY AREA

In February 2023, São Sebastião, located on the northern coast of the Serra do Mar, experienced an extreme rainfall event with over 450 mm of precipitation recorded within a 24-hour period. This unprecedented event triggered widespread shallow landslides (Fig. 1), resulting in severe social, economic, and environmental consequences. Most of the landslides were concentrated along the steep escarpments, where natural vulnerability is heightened by the region's geomorphological characteristics and shallow soil profiles.

III. METHODS

For the comparison between different models, two DSMs with distinct spatial resolutions were used: a 5 m DSM provided by the São Paulo State Government (IDE-DSM) [4] and Copernicus DEM (Cop-DEM) with a spatial resolution of 30 meters [5].

The landslide inventory consists of 1,068 records representing documented locations of landslide events within the study area [6]. To develop the susceptibility models, an equivalent set of absence points (1,068) was generated through

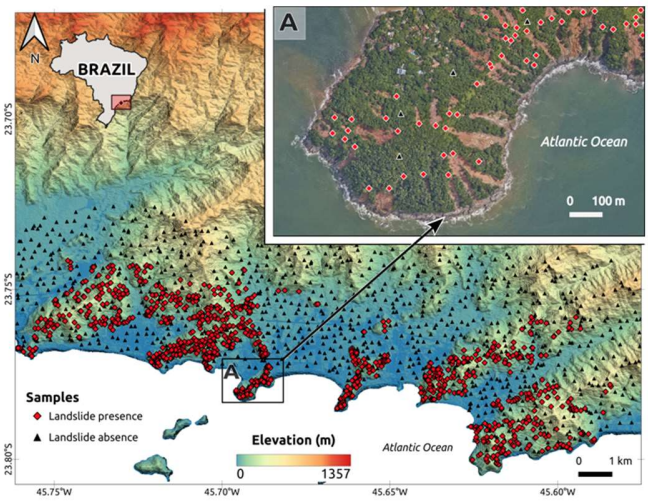

Figure 1. Location of the Study Area and Samples Distribution. A) Detailed view of landslide points within the study area, overlaid on a high-resolution background image

random sampling using QGIS software, representing areas without documented landslides. These absence points were integrated into the landslide inventory, resulting in a balanced dataset for model training and evaluation (Fig. 1).

The morphometric parameters used in this study - slope, aspect, curvatures, and Topographic Position Index (TPI) - were extracted from the rasters using WhiteboxTools [7]. Based on these data, three model configurations were developed using LR: (M1) Model trained and tested on 5 m data (IDE-DSM), (M2) Model trained and tested on 30 m data (Cop-DEM), (M3) Model trained on 5 m data and tested on 30 m data (IDE-DSM to Cop-DEM).

LR establishes a relationship between a dependent variable and multiple predictor variables (independent variables), allowing the inclusion of continuous, discrete, or mixed data types without requiring normal distribution. Recognized as a widely accepted statistical approach, LR has been extensively applied in landslide susceptibility modeling, demonstrating its effectiveness across various geographic and environmental contexts [8][9].

The landslide susceptibility maps generated from the three models were evaluated using statistical metrics calculated by the Python programming language. This process involved a suite of Python libraries: Rasterio for raster data processing, NumPy for numerical and matrix operations, Pandas for data management

and analysis, Scikit-learn for implementing Logistic Regression, and Matplotlib for data visualization.

IV. RESULTS AND DISCUSSIONS

The results revealed significant differences in performance across the models. M2 achieved the highest accuracy (0.7067) and ROC AUC (0.7840), demonstrating robustness for regional-scale analyses (Table I). In contrast, M1 captured finer spatial patterns (Fig. 2A) but underperformed in accuracy (0.6630) and ROC AUC (0.7101), reflecting challenges in balancing high-resolution detail with generalization. Despite this, M1 exhibited moderate capability in detecting localized instability (recall = 0.6442; F1-score = 0.6604). Notably, M3 demonstrated the highest sensitivity (recall = 0.8034), suggesting strong utility for landslide detection, albeit with reduced precision (0.6719) compared to M2 (Table I).

TABLE 1. PERFORMANCE COMPARISON OF LOGISTIC REGRESSION MODELS ACROSS TRAINING AND PREDICTION SPATIAL RESOLUTIONS

Model	*Train Data*	*Pred Data*	*Accuracy*	*Precision*	*Recall*	*F1-Score*	*ROC AUC*
M1	5 m	5 m	0.6630	0.6774	0.6442	0.6604	0.7101
M2	30 m	30 m	0.7067	0.7054	0.7270	0.7160	0.7840
M3	5 m	30 m	0.7055	0.6719	0.8034	0.7318	0.7565

In contrast, M3 demonstrated the highest sensitivity (recall = 0.8034), suggesting its efficacy in detecting landslide-susceptible areas. However, this model exhibited a modest decline in overall performance (AUC = 0.7565), reflecting the capacity of high-resolution-trained models to retain predictive capability when applied to lower-resolution data. The reduction in precision (0.6719) indicates a greater tendency for false positives, a critical limitation for practical applications. These findings align with studies highlighting challenges in cross-resolution model transfer, particularly increased false positives and reduced precision when applying high-resolution-trained models to coarser datasets [10].

A visual analysis of the susceptibility maps revealed notable spatial distinctions (Fig. 2). M1 (Fig. 2A) demonstrated superior capability in identifying critical zones, with fragmented high-susceptibility areas and well-defined boundaries. However, reliance on a DSM introduced noise from anthropogenic features (e.g., roads, rooftops). In contrast, M2 (Fig. 2B) exhibited broader generalization, with continuous high-susceptibility regions that may oversimplify localized geomorphic characteristics.

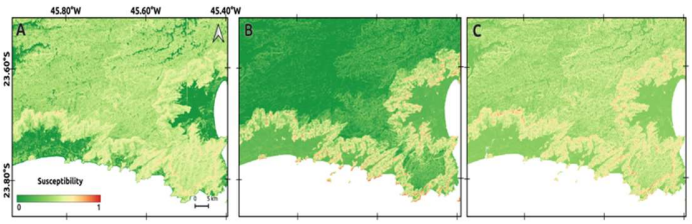

Figure. 2. Landslide susceptibility maps: (A) M1 (trained and tested on 5 m data, IDE-DSM), (B) M2 (trained and tested on 30 m data, Copernicus DEM), (C) M3 (trained on 5 m data and tested on 30 m data, IDE-DSM to Cop-DEM)

Conversely, M3 (Fig. 2C) exhibited an intermediate pattern, retaining some detail from M1 while demonstrating smoothing effects due to the lower resolution of the applied raster. This analysis underscores the importance of aligning data resolution with study objectives, as emphasized by recent studies on spatial resolution in landslide susceptibility mapping [11].

The results highlight the relevance of high-resolution data for local-scale analyses and detailed mapping, essential for urban planning and risk mitigation. M1 demonstrated stronger performance in metrics such as F1-score (0.6604) and AUC (0.7101), reflecting its ability to capture localized susceptibility patterns in areas with pronounced topographic variation. In contrast, M2 proved more suitable for regional applications, where spatial generalization enhances robustness. However, M3 demonstrated potential for cross-resolution applications, albeit with trade-offs such as increased false positives (precision = 0.6719).

V. CONCLUSIONS

This study underscores the critical influence of data resolution on landslide susceptibility modeling, revealing distinct trade-offs between spatial detail and generalizability. M2 emerged as the optimal choice for regional-scale applications, where robustness and noise reduction (e.g., roads, buildings) are prioritized. In contrast, M1 demonstrated strengths in capturing fine-scale topographic patterns, albeit with limitations in broader generalization. M3 bridged these scales, highlighting the potential and challenges of transferring high-resolution models to coarser data, as evidenced by its high sensitivity but elevated false positives.

These findings advocate for context-driven resolution selection: high-resolution data for localized precision, lower resolution for regional insights, and hybrid approaches to harmonize these strengths. Future work should focus on optimizing cross-resolution compatibility to enhance model adaptability in data-scarce environments.

VI. ACKNOWLEDGMENTS

The authors acknowledge the financial support provided by CAPES (Finance code 001) and FAPESP (#2023/11197-1).

REFERENCES

[1] Goetz, J. N., A. Brenning, H. Petschko, and P. Leopold. 2015. "Evaluating Machine Learning and Statistical Prediction Techniques for Landslide Susceptibility Modeling." *Computers & Geosciences* 81: 1–11. https://doi.org/10.1016/j.cageo.2015.04.007

[2] Wolle, C. M., and W. C. Hachich. 1989. "Rain-Induced Landslides in Southeastern Brazil." In *Proceedings of the International Conference on Soil Mechanics and Foundation Engineering*. Balkema. Available at https://www.issmge.org/uploads/publications/1/33/1989_03_0041.pdf

[3] De Ploey, J., and O. Cruz. 1979. "Landslides in the Serra do Mar, Brazil." *Catena* 6 (2): 111–122. https://doi.org/10.1016/0341-8162(79)90001-8

[4] Spatial Data Infrastructure of the State of São Paulo (IDE-SP). 2010–2011. *Digital Surface Model (DSM) – 5-Meter Spatial Resolution – Raster Format – Coverage: State of São Paulo*. Government of the State of São Paulo. Retrieved in November 2024, from http://www.metadados.idesp.sp.gov.br/catalogo/srv/por/catalog.search#/metadata/a3f7abc5-d134-43e9-a71f-3e21128d873b

[5] European Space Agency (ESA). 2021. Copernicus DEM GLO-30 – Copernicus Digital Elevation Model [Data set]. European Space Agency. https://doi.org/10.5270/ESA-c5d3d65

[6] Coelho, R. D., C. D. Viana, V. C. Dias, and C. H. Grohmann. 2024. "Landslides of the 2023 Summer Event of São Sebastião, Southeastern Brazil: Spatial Dataset." *Brazilian Journal of Geology* 54 (2): e20240006. https://doi.org/10.1590/2317-4889202420240006

[7] Lindsay, J. 2016. "Whitebox GAT: A Case Study in Geomorphometric Analysis." *Computers & Geosciences* 95: 75–84. https://doi.org/10.1016/j.cageo.2016.07.003

[8] Lee, S., and B. Pradhan. 2007. "Landslide Hazard Mapping at Selangor, Malaysia, Using Frequency Ratio and Logistic Regression Models." *Landslides* 4 (1): 33–41. https://doi.org/10.1007/s10346-006-0047-y

[9] Akinci, H., and M. Zeybek. 2021. "Comparing Classical Statistic and Machine Learning Models in Landslide Susceptibility Mapping in Ardanuc (Artvin), Turkey." *Natural Hazards* 108 (2): 1515–1543. https://doi.org/10.1007/s11069-021-04743-4

[10] Yu, X., and H. Chen. 2024. "Research on the Influence of Different Sampling Resolution and Spatial Resolution in Sampling Strategy on Landslide Susceptibility Mapping Results." *Scientific Reports* 14: Article 1549. https://doi.org/10.1038/s41598-024-52145-w

[11] Meena, S. R., and T. Gudiyangada Nachappa. 2019. "Impact of Spatial Resolution of Digital Elevation Model on Landslide Susceptibility Mapping: A Case Study in Kullu Valley, Himalayas." *Geosciences* 9 (8): 360. https://doi.org/10.3390/geosciences9080360.

Rockfall susceptibility along communication routes and in urban areas in Italy based on physical and statistical models

Nabanita Sarkar [1], Massimiliano Alvioli [2]
Istituto di Ricerca per la Protezione Idrogeologica, Consiglio Nazionale delle Ricerche, CNR IRPI, Perugia, Italy
[1] nabanitasarkar@cnr.it, [2] massimiliano.alvioli@irpi.cnr.it

Cite as: Sarkar, N., Alvioli, M. (2025). Rockfall susceptibility along communication routes and in urban areas in Italy based on physical and statistical models. In: Proceedings of Geomorphometry 2025, 9-13 June, Perugia, Italy. M. Alvioli, L. Melelli, I. Marchesini eds. CNR Edizioni, Rome. ISBN 978-88-8080-765-0. DOI: 10.5281/zenodo.15274240

***Abstract*— Landslide susceptibility, the likelihood of landslide occurrence in different locations of a specific area, can be obtained with many different methods. Here, we aim at comparing two state-of-the art susceptibility zonations obtained within two such methods, and their predictions at the location of different infrastructure in the whole of Italy. The study considers rockfall landslide type, and susceptibility zonations obtained by a grid-based three-dimensional physically based models and one slope-unit based statistically based model. We first compare the two susceptibility zonations on the whole of Italy, reducing model dependencies by aggregating results of the physical model on the same slope unit zonation as the statistical method. Next, we consider the predictions of both maps restricted to urban areas, railways, and road network. The study shows that the predictions of the two maps are drastically different. We discuss the reasons for such differences, and interpretation of the two versions of rockfalls susceptibility map.**

I. INTRODUCTION

Landslides constitute a significant geo hazard inducing financial losses, injuries and fatalities. Significant research attempts appeared over the past twenty years, on predicting the triggering mechanisms for landslides, as well as their spatial and temporal distributions and related consequences. Consequently, several methods for mapping landslide risk, hazard [6-8], and susceptibility have been developed and put into effect in various geographical regions. Assessments of landslide susceptibility take into account the likelihood for a particular location to experience a landslide, based on terrain attributes and past landslide occurrence and it represents the first stage of landslide hazard and risk assessment process.

The recent literature exhibits different approaches for the spatial zonation of landslide susceptibility. At the opposite sides of the spectrum of possible approaches lie physically based and statistically based methods, which are fundamentally different. Physically based approaches calculate slope stability using well-defined equations, specific of the peculiar landslide type. Statistically based approaches, often mixed with machine learning techniques, establish correlations between several topographic and environmental data and landslide presence. The statistical models usually address a classification problem: given a set of spatial variables and how they are combined to determine whether landslides occur or not, a model should be trained, tested to replicate the desired result, and then applied to data that has not yet been seen.

Past landslide information is useful for both methods, to calibrate model parameters and assess model performance. Other than that, input data may be drastically different. Within the class of statistical and/or machine learning models, many examples exist in the literature; Ref. [9] is a recent critical review on the subject. Examples of physically based methods to obtain landslide susceptibility, applied on large areas as in this work, are probably less abundant in the literature [10, 11].

In particular, rockfalls are one hazardous type of landslide, for their rapidity and destructive potential. They affect infrastructure and transport routes, constituted both by roads [1-3] and railways [4, 5]. This study compares two rockfall susceptibility assessments on the whole of Italy. The first model considered here is an existing statistical zonation [12], calculated across Italy with a slope unit- based spatial granularity [13, 14]. The second is the 3D model STONE, which calculates rockfall trajectories [15-18], which is an inherently grid-based model. In the latter case, we consider here a susceptibility map calculated as an extension to

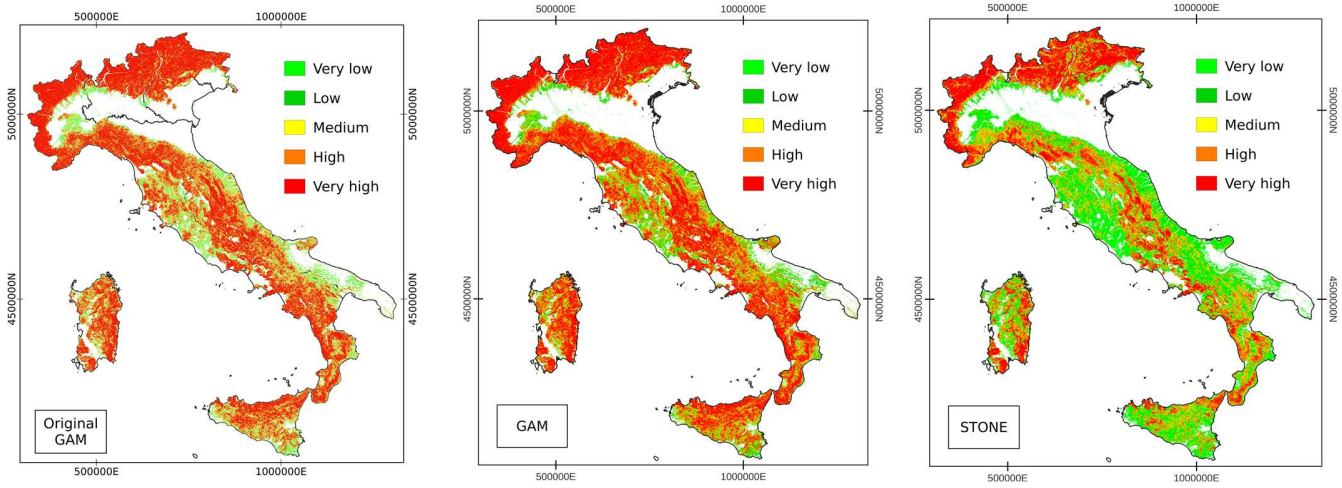

Figure 1. National scale results for the statistical (GAM) and physical (STONE) maps. Physical model results are averaged in each SU. Both maps depict output transformed by ECDF & classified in equal interval.

the whole of Italy of the rockfall susceptibility obtained in Ref. [4] for the only railway network in Italy. We first compared the two maps on a national scale, and next we compared predictions of both methods restricted to urban areas [18], railways, and road network.

II. Materials and Methods

In this study, we compare two state-of-the art susceptibility zonations, and their predictions at the location of different infrastructure in the whole of Italy, obtained by a physically based method [4] and with a slope unit-based statistical method [10].

The physical model STONE requires a digital elevation model (DEM) of the area, predetermined source locations, and numerical parameters controlling the energy restitution at the location of impacts of boulders with the topography. The model performs full three-dimensional simulations of rockfall trajectories, in the approximation of point-like rock blocks. Maps of friction and energy restitution coefficients can be obtained by re-coding lithological or land-use maps based on data obtained from the literature [1,4]. We used the output, a trajectory count per grid cell produced by the model, to calculate rockfall susceptibility. The most relevant input of the model is a map describing the locations of source cells. Here we used the approach of Ref. [4], in which a simple quantile mode was trained in a relatively small (a few hundreds) number of mapped sources, to provide the probability P(S) of a grid cell with slope angle S to represent a rockfall sources.

The statistical model consists of a Bayesian version of a Generalized Additive Model (GAM) with a multiple intercept for each of the 20 Italian region. This allowed selecting the regions with a poor inventory and discard them in training the GAM, and apply the model to the whole of Italy for eight different landslide types. Here, we selected the rockfall susceptibility map. The whole procedure was implemented in R–INLA as described in detail in Ref. [10], including fixed (linear) and random (nonlinear) effects from an interpretative standpoint and produced a full prediction equipped with an estimated uncertainty. The statistical assessment considered several predictors, including morphometric parameters: slope, aspect, curvatures, relative slope position and topographic wetness index.

We compared the two results beyond classification performance. In fact, not only are the models very different in implementation and purpose; they also have been trained against disproportionately different landslide data, which makes comparison of performance very difficult, and probably meaningless. For this reason, we first looked at the predictions of the two models at national scale, with slope unit-aggregation level. Next, we consider urban areas, roads, and railways; in each case, we aggregate the two predictions in a different way (road/railway segments and urban areas polygons), in the attempt of reducing as much as possible model dependencies and make results comparable.

At national level, in the statistical model case, spatial aggregation occurred before running the model through predictors aggregated at slope unit level. To run the physical model, instead, the grid input was mandatory, and aggregation was only possible on the result grids. We opted for an average of the trajectory count grids; other aggregation functions are a valid choice. Next, we calculate empirical cumulative density functions (ECDFs) on both models' result, ending up with values ranging from 0 to 1 in both cases. We classify the two maps with equal intervals in ECDFs, corresponding to classes with equal number of slope units. Results

of this procedure are in Fig. 1 including results of original GAM.

Table I. Predictions of the two models after aggregation on slope units, at national scale. The values show the total surface area in each susceptibility class, obtained as described in Section II. In the GAM case, each non-null class contains 65,104 slope units, and 44,163 in the STONE case. The null class in the case of STONE model encompasses the following number of slope units in different GAM classes: 55,385 (class 1), 32,522 (2), 11,536 (3), 2,949 (4), 372 (5).

Class	Surface area (STONE) [km²]	%	Surface area (Original GAM)	%	Surface area (GAM) [km²]	%
Null	40,889	18.2	-	0	-	0
1	32,045	14.3	18,566	8.3	18,538	8.3
2	32,933	14.7	26,153	11.6	26,15	11.6
3	34,897	15.5	32,989	14.7	32,994	14.7
4	37,543	16.7	47,887	21.3	47,892	21.3
5	46,226	20.6	98,934	44.0	98,907	44.0

We developed another procedure to compare the predictions of the two results restricted to urban areas, railways, and road network. We faced a similar problem as in the comparison at the national scale, except that in this case a mismatch exist with the format of both model results and the target infrastructure. To cope with this issue, we considered the target linear features (roads, railways) as individual segments. We used road and railway data from OpenStreetMap. We calculated ECDFs of the cell-by-cell values of the two model outputs along the segments, assigning to each segment a value between 0 and 1, suitable for classification. Figure 2 shows the classified results.

III. Results

The results portray comparisons of the physical and statistical models at i) national scale, Fig. 1 and Table I, ii) along roads and railway lines and Fig. 2 and Table II.

Table I refers to the national scale comparison. Table I lists the total surface area under each class predicted by the two methods, within the classification scheme described in Section II. Transforming both results by ECDFs, each class in the final classification contains the same number of slope units - 65,104 and 44,163 in the GAM and STONE cases, respectively. One striking difference is that the STONE model predicts a null value about 1/3 of the slope units. This stems from the location of rockfall sources, which are absent in several slope units: consequently, there are no trajectories modeled in the output, in these SUs. The GAM, on the other hand, assigns a result to each SU. We checked that most of the SUs in which STONE predicts a null value are in the "very low" susceptibility class from GAM (55,385 out of 102,764 SUs), and the number of SUs in the other classes decreases as the class increase.

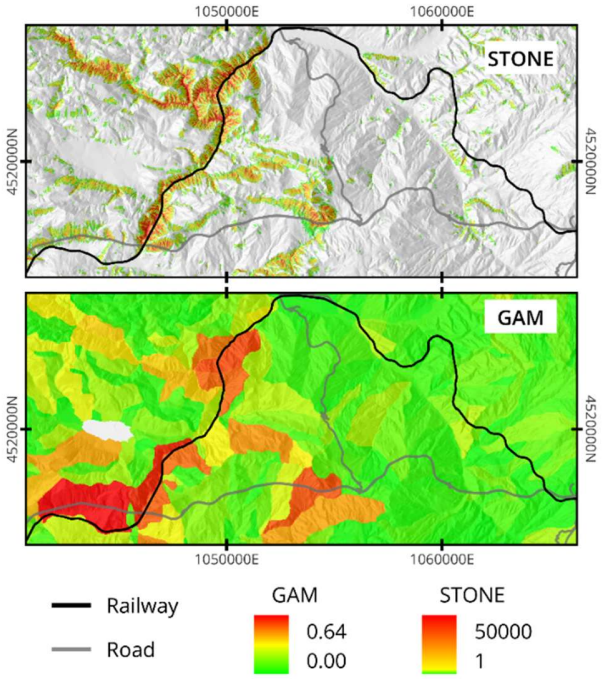

Figure 2. Map showing comparison of roads and railways based on the two methods considered here. Maps obtained aggregating the values of models results along each linear segment (road or railway). The resulting maps were prepared after classification of the calculated ECDF values based on equal interval method

Figure 2 shows two sample locations where both a road and a railway segment is present, overlapped with result from the GAM and STONE models. The figure does not show the classified results, but the original model output values, to illustrate the aggregation procedure of these values along the linear features. Table II refers to the comparison of model predictions along the road network, about 21,000 km in the OpenStreetMap layer. In this case, we can spot a pattern, as in both models the highest class contains the largest percentage of road segments. As in the national scale comparison, the striking difference is the number of road segments which are assigned a null value by the model STONE, for the same reasons as in the previous case.

IV. Discussion and Conclusions

The results of the comparison between GAM and STONE results indicate that the maps based on the considered models are drastically different. The observed disparities stem from the

Table II. Susceptibility classes on road network, aggregated on individual road segments using ECDFs, and classified with equal intervals.

Class	Original (GAM)		Statistical (GAM)		Physical (STONE)	
	Total length [km]	%	Total length [km]	%	Total length [km]	%
Null	31,909	59.9	11,119	34.2	23,802	73.4
1	2,184	4.1	2,186	6.7	939	2.8
2	2,882	5.4	2,885	8.8	1,592	4.9
3	3,650	6.9	3,651	11.2	1,658	5.1
4	5,171	9.7	5,172	15.9	1,982	6.1
5	7,408	13.9	7,409	22.8	2,447	7.5

distinct conceptual frameworks and data dependencies of the two methods. We should stress that the comparison strategy adopted here makes use of ECDFs to transform the two model results into comparable ranges. This surely affects the outcome of the comparison, and investigation of additional strategies is in order.

Reconciling the two maps still looks challenging, and these preliminary results suggest complementary use of both methods. The physically based method can easily capture the details of rockfall propagation, strongly dependent of the knowledge of source locations. Even if we applied the model consistently at national scale, increasing its predictive power requires input potentially limiting its use to data-rich locations. In contrast, the statistically based method is more flexible, and suitable for regional-scale mapping. The findings from these comparative analyses offer valuable insights into the strengths and limitations of physically based and statistically based landslide susceptibility models, aiding in the development of improved methodologies for future large-scale hazard assessments.

V. Acknowledgments

Research supported by the MUR PRIN Project 'URGERE: URban Geodiversity for a Resilient Environment' (2022M7EP3M_PE10_PRIN2022 - PNRR M4.C2.1.1), funded by the European Union – Next Generation EU (CUP: B53D23007260006).

References

[1] Guzzetti, F., Reichenbach, P., Ghigi, S. (2004). Rockfall Hazard and Risk Assessment Along a Transportation Corridor in the Nera Valley, Central Italy. Environmental Management 34, 191–208. https://doi.org/10.1007/s00267-003-0021-6

[2] Pokharel, B., Lim, S., Bhattarai, T.N. *et al.* (2023). Rockfall susceptibility along Pasang Lhamu and Galchhi-Rasuwagadhi highways, Rasuwa, Central Nepal. Bulletin of Engineering Geology and the Environment 82, 183. https://doi.org/10.1007/s10064-023-03174-8

[3] Agliardi, F., Frattini, P., Stock, G.M. et al. (2024). Probabilistic rockfall hazard and risk analysis along the El Portal Road in Yosemite National Park (California, USA). EGU General Assembly 2024, Vienna, Austria, 14–19 Apr 2024, EGU24-9085, https://doi.org/10.5194/egusphere-egu24-9085

[4] Alvioli, M., Santangelo, M., Fiorucci, F., *et al.* (2021). Rockfall susceptibility and network-ranked susceptibility along the Italian railway. Engineering Geology 293, 106301. https://doi.org/10.1016/j.enggeo.2021.106301

[5] Marchesini, I., Althuwaynee, O., Santangelo, M., *et al.* (2024). National-scale assessment of railways exposure to rapid flow-like landslides. Engineering Geology 332, 107474. https://doi.org/10.1016/j.enggeo.2024.107474

[6] P. Jaiswal, C.J. van Westen, V. Jetten Quantitative assessment of direct and indirect landslide risk along transportation lines in southern India (2010). Nat. Hazards Earth Syst. Sci. 10, 1253-1267, https://doi.org/10.5194/nhess-10-1253-2010

[7] Alvioli, M., Poggi, V., Peresan, A. *et al.* (2024b). A scenario-based approach for immediate post-earthquake rockfall impact assessment. Landslides 21, 1–16. https://doi.org/10.1007/s10346-023-02127-2

[8] Sarkar, N., Devoto, S., Vandelli, V. *et al.* (2024). Rock-fall runout simulation using a QGIS plugin along north–west coast of Malta (Mediterranean Sea). *Natural Hazards*. https://doi.org/10.1007/s11069-024-06821-9

[9] Frattini, P., Crosta, G., Carrara, A. *et al.* (2008). Assessment of rockfall susceptibility by integrating statistical and physically-based approaches. Geomorphology 94(3-4), Pages 419-437. https://doi.org/10.1016/j.geomorph.2006.10.037

[10] Alvioli, M., Loche, M., Jacobs, L., *et al.* (2024a). A benchmark dataset and workflow for landslide susceptibility zonation. Earth-Science Reviews 258, 104927. https://doi.org/10.1016/j.earscirev.2024.104927

[11] Alvioli, M., Falcone, G., Mendicelli, A., *et al.* (2023). Seismically induced rockfall hazard from a physically based model and ground motion scenarios in Italy. Geomorphology 429, 108652. https://doi.org/10.1016/j.geomorph.2023.108652

[12] Alvioli, M., Marchesini, I., Reichenbach, P. (2016). Automatic delineation of geomorphological slope units with r.slopeunits v1.0 and their optimization for landslide susceptibility modeling. Scientific Model Development 9(11), 3975–3991. https://doi.org/10.5194/gmd-9-3975-2016

[13] Alvioli, M., Guzzetti, F., Marchesini, I. (2020b). Parameter-free delineation of slope units and terrain subdivision of Italy. Geomorphology 358, 107124. https://doi.org/10.1016/j.geomorph.2020.107124

[14] Loche, M., Alvioli, M., Marchesini, I., *et al.* (2022). Landslide susceptibility maps of Italy: Lesson learnt from dealing with multiple landslide types and the uneven spatial distribution of the national inventory. Earth-Science Reviews 232, 104125. https://doi.org/10.1016/j.earscirev.2022.104125

[15] Guzzetti, F., Crosta, G., Detti, R., et al. (2002). STONE: a computer program for the three-dimensional simulation of rock-falls, Computers & Geosciences, 28(9), Pages 1079-1093. https://doi.org/10.1016/S0098-3004(02)00025-0

[16] Alvioli, M., De Matteo, A., Castaldo, R., *et al.* (2022). Three-dimensional simulations of rockfalls in Ischia, Southern Italy, and preliminary susceptibility zonation. Geomatics, Natural Hazards and Risk 13(1), 2712–2736. https://doi.org/10.1080/19475705.2022.2131472

[17] Santangelo, M., Alvioli, M., Baldo, M. et al. (2019). Brief communication: Remotely piloted aircraft systems for rapid emergency response: road exposure to rockfall in Villanova di Accumoli (central Italy). Natural Hazards and Earth system Sciences 19(2) 325-335. https://doi.org/10.5194/nhess-19-325-2019

[18] Alvioli, M. (2020a). Administrative boundaries and urban areas in Italy: A perspective from scaling laws. Landscape and Urban Planning, 204, 103906. https://doi.org/10.1016/j.landurbplan.2020.103906

On two implicit issues in prediction modeling of landslide susceptibility

Andrea G. Fabbri

Universitá di Milano-Bicocca, Dipartimento di Scienze dell'Ambiente e della Terra, DISAT, Milan, Italy

andrea.fabbri@unimib.it

Cite as: Fabbri, A.G. (2025). On two implicit issues in prediction modeling of landslide susceptibility. In: Proceedings of Geomorphometry 2025, 9-13 June, Perugia, Italy. M. Alvioli, L. Melelli, I. Marchesini eds. CNR Edizioni, Rome. ISBN 978-88-8080-765-0. DOI: 10.5281/zenodo.15026425

Abstract—**this contribution argues the interpretation of prediction-rate curves of landslide susceptibility and the corresponding prediction-pattern uncertainties. The focus is on two main issues in any kind of spatial prediction modeling: (1) isolating the meaningful parts of prediction-rate curves from a cost-benefit point of view and (2) comparing the qualities of prediction patterns obtained by different mathematical models and/or dissimilar spatial evidences. Mathematical models, methods, and databases generated prediction maps (we prefer the term prediction patterns) hard to evaluate due to inevitable relativity of measures, representations and confidence. This is a major problem, with modelling assumptions and justifications mostly ignored or poorly discussed. We consider prediction-rate curves, obtained by cross-validation, as standardized procedure. The curves are the result of cross-validating prediction patterns with the distribution of occurrences more recent than the ones used to generate the patterns. The two issues concern all types of modeling independently of algorithmic complexity or database formats. We examine an application example and its analytical strategy to point at resolving problems of pattern evaluation, comparison and uncertainty measure. The need becomes evident of collaborative efforts towards solutions analyzing a common multi-format database.**

Keywords— **prediction-rate curves, prediction pattern, landslide susceptibility, cross validation, uncertainty**

I. INTRODUCTION

This contribution argues the interpretation of prediction-rate curves and the corresponding prediction-pattern uncertainties.

During the past four decades, with the increasing availability of spatially distributed data, an army of numerical applications attempted predicting the likely locations of future landslide occurrences. Researches in selected study areas captured past evidential settings at the location of known occurrences to recognize the distribution of future ones. Mathematical models, methods, and databases generated prediction maps that were hard to evaluate and compare due to the inevitable relativity of measures, representations and confidence [1]. This is a major problem, with modelling assumptions and justifications mostly ignored or poorly discussed.

Wide use has been made of the Receiving Operator Characteristic curve, ROC, to assess and compare the validity of binary classifiers and their discrimination thresholds. An example is the identification of the proportion of occurrences captured by cumulative proportions of the study area by using a point of significant inflection where the slope of the curve changes from steep to gentle [2]. However, it is debatable whether it is a reliable tool for comparisons. Instances of ROC curves generated by different mathematical models could have equal area under the curve, AUC, but different curve shapes with corresponding dissimilar prediction patterns of landslide susceptibility. Such curves appear unable to compare the patterns satisfactorily and to reveal their uncertainty. In particular, the AUC value of the ROC curve itself represents just an indicator of general reliability [3].

McClish [4] considers interpretation and comparison of the ROC curves when interests do not lie in the entire range of rates and suggests evaluating the area under a portion of the curve or under a specific point of the curve. Furthermore, Dodd and Pepe [5] propose an estimator to interpret a partial area under the ROC curve. They point at costs and benefits associated with the curve rates and corresponding choices. Chung and Fabbri [6] recommend the ratio-of-effectiveness for rate intervals that satisfy monotonically decreasing tangents (slopes) of the curve. That is to contrast them from the slope of random distribution and isolate the corresponding parts of the prediction pattern.

The focus here is on two main issues: (1) isolating the meaningful parts of prediction-rate curves from a cost/benefit point of view and (2) comparing the qualities of prediction patterns obtained by different mathematical models and/or dissimilar

spatial evidences. These are very general critical requirements in spatial prediction modeling. The next section defines the concepts related with the issues and is followed by a section on application examples. The last section provides some suggestive solutions and complex questions related to the two issues in spatial prediction modeling.

II. Prediction Patterns, Prediction-Rate Curves, and Cross-Validation

The term "prediction pattern" indicates the spatial configuration of the prediction rates when converted into equal-area ranks. This is why we do not use the term prediction map. Mathematical models integrate spatial relationships into "likelihood" of landslide occurrence, the prediction rates [6]. A prediction-rate curve is a graphical representation of ordered equal-area ranks of prediction rates.

We propose an interpretation of prediction-rate curves, obtained by cross-validation, as a convenient standardized procedure for any modeling. The curve is the result of cross-validation of a prediction pattern with the distribution of occurrences more recent than the ones used to generate the pattern [7]. The very process leads to estimating pattern uncertainty [8]. The following section provides examples of patterns, curves and comparisons.

III. Examples of Applications

The examples used here of prediction-rate curves, from prediction patterns of landslide susceptibility, derive from the works on Lake Albano, a volcanic crater 20 Km south of the metropolitan city of Rome, in Italy [9].

Mass movements of various dynamic types affect the inner slopes of the crater. They are either sub-aerial or sub-aqueous. Seismicity, uplifting and gas exhalations of H_2S and CO_2 make the lake a multi-hazard site. The gases might have contributed to the flood in 398 BC. Fig. 1 shows the distribution of 120 subaerial linear (blue) and 29 polygonal (red) landslide forms. No information is available on the temporal sequence of the mass movements. We grouped dynamic types of landslides due to the closeness of their settings. We used a 5m-resolution raster database, of 1002x1202 pixels, constructed for susceptibility studies, which implied a variety of assumptions [9]. The study area excluding the lake itself covers 975,093 pixels of which 9,379 indicate the location of the subaerial landslides. We assumed that the remainder of the study area indicates the locations without known landslides. The database contained eight raster images of the settings as follows: land use, **u**, lithology, **l**, categorical, and six continuous fields extracted from high-resolution digital elevation points, aspect, **a**, digital terrain model, **d**, slope, **s**, curvature, **c**, planform, **f** and profile, **p**.

We converted the images into spatial evidence of landslide presence or absence in support of modeling susceptibility as likelihood ratios then integrated into prediction patterns by mathematical models. For all the patterns, we grouped the sorted ratios from 200 equal area ranks into 14 classes as shown in the legend: narrower classes for higher ranks. Each rank has approximately 4875 pixels (i.e. 0.5% of study area).

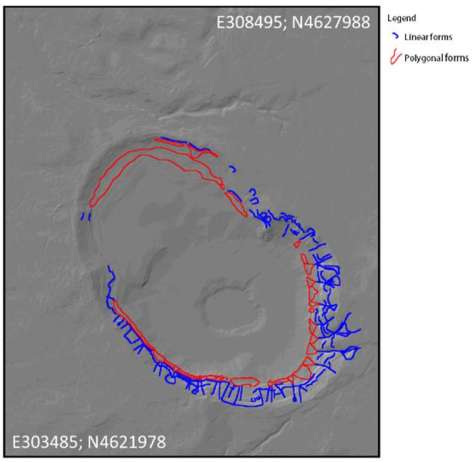

Figure 1. Over the hill-shaded relief are the 120 linear and 29 polygonal subaerial forms in the Lake Albano study area.

Fig. 2 shows the prediction pattern obtained using the 120 subaerial linear forms, the eight images of the settings and the Empirical Likelihood Ratio function, ELR. Fig. 3 shows the prediction pattern using the higher 15% of 29 subaerial polygonal forms and a Logistic Discriminant Function, LOG. Ranks with different models and forms are thus comparable.

The diagram in Fig. 4 compares the prediction-rate curves for both the subaerial forms using the two modelling functions. Sequential exclusion of four occurrences for the 120 and of one for the 29 forms generated iterative cross-validations. The curves captured the prediction rates at the locations of the excluded occurrences in each partial prediction pattern obtained using the remaining occurrences. The ELR and LOG curves in Fig. 4 for the linear forms are very steep and almost coinciding. An inflexion point occurs at the top 4.2% ranks of study area corresponding to the 60% of the 120 occurrences. A sharper inflexion point for the polygonal form curves occurs at the top 8.5% rank of the study area with the 58% of the 29 occurrences.

Using the ratio of effectiveness [6] in Fig 4, the top 12% classes of the red curve for the 120 linear and the top 8% classes of the broken blue curve for the 29 polygonal forms are acceptable from a cost/benefit point of view. The remainder of the curves show no benefit. We could use all the techniques cited in the introduction to threshold critical ranges of ranks or proportions.

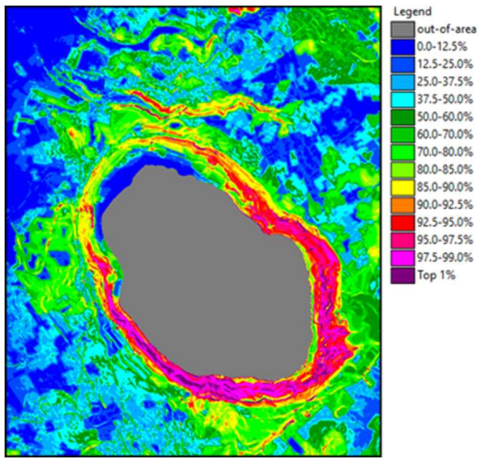

Figure 2. ELR prediction pattern of the 120 linear forms (6440 pixels).

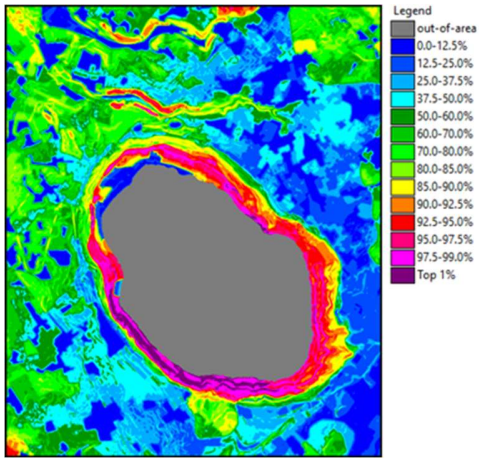

Figure 3. LOG prediction pattern of the 29 polygonal forms (2939 pixels).

The curves compare the predictive quality of different models and different forms in terms of "likelihood" of the next four linear or next polygonal occurrences, respectively. Each model uses a particular type of normalization and combination rules for integrating the spatial evidence. We can interpret the original incommensurable prediction rates only as equal-area ranks.

Furthermore, we can take the set of partial prediction patterns from the iterative process of sequential exclusion and compute some revealing statistic on them. Out of the 29 iterations for the polygonal form LOG curve, shown as blue broken line in Fig. 4, we have computed a "Target pattern" with the median rank of the 29 for each pixel and then an "Uncertainty pattern" ranking the ranges around the median. Fig. 5 shows the LOG Uncertainty pattern for the 29 polygonal forms.

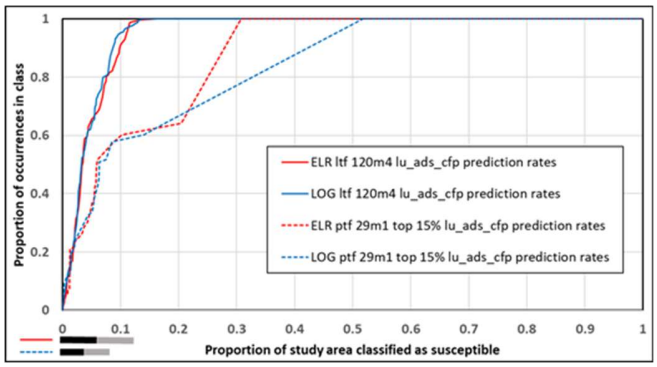

Figure 4. ELR and LOG prediction-rate curves for linear and polygonal terrestrial (subaerial) forms. The top 8 to 12% ranks are of concern as indicated by the bars on the lower left; lower ranks show relatively higher uncertainty.

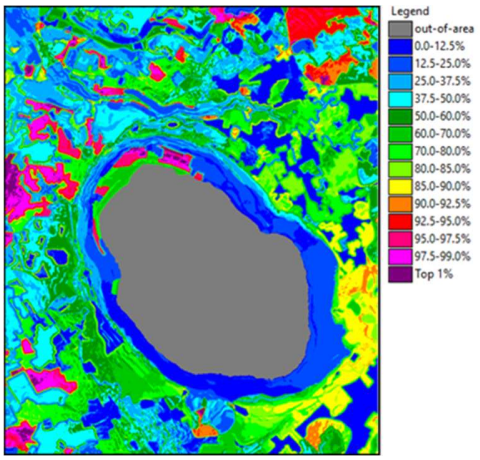

Figure 5. LOG Uncertainty pattern of the 29 polygonal forms.

Here low values are more important than high values. The Target pattern, not shown here, appears indistinguishable from the prediction pattern in Fig. 3. However, it allows us to measure the associated relative uncertainty. Clearly, we have a relationship between the prediction-rate curve and the Uncertainty pattern. Comparing the pattern in Figure 3 with the one in Fig. 5, we can see that higher prediction ranks (colors from red to purple) correspond to lower uncertainty ranks (light blue to dark blue colors). Intermediate and low prediction ranks show relatively higher uncertainties. Other studies using a variety of prediction models confirm the presence of higher uncertainties for intermediate ranks with respect to the two extremes of highest and lowest ranks [8].

IV. Resolving the Issues

We have described a basic modelling strategy that implies a baseline stepwise approach of a very general nature. **Firstly**, we capture spatial relationships between landslide occurrences and

their spatial context in the study area: for instance using an empirical likelihood ratio, ELR, to measure the contrast between settings of presence of occurrences and settings of presumed absence. **Secondly**, we integrate the likelihood ratios of all the pieces of spatial evidence using an ELR function (or an LOG function or some other function) with its combination rules. **Thirdly**, we group the occurrences into older and presumed younger ones and use the older ones to generate a prediction pattern for the younger ones: cross-validation captures the prediction rate for each occurrence to construct the prediction-rate curve for interpretation in addition to providing a set of partial prediction patterns. **Fourthly**, we compute Target and Uncertainty patterns by rank-based statistics (for instance computing median and range or some other statistics): we can threshold the Uncertainty pattern at tentatively lower levels to show only the corresponding ranks of the initial prediction pattern (or of the Target pattern) for geomorphologic interpretation.

The two issues concern all types of modeling independently of the algorithmic complexity or database format. Two examples are raster-based and vector-based modeling, with either pixels or slope units as indicators of landslide occurrences and of their physical context as spatial evidence. This also applies to other tabular database formats.

Besides answering the obvious questions, "Where is the square kilometer with the highest susceptibility and is at least 10 m from the known occurrences?" or "Can we do any better with our database and study area?" We can consider now a multitude of complex questions with many answers like the following ones.

- Are slope-unit based prediction patterns preferable to the raster-based ones?
- For modeling, should we select the remainder of the study area as non-occurrence locations or chose randomly as many locations as those of the occurrences?
- What part of the prediction pattern is of relevance for generating susceptibility classes of practical utility?
- How should we compute and threshold the Uncertainty patterns? Which Statistics?
- If we know or suspect spatial evidence being conditionally dependent, how severely would it disturb the prediction pattern?
- Would sophisticated modeling functions, such as Random Forest or Artificial Neural Networks, generate preferable results to justify their use? Would a simpler modeled prediction pattern be as good or help in their interpretation?

The application examples with their analytical strategies and corresponding assumptions point at unresolved problems and at some solutions out of many. The key point for comparison of prediction patterns is to keep all selections fixed, whatever they are: equal-area ranks, etc. Given the implicit complexity of the two issues, the need becomes evident of collaborative efforts ideally analyzing a common raster-and-polygon database: as recommended in [7], further motivated in [8] or attempted in [10] with a slope-unit based benchmark dataset.

V. Acknowledgment

Dr. Antonio Patera, Istituto Nazionale di Geofisica e Vulcanologia, in Rome (Italy) has constructed and provided the Lake Albano database.

References

[1] Reichenbach P., Rossi M., Malamud B.D., Mihir M. and Guzzetti F., 2018, A review of statistically based landslide susceptibility models. Earth-Science Reviews, 180, 60-91. https://doi.org/10.1016/j.earscirev.2018.03.001

[2] Baddeley A., Brown W., Milne R.K., Nair G., Rakshit S., Lawrence T., Phatak A. and Ching Fu S., 2020, Optimal thresholding of prediction in mineral prospectivity analysis. Natural Resources Research, 30, 923-969. https://doi.org/10.1007/s11053-020-09769-2

[3] Vakhshoori V. and Zare M., 2018, Is the ROC curve a reliable tool to compare the validity of landslide susceptibility Maps? Geomatics, Natural Hazards and Risk, 9:1, 249-266. https://doi.org/10.1080/19475705.2018.1424043

[4] McClish, D.K., 1989, Analyzing a portion of the ROC curve. Medical Decision Making. 9 (3): 190-195. https://doi.org/10.1177%2F0272989X8900900307.

[5] Dodd L.E., Pepe M.S., 2003, Partial AUC Estimation and Regression. Biometrics, 59 (3): 614-723. https://doi.org/10.1111/1541-0420.00071

[6] Chung C.J., Fabbri A.G., 2003, Validation of spatial prediction models for landslide hazard mapping. Natural Hazards, 30: 451–472. https://doi.org/10.1023/B:NHAZ.0000007172.62651.2b

[7] Fabbri A.G. and Chung C-J., 2008, On blind tests and spatial prediction models. Natural Resources Research, v. 17, n. 2, p. 107-118. https://doi.org/10.1007/s11053-008-9072-y

[8] Fabbri A.G., Patera A., 2021, Spatial Uncertainty of Target Patterns Generated by Different Prediction Models of Landslide Susceptibility. Applied Sciences, 11, 3341. https://doi.org/10.3390/app11083341

[9] Patera A, Fabbri AG (2022) Can we assess landslide hazards in the volcanic crater of Lake Albano? WIT Transactions on THE BUILT Environment, WIT Press. In, Hernández S., Garzia F., Lombardi M., Fabbri A. (Eds.), Risk Analysis, Hazard Mitigation and Safety and Security Engineering XIII, 214:3-25. https://doi.org/10.2495/SSR220011

[10] Alvioli M., Loche M., Jacobs L., Carlos H. Grohmann C.H., L.C., , Abraham M.T., Gupta K., Satyam N., Scaringi G., Bornaetxea T., Mauro Rossi M., Marchesini I., Lombardo L., Moreno M., Steger S., Camera C., Bajni G., Samodra G., Wahyudi E.E., Susyanto N., , Marko Sinčic M., Gazibara S.B., Sirbu F., Torizin J., Schüßler N., Benjamin Mirus B., Woodard J., Aguilera H. and Rivera–Rivera J.S., 2024, A benchmark dataset and workflow for landslide susceptibility zonation. Earth-Science Reviews, 258, Article 104927. https://doi.org/10.1016/j.earscirev.2024.104927.

Forest cover controls on debris flow sediment connectivity in the Stolla Basin, Italy

Jason Goetz [1], Stefan Steger [2,3], Vittoria Scorpio [4]

[1] Department of Geography and Environmental Studies, Wilfrid Laurier University, Waterloo, Canada (jgoetz@wlu.ca)

2 Geosphere Austria, Vienna, Austria (stefan.steger@geosphere.at)

3 Eurac Research, Centre for Climate Change and Transformation, Bolzano, Italy

4 Department of Chemical and Geological Sciences, University of Modena and Reggio Emilia, Modena, Italy (vittoria.scorpio@unimore.it)

Cite as: Goetz, J., Steger, S., Scorpio, V. (2025). Forest cover controls on debris flow sediment connectivity in the Stolla Basin, Italy. In: Proceedings of Geomorphometry 2025, 9-13 June, Perugia, Italy. M. Alvioli, L. Melelli, I. Marchesini eds. CNR Edizioni, Rome. ISBN 978-88-8080-765-0. DOI: 10.5281/zenodo.15276730

Abstract—**Detailed knowledge of debris flow runout is essential for hazard mitigation – this study examines the influence of forest cover on debris flow runout and sediment connectivity in the Stolla basin, South Tyrol, Italy. An open-source Gravitational Process Path (GPP) model within SAGA GIS was used to simulate runout paths via a random walk algorithm, with distances constrained by Perla's two-parameter friction model (PCM). Calibration was guided by two primary objectives: accurately reproducing all observed connected debris flows and minimizing the overall relative error across the region. To account for forest cover, we integrated a crown height model (CHM) derived from pre-event LiDAR data, for integrating spatially variable friction parameters. Our results show that incorporating forest cover considerably improves the accuracy of simulated runout paths and distances, especially in terms of sediment connectivity, while also revealing the trade-offs between optimizing for connectivity and reducing regional error.**

I. Introduction

Debris flows are highly destructive natural hazards in mountainous regions, mobilizing large volumes of sediment and posing significant risks to ecosystems, infrastructure, and communities. Understanding debris flow runout is critical for assessing sediment connectivity, especially in river systems where these processes influence sediment delivery and deposition.

The purpose of this study is to explore the controlling impacts of forest cover on connectivity of debris flows to stream channel networks in the Stolla Basin, South Tyrol, Italy. This study calibrates a process-based runout model in the Stolla basin to optimize connectivity predictions while minimizing errors. It integrates forest cover to refine spatially variable friction parameters and improve the model's representation of debris flow dynamics. The model is validated by comparing predicted and observed connectivity for both connected and non-connected debris flows. By incorporating forest cover into the modeling framework, this research aims to advance the understanding of debris flow sediment transport and connectivity in forested mountain landscapes.

II. Study Area

The Stolla Creek basin, located in eastern South Tyrol, Italy spans 40 km² and ranges in elevation from 1185 m at its outlet to 3146 m at its highest peak. Formerly glaciated during the Pleistocene, the catchment now receives 860 mm of mean annual precipitation and has a mean annual temperature of 5.5 °C [1]. The 11.5 km-long Stolla Creek flows into the Prags/Braies River, a tributary of the Rienz/Rienza within the Etsch/Adige river basin. Vegetation includes conifer forests (48%), primarily Norway spruce (*Picea abies*) and silver fir (*Abies alba*), up to the 2200–2300 m tree line, transitioning to grasslands (15%) and shrublands (11%) dominated by mugo pine (*Pinus mugo*) at higher elevations. Unvegetated areas, comprised of bedrock and sediments, account for 26% of the basin [1].

This analysis focuses on more than 600 debris flows that were triggered in the Stolla basin during a 2017 extreme rainfall event. The complete runout (source to deposition area) of the flows were mapped using high-resolution aerial imagery and LiDAR data [1].

III. METHODS

A. GPP Runout Modelling

The Gravitational Process Path (GPP) [2] model was used to regionally simulate runout for the purpose of exploring process-based characteristics controlling connectivity to the main river channel in the Stolla basin. The GPP model is an open-source framework in the SAGA-GIS software that provides users with various model components to simulate runout path, distance, velocity and deposition of material of mass movements.

Runout path was modelled using the random walk process path component of the GPP model. Random walks model the potential paths of runout by iteratively simulating (via Monte Carlo simulation) the downslope movement path of debris flows originating in an individual source-area grid cell. This simulation results in a grid with runout frequencies that indicate how many times a grid cell has been traversed. There are three parameters that need to be calibrated to obtain a desired runout path: (1) a slope threshold (°) defining where divergent flow is allowed; (2) the exponent of divergence that controls the amount of divergence, or lateral spreading; and (3) a persistence factor that controls the direction of movement [2].

Runout distance was constrained using Perla's two-parameter friction model (PCM) component of the GPP model. It is a center-of-mass model where motion is controlled by (1) the sliding friction coefficient and (2) the mass-to-drag ratio. The sliding friction coefficient μ controls the velocity of movement and the mass-to-drag ratio M/D (m) controls velocity movement over steep terrain [2].

To simulate runout on a regional scale, the runout path and distance needs to be calibrated. This was done using the runoptGPP R package [3]. First the path was calibrated by finding optimal random walk model parameters based on a random sample of 100 debris flows across the entire Stolla basin using 1000 walks per source cell. Runout path was calibrated using two approaches in this work: (1) calibrating the model for connectivity and (2) for the entire region. Please see Goetz et al (2021) for more optimization procedure details.

Source areas for each event were automatically selected by selecting the cells within the top 5% elevations for each observed runout path. The runout modelling was performed on a 5 x 5 m spatial resolution sink-filled digital terrain model (DTM). The DTM was sink filled to help simulate the infilling process that can occur during a debris flow event.

B. Calibrating for connectivity and relative error

The PCM model was optimized to find the μ and M/D values with lowest relative error that also resulted in all observed connected debris flows simulated as connected. The objective of this approach was to ensure that the calibrated model is capable of simulating events that connect to the main river channel. In contrast, when optimizing the regional model for higher performance, it is likely that larger debris flow events that reach the river are underestimated, since they usually have much lower μ than medium to small debris flows.

Additionally, several models were calibrated using subsets of only the connected debris flows, the not connected debris flows and all the sampled debris flows. This allowed for comparison in performance to previous approaches for regional model calibration [3].

C. Accounting for forest cover in the GPP model

The pre-event forest conditions were based on a crown height model (CHM) computed from a 1 m resolution DTM and digital surface model (DSM) surveyed in 2010 (Eqn. 1), which was resampled to 5 m spatial resolution.

$$CHM = DSM - DTM \tag{1}$$

To ensure that the differences in the CHM were only attributed to changes in vegetation and not artefacts in steep terrain, a land cover map was used to mask out elevation changes detected in non-vegetation classes (e.g. loose debris and outcrops).

The pre-event forest conditions were introduced into the GPP model by creating grids for μ and M/D values, where grid cells that contained forest were assigned higher μ and lower M/D values, which reduce runout distance due to higher friction and lower runout velocities, respectively. The values assigned to forest and non-forest areas were based on optimal parameter sets determined for the connected debris flow events and across the entire region. This is illustrated in the following equations,

$$\mu_i = \begin{Bmatrix} \mu_{conn} A_i, & if\ A_i = 0; \\ \mu_{relerr} A_{i,} & if\ A_i = 1 \end{Bmatrix} \tag{2}$$

and

$$M/D_i = \begin{Bmatrix} M/D_{conn} A_i, & if\ A_i = 0; \\ M/D_{relerr} A_i, & if\ A_i = 1 \end{Bmatrix}, \tag{3}$$

where μ_i and M/D_i are parameters at grid cell locations i, μ_{conn} and M/D_{conn} are optimal global parameter sets for connected runout events, μ_{relerr} and M/D_{relerr} are optimal global parameter sets that resulted in the lowest median relative errors for all sampled runout events, and A_i is forest cover. A_i = 1 are grid cells classified with forest and A_i = 0 are grid cells without forest cover. The final parameters for Equations 2 and 3 were determined by a trial-and-error approach and visual inspection of the simulated runout paths. The calibrated parameters from the connectivity optimization and lower median relative error served as a starting point in parameter testing.

D. Model sample and validation

To reduce computational time during the exhaustive grid search optimization procedure a subsample of the Stolla basin runout tracks was sampled below a tree line (< 2100 m.a.s.l). In

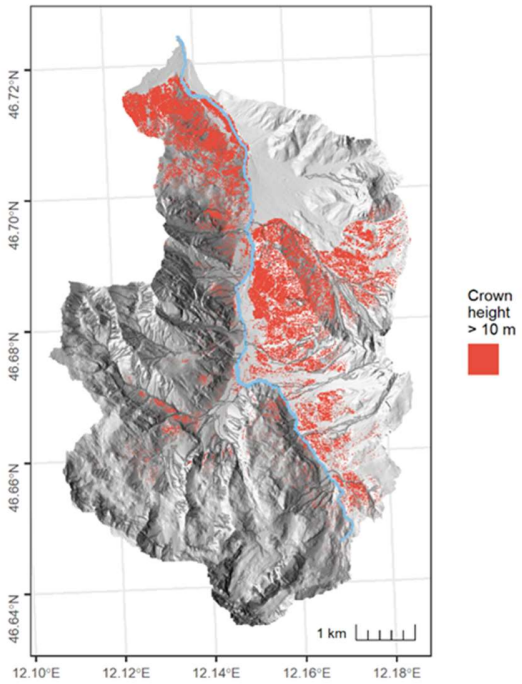

Figure 1. *Map of crown height model and cutoff/threshold > 10 m.*

total 154 debris flows were sampled of which 22 were classified as connected to the Stolla basin river channel.

The performance of the calibrated parameters was assessed using the median relative error of observed runout length and simulated/estimated runout length. These lengths were computed using the minimum area bounding box method [3]. To gain insights on how the model performs for connected and non-connected debris flows, the performance was estimated for data subsets containing (1) only the debris flows that connected to the main channel, (2) only the debris flows that did not connect to the main channel, and (3) all of the debris flows in the sample. The performance was also qualitatively explored for geomorphic plausibility by visual inspection of the corresponding simulated runout maps for individual events and the regionally applied models.

IV. Results and Discussion

A. Crown height modelling

The resulting crown height modelling illustrates much higher and denser forest cover in the north-western and east hillslopes in the Stolla basin. When testing for a suitable crown height model cut-off for spatial modelling of μ and M/D, it was found that simulated runout behavior of debris flows appeared most similar to the observed events when areas with a crown height > 10 m was used (Fig. 1). This threshold provided "openings" in the forested landscape where simulated debris flows could follow observed debris flow paths. Lower thresholds often resulted in closing these "openings", which prevented simulated debris flows from connecting to the main river channel.

B. Parameter calibration and validation

The optimal parameters for ensuring all observed connected debris flows were simulated as connected were μ = 0.04 and M/D = 55. The optimal parameters for a model trained to minimize the median relative error with all the sample debris flows were a μ = 0.38 and M/D = 35. It is evident that the μ values are much higher when training the model with all sampled data. This higher μ results in overall lower simulated runout lengths, which can result in under predicting the number of debris flows that connected to the river channel.

The median relative errors were low (0.06 and 0.10) for GPP models that were independently calibrated for minimizing the relative error for connected and non-connected debris flows compared to the globally calibrated model (0.33). This result hints that there could be spatial attributes, such as terrain conditions, forest cover, available source material, that account for the differences in optimal μ.

Calibrating for connectivity came at the cost of reducing the overall performance of simulated connected debris. That is, debris flow lengths were either similar to the observed length or overestimated. When using the median relative error approach for optimization with only connected debris flows, the overall median error was reduced (0.06 vs. 0.17), however this came at the cost of underestimating the length of some debris flows, including ones that were observed to connect with the main river channel.

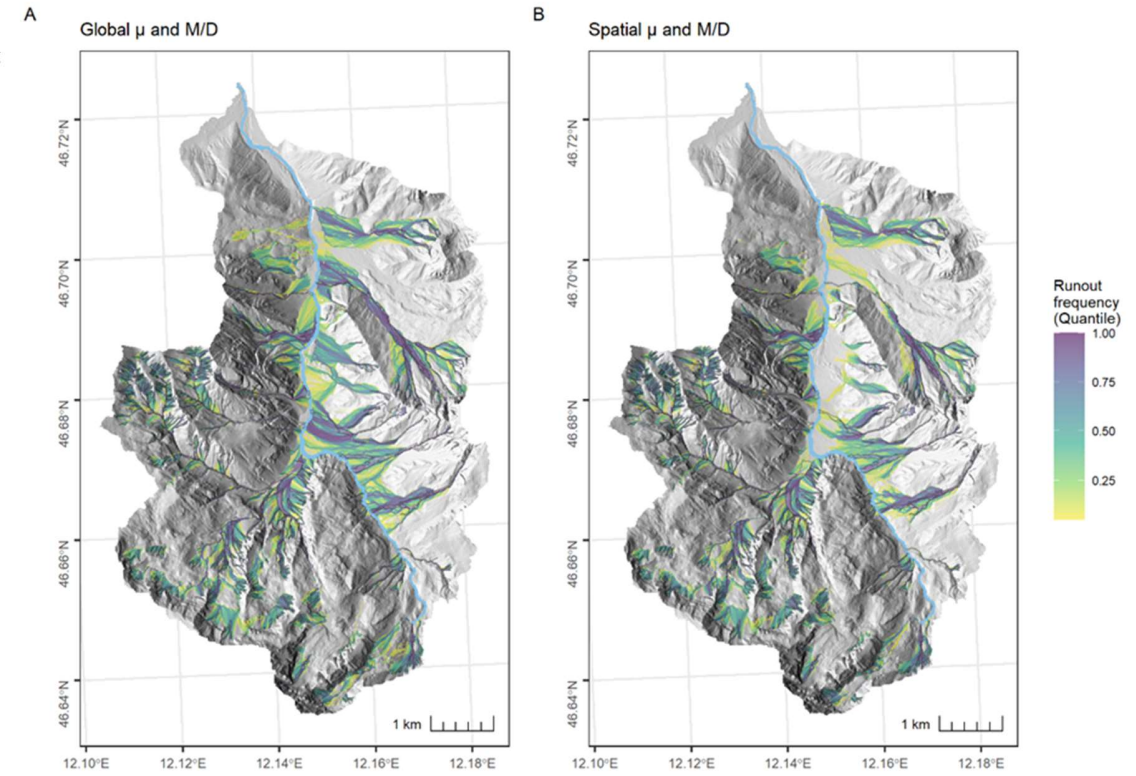

Figure 2. *Maps of simulated runout paths for each event in the Stolla basin. (A) μ and M/D globally optimized for connectivity, and (B) spatial varying μ and M/D ratio to account for forest cover influence.*

Overall, the GPP model calibrated to minimize the relative error of connected debris flows had the best performance in terms of lowest median relative error, followed by the spatial μ and M/D model that accounted for forest cover, and then the model calibrated for connectivity. The model that accounted for forest cover was able to decrease the overall median relative error of the calibrated for connectivity model by 30% (Fig. 2B). It also managed to simulate 22/22 connected debris flows as connected. Through visual inspection, the model with forest cover appears to perform better at matching the observed runout paths, particularly in forest areas, compared to the model calibrated for connectivity.

V. Conclusions

Overall, the calibration for connectivity GPP model in the Stolla basin does perform well at simulating connected slides but comes at the cost of over predicting the runout lengths of non-connected debris flows. The connected debris flows tended to have low sliding friction coefficients compared to non-connected. Typically, larger events were related to lower sliding coefficients, which hints that regional GPP modelling can be improved by better representing the controls of runout length (e.g. catchment area, source areas size, and presence of forest in the runout path) in a model with spatially varying parameters.

The best connectivity results were obtained using a spatial model of the runout parameters that considered forest cover. This indicates that the distribution of forest does play an important role in debris flow sediment transport connectivity in this basin. Likely, changes in the forest cover would result in increased sediment transport to the main river channel.

V. Acknowledgments

This research was funded by the project ‘CoupEvent: Hillslope – Channel coupling during extreme events in South Tyrol, supported by the Autonomous Province of Bozen-Bolzano.

References

[1] Scorpio, V., Cavalli, M., Steger, S., …, Comiti F. 2022. Storm characteristics dictate sediment dynamics and geomorphic changes in mountain channels: A case study in the Italian Alps. Geomorphology, 403, 108173.

[2] Wichmann, V. 2017.The Gravitational Process Path (GPP) model (v1.0) – a GIS-based simulation framework for gravitational processes, Geosci. Model Dev., 10, 3309–3327.

[3] Goetz, J., Kohrs, R., Parra Hormazábal, E., …, Brenning A. 2021. Optimizing and validating the Gravitational Process Path model for regional debris-flow runout modelling, Nat. Hazards Earth Syst. Sci., 21, 2543–2562.

[4] Steger, S., Scorpio, V., Comiti, F., Cavalli, M. 2022. Data-driven modelling of join debris flow release susceptibility and connectivity. Earth Surface Processes and Landforms, 47, 2740-2764.

Regional-Scale Debris-Flow Susceptibility Modelling. A case study in the Rocky Mountains

Txomin Bornaetxea
Dept. of Geography, Prehistory and Archaeology
University of the Basque Country (UPV/EHU)
Vitoria-Gasteiz, Spain
txomin.bornaetxea@ehu.eus

Ivan Marchesini
Research Institute for Geo-Hydrological Protection,
Italian National Research Council
Perugia, Italy
ivan.marchesini@cnr.it

Andrée Blais-Stevens
Natural Resources Canada
Ottawa, Canada
andree.blais-stevens@nrcan-rncan.gc.c

Cite as: Bornaetxea, T., Marchesini, I., Blais-Stevens, A. (2025). Regional-Scale Debris-Flow Susceptibility Modelling. A case study in the Rocky Mountains. In: Proceedings of Geomorphometry 2025, 9-13 June, Perugia, Italy. M. Alvioli, L. Melelli, I. Marchesini eds. CNR Edizioni, Rome. ISBN 978-88-8080-765-0. DOI: 10.5281/zenodo.15094827

Abstract—**This study outlines the datasets and techniques employed to evaluate debris-flow runout susceptibility in the Valemount region, located in east-central British Columbia, Canada. The research spans an area of approximately 1200 km². A comprehensive landslide inventory exists for this region, which maps historical debris-flows by delineating both source zones and valley deposits. The inventory distinguishes between hillslope and channelized debris-flows, enabling separate modelling approaches for these phenomena. The outputs of both models were integrated to classify the region according to its vulnerability to debris-flow runout events. Landslide datasets independent of the training process were used for map validation and optimization. The results demonstrate a strong ability of the models to differentiate between areas likely to form debris-flow fans and regions outside the expected runout paths.**

I. Introduction

Estimating the susceptibility of debris-flows is an important part of mitigation design, and consists of classifying the terrain according to the propensity to experience debris-flows. The goal of such studies is to provide a quantifiable relationship between the occurrence of debris-flows and environmental or physical factors observed on the slopes [1].

Despite the big effort made by researchers to date, modelling debris-flow susceptibility at a regional scale (including the initiation, transportation, and deposition zones) can be extremely challenging due to the complex and variable interactions existing during each event.

At regional scale, only few studies consider the debris-flow susceptibility as a combination of the likelihood to initiate a movement and propagate downhill [2, 3, 4]. In this study, we propose and describe a new framework to assess debris-flow susceptibility. We use a data-driven approach that combines both statistical and conceptual modelling by using a digital elevation model (DEM) and a landslide inventory as the main input data. We tested it over a large area in the Canadian Rocky Mountains, east central British Columbia (Fig. 1).

II. Available Data

A. Debris-flow inventory

The available landslide inventory, compiled from air photo interpretation, consisted of 1286 landslides classified into 11 types (debris-flow, rock avalanche, rotational slide, etc.) with three levels of certainty [5]. For this study, we used only the landslide features classified as “debris-flows”.

However, since under the general term of debris-flow there might be considerable differences in their behaviour, we manually reclassified each debris-flow of the inventory into either hillslope or channelized subtype [6]. To do so, we analyzed each landslide movement in relation to the morphology of the area on which it was triggered. This created two inventories: one consisting of 278 hillslope debris-flows, and the other of 68 channelized debris-flows. Most entries included the entire debris-flow body (source area, transportation zone and deposition zone). For some hillslope debris-flows, only the source area and zone of deposition were delineated. As a final step, we reserved a group of isolated debris-flow deposit polygons for use in the validation.

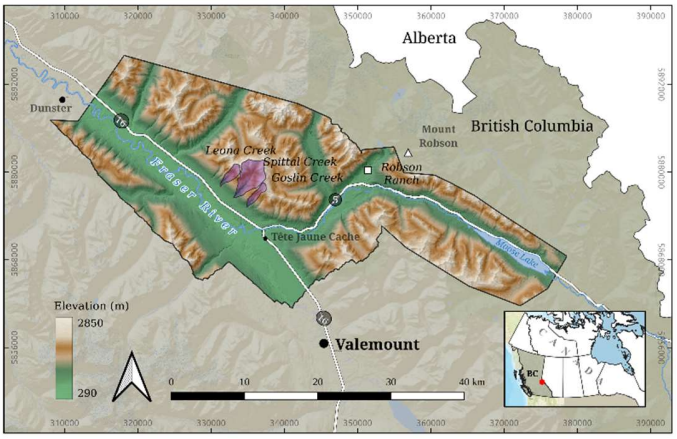

Figure 1. Location map of the study area.

B. *Digital elevation model (DEM) and environmental variables*

A LiDAR-derived DEM served as the primary spatial reference throughout all phases of the experiment. This elevation map was created by manually merging LiDAR data collected between 2019 and 2021 at a resolution of 5 meters [5]. Based on the DEM, we also generated up to 49 derived maps to identify a suitable set of environmental variables for step 2 of the proposed framework (see Fig. 2). These derived maps represent commonly used indicators of terrain morphology, either resampled at different grid-cell resolutions or smoothed using a variable window-size filter [7].

III. Proposed Framework

The proposed framework consists of a sequence of steps (Fig. 2) in which the debris-flow inventory is used to statistically train the models for both the initiation zones and potential runout. Other authors have recently used a similar approach [3, 8].

First, we applied logistic regression to generate a release area zone map specifically for hillslope debris-flows. This step was performed using the LAND-SUITE software [9] and a selection of 7 environmental variables from the original set of 49: cross-sectional curvature, longitudinal curvature, elevation range, sinusoidal slope, insolation time, stream power index, and topographic index. Next, we used the r.randomwalk tool with the obtained release area zone map to train and apply the runout model across the entire study area [9]. As a result, we produced a susceptibility map for hillslope debris-flow runout.

For channelized debris-flows, we assumed that movement typically triggers with the mobilization of debris within a confined valley or channel, where material is progressively supplied from adjacent slopes. To identify potential source areas, we combined the hillslope debris-flow susceptibility map with downstream slope gradient values. As a result, we identified segments of the channel network most prone to channelized debris-flow initiation in areas where the hillslope debris-flow runout model reaches the channel and the downstream slope is between 15º and 24º, as suggested in the literature [10].

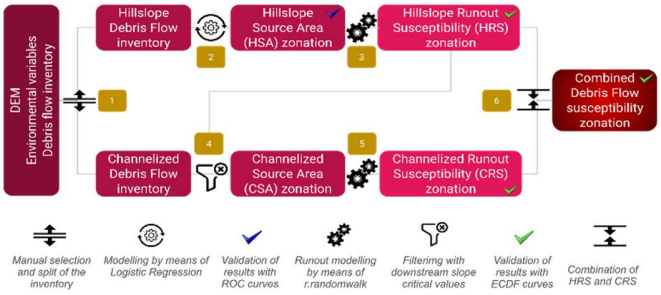

Figure 2. Simplified flowchart of the applied methodology. HAS = hillslope source area; HRS = hillslope runout susceptibility; CSA = channelized source area; CRS = channelized runout susceptibility.

The channelized debris-flow inventory was used to train the channelized runout-trajectory model and to simulate debris-flow trajectories, resulting in a map of the susceptibility of the channelized debris-flows to runout. Finally, the two susceptibility maps were combined to represent the likelihood of each pixel being crossed by one of these debris-flow sub-types, or both. To do so, we normalized the two original maps and then summed the normalized values.

Hillslope, channelized, and combined susceptibility maps were validated by using independent data from the debris-flow inventory. We followed a validation approach proposed by other authors in the past [8]. It consisted in building and comparing specific empirical cumulative distribution function (ECDF) curves based on the runout susceptibility values predicted inside the validation polygons and in the rest of the study area. Figure 5 displays the ECDF curves for each region alongside the Kolmogorov–Smirnov D parameter. This statistic measures the maximum vertical distance between the ECDFs of susceptibility values within independent landslide polygons and those across the entire study area. A notably large D value indicates significant dissimilarity between the two functions, suggesting differences in susceptibility values within the validation inventory polygons compared to the broader region, as expected for a susceptibility map. Conversely, a very small D value suggests random sampling of susceptibility values by landslide polygons, pointing at potential biases in either the susceptibility map, the landslide inventory, or both. The advantage of using the ECDF lies in its ability to autonomously evaluate model performance, even with limited validation data and without the need for binary representation of the dependent variable.

IV. RESULTS

A. *Hillslope debris-flow runout susceptibility*

Following the r.randomwalk approach [11], we released 10 random trajectories from each cell enclosed in the source areas from the hillslope landslide inventory. The r.randomwalk tool keeps track of the angles of reach (Ω) corresponding to the moment when each trajectory leaves the boundaries of the deposition polygon. We collected all these values and obtained a correct fit with a Gaussian distribution model, where the peak can be found around the value of 29. This means that most of the simulated trajectories inside the landslide polygons stop when Ω = 29°. After that, we simulated debris-flow trajectories in the complete study area.

Fig. 4 we show the hillslope debris-flow runout susceptibility map. It was obtained by generating multiple trajectories from the hillslope source area model and using, as a break criterion, random values of the angle of reach (see r.randomwalk manual for more details). The legend and colours allow us to identify the areas where the relative probability of spatial occurrence of hillslope debris-flows is higher or lower than 0.5, with higher areas being the more susceptible to debris-flow runout.

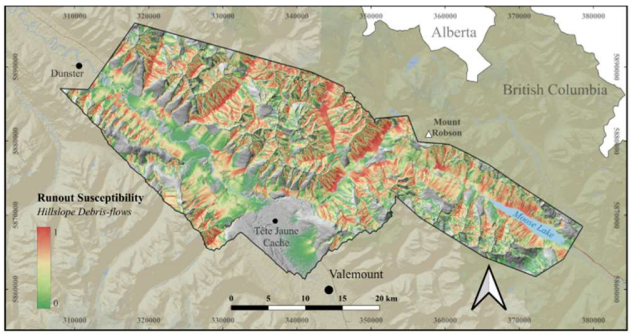

Figure 3. Results of Hillslope Debris-Flow susceptibility modelling.

The plot in Fig. 5a shows the ECDF curves of the susceptibility values for both the validation dataset and the study area where D parameter = 0.45. This indicates that the model can recognize actual debris-flow susceptible areas. Therefore, such a large difference in susceptibility values reflects good modelling performance.

B. *Channelized debris-flow runout susceptibility*

According to the inventory, the areas mapped as channelized source areas equals a total of 5157 pixels, each of these releasing 100 random walks, for a total of 515,700 training trajectories. In this case, the distribution of the collected angle of reach values fits well with a log-normal distribution model, where the mode is observed around the value of 14. This means that most of the channelized debris-flow deposits in the study area will not stop until Ω = 14°.

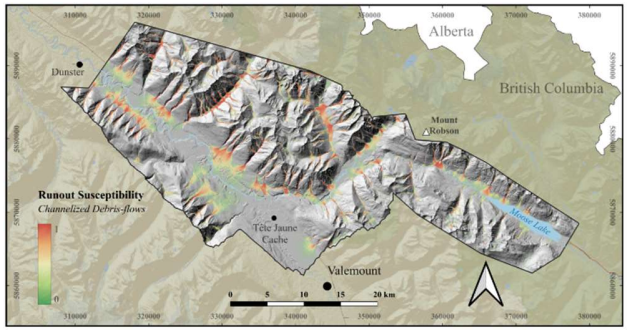

Figure 4. Results of Channelized Debris-Flow susceptibility modelling.

As it can be observed in Fig. 5b, the difference between the curve of the validation dataset and that of the whole study area is significant, with D parameter = 0.80.

The map in Fig. 4 represents the runout susceptibility map of channelized debris-flows. Fan deposits generated from the steep incised valleys are evident. They display a runout zone reaching the main valley bottom, where principal infrastructure and urban settlements are located.

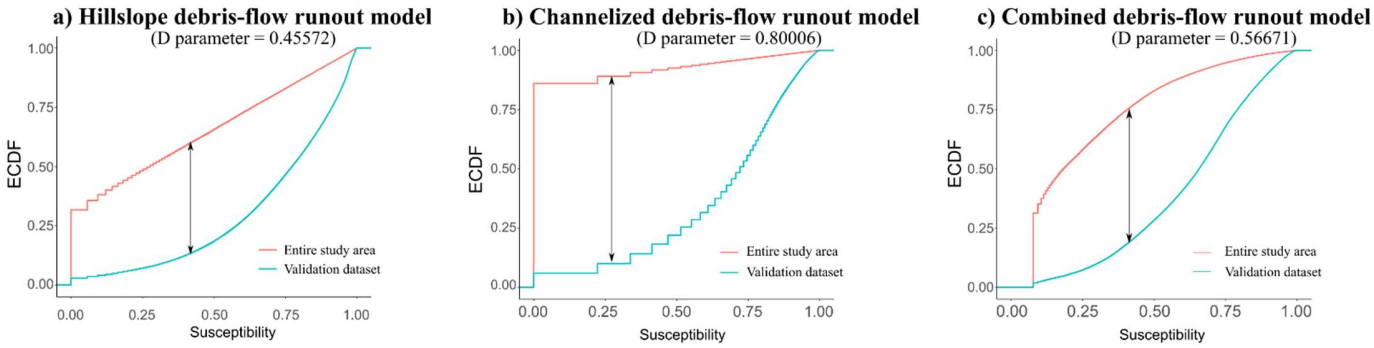

Figure 5. From left to the right, validation results of Hillslope, Channelized and Combined debris-flow susceptibility models.

C. *Combined debris-flow susceptibility map*

For defining possible prevention and mitigation zones, we combined the results of both hillslope and channelized susceptibility maps to produce a single debris-flow runout susceptibility map (Fig. 6).

The resulting D = 0.57 value (Fig. 5ct) demonstrates the model's capability to display higher relative susceptibility values within the validation zones than over the entire study area. Specifically, the plot highlights that only 25% of the validation data pixels have susceptibility values less than 0.5, compared to the entire study area, where more than 75% are at less than 0.5. Thus, this represents a valuable final step in the modelling.

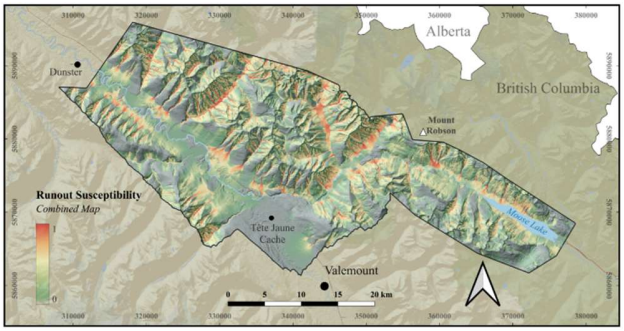

Figure 6. Results of Combined Debris-Flow susceptibility modelling.

V. CONCLUSIONS

We produced three debris-flow runout susceptibility maps for a mountainous area, covering about 1200 km², located near Valemount, British Columbia, in the Canadian Rocky Mountains, where no regional susceptibility models previously existed. We applied statistical and conceptual modelling in the study area with high-resolution digital elevation model (5x5 m grid cells).

We considered two mechanical movements for the debris-flow types: hillslope and channelized. This duality was applied not only for the runout susceptibility modelling, but also for the source-area characterization. This allowed us to combine the resulting models into one final map product that ranks the terrain's susceptibility to either channelized or hillslope debris-flows or both. The two susceptibility models developed solely for hillslope and channelized debris-flows, as well as the final combined model, were validated by using independent sub-datasets, which showed good capabilities to detect potential debris-flow susceptible areas, even in places where no debris-flows have occurred or have yet been mapped.

The primary advantage of this methodology is its utility for regional analyses, since relatively little data are required for its application. Our approach can be used to identify areas most vulnerable to debris-flow runout and, conversely, those that are less vulnerable to these phenomena. In addition, identification of intersections of the highest susceptibility zones with anthropogenic elements-at-risk will help to inform further detailed studies.

ACKNOWLEDGMENTS

During this work Txomin Bornaetxea was supported by a postdoctoral fellowship, granted by the Basque government and the University of the Basque Country (UPV/EHU, group IT1678-22). Funding: This research was supported by Natural Resources Canada's Office of Energy Research and Development (Pipeline Geohazards projects GSC-19-103 and GSC-23-104) within the Public Safety Geoscience Program at the Geological Survey of Canada.

REFERENCES

[1] D'Agostino, V., and L. Marchi, 2001. Debris flow magnitude in the eastern Italian Alps: data collection and analysis. Phys. Chem. Earth, Pt. C, 26 (9), 657–663. https://doi.org/10.1016/S1464-1917(01)00064-2

[2] Blais-Stevens, A., and P. Behnia, 2016. Debris flow susceptibility mapping using a qualitative heuristic method and Flow-R along the Yukon Alaska Highway Corridor, Canada. Nat. Hazards Earth Syst. Sci, 16 (2), 449–462. https://doi.org/10.5194/nhess-16-449-2016

[3] Liang, X., Y. Ge, L. Zeng, L. Lyu, Q Sun, Y. Sun, and X. Wang, 2023. Debris flow susceptibility based on the connectivity of potential material sources in the Dadu River basin. Eng. Geol, 312, 106947. https://doi.org/10.1016/j.enggeo.2022.106947

[4] Steger, S., V. Scorpio, F. Comiti, and M. Cavalli, 2022. Data-driven modelling of joint debris flow release susceptibility and connectivity. Earth Surf. Process. Landf, 47 (11), 2740–2764. https://doi.org/10.1002/esp.5421

[5] Bornaetxea, T., A. Blais-Stevens, and B. Miller, 2023. Landslide inventory map of the Valemount area, British Columbia, Canada. A detailed methodological description, in: Progress in Landslide Research and Technology, Volume 1 Issue 2, Springer, pp. 373–381. https://doi.org/10.1007/978-3-031-18471-0_27

[6] Zhang, S., L.M. Zhang, H.X. Chen, Q. Yuan, and H. Pan, 2013. Changes in runout distances of debris flows over time in the Wenchuan earthquake zone. J. Mt. Sci, 10 (2), 281–292. https://doi.org/10.1007/s11629-012-2506-y

[7] Chang, K.T., A. Merghadi, A.P. Yunus, B.T. Pham, and J. Dou, 2019. Evaluating scale effects of topographic variables in landslide susceptibility models using GIS-based machine learning techniques. Sci. Rep. 9 (1), 12296. https://doi.org/10.1038/s41598-019-48773-2

[8] Marchesini, I., O. Althuwaynee, M. Santangelo, M. Alvioli, M Cardinali, M. Mergili, P. Reichenbach, S. Peruccacci, V. Balducci, I. Agostino, R. Esposito, and M. Rossi, 2024. National-scale assessment of railways exposure to rapid flow-like landslides. Eng. Geol, 332, 107474. https://doi.org/10.1016/j.enggeo.2024.107474

[9] Rossi, M., T. Bornaetxea, and P. Reichenbach, 2022. LAND-SUITE V1.0: a suite of tools for statistically based landslide susceptibility zonation. Geosci. Model Dev, 15 (14), 5651–5666. https://doi.org/10.5194/gmd-15-5651-2022

[10] Armanini, A., L. Fraccarollo, and M. Larcher, 2005. Debris flow. 142. Encyclopedia of Hydrological Sciences. John Wiley & Sons, pp. 2173–2185.

[11] Mergili, M., L. Schwarz, and A. Kociu, 2019. Combining release and runout in statistical landslide susceptibility modeling. Landslides, 16 (11), 2151–2165. https://doi.org/10.1007/s10346-019-01222-7

Automatic Landslide Detection Using Google Earth Engine, a case study for Quang Nam Province, Vietnam

Nguyen Tra My [1], Matthieu Kervyn, Benoît Smets
Department of Geography
Vrije Universiteit Brussel, Brussels, Belgium

Nguyen Thanh Long
Vietnam Institute of Geosciences and Mineral Resources, Hanoi, Vietnam

Nguyen Quoc Dinh
Phenikaa University, Hanoi, Vietnam

Chinh Luu
Faculty of Hydraulic Engineering
Hanoi University of Civil Engineering, Hanoi, Vietnam

[1] Tra.my.nguyen@vub.be

Cite As: Nguyen, T. M., Kervyn, M., Smets, B., Nguyen, Q. D., Nguyen, T. L., Luu, C. (2025). In: Proceedings of Geomorphometry 2025, 9-13 June, Perugia, Italy. M. Alvioli, L. Melelli, I. Marchesini eds. CNR Edizioni, Rome. ISBN 978-88-8080-765-0. DOI: 10.5281/zenodo.15281399

Abstract— **Accurate and timely detection of new landslides is critical for updating landslide susceptibility assessment and developing effective mitigation and response strategies. In this study, an automated procedure for detecting landslides is developed using Sentinel-2 images and Google Earth Engine. Based on a known event date, the best pair of pre- and post-event satellite images is first selected to make a change detection analysis based on the difference of normalised difference vegetation index (dNDVI). Geomorphological filters are then used to select potential landslides from pixels affected by large vegetation changes. This automatic-landslide inventory is compared with a benchmark landslide inventory manually drawn on high-resolution images to assess whether the technique is sufficiently robust. We calibrated this approach in Phuoc Thanh commune, Phuoc Son district, Quang Nam province, which was severely affected by a storm in October 2020. The method is then applied to all mountainous districts of the Quang Nam Province for each rainy season between 2020 and 2024 to produce a multi-temporal landslide inventory in this highly forested region. The Google Earth Engine scripts allow this procedure to be quickly repeated in new areas and create an inventory map for large areas. However, other ground surface changes due to deforestation, wildfires, accelerated erosion, construction, and logging can also cause a decrease in vegetation cover, which can lead to false positives.**

I. INTRODUCTION

On the morning of October 28th 2020, heavy downpours and strong winds triggered by storm struck the mountainous regions of central Vietnam, leading to the occurrence of thousands of landslides and flashfloods in Quang Nam province. These events led to tens of fatalities, and the destruction of multiple houses and roads [1].

Landslide detection with reliable information regarding landslide location and timing is critical for assessing landslide susceptibility and developing effective mitigation and prevention strategies. In the past, this task remained challenging due to the lack of remote sensing and geographic information systems. Therefore, traditional methods for detecting landslides involved intensive fieldwork and manual image interpretation of aerial photographs [2]. These approaches demand expert knowledge, specialized training, and adherence to a standardized detection protocol. Besides, these conventional techniques entail significant labor and are time-consuming.

Nowadays, remote sensing data plays a vital role in landslide detection and mapping due to the provision of critical information on land cover that facilitates the identification of a landslide affected areas [3]. New methodologies have been proposed in recent years to semi-automatically or automatically map landslides with the use of earth observation data.

This study focuses on calibrating an algorithm for automatic detection and mapping of landslides caused by the storm in October 2020, in Phuoc Thanh commune, Quang Nam, Vietnam, through free optical satellite data in Google Earth Engine (GEE). The developed approach is then applied to all mountainous districts of the Quang Nam Province for each rainy season between 2020 and 2024 to produce a multi-annual landslide inventory in this highly forested region.

II. MATERIALS AND METHODS

A. Study area

Quang Nam province is located in the center of Vietnam [4] and is extent over 10,574 km^2 (Figure 1). The population of the province was 1,945,000 people in 2022, representing a population density of 183 inhab/km^2, with most people living in the coastal districts [4]. Quang Nam province has a relatively complex topography that progressively descends from the West to the East. There are six mountainous districts in the West, including Dong Giang, Tay Giang, Nam Giang, Nam Tra My, Bac Tra My, and Phuoc Son districts.

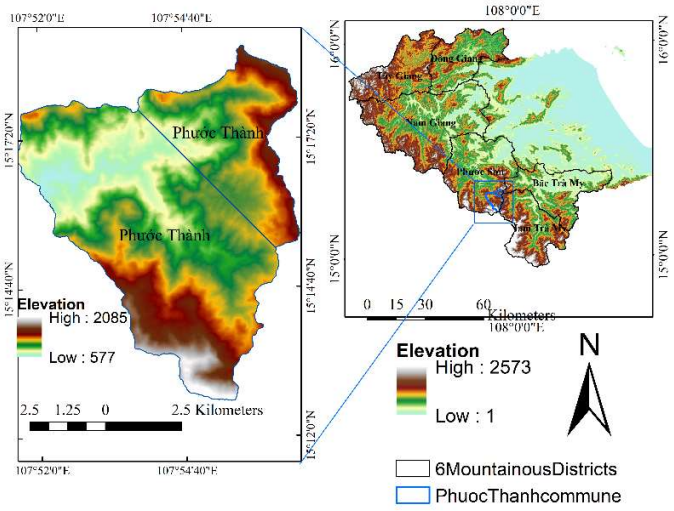

Figure 1. Map showing the study area, Quang Nam province in Vietnam (source: Shuttle Radar Topography Mission Digital Elevation Model with a 30m spatial resolution)

The test area is Phuoc Thanh commune, with an area of 62 km^2, a mountainous commune located in Phuoc Son district (Fig. 1). The population of the commune was 1,891 people in 2019 [4], representing a population density of 30 inhab/km^2 [6]. The population in the area is quite sparse, principally composed of ethnic minorities depending on farming, with a poor livelihood.

This area experiences a tropical climate with the highest rainfall levels in Vietnam [7]. It has one rainy season and one dry season, with an average annual temperature of about 25.6°C [6]. The rainy season begins in August-September, reaching a peak in October and November before ending in November - December, with mean annual rainfall ranging from 2000 to 2500 mm/year [8].

B. Data

In this study, an automated procedure for the detection of landslides is developed using Sentinel-2 with 10 m visible and near-infrared bands. Shuttle Radar Topography Mission (SRTM) Digital Elevation Model (DEM) with a 30-meter spatial resolution (https://earthexplorer.usgs.gov/) is used to describe the topography (Table I). Moreover, high-resolution images from Google Earth will be used to conduct a manual inventory of landslides. The pre- and post-event images available for analysis are from March 6, 2019, and October 1, 2021, respectively ((Table II).

TABLE I. SETINEL-2 IMAGES USED IN THIS STUDY

Variable	Remarks	Value
Image source	Sentinel-2	Band RGB; NIR 10 m spatial resolution
Topographic map	SRTM DEM	30 m resolution
Event date	Date of the storm-trigger landslide occurred in the study area	October 28th, 2020
Pre-event image	Use for automatic detection	January 23rd, 2020
Post-event image	Use for automatic detection	February 16th, 2021

TABLE II. HIGH-RESOLUTION IMAGES USED FOR MANUAL LANDSLIDE MAPPING IN THIS STUDY

Variable	Remarks	Value
Image source	Google Earth	0.3 m spatial resolution
Pre-event image	Use for manual inventory mapping	March 6th, 2019
Post-event image	Use for manual inventory mapping	October 1st, 2021

C. Methods

Our landslide detection approach aims to detect landslides based on change in vegetation cover (measured by NDVI) and geomorphological filters (Fig. 2). An image pair is selected based on the known date of the event during the rainy season. The selection criteria for the pre-event and post-event image prioritize images with the least cloud cover available, acquired during the same time of year to minimize the effects of canopy cover changes across seasons [9].

To improve the identification of the best pair of images, we manually draw sample of landslides and non-landslides areas on the GEE interface, to extract NDVI time series from Sentinel-2 data from 2019 to the present and process with GEE. This step aims to assess the changes in vegetation cover in the time series of images and identify the landslide occurrence. This process aids in establishing the likely date range for a landslide occurrence and provides an initial assessment of the event's timing.

In the second step, one cloud-free scene is selected in the dry season preceding the event and one following it, to compute the dNDVI by subtracting the pre-event from the post-event NDVI image. The dNDVI threshold was defined based on the comparison of the NDVI time series of the affected and not affected areas by landslide, and a comparing the dNDVI statistical distribution for landslide and non-landslides areas. Moreover, a digital elevation model (DEM) is used for filtering results of the landslide detection based on dNDVI, as the slope is one of the contributing factors in landslide mapping [10, 11]. A manual

inventory of landslides conducted on Google Earth for the study area is used to calibrate our automatic algorithm and geomorphological filters. Part of the manual landslide inventory also serves as validation data for the automated detection methods.

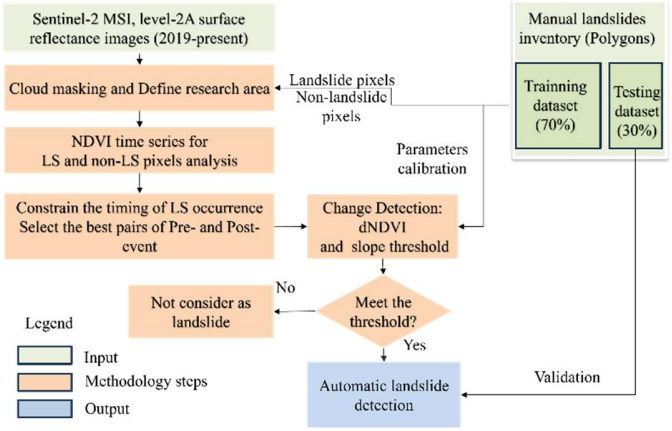

Figure 2. Schematic overview of the landslide detection algorirthm

III. RESULTS AND DISCUSSION

The proposed methodology was calibrated to the automatic detection of landslides in Phuoc Thanh commune, Phuoc Son district, Quang Nam province, based on dNDVI of pre-event (23 January 2020) and post-event (16 February 2021) Sentinel-2 images. Figure 3 shows the NDVI time series of the area affected and the unaffected area by landslides.

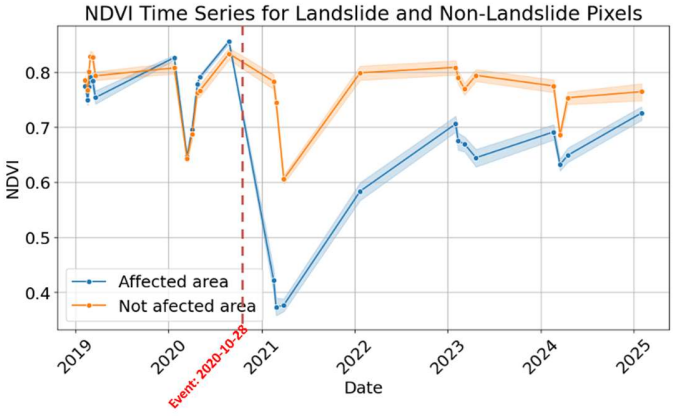

Figure 3. The NDVI time series of the area affected by landslides compared with the time series averaged over a region not affected by landslides.

In areas unaffected by landslides, the NDVI time series exhibit a relatively stable seasonal pattern from 2019 to the present, fluctuating between 0.6 and 0.85. In contrast, regions impacted by landslides experienced a significant drop in NDVI, decreasing from 0.85 to 0.35 after the event. Over the subsequent years, NDVI gradually recovered, reaching 0.7 by 2023.

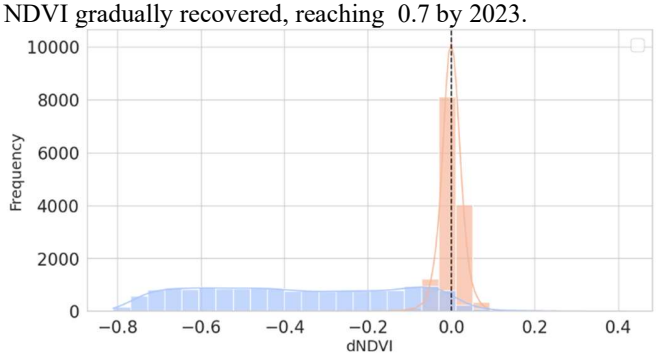

Figure 4. The distribution of dNDVI of the area affected by landslides (blue) compared with the dNDVI of the areas unaffected by landslides (red).

To define the dNDVI threshold for landslide detection, the training dataset was used for parameter calibration. A threshold value can be selected where the separation between the two classes (landslide and non-landslide) is most evident by analyzing their distributions using boxplots and histograms, as in Figure 4. A dNDVI threshold of -0.1 is identified as delivering the best detection accuracy when applied for validation. Moreover, a slope threshold of 10° is selected, to differentiate landslide affected areas (on steep slopes) from zones affected by material deposition (lower slopes).

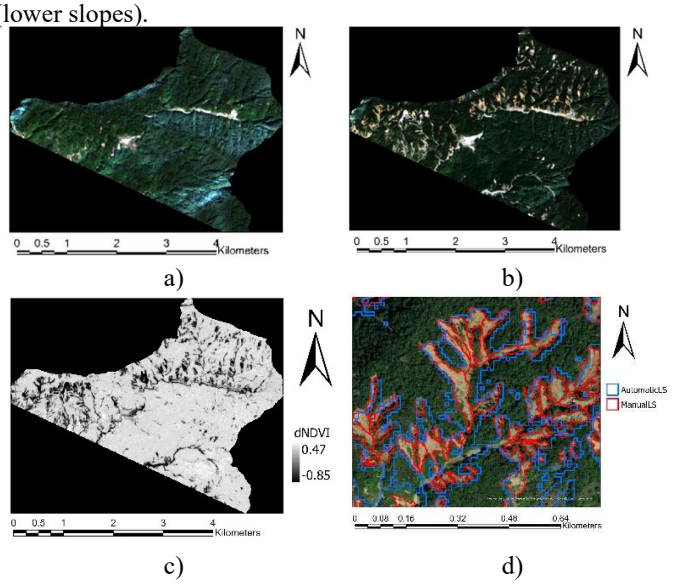

Figure 5. (a) Sentinel-2 pre-event image acquired on 23 January 2020, (b) Sentinel-2 post-event image acquired on 16 February 2021, (c) dNDVI map, (d) comparison between automatic landslide and manual landslide inventory

From the pre- and post-event images (Fig. 4a and Fig. 4b), we obtained the dNDVI (Fig. 4c) that was applied for landslide detection. Finally, the automatic landslide inventory was

compared visually with the manual mapping (Fig. 4d) based on high-resolution images. Visual comparison highlight good performance of the automatic mapping, except for some locations where images are affected by cloud or cloud shadows. Mapping of the full extent and complex shapes of landslides affected areas remains more challenging. A quantitative accuracy assessment needs to be carried out after applying the algorithm to all districts affected by landslides.

IV. CONCLUSIONS

This work developed a method for rapidly detecting landslides with promising performance. The process is automatic, resulting in a landslide inventory map. This approach does not require expensive, high-resolution data. Additionally, the Google Earth Engine scripts are simple, allowing the procedure to be quickly replicated in new areas and enabling the creation of inventory maps for large regions. The method will be applied to all mountainous districts of Quang Nam Province for each rainy season between 2020 and 2024 to generate a multi-annual landslide inventory in this highly forested region. However, it is also noted that other ground surface changes, for instance, due to deforestation, wildfires, accelerated erosion, construction, and logging, can also cause a decrease in vegetation cover, which can lead to false positives.

V. ACKNOWLEGMENTS

We sincerely thank the TEAM VLIR-UOS collaboration project between Vrije Universiteit Brussel (VUB) and Hanoi University of Civil Engineering (VN2022TEA533A105), “GEOdata infrastructures and citizen SCIences to support REsilient development of rural communities in Quang Nam province (GEOSCIRE)” for funding and supporting the study.

REFERENCES

[1] M. Nguyen. "Quang Ngai, Quang Nam in central Vietnam left desolate after fierce storm Molave." https://vietnamtimes.org.vn/quang-ngai-quang-nam-in-central-vietnam-left-desolate-after-fierce-storm-molave-25484.html (accessed Jannuary 10th, 2025).

[2] F. Guzzetti, A. C. Mondini, M. Cardinali, F. Fiorucci, M. Santangelo, and K.-T. Chang, "Landslide inventory maps: New tools for an old problem," *Earth-Science Reviews,* vol. 112, no. 1-2, pp. 42-66, 2012.

[3] H.-J. Park, J.-Y. Jang, and J.-H. Lee, "Physically Based Susceptibility Assessment of Rainfall-Induced Shallow Landslides Using a Fuzzy Point Estimate Method," *Remote Sensing,* vol. 9, no. 5, 2017, doi: 10.3390/rs9050487.

[4] "Statistical Handbook of Vietnam " the Wayback Machine, General Statistics Office Of Vietnam, 2022-01-08 2022.

[5] B. T. Pham *et al.*, "Landslide susceptibility mapping using state-of-the-art machine learning ensembles," *Geocarto International,* vol. 37, no. 18, pp. 5175-5200, 2021, doi: 10.1080/10106049.2021.1914746.

[6] Wikipedia. "Quảng Nam province." https://en.wikipedia.org/wiki/Qu%E1%BA%A3ng_Nam_province (accessed December 29, 2023).

[7] T. A. Tuan, P. D. Pha, T. T. Tam, and D. T. Bui, "A New Approach Based on Balancing Composite Motion Optimization and Deep Neural Networks for Spatial Prediction of Landslides at Tropical Cyclone Areas," *IEEE Access,* vol. 11, pp. 69495-69511, 2023, doi: 10.1109/access.2023.3291411.

[8] H. N. Tuấn and V. T. Tuyết, "Nghiên cứu xây dựng bản đồ phân vùng nguy cơ sạt lở đất cho khu vực miền núi tỉnh Quảng Nam," *Tạp chí Khoa học và Công nghệ thủy lợi, số,* vol. 68, 2021.

[9] D. Notti, M. Cignetti, D. Godone, and D. Giordan, "Semi-automatic mapping of shallow landslides using free Sentinel-2 images and Google Earth Engine," *Natural Hazards and Earth System Sciences,* vol. 23, no. 7, pp. 2625-2648, 2023, doi: 10.5194/nhess-23-2625-2023.

[10] A. D. Luigi Lombardo, Kushanav Bhuyan, Mateo Moreno, Zhice Fang, Said Ahmed Muhtar, Diana Collazos Cortes , Maria Arango Carmona, Nitheshnirmal Sadhasivam, Mahnoor M. Ahmed, Xuetong Wang, Tanuj Pareek, Priscilla and H. T. Niyokwiringirwa, Muhammad Aufaristama , Sansar Raj Meena, Bastian van den Bout ,Cees van Westen, "Developments in landslide inventory, susceptibility, hazard and risk assessments at the UT-Centre for Disaster Resilience," *First South American Geotechnical Seminar,* Seminar 14th-18th November, 2022 2022.

[11] S. Siyahghalati, A. K. Saraf, B. Pradhan, M. N. Jebur, and M. S. Tehrany, "Rule-based semi-automated approach for the detection of landslides induced by 18 September 2011 Sikkim, Himalaya, earthquake using IRS LISS3 satellite images," *Geomatics, Natural Hazards and Risk,* vol. 7, no. 1, pp. 326-344, 2016.

[12] J. Sekajugo *et al.*, "Can citizen scientists provide a reliable geo-hydrological hazard inventory? An analysis of biases, sensitivity and precision for the Rwenzori Mountains, Uganda," *Environmental Research Letters,* vol. 17, no. 4, 2022, doi: 10.1088/1748-9326/ac5bb5.

Assessing the morphological changes of a large landslide using high-resolution UAS and airborne LiDAR data

Manuel Stark
Department of Physical Geography,
Catholic University of Eichstätt-Ingolstadt
Eichstätt, Germany

Annalisa Sannino, Francesca Vergari
Department of Earth Sciences
Sapienza University of Rome
Rome, Italy

Cite as: Stark, M., Sannino, A., Vergari, F. (2025). Assessing the morphological changes of a large landslide using high-resolution UAS and airborne LiDAR data. In: Proceedings of Geomorphometry 2025, 9-13 June, Perugia, Italy. M. Alvioli, L. Melelli, I. Marchesini eds. CNR Edizioni, Rome. ISBN 978-88-8080-765-0. DOI: 10.5281/zenodo.15222233

Abstract -- **The Upper Orcia Valley exhibits a high geomorphological susceptibility to denudation processes, which manifest through continuous water erosion and the frequent occurrence of landslides, due to the high erodibility of its clay-rich marine and fluvial Pliocene deposits in a sub-humid environment. A significant landslide event occurred in January 2021 on a badland hillslope, affecting an area of 0.54 km² within the Formone sub-catchment, approximately 6 km northwest of the Radicofani village. The landslide occurred in a badland hillslope, marking a transition from water-driven denudation processes to gravitational mass movements, thus leading to a complete reconfiguration of the hillslope. This study aims to quantify the morphological changes induced by the landslide and analyze the erosion dynamics of complex landslides in clay-rich substrates. UAS photogrammetry (SfM-MVS), available airborne LiDAR, and DGNSS surveys were employed to analyze volumetric changes over a decade (2012–2022), identify the most affected areas, and investigate the internal morphological evolution of the landslide. The results indicate a total displacement of 17302 m³ of material, with a maximum surface lowering of -6.49 m in the landslide scarp and a maximum deposition of +5.01 m in the westernmost section, resulting in a negative sediment balance of 9980 m³. The landslide, which exhibits a complex dynamic, evolved into a debris flow, with secondary erosion processes further reshaping the landscape. Given the region's susceptibility to denudation and anthropogenic modifications, understanding these processes is crucial for hazard assessment and mitigation strategies. This study highlights the importance of high-resolution topographic surveys for detecting morphological changes and evaluating landslide-prone areas in similar environments.**

I. Introduction

The landscape of the Upper Orcia Valley in Tuscany (Italy) is distinguished by rapid denudation dynamics primarily attributable to the high erodibility of the lithological outcrops (clay-rich marine and fluvial Pliocene deposits). This morphodynamics is further intensified by the Mediterranean climate regime and steep slope gradients, resulting in widespread badlands, where water erosion is predominant and frequent landslides occur [1],[2],[3]. A notable example occurred in January 2021, when a significant landslide (0,54 km²) affected the Provinciale del Monte Amiata road between the villages of Contignano and Le Conie, causing road closure, damage to infrastructures (supply networks for electricity, gas and water) and disruptions to local residents [4]. This landslide took place on a badlands surface (locally called "calanchi") on which it developed, leading to a total reconfiguration of the hillslope. This study aims to examine and quantify the morphological change caused by this landslide. Therefore, advanced methods like UAS photogrammetry (SfM-MVS), airborne LiDAR and DGNSS are used. Key research questions include assessing volumetric changes (2012-2022), identifying areas with the most significant transformations and gaining more insights into the erosion dynamics of complex landslides in clay-rich substrate.

II. Study Site

The study area (Fig. 1) is located in the Formone catchment, about 6 km north-west of the village of Radicofani between 475 m and 575 m a.s.l. It is part of the Radicofani basin, a NW-SE facing depression bordered to the east by the Cetona ridge and to the west by the ridge between Monte Amiata and Castell'Azzara. The topography is predominantly characterised by fluvial landscapes [5],[6]. The climatic conditions of the region are typically Mediterranean (annual mean temperature: 14° C; precipitation: ~700 mm [7]). Rainfall amounts and intensities reach its peaks during the autumn and spring months.

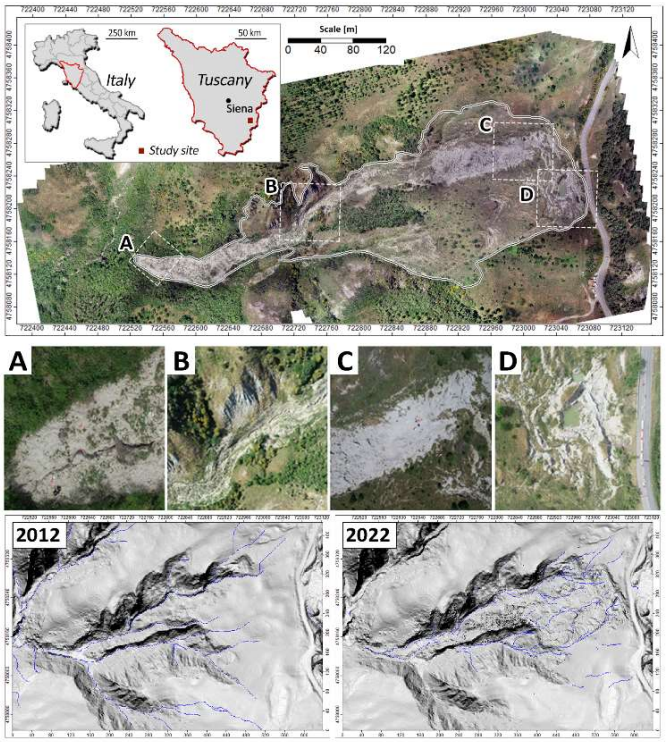

Figure 1, top: Study site with area of interest (AoI) with sub-regions (A-D) of the process area (middle). Bottom: Pre- and post-event hillshaded topography. The blue lines show the respective main channel system.

III. Data Survey and Processing

A. Airborne LiDAR DEM

The available 2012 airborne LiDAR data was acquired by the Ministry of the Environment and the Tutela del Territorio and del Mare as part of the Extraordinary Environmental Remote Sensing Plan [8].The data is available as DEM in a 1 m resolution.

B. Photogrammetric data & ground control points

Table 1 shows the main parameters of data survey. The ground control points (GCPs) were evenly distributed [9], at a distance of 15-80 m [10],[11] and measured with a DGNSS (Stonex S9III and S9i; rover-base-mode; accuracy: $9x10^{-3}$ m). DSMs (resolution: 0.2 m) and orthomosaics (resolution: 0.03 m) were than calculated using structure from motion and multi-view stereo (SfM-MVS) methods [12],[13]. A self-calibration was conducted for the camera parameters (cx, cy, k1, k2, k3, p1, p2), with the exception of the focal length, which was set to a pre-defined value (see table 1). The GCPs were incorporated to ascertain the exterior orientation of the data, (UTM Zone 32N; EPSG code: 25832). Subsequent to the completion of the SfM process, a 3D point cloud and an orthomosaic were calculated for each dataset. Following a comprehensive refinement of the point cloud, which included the filtering of outliers, poorly projected and reconstructed points and major vegetation (trees and shrubs). The photogrammetric DSMs were then resampled from 0.2 m resolution to 1 m (aggregation: lowest z-value corresponding to a grid cell) using a bilinear resampling tool [14].

C. Geomorphic change detection

Figure 2 shows the general workflow employed to ascertain the topographical changes. To distinguish real surface changes from noise the respective uncertainties need to be excluded from the DoD analysis. The individual DEM/DSM uncertainties can be estimated from repeated measurements or from unmodified, geomorphic stable areas (SA) [15]. Here, the SA approach was used to provide a level of detection (LoD) [16] as follows:

$$\sigma\text{DoD} = \frac{\Sigma \sigma DoD}{n\ SA}$$

where σDoD represent the mean of standard deviations of the height values of all stable area pixels in the DEM of Differences (DoD). We used a significance threshold at a critical t-value t crit of 1.96 from Student's t-distribution, corresponding to a confidence level of 95%. The level of detection (LoD) was calculated based on the following equation:

$$\text{LoD} = 1.96 * \sigma\text{DoD}$$

The approach yielded a LoD of 0.18 m. Consequently, all DoD values below are excluded from further analysis. Subsequent to the co-registration and accuracy analysis the models recorded at two different points in time are utilised to calculate the height (surface) changes and, consequently, the volume changes caused by the landslide. The DoD is calculated at a grid size of 1m.

TABLE I: Main Parameters of UAS Survey and SfM-MVS pointcloud

Date:	06/2022
Weather conditions:	dry / sunny
UAS / camera type & focal length:	Phantom 4 Pro + / 8.8 mm
Flight pattern:	Cross grid
Image overlaps (front- & sidelap):	85%
Image count:	1507
Flight altitude (above ground):	80 & 85 m
Point density:	424 $p*m^{-1}$
GCP count:	39
GCP RMSE:	0.03 m
Mean error/ std. dev. (stable areas):	-0.09 m/ 0.08 m

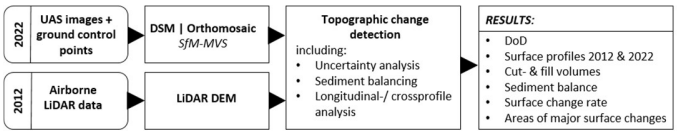

Figure 2: Workflow for UAS and LiDAR data processing and analysis.

IV. RESULTS AND DISCUSSION

The landslide caused a huge morphological change with an erosion volume of 17302 m³ and a deposition volume of 7322 m³ of material. This results in a total mass loss of 9980 m³ transported from the slope to the channel system and further downstream to the Formone River through runoff and other water-driven processes. The most pronounced surface variations occurred in the landslide scarp, in the uppermost part of the Area of Interest (AoI) west of the road, where the terrain subsided by up to -6.49 m (fig. 3). In contrast, the westernmost and lowest sections of the AoI experienced the greatest deposition, with a maximum surface increase of +5.01 m. Linear erosion has been observed to occur exclusively within the primary channel, characterised by gullying and piping, with maximum values reaching -2 m. This area is distinguished by the presence of highly erodible fine-grained material with a high clay content. The presence of numerous subsurface channels on the so-called "popcorn surface" indicates an extensive drainage network piping enhanced after the landslide event, especially in the remolded deposition area. Overall, the event can be described as a complex landslide composed of distinct process zones, each exhibiting different forms of movement. The landslide is characterized by rotational movements in the upper scarp, as indicated by tilted power poles, transitioning into translational movements, mudflows, and gully formation processes in the lower sections. The landslide evolved downstream into a debris flow, particularly west of cross-profile *2 in figure 3, where steeper slopes (max. inclination of 52°) facilitated further material transport. The transport zone of the debris flow is defined by a narrow, incised channel with alternating gullying and piping. Furthermore, the unvegetated slopes north of the debris channel demonstrate a substantial erosion, exhibiting a pronounced slope-channel coupling (cross-profile 3 in figure 3).

According to the surface forms/process signatures, the changes were caused by a combination of shallow landslides and water-driven processes. The material eroded on the slopes was deposited directly on the depth contour after a transport distance of 5-20 metres from where the unconsolidated substrates can now be relatively easily displaced by secondary processes. In the north-western part of the study area, the main slide surface is characterized by significant rill formation (width: 5-60 cm/ depth: 2-40 cm), secondary scarps, and transversal cracks, all indicating ongoing secondary surface movements. The steep slopes in this area and the presence of large cracks suggest active surface processes and a potential future landslide event. The depth of the slide caused partial destruction of key infrastructure, including gas lines. Additionally, minor deposition zones acting as counter-slopes/dams led to the formation of small ponds and pools south of the central slide surface. Tilted power poles point towards

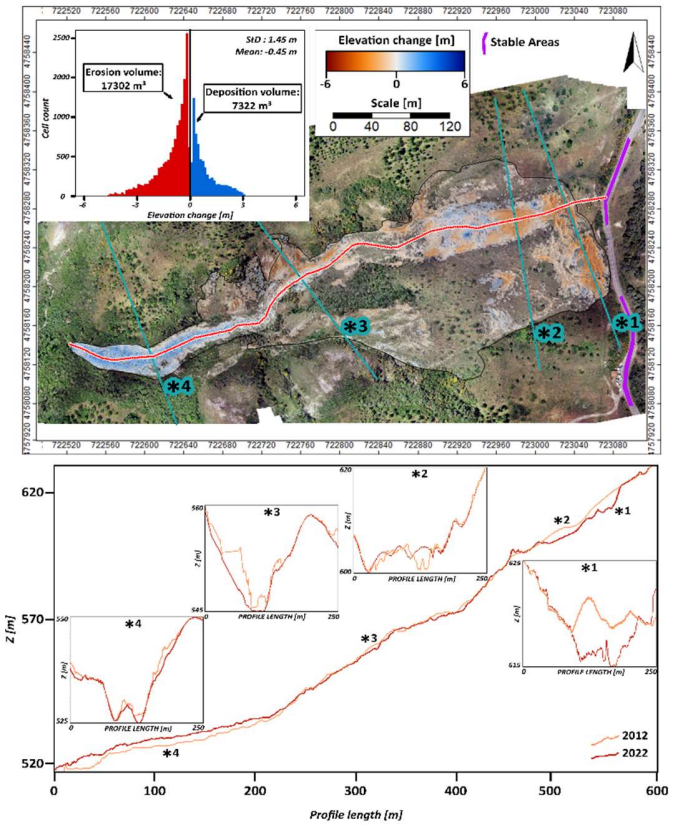

Figure 3: DoD with histogram, location of longitudinal-profile, cross-profiles (*1-*4) and stable areas.

rotational movements here and underlies the complexity of the landslide as it evolved into a debris flow further downstream.

The multitemporal geomorphological analysis showed that the landslide reshaped an hillslope previously affected by badlands, marking a transition from water-driven denudation to gravitational mass movements. This shift highlights how badlands landforms are prone to evolving through landslides and supports the interpretation of the complex cause-effect relationship between calanchi and landslide occurrence in sub-humid climates [17]. Calanchi, which often initiate in landslide scars where vegetation has been removed, are then frequently affected by mass wasting. Future geomorphic processes will likely continue to reshape the landscape, particularly in unvegetated areas prone to secondary sub-events, primarily

driven by water erosion on both hillslopes and within the channel network. With peak precipitation in spring and autumn, these seasons are expected to have the strongest geomorphological effects. The reactivation and further development of existing landforms will most likely include the deepening or filling of rills and channels, the merging of erosional features, and the formation of new active spots [18]. As water erosion proceeds in basal channels, the fluvial domain could extend uphill, re-establishing the system functional sediment connectivity [17]. This could lead, in the near future, to the formation, again, of well-developed badlands in the landslide source area. Further studies on the evolution of dynamic sediment connectivity on this slope could enhance the accuracy of predicting its future development. Considering the natural predisposition of the area to denudation processes and anthropogenic modifications, a deeper understanding of these processes is crucial for early interventions and risk mitigation. Moreover, Structure-from-Motion Multi-View Stereo (SfM-MVS) photogrammetry has proven to be a valuable tool for detecting and quantifying landscape changes, especially at the catchment scale [7], [19].

V. REFERENCES

[1] Della Seta, M., Del Monte, M., Fredi, P., Lupia Palmieri, E. (2009). Space–time variability of denudation rates at the catchment and hillslope scales on the Tyrrhenian side of Central Italy. *Geomorphology*, 107, 161–177. https://doi.org/10.1016/j.geomorph.2008.12.004

[2] Castaldi F., and Chiocchini U. (2012). Effects of land use changes on badland erosion in clayey drainage basins, Radicofani, Central Italy. *Geomorphology* 169–170, 98–108. https://doi.org/10.1016/j.geomorph.2012.04.016

[3] Vergari, F., Della Seta, M., Del Monte, M., Fredi, P., Lupia Palmieri, E. (2013a). Long- and short-term evolution of several Mediterranean denudation hot spots: the role of rainfall variations and human impact. *Geomorphology*, 183, 14–27. https://doi.org/10.1016/j.geomorph.2012.08.002

[4] Cherubini, D. (2021). Radicofani, nuova frana sulla Sp96 Il sindaco: "Ora è chiusa al traffico". In: La Nazione, January 21, https://www.lanazione.it/siena/cronaca/radicofani-nuova-frana-sulla-sp96-il-sindaco-ora-è-chiusa-al-traffico-1.5955089, accessed: 2023-02-09)

[5] Ciccacci, S., Galiano, M., Roma, M.A., Salvatore, M.C. (2008). Morphological analysis and erosion rate evaluation in badlands of Radicofani area (Southern Tuscany—Italy). *Catena*, 74, 87–97. https://doi.org/10.1016/j.catena.2008.03.012

[6] Vergari, F., Della Seta, M., Del Monte, M., Fredi, P., Lupia Palmieri, E. (2013a). Long- and short-term evolution of several Mediterranean denudation hot spots: the role of rainfall variations and human impact. *Geomorphology*, 183, 14–27. https://doi.org/10.1016/j.geomorph.2012.08.002

[7] Aucelli, P.P.C., Conforti, M., Della Seta, M., Del Monte, M., D'Uva, L., Rosskopf, C.M., Vergari, F. (2014). Multi-temporal digital photogrammetric analysis for quantitative assessment of soil erosion rates in the Landola catchment of the Upper Orcia Valley (Tuscany, Italy). *Land Degradation & Development*, 27(4), 1075-1092. https://doi.org/10.1002/ldr.2324

[8] 'DTM LiDAR with ground resolution 1 meter — Tuscany Region', 2013, accessed 2025-01-30, http://data.europa.eu/88u/dataset/m_amte-299fn3-6f2da530-bfde-4dfc-ba76-7e9bc3f8247f

[9] James, M.R., Robson, S. (2012). Straightforward reconstruction of 3D surfaces and topography with a camera: accuracy and geoscience application. *Journal of Geophysical Research: Earth Surface*, 117, F03017. https://doi.org/10.1029/2011JF002289

[10] Gindraux, S., Boesch, R., & Farinotti, D. (2017). Accuracy assessment of digital surface models from unmanned aerial vehicles' imagery on glaciers. *Remote Sensing*, 9(2), 186. https://doi.org/10.3390/rs9020186

[11] James, M.R., Robson, S., d'Oleire-Oltmanns, S., & Niethammer, U. (2017a). Optimising UAV topographic surveys processed with structure-from-motion: Ground control quality, quantity and bundle adjustment. Geomorphology, 280, 51–66. https://doi.org/10.1016/j.geomorph.2016.11.021

[12] Westoby, M.J., Brasington, J., Glasser, M.J., Hambrey, M.J., & Reynolds, J.M. (2012). Structure-from-Motion photogrammetry: a low-cost, effective tool for geoscience applications. *Geomorphology*, 179, 300–314. https://doi.org/10.1016/j.geomorph.2012.08.021

[13] Eltner, A. & Schneider, D. (2015). Analysis of different methods for 3D reconstruction of natural surfaces from parallel-axes UAV images. *The Photogrammetric Record*, 30(151), 279–299. https://doi.org/10.1111/phor.12115

[14] Conrad, O., Bechtel, B., Bock, M., Dietrich, H., Fischer, E.,Gerlitz, L., … Böhner, J. (2015). System for Automated Geoscientific Analysis (SAGA) v. 2.1.4. Geoscientific Model Development, 8(7), 1991–2007. https://doi.org/10.5194/gmd-8-1991-2015

[15] Westaway, R. M., Lane, S. N., & Hicks, D. M. (2000). The development of an automated correction procedure for digital photogrammetry for the study of wide, shallow, gravelbed rivers. Earth Surface Processes and Landforms 25(2), 209–226. https://doi.org/10.1002/(SICI)1096-9837(200002)25:2<209::AID-ESP84>3.0.CO;2-Z

[16] Wheaton, J. M., Brasington, J., Darby, S. E., & Sear, D. A. (2010). Accounting for uncertainty in DEMs from repeat topographic surveys: improved sediment budgets. Earth surface processes and landforms: the journal of the British Geomorphological Research Group, 35(2), 136-156. https://doi.org/10.1002/esp.1886

[17] Vergari, F., Troiani, F., Faulkner, H., Del Monte, M., Della Seta, M., Ciccacci, S., Fredi, P., 2019. The use of the slope–area function to analyse process domains in complex badland landscapes. Earth Surf. Process. Landf. 44, 273–286. https://doi.org/10.1002/esp.4496

[18] Neugirg, F., Stark, M., Kaiser, A., Vlacilova, M., Della Seta, M., Vergari, F., Schmidt, J., Becht, M., Haas, F. (2016). Erosion processes in calanchi in the Upper Orcia Valley, Southern Tuscany, Italy based on multitemporal high-resolution terrestrial LiDAR and UAV surveys. Geomorphology, 269, 8–22. https://doi.org/10.1016/j.geomorph.2016.06.027

[19] Stark M., Heckmann T., Piermattei L., Dremel F., Kaiser A., Machwski P., Haas F., and Becht M. (2021). From consumer to enterprise grade: How the choice of four UAS impacts point cloud quality. *Earth Surface Processes and Landforms* 46:2019–2043. https://doi.org/10.1002/esp.5142

A new perspective on geohazards assessment: leveraging gigapixel imaging technique

Saverio Romeo[1], Alessandro Fraccica, Valerio Vitale
Geological Survey of Italy, ISPRA - Italian Institute for Environmental Protection and Research
Via Vitaliano Brancati, 60 - 00144 Roma, Italy
[1] saverio.romeo@isprambiente.it

Cite as: Romeo, S., Fraccica, A., Vitale, V. (2025). A new perspective on geohazards assessment: leveraging gigapixel imaging technique. In: Proceedings of Geomorphometry 2025, 9-13 June, Perugia, Italy. M. Alvioli, L. Melelli, I. Marchesini eds. CNR Edizioni, Rome. ISBN 978-88-8080-765-0. DOI: 10.5281/zenodo.15425893

Abstract—**The growing frequency of geohazards such as landslides, rockfalls, and slope instabilities, often intensified by climate change and human activities, underscores the urgent need for effective assessment and monitoring tools. Conventional remote sensing techniques like LiDAR, aerial photogrammetry, and satellite interferometry (InSAR) often rely on substantial financial and technical resources, which limit their accessibility. In response, Gigapixel imaging emerges as an innovative and cost-effective alternative, offering ultra-high-resolution visual data to support geohazard assessment while raising awareness among stakeholders and the public. The system used captures hundreds of partially overlapping images in sequence using a robotic head, effectively minimizing parallax errors. With accurate image stitching, it becomes possible to reconstruct an exceptionally detailed 2D gigapixel image. Also, the use of well-known photogrammetric technique allows the generation of 3D models from very high-quality images obtaining Very-High Resolution products. The CDRI's fellowship GIGA^2 - Gigapixel Imaging for Geohazards Assessment and Awareness is aimed at exploring the practical implications of integrating Gigapixel imaging into geohazard monitoring. Beyond its technical advantages, it promotes inclusivity in geoscience by providing an accessible and impactful tool for communicating risks and fostering preparedness. By bridging the gap between advanced technology and practical applications, Gigapixel imaging offers a promising pathway for enhancing geohazard assessment and resilience in vulnerable areas.**

I. INTRODUCTION

Nowadays, many geological representations are available, with the majority existing in 2D formats (e.g., geological maps), and only a sparse few in 3D formats (e.g., point clouds, block diagrams, etc.). Enhancing geological mapping poses a challenge, demanding more precise data collection and the seamless integration of information for the development of improved 3D models. Advancements in remote sensing, computer vision, and photogrammetry have significantly enhanced our ability to analyze and interpret geohazards, enabling early warnings and informed decision-making. Terrestrial remote techniques providing high-resolution 3D products for geohazard mapping and monitoring have undergone extensive testing, offering detailed insights into processes such as landslides, rockfalls, slope instabilities, and subsidence, especially where there is poor site accessibility. Despite this, their widespread usage remains limited. Indeed, conventional remote sensing techniques like LiDAR, aerial photogrammetry, and satellite interferometry (InSAR) often offer limited accessibility due to substantial financial and technical requirements, especially in Low-Income Countries. Gigapixel imaging could become a valid and cost-effective alternative. This technique captures ultra-high-definition optical images composed of billions of pixels. It allows combination with photogrammetric and imaging techniques like Structure from Motion (SfM) and Image stitching. This approach enables the creation of detailed two- and three-dimensional representations of geological features and processes which are strongly affected by spatial variability. These capabilities make it a versatile tool for geotechnical monitoring, back-analysis support tool, geoscience education, and public awareness campaigns [e.g., 1, 2, 3, 4, 5].

For instance, the ultra-detailed data produced by Gigapixel imaging can effectively convey geohazard risks to policymakers and local communities, enhancing understanding and preparedness. Its affordability and ease of use further broaden its appeal, making it accessible to researchers, professionals, public agencies, and NGOs.

Within this context, the CDRI (Coalition for Disaster Resilient Infrastructures) fellowship named "GIGA^2" is aimed at exploring practical uses and implications of integrating Gigapixel imaging

into more conventional monitoring and site assessment, through study sites presenting different geohazard typologies.

Following, Section 2 describes the experimental setup, the methods and instruments used, and the processing procedures. Section 3 introduces the selected case studies identified in the context of this project. Finally, Section 4 summarizes the gained knowledge, highlights the main limitations of the presented approach, and provides an outlook for future work.

II. METODOLOGY

Gigapixel images consisting of digital images comprised of billions of pixels or more. While typical modern cameras boast sensors with over 20 million pixels (20MP), they fall short of directly creating Gigapixel images. However, leveraging innovative technologies and instruments (e.g., GigaPan) enables achieving remarkable results. More in detail, the proposed research is performed by coupling Image stitching with Structure from Motion (SfM) photogrammetric technique to analyse geohazards within complex contexts obtaining Very-High Resolution products (e.g. Point Cloud). In other words, the integration of such techniques allows the generation of 3D models from very high-quality images. This also allows assessing scenarios from remote locations (e.g. 1km away) ensuring the safety of the technicians involved. Moreover, such Gigapixel images, if acquired in different time periods, can also be compared by using Digital Image Correlation (DIC) techniques.

Therefore, this study is based on a mixed-method research methodology which uses the characteristics of both quantitative and qualitative research methodologies in the same study. This is because by combining the two types of data (quantitative and qualitative) it is possible to benefit from both the detailed and contextualized insights of qualitative data (e.g., gigapixel images and its geological interpretation) and quantitative data (e.g., point clouds and geo-structural analysis). Image acquisition is performed through a 20MP DSLR camera equipped with a telephoto zoom lens (200-500mm). This acquisition stage is performed by means of robotic mounts empower DSLR camera to take thousands of aligned and overlaid photos, which are combined and stitched to create a single highly defined image allowing the view of many details.

III. PRACTICAL APPLICATION AND IMPLICATIONS

The Gigapixel approach has various practical applications depending on the context where it is used as it allows 3D information to be obtained from 2D image sequences. Three main geohazards are addressed in the present research work: rockfalls, shallow landslides and debris flow. Study sites have been selected as part of research projects currently in progress and which directly involve the Geological Survey of Italy (ISPRA, Italian Institute for Environmental Protection and Research). Also, in order to make the experiment more efficient also from a logistical point of view, nearby sites within a radius of 150 km were considered (Figure 1). However, sites with very different conditions in terms of geological setting, topography and geohazards and exposed value were identified (Table I).

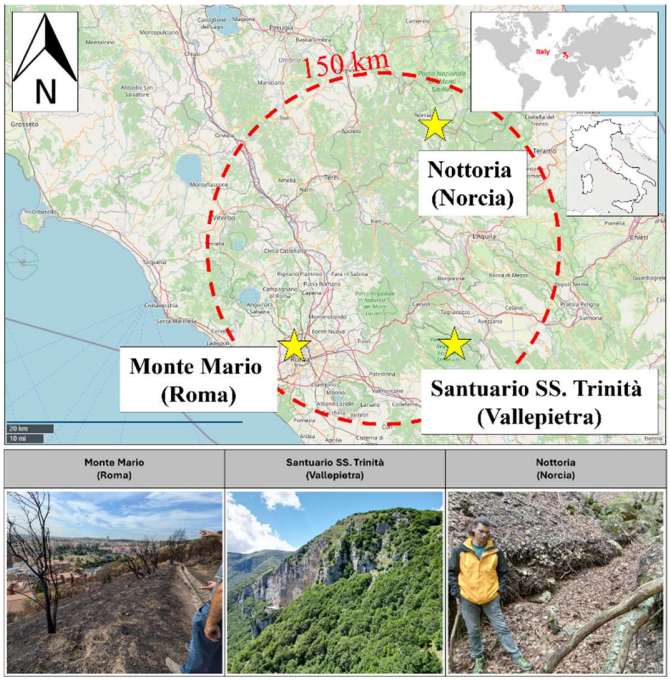

Figure 1. Location of the three study sites used in this work.

TABLE I. DRIVING PARAMETERS FOR THE SELECTION OF STUDY SITES.

	Study sites		
	Monte Mario (Roma)	***Santuario S. Trinità (Vallepietra)***	***Nottoria (Norcia)***
Geohazards	Rainfall-triggered shallow landslide	Rockfall	Debris flow
Exposed items	Densely populated urban area	Historical shrine	Mountain village
Main stakeholders	Civil Protection Department (Municipality of Rome)	Municipality of Vallepietra	Local university

As regards the rockfall case study (Santuario S. Trinità, Vallepietra), a discontinuity set detection and assessment have been carried out from a very high-resolution point cloud. Such a point cloud has been generated starting from 3 Gigapixel acquisitions, the results of which have been in turn processed

through SfM technique. Therefore, by using the open-source software Discontinuity Set Extractor (DSE) which enables the assessment of the joint families' orientation and spacing (Figure 2b), the jointed rock wall has been characterized [6]. Traditional geological survey allowed to confirm data obtained from images (Figure 2a). Such quantitative representation of the rock-wall permitted building a 3D model in RocScience finite element code, considering the discontinuities' geometry (Figure 3). Rock materials and joints were attributed to the respective stiffness and strength properties evaluated by a rock mechanics laboratory and field investigation [7].

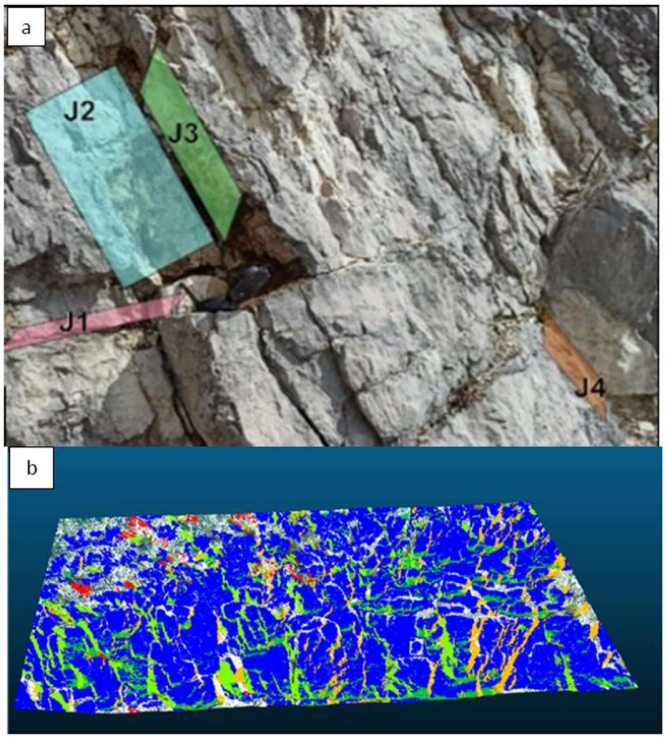

Figure 2. a) Jointed rock-wall under study, with rock joints identification by a field survey, b) Joint families detected from DSE software.

For the represented case, a boundary condition of null displacements only was imposed on the bottom and on the two smaller lateral faces of the model. This allowed us to represent continuity with the adjacent rock-wall portions and with the intact background, in order to limit the extent of the 3D model and to reduce the computational effort. A stability analysis was conducted, revealing the main rockfall kinematics (wedge failure, Figure 3) to be expected given the discontinuities orientations and the mechanical properties of the rock mass. This model could be also used to perform back-analyses referring to past rockfall events within the monitored area.

Within the shallow landslide case (Monte Mario, Roma), from a Digital Surface Model (DSM) derived from gigapixel photogrammetry a 2-dimensional simulation with limit equilibrium and finite element models have been performed by transposing the geological-technical slope model to a numerical model.

Finally, a debris flow case (Nottoria, Norcia) has been analyzed: in this case, given the presence of dense vegetation, Gigapixel images were used for a qualitative assessment of the scenario investigated (e.g., shape detection, vegetation regrowth, presence of debris, etc.). Using the approach presented in this paper, an attempt was made to create a Digital Terrain Model (DTM) and then derive some of the main Geomorphic indexes (e.g. Terrain Ruggedness Index, Slope, Valley Depth, etc.). Due to the noisy data, the data are not considered to be reliable.

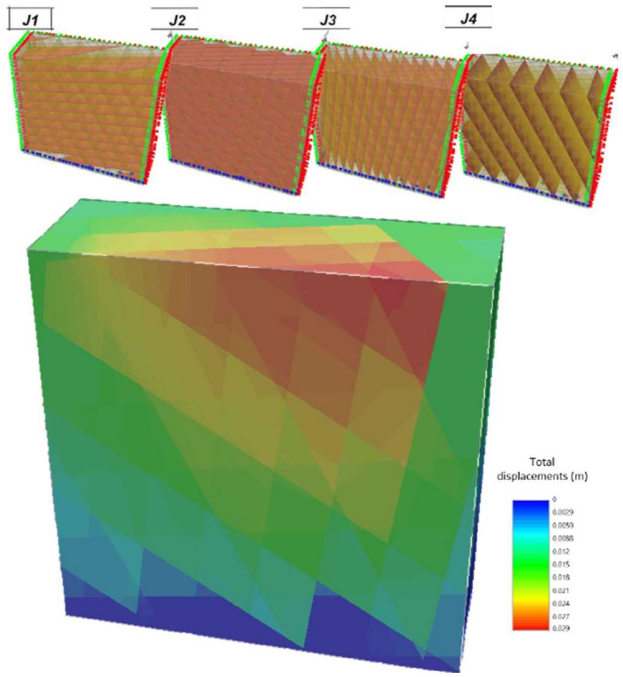

Figure 3. Joint sets used in the model and results from the FEM stability analysis.

IV. RESULTS AND CONCLUSIONS

The photogrammetric processing of Gigapixel data represents an unconventional approach in the analysis for geohazard assessment. Given its low cost and ease of deployment and use, it would be particularly relevant for the safety of linear infrastructure including roads, railways, and pipelines, with a special focus on mountainous regions. The main limitation is due to the nature of the photographic sensor: with low light conditions expect poor results. Although tests have been carried out at multiple sites affected by different geohazards, the proposed approach can be

expected to have further limitations due to the geometry of the survey. For example, in the case of considerable sensor-scenario distances, or a limited field of view due to shadow areas, the acquisition of the data and therefore the creation of a three-dimensional model would be of poor definition or with sectors with missing data (e.g., holes) respectively.

Both new technology and techniques tested and validated in this project and still underestimated in the field of geosciences, fully fall within the field of terrestrial remote sensing. The photogrammetric processing of Gigapixel data would represent an innovative turning point in quantitative analysis for geohazard assessment. Potentially, the results achieved during the project could open new lines of research and experiments in the field of terrestrial remote sensing using optical sensors. In any case, the products that will be achieved and their impact will be easily assessable as they are basic products that are usually used in professional work. Potential stakeholders are researchers, technologists as well as practitioners. Further potential implementation will concern the use of thermal sensors (e.g. thermal cameras) which the proponents undertake to evaluate as a further test to be carried out on the field.

V. ACKNOWLEGMENTS

The authors want to thank the Coalition for Disaster Resilient Infrastructure (CDRI), which funded the project "*GIGA^2: Gigapixel Imaging for Geohazards Assessment and Awareness*" under the Fellowship Program (Cohort 2024-25). This paper was written as part of the aforementioned project.

REFERENCES

[1] Lato M.J., G. Bevan, and M. Fergusson, 2012. "Gigapixel Imaging and Photogrammetry: Development of a New Long Range Remote Imaging Technique". Remote Sens. 2012, 4, 3006-3021; https://doi.org/10.3390/rs4103006.

[2] Romeo S., L. Di Matteo, D.S. Kieffer, G. Tosi, A. Stoppini, and and F. Radicioni, 2019. "The Use of Gigapixel Photogrammetry for the Understanding of Landslide Processes in Alpine Terrain". Geosciences 2019, 9, 99; https://doi.org/10.3390/geosciences9020099.

[3] Romeo S., A. Cosentino, F. Giani, G. Mastrantoni, and P. Mazzanti, 2021. "Combining Ground Based Remote Sensing Tools for Rockfalls Assessment and Monitoring: The Poggio Baldi Landslide Natural Laboratory". Sensors 2021, 21, 2632. https://doi.org/10.3390/s21082632.

[4] Javadi P., L. García-Asenjo, R. Luján, and J.L. Lerma, 2024. "Assessment of Panorama Photogrammetry as a Tool for Long-Range Deformation Monitoring". Sensors 2024, 24, 3298. https://doi.org/10.3390/s24113298.

[5] Nourbakhsh I., C. Acedo, R. Sargent, C. Strebel, L. Tomokiyo, and C. Belalcazar, 2010. "GigaPan conversations: Diversity and inclusion in the community" in Proc. Int. Sci. Conf. Technology Development, United Nations, Lausanne, Switzerland, 2010.

[6] Riquelme, A., Tomás, R., Cano, M., & Abellán, A. (2016). Using open-source software for extract-ing geomechanical parameters of a rock mass from 3D point clouds: Discontinuity Set Extractor and SMRTool. In Rock Mechanics and Rock Engineering: from the past to the future, 2016 International Symposium of the International Society for Rock Mechanics (ISRM 2016).

[7] Fraccica, A., Romeo, S., D'Angiò, D., Chiessi, V., Monti, G. M., Spiniello, O., ... & De Santis, F. (2024). Manual and semi-automatic approaches for rock mass discontinuities recognition and kinematic analyses: A case study on the rock wall of the Vallepietra Shrine (Central Italy). In New Challenges in Rock Mechanics and Rock Engineering (pp. 1174-1179). CRC Press.

A comparative study of mass movement morphometry in two adjacent watersheds of southern Italy

Lucia Contillo[1], Giusy Dimola, Giuseppe Corrado, Marcello Schiattarella
Department for Human, Scientific and Social Innovation (DIUSS)
Basilicata University
Matera, Italy
[1]lucia.contillo@unibas.it

Cite as: Contillo, L., Dimola, G., Corrado, G., Schiattarella, M. (2025). A comparative study of mass movement morphometry in two adjacent watersheds of southern Italy. In: Proceedings of Geomorphometry 2025, 9-13 June, Perugia, Italy. M. Alvioli, L. Melelli, I. Marchesini eds. CNR Edizioni, Rome. ISBN 978-88-8080-765-0. DOI: 10.5281/zenodo.15148025

Abstract— **This study examines the integration of geomorphometric and geological data to understand landslide dynamics in the Bradano and Basento river basins in southern Italy. Despite their proximity and shared climatic conditions, these basins display distinct geomorphological and lithological features, making them ideal for a comparative analysis.**

High-resolution digital elevation models (DEMs) and landslide data from official databases were combined with key geomorphometric indices. This approach allowed a detailed assessment of mass movement distributions and their relationships with geological and morphological factors. Results reveal substantial differences between the basins. Furthermore, significant variability inside the same basin was observed, with landslides unevenly distributed across lithological units and valley sides.

This research underlines the value of integrating geomorphometric and geological analyses to identify patterns in landslide susceptibility and spatial variability. The findings highlight the critical role of local geological settings in shaping mass movement dynamics and stress the need for basin-specific strategies for risk assessment and land-use planning. Future work will refine this integrated methodology and explore predictive models to evaluate the potential impacts of climate change on landslide activity in the region's diverse landscapes.

I. Introduction

This study focuses on two adjacent fluvial basins, the Bradano and Basento river catchments, significatively different from geological and geomorphological viewpoints. Such basins are located astride the border between Lucanian and Apulian regions in the case of the Bradano River catchment [1], and entirely in Basilicata in the case of the southernmost Basento basin. Both are in southern Italy and therefore share similar climatic conditions [2, 3], but their divergent topographical and geological attributes make them the ideal candidates for this kind of investigation, aiming to stress the different mass movement arrangement eventually linked to local control factors. As a matter of fact, landslides represent the expression of a cumulative geomorphological vulnerability, influenced by climatic, geomorphometric and geological factors [4, 5, 6, among others]. Although it is not possible, in many cases, to precisely date landslide events, multi-temporal climate analysis provides valuable information on predisposing conditions and potential climate-related triggers by the identification of climate trends and critical rainfall thresholds [7, 8, 9]. On the other hand, the morphometric comparison between two basins under the same climatic forcing may furnish the keys for a better comprehension of spatial distributions of gravitative events [6].

The study area is characterized by a complex setting, hosting river basins with distinct lithological, structural, and morphological features, whose watercourses cut geological units of both the orogenic chain and foredeep domain. The increasing frequency of extreme weather events, driven by climate change, necessitates a deeper understanding of how these phenomena manifest in regions with varying geomorphological characteristics.

II. Methodology

High-resolution digital elevation models (DEMs) integrated by new field data were employed to analyse the spatial distribution and characteristics of landslides in the two basins.

Landslide data were acquired and processed from official databases, including PAI (*Piano Assetto Idrogeologico*) and IFFI (*Inventario dei Fenomeni Franosi in Italia*), besides from published and/or original geothematic maps and geodatabases of the authors. Key geomorphometric indices [10] were calculated to provide a quantitative comparison of the two basins, including Asymmetry Factor (Af); Transverse Topographic Symmetry Factor (T); Valley Floor Width-to-Height Ratio (Vf). In addition, more landslide-related parameters were calculated in function of different geological and morphological zonation of the study area.

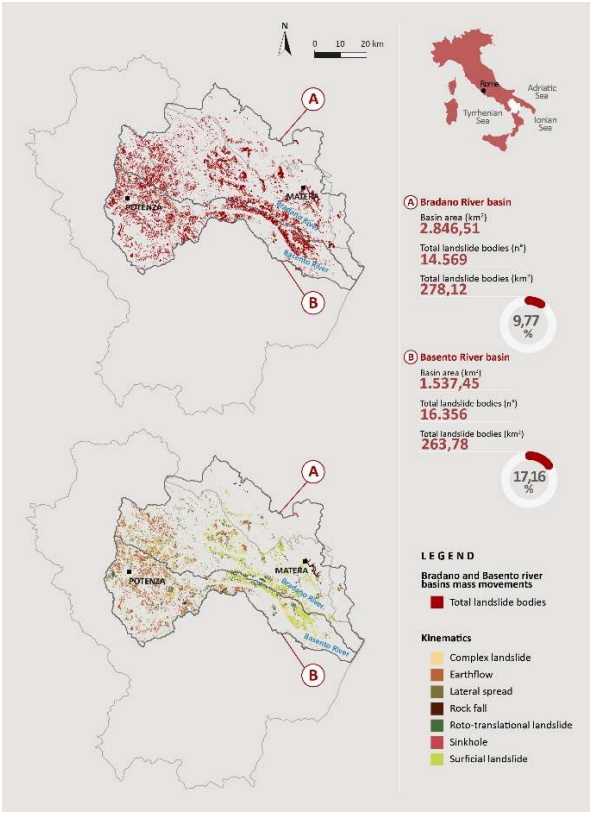

Figure 1. Data comparison of mass movements of the Bradano and Basento river basins.

III. DATA ANALYSIS AND PRELIMINARY REMARKS

The comparative analysis revealed significant differences in the frequency, type, and spatial distribution of mass movements between the two basins. As Fig. 1 shows, in the Bradano river basin (covering an area of 2.846,51 km²), 14.569 landslide bodies were identified, corresponding to 278,12 km² of landslide-affected area (about 9,77% of the total basin area). In contrast, the Basento river catchment (1.537,45 km²) exhibited 16.356 landslides, affecting 263,7 km² (about 17,2% of the basin's area).

The quantitative geomorphic analysis of landslides and their morphometric parameters showed that significant differences exist also inside the same catchment, such as unequal distributions of mass movements in the left and right orographic side of the main valleys. The right orographic sides of the Bradano and Basento river basins show similar patterns in terms of landslide density, but the percentage of landslide-affected area is higher in the Basento river valley (7,66% vs. 4,67%). The left orographic side of the Basento watershed, despite its smaller area compared to the left side of the Bradano ones (Fig. 2), shows a significantly higher percentage of landslide-affected area (9,49% vs. 5,10%). Overall, the Basento fluvial basin is more prone to landslides, with nearly double the percentage of landslide-affected area compared to the Bradano basin (17,15% vs. 9,77%). These findings underline how landslide distribution is strongly influenced by the morphology, lithology, and local control factors specific to each orographic side and orographic basin. The high density and extent of landslides on the left side of the Basento river valley suggest particularly predisposing geomorphological and geological conditions to be investigated (Table 1). Calculations of morphotectonic indices, in progress, will help to detect the recent to present deformational behaviour of the basins.

The analysis of the single lithological units shows percentage peaks of landslides in the arenaceous and clayey units of the foredeep, whereas in the Apennine chain higher percentages (up to 30% ca.) are recorded for the clay-dominant formations (deep-water units) and marly-arenaceous stratigraphic successions (mainly Miocene flysch units). In relation to the kinematics, in the entire study area the flows are the landslides that offer a greater contribution, followed by the roto-translational slides (Table 2).

This study highlights the importance of integrating geomorphometric and geological data to understand the arrangement and dynamics of mass movements in diverse landscape units.

TABLE I. DATA COMPARISON OF MASS MOVEMENTS IN THE RIGHT AND LEFT OROGRAPHIC SIDE OF THE BRADANO AND BASENTO RIVER VALLEYS.

Right and Left orographic side				
Bradano River valley				
	Area (sq.km)	***N. landslide bodies***	***Landslide area (sq.km)***	***%***
Right	851,1	8509	132,89	4,67
Left	1995,41	6113	145,23	5,10
Total	2846,51	14622	278,12	**9,77**
Basento River valley				
	Area (sq.km)	***N. landslide bodies***	***Landslide area (sq.km)***	***%***
Right	910,8	7371	117,80	7,66
Left	626,65	9017	145,94	9,49
Total	1537,45	16388	263,74	**17,15**

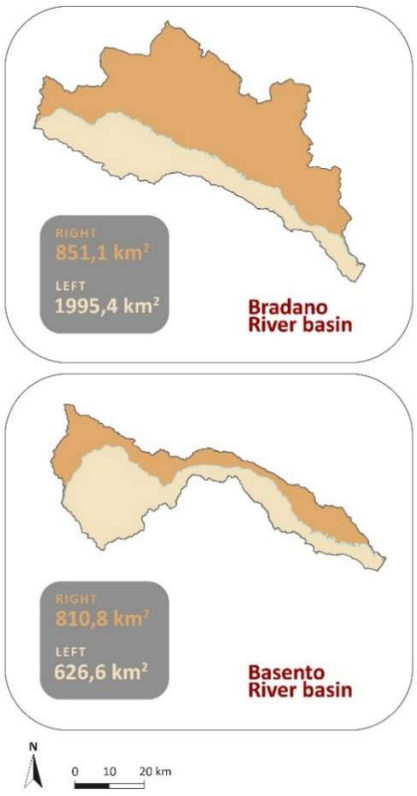

Figure 2. Right and left orographic side areas (km^2) comparison of Bradano and Basento river basins.

TABLE II. DISTRIBUTION OF LANDSLIDE BODIES AND RELATED KINEMATICS IN THE ENTIRE STUDY AREA OF THE BRADANO AND BASENTO RIVER BASINS (4383,96 KM^2).

Bradano and Basento river valleys landslide types			
Kinematics	***N. landslide bodies***	***Area (sq.km)***	***%***
Complex landslide	503	11,77	**0,27**
Earthflow	16307	205,95	**4,70**
Lateral spread	16	0,61	**0,01**
Rock fall	545	14,54	**0,33**
Roto-translational landslide	6211	72,43	**1,65**
Sinkhole	86	1,52	**0,03**
Surficial landslide	7257	235,06	**5,36**
Total	30925	541,87	**12,36**

The findings emphasize the need for tailored risk management strategies [11], considering the complex interplay among landslide-triggering factors of each basin, and represent the grounds for the construction of geomorphic susceptibility maps and related predictive scenarios under a changing climate.

IV. ACKNOWLEDGMENTS

This work was granted by Next Generation UE - PNRR Tech4You Project funds assigned to Basilicata University (PP4.3.2 - Parks, forests, landforms, rural landscapes, and multifunctional agriculture, Scientific Coordinator: Professor Marcello Schiattarella) - Technologies for climate change adaptation and quality of life improvement", field of intervention "5. Climate, Energy 289 and Sustainable Mobility", Code ECS00000009 – CUP C43C22000400006.

REFERENCES

[1] Azzillonna, V., L. Contillo, G. Corrado, G. Dimola, E. Giaccari, P. Giannandrea, D. Gioia, and M. Schiattarella, 2023, Multistadial physiographic evolution of the Bradano River catchment in Southern Italy. Geografia Fisica e Dinamica Quaternaria, 46(1-2), 125-134.

[2] Piccarreta, M., A. Pasini, D. Capolongo, and M. Lazzari M., 2013, Changes in daily precipitation extremes in the Mediterranean from 1951 to 2010: The Basilicata region, southern Italy. International Journal of Climatology, 33.

[3] Samela, C., V. Imbrenda, R. Coluzzi, L. Pace, T. Simoniello, and M. Lanfredi, 2022, Multi-Decadal Assessment of Soil Loss in a Mediterranean Region Characterized by Contrasting Local Climates. Land, 11, 1010.

[4] Lazzari M., Piccarreta M., Capolongo D. (2013) - Landslide Triggering and Local Rainfall Thresholds in Bradanic Foredeep, Basilicata Region (Southern Italy). Landslide Science and Practice, 671-677.

[5] Lazzari, M., D. Gioia, and B. Anzidei, 2018, Landslide inventory of the Basilicata region (Southern Italy). Journal of Maps, 14(2), 348-356.

[6] Marchesini, I., M. Rossi, A. Mondini, M. Santangelo, and F. Bucci, 2014, Morphometric signatures of landslides. Proceed. Third Open Source Geospatial Research & Education Symposium (OGRS), Espoo, Finland, 10-13 June 2014.

[7] Gariano, S.L., G.G.R. Iovine, M.T. Brunetti, S. Peruccacci, S. Luciani, D. Bartolini, M.R. Palladino, G. Vessia, A. Viero, C. Vennari, L. Antronico, A.M. Deganutti, F. Luino, M. Parise, O.G. Terranova, and F. Guzzetti F., 2012 Populating a catalogue of rainfall events that triggered shallow landslides in Italy. Rend. Online Soc. Geol. It., 21, 396-398.

[8] Vennari, C., S. L. Gariano, L. Antronico, M. T. Brunetti, G. Iovine, S. Peruccacci, O. Terranova, and F. Guzzetti, 2014, Rainfall thresholds for shallow landslide occurrence in Calabria, southern Italy. Nat. Hazards Earth Syst. Sci., 14, 317-330.

[9] Pánek, T., 2019, Landslides and Quaternary climate changes—The state of the art. Earth-Science Reviews, 196, 102871.

[10] Keller, E.A., and N. Pinter, 2002, Active Tectonics, Earthquakes, Uplift and Landscape. 2nd Edition, Prentice Hall, Upper Saddle River, 362 pp.

[11] Guadagno, F. M., and P. Revellino (eds.), 2009, Future Risk Assessment as a New European approach to landslide hazards (FRANE). Guidelines & Relevant Reports. Lengua, Cervinara (AV), 235 pp.

Comparing hybrid and machine learning models for rainfall-induced shallow landslide susceptibility

Florian Strohmaier
Department of Geography
Friedrich Schiller University Jena
Jena, Germany
florian.strohmaier@uni-jena.de

Alexander Brenning
Department of Geography
Friedrich Schiller University Jena
Jena, Germany

Cite as: Strohmaier, F., Brenning, A. (2025). Comparing hybrid and machine learning models for rainfall-induced shallow landslide susceptibility. In: Proceedings of Geomorphometry 2025, 9-13 June, Perugia, Italy. M. Alvioli, L. Melelli, I. Marchesini eds. CNR Edizioni, Rome. ISBN 978-88-8080-765-0. DOI: 10.5281/zenodo.15276265

Abstract— **Effective risk management for rainfall-induced mass movements necessitates models that simultaneously have predictive power and are interpretable. This study introduces a hybrid model combining machine learning and physical principles to enhance landslide susceptibility predictions under rainfall conditions. By integrating the predictive power of machine learning with an infinite-slope stability approach, we overcome traditional limitations in model parametrization. We utilized static and dynamic key factors such as terrain surface properties, lithological and tectonic setting, land cover/land use and accumulated precipitation to estimate effective cohesion, internal friction angle and soil parameters as latent variables of a Factor-of-Safety model based on the law of Mohr-Coulomb. We compared this approach with established physically-based and empirical models for a landslide/non-landslide point sample of 620 observations in a study area in northern and western Slovenia (400km²) where disastrous rainfall events happened in August and autumn 2023. A spatial block cross-validation yielded median Area under the Receiver Operating Curve values of 0.53 for the physical model, 0.85 for the benchmark empirical model and 0.66 for the hybrid model. Despite inferior model performance in discriminating between landslide and non-landslide points compared to the benchmark, the hybrid model allows for the interpretation, mapping and plausibility check of geomechanical and hydrological slope stability parameters.**

I. Introduction

Rainfall triggered landslides pose a significant threat to communities worldwide. Models that accurately predict landslide susceptibility can allow for more effective planning and risk management strategies.

Machine learning models have proven their predictive power in modelling landslide susceptibility, as they are capable of effectively capturing patterns and trends in large datasets without relying on explicit physical equations. Physically-based models, by contrast, reflect the underlying geomechanical and hydrological slope processes more plausibly. However, they require sophisticated parametrization through field work and laboratory testing and are not easily transferable from individual slopes to the regional-scale susceptibility mapping for spatial planning purposes.

In recent years, in an attempt to overcome the drawbacks of each of the modelling approaches, researchers successfully developed physically constrained machine learning models in the Earth system sciences [1,2]. The seminal paper by Reichstein et al. [3] provides an overview on how physical knowledge and machine learning techniques can be interlinked.

Following this paradigm we have developed a machine-learning approach that is constrained by a hybrid infinite-slope stability model. In comparison with traditional approaches to the parametrization of physically-based models, we use machine learning to estimate model parameters as latent variables by fitting the physical and machine learning part simultaneously.

We compared this hybrid, physically-informed machine learning approach with a traditional Factor-of-Safety model, and with established machine learning models (Generalized Additive Model, GAM) with the influence of dynamic predictors (antecedent rainfall) in terms of predictive performance.

II. Study Area

The study area of 400km² comprises three Slovenian municipalities located in those regions which have been most severely struck by flooding and rainfall-triggered mass movements after a rainfall event in August 2023 [4,5], and, to a lesser extent, in October and November 2023. Landslide data has been mapped in the field and from remote sensing data by GeoZS; mapping in other affected regions is still ongoing.

The neighbouring municipalities Ravne na Koroškem and Slovenj Gradec are located in north-central Slovenia at the border to Austria. The landscape is dominated by mountainous terrain and an inner alpine valley with alluvial sediment. Železniki in north-eastern Slovenia lies in the Southern Alps and their hilly karst forelands.

The complex lithology is governed by a tectonic setting in the border zone between the Dinarides and the Southern and Eastern Alps. In the Southern Alps and in the karstic area, limestones, dolomites and complex alternating sedimentary rocks prevail; metamorphic and volcanic rock types are predominant in the Eastern Alps. Especially the alternating sedimentary rocks are susceptible to landsliding.

Climate ranges from temperate-humid to alpine at higher elevations with maritime influence by the Mediterranean sea.

From August 3rd to 5th 2023, northern Slovenia was hit by severe rainfall with cumulative precipitation of more than 300mm within 72 hours, following an exceptionally wet period in May – July. This led to flooding and triggered mass movements such as debris flows and shallow landslides and caused fatalities and damage to infrastructure. The study area is located in the most affected areas. At the end of October and beginning November 2023 another series of rainfall events triggered further landslides in the study region, however to a lesser extent than in summer 2023.

III. Data and Methods

An inventory of landslide initiation points was compiled by GeoZS in a field survey and satellite-based mapping campaign shortly after the events. After the exclusion of areas flatter than a slope angle of 5°, 310 landslide initiation points were left for fitting the model. We randomly selected 310 non-landslide points in the study area with a minimum separation distance of 500m from the identified landslide points to account for the typical areal extent of shallow landslides, resulting in a total of 620 training points.

We generated a 10m digital elevation model (DEM) from a LiDAR point cloud with 1m ground resolution. We calculated slope angle, slope aspect, longitudinal and cross-sectional curvature after [6] as well as upslope contributing area and topographic wetness index (TWI) with a multiple flow direction algorithm [7] with SAGA GIS modules.

We calculated the distance of every landslide initiation point to active and probably active tectonic faults and reduced a lithological map to five classes of mineral types with similar mechanic properties. We reclassified Land Cover and Land Use (LULC) data to four classes. The datasets were provided by GeoZS.

For the northern part of Slovenia, integrated nowcast precipitation (INCA) data from Geosphere Austria is available. We aggregated hourly rainfall amounts to cumulative precipitation one day and 2-5 days before the landslide occurred.

As machine-learning benchmark models, we fitted a logistic GAM [8] with lithology and LULC as linear predictors and smoothing terms for topographic and tectonic variables and dynamic rainfall amounts. As our physically-based benchmark, following [9,10] we calibrated a Factor-of-Safety model where we consider bulk dry soil density ρ and a transmissivity-to-recharge ratio T/R as indicators for pore water pressure

$$FS = \frac{C' + cos(\beta)tan(\phi') \dfrac{1 - a/(sin(\beta)\, T/R)}{\rho}}{sin(\beta)}$$

with effective cohesion C', and effective friction angle ϕ' as well as ρ and T/R as unknown model parameters at each landslide initiation point. The local slope angle β and upslope contributing area a are given at each location. In the literature on infinite slope model calibration, C' is commonly assumed to be zero and stabilizing forces are attributed solely to the friction angle. Instead, in our model, we calibrated all model parameters for physical plausibility and comparability.

In the hybrid framework, we conceptualized the parameters C', ϕ', T/R and ρ as latent variables. Each of them was represented by a linear combination, or weighted sum, of terrain properties, LULC, geological units and precipitation. This hybrid Factor-of-Safety model was fitted with landslide occurrence as target variable.

We estimated model performance with spatial block k-fold cross validation with six folds and ten repetitions, resulting in a total of 60 training/test set splits. A comparison between spatial and non-spatial (random with 60 splits) cross-validation errors allowed for an assessment of the ability to generalize the modelled relationships. We used the Receiver Operating Curve (ROC) and the area under this curve (AUC) to compare the models' ability to discriminate between landslide and non-landslide initiation points.

We used R 4.3.3 with mgcv, SAGA GIS 9.5.1 for terrain model preprocessing and CloudCompare v2.12.x. All data was projected into EPSG:3794 Slovene National Grid 1996.

IV. Results and Discussion

Looking at model performance (fig. 1), preliminary results indicate that the hybrid model (median AUC 0.66) performs better than the physically-based slope stability model (median AUC 0.53, up to 0.68) but worse than the GAM (median AUC 0.85); all performance measures estimated by spatial block cross validation. However, the hybrid model is less prone to overfitting

than the GAM, indicated by just a slight drop in model performance for the spatial CV compared to non-spatial CV.

In the hybrid model, physically meaningful parameters are estimated as latent variables. Compared to purely machine-learning approaches, those latent variables can be mapped in space. Each latent variable is estimated by a separate regression model which is interpretable with established statistical means. This allows checks for plausibility of each of the model coefficients and thus predictor influences.

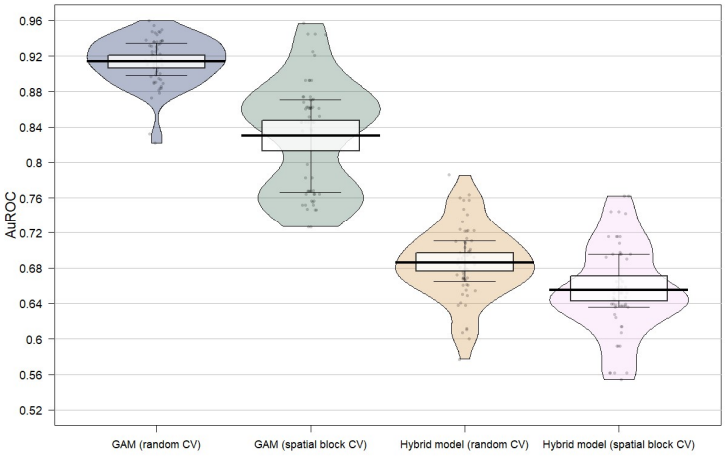

Figure 1. Distribution of Area under the Receiver Operating Curve (AUC) values estimated by random and spatial block cross validation for: GAM random CV (median AUC 0.92), GAM spatial CV (median AUC 0.85), Hybrid random CV (median AUC 0.68) and Hybrid model spatial CV (median AUC 0.66).

V. Outlook

The presented integration of physical with machine learning techniques in modelling rainfall-induced shallow landslide susceptibility demonstrates a robust and straightforward approach, achieving both satisfactory predictive power and interpretability.

Despite its effectiveness, opportunities for enhancement exist. Future work will focus on expanding the current linear regression model towards a more sophisticated non-linear modelling framework. Additionally, exploring the capabilities of more flexible artificial neural networks will offer a comparative assessment of model performance.

Given the significant influence of climate and weather dynamics on rainfall-induced landslide occurrence [11,12], incorporating rainfall thresholds into a hybrid hazard model is imperative when aiming at an integrated early warning system.

V. Acknowledgments

We are grateful to GeoZS and the Slovenian Environment Agency (ARSO) for providing terrain and landslide data. We especially thank Mateja Jemec Auflič and Jernej Jež from GeoZS for the discussions and their support.

References

[1] Kraft, B., Jung, M., Körner, M., Koirala, S., Reichstein, M., 2022. *Towards hybrid modeling of the global hydrological cycle.* Hydrol. Earth Syst. Sci. 26, 1579–1614. https://doi.org/10.5194/hess-26-1579-2022

[2] Dahal, A., Lombardo, L., 2025. *Towards physics-informed neural networks for landslide prediction.* Engineering Geology 344, 107852. https://doi.org/10.1016/j.enggeo.2024.107852

[3] Reichstein, M., Camps-Valls, G., Stevens, B., Jung, M., Denzler, J., Carvalhais, N., Prabhat, 2019. *Deep learning and process understanding for data-driven Earth system science.* Nature 566, 195–204. https://doi.org/10.1038/s41586-019-0912-1

[4] Bezak, N., Panagos, P., Liakos, L., Mikoš, M., 2023. *Brief communication: A first hydrological investigation of extreme August 2023 floods in Slovenia, Europe.* Nat. Hazards Earth Syst. Sci. 23, 3885–3893. https://doi.org/10.5194/nhess-23-3885-2023

[5] Peternel, T., Jemec Auflič, M., Šegina, E., Turk, D., Jež, J., Bavec, M., 2024. *May and August 2023: the extreme landslide events in Slovenia, triggered by extreme rainfall.* (poster) https://doi.org/10.5194/egusphere-egu24-16859

[6] Zevenbergen, L.W., Thorne, C.R., 1987. *Quantitative analysis of land surface topography.* Earth Surf Processes Landf 12, 47–56. https://doi.org/10.1002/esp.3290120107

[7] Freeman, T.G., 1991. *Calculating catchment area with divergent flow based on a regular grid.* Computers & Geosciences 17, 413–422. https://doi.org/10.1016/0098-3004(91)90048-I

[8] Hastie, T., Tibshirani, R., 1999. *Generalized additive models.* Chapman & Hall/CRC, Boca Raton.

[9] Goetz, J.N., Guthrie, R.H., Brenning, A., 2011. *Integrating physical and empirical landslide susceptibility models using generalized additive models.* Geomorphology 129, 376–386. https://doi.org/10.1016/j.geomorph.2011.03.001

[10] Meisina, C., Scarabelli, S., 2007. *A comparative analysis of terrain stability models for predicting shallow landslides in colluvial soils.* Geomorphology 87, 207–223. https://doi.org/10.1016/j.geomorph.2006.03.039

[11] Maraun, D., Knevels, R., Mishra, A.N., Truhetz, H., Bevacqua, E., Proske, H., Zappa, G., Brenning, A., Petschko, H., Schaffer, A., Leopold, P., Puxley, B.L., 2022. *A severe landslide event in the Alpine foreland under possible future climate and land-use changes.* Commun Earth Environ 3, 87. https://doi.org/10.1038/s43247-022-00408-7

[12] Jemec Auflič, M., Bezak, N., Šegina, E., Frantar, P., Gariano, S.L., Medved, A., Peternel, T., 2023. *Climate change increases the number of landslides at the juncture of the Alpine, Pannonian and Mediterranean regions.* Sci Rep 13, 23085. https://doi.org/10.1038/s41598-023-50314-x

Regional landslide prediction: comparing open-access Digital Elevation Models to delineate slope units

Mahnoor Ahmed [1], Giacomo Titti [2*], Sebastiano Trevisani [3], Lisa Borgatti [2], Mirko Francioni [1]

[1] Department of Pure and Applied Sciences, University of Urbino Carlo Bo, Urbino, Italy
[2] Department of Civil, Chemical, Environmental and Materials Engineering, ALMA MATER STUDIORUM University of Bologna, Bologna, Italy - *giacomo.titti@unibo.it

[3] Dipartimento di Culture del Progetto, University Iuav of Venice, Venice, Italy

Cite as: Ahmed, M., Titti, G., Trevisani, S., Borgatti, L., Francioni, M. (2025). Regional landslide prediction: comparing open-access Digital Elevation Models to delineate slope units. In: Proceedings of Geomorphometry 2025, 9-13 June, Perugia, Italy. M. Alvioli, L. Melelli, I. Marchesini eds. CNR Edizioni, Rome. ISBN 978-88-8080-765-0. DOI: 10.5281/zenodo.15284492

Abstract— **Digital Elevation Models (DEMs) significantly influence landslide studies including detection and prediction. Often, DEM selection is based on accessibility and resolution rather than accuracy. This study compares freely available global DEMs (ALOS, COP, FABDEM) and a national DEM (TINITALY) against a reference DEM (airborne LiDAR) to determine the most suitable model for capturing fine-scale morphology and SU partitioning in the Marche Region of Italy to contribute towards landslide susceptibility studies. The evaluation considered multiple factors, including differences in elevation, residual DEMs, roughness indices, slope variations, and SU delineation capability. Among the tested models, TINITALY, resampled to a 30x30m resolution, proved most effective for representing detailed terrain morphology. It was subsequently used to generate the optimal SU partition from 18 different configurations. These combinations were assessed using existing and newly integrated metrics, using mapped polygonal landslide inventories.**

I. INTRODUCTION

Freely accessible global Digital Elevation Models (DEMs) have been widely utilized for extensive geomorphological studies, which require modelling or analysis for mountainous terrains, where the DEMs accuracy is lower than in flat terrains [1], [2]. DEMs are commonly used in landslide modelling to predict and detect slope failures as well as derive terrain based characteristics where the accuracy is influenced by the quality and resolution of the DEM.

To assess the suitability of DEMs for landslide susceptibility and prediction, quality assessments have essentially been conducted. Therefore, global DSMs and a national Italian Digital Terrain Model (DTM) have been compared with a local high resolution (1m) elevation model (Airborne LiDAR) in the context of terrain representation and its delineation, referred to as "reference DEM" in the following text. Once the most accurate DEM has been selected, it was used to delineate the optimal Slope Units (SUs) partition. The Marche region, shown in Figure 1, was selected to test the two approaches proposed. The study area AOIa represents the Marche region which was used in the second methodological phase of SU delineation, while AOIb is a subset of the Marche region which is equipped with the necessary information required to complete a DEM comparison.

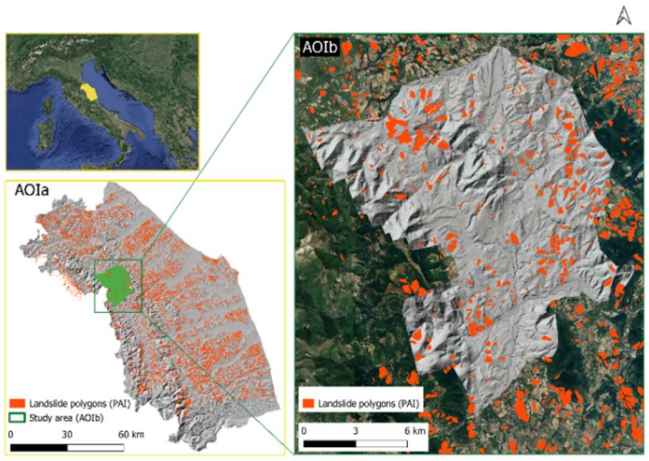

Figure 1. Central Italy divided in two study areas. AOIa; used in the second phase of analyses representing the Marche region. AOIb; used in the first phase of analysis by comparing LiDAR with public DEMs. Adapted from [3]

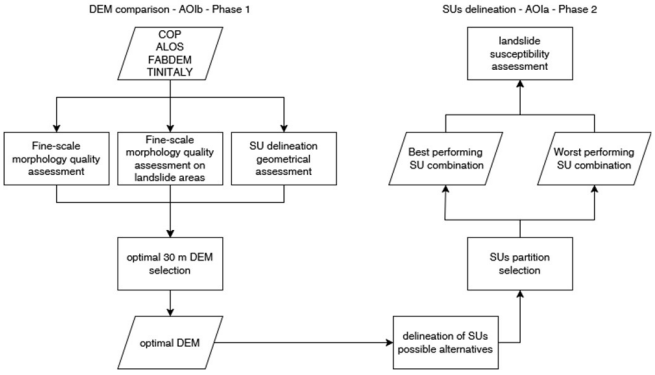

Figure 2. Methodology described according the two-phased analysis where Phase 1 involved DEM comparisons (AOIb) and Phase 2 is dedicated to SU delineations (AOIa). Adapted from [3].

II. MATERIALS AND METHODS

A. Phase 1: DEM assessment

The first phase (Figure 2) comprises of comparing global DEMs; Advanced Land Observing Satellite (ALOS) surveyed in 2006-2011, Copernicus Glo-30 (COP) from a mission of 2011-2015, Forest And Buildings removed Copernicus DEM (FABDEM), as well as the national Italian DEM TINITALY. These DEMs are compared with the reference DEM, which is an airborne LiDAR DTM at 1m resolution acquired in 2012 (https://gn.mase.gov.it/portale/pst-dati-lidar). The comparisons were made for the representation of fine-scale morphological characteristics such as roughness, slope and elevation in AOIb area.

B. Phase 2: Slope Unit delineation

Once the most suitable DEM has been identified, it was used to subdivide the AOIa area in SUs. Several combinations of input parameters have been compared to understand the most representative terrain partitioning (Figure 2). The software *r.slopeunits* [4] was used for SU generation and in particular two parameters were changed to create 18 combinations: the *minimum surface area* of SU (a) and the *minimum circular variance* for terrain (c). The combinations were evaluated by using three performance metrics: i) aspect segmentation (F) proposed by Alvioli et al. [4] that evaluates the segmentation based on internal homogeneity and external heterogeneity of SUs; ii) landslide density (D) which is representative of the mean number of landslides within a unstable terrain unit, signifying the use of landslide inventories to delineate SUs; iii) landslide extension (A) is the sum of the landslide areas contained within a SU respect to the total landslide areas. The product (S) of their normalized values ($\tilde{F}, \tilde{A}, \tilde{D}$), has been used to select the optimal SU delineation (Eq. 1).

$$S = \tilde{F} \cdot \tilde{A} \cdot \frac{1}{\tilde{D}} \quad (1)$$

These metrics have been introduced in this study as a new approach to integrate landslide polygons in terrain partitioning for landslide susceptibility modelling.

III. RESULTS

The differences in elevation, slope, isotropic roughness, radial roughness and residual elevation between the DEMs and the reference DEM are reported in Figure 3.

A notable observation is the similarity between COP and FABDEM. Since FABDEM (a DTM) is an improvement of a DSM (COP), it should theoretically provide a more accurate representation of the terrain, making it similar to the LiDAR reference. However, FABDEM does not exhibit smaller differences in comparison to COP when compared with the reference DEM. This can be explained by the motivation of FABDEM construction being for flood modelling [5]. Thus, the application of a DTM generated for hydrogeomorphology purposes may not perform strongly in applications of slope instability.

TINITALY10m and TINITALY30m were also compared with their respective resolutions to the LiDAR as shown in Figure 4. TINITALY30m shows lower differences across the metrics used. At the conclusion of Phase 1 the resampled 30m TINITALY DEM is the most suitable choice for SU delineation in the Marche region conducted within the Phase 2.

SU delineations were tested across a combination of parameters (18 combinations) and tested with F, A and D metrics, summarized in the S metric as shown in Table 1. The higher the S value, the better the SU representation is considered. The behavior of combinations shows that extreme values (low c and a, and high c and a) almost nullifies the S metric value since the SU are represented out of proportion.

Table 1. S metric values for corresponding parameters of 18 SU combinations. Adapted from [3].

S	**Minimum surface area (a) m²**					
Circular variance (c)	*40000*	*80000*	*150000*	*200000*	*300000*	*500000*
0.1	0	0.048	0.243	0.301	0.317	0.005
0.4	0.087	0.087	0.083	0.080	0.028	0.014
0.7	8.17 x10^{-5}	8.17 x10^{-5}	6.91 x10^{-5}	9.73 x10^{-5}	3.26 x10^{-5}	0

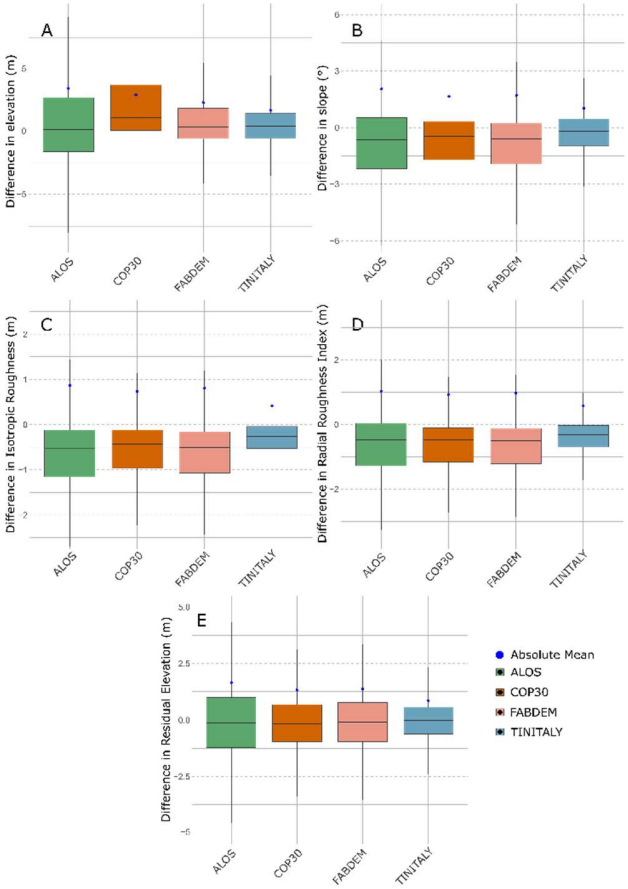

Figure 3. Boxplots showing the differences in metrics used to describe fine-scale morphology using the global/national DEMs and the reference DEM (30m). The metrics represented are; A) Elevation, B) Slope, C) Isotropic Roughness Index, D) Radial Roughness Index and E) Residual DEM. Adapted from [3].

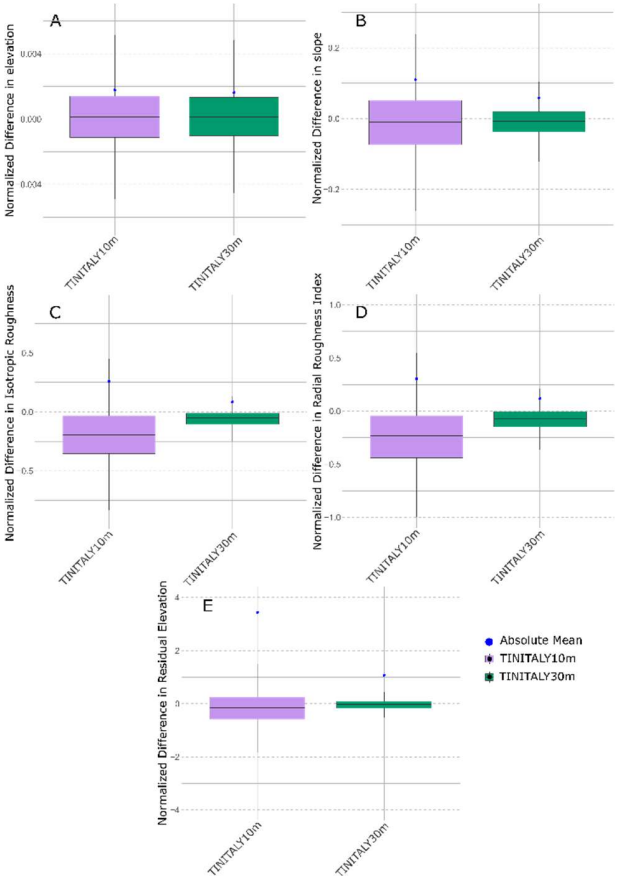

Figure 4. Boxplots depicting the differences in TINITALY at 10m and 30m against the reference DEM. The metrics represented are; A) Elevation, B) Slope, C) Isotropic Roughness Index, D) Radial Roughness Index and E) Residual DEM. Adapted from [3].

IV. Discussion

A comparison of global DEMs and the resampled 30m TINITALY against the reference airborne LiDAR DEM (resampled to 30m to match the resolution) revealed significant differences in selected geomorphometric derivatives within AOIb. While TINITALY 30m performs better against all other DEMs, it is also interesting to observe the low performance of TINITALY 10m. This can signify that areas of low-sampling density generate artifacts which are smoothed while upscaling the DEM and thus, affects the geomorphometric derivatives. Figure 5 also shows the visual differences in slope where TINITALY30m variates the least with the reference DEM and became an ideal choice to test SU parameters.

To assess the impact of terrain partitioning on the landslide susceptibility model, both the best SU partition (c = 0.1 and a = 300 × 10^3 m^2) and worst case (c = 0.7 and a = 150 × 10^3 m^2) landslide susceptibility scenarios were analyzed using a Generalized Additive Model. Notably, performance metrics such as Area Under the Curve (AUC), F1 score (F1), and Cohen's Kappa Index (Kappa) exhibited trends opposite to those of the S metric, indicating that higher S metric performance does not necessarily correspond to a better susceptibility model performance. This is a well-known behavior related to the smoothing effect of large SU on the explanatory variables which is represented by a single value per SU.

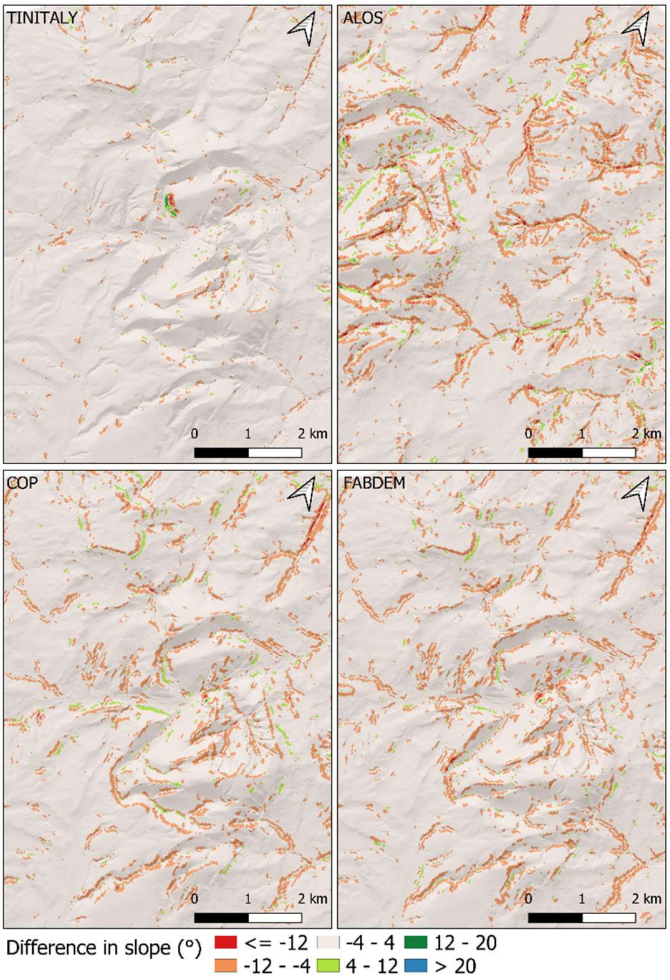

Figure 5. Mapped differences in slope (degrees) between the tested DEMs (30m) and the reference DEM, in a local zoom in of AOIb. Adapted from [3].

V. CONCLUSIONS

This study evaluates global and national DEMs for their ability to derive fine-scale terrain features. Among the tested DEMs (ALOS, COP, FABDEM, TINITALY), TINITALY30m showed superior performance and was used to generate optimized SU partitions.

Moreover, a new method to assess SU configurations based on internal homogeneity, external heterogeneity, landslide presence and landslide area has been proposed. Results show that terrain partitioning influences susceptibility modeling, though model performance metrics (AUC, F1, Kappa) don't always align with SU quality.

Future research should explore multi-temporal SU delineations using space-time inventories. Adapting SU delineation to evolving terrains, could significantly enhance landslide prediction accuracy.

REFERENCES

[1] Guth, P. L., Trevisani, S., Grohmann, C. H., Lindsay, J., Gesch, D., Hawker, L., Bielski, C., "Ranking of 10 Global One-Arc-Second DEMs Reveals Limitations in Terrain Morphology Representation," *Remote Sens (Basel)*, vol. 16, no. 17, p. 3273, 2024, doi: 10.3390/RS16173273.

[2] Trevisani, S., Skrypitsyna, T. N., Florinsky, I. V., "Global digital elevation models for terrain morphology analysis in mountain environments: insights on Copernicus GLO-30 and ALOS AW3D30 for a large Alpine area," Environ Earth Sci, vol. 82, no. 9, May 2023, doi: 10.1007/s12665-023-10882-7.

[3] Ahmed, M., Titti, G., Trevisani, S., Borgatti, L., Francioni, M., "Is higher resolution always better? Open-access DEM comparison for Slope Units delineation and regional landslide prediction," Natural Hazards and Earth System Sciences, 2025, doi: 10.5194/NHESS-2024-211.

[4] Alvioli, M., Marchesini, I., Reichenbach, P., Rossi, M., Ardizzone, F., Fiorucci, F., Guzzetti, F., "Automatic delineation of geomorphological slope units with r.slopeunits v1.0 and their optimization for landslide susceptibility modeling," *Geosci Model Dev*, vol. 9, no. 11, pp. 3975–3991, Nov. 2016, doi: 10.5194/gmd-9-3975-2016.

[5] Hawker, L., Uhe, P., Paulo, L., Sosa, J., Savage, J., Sampson, C., Neal, J., "A 30 m global map of elevation with forests and buildings removed," *Environmental Research Letters*, vol. 17, no. 2, 2022, doi: 10.1088/1748-9326/AC4D4F.

2.2 - Fluvial processes

Soil Erosion And Intensive Agriculture (Lessini Veronesi, NE Italy): Multi-Temporal Modelling On DEMs From Photogrammetry And Lidar

Barbara Rigon[1], Sandro Rossato[2], Giacomo Vinci[1], Stefano Castelli[1], Paolo Mozzi[1]

[1] Department of Geosciences, University of Padua
Via Gradenigo 6 – 35131 - Padova, Italy

[2]Institute of Geosciences and Georesources, National Research Council of Italy
Corso Stati Uniti, 4 - 35127 – Padova, Italy

Cite as: Rigon, B., Rossato, S., Vinci, G., Castelli, S., Mozzi, P. (2025). Soil Erosion And Intensive Agriculture (Lessini Veronesi, NE Italy): Multi-Temporal Modelling On DEMs From Photogrammetry And Lidar. In: Proceedings of Geomorphometry 2025, 9-13 June, Perugia, Italy. M. Alvioli, L. Melelli, I. Marchesini eds. CNR Edizioni, Rome. ISBN 978-88-8080-765-0. DOI: 10.5281/zenodo.15166872

Abstract—**The study evaluates the impact of intensive vine cultivation on soil erosion near Verona, in the Monteforte d'Alpone area, with an innovative technique consisting of the multi-temporal analysis of Digital Elevation Models (DEMs) derived from photogrammetry and LiDAR (Light Detection and Ranging).**
By applying the Revised Universal Soil Loss Equation (RUSLE) model to a 1981 DTM (Digital Terrain Model) generated through photogrammetry of aerial photos and to a LiDAR-derived DTM from 2008, the study analyses changes in soil erosion over time. The mean potential soil erosion rates calculated for the study area are 20.95 (Mg ha^{-1} yr^{-1}) in 1981 and 15.72 (Mg ha^{-1} yr^{-1}) in 2008, which are 20 and 15 times higher, respectively, than the thresholds considered sustainable in a comparable European-scale analysis (Verheijen et al., 2009). The results have been compared with DEMs generated in summer 2024 by drone-based photogrammetry and LiDAR, to evaluate accuracy and verify the correlation between erosion predictions and present field conditions.
The application of RUSLE modelling to estimate soil erosion yielded consistent results across the years 1981, 2008 and 2024, that were corroborated by observations carried out in the field, demonstrating it is possible to generate high-resolution DEMs from aerial photogrammetry, which are suitable for the application of soil erosion models, such as RUSLE.

I. INTRODUCTION

Vineyards are among the agricultural crops causing the highest rates of soil erosion (Pappalardo et al., 2019; Strafellini et al., 2022), a significant environmental issue that reduces biodiversity and increases slope instability (Pimentel et al., 2006). The hills of Monteforte d'Alpone, the production area of Soave DOC wine, provide an ideal setting to study soil erosion using the Revised Universal Soil Loss Equation (RUSLE) model (Renard et al., 1997). Widely adopted by the European Union for land management assessments, this empirical model combines data on topography, soil, precipitation, and land use within a GIS framework, relying on Digital Elevation Models (DEMs) (Pappalardo et al., 2019).
Until recently, the application of RUSLE has been constrained to recent scenarios due to the need for high-resolution DEMs that were poorly available before the advent of LiDAR technology. Nowadays, advancements in photogrammetric techniques allow for the generation of detailed DEMs from historical aerial photos (Natale et al., 2024), that enable multi-temporal analyses of soil erosion.
The aim of this study is to estimate the diachronic soil erosion in the Monteforte d'Alpone area by applying the RUSLE model to two DEMs from different time periods: the first one generated through photogrammetry from 1981 aerial photos, and the second one from 2008, obtained through LiDAR aerial surveys, in order to evaluate changes in potential soil erosion over time.

II. MATERIAL AND METHODS

A. Aerial photos

To assess the evolution of the morphology of the area, aerial photographs freely available on the Geoportal of the Veneto Region (https://idt2.regione.veneto.it/) were used. All photos

were georeferenced in QGIS, in order to evaluate the geomorphological evolution over time and identify areas subject to instability or frequent human interventions, indicators of potentially high soil erosion rates. Five areas of interest (A, B, C, D, E) were identified (Fig. 1). The reference system used is Monte Mario Zone 1 (EPSG: 3003), as it minimizes the distortion of the aerial photos during the georeferencing process. Once identified the five zones, direct observations were conducted in the field to evaluate the actual slope stability conditions.

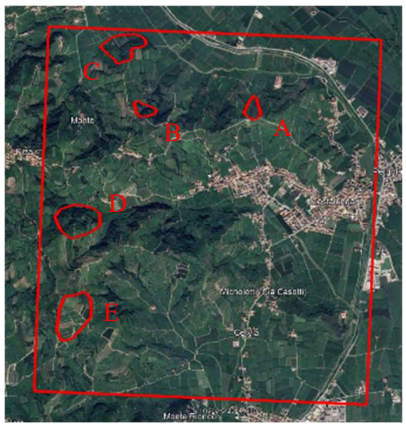

Figure 1: areas with probable instabilities identified through aerial photographs in QGIS.

B. Aerial photogrammetry

The 1981 DEM of the Monteforte d'Alpone area was created from 11 black-and-white aerial photos taken during the Reven flight (12 April–13 October 1981). Pre-processing involved FIJI/ImageJ software to improve image quality and align the photos for the subsequent photogrammetry in Agisoft MetaShape. Fiducial points ensured precise alignment, with one photo set as reference, oriented to cardinal directions. The BigWarp plugin helped match fiducial points between fixed and moving images, rotating them for accurate overlap. After alignment, the image contrast was adjusted based on the sharpest photo. The enhanced images were imported into Agisoft MetaShape, where masks excluded irrelevant areas, and a sparse points cloud (Fig. 2) was generated and georeferenced by placing markers. Image alignment was optimized using all available parameters, resulting in dense point clouds (Fig. 3).

Processing was done on a standard laptop (Intel Core i5-8265U, 24GB RAM) and took about 1.5 hours, demonstrating MetaShape's efficiency. Finally, the dense point cloud was used to create an orthomosaic and a DTM with a resolution of 1.48 m/pix and a Root Mean Square Error (RMSE) of 0.242 m (Fig. 4).

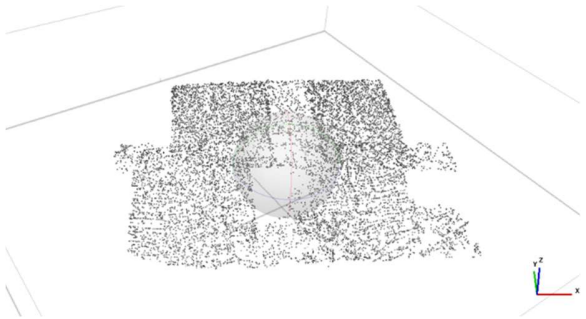

Figure 2: sparse point cloud obtained from photo alignment in Agisoft MetaShape.

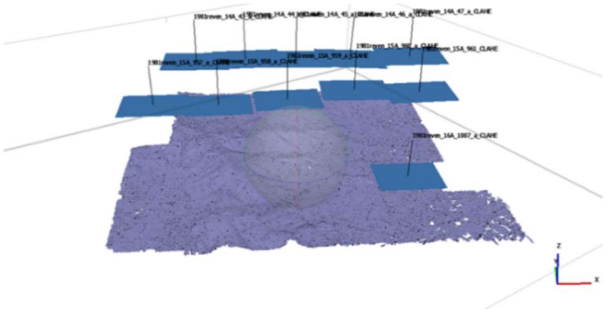

Figure 3: high quality dense cloud generated from the sparse points cloud in Agisoft MetaShape.

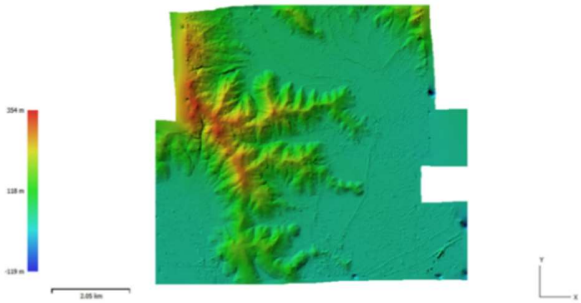

Figure 4: DTM obtained from 1981 aerial photos through photogrammetry with Agisoft MetaShape.

C. Drone photogrammetry and LiDAR.

Drones equipped for photogrammetry and LiDAR surveys were used to generate high-resolution DEMs, offering precise data on current conditions in the study area. These datasets were compared with 1981 and 2008 models to evaluate erosion and other terrain changes and provide images of the landslides occurring in the study area. The surveys were conducted in August 2024.

A drone-based photogrammetric DSM was produced for Zone B, which shows notable evidence of surface erosion. Data collection was carried out with a DJI MAVIC 3 ENTERPRISE drone, featuring a GNSS system with RTK corrections. Images were

taken during two flights along perpendicular paths to optimize coverage and reduce vegetation interference. Georeferencing used a "base-rover" system, with an Emlid Reach RS2+ GPS providing RTK corrections via the NTRIP network. The 422 images collected were processed in Agisoft MetaShape, creating a medium-quality dense cloud and a final DSM with 8.47 cm/pix resolution (Fig. 5).

LiDAR surveys were performed in zones B and C. Zone B, with significant surface erosion, and zone C, covered in dense vegetation, were surveyed using the Zenmuse L2 system mounted on a MATRICE 350 RTK drone. The LiDAR system produced DSM with resolution 0.5 m/pixel (Fig. 6). The RMSE has a value of 0.227 m.

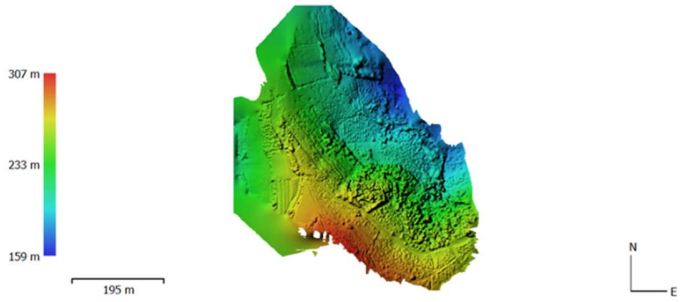

Figure 5: zone B DSM obtained from drone images through photogrammetry with Agisoft Metashape.

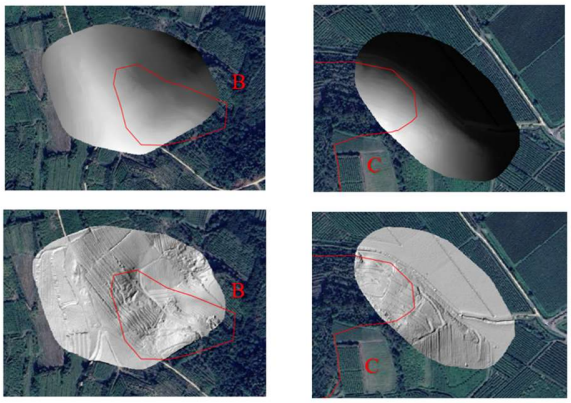

Fig. 6: zones B and C DSM obtained from LiDAR acquisitions. QGIS.

D. RUSLE

The RUSLE model (Renard et al., 1997), widely used in the European Union for land management assessments, was chosen for this study due to its proven effectiveness in similar contexts, such as the Prosecco DOCG region (Pappalardo et al., 2019). RUSLE calculates soil erosion rates (A) by integrating factors like rainfall erosivity (R), soil erodibility (K), slope length and steepness (LS), vegetation cover (C), and cultivation practices (P). Due to limited historical data and time constraints, the P factor was excluded from the equation. For each variable, separate raster datasets were generated in QGIS for 1981 and 2008.

Rainfall erosivity (R) was modeled using Panagos et al. (2021) data from the REDES (Rainfall Erosivity Database at European Scale) database. Precipitation data from seven ARPAV (Agenzia Regionale per la Prevenzione e Protezione Ambientale del Veneto) stations were interpolated to create raster layers for 1981 and 2008. The soil erodibility factor (K) was taken from the ESDAC (European Soil Data Centre) 2014 soil erodibility map, based on the 2009 LUCAS (Land Use/Cover Area frame Survey) survey. Slope length and steepness (LS), key morphological factors, were calculated using 1981 and 2008 DEMs processed for hydrological consistency with the Erosion Flow plugin. LS overestimations on structural highs matched findings by Benavidez et al. (2018) and were higher for 1981, due to the lower DEM resolution. Vegetation and land use (C) were derived from CORINE Land Cover data and ARPAV (2017) coefficients. Land cover polygons for 1981 and 2008 were manually digitized in QGIS, based on aerial photographs for 1981 and satellite imagery for 2008 and C values were accordingly assigned. Final soil erosion maps for 1981 and 2008 were generated by combining R, K, LS, and C rasters with the Raster Calculator tool of QGIS, using the 1981 DEM as the resolution reference. This ensured that all input and output rasters had a uniform resolution of 1.48 m/pix.

III. RESULTS AND DISCUSSION

The application of RUSLE in the Monteforte d'Alpone area for 1981 showed an average potential soil erosion rate of 20.95 (Mg ha^{-1} yr^{-1}), significantly higher than the European sustainable threshold of 1 (Mg ha^{-1} yr^{-1}) based on the expected soil formation rate of 1.4 (Mg ha^{-1} yr^{-1}) (Verheijen et al., 2009). Erosion was most severe on slopes and incisions due to surface runoff, while lower values were observed on flat areas (Fig. 7). Vineyards and arable lands, having the highest C values, contributed the most to erosion, while areas with dense vegetation, which have the lowest C values, had reduced rates.

By 2008, the average erosion rate decreased to 15.72 (Mg ha^{-1} yr^{-1}), showing modest improvement, but still exceeding the expected soil formation rate (Fig. 8). Erosion patterns remained similar, with high rates along steep slopes, indicating LS as the determining factor for the erosion rate. Land use remained a key factor, with vineyards and arable lands showing the highest erosion and vegetated areas offering a stabilizing effect.

A comparison between 1981 and 2008 highlighted the improved accuracy of the 2008 DTM, reducing overestimation of the LS factor on steep slopes. Changes in vegetation also affected erosion patterns: abandoned vineyards replaced by chestnut forests in Zone C reduced erosion, while vegetation loss in Zone D increased instability. Remedial measures such as afforestation and terracing stabilized soils in erosion-prone areas.

Results were confirmed through field observation and visual analysis of 2024 LiDAR and photogrammetric DEMs from drone on the small test areas. These data were compared with previous studies in the region (Pappalardo et al., 2019) and the 2016 ESDAC European erosion map, confirming its usefulness in assessing and predicting soil erosion.

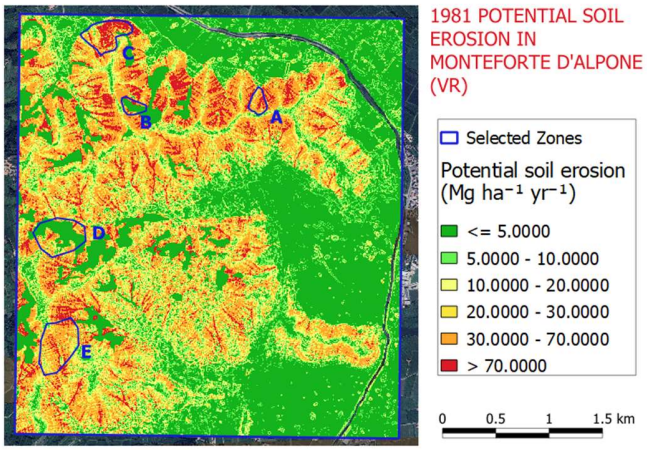

Figure 7: Soil erosion map of 1981 near Monteforte d'Alpone, produced using the application of RUSLE in QGIS**.**

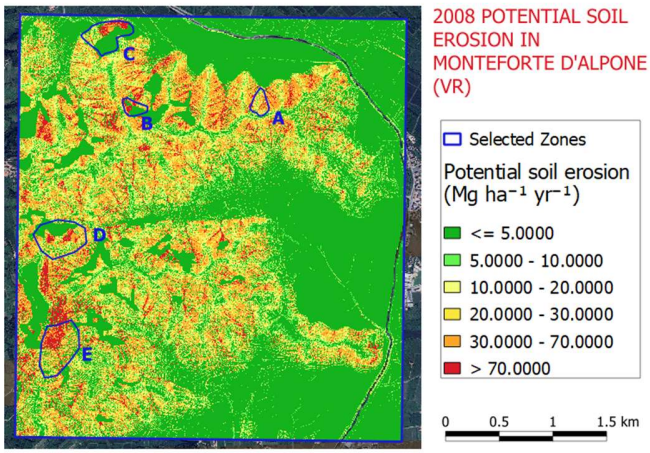

Fig. 8: Soil erosion map of 2008 near Monteforte d'Alpone, produced using the application of RUSLE in QGIS**.**

IV. CONCLUSIONS

In conclusion, it is possible to reconstruct high-resolution digital elevation models from historical aerial photographs using photogrammetry and to apply soil erosion models to analyze past and present land conditions. Using the RUSLE model, soil erosion was estimated for a 1981 DEM derived from photogrammetry and a 2008 DEM generated from LiDAR data, yielding results consistent with current field observations and land management practices.

The analysis of soil erosion changes between 1981 and 2008 correlates with land-use changes and slope modifications. Findings are consistent with similar studies, such as Pappalardo et al.'s 2019 erosion estimates in the Prosecco DOCG area and ESDAC's 2016 European soil erosion map.

There were difficulties in acquiring historical rainfall and soil data, particularly for 1981, which required making approximations to address the gaps.

The study emphasizes the critical role of DEM accuracy and resolution in determining soil erosion rates. Applying RUSLE to multi-temporal DEMs allows for comprehensive soil erosion analyses over time. Future improvements include refining the K factor with detailed soil data and incorporating the P factor through historical conservation and cultivation data to enhance result precision and support sustainable land management planning.

REFERENCES

[1] Pappalardo, S. E., Gislimberti, L., Ferrarese, F., De Marchi, M., & Mozzi, P., 2019. Estimation of potential soil erosion in the Prosecco DOCG area (NE Italy), toward a soil footprint of bottled sparkling wine production in different land-management scenarios. *PLOS ONE, 14*(2), e0210922. https://doi.org/10.1371/journal.pone.0210922

[2] Straffelini, E., Pijl, A., Otto, S., Marchesini, E., Pitacco, A., & Tarolli, P., 2022. A high-resolution physical modelling approach to assess runoff and soil erosion in vineyards under different soil managements. *Soil & Tillage Research, 222*, 105418. https://doi.org/10.1016/j.still.2022.105418

[3] Pimentel, D., 2006. Soil erosion: a food and environmental threat. *Environment, Development and Sustainability, 8*(1), 119–137. https://doi.org/10.1007/s10668-005-1262-8

[4] Renard, K. G., Foster, G. R., Weesies, G. A., McCool, D. K., & Yoder, D. C., 1997. Predicting Soil Erosion by Water: A Guide to Conservation Planning with the Revised Universal Soil Loss Equation (RUSLE). *USDA Agricultural Research Service*, Agriculture Handbook No. 703.

[5] Natale, J., Vitale, S., Repola, L., Monti, L., & Isaia, R., 2024. Geomorphic analysis of digital elevation model generated from vintage aerial photographs: A glance at the pre-urbanization morphology of the active Campi Flegrei caldera. *Geomorphology, 460*, 109267. https://doi.org/10.1016/j.geomorph.2024.109267

[6] Panagos, P., Ballabio, C., Borrelli, P., Meusburger, K., Klik, A., et al., 2021. Reconstruction of past rainfall erosivity and trend detection based on the REDES database and reanalysis rainfall. *Journal of Hydrology, 603*, 126984. https://doi.org/10.1016/j.jhydrol.2020.126984

[7] ARPAV, 2017. Valutazione del rischio di erosione per la Regione Veneto - Aggiornamento 2017. Agenzia Regionale per la Prevenzione e Protezione Ambientale del Veneto. https://www.arpa.veneto.it

[8] Benavidez, R., Jackson, B., Maxwell, D., & Norton, K., 2018. A review of the (Revised) Universal Soil Loss Equation ((R)USLE): with a view to increasing its global applicability and improving soil loss estimates. *Hydrology and Earth System Sciences, 22*(11), 6059–6086. https://doi.org/10.5194/hess-22-6059-2018

[9] Verheijen, F. G. A., Jones, R. J. A., Rickson, R. J., & Smith, C. J., 2009. Tolerable versus actual soil erosion rates in Europe. *Earth-Science Reviews, 94*(1–4), 23–38. https://doi.org/10.1016/j.earscirev.2009.02.003

Gully erosion potential by hypsometric curve and morphometric analysis

Margherita Bufalini [1,§], Ugo Ciccolini [2,¥], Francesco Dramis [3, †], Marco Materazzi [1]

[1] School of Science and Technology, Geology Division, University of Camerino, Camerino, Italy
[2] Gallese, VT, Italy; ciccolini50@hotmail.it
[3] Department of Sciences, University of Roma Tre, Rome, Italy

[§] margherita.bufalini@unicam.it, [¥] ciccolini50@hotmail.it, [†] francesco.dramis@uniroma3.it

Cite as: Bufalini, M., Ciccolini, U., Dramis, F., Materazzi, M. (2025). Gully erosion potential by hypsometric curve and morphometric analysis. In: Proceedings of Geomorphometry 2025, 9-13 June, Perugia, Italy. M. Alvioli, L. Melelli, I. Marchesini eds. CNR Edizioni, Rome. ISBN 978-88-8080-765-0. DOI: 10.5281/zenodo.15267475

Abstract— The formation and development of gullies is a highly intensive process of soil erosion that is often overlooked in river basin policies and strategies. Despite the worldwide spread of the phenomenon, our ability to assess and simulate gullying and its impacts remains limited. Our study shows how an exclusively morphometric approach, based on the construction of the hypsometric curve and applied to small catchments that are lithologically homogeneous, is able to predict the triggering height of gullies and the energy (in terms of "energy efficiency" along the hypsographic curve) required for their activation; these two points are found to coincide.

I. Introduction

The formation and development of gullies is a very intensive soil erosion process that is often overlooked in river basin policies and strategies and is responsible for more than 90% of the sediment load in streams [1-5].

Despite the worldwide distribution of the phenomenon, some particular aspects of these processes have been little studied, i.e. the development of reliable models for their formation and evolution. The latter is mainly due to the diversity of geomorphological features and processes involved [6-8].

The present study, based on studies already begun by the authors on this topic [9], allows us to mark, with an original morphometric approach and simple tools implemented in a GIS environment, the transition between the sectors of the basin characterized by the different erosive capacity of running waters, confirming the intuition of Strahler [10, 11] that the inflection point of the hypsometric curve would have a significant geomorphological value; furthermore, it shows that the height of the gully heads and the potential energy required for their activation can be related to the mean elevation of the basin.

II. Data and Methods

We tested our approach on 35 sample basins in three test areas: one in central Italy, another in the Mountain States (U.S.A.-Wyoming) and a third in New Zealand (Fig.1). These basins are characterized by different climatic, morphometric, geomorphological and land-use conditions, as well as different degrees of anthropization. The only similarities are the less permeable bedrock, which allows the formation of a well-developed hydrographic network, and the low degree of tectonic conditioning.

The study has been organized in several steps:

- Calculation of the basic morphometric parameters with the aid of GIS procedures using DTMs with a resolution of 10 m, which can be downloaded free of charge from the links https://doi.org/10.13127/tinitaly/1 , https://portal.opentopography.org/ and https://maps.gns.cri.nz/ for the Italian, US and New Zealand catchments respectively.
- Construction of the hypsometric curve;
- Analytical determination of the energy potential of running waters within the river catchment area
- Detection of gully heads by satellite image interpretation and verification of the proposed model;

- Calculation of Şen's "energy index" [12] for gully head formation.

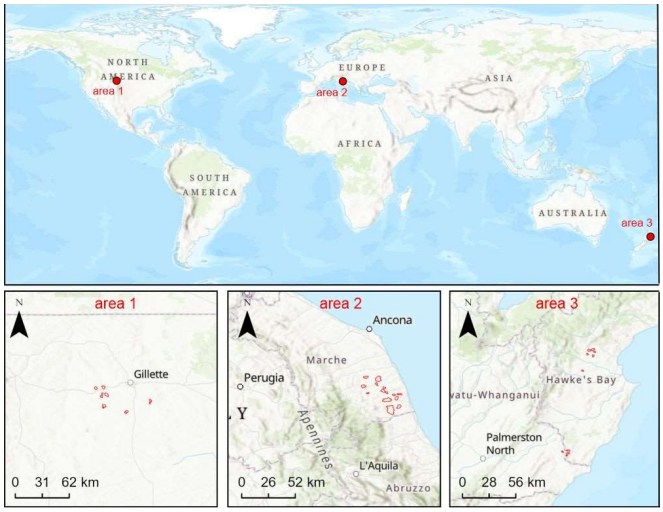

Figure 1. Location map of the study areas with indication of the catchments analyzed (red polygons)

III. RESULTS AND DISCUSSION

In a first step, we carried out the morphometric analysis of the 35 basins using the DTMs described above with a resolution of 10 m (Fig.2a). To estimate the mean elevation of each catchment, we constructed the hypsometric curve, which represents the fraction of the area of a catchment above a given elevation. The curves obtained are presented in non-dimensional form (i.e. plots of the relative height (h/H) against the relative area (a/A) of the studied region), which allows comparison between different hydrographic catchments. For the specific objectives of this work and to make the correlations between the relative elevations of the analyzed basins clearer, we created the hypsometric curve in a semi-dimensional form with the "normalized" basin area values (a/A between 0 and 1, Fig.2b).

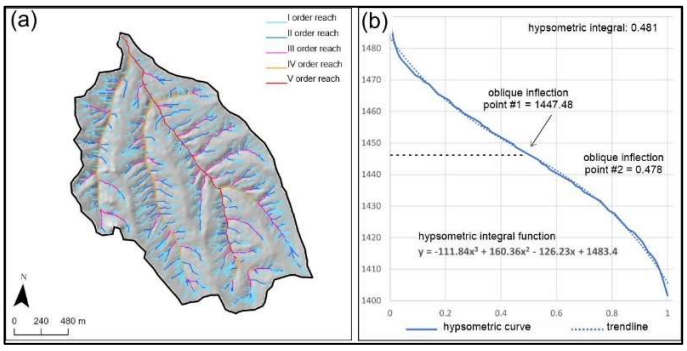

Figure 2. a) GIS elaboration from a DTM with a resolution of 10 m; b) Example of a hypsometric curve with indication of the value and position of the relative Oblique Inflection Points (OIPs). Modified after [9]

The equation of the hypsometric curve, which is expressed with a 3rd degree polynomial function, shows two special points (Oblique Inflection Points - OIPs), one of which corresponds to the change in curve slope in the upper part of the basin and the other lies outside the diagram area. In real-world applications where a system is modeled using a curve, finding the inflection point is crucial to predict the behavior of the system. In the specific case of a hydrographic basin, Strahler [10] has emphasized that this change in concavity (corresponding to the "higher" point) marks the point […at which the rate of decrease of mass upwards changes from an increasingly rapid rate of decline to a diminishing rate of decline]; in other words, this point represents the transition from a region of greater to a region of lower energy on the slope. As far as the determination of the energy potential within a watershed is concerned, it can be shown that the power of a water particle moving without friction and descending by a value dh can be expressed in the form

$$P = (\mathrm{mg}\sin\alpha)\sqrt{2gh} \qquad (1)$$

with P expressed in watt (Joule/sec).

This formula tells us that in the hypsometric curve for h=0 the power P =0 and that for h=1 P is equal to (mg sin α) √(2g). Of course, this is an "ideal" system that does not take into account the energy dissipated by friction, but in absolute terms it can be compared with the morphometric evaluations.

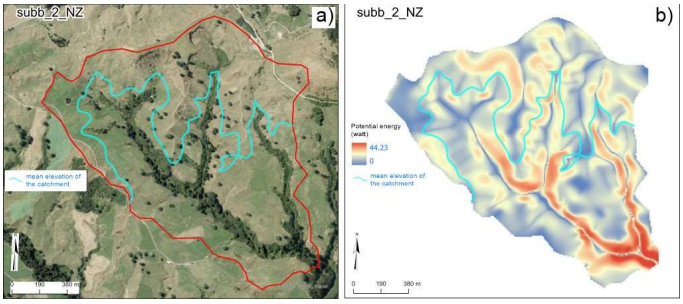

Figure 3. a) An example of a catchment in New Zealand showing the relationship between gully heads and the mean elevation of the basin (light blue polyline). b) The same catchment with a comparison between potential energy and mean elevation of the basin

As can be seen from the example in Fig. 3a (referring to a sample basin in New Zealand), the gully heads are generally in line with the contour line corresponding to the mean elevation of the basin (calculated from the hypsometric curve); this height is practically identical to that of the inflection point (between the two calculated along the same hypsometric curve), which is at a higher elevation (Table 1). The gully heads are also located at an altitude

corresponding to the relative maximum of energy that runs from the watershed downward (Fig.3b).

Although the calculated energy value is significant, it cannot be directly linked to the relationships between relative height and area (hypsometric curve) in a drainage basin.

To overcome this problem, an approach similar to that used in literature to measure the hydroelectric potential in a catchment was used (single point method, [12]). The single point method relates the "hydropower" P to the specific density of the water γ, the flow rate Q and the falling head H.

$$P = \gamma\, Q\, H \qquad (2)$$

It can be shown that if, starting from equation (2), we write the differences in terms of power gain dP, height dH and flow rate dQ and use the well-known formula of the Rational method Q = C I A to determine the flow rate (where C corresponds to the runoff coefficient, which varies between 0 and 1, I is the rainfall intensity and A is the basin area), we obtain the following relationship

$$dP = \gamma\, C\, i\, (dH)(dA) \qquad (3)$$

If we consider the density of the water equal to 1, the runoff coefficient equal to 1 (only the drainage area and the altitude are taken into account without geological influences) and the rainfall intensity also equal to 1 (i.e. the drainage basin, which is effective in the whole area, can be adjusted according to the rainfall intensity), we can write

$$dP = (dH)(dA) \qquad (4)$$

The product of the infinitesimal increase in drainage area and the decrease in height is defined as the "energy index" (Ei) of the catchment [12], in which hydrometeorological and geological effects do not play any role. In practice, Ei can be defined as the infinitesimal energy per unit density of a catchment subject to a constant precipitation intensity and a uniform runoff coefficient.

Based on these assumptions, it is possible to fit (4) to the hypsographic curve of the catchment as follows:

$$\mathrm{Ei} = h/H * a/A \qquad (5)$$

Once the Ei values have been calculated for a given number of pairs of h/H and a/A values along the hypsometric curve, it is possible to choose the value associated with the mean elevation of the selected basin (Fig. 4a); the summary of the results for all 35 basins analyzed can be found in Table 1.

Looking at the values obtained, it is noticeable that the average value of Ei is 0.24, with a small standard deviation (0.05). If we want to calculate the interquartile range (IQR), which measures the dispersion of the central values of the data set (difference between the third quartile Q3 and the first quartile Q1), we obtain a value of 0.045, which represents the values between 0.21 and 0.26. The mean value of 0.24 obtained is compatible with the efficiency classes of energy potential for hydropower generation proposed by Şen [12], which considers the interval of Ei between 0.3 and 0.6 as "normal".

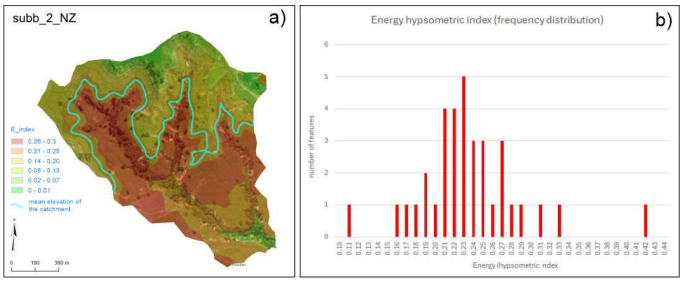

Figure 4. a) Energy hypsometric index calculated for the sample catchment; b) frequency distribution of the Ei values for all the basins analyzed

TABLE I. SUMMARY TABLE WITH ALL THE RESULTS OF THE PROCESSING DESCRIBED IN THE TEXT. STANDARD DEVIATION σ REFERS TO COLUMNS 2, 4 AND 5

BASIN	OIP (m)	Hypso Int	Hmean gullies Field (m)	Hmean (m)	Ei	Std. Dev. σ
Basin 1 ITALY	230.16	0.431	230.50	227.35	0.23	1.41
Basin 2 ITALY	181.40	0.473	196.50	184.90	0.23	6.45
Basin 3 ITALY	192.07	0.483	195.91	202.04	0.24	4.11
Basin 4 ITALY	165.45	0.459	177.20	166.69	0.22	5.27
Basin 5 ITALY	151.46	0.401	169.12	162.08	0.19	7.26
Basin 6 ITALY	300.18	0.487	305.15	287.85	0.25	7.27
Basin 7 ITALY	227.69	0.402	239.11	236.99	0.19	4.96
Basin 8 ITALY	180.31	0.355	196.15	198.23	0.16	8.00
Basin 9 ITALY	201.14	0.378	245.30	229.78	0.18	18.29
Basin 10 ITALY	173.46	0.417	185.40	177.92	0.20	4.93
Basin 11 ITALY	288.55	0.472	284.64	295.61	0.23	4.54
Basin 12 ITALY	222.57	0.439	193.81	229.48	0.21	15.45
Basin 13 ITALY	230.34	0.461	244.94	231.95	0.23	6.54
Basin 14 ITALY	174.71	0.376	171.35	182.83	0.17	4.82
Basin 1 USA	1482.57	0.529	1485.21	1474.72	0.29	4.46
Basin 2 USA	1504.98	0.559	1512.44	1502.05	0.28	4.37
Basin 3 USA	1447.48	0.481	1453.69	1445.21	0.24	3.58

Basin 4 USA	1514.94	0.443	1523.71	1516.26	0.21	3.86
Basin 5 USA	1532.76	0.465	1544.26	1535.71	0.22	4.88
Basin 6 USA	1454.10	0.530	1449.98	1451.71	0.27	1.69
Basin 7 USA	1450.01	0.598	1452.55	1445.61	0.31	2.87
Basin 8 USA	1401.72	0.472	1400.84	1395.11	0.25	2.93
Basin 9 USA	1427.15	0.601	1419.11	1411.31	0.33	6.47
Basin 10 USA	1501.15	0.506	1511.69	1501.36	0.24	4.92
Basin 11 USA	1502.48	0.526	1504.36	1498.66	0.27	2.37
Basin 1 NZ	395.41	0.315	418.77	426.09	0.11	13.08
Basin 2 NZ	337.64	0.442	340.16	341.92	0.22	1.76
Basin 3 NZ	326.47	0.643	329.12	303.81	0.42	11.36
Basin 4 NZ	261.54	0.419	255.65	259.25	0.26	2.42
Basin 5 NZ	353.23	0.487	348.29	342.02	0.27	4.59
Basin 6 NZ	466.11	0.428	474.32	469.60	0.23	3.36
Basin 7 NZ	324.75	0.472	325.15	321.07	0.25	1.84
Basin 8 NZ	316.10	0.423	332.28	328.15	0.22	6.86
Basin 9 NZ	328.34	0.465	331.88	334.28	0.21	2.44
Basin 10 NZ	294.08	0.366	298.39	294.34	0.21	1.97

IV. CONCLUSIONS

This work shows that morphometric analysis, and in particular the use of the hypsometric curve, is an extremely valid tool for a qualitative-quantitative assessment of erosion processes in a hydrographic basin. The analysis of 35 sample basins, which are essentially homogeneous from a lithological point of view, has shown that the trigger altitude of the deepening processes (gullies) essentially coincides with the mean elevation of the basin and with the height in the hypsometric curve corresponding to their inflection point; this height corresponds, among other things, to the relative maximum of the energy flowing downwards from the watershed.

Finally, the study defines an "energy index" Ei that is compatible with the efficiency classes of energy potential proposed in literature for hydropower generation.

REFERENCES

[1] Dube, H. B., Mutema, M., Muchaonyerwa, P., Poesen, J., & Chaplot, V. 2020. A global analysis of the morphology of linear erosion features. Catena, 190, 104542. https://doi.org/10.1016/j.catena.2020.104542

[2] García-Ruiz, J.M.; Beguería, S.; Nadal-Romero, E.; González-Hidalgo, J.C.; Lana-Renault, N.; Sanjuán, Y. A meta-analysis of soil erosion rates across the world. Geomorphology 2015, 239, 160–173. https://doi.org/10.1016/j.geomorph.2015.03.008

[3] Poesen, J.; Nachtergaele, J.; Verstraeten, G.; Valentin, C. Gully erosion and environmental change: Importance and research needs. CATENA 2003, 50, 91–133. https://doi.org/10.1016/S0341-8162(02)00143-1

[4] Li, G.; Klik, A.; Wu, F. Gully Erosion Features and Its Causes of Formation on the (Yuan) Land in the Loess Plateau, China; Li, Y., Poesen, J., Valentin, C., Eds.; Gully Erosion under Global Change, Sichuan Science and Technology Press: Chengdu, China, 2004.

[5] Torri, D.; Poesen, J.; Rossi, M.; Amici, V.; Spennacchi, D.; Cremer, C. Gully head modelling: A Mediterranean badland case study. Earth Surf. Process. Landf. 2018, 43, 2547–2561. https://doi.org/10.1002/esp.4414

[6] Nadal-Romero, E.; Martínez-Murillo, J.F.; Vanmaercke, M.; Poesen, J. Scale-dependency of sediment yield from badland areas in Mediterranean environments. Prog. Phys. Geogr. 2011, 35, 297–332. https://doi.org/10.1177/0309133311400330

[7] Siepel, A.C.; Steenhuis, T.S.; Rose, C.W.; Parlange, J.Y.; McIsaac, G.F. A simplified hillslope erosion model with vegetation elements for practical applications. J. Hydrol. 2002, 258, 111–121.

[8] Gutiérrez, Á.G.; Schnabel, S.; Contador, F.L. Gully erosion, land use and topographical thresholds during the last 60 years in a small rangeland catchment in SW Spain. Land Degrad. Dev. 2009, 20, 535–550. https://doi.org/10.1002/ldr.931

[9] Ciccolini, U., Bufalini, M., Materazzi, M., & Dramis, F. (2024). Gully Erosion Development in Drainage Basins: A New Morphometric Approach. Land, 13(6), 792. https://doi.org/10.3390/land13060792

[10] Strahler, A.N. Hypsometric (area-altitude) analysis of erosional topography. Bull. Geol. Soc. Am. 1952, 63, 1117–1142.

[11] Schumm, S.A. Evolution of drainage systems and slopes in badlands at Perth Amboy, New Jersey. Bull. Geol. Soc. Am. 1956, 67, 597–646.

[12] Şen, Z. (2019). Innovative methodologies in renewable energy: A review. International Journal of Energy Research, 43(11), 5621-5658. https://doi.org/10.1002/er.4619

An open-source tool for modelling reservoir bottom gully head erosion volume

Alex-Andrei Cuvuliuc [1], Denisa-Elena Ursu [2], Mihai Niculiță [3]
Department of Geography, Faculty of Geography and Geology - Alexandru Ioan Cuza University of Iași, Iași, Romania
[1] alex.cuvuliuc@student.uaic.ro, [2] denisa.ursu@student.uaic.ro, [3] niculita.mihai@uaic.ro

Cite as: Cuvuliuc, A.-A., Ursu, D.-E., Niculiță, M. (2025). An open-source tool for modelling reservoir bottom gully head erosion volume. In: Proceedings of Geomorphometry 2025, 9-13 June, Perugia, Italy. M. Alvioli, L. Melelli, I. Marchesini eds. CNR Edizioni, Rome. ISBN 978-88-8080-765-0. DOI: 10.5281/zenodo.15284237

***Abstract*— The study proposes a methodology for estimating the volume of gully head erosion using high-resolution datasets obtained through LiDAR technology and/or Structure from Motion (SfM), along with satellite images from Google Earth archives and orthophotos. Manual extraction of the boundaries of four active reservoir bottom gullies was performed across two different time periods. For 2012 – a high-resolution digital elevation model (0.25 m) derived from LiDAR data and Google Earth imagery were utilized; for 2019 – a high-resolution digital elevation model (0.25 m) derived from SfM data and orthophotos were employed. A Geographic Information System (GIS) methodology was developed that uses a single DEM to backcast or forecast topographic data for the computation of the gully head eroded volume between two time periods: 2012–2019 and 2019–2012 respectively. The reconstruction of the topography was achieved by interpolating the gully boundary and a series of simulated flow paths. As topography is known for both 2012 and 2019, the validation of the method could be performed.**

The proposed methodology was implemented as a processing plugin within the Quantum GIS (QGIS) environment using the API for Python. This allowed for the development of a Processing Toolbox which includes two algorithms designed to backcast and forecast erosion processes.

I. INTRODUCTION

The estimation of geomorphological process rates has become an increasingly prominent research direction in geomorphology in recent years, largely due to the increasing accessibility of remote sensing data and techniques [1-5]. High-resolution topographic data acquired through LiDAR or Structure from Motion (SfM), combined with spatial information from aerial and satellite imagery, allow regional-scale analyses of process rates over the past two decades [6].

The lowland area of northeastern Romania, known as the Moldavian Plain (though more accurately a hilly landscape), has a long history of pond construction over the past 500 years. These reservoirs were typically small (under 1 million m³), shallow (4–5 meters deep, with water levels reaching up to 3 meters), and often dried up during summer or winter [7]. Built in response to the region's arid climate, they served as water storage, fish farming, and powering grain mills.

After their sedimentation, the dams were cut in the spillway area to facilitate underground water drainage, allowing the reservoir bottoms to be used as pastureland. This human intervention led to concentrated water flow in the spillway area during high discharge events, which facilitated the formation and evolution of gullies on the flat lacustrine deposits. Over 500 such gullies have been identified and mapped [7-8], some of which continue to evolve through headward retreat [6]. From the identified gullies, we selected four for which topographic data was available for both 2012 and 2019 to test the proposed methodology in this study.

II. MATERIALS AND METHODOLOGY

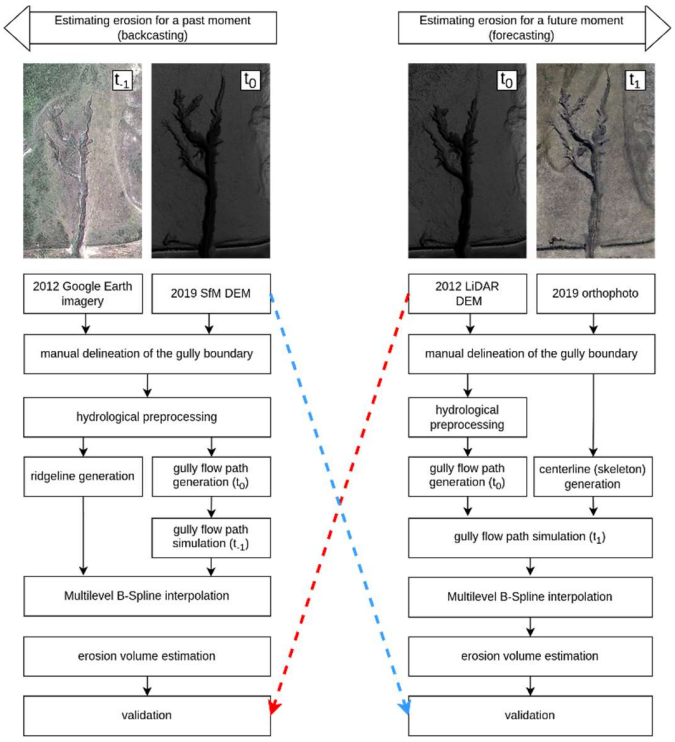

Figure 1. The methodology employed to backcast or forecast a DEM used for estimating the eroded volume of the gully heads

For each of the four gullies, boundaries from two different time periods were manually delineated using four different datasets: LiDAR DEMs and Google Earth imagery for the year 2012 and SfM DEMs and orthophotos for 2019. We have resorted to a manual delineation as the attempted automatic approaches on the DEM were not outlining the banks of the gully heads. As there is no straightforward approach to access historical imagery from Google Earth in QGIS, we have resorted to georeferencing them ourselves with the *Georeferencer* tool (Fig. 2).

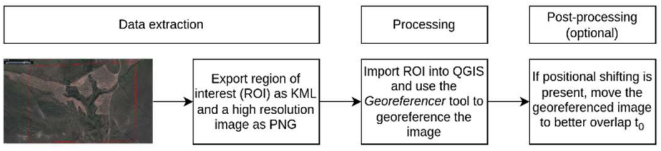

Figure 2. Workflow used in georeferencing the Google Earth imagery for 2012

The methodology makes use of a reference (t_0) high resolution DEM, to either forecast (t_1) or backcast (t_{-1}) another DEM. With our data, for forecasting, t_0 is the DEM for 2012 and t_1 the simulated DEM for 2019. For backcasting, t_0 is the DEM for 2019 and t_{-1} the simulated DEM for 2012. The simulated DEM is used to estimate the eroded volume in the gully head areas. This is achieved by knowing the extent of the gully for either t_1 or t_{-1} from auxiliary data (Google Earth historical imagery, orthophotos). Validation is possible, as real DEM data is available for both 2012 and 2019, allowing the estimated eroded volumes for both t_{-1} and t_1 to be compared with the ground truth ones.

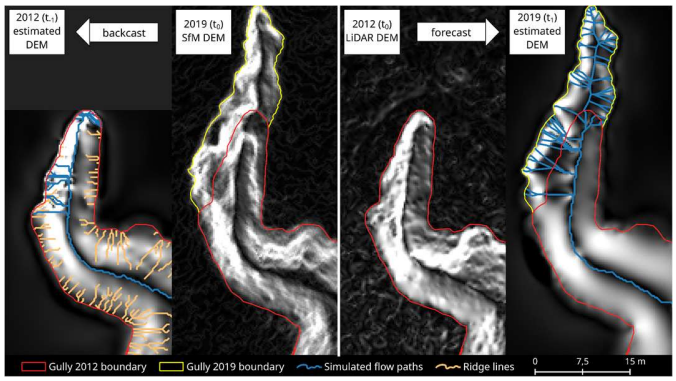

Figure 3. The simulated flow paths and ridge lines used in simulating a DEM

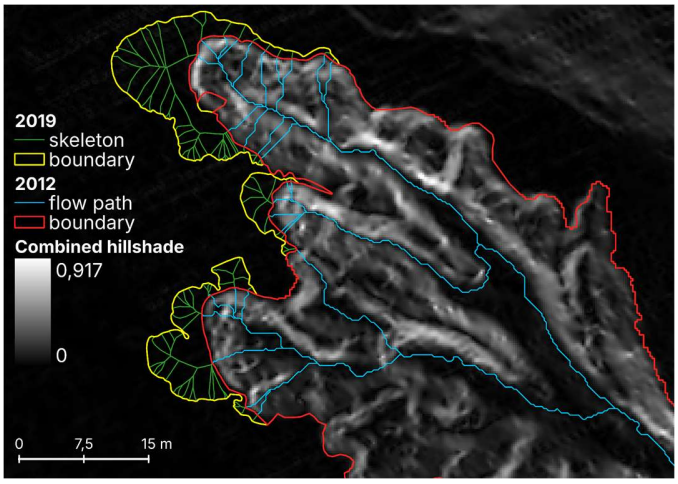

Figure 4. Example illustrating the simulated flow paths for forecasting, where t_0 is 2012. The skeleton and the real flow paths are merged to create multiple contiguous lines

The t_1 and t_{-1} DEMs are generated by estimating the elevation along simulated flow paths. For forecasting, the geometry of the flow paths for t_1 is simulated by merging the polygon centerlines generated based on the t_1 gully boundary with the flow paths from t_0 (Fig. 3, 4). The centerline was generated with the *v.voronoi.skeleton* GRASS GIS tool.

In the case of backcasting, the geometry of the flow paths for t_{-1} are assumed to coincide with the flow paths generated from t_0 (Fig. 3, 5) of which source points are located at the grid pixels which overlap the t_0 gully limit. For t_{-1}, in addition to the

simulated flow paths, the ridgelines from t_0 were also computed. The sampled elevation along the ridgelines of t_0 helps preserve the morphology of the terrain for and around the gully heads. After generating the flow paths and the ridge lines (Fig. 5), their geometries are intersected with the t_{-1} gully polygon.

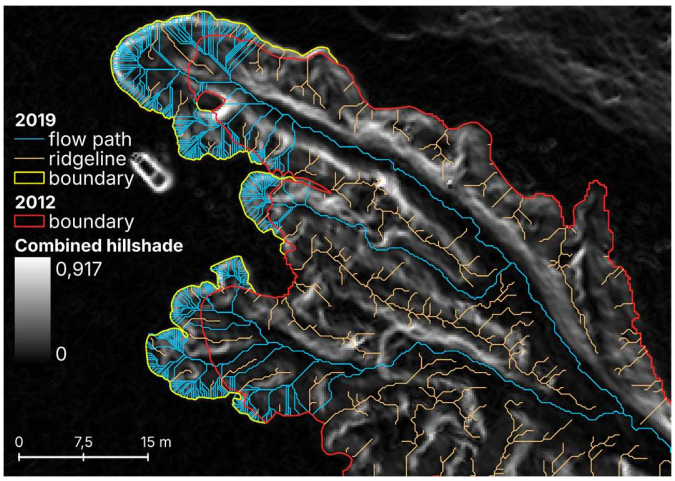

Figure 5. Example illustrating the simulated flow paths and ridgelines in the backcasting case, where t_0 is 2019. The resulting geometries are intersected with the t_{-1} gully boundary and used for backcasting the t_{-1} DEM

The estimation of the topography along the simulated flow paths was based on the topography of the gully head at t_0 (Fig. 6). To extract the gully head at t_0, a changepoint analysis was performed using the linearly penalized segmentation algorithm [9], implemented in the Ruptures Python library [10].

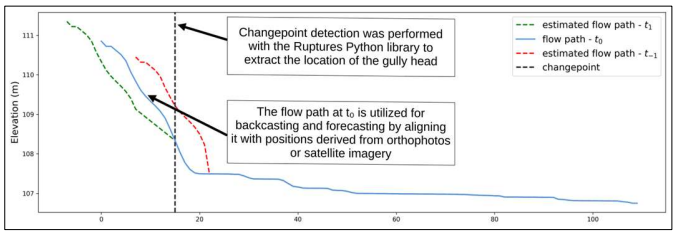

Figure 6. A theoretical example of generating the t_1 and t_{-1} heads using the topography of the t_0 head

Together with the sampled elevation along the boundary of the gully for either t_1 or t_{-1}, the generated set of points can be interpolated to obtain a simulated DEM. An interpolation method suited for scattered datasets is Multilevel B-Spline [11], which is implemented in the SAGA-GIS software [12]. After interpolation, a Gaussian filter was applied to smooth the final output.

III. Results

We identified 27 active gully heads across the four analyzed gullies. For each, the eroded volumes between 2012–2019 were computed using both methods: backcasting and forecasting. After summing the eroded volumes of the heads in each gully, the estimations and associated errors are reported in Table 1. Errors are defined as the absolute difference between the ground truth and the estimated eroded volumes, expressed as a percentage of the ground truth volume.

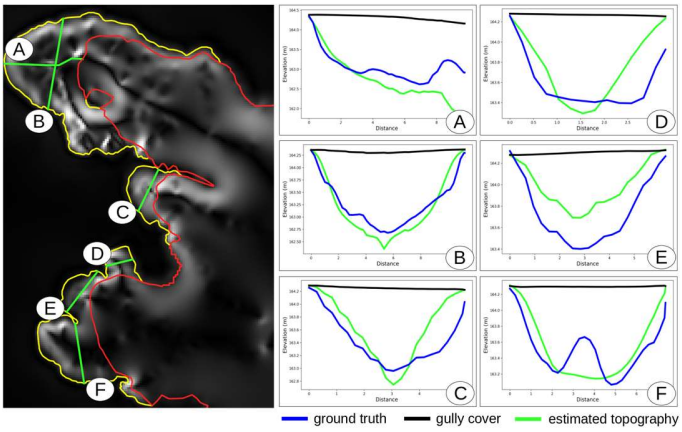

Figure 7. Cross profiles for the forecasted 2019 DEM, comparing it with the ground truth

The forecasting approach proved to be robust, with errors ranging from 5.5% to 10.5% in estimated eroded gully head volume during the 2012–2019 interval, including two cases of overestimation and two of underestimation.

The backcasting approach produced significantly larger errors for two of the tested gullies, indicating that the methodology requires further refinement. Notably, all backcasting errors are cases of underestimation of eroded volume. These errors stem from the method's inability to accurately reconstruct the morphology of the gully head at t_{-1}, leading to underestimation of elevation (Fig. 8), and consequently, of eroded volume.

IV. Discussions and Conclusions

For the analyzed gullies, the forecasting approach yielded the best results, with errors up to 10%. However, the backcasting methodology needs further improvements. Some limitations are positional shifts between datasets and the subjectivity involved in delineating gully boundaries, especially those digitized from Google Earth imagery. The lack of higher quality imagery affected the proper delineation of the gully boundaries for t_{-1}. As the method assumes a simple relationship between a series of simulated gully channels and the gully boundary, complex topographic scenarios in the gully head fail to be simulated properly, which increases the errors.

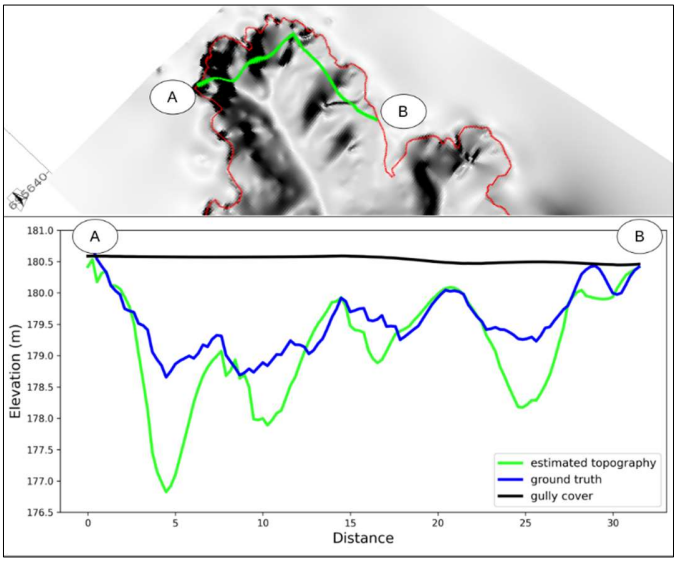

Figure 8. Profile through the backcasted t_{-1} DEM for the gully with the highest error, comparing it with its ground truth

TABLE I. THE FORECASTED AND BACKCASTED ERODED VOLUMES AND THE ERRORS FOR EACH OF THE FOUR ANALYZED GULLIES

	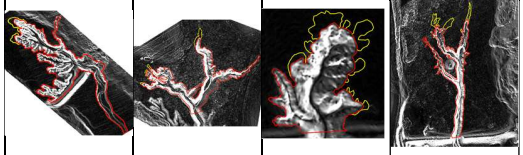			
Latitude Longitude	**47.7355 N 26.9390 E**	**47.8937 N 26.8951 E**	**47.7437 N 26.9243 E**	**47.8765 N 26.8831 E**
Eroded truth 2012-2019 (m^3)	**305.245**	**325.986**	**475.018**	**525.89**
Estimated t_1 (m^3)	**337.131**	**345.569**	**449.073**	**474.834**
Error t_1 (%)	**10.446**	**6.007**	**5.462**	**9.708**
Estimated t_{-1} (m^3)	**268.739**	**318.941**	**331.715**	**393.336**
Error t_{-1} (%)	**11.96**	**2.161**	**30.168**	**25.205**

A QGIS processing toolbox plugin was developed to automate the process described and is available on GitHub (https://github.com/alecsandrei/gully-erosion-modelling). The plugin depends on the processing providers of GRASS GIS and SAGA GIS, as well as the Ruptures Python library which was used to perform the changepoint analysis. With this open-source approach we encourage reproducibility, suggestions and improvements from potential contributors. Upon further improvements, the plugin will also be available on the QGIS official plugin repository.

V. ACKNOWLEGMENTS

We are grateful to the Prut-Bârlad Water Administration who provided us with the LiDAR data regarding the study area.

REFERENCES

[1] R. J. Pike, "Advances in geomorphometry," in *Proceedings of the Walter F. Wood Memorial Symposium*, vol. 101, pp. 1–238, 1995.

[2] T. Oguchi and T. A. Wasklewicz, "Geographic information systems in geomorphology," in *The SAGE Handbook of Geomorphology*, SAGE, London, pp. 227–245, 2011.

[3] M. J. Westoby, J. Brasington, N. F. Glasser, M. J. Hambrey, and J. M. Reynolds, "'Structure-from-Motion' photogrammetry: A low-cost, effective tool for geoscience applications," *Geomorphology*, vol. 179, pp. 300–314, 2012, https://doi.org/10.1016/j.geomorph.2012.08.021

[4] J. P. Wilson and M. P. Bishop, "Geomorphometry," in *Treatise on Geomorphology*, vol. 3, J. F. Shroder and M. P. Bishop, Eds. San Diego: Academic Press, pp. 162–186, 2013.

[5] J.-C. Otto, G. Prasicek, J. Blöthe, și L. Schrott, "2.05 - GIS Applications in Geomorphology," *Comprehensive Geographic Information Systems*, Elsevier, Oxford, pp. 81–111, 2017, doi: 10.1016/B978-0-12-409548-9.10029-6.

[6] M. Niculiță, M. C. Mărgărint, and P. Tarolli, "Chapter 10 - Using UAV and LiDAR data for gully geomorphic changes monitoring," *Remote Sensing of Geomorphology*, Developments in Earth Surface Processes, vol. 23, pp. 271-315, 2020, https://doi.org/10.1016/B978-0-444-64177-9.00010-2

[7] M. C. Mărgărint, N. Mihai, D. S. Doru, N. Necula, and A. Cristea, "Old anthropic dams, lacustrine deposits, and gullies from Șoldănești village", 2017, doi: 10.15551/prgs.2017.133

[8] M. Niculiță, M. C. Mărgărint, N. Necula, and P. Tarolli, "Gully erosion of lowland old anthropic lakes beds," in *EGU General Assembly Conference Abstracts*, p. 9037, 2018.

[9] R. Killick, P. Fearnhead, and I. A. Eckley, "Optimal detection of changepoints with a linear computational cost," Journal of the American Statistical Association, vol. 107, no. 500, pp. 1590–1598, 2012, https://doi.org/10.1080/01621459.2012.737745

[10] C. Truong, L. Oudre, and N. Vayatis, "Selective review of offline change point detection methods," *Signal Processing*, vol. 167, p. 107299, 2019, https://doi.org/10.1016/j.sigpro.2019.107299

[11] S. Lee, G. Wolberg, and S. Y. Shin, "Scattered data interpolation with multilevel B-splines," *IEEE Transactions on Visualization and Computer Graphics*, vol. 3, no. 3, pp. 228–244, 1997, doi: 10.1109/2945.620490

[12] O. Conrad, B. Bechtel, M. Bock, H. Dietrich, E. Fischer, L. Gerlitz, J. Wehberg, V. Wichmann, and J. Böhner, "System for automated geoscientific analyses (SAGA) v. 2.1. 4," *Geoscientific Model Development*, vol. 8, no. 7, pp. 1991–2007, 2015, https://doi.org/10.5194/gmd-8-1991-2015

Monitoring Badlands Features through TLS and UAV Technology

Antonella Marsico*, Rosa Colacicco, Marco La Salandra, Rodolfo Roseto, Teresa Scolamacchia, Domenico Capolongo
Department of Earth and Geoenvironmental Sciences, University of Bari
via E. Orabona, 70125 Bari, Italy
*antonella.marsico@uniba.it

Cite as: Marsico, A., Colacicco, R., La Salandra, M., Roseto, R., Scolamacchia, T., Capolongo, D. (2025). Monitoring Badlands Features through TLS and UAV Technology. In: Proceedings of Geomorphometry 2025, 9-13 June, Perugia, Italy. M. Alvioli, L. Melelli, I. Marchesini eds. CNR Edizioni, Rome. ISBN 978-88-8080-765-0. DOI: 10.5281/zenodo.15195715

Abstract—**High-resolution Point Clouds (PC), obtained from Terrestrial Laser Scanner and Unmanned Aerial Vehicle (UAV)-based surveys (both LiDAR and RGB), enables the precise detection of topographical changes, essential for advanced geomorphological analysis. This study evaluates the performance of both methods in a badlands area near Aliano (Basilicata region, southern Italy), characterized by distinctive dome-shaped landforms known as *biancane*. The complex morphology investigated presents challenges for these techniques, requiring exceptionally detailed modeling to capture subtle topographical variations with accuracy. These factors introduce potential sources of error that must be addressed to ensure reliable analysis. Furthermore, another source of errors depends on the type of landscape monitored. In this study we compare PCs derived from different monitoring techniques to define the best practices in combining remote sensing surveys, and to evaluate their strengths, limitations, and potential synergies in monitoring highly complex geomorphological features. By integrating insights from both approaches, we aim to establish best practices for combined remote sensing techniques in the study of badlands and other complex terrains. The preliminary results provide a framework for the selection and optimization of monitoring methodologies based on landscape complexity and project objectives, contributing to the broader application of remote sensing in geomorphology.**

I. INTRODUCTION

High-resolution Point Cloud (PC) reconstructions from Terrestrial Laser Scanner (TLS) and Unmanned Aerial Vehicle (UAV)-based surveys have significantly improved advancements in geomorphological analyses. Thanks to their very high resolution, PCs enable the detection of topographical changes in ranges of few cm/y to some mm/y [1,2]. However, both technologies present distinct advantages and limitations. UAV and TLS provide complementary benefits in terms of geomorphological analysis, offering high-resolution data for mapping, and monitoring landscape features. UAVs are cost-effective and versatile, making them ideal for surveying remote areas, while TLS provides detailed 3D measurements of surface features [3,4].

Therefore, the integration of these two technologies has the potential to improve spatial coverage, and data accuracy, by combining the broad accessibility of UAV, with the precision of laser scanning. Nonetheless, challenges including specialized expertise, data processing and accuracy, and potential limitations in distance range and line of sight in variable environmental conditions, highlight the importance of addressing these issues for their effective integration into geomorphological research.

In this context, we assessed the combined PC reconstructions derived from UAV-based Light Detection and Ranging (LiDAR) and RGB sensors, comparing them with those generated from TLS. Key evaluation parameters included point density, scene coverage, surface roughness, and accuracy, giving particular attention to errors introduced by the area's complex morphology [5]. TLS-derived PCs offer a superior resolution for those areas that are in the line of sight, but the lack of complete coverage on complex slopes represents a drawback. On the contrary, UAV-based PCs (both RGB and LiDAR) provide broader scene coverage, suffering, however, from lower point density and a limited penetration under vegetation [6,7].

This study aims to evaluate the effectiveness of PCs derived from the above-described methodologies in characterizing complex terrain morphology of *biancane* landforms in Basilicata to state the best strategy for integration. PCs were further validated against in-situ data allowing a more effective analysis. The results facilitated the assessment of geomorphological changes, including the rates of erosion and deposition, while offering insights into the underlying factors driving these processes. This combined

approach provides a robust framework to understand the *biancane* landforms dynamics.

The study area, ~55000m^2 wide, is located near Aliano, (Matera) in Basilicata (southern Italy), close the Sauro-Agri river confluence, at an altitude of about 200 m above sea level (Fig. 1). The topography is characterised by a gently NE-dipping monocline with rocks exposed to the S and SW steeper slopes. The area represents the NE portion of the Plio-Pleistocene Sant'Arcangelo basin [8–10], where grey-blue, shallow-marine marly clays, and limited beds of yellowish silty-sandy clays, are the main geological formations [11]. *Biancane*, micropediments, and gullies are the main landforms in the area [2,12,13].

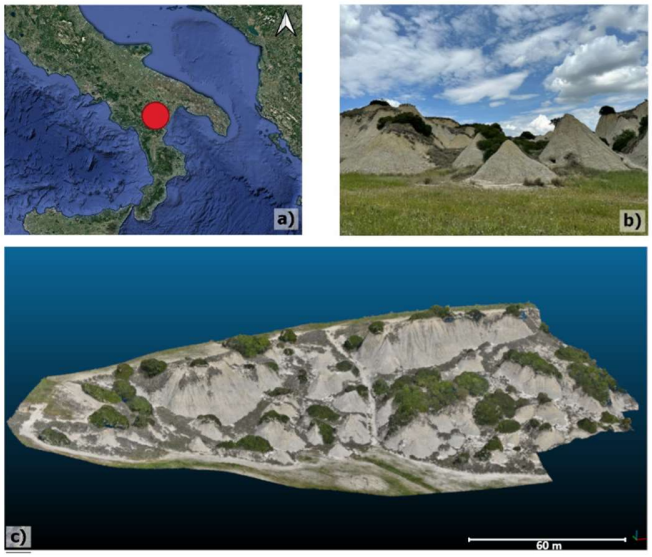

Figure 1. a) Location of the studied area in southern Italy. Base map: Google Satellite; b) view of dome shaped features (*biancane*) in the area; c) extend of UAV-based and TLS surveys.

Figure 2.

II. METHODS

All datasets were collected at the same time, on May 10, 2024. The acquisitions were performed with a DJI Mavic 3M, equipped with a 20 MP RGB camera and with a DJI Matrice 350 with a LiDAR sensor Zenmuse L1. Both sensors were used to conduct flight missions at angles of 90° (ortho collection) and 45° (oblique collection). The flight mission's settings are summarized in Table I.

DJI Terra [14] was used for both RGB and LiDAR data processing: image post-processing followed the principles of Structure-from-Motion techniques [15].

TABLE I. FLIGHT MISSION SETTINGS

	DJI Mavic 3M (RGB)	**DJI Matrice 350 RTK (LiDAR)**
Flight height (m)	50	50
Paths direction	E-W	E-W
Ortho GSD (cm/pix)	1.34	1.36
Oblique GSD (cm/pix)	1.9	1.93
Side Overlap (%)	70	20
Forward Overlap (%)	80	

TLS data were collected with a FARO Laser Scanner Focus 3D in 7 positions in and around the study site. PCs registration, georeferencing, and dataset comparison were done using the Cloud Compare free software (www.cloudcompare.org, version 2.13.2 Kharkiv, 2024). The total root mean square (RMS) error for registration processing is 2.23 cm and 3.01 cm for georeferencing. Point cloud roughness was computed to monitor how the points are scattered on the model. We applied Cloud Compare roughness tool, that is the distance between each point, and the best fitting plane computed on its nearest neighbors (https://www.cloudcompare.org/doc/wiki/index.php/Roughness). In addition, we used the M3C2 plugin [16] to detect changes among different datasets.

III. RESULTS

Multi-platform, and multi-sensor surveys, generated different datasets (Table II). Among these, TLS surveys exhibited the highest point density.

TABLE II. MAIN PARAMETERS OF DATASET USED IN THIS WORK

Device		**Dataset parameters**		
		Total area (m^2)	***Total point***	***Mean density (p/m^2)***
TLS		37,818.1	38,073,840	1,006.76
UAV-based	LiDAR 90°	55,771.4	1,318,242	23.64
	LiDAR 45°	55,771.4	1,284,590	23.03
	LiDAR 45°+90°	55,771.4	2,602,832	46.67
	RGB sensor 90°	55,771.4	6,610,201	118.52
	RGB sensor 90°+45°	55,771.4	8,093,026	145.11

However, despite significant efforts to maximize TLS survey coverage, this PC covered only 68% of the area surveyed by UAVs due to the complex topography of *biancane* landforms.

UAV-based sensors generate PCs of variable quality. The point density improves only when point clouds captured by the same sensor at different angles, are merged.

Roughness analysis (Fig. 2) shows that points' scattering is directly related to higher point density. In the TLS PC, the highest roughness value seems to be directly related to the vegetation cover on top of the *biancane* landforms, and it is lower on the domes' slopes.

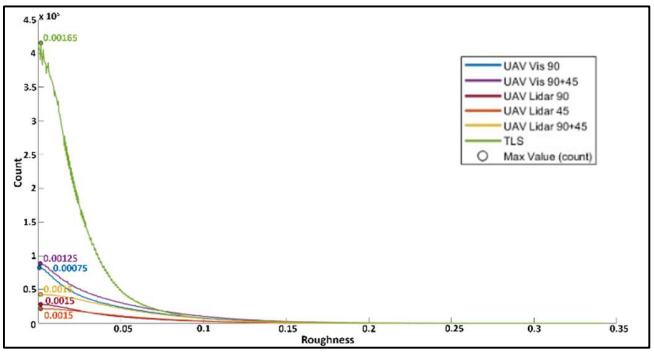

Figure 3. Cloud roughness distribution on the analyzed PCs.

On the contrary, roughness is generally lower on the UAV-based PCs, due to the lower number of points generated. In this case, the highest values span the whole PC, not only vegetation. UAV-based RGB PCs show a lower roughness than LiDAR PCs, according to the smoothest surface derived from the photogrammetry processing. By merging different UAV-based points clouds, also the roughness increases, confirming that this parameter is influenced by a greater number of points.

Even if the TLS PC has the highest roughness, this parameter decreases more rapidly than what is observed on the UAV-based PCs.

Differences in the dataset used are also highlighted by comparing the high density (Table II) merged (i.e. 45°+90°) UAV-based RGB PC, with the TLS PC. Multiple, horizontal, cross sections through these combined PCs (Fig. 3), disclose the points setting on each dataset. Such configuration indicates a more accurate slope reproduction on TLS PC than on UAV-based RGB PC. The cloud of difference (CoD) obtained from the M3C2 plugin (Fig. 4) shows better surface records specifics using the terrestrial device, which reproduces slopes features. Both herbaceous vegetation on micropediments, and other features at the slope foot, seem to cause points scattering on the model. The CoD also highlights that the TLS survey is not continuous with respect to UAV-based monitoring.

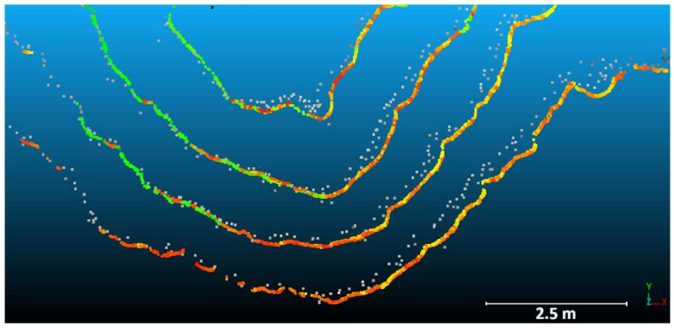

Figure 3. I Multiple cross sections obtained through TLS (green, yellow, red scale), and UAV-based (45°+90°) RGB (gray scale) PCs of a slope of one single dome landform.

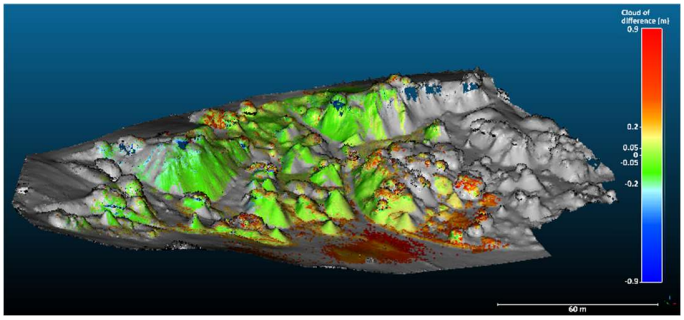

Figure 4. I Multiscale Model to Model Cloud Comparison (M3C2) between UAV-based (45°+90°) RGB and Terrestrial Laser Scanner PCs. Color scale on the right indicates distance between PCs

However, TLS high-quality-survey is confirmed by comparing in-situ, and 3D model rill width measurements, performed on marked features clearly recognizable on the TLS PC (Fig. 5).

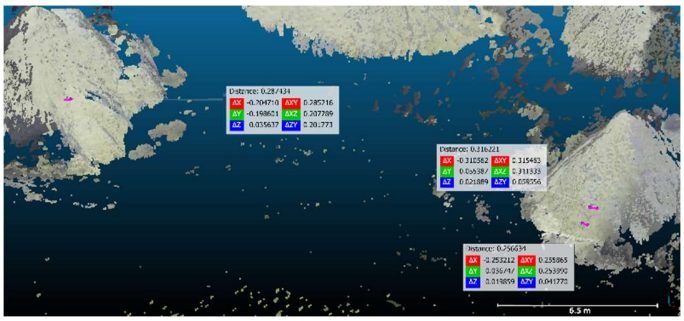

Figure 5. Measurements of the rill width carried out with the TLS PC at marked features compared to corresponding in-situ measurements

IV. Discussions and Conclusion

This preliminary study confirms that high-resolution PCs, obtained from TLS and UAV-based surveys, have different characteristics when used in a complex terrain morphology. Point density is significantly higher for TLS PC than for UAV-based surveys. TLS survey produces high-detailed PC that quite accurately reproduces slopes surface complexity. Based on *in situ* monitoring, TLS data seem to offer a superior resolution than UAV-based PCs, and measurements on TLS PC are similar to those collected in field surveys. In fact, the roughness is proportionally lower, and the points are less scattered on the scene, better reproducing the details occurring on the domes' slopes.

However, on complex landscapes, such those we have been monitoring, TLS technology is a time-consuming survey requiring many scan positions, in order to acquire the landforms' features since both domes' morphology, and vegetation, obstacle the laser flight. TLS implementation requires long time (order of hours) of dedicated processing, and PCs are affected by great uncertainties such as registration, and georeferencing errors.

On the contrary, UAV-based surveys can provide broader, and full scene coverage, a lower impact of registration, and less georeferencing errors, therefore representing an easy and quick procedure.

UAV-based sensors affect PCs densities. In fact, UAV-based RGB processing produces denser PC than UAV-based LiDAR. By merging PCs acquired from the same sensor at different angles, we improved the datasets, as the number of points increases per square meter. Even though the TLS PCs are characterized by a greater point density than the UAV-based PCs, and the quality, the density, and the accuracy of TLS PC are higher than those of UAV-based PCs, an integrated survey can help in the full coverage of the articulated *biancane* morphology. In fact, by merging high-detailed TLS PCs of dome slopes in the UAV-based PC, we can obtain full coverage of the landscape maintaining the main information about geomorphological process acting on slopes.

V. Acknowlegments

The research activities are carried out in the framework of the Next Generation EU, Mission 4 Component 1 PRIN2022-BAD2BED- BADland morphodynamics assessment and hillslope-channel BED coupling in the context of global change (no. 2022C7K7RR, CUP CUPH53D23001540006) and of the Enlarged Partnerships supported under the National Recovery and Resilience Plan (NRRP), Mission 4, Component 2, Investment 1.3 funded by the European Union— Next Generation EU RETURN project "Multi-risk science for resilient communities under a changing climate" (no. PE00000005, CUP B53C22004020002).

References

[1] Llena, M.; Vericat, D.; Smith, M.W.; Wheaton, J.M. Geomorphic Process Signatures Reshaping Sub-Humid Mediterranean Badlands: 1. Methodological Development Based on High-Resolution Topography. *Earth Surf Process Landf* **2020**, *45*, 1335–1346, doi:10.1002/esp.4821.

[2] Marsico, A.; De Santis, V.; Capolongo, D. Erosion Rate of the Aliano Biancana Badlands Based on a 3d Multi-Temporal High-Resolution Survey and Implications for Wind-Driven Rain. *Land (Basel)* **2021**, *10*, doi:10.3390/land10080828.

[3] Kasprak, A.; Bransky, N.D.; Sankey, J.B.; Caster, J.; Sankey, T.T. The Effects of Topographic Surveying Technique and Data Resolution on the Detection and Interpretation of Geomorphic Change. *Geomorphology* **2019**, *333*, 1–15, doi:10.1016/J.GEOMORPH.2019.02.020.

[4] Smith, M.W.; Vericat, D. From Experimental Plots to Experimental Landscapes: Topography, Erosion and Deposition in Sub-Humid Badlands from Structure-from-Motion Photogrammetry Measuring Erosion in Dynamic Landscapes. **2015**, doi:10.1002/esp.3747.

[5] Kamp, N.; Krenn, P.; Avian, M.; Sass, O. Comparability of Multi-Temporal DTMs Derived from Different LiDAR Platforms: Error Sources and Uncertainties in the Application of Geomorphic Impact Studies. *Earth Surf Process Landf* **2022**, doi:10.1002/esp.5540.

[6] Del Río, L.; Posanski, D.; Gracia, F.J.; Pérez-Romero, A.M. A Comparative Approach of Monitoring Techniques to Assess Erosion Processes on Soft Cliffs. *Bulletin of Engineering Geology and the Environment* **2020**, *79*, 1797–1814, doi:10.1007/S10064-019-01680-2/TABLES/5.

[7] Wilkinson, M.W.; Jones, R.R.; Woods, C.E.; Gilment, S.R.; McCaffrey, K.J.W.; Kokkalas, S.; Long, J.J. A Comparison of Terrestrial Laser Scanning and Structure-Frommotion Photogrammetry as Methods for Digital Outcrop Acquisition. *Geosphere* **2016**, *12*, 1865–1880, doi:10.1130/GES01342.1.

[8] Onofrio, V.; Tropeano, M.; Festa, V.; Moretti, M.; Sabato, L. Quaternary Transpression and Lacustrine Sedimentation in the San Lorenzo Area (Sant'Arcangelo Basin, Italy). *Sediment Geol* **2009**, *222*, 78–88, doi:10.1016/j.sedgeo.2009.08.001.

[9] De Santis, F.; Giannossi, M.L.; Medici, L.; Summa, V.; Tateo, F. Impact of Physico-Chemical Soil Properties on Erosion Features in the Aliano Area (Southern Italy). *Catena (Amst)* **2010**, *81*, 172–181, doi:10.1016/j.catena.2010.03.001.

[10] Sabato, L.; Bertini, A.; Masini, F.; Albianelli, A.; Napoleone, G.; Pieri, P. The Lower and Middle Pleistocene Geological Record of the San Lorenzo Lacustrine Succession in the Sant'Arcangelo Basin (Southern Apennines, Italy). *Quaternary International* **2005**, *131*, 59–69, doi:10.1016/j.quaint.2004.07.001.

[11] Pieri, P.; Sabato, L.; Loiacono, F.; Marino, M. Il Bacino Di "Piggyback" Di Sant'Arcangelo; Evoluzione Tettonico-Sedimentaria. *Bollettino della Societa Geologica Italiana* **1994**, *113*.

[12] Bentivenga, M.; Piccarreta, M. Rapid Geomorphological Evolution in the Mediterranean Basilicata Region (Southern Italy) during Little Ice Age. *Catena (Amst)* **2023**, *231*, doi:10.1016/j.catena.2023.107362.

[13] Farifteh, J.; Soeters, R. Origin of Biancane and Calanchi in East Aliano, Southern Italy. *Geomorphology* **2006**, *77*, 142–152, doi:10.1016/j.geomorph.2005.12.012.

[14] Tamimi, R.; Toth, C. Accuracy Assessment of UAV LiDAR Compared to Traditional Total Station for Geospatial Data Collection in Land Surveying Contexts. In Proceedings of the International Archives of the Photogrammetry, Remote Sensing and Spatial Information Sciences - ISPRS Archives; International Society for Photogrammetry and Remote Sensing, June 11 2024; Vol. 48-2–2024, pp. 421–426.

[15] Westoby, M.J.; Brasington, J.; Glasser, N.F.; Hambrey, M.J.; Reynolds, J.M. 'Structure-from-Motion' Photogrammetry: A Low-Cost, Effective Tool for Geoscience Applications. *Geomorphology* **2012**, *179*, 300–314, doi:10.1016/J.GEOMORPH.2012.08.021.

[16] Lague, D.; Brodu, N.; Leroux, J. Accurate 3D Comparison of Complex Topography with Terrestrial Laser Scanner: Application to the Rangitikei Canyon (N-Z). *ISPRS Journal of Photogrammetry and Remote Sensing* **2013**, *82*, 10–26, doi:10.1016/j.isprsjprs.2013.04.009.

2.3 - Glacial processes

Geomorphic evolution of the Miage Lake: a morphometric evaluation of the changes from 2018 to 2024

Francesco Parizia [1,2], Walter Alberto [3], Marco Giardino [3,4], Luigi Perotti [2,3]
1 Università di Roma Sapienza
2 Dipartimento di Scienze Agrarie, Forestali e Alimentari
Università degli Studi di Torino, Largo Paolo Braccini, 2, 10095 Grugliasco, Torino
3 Comitato Glaciologico Italiano
4 Dipartimento di Scienze della Terra - Università degli Studi di Torino, Via Valperga Caluso 35, 10125, Torino;

Cite as: Parizia, F., Alberto, W., Giardino, M., Perotti, L. (2025). Geomorphic evolution of the Miage Lake: a morphometric evaluation of the changes from 2018 to 2024. In: Proceedings of Geomorphometry 2025, 9-13 June, Perugia, Italy. M. Alvioli, L. Melelli, I. Marchesini eds. CNR Edizioni, Rome. ISBN 978-88-8080-765-0. DOI: 10.5281/zenodo.15166555

1

Abstract — **The Miage Glacier, located on the Italian side of Mont Blanc, features the popular Lake Miage. This lake has experienced significant changes in recent years, including a Glacial Lake Outburst Flood (GLOF) in July 2022. This study uses geomorphometry to analyze the lake's evolution and increasing hazard. Comparing photogrammetric surveys from 2018, 2022, and 2024, changes were tracked in the lake's volume. In 2018, the lake held 170,000 m³ of water, with a potential capacity of 340,000 m³. By 2022, the volume increased to 450,000 m³. In 2024, the actual volume was 137,000 m³ and the potential volume decreased to 210,000 m³. These changes highlight the complex role of factors influencing the lake's dynamics, including glacier flow, ice melt, and debris input. Continuous monitoring is crucial to understanding these evolving processes including the natural risks that can affect the area.**

I. Introduction

The Miage Glacier is a debris-covered glacier located at the bottom of the Italian side of Mont Blanc (Val Veny, Courmayeur, AO). On the right flank of the glacier there is the Miage Lake, an important touristic place, due to its landscape value and also because of its location along the famous "Tour du Mont Blanc" trekking route [1–4] (Fig. 1). In recent years, a series of different proglacial lakes originated in the area, with seasonal life, filling up during the spring and emptying in the summer, remaining full for varying periods annually.

Lake Miage - empty after July 2021 – starting on June 2022 fills up reaching maximum flooding level in early July 2022, culminating at about 2006 m a.s.l. (Fig. 2). Thereafter, a weak eastward overflow occurred during the night of July, 11 when the sudden emptying of the lake generated a Glacial Lake Outburst Flood (GLOF). Flood propagated within the endoglacial conduits until it escaped from the front of the South Lobe; the ejection of pressurized water resulted in the collapse of the latero-frontal moraine at several points. The occurrence of a GLOF made it essential to monitor the Lake sector in order to better understand the evolution dynamics of the area to be able to make a proper assessment of environmental hazard characters. In this work, we want to bring into attention the role of geomorphometry for interpreting the recent evolution of the lake, the increase in volume that can be stored in it, and the increase in hazard that afflicts the Miage Glacier area.

Figure 1. View of the whole Miage Glacier (helicopter photogrammetry, 2022). The Miage Lake is empty after the event of July 11, 2022.

Figure 2. Miage Lake as seen from the NE. At its maximum fill level, reached in early July 2022, the lake filled the entire depression to a natural overflow level on the downstream side. Photo courtesy by F. Pollicini

II. MATERIAL AND METHODS

In the context of Glacial Monitoring carried out by the Italian Glaciological Committee (CGI), the Miage Glacier is one of the glaciers with the largest amount of data collected over the years. In particular, the sector related to Lake Miage was particularly studied over the past few years. Since 2018, photogrammetric surveys of Lake Miage was carried out, first by drone photogrammetry, and later by photogrammetric helicopter flyovers. In this paper, 3 datasets obtained from Structure from Motion (SfM) [5,6] photogrammetry shown in Table 1 are compared.

TABLE I. TECHNICAL DETAILS OF THE CAMERAS USED IN THE SURVEYS

Cameras used in photogrammetric surveys				
Survey year	***Camera type***	***Sensor type***	***Focal length [mm]***	***Mega pixel***
2018	DJI Phantom 4 Pro	CMOS 1”	8,8	20
2022	Sony a6400	APS-C	16	24.2
2024	Sony a6400	APS-C	16	24.2

Photogrammetric surveys were georeferenced using Groud Control Points (GCPs) acquired by geodetic GNSS systems in order to obtain the best possible coregistration among the obtainable products. Therefore, each survey was processed in Agisoft Metashape [7] in order to obtain detailed Digital Surface Models (DSMs) and orthophotos. In this work we compare the dataset presented in table 2 in order to quantify the modification of the Lake Miage.

TABLE II. DETAILS OF THE PHOTOGRAMMETRIC SURVEYS (PREFORMED WITH EMPTY LAKE)

Dataset		
Year	***Product***	***Resolution [cm]***
August 2018	DSM	20
	Ortophoto	5
August 2022	DSM	26
	Ortophoto	13
October 2024	DSM	20
	Ortophoto	10

The products obtained were compared in a GIS environment to identify the levels of water recorded and contained in the reservoir in 2018, 2022 (the lake was filled to the maximum possible), 2024 (Fig. 3) and that potentially contained in 2018, 2024.

Figure 3. Miage Lake as seen from the NE. At its maximum fill level, reached in early June 2024, two lakes filled part of the whole depression. Photo courtesy by P. Deline

III. RESULTS

The image datasets were analyzed individually. In 2018 the erosional notch generated by waves into the ice cliff was clearly visible, indicating the lake’s settling level (2006 m a.s.l.). That level was maintained by the lake until it was completely drained (in August). Both notch line and the DSM of the empty depression of the lake allowed to calculate the actual volume of the lake (170’000 m^3) and the potential volume, achievable if the whole lacustrine basin were full (340’000 m^3). Shifting to year 2022, we consider the lake being full before its complete emptying as a

result of a GLOF. The highest possible "closed" contour line were used to calculate the volume of the lake depression: 450'000 m^3. Finally, the same process was carried out for 2024 in order to obtain the volume reached by the lake (137'000 m^3) and the maximum potential value (210'000 m^3). All the geomorphometric results are summarized in Tab. 3.

TABLE III. POTENTIAL AND REACHED DIMENSIONS OF THE LACUSTRINE BASIN OF MIAGE LAKE

Miage Lake			
Year			***Dimension***
2018	Reached	Area	18'000 m^2
		Volume	170'000 m^3
		Water height a.s.l.	2006 m
	Potential	Area	25'000 m^2
		Volume	340'000 m^3
		Water height a.s.l	2014 m
2022	Reached and Potential	Area	33'000 m^2
		Volume	450'000 m^3
		Water height a.s.l	2006 m
2024	Reached	Area	16'000 m^2 (two lakes)
		Volume	137'000 m^3
		Water height a.s.l	1990 m
	Potential	Area	22'000 m^2
		Volume	210'000 m^3
		Water height a.s.l	1994 m

IV. DISCUSSION AND CONCLUSION

According to the interpretation of dataset created by means of photogrammetric surveys, The Miage Lake area is spreading in time span 2018 – 2022. Possible causes of this expansion are: the accelerating rates of erosion on the ice cliffs that surround the Lake; the decreasing velocity of the glacier itself preventing the icecliff advance. Therefore, the geomorphological equilibrium of the Lake sector was broken creating a much larger depression, more than 130% increase from 2018 to 2022 (Fig. 4). But the contraction of the glacier and the lowering of the whole surface led to a progressive reduction in the area that can potentially be filled. Additional factors contributing to determine the reduction in volume of the Lake are: the accumulation of debris carried by ice and the landslide of the moraine at the southern lake shore.

As result, the shape, the depth and potential invadable volume of the lake are the result of a complex dynamic balance between many factors: glacier flow velocity, ice melt and debris input from the glacier and moraine. Concerning the amount of water in the depression, both potential (fig. 5A) and reached level (fig. 5B), it is affected by snow and ice melt rates, precipitation, incoming/outgoing endoglacial water flows, and finally by stress conditions within the glacier that result in the opening or closing of endoglacial conduits. An example of the effects of the morphoevolutive dynamics on the southern ice cliff is shown in figure 5. These processes are in continuous changing due to climate change and it is hard to predict future shape of the lake area. This work emphasises the importance of continuous monitoring of the area in order to better understand and control the changes can occur in the Lake Miage area in order to reduce the multiple potential risk (GLOF, moraines instability, ice falls, …) that can born in the area.

Figure 4. Detail of the area of Miage Lake. It is observable the evolution of the maximum dimension of the lake's basin through the time.

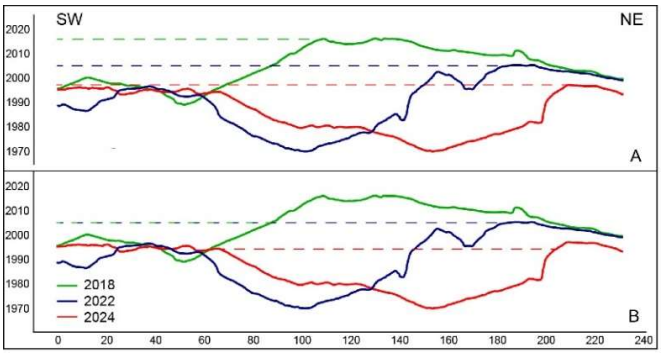

Figure 5. Topographic profiles of the Ice Cliff bordering the lake downstream. It is possible to appreciate the East-migration of the cliff and the lowering of the surface downstream. Furthermore, Dashed lines show the potential level of water

(A) and the reached level of water (B) in each investigated year. The location of the profile is shown in Figure 4

V. Acknowlegments

We acknowledge the whole Miage team of the Italian Glaciological Committee and the participant researchers from Università di Torino, Fondazione Montagna Sicura.

References

[1] Deline, P. Les Variations Holocènes Récentes Du Glacier Du Miage (Val Veny, Val d'Aoste) [Late Holocène Fluctuations of the Miage Glacier (Val Veny, Valley of Aosta)]. *Quaternaire* **1999**, *10*, 5–13, doi:10.3406/quate.1999.1624.

[2] Deline, P. La Mise En Place de l'amphithéâtre Morainique Du Miage (Val Vény, Val d'Aoste)/The Setting up of the Miage Morainic Amphitheatre (Val Vény, Valley of Aosta). *Géomorphologie* **1999**, *5*, 59–72, doi:https://doi.org/10.3406/morfo.1999.975.

[3] Diolaiuti, G.; D'Agata, C.; Meazza, A.; Zanutta, A.; Smiraglia, C. Recent (1975-2003) Changes in the Miage Debris-Covered Glacier Tongue (Mont Blanc, Italy) from Analysis of Aerial Photos and Maps. *Geogr. Fis. E Din. Quat.* **2024**, *32*, 117–127.

[4] Reid, T.D.; Brock, B.W. Assessing Ice-Cliff Backwasting and Its Contribution to Total Ablation of Debris-Covered Miage Glacier, Mont Blanc Massif, Italy. *J. Glaciol.* **2014**, *60*, 3–13, doi:10.3189/2014JoG13J045.

[5] Westoby, M.J.; Brasington, J.; Glasser, N.F.; Hambrey, M.J.; Reynolds, J.M. 'Structure-from-Motion'Photogrammetry: A Low-Cost, Effective Tool for Geoscience Applications. *Geomorphology* **2012**, *179*, 300–314.

[6] Parizia, F.; Roberti, G.; Clague, J.J.; Alberto, W.; Giardino, M.; Ward, B.; Perotti, L. Landslide Deposit Erosion and Reworking Documented by Geomatic Surveys at Mount Meager, BC, Canada. *Remote Sens.* **2024**, *16*, 1599, doi:10.3390/rs16091599.

[7] Agisoft Metashape 2025.

Rocks from the ice: DEMs of subglacial concretions through photogrammetry

Veronica Chiarini[1], Stefano Castelli, Alessandro Fontana
Department of Geosciences
University of Padova
Padova, Italy
[1]veronica.chiarini@unipd.it

Cite as: Chiarini, V., Castelli, S., Fontana, A. (2025). Rocks from the ice: DEMs of subglacial concretions through photogrammetry. In: Proceedings of Geomorphometry 2025, 9-13 June, Perugia, Italy. M. Alvioli, L. Melelli, I. Marchesini eds. CNR Edizioni, Rome. ISBN 978-88-8080-765-0. DOI: 10.5281/zenodo.15242239

Abstract— **At the ice-rock interface of glaciers developing on carbonate bedrocks, carbonate deposits known as "subglacial concretions" can form. These deposits are usually found on the lee side of obstacles and are the results of melting of the basal ice at the stoss side of the same obstacles and subsequent regelation at the lee side. Although their potential as palaeonvironmental proxies is still not clear, it has been demonstrated that these deposits can provide information about past glacier dynamics. However, their fragility prevents their conservation over long periods of time, and they can be destroyed by erosion and weathering processes within approximately 50 years since their exposure. Considering the fast glacier retreat we are experiencing, it is important to document and study subglacial concretions before they are forever gone. Subglacial concretions documentation was carried out producing DEMs with sub-millimetric resolution through photogrammetry. These models allow the morphometric analyses of subglacial carbonate deposits and represent an important tool to understand their formation and provide a solid base for investigating the relation between the development of specific micro landforms and glacier dynamics. Subglacial concretions are generally located in not easily accessible sites, which can present extreme environmental conditions, we thus tested an affordable and efficient way to produce reliable data in these environments. In this work we investigate three sites in the Dolomites (NE Italy), exploring the use of photogrammetry in providing high resolution DEMs of subglacial concretions to support their morphometric analyses.**

I. INTRODUCTION

Global warming is causing rapid continental glacier retreat worldwide. The Alpine area appears to be one of the most affected regions with an annual glacier mass loss of about 1.2 kg/m^2 between 1997 and 2017 (Copernicus Climate Change Service (C3S)/WGMS). LiDAR and both aerial and terrestrial photogrammetry technologies are widely used to measure changes in glacier mass balance and monitor glacier evolution [1][2]. These methods can provide important data on a large scale but can also be useful to document morphologies related to glacier evolution at a smaller scale.

Indeed, at the ice rock interface several processes occur which can lead to the development of specific morphologies and to the deposition of carbonate crusts which are generally defined as "subglacial concretions", where carbonate bedrocks are present. These deposits have been first observed and described in the early '70s in the Canadian Rocky Mountains [3] and consist in carbonate crusts deposited on the lee side of obstacles. Their formation has been related to melting and re-gelation processes of thin films of water at the base of glaciers [3][4][5][6][7].

Subglacial concretions potential as paleoenvironmental proxies is not clear since their isotopic signals ($\delta^{13}C$ and $\delta^{18}O$) can be affected by strong kinetic fractionation [8][9]. Lipar et al. (2021) [10] dated back to the Younger Dryas and the LGM some subglacial concretions from the Triglav Glacier (Slovenia), showing their potential in providing information about glaciers development during the current interglacial phase. Indeed, once exposed to weathering, these subglacial deposits soon disappear: Frisia and Borsato (1994) [11] estimated a maximum duration of subglacial concretions of about 50 years in the "Dolomiti di Brenta" area. This suggests that subglacial carbonate deposits, when found, indicate the absence of an icecap for a maximum of about 50 years. If we consider the widespread presence of

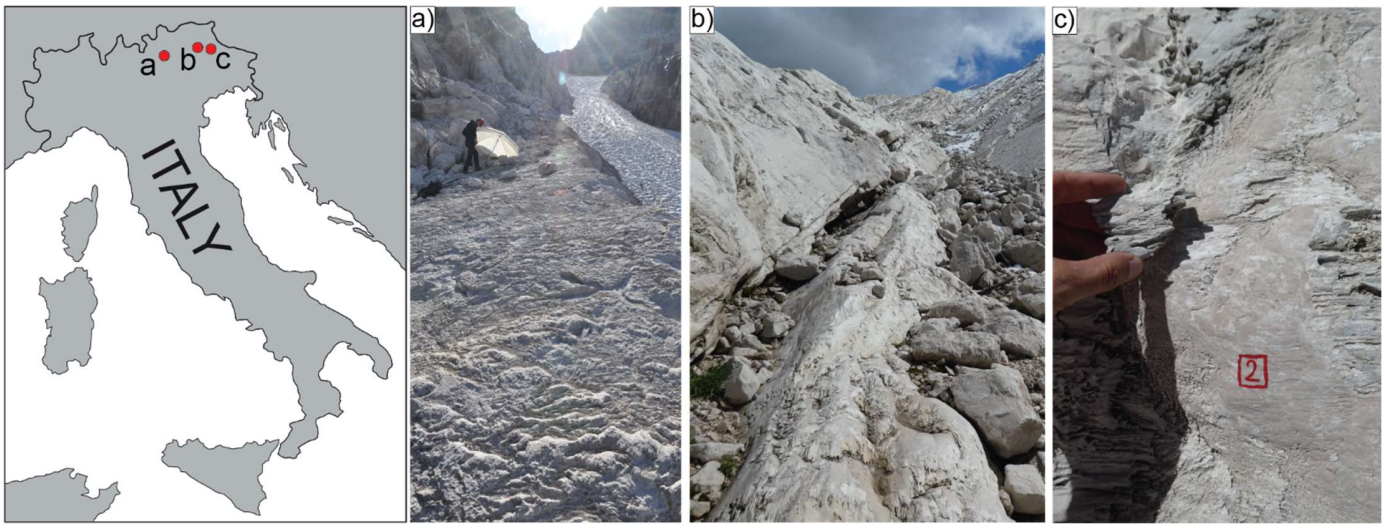

Figure 1. Sites where subglacial concretions were documented. a) Tuckett glacier; b) Marmolada glacier; c) Antelao glacier. In a) it is possible to observe evident erosion/corrosion morphologies. In b) and c) fluted carbonate crusts are elongated according to the direction of the ice flow.

carbonate bedrock in the central and eastern part of the Italian Alps and the massive glacier retreat this region is experiencing, it comes out that new subglacial concretions are being exposing rapidly. But they will not last for long. It is thus important to document and study them before they are destroyed by weathering and erosion processes. For this purpose, it is useful to investigate methods which can be easily performed in extreme environments, and which can be affordable for the documentation of these ephemeral witnesses of past glaciers, such as photogrammetric techniques, which are widely used to document archaeological findings.

II. MATERIALS AND METHODS AND PRELIMINARY RESULTS

A. The surveyed area

The prevalent rock type in the Dolomites is represented by carbonates. In this area the glacier coverage is disappearing fast. Indeed, of the 33 glaciers documented in the late 1950's, only 9 are still active [12]. Considering this massive retreat and the type of bedrock characterizing this region, in several areas subglacial concretions have been recently exposed and are prone to their rapid disappearance. In this study we considered three of the most representative sites of the Dolomites, surveyed in 2020 and 2021: Marmolada, Antelao and Tuckett glaciers (Fig.1). Marmolada massif hosts the largest glacier of the Dolomites which currently represents the 55 % of the total glacier area of this region, and that has lost 65.7 % of its volume since the 1980s [12]. On the freshly exposed areas at the glacier front it is possible to observe abundant subglacial concretions characterized by carbonate crusts and deposits elongated in the same direction of the ice flow (Fig.1). Similar deposits can be observed on bedrock and boulder surfaces recently exposed by the Antelao glacier retreat (Fig.1). Less developed subglacial concretions associated with marked erosion/corrosion morphologies partly due to subglacial karst processes have been instead observed at the flanks of the area recently occupied by Tuckett glacier (Fig.1).

B. Photogrammetric survey

Eight boulders in Marmolada massif, five in Antelao and ten in Tuckett site were chosen for photogrammetric documentation. Their dimension ranges between 2.12 and 47.6 m^2 in the first site, 0.76 and 6.17 m^2 in the second, and between 0.2 and 3.26 m^2 in the latter.

A total of 1257, 1878 and 1559 photos were taken in the three sites, respectively. These photographs were taken using the SLR camera NIKON D810 with a focal length of 35, 24 and 50 mm in the Marmolada site, the full frame mirrorless camera SONY

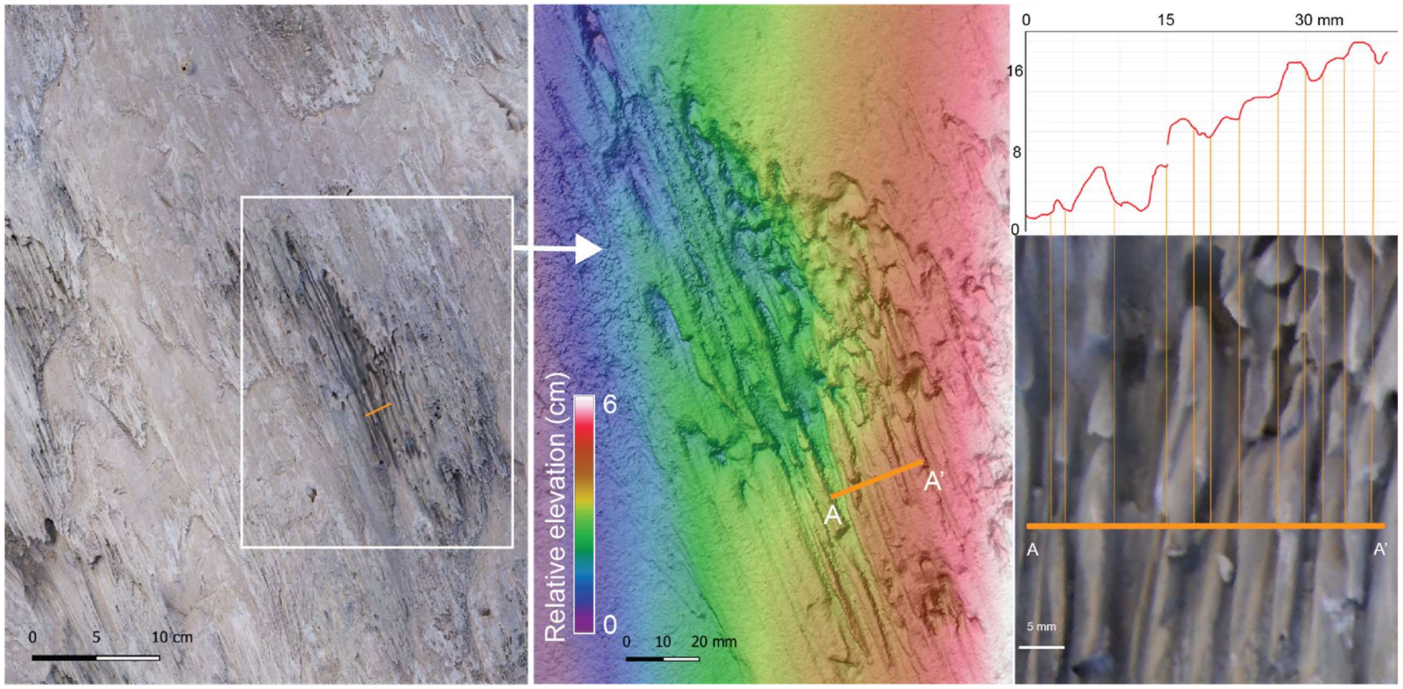

Figure 2. On the left the orthomosaic of the surface of a surveyed boulder from Antelao glacier. The white square indicates a subglacial concretion. In the center a closeup on the DEM in correspondence of the subglacial concretion. On the right a profile of the subglacial concretion realized with the profile tool in QGIS.

ILCE-7RM3 with a focal length of 47 mm in Antelao site, and the RICOH GR III camera with a focal length of 18 mm. All photos were taken manually, without the help of a tripod. For each documented boulder, at least two metersticks have been placed as a reference. The calculation of 3D models of all the surveyed boulders has been performed using the Agisoft Metashape software. Each model has been scaled using the references placed during the fieldwork reaching a scale bar error between 0.01 and 0.4 mm. The ground resolution of the calculated models ranges between 0.074 and 0.194 mm/pixel with a reprojection error between 0.33 and 0.766 pixels for the Marmolada site, between 0.0491 and 0.104 mm/pixel with a reprojection error between 0.745 and 1.58 mm pixels in the Antelao site, and between 0.0425 and 0.106 mm/pixel with a reprojection error between 0.572 and 1.3 pixels in Tuckett site. From each point cloud a digital elevation model and an orthomosaic have been calculated to be used in a GIS environment. The models of the boulders presenting the most representative subglacial concretions and erosion morphologies have been analysed using the QGIS 3.22.4 software (Fig.2). These models allowed to highlight and measure the morphologies of these concretions, which are mainly formed of crusts and ribbon shaped deposits with crests and furrows elongated in the same direction of the ice flow, sometimes ending with stalactite-shape protrusions, and to analyze the pattern and distribution of the erosion/corrosion morphologies. Using this procedure it has thus been possible to investigate glacial micro-landforms at the sub-millimetric scale, leading to the identification of at least four different types of subglacial concretions according to their morphometric characteristics, mainly consisting in differences in crest length, surface roughness, crest width, and furrow depth. Petrographic and geochemical analyses will be carried out to investigate the eventual presence of specific patterns characterizing the identified subglacial concretion types. The distribution of each subglacial concretion type with respect to the past glacier flow will be also examined, thus investigating the potential of morphometric analyses in the identification of subglacial deposits which may provide further information about past glacier dynamics. This work confirms photogrammetry as an efficient and affordable method for the production of high-quality models for the description of small-scale morphologies in extreme environments.

References

[1] Geissler, J., Mayer, C., Jubanski, J., Münzer, U., and Siegert, F.: Analyzing glacier retreat and mass balances using aerial and UAV photogrammetry in the Ötztal Alps, Austria, The Cryosphere, 15, 3699–3717, https://doi.org/10.5194/tc-15-3699-2021, 2021.

[2] Telling, J. W., Glennie, C., Fountain, A. G., & Finnegan, D. C. (2017). Analyzing Glacier Surface Motion Using LiDAR Data. *Remote Sensing*, *9*(3), 283. https://doi.org/10.3390/rs9030283.

[3] Ford, D., Fuller, P., Drake, J, 1970. Calcite Precipitates at the Soles of Temperate Glaciers. Nature 226, 441–442.

[4] Hallet, B., 1976. Deposits formed by subglacial precipitation of $CaCO_3$. Geological Society of America Bulletin, 87(7), 1003-1015.

[5] Hallet, B., 1979. Subglacial regelation water film. Journal of Glaciology, 23(89), 321-334.

[6] Frisia, S., Borsato, A., 1994. Composizione, precipitazione e dissoluzione di carbonati subglaciali nelle Dolomiti di Brenta. Museo tridentino di scienze naturali.

[7] Ng, F., & Hallet, B., 2002. Patterning mechanisms in subglacial carbonate dissolution and deposition. Journal of Glaciology, 48(162), 386-400. https://doi.org/10.3189/172756502781831214.

[8] Hanshaw, B. B., & Hallet, B., 1978. Oxygen isotope composition of subglacially precipitated calcite: possible paleoclimatic implications. Science, 200(4347), 1267-1270. DOI: 10.1126/science.200.4347.1267.

[9] Lemmens, M., Lorrain, R., & Haren, J., 1982. Isotopic composition of ice and subglacially precipitated calcite in an alpine area. Zeitschrift für Gletscherkunde und Glazialgeologie, 18(2), 151-159.

[10] Lipar, M., Martín-Pérez, A., Tičar, J., Pavšek, M., Gabrovec, M., Hrvatin, M., Komac, B., Zorn, M., Zupan Hajna, N., Zhao J.-X., Drysdale, R.N., Ferk, M., 2021. Subglacial carbonate deposits as a potential proxy for a glacier's former presence. The Cryosphere, 15(1), 17-30. https://doi.org/10.5194/tc-15-17-2021.

[11] Frisia, S., Borsato, A., 1994. Composizione, precipitazione e dissoluzione di carbonati subglaciali nelle Dolomiti di Brenta. Museo tridentino di scienze naturali.

[12] Securo, A., Del Gobbo, C., Baccolo, G., Barbante, C., Citterio, M., De Blasi, F., Marcer, M., Valt, M., and Colucci, R. R.: The Glaciers of the Dolomites: last 40 years of melting, EGUsphere [preprint], https://doi.org/10.5194/egusphere-2024-1357, 2024.

2.4 - Tectonic processes

Coupling UAV-derived Lidar and geophysical data for the reconstruction of high-resolution 3D model of active faults: an example from the Piano di Pecore intramontane basin (Mt. Marzano, southern Italy)

Dario Gioia [1], Antonio Minervino Amodio [1], Nicodemo Abate[1], Alessandra Ascione[2], Pietro Patrizio Ciro Aucelli[3], Mauro Bonasera[4], Ciro Cerrone[2,5], Lucia Contillo[6], Rosa Colacicco[7], Giuseppe Corrado[1,6], Michele Delchiaro[8], Marta Della Seta[8], Gianluigi Di Paola[4], Giandomenico Fubelli[9], Andrea Gionta[3], Fabio Matano[10], Francesco Pavano[2], Valeria Ruscitto[8], Marcello Schiattarella[6], Carlo Scirocco[2], Fabio Silvani[11], Ettore Valente[2]

1 ISPC-CNR, Tito Scalo (Potenza), Italy
2 Department of Earth, Environmental and Resources Science, University of Naples Federico II, Naples, Italy
3 Department of Science and Technology, University of Naples Parthenope, Naples, Italy
4 ISPRA, Rome, Italy
5 1 Department of Environmental Sciences, Informatics and Statistics, University of Venice Ca' Foscari, Venice, Italy
6 Department for Humanistic, Scientific and Social Innovation, University of Basilicata, Matera, Italy
7 Department of Earth and GeoEnvironmental Science, University of Bari Aldo Moro, Bari, Italy
8 Department of Earth Science, Sapienza University of Rome, Rome, Italy
9 Department of Earth Science, University of Torino, Turin, Italy
10 CNR-ISMAR, Naples, Italy
11 Department of Physics and Geology, University of Perugia, Perugia, Italy

Cite as: Gioia, D., Amodio, A. M., Abate, N. et al. (2025). Coupling UAV-derived Lidar and geophysical data for the reconstruction of high-resolution 3D model of active faults: an example from the Piano di Pecore intramontane basin (Mt. Marzano, southern Italy). In: Proceedings of Geomorphometry 2025, 9-13 June, Perugia, Italy. M. Alvioli, L. Melelli, I. Marchesini eds. CNR Edizioni, Rome. ISBN 978-88-8080-765-0. DOI: https://doi.org/10.5281/zenodo.15234620

Abstract— **We explore the integration of UAV-derived LIDAR DTM and multiple geophysical data to derive a 3D model of an area (e.g., the Piano di Pecore intramontane basin) affected by the co-seismic rupture during the M 6.9, 1980 Irpinia earthquake. Surface expression of late Quaternary faulting was reconstructed by interpreting an ultrahigh-resolution LIDAR-derived 3D model whereas seismic prospections (i.e. MASW; ESAC and HVSR) allowed us to define the thickness of the basin infill and to reveal a complex architecture of the fault zone. Our approach can represent an effective workflow in modern morphotectonic studies and can be able to reconstruct surface and subsurface features of tectonically active landscapes.**

I. INTRODUCTION

Reconstruction of the surface and subsurface expression of active faults is a crucial step for many derivatives of seismotectonic studies, including the assessment of the seismic hazard and the definition of the magnitude and recurrence time of the stronger earthquakes [1, 2]. In the seismogenic belt of the southern Apennines, geomorphic evidence of Holocene faulting is frequently obliterated by erosion processes, deposition of colluvial slope deposits and human activity. The low degree of conservation of co-seismic fault ruptures and/or their subtle topographic expression mislead to contrasting and debated structural models for active faulting of the southern Apennines [3-6]. Therefore, there is a growing interest in developing new methodologies and procedures to define the detailed geometry of active fault

segments. Useful to this topic are high-resolution (less than 1 m of horizontal resolution) digital terrain models and geophysical analyses. The former may reveal the surface evidence of active faulting while the latter may constrain the subsurface geometry of these structures, although an in-depth integration between these techniques is lacking. Moreover, emerging but limited applied techniques such as Unmanned Aerial Vehicle (UAV)-derived LIDAR can be an effective approach to derive high-resolution DTMs of tectonically areas, even when vegetated. In this work, we explore the integration of UAV-derived LIDAR DTM and seismic prospections with the goal of building a 3D model of the area affected by co-seismic rupture during the M 6.9, 1980 Irpinia earthquake (e.g., the Piano di Pecore intramontane basin, [7-8]).

II. STUDY AREA

The study area is the Piano di Pecore intramontane basin (Fig. 1), a small tectonic depression located in the north-western sector of the Marzano Mt. The latter is a carbonate massif located in the axial belt of the Southern Apennines. This area has been struck by normal faulting-related moderate to high magnitude earthquakes [9], the last of which was the destructive M 6.9, 23 November 1980 Irpinia earthquake [8]. Related to the 1980 earthquake is the formation of 50 to 70 cm high co-seismic fault scarps both in the core of the Mt. Marzano and in the adjoining San Gregorio Magno basin [5, 6].

In the Mt. Marzano area, the trace of the co-seismic fault scarp crosses the Piano di Pecore basin in its southwestern sector. Available 2D P-wave seismic analysis, Electrical Resistivity Tomography (ERT) and Horizontal to Vertical Spectral Ratio Analysis (HVSR) measurements indicate a maximum thickness of ca. 40 m of the late Quaternary filling of the basin [5, 6, 10]. These analyses provide a detailed subsurface reconstruction along a single profile trace, but a reconstruction of the 3D subsurface geometry of the entire Piano di Pecore basin has not been carried out up to now. Moreover, geochemical analyses on gas emissions reveal a complex subsurface setting of the Piano di Pecore basin, whit the occurrence of small E-W trending fault strands in the southern and northern sectors of the basin [11].

III. METHODS

Our approach includes the integration of traditional and consolidated tools of morphotectonic analysis (i.e., fieldwork and geomorphological analysis of detailed scale topographic maps) with high-resolution point cloud from LIDAR UAV survey and geophysical prospections. Quantitative geomorphic analysis of LIDAR-derived 3D model adopts common techniques of geomorphological photointerpretation and visual inspection of DEM derivatives for the delineation of active fault traces (Fig. 2).

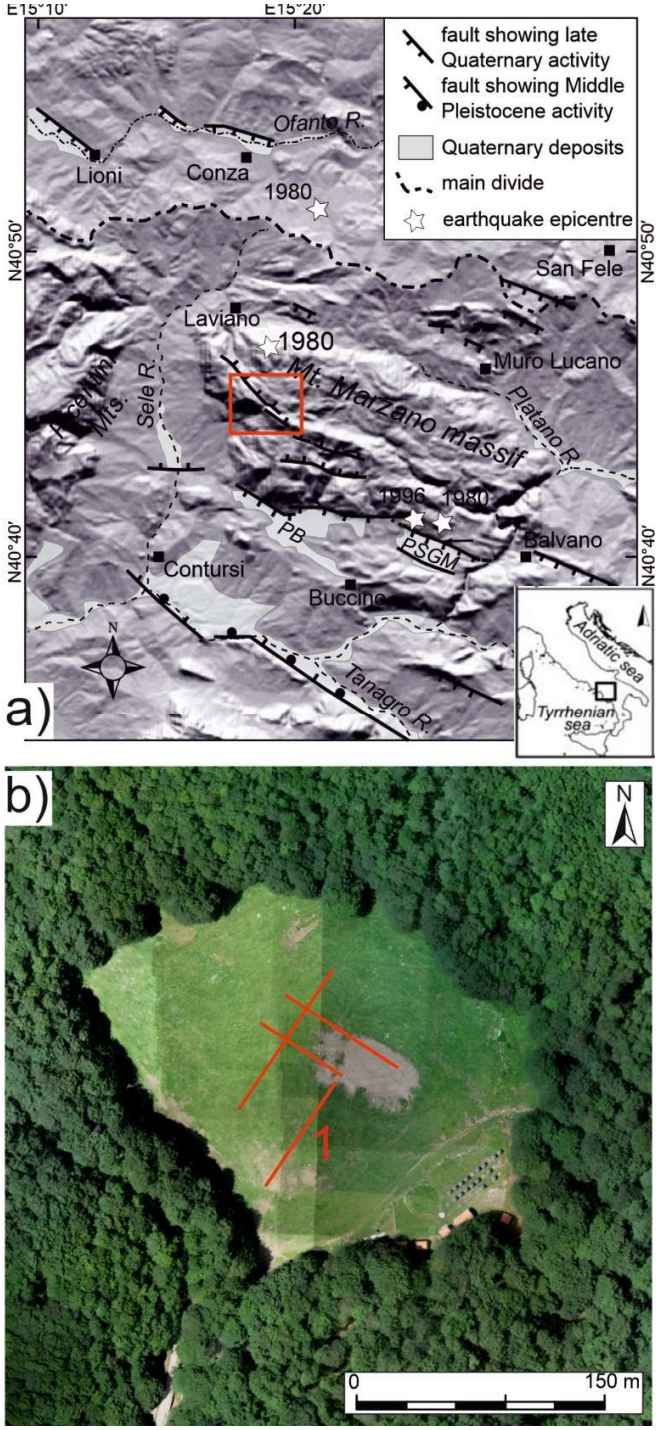

Figure 1. a) Hillshade of the Marzano Mt area showing the main Quaternary faults. The red box portrays the study area (mod. after [7]). b) Orthophoto derived by UAV survey showing the traces of the seismic prospections.

Lidar data acquisition was carried out using a DJI Matrice 300 equipped with the Zenmuse L1 Lidar sensor. The study area is about 66 ha, the point cloud acquired is approximately 440 million points. The point cloud obtained was processed by CloudCompare software. The workflow followed several steps: i) filtering the cloud from vegetation; ii) applying the kriging interpolator on the point cloud to obtain more robust data; iii) identifying the surface break trace and generating the topographic profile.

Geophysical prospections consist of active and passive seismic data (Fig. 3). More specifically, seismic dataset includes multi-component surface-wave analysis (single-offset MASW), ESAC and HVSR along key sectors of the basin. The integration between the different seismic survey methods provided robust information at different depths. ESAC and MASW have been used for the delineation of the shallower layers whereas HVSR furnished information at a depth higher than the thickness of the basin infill. 3D model of the surface and subsurface features of the study area provides new constraints on the morphotectonic framework of the tectonic basin.

IV. Preliminary Results

Here, we present some preliminary results regarding both the geomorphic and the geophysical (HVSR and ESAC data) investigations.

3D LIDAR-derived model allowed us to delineate the trace of the scarp as well as its height, orientation and slope. The trace of the different segments of the fault scarp can be delineated across the dense-vegetated carbonate slope crossing the Piano di Pecore endorheic basin. The scarp exhibits a clear geomorphic expression, which can be preliminarily ascribed to the co-seismic ruptures of the Irpinia earthquake.

Figure 2 shows the UAV derived DSM with a horizontal resolution of 5 centimeters (Figure 2a) and the derived slope map (Figure 2b). The DSM enhanced the occurrence of a low elevation area in the core of the Piano di Pecore basin. The lowest altitude area is roughly N-S oriented and is interrupted by a NW-SE scarp that is the co-seismic scarp of the 1980 Irpinia earthquake. The scarp is also recognizable in the slope map despite the diffuse presence of a sparse vegetation that causes local increments in the slope values. Improvement of the terrain model will be the next step of the research. Furthermore, high slope values in the southern portion of the Piano di Pecore basin are aligned along a NW-SE trend that mirrors the co-seismic scarp. The scarp is also highlighted through a topographic profile (Figure 2c) which enhances the ca. 35 cm high scarp.

Geophysical prospections provide additional information on the subsurface features of the Piano di Pecore endorheic basin, highlighting a high degree of structural complexity of the basin. For example, HVSR curves (Fig. 3a) show a maximum at a relatively high frequency which can be correlated to a strong surficial discontinuity in the Vs profile.

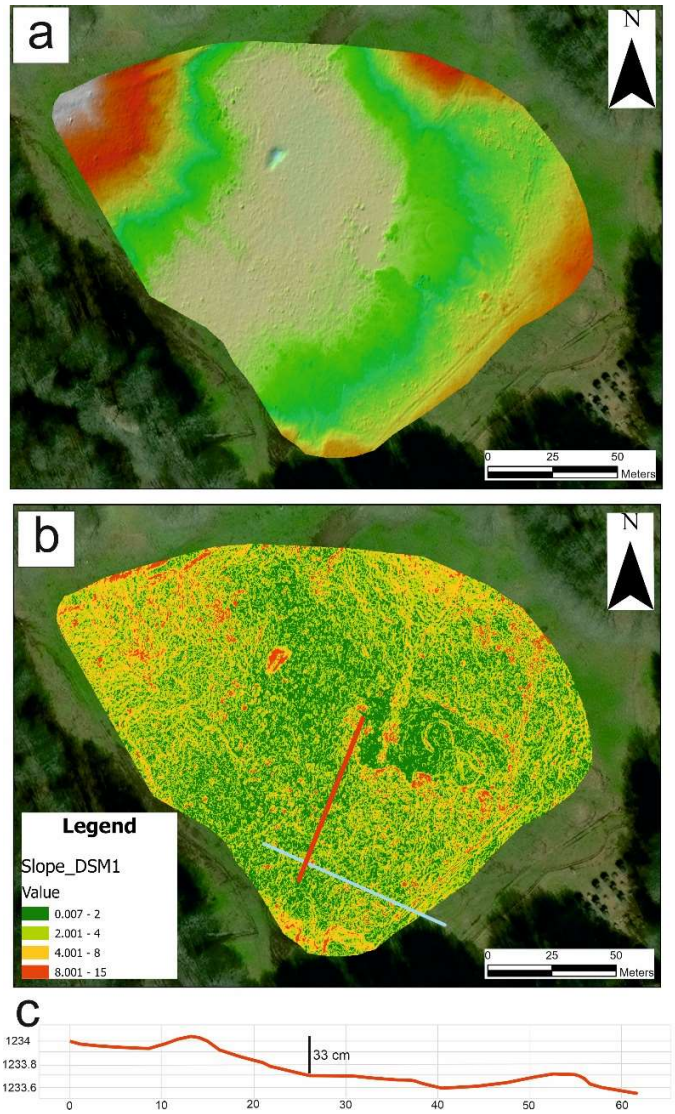

Figure 2. a) UAV derived DSM of the Piano di Pecore basin; b) slope map of the Piano di Pecore basin; c) topographic profile across the 1980 Irpinia earthquake co-seismic scarp. Blue line in maps a and b is the co-seismic scarp trace. Red line in map b is the trace of the topographic profile in figure c.

The 2D-section of the Vs derived by the ESAC array (Fig. 3b) also highlights a complex alternation of subvertical zones with a high discontinuity of the Vs velocity, which can be interpreted as due to the presence of different fault segments. HVSR and ESAC data clearly depicted a strong Vs contrast, which can be correlated to the abrupt discontinuity between unconsolidated basin deposits and carbonate bedrock. Such discontinuity can be roughly observed at a depth of about 10-15 m in the south-west sector of the seismic line (Fig. 3b). The main peak in the H/V curves tends

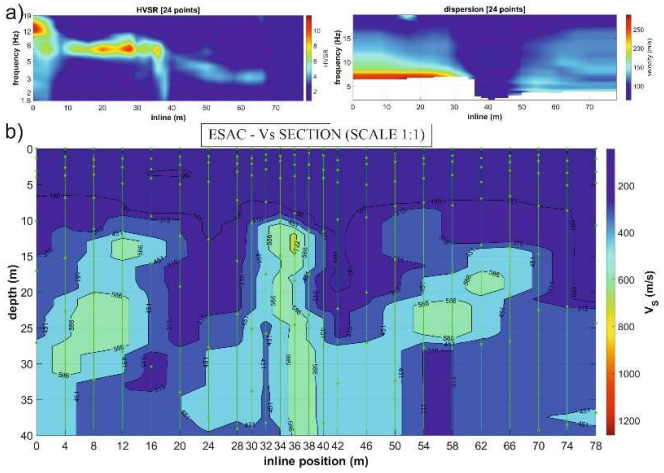

Figure 3. Main results of the passive seismic data (location in Fig. 1, trace 1: a) 2D section derived by the inversion of the HVSR (to the left) and ESAC dispersion curves (to the right); b) 2D-section of the Vs derived by the joint inversion of ESAC and HVSR data.

to move towards lower frequencies from lower inline values to higher ones (red tones in Fig. 3a).

This pattern suggests a northward deepening of the bedrock depth, which should amount to about 35 m in the depocentral zone of the basin.

V. Concluding Remarks

In summary, the integration between morphometric analysis of LiDAR-derived data and geophysical prospections can represent an effective approach for the surface and subsurface characterization of areas with a high degree of geological complexity. Our data can support the reconstruction of the spatial distribution of fault scarps and the definition of the relationships among surface ruptures, fault zone geometry and basin infill.

VI. Acknowlegments

This work benefited from the support and discussion of the members of the AIGeo (Associazione Italiana di Geografia Fisica e Gemorfologia) Working Group of 'SIStemi e TECnologie integrati per l'analisi morfoTettonica' (SISTECT).

References

[1] Maurya, D.M., et al., *Mapping the near-surface trace of the seismically active Kachchh Mainland Fault and its lateral extension in the blind zone, Western India.* Near Surface Geophysics, 2022. **20**(5): p. 544-566.

[2] Hinsch, R., K. Decker, and M. Wagreich, 3-D mapping of segmented active faults in the southern Vienna Basin. Quaternary Science Reviews, 2005. 24(3-4 SPEC. ISS.): p. 321-336.

[3] Schiattarella, M., S.I. Giano, and D. Gioia, *Long-term geomorphological evolution of the axial zone of the Campania-Lucania Apennine, southern Italy: A review.* Geologica Carpathica, 2017. **68**(1): p. 57-67.

[4] Ascione, A. and A. Cinque, *Fault scarps in the southern apennines: Origin, age and tectonic significance.* Alpine and Mediterranean Quaternary, 1997. **10**(2): p. 285-291.

[5] Ascione, A., et al., *Late Quaternary faulting within the Southern Apennines seismic belt: New data from Mt. Marzano area (Southern Italy).* Quaternary International, 2003. **101-102**(1): p. 27-41.

[6] Galli, P. and E. Peronace, *New paleoseismic data from the Irpinia Fault. A different seismogenic perspective for southern Apennines (Italy).* Earth-Science Reviews, 2014. **136**: p. 175-201.

[7] Ascione, A., et al., *A decoupled kinematic model for active normal faults: Insights from the 1980, ms = 6.9 irpinia earthquake, southern italy.* Bulletin of the Geological Society of America, 2013. **125**(7-8): p. 1239-1259.

[8] Pantosti, D., D.P. Schwartz, and G. Valensise, *Paleoseismology along the 1980 surface rupture of the irpinia fault: Implications for earthquake recurrence in the southern apennines, Italy.* Journal of Geophysical Research: Solid Earth, 1993. **98**(B4): p. 6561-6577.

[9] Rovida, A., et al., *The Italian earthquake catalogue CPTI15.* Bulletin of Earthquake Engineering, 2020. **18**(7): p. 2953-2984.

[10] Galli, P.A.C., et al., *Integrated near surface geophysics across the active Mount Marzano Fault System (southern Italy): seismogenic hints.* International Journal of Earth Sciences, 2013. **103**(1): p. 315-325.

[11] Ciotoli, G., et al., *Soil gas distribution in the main coseismic surface rupture zone of the 1980, Ms = 6.9, Irpinia earthquake (southern Italy).* Journal of Geophysical Research: Solid Earth, 2014. **119**(3): p. 2440-2461.

The Central Italy's 1997-2009-2016 Seismic Sequences: a comparison of surface deformation from a review of DinSAR results

[1]Carlo Alberto Brunori, [2]Massimiliano Rinaldo Barchi,
[2]Massimiliano Porreca, [2]Laura Melelli
Dip. Di Fisica e Geologia, Università degli Studi di Perugia
[1] carloalberto.brunori@ingv.it, [2]{massimiliano.barchi,
massimiliano.porreca, laura.melelli}@unipg.it

[3]Vincenzo De Novellis, [3]Diego Reale, [3]Eugenio Sansosti
Institute for Electromagnetic Sensing of Environment (IREA)
National Research Council (CNR) Napoli, Italy
[3]{denovellis.v, reale.d, sansosti.e}@irea.cnr.it

Cite as: Brunori, C. A., Barchi, M. R., De Novellis, V., Reale, D., Sansosti, E., Porreca, M., Melelli, L. (2025). In: Proceedings of Geomorphometry 2025, 9-13 June, Perugia, Italy. M. Alvioli, L. Melelli, I. Marchesini eds. CNR Edizioni, Rome. ISBN 978-88-8080-765-0. DOI: 10.5281/zenodo.15204330

Abstract — **Between 1997 and 2017, the Central Apennines experienced three seismic sequences—Colfiorito-Gualdo Tadino (1997-1998), L'Aquila (2009), and Amatrice-Visso-Norcia (2016-2017)—which share similar characteristics in terms of fault kinematics and crustal structure. These sequences, driven by extensional tectonics, can be viewed as resulting from the longitudinal propagation of a complex NNW-SSE trending normal fault setting along a distance of about 130 km. These seismic sequences can be interpreted as manifestations of the same geodynamic process, occurring within a relatively short spatial and temporal range in comparable tectonic and geological settings. This repetition creates a natural laboratory where, using similar observation techniques, the impact of these events on the Earth's surface can be quantitatively assessed and analysed. In this study, we review the surface deformation induced by four mainshocks of these sequences using InSAR data from SAR missions ERS (1992-2000), Envisat (2003-2011), and Sentinel-1 (2014-present), with the aim of proposing a direct comparison of the size, shape, and spatial distribution of ground displacement across different events. The results highlight both commonalities and differences of ground deformation patterns across the different analysed events. This methodological approach, after the experiences acquired in more than 30 years of InSAR-derived observations, offers a deeper understanding of the potential and limitations of InSAR for monitoring earthquake-induced surface deformation. By considering four different earthquakes, occurred in the same geological context, we will compare and discuss the relationships between the observed surface deformation and the magnitude and fault mechanism at depth of the causative events.**

I. INTRODUCTION

Italy is among the most tectonically active regions, as evidenced by historical and recent earthquakes [1]. The tectonic activity is marked by compressional mechanisms along the Alpine and Apennine fronts and extensional mechanisms along the Apennine belt, which extend northeast-southwest to Calabria, where the orientation shifts to northwest-southeast, reflecting the curvature of the Calabrian arc. The Apennines are characterized predominantly by extensional seismicity along the ridge at depths of 10–15 km. Advances in data acquisition, including Differential Synthetic Aperture Radar Interferometry (DInSAR) and seismology, allow detailed analysis of seismic sequences and faulting processes. Since 1997, three major seismic sequences, nucleated within same tectonic settings (i.e., extensional environments) along the Central and Northern Apennines chain, causing several casualties and large damage: the 1) 1997 1 Colfiorito, 2) the 2009 L'Aquila, and the most recent 3) 2016-2017 Central Italy seismic sequences [2- 6, Fig. 1, Table 1]. The aim of this study is to carry out a consistent comparison across the three sequences by means the analysis of DInSAR products, thus better identifying common patterns in the deformation fields. By comparing the spatial and geometric relationships of the deformed masses with the corresponding fault sources, we aim to gain a deeper understanding of the mechanical processes

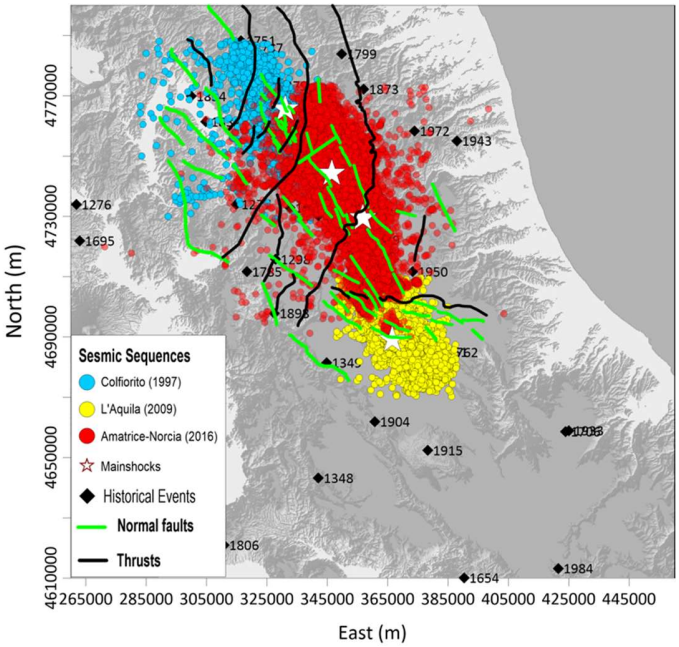

Figure 1. The 1997-2017 seismic sequences in the Central Apennines

governing these seismic events and their spatial impact on the landforms of this region.

I. Material and Methods

An interferogram is generated by processing a pair of SAR images captured over the same area at different times. This process, known DInSAR, involves comparing the phase difference between the two images to detect subtle changes in the Earth's surface. The resulting interferogram displays deformation patterns as a series of concentric colored fringes, each representing a displacement of approximately half the radar wavelength (e.g., ~2.8 cm) for C-band sensors available and exploited for the purposes of this work.

Deformation fringes in an interferogram represent phase differences between two SAR images acquired at different times over the same area. Each fringe (or cycle of color) corresponds to a specific displacement of the ground along the satellite's Line of Sight (LOS), typically equal to half the radar wavelength. The fringes provide a visual representation of ground deformation patterns, allowing scientists to quantify surface movements with high precision. The concentric pattern of a series of fringes indicates a localized deformation source, often associated with phenomena such as in our case earthquakes, but also for volcanic inflation/deflation, or subsidence. The direction of motion can be inferred from the shape and distribution of the fringes. The phase shift measured in an interferogram is a cyclic signal, meaning that the radar measures phase differences within a range of 0 to 2π. Once the phase shift exceeds 2π, it "resets" creating a cyclic pattern known as phase wrapping. The interferogram represented using fringes is called “wrapped”. To measure the total ground displacement, the phase must be "unwrapped" by adding successive 2π cycles to account for the cumulative displacement. This process is critical for distinguishing between large and small displacements and for deriving continuous deformation maps.

In summary, deformation fringes provide valuable insight into ground displacement patterns, and the cyclic delay of the SAR signal allows precise measurements of these displacements. However, interpreting these fringes requires careful phase unwrapping to account for the periodic nature of the radar signal and to convert the cyclic phase values into real-world displacement measurements.

TABLE I. THE 4 MAIN SHOCKS PARAMETERS FOR THE CENTRAL ITALY 1997-2016 SEISMIC SEQUENCES

#	*Locality*	*date*	*Mw*	*depth*
1	COLFIORITO	SEPT. 27, 1997	6.0	7.5
2	L’AQUILA	APR., 09, 2009	6.3	8
3	AMATRICE	AUG., 24, 2016	6.1	8
3	NORCIA	OCT., 30, 2016	6.5	7

On 26 September 1997, a Mw 6.0 earthquake struck the Central Apennines region of Central Italy (Fig. 1) [7, 8] near the Colfiorito village; the mainshock occurred at a depth of 7.5 km, along the approximately 12-km-long Mt. Pennino-Mt. Prefoglio normal fault, which is part of the Apenninic extensional system [9]. This event was followed by 5,410 aftershocks with Mw ≥ 1.6, including two notable events on 6 October and 14 October, with magnitudes Mw 5.4 and Mw 5.6, respectively. Additionally, six months later, on 3 April 1998, another earthquake with a magnitude of Mw 5.1 was recorded. The ground displacements caused by the Colfiorito earthquake were investigated through Differential Interferometric Synthetic Aperture Radar measurements (DInSAR) acquired via ERS satellites. A selection of such interferogram is shown in Figure 2a and 2b for ascending and descending orbit, respectively; the corresponding displacement maps (Fig. 2 i, j) reveal a maximum displacement along the radar line of sight (LOS) of approximately 25 cm. The largest subsidence was observed on the hanging wall block, consistent with a normal faulting mechanism. On 6 April 2009, a Mw 6.3 earthquake took place at a depth of 8 km, along the approximately 15-18 km-long Paganica normal fault [10,11]; it was followed by 19,939 aftershocks with Mw ≥ 0.1, the strongest of which was a Mw 5.4 earthquake on 7 April (Fig. 1). Ground displacements associated with the L’Aquila earthquake were analysed using DInSAR measurements from ENVISAT satellites, derived from both ascending and descending orbits (Fig. 2c, d, k,

l). Figures 2k, l display displacement maps from ascending and descending orbits, based on acquisitions from 11 March to 15 April 2009 and 1 February to 12 April 2009, respectively. As highlighted by [5], the deformation patterns retrieved reveal an asymmetric distribution of LOS displacement. In the northwestern region, LOS subsidence values of 17-18 cm and 23-24 cm were observed for the ascending and descending orbits, respectively. Conversely, the northeastern region exhibited a maximum LOS uplift of 4-5 cm, visible only in the descending map. The vertical deformation map highlights a maximum subsidence of 25 cm on the hanging wall block, consistent with the normal faulting mechanism [5].

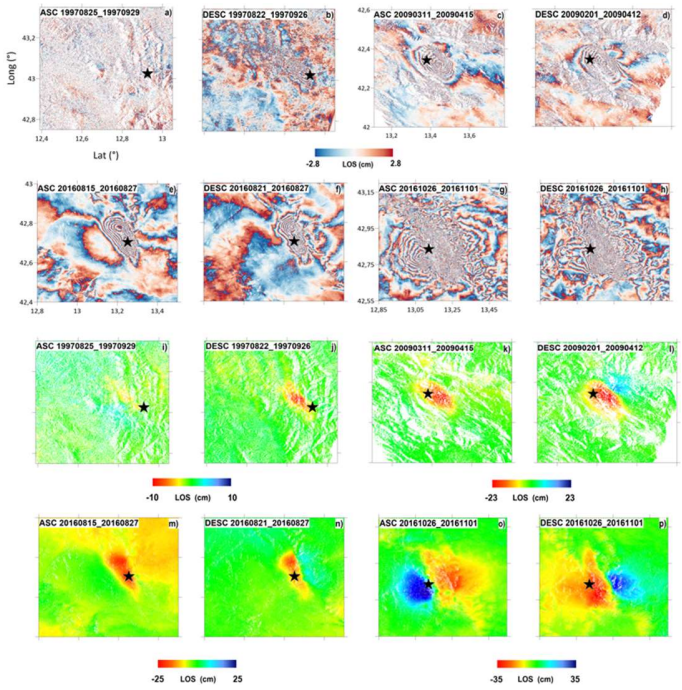

Figure 2. Interferograms for data acquired in both ascending and descending (ASC and DESC) orbits of the four mainshocks: "wrapped" deformation maps ERS (a-b); Envisat (c-d); Sentinel 1(e-h); the i-p images are the above deformation maps "unwrapped" with the displacements expressed in cm.

Finally, the 2016-2017 Central Italy seismic sequence began with the Mw 6.0 Amatrice earthquake on 24 August 2016, which activated the northernmost segment of the SW-dipping Mt. Gorzano extensional fault and the southernmost section of the SW-dipping Mt. Vettore Fault System. Subsequently, on 26 October, two earthquakes with magnitudes Mw 5.4 and Mw 5.9 occurred near Visso, affecting the northern portion of the Mt. Vettore Fault System. The sequence culminated on 30 October with the Mw 6.5 Norcia earthquake, the largest event of the series, located at a depth of approximately 7 km along the Mt. Vettore Fault System. Additionally, in the January 2017 four significant events (Mw 5.1, 5.5, 5.4, and 5.0) were recorded in the Campotosto area south of Amatrice, originating from the deeper portions of the northwestern segment of the Campotosto fault at depths between 9–11 km [12]. This entire sequence occurred within a seismic gap situated between the 1997 Colfiorito and 2009 L'Aquila earthquakes (Fig. 1) and more than 100,000 events (Mw ≥ 0.1) were recorded by the INGV seismometric network. All major earthquakes were characterized by normal faulting mechanisms, consistent with the NE–SW extension direction that defines this sector of the Central Apennines. Ground displacements associated with the mainshocks were analysed using Sentinel-1 data from both ascending and descending orbits. Interferometric pairs with minimal phase artifacts (e.g., atmospheric delays and decorrelation noise) were selected to ensure spatial coverage and coherence (Fig. 2 e, f, m, n). Fig. 2m, n shows the displacement maps derived from the acquisitions of 21-27 August 2016 and 15-27 August 2016 respectively showing an ellipsoidal deformation pattern, characterized by two lobes elongated in the NNW-SSE direction. The Line of Sight (LOS) deformation map showed a maximum subsidence of 20 cm on the hanging wall block, consistent with a normal faulting mechanism.

The ground displacements caused by the Mw 6.5 Norcia earthquake (30 October 2016) were similarly analysed using Sentinel-1 DInSAR measurements from ascending and descending orbits (Fig. 2g, h, o, p). The displacement analysis revealed two NNW–SSE striking lobes, and deformation maps were combined to determine vertical and east-west displacement components (Fig. 2o, p) [4]. The LOS deformation map highlights a maximum subsidence of 70 cm on the hanging wall block and a maximum uplift of 10 cm on the adjacent footwall block. These represent the largest ground displacements ever recorded in Italy using the DInSAR technique, caused by an earthquake.

II. Discussion and Conclusions

For the first time, both "wrapped" and "unwrapped" interferograms capturing the deformations associated with the main events of the 1997, 2009, and 2016 seismic sequences in the Apennines are shown and compared to allow both qualitative and quantitative analysis (Fig. 2). Preliminary observation highlights differences in the quality of the interferometric fringes (Fig. 2a-h) and the derived displacement fields (Fig. 2i-p). As expected, the quality of the results improves continuously through time: for the 1997 Colfiorito earthquake, the ERS acquisition pairs from both ascending and descending orbits (Fig. 2a-b) show discontinuous measurements, with grainy and poorly defined images, particularly for the ascending pair (Fig. 2i-j). In contrast,

better results were obtained with ENVISAT acquisitions (Fig. 2c-d) for the 2009 L'Aquila earthquake, and even more detailed results were achieved using Sentinel-1 data (Fig. 2e-h) for the 2016 Amatrice and Norcia earthquakes. Sentinel-1 acquisitions offer higher detail in the distribution and continuity of the interferometric fringes and the derived displacement maps (Fig. 2 k-l), offering a clearer identification of the affected areas and rate of ground subsidence or uplift.

This study provides a comprehensive comparison of the ground deformation patterns associated with three major seismic sequences in Central Italy, spanning 1997 to 2016. Using DInSAR techniques, significant insights were gained into the variability and consistency of deformation fields caused by extensional faulting mechanisms in the Apennine region.

The results underline the progression in satellite technology and its impact on the quality of interferometric measurements. While ERS data allowed a first assessment of the 1997 Colfiorito sequence, ENVISAT and Sentinel-1 data offered increasingly detailed and reliable results for the 2009 L'Aquila and 2016 Amatrice-Visso-Norcia events, respectively. This progression highlights the role of technological advancements in refining our understanding of seismic phenomena.

The analysis of displacement fields revealed not only shared characteristics but also significant differences in deformation geometry, spatial distribution, and magnitudes across the sequences. These variations are closely linked to the faulting mechanisms and regional geological context, underscoring the importance of site-specific studies for seismic risk assessment.

Moreover, analysing the differences in the topographic response to similar seismic events (in terms of depth, magnitude and geological context) opens the way to observing other variables in ground deformation, as the role of topographic parameters as the relief energy or the spatial relationship between the fault lines as a key factor in the topographic surface model.

Future work will aim to integrate these observations with source modelling to establish a more detailed relationship between fault dynamics and surface deformation. By coupling advanced geodetic techniques with geological and seismological data, we can further improve our predictive capabilities and support efforts in seismic hazard mitigation.

REFERENCES

[1] Rovida A., Locati M., Camassi R., Lolli B., Gasperini P. (eds), 2016. CPTI15, the 2015 version of the Parametric Catalogue of Italian Earthquakes. Istituto Nazionale di Geofisica e Vulcanologia. doi:http://doi.org/10.6092/INGV.IT-CPTI15.

[2] Salvi S., Stramondo S., Cocco M., Tesauro M., Hunstad I., Anzidei M., P. Briole, Baldi P.,Sansosti E. , Fornaro G., Lanari R., Doumaz F., Pesci A., Galvani A. (2000) Modeling coseismic displacements resulting from SAR interferometry and GPS measurements during the 1997 Umbria-Marche seismic sequence. *J. Seism.* **2000**, 4, 479-499, doi: 10.1023/A:1026502803579

[3] Lavecchia G., Castaldo R., Nardis R., De Novellis V., Ferrarini F., Pepe S., Brozzetti F., Solaro G., Cirillo D., Bonano M., Boncio P., Casu F., De Luca C., Lanari R., Manunta M., Manzo M., Pepe A., Zinno I., Tizzani P. (2016) Ground deformation and source geometry of the 24 August 2016 Amatrice earthquake (Central Italy) investigated through analytical and numerical modeling of DInSAR measurements and structural ‐ geological data. Geophys. Res. Lett. 2016, 43, 12-389, doi: 10.1002/2016GL071723.

[4] Cheloni D., De Novellis V., Albano M., Antonioli A., Anzidei M., Atzori S., Avallone A., Bignami C., Bonano M., Calcaterra S., Castaldo R., Casu F., Cecere G., De Luca C., Devoti R.,Di Bucci D.,A. Esposito,A. Galvani,P. Gambino ,R. Giuliani ,R. Lanari , Manunta M.,Manzo M., M. Mattone4,A. Montuori,A. Pepe ,S. Pepe ,G. Pezzo,G. Pietrantonio, M. Polcari, Riguzzi F., S. Salvi, V. Sepe, E. Serpelloni, G. Solaro,S. Stramondo,P. Tizzani ,C. Tolomei, Trasatti E., Valerio E., Zinno I., Doglioni C. (2016) Geodetic model of the 2016 Central Italy earthquake sequence inferred from InSAR and GPS data. Geophys. Res. Lett. 2017, 44, 6778-6787, doi: 10.1002/2017GL073580.

[5] Castaldo R., De Nardis R., De Novellis V., Ferrarini F., Lanari R., Lavecchia G., Pepe S., Solaro G., Tizzani P. (2018) Coseismic Stress and Strain Field Changes Investigation Through 3 ‐ D Finite Element Modeling of DInSAR and GPS Measurements and Geological/Seismological Data: The L'Aquila (Italy) 2009 Earthquake Case Study. J. Geophys. Res. Solid Earth 2018, 123, 4193-4222, doi: 10.1002/2017JB014453.

[6] Valerio, E., Tizzani, P., Carminati, E., Doglioni, C., Pepe, S., Petricca, P., De Luca, C., Bignami, C., Solaro, G., Castaldo, R., De Novellis, V., & Lanari, R. (2018) Ground Deformation and Source Geometry of the 30 October 2016 Mw 6.5 Norcia Earthquake (Central Italy) Investigated Through Seismological Data, DInSAR Measurements, and Numerical Modelling. Rem. Sens. 2018, 10, doi: 10.3390/rs10121901.

[7] Amato A., Azzara R., Chiarabba C., Cimini G.B., Cocco M., Di Bona M., Margheriti L., Mazza S., Mele F., Selvaggi G., Basili A., Boschi E., Courboulex F., Deschamps A., Gaffet S., Bittarelli G., Chiaraluce L., Piccinini D., Ripepe M. (1998). The 1997 Umbria-Marche, Italy, earthquake sequence: A first look at the main shocks and aftershocks. *Geophys. Res. Lett.* **1998**, 25, 2861-2864, doi: 10.1029/98GL51842.

[8] Ripepe, M., Piccinini, D., Chiaraluce, L. Foreshock sequence of September 26th, 1997 Umbria-Marche earthquakes. *J. Seism.* **2000**, 4, 387–399, doi: 10.1023/A:102650842.

[9] Ferrarini, F., Lavecchia, G., de Nardis, R., Brozzetti, F. (2015)Fault geometry and active stress from earthquakes and field geology data analysis: the Colfiorito 1997 and L'Aquila 2009 Cases (Central Italy). Pure Appl. Geophys. 2015, 172, 1079-1103, doi: 10.1007/s00024-014-0931-7.

[10] Chiaraluce L., Chiarabba C., De Gori P., Di Stefano R., Improta L., Piccinini D, Schlagenhauf A., Traversa P., ValorosoL and Voisin C (2010) . The 2009 L'Aquila (Central Italy) Seismic Sequence. Boll. Geofis. Teor. Appl. 2010. Doi 10.4430/bgta0019

[11] Bagagli M., Valoroso L., Michelini A., Cianetti S., Gaviano S., Giunchi C., Jozinović D., Lauciani V. (2023) Radiography of a normal fault system by 64,000 high ‐ precision earthquake locations: The 2009 L'Aquila (central Italy) case study. J. Geophys. Res. Solid Earth 2013, 118, 1156-1176, doi: 10.1002/jgrb.50130.

Airborne LiDAR survey for Monte Cefalone Fault structural analysis

Muhammad Muneeb[1,a], Andrea Ermini[1,2,b], Riccardo Salvini[1,c], Stefano Pucci[3,d], Riccardo Civico[3,e], Paolo M. De Martini[3,f]

[1] Department of Physical Sciences, Earth and Environment and Centre of Geotechnologies CGT, University of Siena, Via Vetri Vecchi 34, San Giovanni Valdarno (Arezzo), Italy

[2] National PhD Programme in Space Science and Technology, University of Trento and Centre of Geotechnologies CGT, University of Siena, Via Vetri Vecchi 34, San Giovanni Valdarno (Arezzo), Italy

[3] Istituto Nazionale di Geofisica e Vulcanologia, Via di Vigna Murata 605, 00143 Rome, Italy

[a] m.muneeb@student.unisi.it, [b] andrea.ermini@unisi.it/andrea.ermini@unitn.it, [c] riccardo.salvini@unisi.it, [d] stefano.pucci@ingv.it, [e] riccardo.civico@ingv.it, [f] paolomarco.demartini@ingv.it

Cite as: Muneeb, M., Ermini, A., Salvini, R., Pucci, S., Civico, R., De Martini, P. M. (2025). Airborne LiDAR survey for Monte Cefalone Fault structural analysis. In: Proceedings of Geomorphometry 2025, 9-13 June, Perugia, Italy. M. Alvioli, L. Melelli, I. Marchesini eds. CNR Edizioni, Rome. ISBN 978-88-8080-765-0. DOI: 10.5281/zenodo.15284961

***Abstract* — High-resolution airborne LiDAR (Light Detection And Ranging) products can enable precise fault scarp morphometry in active tectonic regions. In this work, we performed geomorphometric and structural analyses of the NW-SE-trending Monte Cefalone Fault (MCF), the main segment controlling the Campo Felice Basin, in Italy, using a High-Resolution Digital Elevation Model (HR-DEM) derived from a LiDAR point cloud.**

The integrated use of HR-DEM-derived products and 3D processing software, complemented by high-precision field data, allowed the precise extraction of key information regarding tectonic morphostructures. The DEM spatial resolution, along with optimized slope analysis, allowed actual scarp identification and improved the detection of the affected geomorphic markers, enabling a detailed along-strike throw measurement. The MCF exhibits a more than 10 m-high post-Last Glacial Maximum (LGM) scarp characterized by variable depositional and erosional processes responding to the long-term (late-Pleistocene/Holocene) fault activity. Morpho-structural analysis reveals the fault system's geometric complexity, demonstrating that highly detailed data is essential for understanding tectonic evolution. The adopted workflow demonstrates how integrated geomorphometric techniques can enhance fault scarp detection in complex terrains, advancing regional tectonic mapping.

I. Introduction

Airborne LiDAR data and derived products may enable high- resolution mapping of fault scarps and geomorphological features, making this approach particularly valuable in densely forested, rugged or inaccessible terrain. A high-resolution DEM elaborated from aerial LiDAR data reveal fault-related structures with high spatial accuracy and detail. Moreover, GIS-based geomorphometric analysis can allow for the quantification of fault scarp geometry and system dynamics. These methods contribute to standardized fault scarp characterization, reducing reliance on field surveys [1,2]. In this work, we integrated LiDAR-based data with geomorphometric analyses to quantify fault throws post-LGM landscape evolution in the area of the Campo Felice Basin tectonic depression (Central Apennines, Italy). We analyzed MCF-related morphology using a LiDAR-derived DEM, from which elevation profiles were extracted to quantify post-LGM throws. Our findings may contribute to paleoseismic reconstructions and enhance the understanding of fault segmentation patterns in this tectonically active region.The study highlights the necessity of integrating high-resolution remote sensing techniques with conventional field-based geological data to achieve comprehensive structural interpretations.

The study area (Fig. 1) is located in the Abruzzo Region, south of L'Aquila city (Italy), and includes the Campo Felice intramontane depression. The Campo Felice plain lies at 1,400– 1,500 m a.s.l. and it is bordered by mountain peaks such as Mt.Cefalone (2,142 m) and Mt. Serralunga (1,909 m). The Campo Felice depression is located on the hanging wall of the SW- dipping Monte Cefalone Fault (MCF), part, together with the Monte Orsello Fault (MOF), of a > 30 km-long segmented fault system called L'Aquila-Ovindoli-Celano with evidence of Holocene activity.

The MCF extends NW-SE along Monte Cefalone's southwestern slope with a cumulative throw of 100–250 m since 0.5 Ma and an average dip of 53° [1,2]. It displays a ~ 5 km-long prominent bedrock fault scarp, interpreted as mostly due to the coseismic exhumation occurring during discrete slip episodes since the demise of the LGM (19-20 cal ka BP). Cosmogenic dating and micro-morphology analyses identify four earthquakes with moment magnitude

(Mw) greater than 6 on the MCF over the past 10 ka [1,4].

The Campo Felice Basin is bounded by significant geological structures, including active normal faults and inherited thrust faults of the Italian Central-Southern Apennines. The area belongs to the Lazio-Abruzzo carbonate platform, characterized by a complex geological and structural framework.

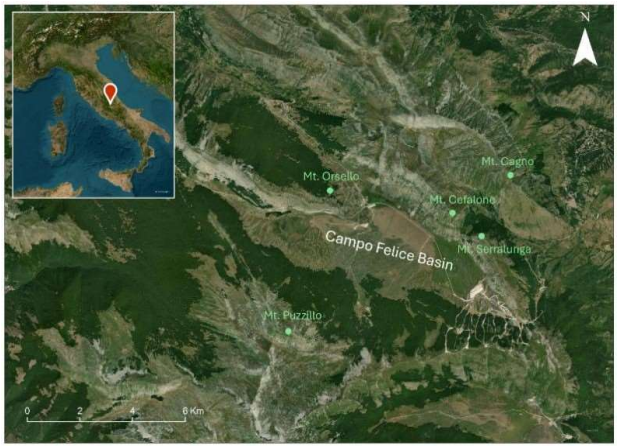

Figure 1 - Geographical location of the Campo Felice Basin, in Italy.

II. MATERIALS

A. Airborne Data Acquisition

A flight was carried out over the area under investigation by using an autogyro that was equipped with a LiDAR sensor, including GNSS (Global Navigation Satellite System) and IMU (Inertial Measurement Unit) systems, and a digital RGB camera for digital imagery acquisition. The aim of the flight was to get georeferenced data to be used for topographic and photogrammetric mapping.

B. Airborne Data Acquisition

A flight was carried out over the area under investigation by using an autogyro that was equipped with a LiDAR sensor, including GNSS (Global Navigation Satellite System) and IMU (Inertial Measurement Unit) systems, and a digital RGB camera for digital imagery acquisition. The aim of the flight was to get georeferenced data to be used for topographic and photogrammetric mapping.

C. LiDAR Survey

The sensor used consists of a RIEGL™ miniVUX-1DL laser scanner, optimized for surveying natural areas due to its "downward-looking" configuration. Its wedge-shaped prism provides a ±23° field of view at 100,000 pulses/sec. A key feature of this scanner is its ability to digitize different return echoes and process the waveforms in real-time. Although the system can record multiple returns for vegetation penetration, this capability was not utilized in the present study due to the bare cover of the slopes. The instrument generated a high-resolution three- dimensional point cloud, enabling the production of a DEM that was subsequently utilized for geological-structural investigations.

D. LiDAR Survey

The sensor used consists of a RIEGL™ miniVUX-1DL laser scanner, optimized for surveying natural areas due to its "downward-looking" configuration. Its wedge-shaped prism provides a ±23° field of view at 100,000 pulses/sec. A key feature of this scanner is its ability to digitize different return echoes and process the waveforms in real-time. Although the system can record multiple returns for vegetation penetration, this capability was not utilized in the present study due to the bare cover of the slopes. The instrument generated a high-resolution three- dimensional point cloud, enabling the production of a DEM that was subsequently utilized for geological-structural investigations.

E. Digital Elevation Model

The LiDAR-derived DEM was generated at a 0.3 m spatial resolution (Fig. 2). This level of detail surpassed the resolution of the 1:50,000 Geological Map of Abruzzo Region provided by the Italian Institute for Environmental Protection and Research (Istituto Superiore per la Protezione e la Ricerca Ambientale - ISPRA). The model allowed for various terrain analyses, including the evaluation of slope gradients, dip directions towards North, and the identification of geomorphological and tectonic structures along the actual MCF surface. Positional checks conducted on selected Ground Control Points (GCPs), measured by differential GNSS surveys during the airborne data acquisition phases, revealed average altimetric errors in the DEM of, approximately, ±30 cm.

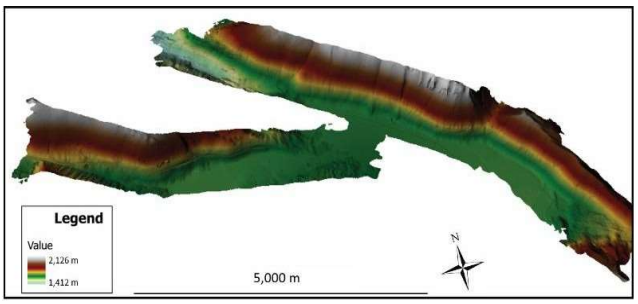

Figure 2 - DEM spatial extension.

III. METHODS

We employed an integrated approach combining ESRI™ ArcGIS Pro software for geomorphometric analysis and AutoCAD™ software for structural measurements to investigate the MCF. This dual-method workflow enabled precise quantification of fault geometry and post-LGM displacements.

A. Geomorphometric Interpretation and Analysis

The High-Resolution DEM was processed using ESRI™ ArcGIS Pro software and was analyzed in combination with Web Map Service (WMS) layers (e.g., RGB orthophotos, geological boundaries, contour lines) enabling detailed identification of: the surface fault trace; fault slickenside location and dip; related tectonic scarp morphology; footwall erosional surfaces; hanging wall depositional bodies; cross-fault drainage incisions. The identified morphostructural features revealed subtle characteristics indicative of fault activity.

B. Structural Analysis

The removal of vegetation, thanks to the map of "slope" and "aspect", allowed unambiguous location of the fault slickenside base in the DEM. A series of elevation profiles extracted from the DEM (Fig. 4) served as the basis for fault throw calculations, calculated using the method described in [5], which assumes minimal post-LGM sediment accumulation at the scarp due to the steep slope gradient.

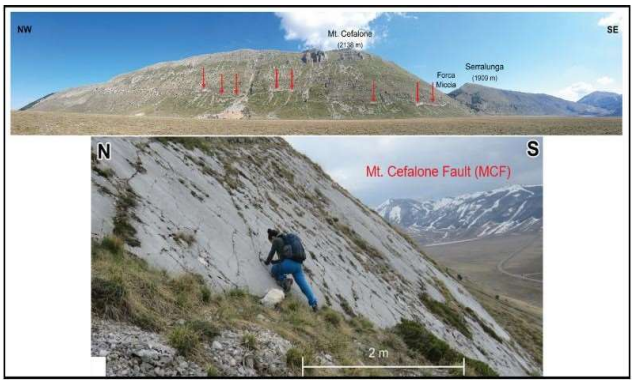

Figure 3 - Fault scarp (MCF). The red arrows at the top image indicate the fault plane along the Monte Cefalone southwestern slope [2].

The fault was characterized in terms of dip direction, dip and slip vector by collecting field data. The parameters of the erosional surface of the footwall, used as LGM geomorphic marker, were extracted from the High-Resolution DEM. Then, the AutoCAD™ software allowed to calculate vertical throws along the fault plane using the following formula as proposed by [5]:

$$T = S / (1 - \tan(\gamma) / \tan(\alpha))$$

where:

- T = vertical offset;
- S = surface displacement;
- γ = dip angle of the erosional surface of the footwall;
- α = dip angle of the fault plane.

IV. RESULTS AND DISCUSSION

A. Analysis of Profiles

Only profiles intersecting the exposed fault plane were retained to ensure reliable measurements (Fig. 4). The High-Resolution DEM captured scarp details, even in otherwise inaccessible terrain.

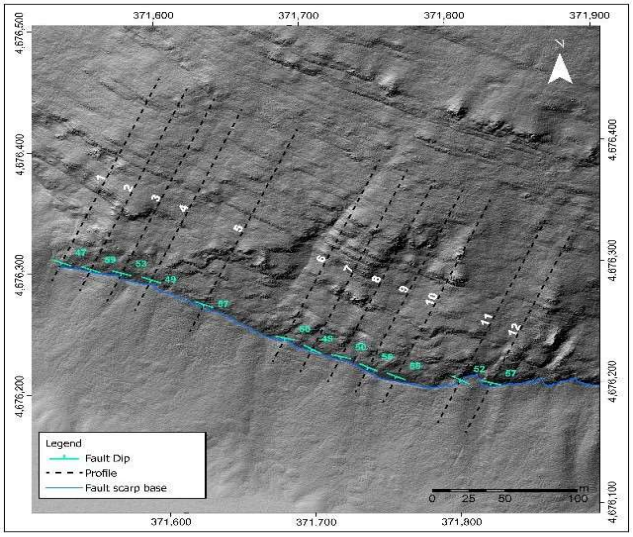

Figure 4 - Black lines represent traces of the profiles utilized for MCF throw analysis. The blue line indicates the MCF scarp base. Cyan symbols indicate the fault plane dip.

B. Dip and Dip Direction Calculation

Dip values computed on the DEM indicate an average fault scarp angle of 52°. The dip angle ranges, from 47° to 59° (Table 1), seems to maintain a quite stable pattern [7] likely modified, locally, by erosion and weathering processes acting throughout time. The along-strike constant dip values suggest coheval exhumation of the scarp. The average computed scarp dip value is lower than the slickensides dip measured in the field and reported on the 1:50,000 geological map (i.e., 58°) due to prolonged erosion that degrades the upper scarp. The slight dip changes detected at morphological bends along the trace can be attributed to lithological variations or erosional processes while remaining inconsistent with fault segmentation. Since the LGM there have been minimal but standard adjustments in fault systems while no major reactivation events have been recorded [5,6]. Overall, the continuous dip values indicate tectonic stability, with little evidence of deformation or secondary faulting since the LGM.

TABLE I. DIP AND DIP DIRECTION MEASUREMENTS ALONG MCF.

Profile Nr. of Fig. 4	*Dip (°)*	*Dip Direction (°)*
1	47	201
2	59	200
3	53	196
4	49	200
5	57	201
6	50	193
7	49	210
8	50	194
9	56	206
10	55	203
11	52	208
12	57	195

C. *Throw Measurements*

The average throws (Fig. 5) resulted equal to 13.01 ± 4.87 m across the analyzed fault segments, indicating post-LGM slip activity. Throw measurements, varying from 5 to 20 meters, reveal fault segmentation due to variable slip across different segments. A segmented fault system exhibits varying throw levels as one of its characteristic features. The outcomes obtained confirm previous investigations by [3], which strengthens the understanding about fault segmentation and its impact on the Campo Felice Basin's geographic development. Analyzing a small segment of the MCF revealed evidence of segmentation according to the results of throw variability. Future studies should explore fault segmentation across broader spatial areas to improve our understanding of regional tectonic dynamics.

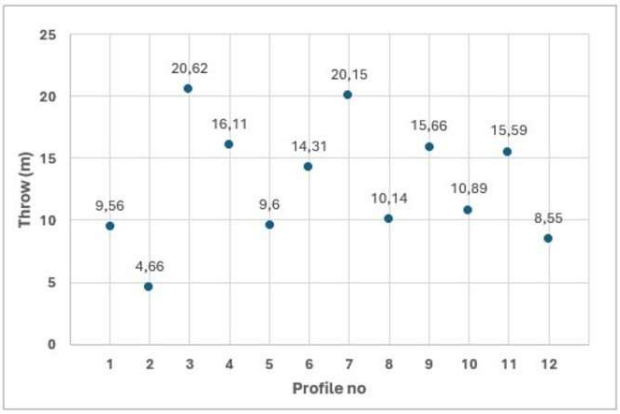

Figure 5 - Fault throw variations along the twelve profiles of Fig. 4.

V. CONCLUSIONS

The MCF's 5 km-long fault scarp (Fig. 3) exhibits clear evidence of post-LGM displacement, likely associated with earthquakes of Mw 6.2–6.5 [3,5,6].

The LiDAR-derived DEM was used extensively for the actual fault surface identification and characterization. The MCF exhibits a 13.01 m post-LGM vertical throw (σ = ±4.87 m) and a consistent 52° SW dip angle, as measured from twelve profiles using ESRI™ ArcGIS Pro and AutoCAD™ software assisted elaboration. This highlights the effectiveness of geomorphometry in regional tectonic assessments, particularly in complex terrains, and further advances tectonic mapping in the area. Future work aims to integrate roughness metrics with slope and curvature analyses to automate fault trace extraction, extending this method to the nearby Monte Orsello Fault (MOF).

VI. ACKNOWLEGMENTS

This extended abstract was produced while Andrea Ermini was attending the PhD program in Space Science and Technology at the University of Trento, Cycle XXXIX, with the support of a scholarship financed by the Ministerial Decree no. 118 of 2nd March 2023, based on the NRRP - funded by the European Union- NextGenerationEU - Mission 4 - CUP E66E23000110001-

REFERENCES

[1] Benedetti, L., Manighetti, I., Gaudemer, Y., Finkel, R., Malavieille, J., Pou, K., Arnold, M., Aumaître, G., Bourlès, D., and Keddadouche, K., 2013. Earthquake synchrony and clustering on Fucino faults (Central Italy) as revealed from in situ 36Cl exposure dating. Journal of Geophysical Research: Solid Earth, 118(9), 4948–4974. https://doi.org/10.1002/jgrb.50299

[2] Villani, F., Maraio, S., Improta, L., Sapia, V., Di Giulio, G., Baccheschi, P., and De Martini, P. M., 2024. High-resolution geophysical investigations in the central Apennines seismic belt (Italy): Results from the Campo Felice tectonic basin.Tectonophysics, 871, 230170. https://doi.org/10.1016/j.tecto.2023.230170

[3] Schirripa Spagnolo, G., Mercuri, M., Billi, A., Carminati, E., and Galli, P., 2021. The segmented Campo Felice normal faults: Seismic potential sappraisal by application of empirical relationships between rupture length and earthquake magnitude in the central Apennines, Italy. Tectonics, 40, e2020TC006465. https://doi.org/10.1029/2020TC006465

[4] Giaccio, B., Galadini, F., Sposato, A., Messina, P., Moro, M., Zreda, M., and Todero, A., 2003. Image processing and roughness analysis of exposed bedrock fault planes as a tool for paleoseismological analysis: Results from the Campo Felice fault (central Apennines, Italy). Geomorphology, 49(3-4), 281–301, https://doi.org/10.1016/S0169-555X(02)00191-5

[5] Pucci, S., Pizzimenti, L., Civico, R., Villani, F., & Brunori, C. A., 2021. High resolution morphometric analysis of the Cordone del Vettore normal fault scarp (2016 central Italy seismic sequence): Insights into age, earthquake recurrence and throw rates. Geomorphology, 384, 107705. https://doi.org/10.1016/j.geomorph.2021.107784

[6] Wilkinson, M., Roberts, G. P., McCaffrey, K., Cowie, P. A., Faure Walker, J. P., Papanikolaou, I., Phillips, R. J., Michetti, A. M., Vittori, E., Gregory, L., Wedmore, L., & Watson, Z. K., 2015. Slip distributions on active normal faults measured from LiDAR and field mapping of geomorphic offsets: An example from L'Aquila, Italy, and implications for modelling seismic moment release. Geomorphology, 237, 130–141. https://doi.org/10.1016/j.geomorph.2014.04.026

[7] Giaccio, B., Galadini, F., Sposato, A., Messina, P., Moro, M., Zreda, M., & Todero, A., 2002. Image processing and roughness analysis of exposed bedrock fault planes as a tool for paleoseismological analysis: Results from the Campo Felice fault (central Apennines, Italy). *Geomorphology, 49*(3-4), 281–301. https://doi.org/10.1016/S0169-555X(02)00191-5.

2.5 - Landform classification

Multidisciplinary Application of Geomorphometry for the Characterization of the Northern Gulf of Mexico Seafloor, United States

Vincent Lecours
Laboratoire d'expertise et de recherche en géographie appliquée Université du Québec à Chicoutimi
Chicoutimi, Canada
vlecours@uqac.ca

Riccardo Arosio
School of Biological, Earth, and Environmental Sciences
University College Cork
Cork, Ireland
rarosio@ucc.ie

Benjamin Misiuk
Department of Geography
Department of Earth Sciences
Memorial University of Newfoundland
St. John's, Canada
bmisiuk@mun.ca

Rachel Barrett
Institute of Geosciences
Christian-Albrechts-Universität zu Kiel
Kiel, Germany
rachel.barrett@ifg.uni-kiel.de

Margaret Dolan
Section for Marine Geology
Geological Survey of Norway
Trondheim, Norway
margaret.dolan@ngu.no

Cite as: Lecours, V., Arosio, R., Misiuk, B., Barret, R., Dolan, M. (2025). Multidisciplinary Application of Geomorphometry for the Characterization of the Northern Gulf of Mexico Seafloor, United States. In: Proceedings of Geomorphometry 2025, 9-13 June, Perugia, Italy. M. Alvioli, L. Melelli, I. Marchesini eds. CNR Edizioni, Rome. ISBN 978-88-8080-765-0. DOI: 10.5281/zenodo.14976146

Abstract—**Geomorphometry is now commonly applied to the study of the marine environment. Here, we present a case study in which multiple disciplinary approaches were integrated with geomorphometry to characterise the northern Gulf of Mexico. A digital bathymetric model spanning 233,000 km^2 and built from 3D seismic data was combined with a smaller bathymetric dataset collected using a multibeam echosounder. Using different software (*e.g.*, R, WhiteboxTools, ArcGIS Pro), terrain variables were derived and submarine landforms were extracted from these datasets. These derivatives were then integrated with other environmental variables to delineate and characterise pockmarks, predict the mean grain size of seafloor substrate, constrain and characterise a submarine landslide, and predict cold-water coral distribution in parts of the Gulf of Mexico. In an area north of the Sigsbee Escarpment, a total of 4,017 pockmarks were delineated. In the area covered by the multibeam data, the range of mean grain size was predicted to be between -0.23 and 6.29 phi (average of 1.12 phi). Important predictor variables included a broad-scale bathymetric position index, mean and standard deviation of bathymetry, and the vector ruggedness measure (VRM). The characterization of a submarine landslide using geomorphometry showed that variations in terrain variables can efficiently demarcate the headwall, but the lateral extent of the landslide toe is more challenging to define, altough the integration of a submarine landform classification helped delineate it. Finally, the ensemble model of cold-water corals enabled the identification of 3,888 km^2 of suitable habitat. Primary predictors included bathymetry, VRM, and slope. These results highlight the potential of geomorphometry to contribute to multidisciplinary environmental studies in the marine realm, which can tell us about seafloor environments' past, present, and future conditions and can be used to inform resource management, conservation, or restoration.**

I. Introduction

In the last decade since [1], the applications of geomorphometry to the marine realm have increased dramatically. More marine scientists are now aware of geomorphometry as a science, which facilitated the adaptation of terrestrial geomorphometric approaches to the specificities of underwater studies and the development of new approaches specific to marine terrain [2-4]. As new marine disciplines adopt geomorphometry to expand their analytical potential, it becomes interesting and relevant to conduct multidisciplinary characterization of areas to understand better how they evolved through time, which natural processes are influenced by their geomorphology, and how they might change in the future under various impacts from anthropogenic activities and climate change. Here, we used digital surface models of the northern Gulf of Mexico to conduct such a multidisciplinary characterization anchored in geomorphometry,

including approaches from marine geology, geomorphology, biology, and ecology.

II. METHODS

A. Data

Two digital bathymetric models were used. First, the northern Gulf of Mexico deepwater bathymetry grid built from 3D seismic data and provided by the United States Bureau of Ocean Energy Management [5] was downloaded at its native resolution of 12 m. This dataset spans approximately 233,000 km^2, with depths ranging from 39 to 3380 m deep (Fig. 1). It shows a relatively high diversity of geomorphic and geomorphological features.

Second, a digital bathymetric model produced with a Kongsberg Maritime EM 1002 multibeam echosounder and provided by the United States Geological Survey (USGS) was used (survey #W00609). The survey was performed in 2001 about 30 nautical miles south of Cape San Blas, in Florida. It has a resolution of 8 m and spans about 394 km^2 (Fig. 1).

The MultiscaleDTM R package [6] was used to derive 17 terrain variables (*e.g.*, slope, rugosity measures, curvatures) from the northern Gulf of Mexico dataset, both on the native 12 m resolution and on a resampled version of the dataset of 40 m

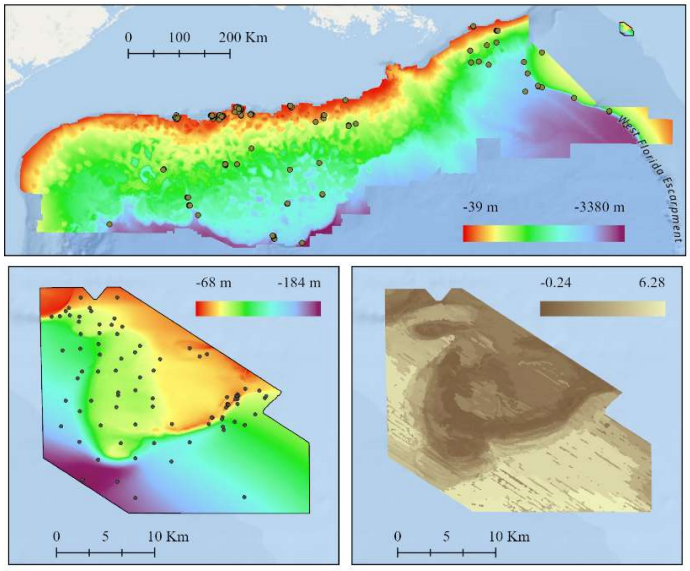

Figure 1. Northern Gulf of Mexico bathymetry grid at 40 m resolution with cold-water coral observations used for the species distribution modelling (top); digital bathymetric model produced from multibeam data with seabed sediment data used for mean grain size modelling (bottom left); and results of the mean grain size modelling (units: phi) (bottom right).

resolution – to facilitate the more computationally-intensive processes. A 3x3 window of analysis was used in both cases. Then, the multiscale capabilities of WhiteboxTools were harnessed to produce a multiscale roughness variable [7], derived using a search neighbourhood varying from 1 (3x3; analysis distance of 120 m) to 1001 (2,003 x 2,003; analysis distance of 80,12 km) and a step size of 1. For the multibeam dataset, common seafloor-surface variables used in marine habitat mapping were calculated in ArcGIS Pro using the Benthic Terrain Modeller toolbox [2]. These included slope, benthic position indices, and a vector ruggedness measure, among others, many with a window of analysis of 36 cells to account for the relative homogeneity of the area.

Seven types of morphometric features were also delineated using the MultiscaleDTM R package, at different window sizes (3x3, 9x9, 15x15, 21x21). The BRESS (Bathymetric and Reflectivity-based Segments) v.2.5.2 tool [3], which uses principles of topographic openness, pattern recognition, and texture classification to identify geomorphic elements of the seafloor, was also used using the default parameters. Four classification schemes were applied, each identifying either 4, 5, 6, or 10 types of landforms.

In terms of the other environmental variables used for the analyses, mean grain size measurements for a portion of the Gulf were obtained from the USGS usSEABED dataset [8]. This dataset is a compilation of seabed sediment data aggregated from multiple sources. Deep-sea coral occurrence data were retrieved from the United States National Oceanic and Atmospheric Administration Deep-Sea Coral Data Portal. Data were filtered to include only coral observations associated with a positional accuracy of 20 m, so they spatially aligned with the 40 m resolution pixels of the bathymetry, which left 5,769 observations.

B. Pockmark Delination and Characterization

The northwestern Gulf of Mexico north of the Sigsbee Escarpment is characterised by a distinctively deformed seafloor surface resulting from the upward migration and dissolution of deep salt deposits. As salt diapirs move up, sediments over them are uplifted creating seafloor doming structures, which are often cracked by a network of extensional faults that provide pathways for fluid and/or gas migration. When these emerge at the seafloor, they create circular or elongated depressions or craters, generally called pockmarks (*e.g.*, gas seeps or mud volcanoes), that often harbour unique ecosystems.

Here, we analysed a subset of the northern Gulf of Mexico dataset (5,135 km^2) associated with some of these doming structures to map pockmarks. A semi-automated procedure enabled by the CoMMa toolbox for ArcGIS Pro [4] was utilised. First, a boundary-based delineation on a directional median derivative was applied to extract polygons using a window of analysis of 21 cells, and a geomorphons layer was produced. Statistics were calculated on both the boundary-delineated objects and the geomorphons. Finally, a rule-based filtering was applied to retain only the polygons with specific characteristics linked to pockmarks.

C. Mean Grain Size Prediction

A number of potential substrate parameters can be mapped, such as sediment composition or presence/absence; here we focus on the mean grain size - a common metric that describes the average sediment grain diameter from a physical seabed sample. Using the multibeam dataset and its terrain derivatives, seafloor substrate patterns were mapped within an object-based image analysis (OBIA) framework. A multiresolution segmentation was applied on the terrain variables in Trimble eCognition v10.2, followed by a Grow region algorithm to merge objects with low rugosity. Objects were then further merged using a spectral difference segmentation. The final objects each contained information on the mean, standard deviation, GLCM homogeneity (all direction) and GLCM entropy (all direction) for all input layers.

Regression was used to model the mean grain size observed within each image object polygon as a function of the terrain variables. The average value of mean grain size measurements was calculated where multiple sediment samples occurred within a single polygon, resulting in 86 complete observations of predictor and response variables available for random forest modelling, which was conducted using the R package randomForest. After training, model diagnostics were investigated, and values of mean grain size were predicted over the entire extent of the multibeam dataset using the predictor values, and validation was conducted.

D. Submarine Landslide Characterisation

Landslide susceptibility at water depths greater than 120 m was modelled by Dyer *et al.* [9] using terrain variables in addition to other geomorphological, geological, and geochemical factors. Their results show that sediment type (mud, sand, gravel, or rock) and slope are the most important predictors of where a landslide will occur, although they note that the importance of slope might be overestimated as a consequence of steeper headwall scarps, which are left behind after failure [9]. To better understand these headwalls, we used the terrain variables derived from the 12 m resolution northern Gulf of Mexico dataset to characterise a specific submarine landslide and its different components quantitatively. The landslide was identified on the edge of the continental shelf in an area of high landslide probability based on the model by Dyer *et al.* [9].

E. Cold-Water Coral Distribution

An iterative ensemble species distribution modelling approach was implemented following Lecours *et al.* [10]. In short, correlations were measured between the 40 m resolution bathymetry and all terrain variables derived from it. Uncorrelated variables were then combined with the coral observation data in the SSDM R package. A geographic resampling was applied to coral occurrences to ensure that no two observations were found in the same pixel so that the importance of the environmental conditions at that location was not artificially amplified. This reduced the number of observations for the modelling to 1,706. Nine different modelling techniques were combined into the ensemble model: generalized linear models (GLM), generalized additive models (GAM), multivariate adaptive regression splines (MARS), classification tree analysis (CTA), generalized boosted models (GBM), maximum entropy (MaxEnt), artificial neural networks (ANN), random forests (RF) and support vector machines (SVM). All parameters used to run the model can be found in Lecours *et al.* [10], with the only difference being that the 10-fold validation method was conducted with only one cross-validation and that the threshold for model selection as part of the ensemble was based solely on the area under the curve (AUC) of the receiver operating characteristic (ROC) curve, which had to be greater than 0.75. Results of this first model were analyzed, and the model was rerun using only the variables that contributed more than 5% to the model.

III. Results

A. Terrain Characterisation

The various terrain variables derived from the bathymetry show a high geomorphometric diversity, hinting at the different geological processes that formed them. The multiscale roughness analysis clearly identified some of the known features in the area with higher values, such as the West Florida Escarpment, the Keathley Canyon, the slopes of the Mississippi Canyon, and the edges of many salt domes. Dominant scales for roughness were identified at 7x7 (280 m by 280 m), 87x87 (3.48 km), and 111x111 (4.44 km), among others. The different characterizations of morphometric features identified that the area is mainly composed of flat areas and slopes, with a significant number of channels and ridges depending on the scale of analysis.

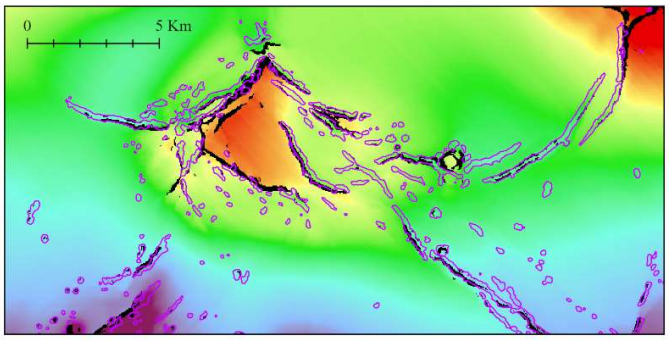

Figure 2. Subset of the northern Gulf of Mexico dataset showing the delineated pockmarks (purple polygons), and the areas identified as suitable for cold-water corals (black pixels). Background bathymetry ranges from about 230 m deep (in red) to 475 m deep (in dark purple).

B. Pockmark Delination and Characterization

A total of 4,017 pockmarks were delineated in the sub-area studied. The pits form within faults (elongated depressions) or are

independent, single structures (about 44% of the pockmarks). Some of these single pockmarks were as deep as 40 m. At many places, trains of pockmarks coalesce to create thin, elongated features (~400 instances), potentially indicating a buried fault that has not breached the surface. There appears to be no correlation between depth and structure type, suggesting that similar processes occur throughout the region. The pockmarks align closely with the valleys and pits identified by the BRESS tool (Fig. 2).

C. Mean Grain Size Prediction

The mean grain size predictions are presented in Fig. 1. The R^2 statistic from the cross-validation suggested that the predictions explained about 61% of the variance of the ground-truthed observations. Results suggested that the mean broad-scale BPI was the most important predictor variable, followed by the mean bathymetry of each image object, the standard deviation of bathymetry, and the mean VRM. All other predictors contributed less than 10% to the model's predictive capacity.

D. Submarine Landslide Characterisation

While the headwall of the submarine landslide was clearly demarcated by variations in the value of most terrain variables, they must be considered together to fully understand the boundaries of the submarine landslide. The lateral extent of the landslide toe was more challenging to define, but can be constrained using northness in combination with the morphometric feature classification. Small variations at the toe are also visible in the plots of relative position variables, the roughness index elevation (RIE), and minimum curvature. The morphometric features characterization highlighted the two-part nature of the landslide: the eroded headwall region, where the slope is incised by channels that drain towards the centre of the headwall; and the translational body of the landslide, characterised by ridges and channels, and slope-parallel compressional ridges at the toe.

E. Cold-Water Coral Distribution

The uncorrelated variables included in the first model were bathymetry, slope, easterness, northerness, topographic position index, vector ruggedness measure (VRM), and maximum, minimum, plan, and twist curvatures. After the first model was run, only bathymetry, VRM, and slope were deemed to contribute enough to the predictions to be retained for the final model, which identified approximately 3,888 km^2 of suitable habitat (>70% of probability of occurrence) for cold-water corals. However, based on the evaluation metrics, the model's performance was only fair. Bathymetry remained the primary driver of coral distribution, followed by VRM and slope. Despite corals being found at all depths, predicted coral distribution generally aligns closely with broad-scale topographic highs in relatively shallower waters, and with finer-scale topographic lows such as valleys and pits identified by the submarine landform classifications and the delineated pockmarks (Fig. 2).

IV. Conclusions

These examples of applications of marine geomorphometry show the benefits of multidisciplinary efforts. Without combining the different analyses, we would not know that some valleys and pits identified by submarine landform classifications correspond to pockmarks that may have been formed by gas seeping through the seafloor, which create suitable habitat for cold-water corals. They also demonstrate the potential of a single data type, digital bathymetric models, to provide relevant information about dynamic and complex marine systems. With the increased interest in marine resources, it becomes critical to map and comprehensively characterize seafloor environments to inform decision-making in several contexts.

References

[1] Lecours, V., V.L. Lucieer, M.F.J. Dolan, and A. Micallef, 2015. "An ocean of possibilities: Applications and challenges of marine geomorphometry" in J. Jasiewicz, Z. Zwoliński, H. Mitasova and T. Hengl, Geomorphometry for geosciences. ISG. Poznań, Poland, 23-26.

[2] Walbridge, S., N. Slocum, M. Pobuda and D.J. Wright, 2018. "Unified geomorphological analysis workflows with Benthic Terrain Modeler" Geosciences, 8(3), 94. https://doi.org/10.3390/geosciences8030094.

[3] Masetti, G., L.A. Mayer and L.G. Ward, 2018. "A bathymetry- and reflectivity-based approach for seafloor segmentation" Geosciences, 8(1), 14. https://doi.org/10.3390/geosciences8010014.

[4] Arosio, R., J. Gafeira, L.H. De Clippele, A.J. Wheeler, V.A.I. Huvenne, F. Sacchetti, L.A. Conti and A. Lim, 2024, "CoMMa: A GIS geomorphometry toolbox to map and measure confined landform" Geomorphology, 458, 109227. https://doi.org/10.1016/j.geomorph.2024.109227.

[5] Bureau of Ocean Energy Management, 2017, "Northern Gulf of Mexico deepwater bathymetry grid from 3D seismic.", https://www.boem.gov/Gulf-of-Mexico-Deepwater-Bathymetry/.

[6] Ilich, A.R., B. Misiuk, V. Lecours and S.A. Murawski, 2023, "MultiscaleDTM: An open-source R package for multiscale geomorphometric analysis." Transactions in GIS, 27, 1164-1204. https://doi.org/10.1111/tgis.13067.

[7] Lindsay, J.B. and D.R. Newman, 2018, "Hyper-scale analysis of surface roughness." Geomorphometry 2018 Peer J Preprints, 6, e27110v1. https://doi.org/10.7287/peerj.preprints.27110v1.

[8] Buczkowski, B.J., J.A. Reid, P.N. Schweitzer, V.A. Cross and C.J. Jenkins, 2020, "usSEABED—Offshore surficial-sediment database for samples collected within the United States Exclusive Economic Zone." U.S. Geological Survey data release, https://doi.org/10.5066/P9H3LGWM.

[9] Dyer, A.S., M. Mark-Moser, R. Duran and J.R. Bauer, 2024, "Offshore application of landslide susceptibility mapping using gradient-boosted decision trees: a Gulf of Mexico case study." Natural Hazards, 120, 6223–6244. https://doi.org/10.1007/s11069-024-06492-6.

[10] Lecours, V., A. Oxton, D. Khor and J. Tiplea, 2024, "High-resolution ensemble modelling of coral distributions in the northern Gulf of Mexico based on geomorphometry: coral diversity and benthic habitat fragmentation from oil and gas infrastructure to inform spatial planning." Aquatic Conservation: Marine and Freshwater Ecosystems, 34(9), e4234. https://doi.org/10.1002/aqc.4234

Introducing the Geomorphometric Atlas of Romania: A Publicly Available Database of Landform Classifications and Land-Surface Variables based on FABDEM

Andrei Ioniță
Institute for Advanced Environmental Research (ICAM)
West University of Timișoara
Timișoara, Romania
andrei.ionita@e-uvt.ro

Lucian Drăguț
Department of Geography
West University of Timișoara
Timișoara, Romania
lucian.dragut@fulbrightmail.org

Cite as: Ioniță, A., Drăguț, L. (2025). Introducing the Geomorphometric Atlas of Romania: A Publicly Available Database of Landform Classifications and Land-Surface Variables based on FABDEM. In: Proceedings of Geomorphometry 2025, 9-13 June, Perugia, Italy. M. Alvioli, L. Melelli, I. Marchesini eds. CNR Edizioni, Rome. ISBN 978-88-8080-765-0. DOI: https://doi.org/10.5281/zenodo.15263729

Abstract— **This paper introduces the first national geomorphometric atlas of Romania, an open-access database developed to support detailed terrain assessment and landform characterization. The atlas integrates established landform classification frameworks and a broad set of morphometric variables derived from the 30 m Forest and Buildings Removed Copernicus Digital Elevation Model (FABDEM). To accurately represent Romania's diverse topography, land-surface parameters (LSPs) and landform types were computed across multiple spatial scales based on the country's specific topographic grain. The atlas includes both common and lesser-used morphometric indices, derived using automated methods in SAGA GIS and WhiteboxTools' Geomorphometric Analysis toolbox. All processing was conducted in Romania's national coordinate system, Stereo70 (EPSG:31700), and results were reprojected to Web Mercator (EPSG:3857) only for web-based visualization. The derived data layers were produced in full compliance with FABDEM's non-commercial license; no redistribution of the raw elevation data occurs. Available through ArcGIS Online and Google Drive, the atlas provides a standardized, high-resolution resource to support geoscientific research, environmental modeling, and spatial planning. Its open-access design enables users to visualize and analyze terrain properties from national to local scales, contributing to improved understanding and practical use of Romania's geomorphological landscape.**

I. Introduction

Geomorphometric atlases provide standardized datasets for applications in geomorphology, environmental research, and land-use planning. Several global and continental-scale atlases have been developed, such as those by [1], which derived core morphometric variables from the SRTM dataset at 90 m resolution, and [2], which focused on statistical terrain attributes. More recently, global initiatives like Geomorpho90m [3] have used MERIT DEM at 90 m to generate multi-variable morphometric datasets for hydrological, geological, and environmental modeling.

At the European scale, projects such as the EcoDataCube [4] have created integrated geospatial platforms linking morphometric indicators with open satellite and environmental data. Other studies [5, 6] have explored automated topographic classification using cloud-based tools like Google Earth Engine.

Despite these advancements, no high-resolution, country-level geomorphometric atlas has been available for Romania. To address this gap, the Geomorphometric Atlas of Romania was developed as an open-access database based on the 30 m FABDEM elevation product. This atlas includes landform classification outputs and a broad set of derived morphometric variables computed at multiple spatial scales tailored to Romania's specific topographic grain.

This work builds upon a previous framework introduced by Ioniță et al. [7], which focused on landform classifications from SRTM and MERIT DEM data. In contrast, the present study integrates FABDEM, expands the morphometric parameter set, introduces topographic grain calibration, and improves public accessibility through a standardized WebApp and downloadable datasets. The atlas is designed to support interdisciplinary applications in geomorphological mapping, environmental monitoring, spatial planning, and hazard assessment.

Mercator (EPSG:3857) for online viewing. Raster datasets were converted to tile layers and vector datasets to vector tiles, enabling smooth multiscale navigation. The updated WebApp, redesigned from the previous [7] version, includes a broader set of thematic layers grouped by LSP type, as well as new tools for base map switching, cross-variable comparison, and location-specific querying.

The full atlas is accessible online via ArcGIS Online and downloadable through Google Drive. All derived products comply with FABDEM's non-commercial license. No raw elevation data is redistributed.

III. RESULTS

Topographic grain analysis identified an optimal analysis window size of 330 m (11 × 11), with a broader grain threshold observed around 810 m (27 × 27). A standard 3 × 3 window was also included for baseline comparison. These three reference scales were used consistently throughout the atlas to compute landform classifications and morphometric variables tailored to Romania's terrain variability.

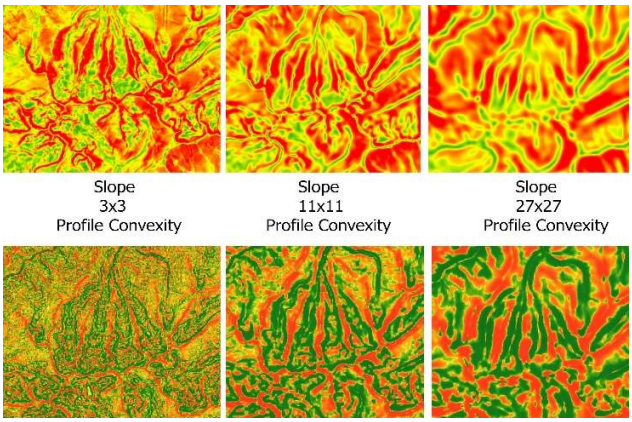

Fig. 2. Comparison of two key land-surface variables—slope and profile convexity—computed at three spatial analysis scales (3×3, 11×11, 27×27). The figure illustrates how increasing topographic grain size generalizes terrain detail and affects morphometric expression.

Based on the methodologies described, a total of twelve landform classification maps were generated, integrating both global models and region-specific frameworks (Fig. 2). Geomorphons-based classifications were computed at all three analysis scales, using a flatness threshold of 1°, to highlight variations in landform structure under different spatial generalizations.

Using WhiteboxTools and SAGA GIS, an expanded set of 27 morphometric variables was derived at multiple scales, including slope, convexity, profile and plan curvature, roughness metrics, and directional derivatives. The core LSVs (Slope, Aspect, PROC, PLAC, LONC, CRSC, PRCM) were initially computed at 3×3, 11×11, and 27×27 window sizes, resulting in a total of 21 terrain maps from this base group alone. Additional variables, such as angular deviation, curvature variance, elevation percentile, elevation extremes, terrain openness, topographic position index, and multiscale deviation indices were computed to support nuanced topographic interpretation.

A notable extension beyond the earlier work [7] is the inclusion of these newly derived LSPs, which were not present in the initial release. These additions substantially enhance the atlas's capacity to represent complex terrain morphologies at both macro and micro scales, supporting a broader range of geospatial analyses.

All results were standardized, thematically grouped, and incorporated into a newly developed WebApp, redesigned from the original version, to support multiscale interactive visualization and spatial exploration.

IV. DISCUSSION

A key innovation introduced by this atlas is the determination of Romania's optimal topographic grain, which is essential for scale-sensitive geomorphometric analysis. By calibrating land-surface parameters across representative spatial windows, the atlas offers a scalable framework applicable to both national and sub-regional studies. The 330 m grain size is tailored to the 30 m FABDEM input and national-scale application; regional analyses or higher/lower resolution DEMs would require recalibration to ensure scale compatibility with terrain variability.

The atlas supports a wide range of disciplines, including geomorphology, hydrology, geology, forestry, environmental sciences, agriculture, and spatial planning. By offering ready-to-use terrain indicators, the database enables users without specialized GIS or DEM processing expertise to access critical morphometric information. This standardization also reduces the need for redundant calculations and facilitates the integration of terrain variables into applied research.

Despite these advantages, certain limitations exist. The atlas is constrained by the 30 m resolution of FABDEM, as no higher-resolution open-access DEM currently exists for Romania.

The WebApp is accessible at the address: https://experience.arcgis.com/experience/9be599ab17c049c9bf1a93203197156f (Fig. 3).

The original dataset can be downloaded publicly from the following address: https://drive.google.com/drive/u/1/folders/1FHn_Jb-QmmiSop0wM77IMLbzAaHt1zTt

V. CONCLUSION

This study addresses a key data gap in Romania by providing a national-scale, open-access geomorphometric atlas based on 30 m FABDEM data. Through the derivation of standardized land-surface parameters and landform classifications across multiple spatial scales, the atlas enables accurate topographic assessment for diverse environmental and geoscientific applications.

By integrating newly derived morphometric variables—such as elevation deviation, curvature variance, and topographic position indicators—the atlas expands its utility for advancedterrain analysis. It supports interdisciplinary research by facilitating integration with variables from fields such as biology,

chemistry, physics, and geosciences, while also serving as a resource for national and regional planning efforts.

The atlas provides decision-makers and practitioners in agriculture, forestry, hydrology, hazard management, and environmental policy with accessible, pre-processed terrain information. Its open-access format encourages reproducibility, promotes cross-sector collaboration, and enhances Romania's capacity for data-driven environmental monitoring and spatial policy development.

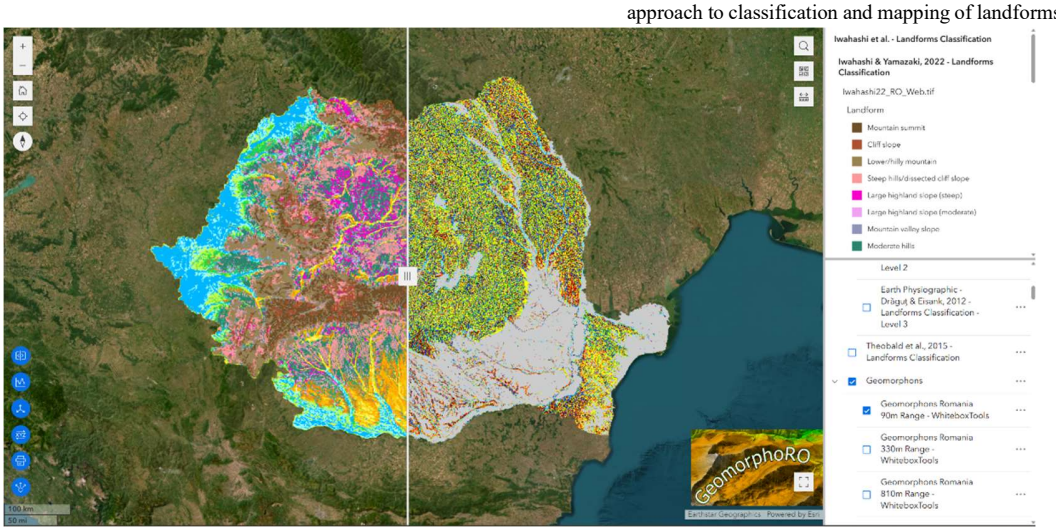

Fig. 3. The interactive WebApp for visualizing the atlas

VI. ACKNOWLEDGEMENTS

We extend our gratitude to the GIS Master's program students at the West University of Timișoara for their contributions to this work. We also thank Ian Evans, Michal Gallay, and Mike Shand for their constructive feedback on our previously published Journal of Maps article [7], which provided valuable insights that contributed to the development of the current extended version.

REFERENCES

[1] H. I. Reuter and A. D. Nelson, "Worldterrain – A Contribution to the Global Geomorphometric Atlas," in *Geomorphometry 2009 Conference Proceedings, Zurich, Switzerland, Edited by: Purves Ross, Gruber Stephan & Straumann Ralph*, Zurich, 2009. [Online]. Available: https://geomorphometry.org/2009-2/

[2] P. L. Guth, "Geomorphometry in MICRODEM," *In Hengl, T., Reuter, H.I. (eds), Geomorphometry: concepts, software, applications. Developments in Soil Science Series, Elsevier*, pp. 351–366, 2009.

[3] G. Amatulli, D. McInerney, T. Sethi, P. Strobl, and S. Domisch, "Geomorpho90m, empirical evaluation and accuracy assessment of global high-resolution geomorphometric layers," *Sci Data*, vol. 7(1), no. 162, 2020.

[4] M. Witjes, L. L. Parente, J. Krizan, T. Hengl, and L. Antonic, "Ecodatacube.eu: Analysis-ready open environmental data cube for Europe," *Res Sq*, 2023.

[5] O. Csillik and L. Drăguț, "Towards a global geomorphometric atlas using Google Earth Engine," *Geomorphometry 2018 Conference Proceedings, Boulder, Colorado, USA, Edited by: Guth Peter, Grohmann Carlos, Peckham Scott & Crosby Chris*, vol. Boulder, 2018, [Online]. Available: https://geomorphometry.org/geomorphometry-2018/

[6] L. Drăguț and C. Eisank, "Automated object-based classification of topography from SRTM data," *Geomorphology*, vol. 141–142, pp. 21–33, Mar. 2012.

[7] A. Ioniță, M. Lungu, M. Baleț, and A. Todor, "The geomorphometric atlas of Romania: an open-access database on landform classifications and morphometric variables," *J Maps*, vol. 20, no. 1, Dec. 2024, https://doi.org/10.1080/17445647.2024.2354712

[8] B. Candrea, "Harta unităților de relief din România." Accessed: Jun. 05, 2023. [Online]. Available: https://geo-spatial.org/vechi/download/harta-unitati-relief-romania

[9] J. Jasiewicz and T. F. Stepinski, "Geomorphons — a pattern recognition approach to classification and mapping of landforms," *Geomorphology*, vol. 182, pp. 147–156, 2013.

[10] J. Iwahashi, I. Kamiya, M. Matsuoka, and D. Yamazaki, "Global terrain classification using 280 m DEMs: segmentation, clustering, and reclassification," *Prog Earth Planet Sci*, vol. 5, no. 1, pp. 1–31, 2018.

[11] J. Iwahashi and R. J. Pike, "Automated classifications of topography from DEMs by an unsupervised nested-means algorithm and a three-part geometric signature," *Geomorphology*, vol. 86, pp. 409–440, 2007.

[12] J. Iwahashi and D. Yamazaki, "Global polygons for terrain classification divided into uniform slopes and basins," *Prog Earth Planet Sci*, vol. 9, no. 33, 2022.

[13] M. Meybeck, P. Green, and C. Vorosmarty, "A New Typology for Mountains and Other Relief Classes," *Mt Res Dev*, vol. 21, no. 1, pp. 34–45, 2001.

[14] L. Hawker *et al.*, "A 30 m global map of elevation with forests and buildings removed," *Environmental Research Letters*, vol. 17, no. 2, 2022.

[15] W. F. Wood and J. B. Snell, "A quantitative system for classifying landforms," *Quartermaster Research & Engineering Command, U.S. Army Technical Report, EP-124.*, 1960.

[16] R. J. Pike, W. Acevedo, and D. H. Card, "Topographic grain automated from digital elevation models," in *In Proceedings, Auto-Carto*, ASPRS/ACSM Baltimore MD, 1989, pp. 128–137

[17] J. B. Lindsay, "Whitebox GAT: A case study in geomorphometric analysis," *Comput Geosci*, vol. 95, pp. 75–84, 2016.

[18] J. Wood, "The Geomorphological Characterisation of Digital Elevation Models," University of Leicester, Leicester, 1996.

[19] "Whitebox Tools User Manual - Geomorphometric Analyses."

[20] T. Hengl and H. I. Reuter, *Geomorphometry: Concepts, Software, Applications*, vol. 33. Developments in Soil Science. Elsevier, 2008.

Geomorphic Distribution Modeling of Desert Pavements: Towards a Global Assessment

Alexander Brenning [1], Lucca Güldner
Department of Geography
Friedrich Schiller University Jena
Jena, Germany

Kerstin Schepanski
Institute of Meteorology
Freie Universität Berlin
Berlin, Germany

Michael Dietze
Institute of Geography
Georg August University Göttingen
Göttingen, Germany
German Research Center for Geosciences (GFZ)
Potsdam, Germany

Markus Fuchs
Department of Geography
Justus Liebig University Giessen
Giessen, Germany

[1] alexander.brenning@uni-jena.de

Cite as: Brenning, A., Güldner, L., Schepanski, K., Dietze, M. Fuchs, M. (2025). Geomorphic Distribution Modeling of Desert Pavements: Towards a Global Assessment In: Proceedings of Geomorphometry 2025, 9-13 June, Perugia, Italy. M. Alvioli, L. Melelli, I. Marchesini eds. CNR Edizioni, Rome. ISBN 978-88-8080-765-0. DOI: 10.5281/zenodo.15014982

Abstract— **Desert pavements, characterized by a stone layer over fine eolian materials, are key geomorphological features in arid regions and play a critical role in the global dust cycle. Despite their importance, quantitative evidence regarding their global distribution remains limited. This study provides a preliminary assessment of desert pavement distribution using a GIS-based multiple-criteria decision analysis (GIS–MCDA) framework. Key environmental factors, including climate, topography, vegetation, soil texture, and anthropogenic disturbance, were incorporated into a global favorability index at a 1 km × 1 km resolution. Validation against 20 documented desert-pavement research sites revealed a significant association with high index values, with 15% of sites exhibiting an index ≥0.90 and 80% ≥0.75. The model estimates that up to 25.7 million km², or 19.0% of the Earth's land surface, holds potential for desert pavements. These results provide a foundation for future studies, emphasizing the need for localized, high-resolution research and the integration of geomorphometric and remote-sensing techniques with machine-learning models. This initial global assessment underscores the utility of GIS–MCDA in geomorphic distribution modeling and highlights the importance of refining global environmental datasets for arid landscapes.**

I. Introduction

Desert pavements are widespread yet complex geomorphological phenomena in desert environments worldwide and are key components of the global dust cycle [1, 2, 3]. Characterized by a distinct stone layer above fine, eolian materials, their distribution is constrained by a combination of topographic, hydroclimatic, geomorphic, and biological processes. Despite their prevalence and geomorphic importance, knowledge regarding their distribution, characteristics, and environmental feedback mechanisms within the Earth system remains limited. Surprisingly, despite global mapping efforts for many other land surface characteristics, quantitative evidence of their distribution and significance is still scarce, though anecdotal estimates suggest that nearly 50% of arid land surfaces feature desert pavements (defining 'arid' as mean annual precipitation < 250 mm) [4].

This study aims to provide an initial assessment of the potential global distribution of desert pavements. Confronted with methodological challenges, particularly the scarcity of suitable training data for supervised classification modeling using machine-learning or statistical techniques, this study adopts a pragmatic approach. By utilizing prescriptive cartographic models within a GIS-based multiple-criteria decision analysis (GIS–MCDA) framework [5], the research integrates geomorphological expertise with available global GIS datasets. This approach, while preliminary, leverages local evidence from existing publications for validation, offering a foundation for more rigorous future studies using supervised statistical and machine-learning models that have been successful in other geomorphic distribution modeling tasks [6, 7].

II. Methods and Data

To explore the geographic distribution of desert pavements, the proposed GIS-MCDA approach leverages global GIS datasets representing first-order limiting factors of desert pavement

TABLE I. CRITERIA AND DATA SOURCES USED FOR THE GIS-BASED MULTICRITERIA ANALYSIS OF POTENTIAL DESERT PAVEMENT DISTRIBUTION.

Theme	**Variable and source**	**Suitable range**	**Locally suitable**
Ecoregion	Köppen–Geiger ecoregions 1991-2020 [8]	BWh, BWk	BSh, BSk
Climate	CHELSA V2.1 precipitation data 1981-2010 [9, 10]	70-200 mm	<70 mm, 200-320 mm
Vegetation	Barren land in Global 1-km Consensus Land Cover [11]	>90%	80-90%
Topography	Slope angle, Standard deviation of elevation from Global 1 km land surface parameters dataset [12]	<2° <25 m	2-5° 25-40 m
Soil texture	Ratio of coarse fraction in top to underlying layer; SoilGrids 250 m [13]	Ratio >0.95	n/a
Anthropogenic disturbance	Nighttime lit surface fraction [14]	<5%	5-10%
Water bodies	Percent water body from Global 1 km land surface parameters dataset [12]	0%	<20%

distribution. The model does not aim to pinpoint exact locations but instead delineates an "envelope" of their potential distribution.

Specifically, the thematic aspects considered are climate [8], topography [9], vegetation [10], soil texture [11], and anthropogenic disturbance [12] (Table 1), sourced at or downscaled to a ~1 km resolution. Each GIS layer is reclassified into "suitable," "locally suitable," and "unsuitable," with ratings of 1.0, 0.5, and 0 assigned, respectively. These ratings layers are combined into a weighted average to create a global favorability index. The climate and the vegetation layer are double weighted.

The chosen criteria reflect general characteristics of environments that are favorable for the presence of desert pavements, while accounting for the fact that the chosen global GIS layers are strongly generalized and therefore exhibit

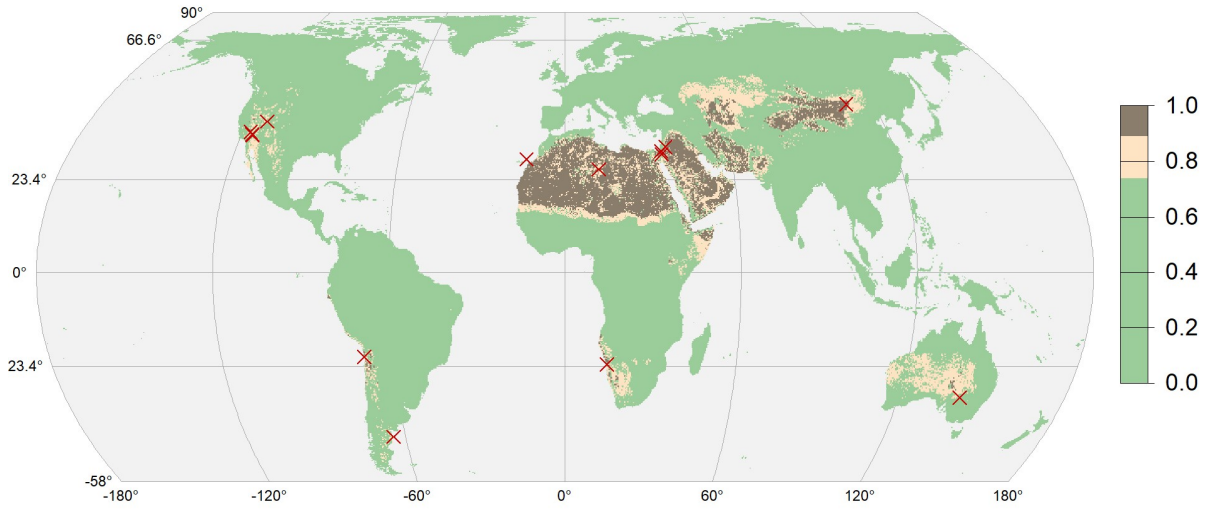

Figure 1. Potential global distribution range of desert pavements based on GIS–MCDA. Larger index values indicate a higher favorability for desert pavements. Field sites with coordinates identifiable in the literature are marked with red crosses (from West to East: Mojave Desert, California; Black Rock Desert, Utah; Atacama, Chile; Patagonia, Argentina; Fuerteventura, Spain; Negev, Israel; Badia Desert, Jordan; Gobi, Mongolia; Strzelecki Desert, Australia).

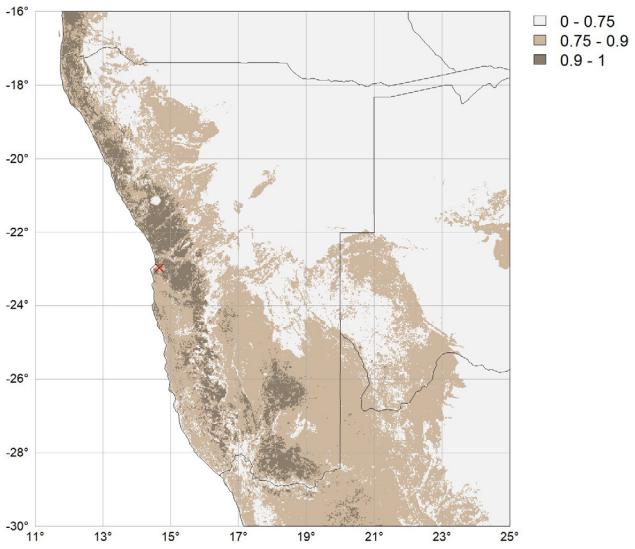

Figure 2. Potential desert pavement distribution in Namibia based on GIS–MCDA.

significant variation in environmental conditions within a grid cell. Moreover, the climatic and soil texture input layers are themselves model outputs that are based on sparse observational data from desert environments, affecting their accuracy, and ultimately all GIS layers are only proxies for possible processes that favor or inhibit the existence of desert pavements. Against this background, the "suitable" and "locally suitable" categories were defined, generally following the distributional statistics of these variables for 20 desert pavement research sites identified in the literature.

Since rainfall events, and even rare high-intensity events, may erode or bury a superficial stone layer, only Köppen–Geiger desert climates were identified as being fully suitable, while steppe ecoregions may be locally suitable [8], and a global precipitation climatology was accessed to obtain quantitative evidence [9, 10]. Desert pavement evidences are also concentrated in barren land based on a consensus vegetation density dataset [11]; it serves as an important exclusion criterion since root-forming plants stabilize the soil and are associated with increased bioturbation. Indirectly, vegetation may also indicate more humid conditions.

Topography controls not only erosion and deposition by wind and water, but also the availability and downslope displacement of clasts forming the surface layer. A coarse-resolution slope angle criterion and the within-cell elevation standard deviation [12] are both informative indicators based on the available evidence. The geomorphometric data from the Global 1-km land surface parameters dataset [12] is based on the Multi-Error-Removed Improved-Terrain DEM (MERIT DEM, 90 m resolution) [13].

By definition, a seemingly ideal indicator of desert pavement is the ratio of coarse material in the top layer versus the underlying layers in globally available gridded soil data products [14]. Nevertheless, the machine-learning models used to generate SoilGrids data must extrapolate empirical rules from more densely sampled, often more humid regions into the extremely data-poor desert environments relevant to this study (e.g., Namibia: 1.7 soil profiles per 1000 km²). Because of this, it was decided to give this layer (only) an equal weight, balancing the high relevance of this layer against its large uncertainties. Finally, anthropogenic disturbance, as represented by a location's nighttime lit surface fraction [15], helps to identify and exclude areas in which soils are more likely disturbed due to urban sprawl or along major infrastructure or mine sites.

A preliminary validation of the model's predictive capacity was conducted by comparing its outputs against the locations of 20 documented desert pavement field sites across diverse arid regions.

III. Results and Discussion

The empirical validation showed that 15% of the desert pavement field sites exhibited a favorability index value ≥0.90, while 80% had an index value greater than ≥0.75. These areas should be prioritized for further refinement using higher-resolution environmental data and supervised classification techniques.

The GIS–MCDA yielded significant insights into the potential global distribution of desert pavements, as shown in Figure 1. According to the derived index, an estimated 12.1 million km², or approximately 9.0% of the Earth's total land surface (excluding Antarctica), has a high favorability index value (≥0.90), indicating that the favorability criteria are nearly fully satisfied. This high-favorability area corresponds to 50.0% of all arid land (<250 mm). Relaxing the threshold to include areas with an index value ≥0.75 expands the potential area to 25.7 million km², or 19.0% of the Earth's land surface. It covers 88.7% of all arid land and partly extends beyond it.

Considering the case of Namibia (Figure 2), where our future research will be focused, it becomes evident that some areas with high favorability index values may exhibit a high dust emission potential, making desert pavements as accretionary features less likely. This is especially true for coastal areas in Namibia.

V. Conclusions and Outlook

Our GIS-based multicriteria analysis demonstrates promise in delineating an initial global distribution of desert pavements using globally available environmental datasets. Despite encouraging validation results using sparse evidence from the literature, this research exposes critical gaps in the specificity and thematic depth of current global soil datasets for arid environments.

This study serves as an exploratory step, suggesting that future efforts should prioritize localized, high-resolution studies to generate refined data that better capture the relationships between local topography and desert pavement formation and preservation. An additional variable that should be incorporated in future model enhancements is modeled atmospheric dust flux [16]. Remote sensing data could further complement this approach, aiding in the differentiation of stable, stone-covered surfaces from other desert soils [17].

REFERENCES

[1] Anderson, K., S. Wells, and R. Graham, 2002. "Pedogenesis of vesicular horizons, Cima volcanic field, Mojave desert, California." Soil Sci. Soc. Am. J., 66, 878–887.

[2] Dietze, M., S. Bartel, M. Lindner, and A. Kleber, 2012. "Formation mechanisms and control factors of vesicular soil structure." Catena, 99, 83–96.

[3] Schepanski, K., 2018. "Transport of mineral dust and its impact on climate." Geosciences, 8(5), 151. https://doi.org/10.3390/geosciences8050151

[4] Walker, A.S., 1986. "Eolian landforms." In: Short, N.M. and R.W. Blair Jr. (Eds.), Geomorphology from space: A global overview of regional landforms. Special Publication 486. NASA Scientific and Technical Branch, Washington DC, 447–520.

[5] Greene, R., R. Devillers, J.E. Luther and B.G. Eddy, 2011. "GIS-based multiple-criteria decision analysis." Geography Compass, 5/6, 412-432. https://doi.org/10.1111/j.1749-8198.2011.00431.x

[6] Hjort, J. and M. Luoto, 2013. "2.6 Statistical Methods for Geomorphic Distribution Modeling." Treatise on Geomorphology, 2, 59-73. https://doi.org/10.1016/b978-0-12-374739-6.00028-2

[7] Goetz, J.N., A. Brenning, H. Petschko, and P. Leopold, 2015. "Evaluating machine learning and statistical prediction techniques for landslide susceptibility modeling." Computers & Geosciences, 81, 1-11.

[8] Beck, H.E., T.R. McVicar, N. Vergopolan, A. Berg, N.J. Lutsko, A. Dufour, Z. Zeng, X. Jiang, A.I.J.M. van Dijk, and D.G. Miralles, 2023. "High-resolution (1 km) Köppen-Geiger maps for 1901–2099 based on constrained CMIP6 projections." Scientific Data, 10, 724. https://doi.org/10.1038/s41597-023-02549-6

[9] Karger, D., O. Conrad, J. Böhner, T. Kawohl, H. Kreft, R.W. Soria-Auza, N.E. Zimmermann, H.P. Linder, and M. Kessler, 2017. "Climatologies at high resolution for the earth's land surface areas." Scientific Data, 4, 170122. https://doi.org/10.1038/sdata.2017.122

[10] Karger, D. N., O. Conrad, J. Böhner, T. Kawohl, H. Kreft, R.W. Soria-Auza, N.E. Zimmermann, H.P. Linder, and M. Kessler, 2021. "Climatologies at high resolution for the earth's land surface areas." EnviDat. https://www.doi.org/10.16904/envidat.228

[11] Tuanmu, M.-N., and W. Jetz, 2014. "A global 1-km consensus land-cover product for biodiversity and ecosystem modeling." Global Ecology and Biogeography, 23(9), 1031-1045. https://doi.org/10.1111/geb.12182

[12] Li, L., G. Bisht, D. Hao, and L.R. Leung, 2024. "Global 1 km land surface parameters for kilometer-scale Earth system modeling." Earth System Science Data, 16, 2007–2032. https://doi.org/10.5194/essd-16-2007-2024

[13] Yamazaki, D., D. Ikeshima, J. Sosa, P.D. Bates, G.H. Allen, and T.M. Pavelsky, 2019. "MERIT Hydro: A high-resolution global hydrography map based on latest topography dataset." Water Resources Research, 55(6), 5053–5073. https://doi.org/10.1029/2019wr024873

[14] Hengl, T., J. Mendes de Jesus, G.B.M. Heuvelink, M. Ruiperez Gonzalez, M. Kilibarda, A. Blagotić, W. Shangguan, M.N. Wright, X. Geng, B. Bauer-Marschallinger, M.A. Guevara, R. Vargas, R.A. MacMillan, N.H. Batjes, J.G.B. Leenaars, E. Ribeiro, I. Wheeler, S. Mantel and B. Kempen, 2017. "SoilGrids250m: Global gridded soil information based on machine learning." PLoS ONE, 12(2), e0169748. https://doi.org/10.1371/journal.pone.0169748

[15] Elvidge, C.D, M. Zhizhin, T. Ghosh, F.C. Hsu, and J. Taneja, 2021. "Annual time series of global VIIRS nighttime lights derived from monthly averages: 2012 to 2019." Remote Sensing, 13(5), 922. https://doi.org/10.3390/rs13050922

[16] Feuerstein, S., and K. Schepanski, 2019. „Identification of dust sources in a Saharan dust hot-spot and their implementation in a dust-emission model." Remote Sensing, 11, 4, https://doi.org/10.3390/rs11010004

[17] Potter, C. 2016. "Mapping changes in desert pavement surfaces of the Lower Colorado Desert of southern California using Landsat time series analysis." Int. J. Adv. Remote Sensing and GIS, 6, 1747-1754.

Application of Physical Geomorphometry in Digital Geomorphological Mapping

Anton B. Popov
Faculty of Geography
MSU-BIT university
Shenzhen, P.R. China
antonmsu1117@gmail.com

Jozef Minár
Department of Physical Geography and Geoinformatics
Comenius University
Bratislava, Slovak Republic
jozef.minar@uniba.sk

Cite as: Popov, A., Minár, J. (2025). Application of Physical Geomorphometry in Digital Geomorphological Mapping. In: Proceedings of Geomorphometry 2025, 9-13 June, Perugia, Italy. M. Alvioli, L. Melelli, I. Marchesini eds. CNR Edizioni, Rome. ISBN 978-88-8080-765-0. DOI: 10.5281/zenodo.15022784

Abstract— **This study builds on the principles of physical geomorphometry, focusing on the relationship between gravitational energy and geomorphometric variables. We applied a modified version of the algorithm for physically-based elementary land surface segmentation which also integrates dynamic least squares (DLS) generalization and GEOBIA. The modified algorithm produced plausible and genetically interpretable results in both areas, reinforcing the value of physical geomorphometry for geomorphological mapping. Additionally, we introduced the concept of a physical-geomorphometric signature, which proved highly effective for quantitatively comparing different genetic groups of landforms.**

I. INTRODUCTION

Geomorphological maps are an essential resource for numerous applications related to land surface studies. Enhancing these maps by integrating geomorphometric approaches with spatial data science techniques significantly improve their accuracy and utility. While machine learning algorithms have become a key tool in this process, their inherent limitations prevent them from serving as a standalone solution for geomorphological mapping. Instead, they function more effectively as a complementary approach.

Physical geomorphometry (PG), on the other hand, is uniquely suited to address these challenges. By directly linking geomorphometric variables to gravitational energy, PG enables land surface partitioning that adheres not only to the principle of regionalization—ensuring internal homogeneity and external differentiation—but also to fundamental physical laws. This integration enriches the resulting segments with deeper geomorphological significance, providing a more robust foundation for interpretation and analysis.

In this paper, we build upon the elementary physically-based land surface segmentation proposed in [1], and the extension of its application to the diverse topographies of karst and glacial landscapes in [2]. This adaptation underscores the versatility and potential of PG in advancing geomorphological mapping techniques.

II. MATERIALS AND METHODS

A. Study areas

The study was conducted in Slovakia across two contrasting topographies: Malá Studená Dolina (58.4 ha) and the Silická planina Plateau (217 ha). The first located in the Tatra Mountains (2,066–2,516 m a.s.l.), represents a classic Pleistocene glacial cirque. The second, Silická planina Plateau, part of the Slovak Karst (404–568 m a.s.l.), is one of Europe's most distinctive karst landscapes.

B. DEM generalization and segmentation

To optimize (generalize) the DEM we applied the dynamic least squares method [3]. A fixed fourth-order polynomial, and flexible the moving window size was used. This process resulted in the computation of nine physical-geomorphometric variables suitable for elementary segmentation according [1]: elevation, slope and aspect, three curvatures (normal slope and contour line curvatures $(k_n)_s$ and $(k_n)_c$, and torsion curvature $(\tau_g)_c$) and three changes of curvatures (normal and contour change of $(k_n)_c - (k_n)_{cs}$ and $(k_n)_{cc}$, and normal change of $(k_n)_s - (k_n)_{ss}$). The multiresolution segmentation of geographical object-based image analysis (GEOBIA) of the territories was done in the eCognition software using ESP 2 tool [4] with increment of step size of 5 (more in [2]).

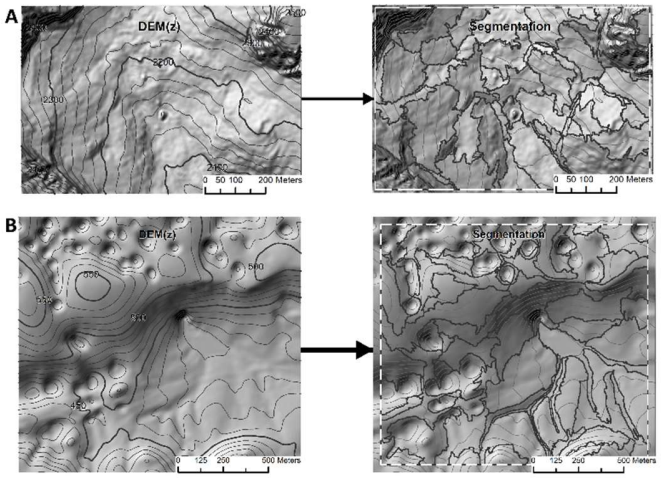

Figure 1. Generalized DEMs and segmentations of study areas: A – Malá Studená Dolina (part of the glacial cirque in the rectangle); B – Silica (part of the karst plateau). According [2], modified.

The resulting generalized DEMs and segmentations used are shown in Fig. 1.

C. *Physical-geomorphometric analysis*

The PG concept was applied to assess segmentation results and classify landforms. It was done in few stages. At the first stage, we computed mean values of various PG indices for elementary forms using the generalized DEM and a segmentation results. For indices with negative values, absolute values were also calculated.

Coefficients of variance of i input variables (CV_i) quantifies the affinity of a derived segment to the homogeneity (constant value) of these variables. According to [1] we computed the magnitude of this affinity as $Af_i = 1 - (CV_i)/2$. The range of the index lies in interval <0,1> (if Affinity < 0, affinity is considered zero).

Expert-based morphogenetic classification of segments preceded the next step of PG analysis. This aggregated PG indices for each morphogenetic landform type by filtering out outlier pixels beyond the standard deviation and normalizing the remaining values to a 0–100 scale (or -100 to +100 for indices with both positive and negative values). The normalized data was used to produce box plot graphs (Fig. 2), hierarchically describing the geomorphic energy influencing each landform type.

The position of a landform determines its global (*GGE*) and regional (*RGE*) geomorphic energy, related to the elevation above sea level or local basis of erosion. Due to their strong correlation in small areas, only *GGE* was used. Local geomorphic energy related to diffusion processes (*PESD*) is defined by mean curvature, while energy associated with mass flow (*PES*) is

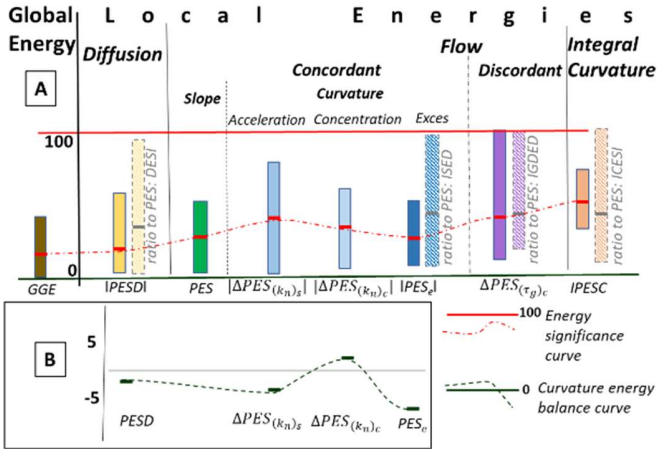

Figure 2. PG signature concept: Mean and range of regionally normalized values (100 = max) of PG indices (A). Mean of energies with positive and negative values (B). After [2].

determined by slope sine. Gravity-concordant profile and plan curvatures ($(k_n)_s$ and $(k_n)_c$) directly influence *PES*, causing flow acceleration ($\Delta PES(k_n)_s$) or concentration ($\Delta PES(k_n)_c$).

The combined effect of these curvatures is represented by excess energy (PES_e) determined by difference curvature. In contrast, twisting curvature $(\tau_g)_c$ captures gravity-discordant changes in *PES* ($\Delta PES(\tau_g)_c$) that do not affect local flow, reflecting the influence of external regulators beyond diffusion or mass flow. Finally, integral curvature energy (*IPESC*) quantifies the total energetic impact of all curvatures, providing a comprehensive measure of the landform's energetic behavior.

The absolute values of energies with both positive and negative components (*PESD*, $\Delta PES(k_n)_s$, $\Delta PES(k_n)_c$, PES_e) indicate the significance of energy within a landform type, similar to purely positive energies. A smaller range of values on Fig.2 A indicates a more specific characteristic for the landform type. The ratio of curvature energy to slope (*PES*) reveals the relative role of curvature in the landform signature. The normalized energy values forming the PG signature, which reflects the balance or dominance of positive (destructive) and negative (constructive) geomorphic energy, are visualized in Fig. 2B. This energy significance curve highlights both positive and negative extreme values, which indicate instability and values close to zero reflect equilibrium.

III. Results

In the territory of Malá Studená Dolina we distinguished 7 morphogenetic types of landforms, namely: Cirque headwall, Morain, Morain residue, Preglacial surface, Sheepback, structural linear feature and Talus landform (Fig. 3). The Silica area was

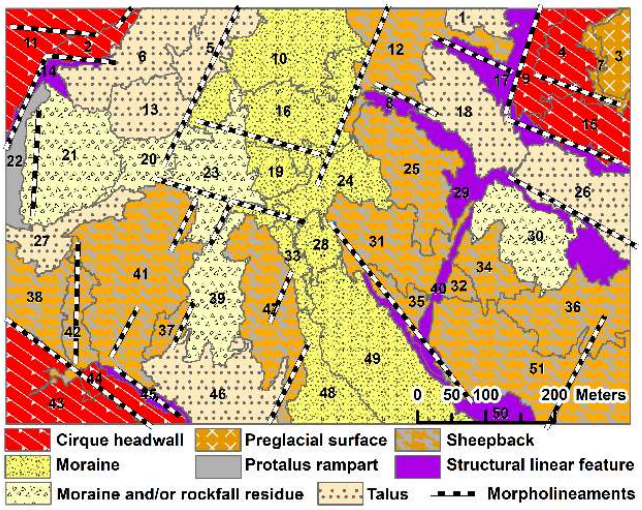

Figure 3. Digital geomorphological map of Malá Studená Dolina – Modified from [2].

classified to five basic landforms (Fig. 4): Karst plateau dissected, karst plateau smooth, Slope on lithological boundary, Tectonic window and tectonic window sinking transition landform.

The affinity of these segments to ideal elementary forms (EF) in Malá Studená Dolina is predominantly driven by the

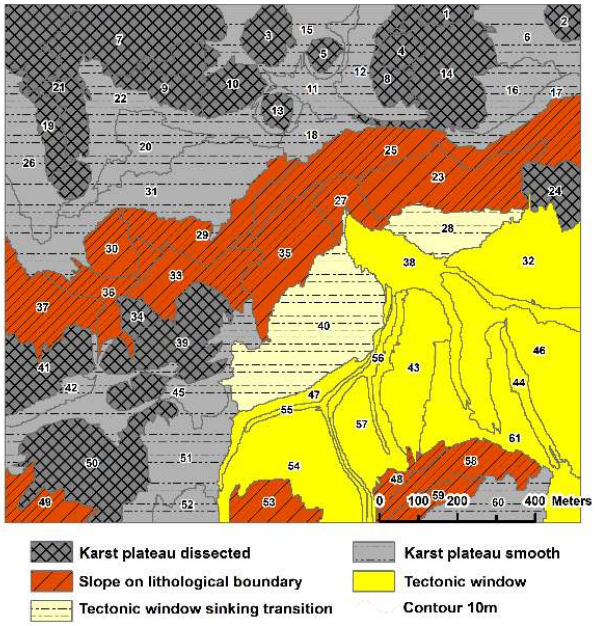

Figure 4. Digital geomorphological map of Silica – expert-based classification of automatically delineated elementary forms. Modified from [2].

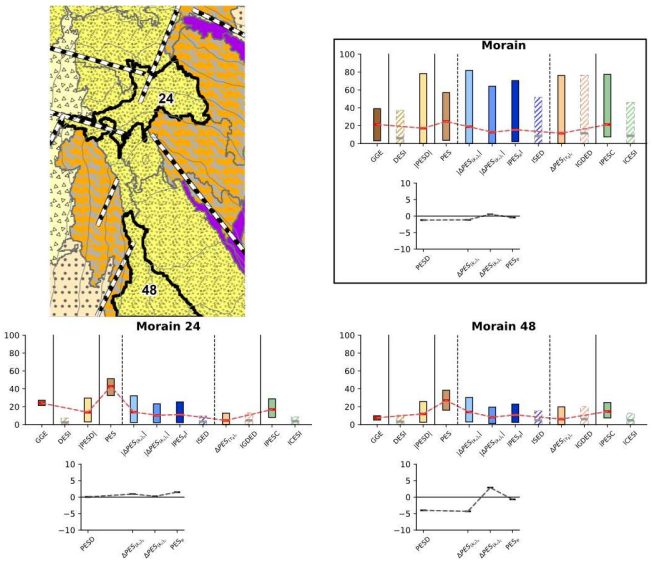

Figure 6. PG signature of moraine segments of Malá Studená Dolina study area

combination of slope and aspect (Fig. 5, upper left), a characteristic feature of mountainous landscapes. This relationship is further emphasized by an exceptionally high magnitude of affinity observed across the area (Fig. 5, upper right). Notably, the large boulder situated at the center of the area, along with certain structural linear features, exhibits the highest affinity to an EF type characterized by a combination of slope and $(k_n)_{c,s}$.

In Silica, the affinity predominantly aligns with two types of EF: constant altitude (horizontality) and the combination of

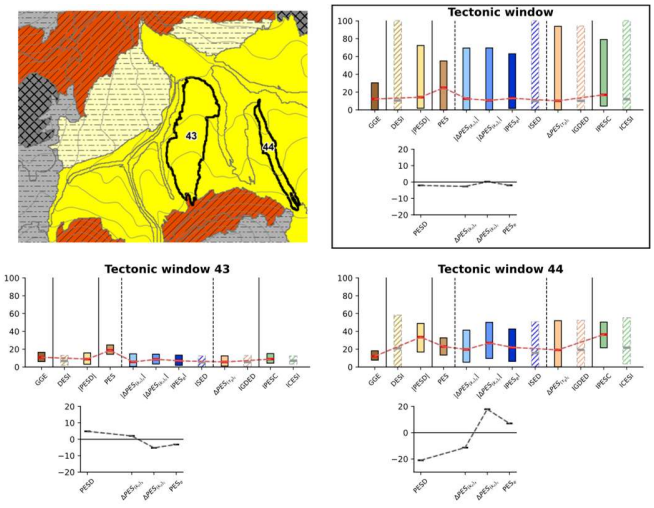

Figure 7. PG signature of tectonic window of Silica study area

constant slope and aspect (linearity) (Fig. 5, lower left). This dominant affinity is evident across the majority of the territory, with only a few isolated segments displaying low affinity magnitudes (Fig. 5, lower right). Overall, the magnitude of affinity to equilibrium elementary forms in the case of the Silica area is significantly lower, which may be characteristic of the karst topography formed more by chemical denudation than by gravity processes.

The PG signature of landform types in Malá Studená Dolina effectively differentiates them and highlights the physical basis of their geometric variations. However, in this study, we focus on a single landform for both Malá Studená Dolina and Silica. In the first territory, the energy balance curve for the moraine landform (Fig. 6, upper right) is surprisingly stable, contrary to expectations of imbalance caused by the abrupt deposition of moraine material on the surface.

Physical geomorphometry analysis at the segment level reveals that while half the segments show imbalance, the others exhibit equilibrium, likely due to underlying factors. Fig. 6 (lower part) highlights two groups: segment 24 (lower left) represents a balanced state, likely due to thinner glacial material and additional gravitational remodelling in the valley bottom, while segment 48 (lower right) represents the most significant signature of the landform.

In Silica (Fig. 7), PG graphs for the Tectonic Window landform reveal extremely low positional energy (GGE) and generally low other energies (Fig. 7, upper right). Some segments exhibit energetic balance, with segment 43 being the most representative (Fig. 7, lower left). Conversely, segments in the valley bottom are characterized by high $\Delta PES(\tau_g)_c$. Values, reflecting the significant influence of streams as regulators of adjacent development, primarily determined by $(\tau_g)_c$ and indirectly by $\Delta PES(\tau_g)_c$. This is illustrated by the balance curve of segment 44 (Fig. 7, lower right).

IV. Discussions and conclusion

In digital geomorphological mapping, it is essential to delineate geomorphic units that are both genetically and geometrically homogeneous. Our method achieves this by emphasizing unique morphogenetic interpretations for each segmented area. By integrating the concept of physical geomorphometry (PG), we extended the approach of [5] to identify unique landform signatures.

For the first time, "signature" refers not only to statistical morphometric measures but also to the physical significance of landforms. While this is a pilot study, it lays the groundwork for further theoretical and applied advancements.

In this framework, landform type signatures can be compared with individual segment signatures (Figs. 6, 7), enabling the identification of genetic variations, reclassification of segments, or recognition of polygenetic origins. PG analysis also highlights uncertainties and variations in genetic classifications, refining our understanding of landform types and their evolution.

Physical geomorphometry analysis proves invaluable for characterizing landforms, offering insights into the physical processes shaping them and improving the accuracy of geomorphological mapping. It identifies subtle features and patterns often overlooked by traditional methods, bridging the gap between qualitative observations and quantitative assessments, and advancing landform studies with a robust analytical framework.

V. Acknowlegments

This work was funded by the Slovak Research and Development Agency under contract No. APVV-22-0024. We sincerely thank the research team at Pavol Jozef Šafárik University, particularly doc. Michal Gallay, for providing the data for the Malá Studená Dolina and Silica study areas.

References

[1] J. Minár, L. Drăguţ, I. Evans, R. Feciskanin, M. Gallay, M. Jenčo, & A. Popov, 2024. Physical geomorphometry for elementary land surface segmentation and digital geomorphological mapping. *Earth-Science Reviews*, *248*, 104631. https://doi.org/10.1016/j.earscirev.2023.104631

[2] A. B. Popov, J. Minár, L. Drăguţ, 2025, Physically-based digital geomorphological mapping: Case study of glacial and karst topography. *Geomorrphology, Vol. 470.* https://doi.org/10.1016/j.geomorph.2024.109539

[3] J. Minár, J. Minár Jr., & I. S. Evans, 2015. Towards exactness in geomorphometry. In: Jasiewicz, J., Zwoli´nski, Z., Mitasova, H., Hengl, T. (Eds.), Geomorphometry for Geosciences. Adam Mickiewicz University in Poznan, Poland, pp. 27–30. Geomorphometry 2015 Conference Proceedings.

[4] L. Drăguţ, O. Csillik, C. Eisank, & D. Tiede, 2014, Automated parameterisation for multi-scale image segmentation on multiple layers. *ISPRS Journal of Photogrammetry and Remote Sensing*, *88*, 119–127. https://doi.org/10.1016/j.isprsjprs.2013.11.018

[5] R. J. Pike, 1988, The Geometric Signature: Quantifying Landslide-Terrain Types from Digital Elevation Models I. *Mathematical Geology 20*(5), 491–511. https://doi.org/10.1007/BF00890333

2.6 - Physical and other surface processes

Advances in theory of physical geomorphometry

Jozef Minár, Richard Feciskanin
Department of Physical Geography and Geoinformatics
Faculty of Natural Sciences, Comenius University in Bratislava, Slovakia
jozef.minar@uniba.sk, richard.feciskanin@uniba.sk

Michal Gallay, Jozef Šupinský
Institute of Geography
Pavol Jozef Šafárik University in Košice
Slovakia
michal.gallay@upjs.sk, jozef.supinsky@upjs.sk

Cite as: Minár, J., Feciskanin, R., Gallay, M., Šupinský, J. (2025). Advances in theory of physical geomorphometry. In: Proceedings of Geomorphometry 2025, 9-13 June, Perugia, Italy. M. Alvioli, L. Melelli, I. Marchesini eds. CNR Edizioni, Rome. ISBN 978-88-8080-765-0. DOI: https://doi.org/10.5281/zenodo.15282902

Abstract— **The development of the physical-geomorphometric (PG) theory is necessary for the development of its methods and applications. The new system of basic 2D PG quantities including both the derivatives (up to changes of curvatures) and dispersions (roughness) in their mutual relationships is the first innovation of the concept presented. Further, the principles of construction of PG indices from these basic quantities are outlined. A new concept of 3D physical geomorphometry of caves is also introduced, linked to the previously defined concept of endogenous and exogenous work. Finally, the role of DEM generalization and its essential properties needed for physically based segmentations are presented.**

I. Introduction

Physical geomorphometry has been defined in [1] and [2] as a specific subfield of geomorphometry that examines the form of the land surface in relation to the principles, procedures, and concepts of physics, such as dimensions, energy, work, force, thermodynamics, and equilibria. As part of the project "Physical Geomorphometry for Physical Geographical Research", we have been developing the theoretical concept, methodology and practical applications of physical geomorphometry since mid-2023. Significant advances in the methodology and applications are presented in separate contributions, here we focus on the theoretical development of the concept.

II. System of Physical-Geomorphometric Quantities

The gravity potential of unit volume of material obtained by the uplift Δz = 1m is the unit Local Geomorphic Energy (LGE_u). In [2], we have documented that the parts of LGE_u applicable to specific geomorphic processes are defined by the first and second derivatives of altitude (slope sine and various curvatures). In [1], we presented a system, which in addition to these local energies, also include the regional energies/works defined in [3] and [4]. Now we extend this system by changes of curvatures and of the energetic significance of different roughness quantities (Fig. 1).

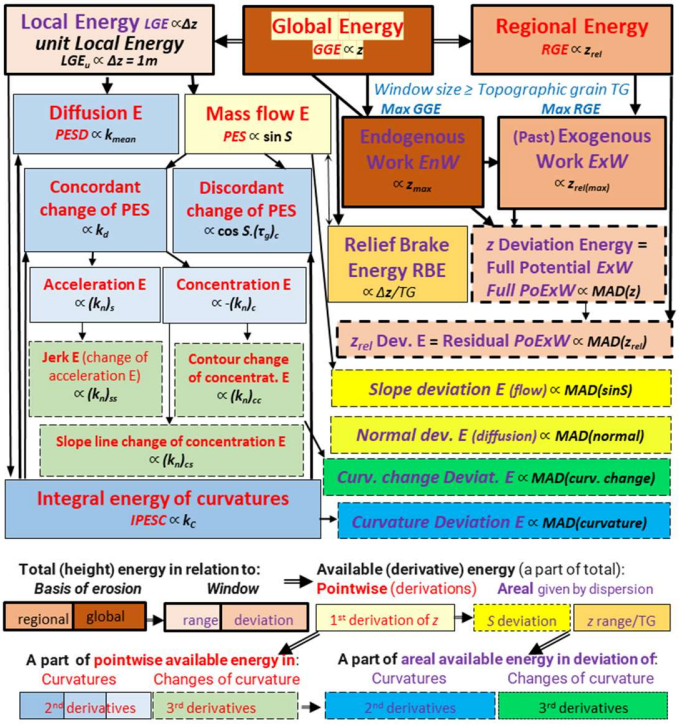

Figure 1. System of PG quantities, defined by *heights*: z (a.s.l.), z_{rel} (above local basis of erosion); *slope* (S); *curvatures*: k_{mean} (mean), k_d (difference), $(\tau_g)_c$ (twisting – contour torsion), $(k_n)_s$ (profile – normal slope line), $(k_n)_c$ (plan/tangential – normal contour), k_C (Casorati); *changes of curvatures*: $(k_n)_{ss}$ (slope line change of normal slope line c.), $(k_n)_{cs}$ (slope line change of normal contour c.), $(k_n)_{cc}$ (contour change of normal contour c.); *dispersions* of the above in moving window: Δ (range), *MAD* (mean absolute deviation). Arrows express the hierarchy (subordination) of quantities. Hitherto unpublished energies are framed in dashes.

The changes in curvature express the changes in the acceleration and concentration energies. The deviations of heights express the ExW that still needs to be done (without considering external influence) in order to achieve a static equilibrium (surface

leveled to z_{mean}). The deviations of the derivatives of the heights can then be interpreted as energy, the removal of which achieves the equilibrium state of the energies resulting from the derivatives.

Two basic dichotomies are contained in this system: division into *Pointwise* and *Areal energy* and *Total* and *Available* energy.

Pointwise energies (in red in Fig. 1) are energies specific to each individual point of the land surface. They are linked with position of the point above global or local basis of erosion (absolute height z and relative height z_{rel}) and *derivatives of height*. The former include fundamental global and regional geomorphic energy (*GGE* and *RGE*) given by heights. In accordance with [5] height derivatives are local point-based geomorphometric variables expressing the behavior (variation) of a surface in the infinitesimal vicinity of a point. Physically, they represent a hierarchy of changes in LGE_u acting at a given point [2].

Areal energies (in violet in Fig. 1) express the energy of the area (window) from which they are calculated. They may represent central tendencies, extremes or dispersion measures of pointwise energies resulting from heights and their derivatives. Maxima and means of altitude were used to define endogenous and exogenous work in [3] and height range was used to define the relief brake force. The whole set of other areal energies can be defined using roughness measures traditionally expressed mainly by standard deviations. However, a more straightforward energetic interpretation is provided by the mean absolute deviation (MAD) used in Fig. 1. In line with [2] local area-based variables can represent the local energies if they are calculated from the smallest possible window, or regional energies if the size of the window corresponds to the wavelength of the land surface (topographic grain *TG*). Therefore, if areal energies are to have a specific regional character, should be computed from window ≥ TG.

Total energies (shades of orange with a thick frame in Fig. 1) represent the total gravitational potential of pointwise and areal characteristics of heights, which can also be interpreted as the entire measurable energy spent on long-term geomorphic work that formed land surface. They are multiples of LGE_u reaching values $\leq z_{max} . LGE_u$. They have their own hierarchy ($GGE \geq RGE$ and $EnW \geq LGE \geq ExW \geq Full\ PoExW \geq Residual\ PoExW$) which results from the statistical relationships between the maximum, mean, range and deviation of z and z_{rel}, but also from their geomorphological (PG) interpretation. Normally, the local base of erosion cannot be below sea level, therefore *GGE* is the superior energy and the *RGE* is the subordinate energy (it is only a part of *GGE*). Likewise, *ExW*, which only eliminates *EnW*, cannot exceed its value, and thus *EnW* is superior and *ExW* is subordinate, etc.

A*vailable energies* (with a thin frame in Fig. 1) can also be both, pointwise and areal. However, compared to the total energies, they are only a fraction of LGE_u, reaching values ≤ LGE_u. They express parts of LGE_u that are available for certain current geomorphic processes (morphodynamics). They are therefore usually significantly smaller than total energies reflecting long-term development (morphogenesis). Their hierarchy (superiority and subordination) again results from both the mathematical essence and the PG interpretation. The higher derivatives of heights are (for physical reasons) smaller than the lower derivatives, so the slope represents more energy than curvatures and those greater than curvature changes. This hierarchy of pointwise energies is also transferred to the areal available energies.

III. DEFINING PHYSICAL-GEOMORPHOMETRIC INDICES

Assigning a clear and compatible physical meaning to basic geomorphometric variables opens space for a new (physical) interpretation and improvement of topographic indices derived from them, as well as the definition of new indices. An example given in [2] is the energy interpretation of the popular Index of Connectivity ([6]) as the sum of upstream regional concentration energy and downstream mass flow energy. Similarly, the χ-index [7] can be interpreted as the ratio of overall regional energy to regional concentration energy, which tends to be constant for equilibrium longitudinal river profiles under conditions of geological homogeneity. The importance of PG insight into the issue lies not only in a clearer interpretation, but also in the possible modification (optimization) of such indices. In the case of the χ-index, it can be, for example, the substitution of the 2D projected catchment area (which by default enters its calculation) with a 3D area considering the distribution of slopes in it.

The construction of completely new PG indices is another significant possibility (see e.g. [2], [3], [4]). In general, these indices can be defined as the ratio, difference or sum of different types of geomorphic energies. The informative value of each such index is substantial. For example, if we compare energies in a hierarchical relationship, it is important to realize that the uniform spatial distribution of superior energies is usually associated with some kind of equilibrium, and hierarchically subordinate energies are generally responsible for instability in the geosystem. An increase in the proportion of subordinate energy thus signals an imbalance of the system, the type of which depends on the nature of the subordinate energy. Currently, we are focused on deriving a set of PG indices to define the PG signature of various genetic landform types [8]. The traditional concept of geometric signature [9] based on descriptive statistics / geomorphometry is now widely applied in modern segmentation and classification methods based on artificial intelligence (machine learning). In addition to its indisputable advantages (they can well replicate known forms), its main shortcoming is its black box approach obscuring the physical reasons for why some variables are most important – e.g. [10]). The clear physical interpretation of the PG signature components makes this concept a white box system.

IV. 3D CAVE PHYSICAL GEOMORPHOMETRY

We have defined the concept of unit total cave work *CW* (concerning the change of gravitational potential of 1m^3 of material) using the ratio of V_{cave} (volume of the cave) and A_{cave} (area of the cave map projection – see Fig. 2a):

$$\boldsymbol{CW} = (1m^3).\frac{V_{cave}}{A_{cave}}\rho.g \qquad (1)$$

The *CW* is defined in this way as a specific subsurface variant of exogenous work (*ExW*). The *ExW* is defined in [3] by the difference in maximum and mean height as the portion of past endogenous work (*EnW*) eliminated by exogenous processes. By analogy, *CW* will present the elimination of *EnW*, which, however, has not yet manifested itself at surface altitudes (theoretically, it would be reflected in them when the cave ceiling collapses). This *CW* concept allows the whole 3D physical geomorphometry of caves to link directly with the surface 2D geomorphometry system (Fig. 1) and to define other PG characteristics of caves using transverse profiles through their passages (Fig. 2b).

Relations in Fig. 2 are derived from relation (1). The CW_{tp} is derived for a horizontal circular passage, with slope of center line $\beta = 0$. In a more general case ($\beta \neq 0$), equation takes the form:

$$\boldsymbol{CW_{tp}} = (1m^3).\frac{Ap(.1m)}{2r_p(.1m).\cos\beta + Ap.\sin\beta}.\rho.g \qquad (2)$$

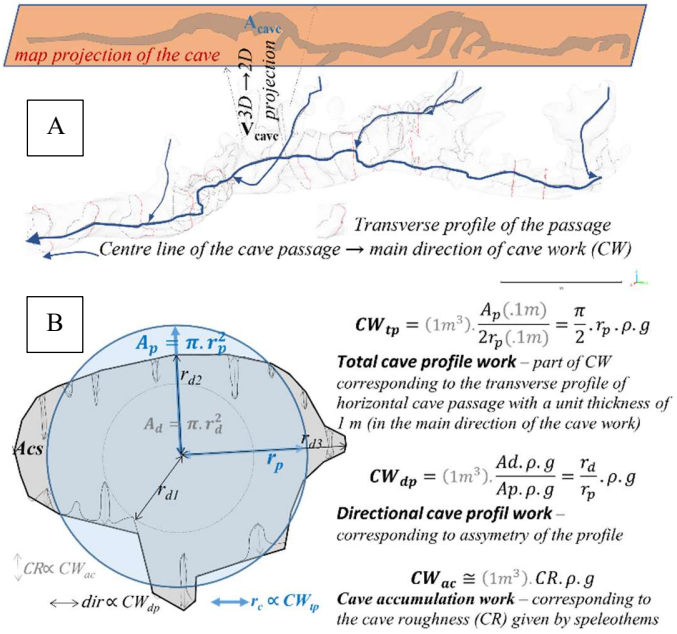

Figure 2. Derivation of cave physical geomorphometry: **A** Total cave work given by relation (1); **B**. Cave profiles works. For more explanation see the text.

The equation for CW_{ac} suggests that the roughness of the 3D cave surface can also be physically interpreted. And it does not have to be only in the sense of total (genetic) categories, but also dynamically as a cave barrier effect.

V. LANDFORM HIERARCHY, GENERALIZATION AND SEGMENTATION

Mild generalization (smoothing) is commonly used to eliminate DEM errors. This is important for the calculation of curvatures and changes of curvatures, where with the size of the DEM errors, the calculation error increases exponentially.

The purpose of major generalization (filtering) is to remove existing smaller forms for easier analysis of superior larger forms. Just as we can efficiently capture and then analyze individual wavelengths of electromagnetic radiation using specialized telescopes, targeted generalization of DEM is a prerequisite for effective PG analysis. In this case, the land surface can be perceived (according to information theory) as a 2D nonstationary signal consisting of multiresolution components and generalization is a filtering of original signal [11].

The profiles on Fig. 3 schematically depict not only the forms of various hierarchical levels, but (in accordance with Fig. 1) they can also be perceived as an expression of the spatial distribution of geomorphic energies. The most important attributes of this signal are wavelength (topographic grain) and amplitude. Generalization (filtering) should preserve them as best as possible until they are not separated from the signal. The most common simple generalization methods are not capable of this. Polygonal simplification method using Quadric Error Metrics is much better, but it limits the subsequent calculation of higher derivatives [14].

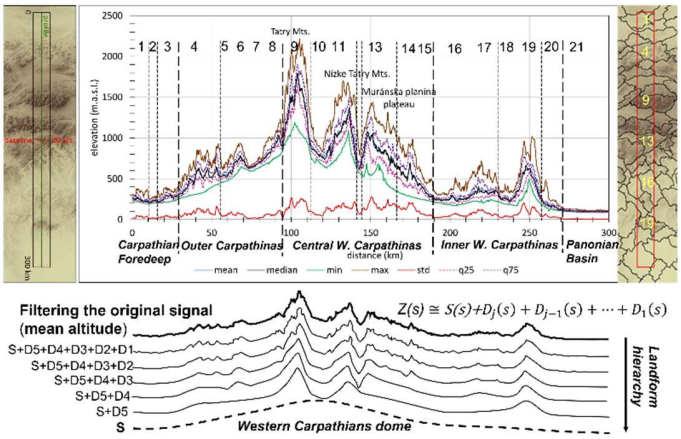

Figure 3. Swath profile across the Western Carpathians (according [12]) as a non-stationary signal of multi-resolution components (according [11]). The signal changes the most at the boundaries of the basic geological units, but it is also specific for each smaller morphostructural unit (on the right, according [13]). *S* – the smoothest component of the signal (form of highest hierarchic level), *D1- D5* –more detailed components (incorporating increasingly smaller forms).

We need generalization method that allows subsequent calculation of all variables and will keep the signal (forms of a

given hierarchical level) as clear as possible until it is deleted. This is important for physically based elementary segmentation [2] – a part of discrete geomorphometry [15], that looks for internally homogeneous objects separated by discrete boundaries. Therefore, the generalization method should not smooth the edges, but rather accentuate and, ideally, also increases the homogeneity of PG variables between edges, as our new method does [16].

Choosing the generalization level most suitable for segmentation is a specific problem. Maximizing the concentration of changes of curvatures values around zero (K_0 index) seems to be a good criterion ([2], [8], [14]), however, so far it has only been applied in small areas and has not been confronted with modern multiscale analysis based on information theory such as Wavelet Transform (WT) and Empirical Mode Decomposition (EMD). As the information signal changes in different morphostructural units (Fig. 3), the most appropriate level of generalization can also change. The same applies to the calculation of the wavelength (topographic grain), which is crucial for the calculation of regional PG variables (Fig. 1). The development of the PG quantities system and the PG indices derived from them allows for the improvement of segmentation algorithms and geomorphological interpretation of segmentation results. It seems appropriate to reconsider the calculation of inputs to morphostructural segmentation [4] and look for an increasingly optimal expression of PG signature relief forms [2].

VI. Conclusions

All analyzed aspects of physical geomorphometry are interconnected and important for the development of its methods. Improving of the system of PG quantities gives new interpretative views on the quantities themselves, but also allows us to see their combinations in traditional geomorphometric indices, improve them or create new PG indices. This enables to improve the methods of physically-based segmentation and their use within digital geomorphological mapping. The proposed concept of cave work connects 2D and 3D PG geomorphometry and outlines the potential of studying the roughness of cave surfaces. The theoretically defined requirements for the DEM generalization in the context of physical geomorphometry are crucial for the development and application of a suitable generalization method and adaptation of PG segmentation algorithms in larger areas. All this points to the need to develop methods of physical geomorphometry in mutual interaction, within its synthetic theoretical concept.

VII. Acknowledgments

This work was supported by the Slovak Research and Development Agency under the contract No. APVV-22-0024. The authors thank to I. S. Evans for inspiring remarks and comments.

References

[1] Minár, J., and I.S. Evans, 2023. Physical geomorphometry. Geomorphometry 2023, Iasi, Romania. Zenodo, https://doi.org/10.5281/zenodo.7802187.

[2] Minár, J., L. Drăguţ, I.S. Evans, R. Feciskanin, M. Gallay, M. Jenčo, and A. Popov, 2024. Physical geomorphometry for elementary land surface segmentation and digital geomorphological mapping. Earth Sci. Rev. 248, 104631. https://doi.org/10.1016/j. earscirev.2023.104631.

[3] Minár, J., P. Bandura, J. Holec, A. Popov, M. Gallay, J. Hofierka, J. Kaňuk, L. Drăguţ, and I.S. Evans, 2018. Physically-based land surface segmentation: Theoretical background and outline of interpretations. PeerJ Preprints 6, e27075v1. https://doi.org/10.7287/peerj.preprints.27075v1.
https://doi.org/10.1111/tgis.12847.

[4] Bandura, P., J. Minár, and M. Bielik, 2021. Physically based morphostructural land surface segmentation: Case of the Alps and Western Carpathians. Trans. GIS 25, 2394–2418.

[5] Evans, I.S., and J. Minár, 2011. A classification of geomorphometric variables. In: Hengl, T., Evans, I.S., Wilson, J.P., Gould, M. (Eds.), Proceedings of Geomorphometry 2011. International Society for Geomorphometry, Redlands, California, pp. 105–108.

[6] Borselli, L., P. Cassi, and D. Torri, 2008. Prolegomena to sediment and flow connectivity in the landscape: a GIS and field numerical assessment. Catena 75, 268–277. https://doi.org/10.1016/j.catena.2008.07.006

[7] Perron, J.T., and L.H. Royden, 2013. An integral approach to bedrock river profile analysis. Earth Surf. Process. Landf. 38 (6), 570‑576. https://doi.org/10.1002/esp.3302. https://doi.org/10.1002/esp.3302

[8] Popov, A.B., J. Minár, and L. Drăguţ, 2025. Physically based digital geomorphological mapping: Case study of glacial and karst topography. In: Geomorphology, 470, 109539.
https://doi.org/10.1016/j.earscirev.2023.104631

[9] Pike, R.J., 1988. The geometric signature: quantifying landslide-terrain types from digital elevation models I. Math. Geol. 20 (5), 491–511. https://doi.org/10.1007/ BF00890333.

[10] Dyba, K., 2024. Explanation of the influence of geomorphometric variables on the landform classification based on selected areas in Poland. Sci. Rep 14 (1), 5447. https://doi.org/10.1038/s41598-024-56066-6

[11] Hengl, T., Evans, I.S., 2009. Mathematical and digital models of the land surface. In: Hengl, T., Reuter, H.I. (Eds.), Geomorphometry—Concepts, Software, Applications: Developments in Soil Science, vol. 33. Elsevier, Amsterdam, 31–63. https://doi.org/10.1016/S0166-2481(08)00002-0

[12] Minár, J., J. Krcho, J. and I.S. Evans, 2016. Geomorphometry: Quantitative Land-Surface Analysis. In: Reference Module in Earth Systems and Environmental Sciences, Elsevier, 13 pp.
http://dx.doi.org/10.1016/B978-0-12-409548-9.10260-X

[13] Bandura, P., J. Minár and L. Drăguţ, 2019. Morphometrical-morphostructural subdivision of the Western Carpathians by Object-based image analysis. In: Geomorphologia Slovaca et Bohemica, 1, 19, 104 pp.

[14] Feciskanin, R., J. Minár, 2021. Polygonal simplification and its use in DEM generalization for land surface segmentation. Transactions in GIS 25 (5), 2361–2375. https://doi.org/10.1111/tgis.12796.

[15] Drăguţ, L. and C, Eisank, 2011. Object representations at multiple scales from digital elevation models. Geomorphology 129 (2011) 183–189. https://doi.org/10.1016/j.geomorph.2011.03.003

[16] Feciskanin, R., and J. Minár, 2025. Advancing Raster DEM Generalization with a Quadric Error Metric Approach. Computers and Geosciences, in review.

Extending Physical Geomorphometry into 3D: A Case Study on Domica Cave, Slovakia

Michal Gallay, Jozef Šupinský, Michaela Nováková
Institute of Geography, Faculty of Science,
Pavol Jozef Šafárik University in Košice, Slovakia
michal.gallay@upjs.sk, jozef.supinsky@upjs.sk,
michela.novakova@upjs.sk

Jozef Minár
Department of Physical Geography and Geoecology
Faculty of Natural Sciences, Comenius University in
Bratislava, Slovakia
jozef.minar@uniba.sk

Cite as: Basta, P., Maresova, J., Moudry, V. (2025). The role of spatial resolution and vertical accuracy of global DEMs in delineating stream networks. In: Proceedings of Geomorphometry 2025, 9-13 June, Perugia, Italy. M. Alvioli, L. Melelli, I. Marchesini eds. CNR Edizioni, Rome. ISBN 978-88-8080-765-0. DOI: 10.5281/zenodo.15306377

Abstract— **We present a novel approach to physical geomorphometry applied to the Domica Cave system in Slovakia. Using a high-resolution terrestrial laser scanning point-cloud, we generated a 3D mesh model of the cave, enabling the application of the framework of physical geomorphometry. A central aspect of this study is the computation of unit total cave work, a specific subsurface variant of exogenous work. This metric links 3D cave physical geomorphometry with 2.5D surface geomorphometry and provides new insights into cave formation processes and their interaction with geomorphic evolution. To operationalize these concepts, we developed an automated methodology for defining the central line of the 3D cave model and systematically slicing it into transverse profiles. The results demonstrate the utility of physical geomorphometry in cave studies, offering a new perspective on subsurface geomorphic processes and their linkages to surface topography.**

I. Introduction

Caves represent a unique geomorphic environment where traditional 2.5D surface-based geomorphometric techniques cannot be directly applied. Physical geomorphometry defined in [1] and [2] provides a robust theoretical framework for describing landform evolution in terms of energy, work, and force, integrating gravity principles with geomorphic processes. While 2D physical geomorphometry has been well-established, its application to 3D cave systems remains in early stages.

This study explores the application of physical geomorphometry to characterize the amount of geomorphic work recorded in a part of the Domica cave (Fig. 1). The cave is a part of 27 km long system formed inside a Triassic limestone plateau that spans the border between Slovakia and Hungary in Central Europe. By defining and applying the concept of unit total cave work (*CW*), we establish a novel approach to quantify effect of subsurface geomorphic processes. Our methodology builds on prior work in digital terrain modeling and expands it into three-dimensional cave environments [3].

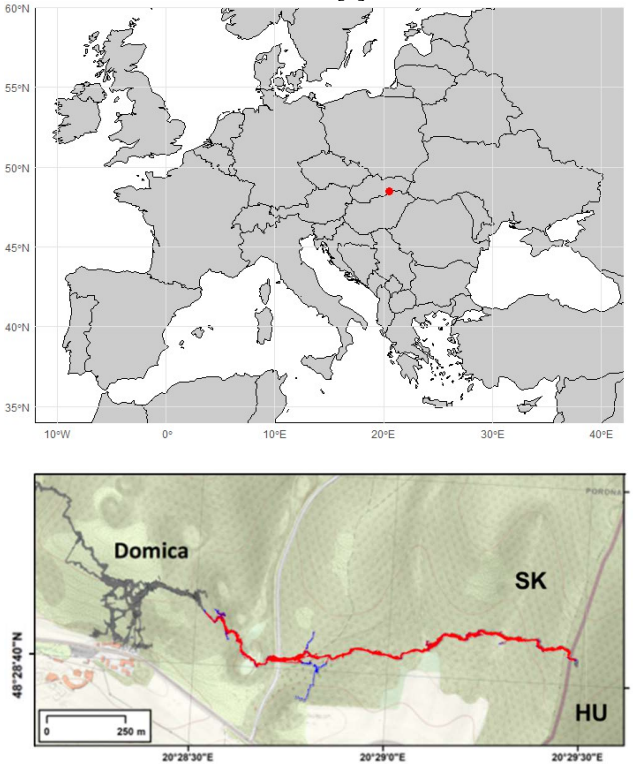

Figure 1. Location of the Domica cave and its part used in the case study (red).

This study presents advances in the methodology and application of physical geomorphometry linking to the development of the theoretical concept explained in another paper by Minár et al. of the Geomorphometry 2025 abstracts.

II. Derivation of Basic Cave Works

In [4], exogenous work (*ExW*) is defined as the part of endogenous work (*EnW*) that has been eliminated by exogenous processes. *EnW* is given by maximum elevations z_{max} and *ExW* corresponds to difference between z_{max} and z_{mean}. By analogy, the ***total cave work*** (***CW***) can be defined as a potential lowering of the surface by the collapse of the cave:

$$\boldsymbol{CW} = \left(1m^3\right).\frac{V_{cave}}{A_{cave}}\rho.g \qquad (1)$$

where ρ is rock density, g is the acceleration of gravity and 1 m^3 represents the unit volume of material on the surface whose potential gravity energy is changed by the potential collapse of the cave (Fig. 2A). The unit total cave work (*CW*) quantifies the change in gravity potential energy associated with 1 m³ of denuded material, calculated from the total cave volume (V_{cave}) and its planimetric projection area (A_{cave}) following Eq. (1) Subsequently, it is possible to investigate how this cave work is distributed in the individual parts of the cave, represented by its transverse profiles through their passages. When we assign a unit width (1m) to each profile (Fig. 2B), the ***total cave profile work*** (***CW_{tp}***) will be given (for horizontal passages) by ratio of the profile area A_p and diameter of the profile (= $2r_p$) that represents its map projection on the land surface:

$$\boldsymbol{CW_{tp}} = (1m^3).\frac{A_p(.1m)}{2r_p(.1m)} = \frac{\pi}{2}.r_p.\rho.g \qquad (2)$$

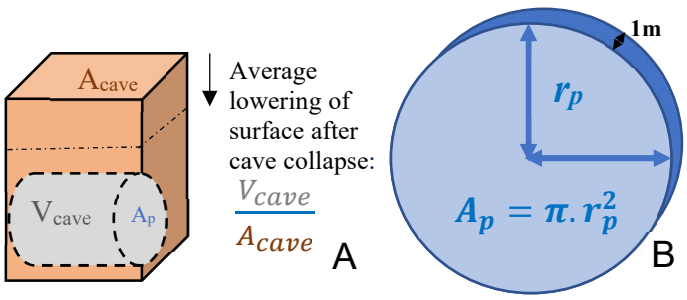

Figure 2. Derivation of cave physical geomorphometry: **A** Total cave work *CW* (1); **B**. Total cave profile works CW_{tp} (2).

In the general case of non-horizontal passages, the calculation of CW_{tp} incorporates the slope correction as shown in Minar et al. of this of the Geomorphometry 2025 abstracts, accounting for both horizontal and vertical components of the gravitational work. The unit total cave work (*CW*) is conceptualized as a specific subsurface variant of exogenous work (ExW). In the context of surface geomorphometry, ExW is defined [3] as the difference between maximum and mean elevation, representing the portion of past endogenous work (EnW) removed by exogenous processes. By analogy, *CW* represents the elimination of EnW within the cave system that has not yet manifested at the surface — theoretically, it would be expressed in surface elevation changes following cave ceiling collapse. This *CW* framework enables a direct link between 3D physical geomorphometry of caves and the established 2D surface geomorphometry system and further supports the definition of additional physical geomorphometric characteristics derived from transverse cave profiles (Fig. 2B).

III. Methods

The research is based on a 3D cave model derived from 3D point clouds acquired during several terrestrial laser scanning campaigns [5]. The data provide a high-resolution 3D representation of cave morphology at the spacing of several millimeters. The 3D model used in this study was generated in the form of a triangulated mesh by Poisson surface reconstruction method [6] implemented in the open-source software CloudCompare [7] at 10 cm spacing of the mesh nodes. A 3D centerline of the cave corridors was extracted using a NeuroMorph [8] plugin in the open-source software Blender [9]. A computational algorithm traced the longest continuous path, representing the cave corridor. Smoothing of the line minimized distortions and ensured profile consistency. The 3D cave model was then systematically sliced at 1-meter intervals, with transverse sections generated perpendicular to the centerline in CloudCompare using a customized Python script of CloudComPy library [10]. The slicing algorithm adapted dynamically to curved and branching passages to prevent profile overlap and segmentation errors. Theoretical expectations suggest that passages with larger cross-sectional areas and lower slopes correspond to higher subsurface geomorphic work values, reflecting zones of intensified speleogenetic activity and preferential dissolution. Complex cave geometry was managed through clustering techniques, ensuring that multi-level sections were correctly categorized. The final slices were classified based on their geomorphometric properties and stored in GIS-compatible formats for further analysis in the Scene interface of ArcGIS Pro by ESRI. We calculated the unit total cave work *CW* (1) and the total cave profile work CW_{tp} (2) assuming the limestone rock density ρ of 2,600 kg/m³ and the gravity acceleration g of 9.80663 kg/m². The r_p was calculated from the slice area A_p by:

$$r_p = \sqrt{A_p/\pi} \qquad (3)$$

All passages were considered horizontally inclined despite a gentle dip of the cave bottom from west to east.

IV. Results and Discussion

Our study confirms that outlined physical geomorphometric principles can be effectively extended into 3D cave environments. The analysed section contained 1,862 transverse slices thus the section was 1,862 m long. The vertical range of the cave bottom was 7 meters between the start and the end of the cave section which is an average dip of 0.215°. The total volume of the analysed section of the cave (V_{cave}) was 68,476 m³, and the horizontally projected area (A_{cave}) was 14,232 m². Based on these values, the computed average CW_{tp} is 120.577 kJ per unit volume of denuded material. The total CW for the analysed cave section amounts to 8.256 GJ, representing the gravity energy that would be released if the cave ceiling were to collapse. Figure 3 demonstrates the CW_{tp} values distributed along the cave centerline, where passages with larger cross-sectional areas correspond to higher values of subsurface geomorphic work, reflecting zones of intensified speleogenetic activity.

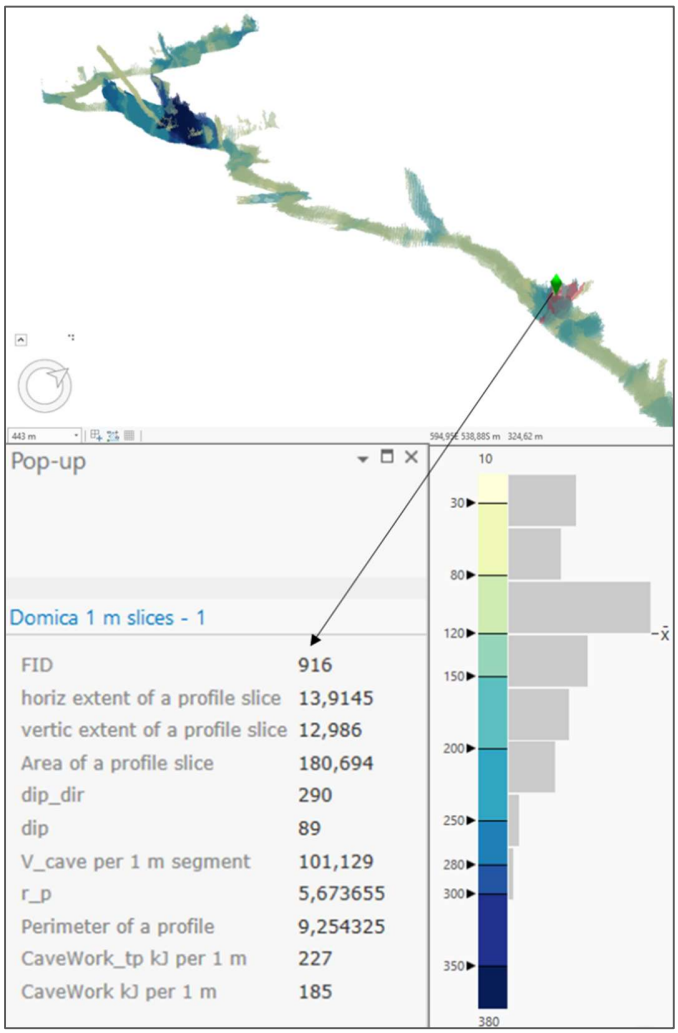

Figure 3. Total cave profile work (CW_{tp}) per unit length in kilo Joules along the cave centreline. The attributes used for calculation and assigned to each cave slice are shown in the pop-up window. The histogram illustrates the distribution of CW in the cave.

The findings, while preliminary, align with these theoretical expectations and reinforce the link between cave evolution and subsurface geomorphic processes. Here, cave evolution refers to the enlargement, collapse, and reshaping of underground voids through dissolution and mechanical processes, while subsurface geomorphic processes include material removal, structural failure, and sediment infill, influencing both underground morphology and surface topography. The CW metric thus provides a foundation for interpreting speleogenetic patterns and the broader evolution of subsurface landscapes.

Advancements in automated cave segmentation also improve the standardization of comparative analyses between different cave systems and enhance morphometric classification approaches. Furthermore, the established connection between 3D cave morphology and 2D surface relief broadens the potential for holistic landscape evolution studies, integrating subsurface and surface geomorphometry into a comprehensive analytical framework. While the planimetric area (A_{cave}) provides a direct 2D projection of the cave system, the calculated CW_{tp} values quantify the gravity work potential that would be released if surface collapse occurred. Thus, 3D cave geometry informs surface processes such as denudation rates, potential sinkhole formation, and broader landscape evolution dynamics.

Nevertheless, interpreting the calculated physical geomorphometric parameters requires careful consideration. Further methodological improvements should focus on better treatment of cave branches in a speleogenetic context and on properly handling vertical chimneys, which, due to their large volume, reflect a different type of geomorphological work than horizontal passages.

V. Conclusions

This study advances the integration of 3D physical geomorphometry into karst research. The development of the unit total cave work (CW) metric and its systematic computation along the cave centerline (CW_{tp}) offer a novel framework for quantifying subsurface geomorphic processes. The distribution of CW_{tp} revealed zones of enhanced passage enlargement corresponding to anticipated speleogenetic activity, particularly in wider and flatter segments. This reinforces the idea that 3D cave morphology retains measurable signatures of subsurface geomorphic evolution processes. Additionally, the proposed methodology offers a framework for comparing different caves and standardizing cave morphometric classification.

Nevertheless, certain limitations should be considered. Interpretation becomes more complex where cave morphology results from multiple phases of accumulation and erosion, and the

present model does not explicitly incorporate variations in rock resistance or solvability, which can influence the distribution of geomorphic work. Critical factors for the reliable application of this method include high-resolution 3D data, accurate centerline extraction, and consistent slicing of cave profiles. Deviations in model quality would significantly affect the reliability of CW values.

The findings reinforce the connection between subsurface cave evolution and surface denudational processes, offering a measurable link between underground void formation and surface topography changes. Future work should explore broader applications across different karst systems, consider vertical features (e.g., chimneys) separately, and further refine automation workflows for large-scale comparisons. Furthermore, extending the analysis to consider additional types of geomorphic work, such as the kinetic energy of water required for cave tube erosion, will enhance the versatility and relevance of the presented approach to karst landscape evolution studies.

VII. ACKNOWLEDGMENTS

This work was supported by the Slovak Research and Development Agency under the contract No. APVV-22-0024.

REFERENCES

[1] Minár, J., and I.S. Evans, 2023. Physical geomorphometry. Geomorphometry 2023, Iasi, Romania. Zenodo, https://doi.org/10.5281/zenodo.7802187.

[2] Minár, J., L. Drăguţ, I.S. Evans, R. Feciskanin, M. Gallay, M. Jenčo, and A. Popov, 2024. Physical geomorphometry for elementary land surface segmentation and digital geomorphological mapping. Earth Sci. Rev. 248, 104631. https://doi.org/10.1016/j. earscirev.2023.104631.

[3] Gallay, M., Hochmuth, Z., Kaňuk, J., and Hofierka, J., 2016: Geomorphometric analysis of cave ceiling channels mapped with 3-D terrestrial laser scanning, Hydrol. Earth Syst. Sci., 20, 1827–1849, https://doi.org/10.5194/hess-20-1827-2016 .

[4] Bandura, P., J. Minár, and M. Bielik, 2021. Physically based morphostructural land surface segmentation: Case of the Alps and Western Carpathians. Trans. GIS 25, 2394–2418. https://doi.org/10.1111/tgis.12847.

[5] Kaňuk J., Šupinský J., Meneely J., Hochmuth Z., Šašak J., Gallay M., Callieri M., 2023. Laser Scanning of a Complex Cave System during Multiple Campaigns: A Case Study of the Domica Cave, Slovakia. In Meneely, J. 3D Imaging of the Environment: Mapping and Monitoring, CRC Press, pp. 56 - 81.

[6] Kazhdan, M., Hoppe, H. (2013). Screened poisson surface reconstruction. ACM Transactions on Graphics (ToG), 32(3), 29.

[7] Girardeau-Montaut, D. (2018). CloudCompare 2.10.2 Zephyrus. http://www.cloudcompare.org/ .

[8] Jorstad A, Blanc J, Knott G (2018) NeuroMorph: A Software Toolset for 3D Analysis of Neurite Morphology and Connectivity. Frontiers in Neuroanatomy 12:59. https://doi.org/10.3389/fnana.2018.00059

[9] Community, B.O., 2018. Blender - a 3D modelling and rendering package, Stichting Blender Foundation, Amsterdam. http://www.blender.org.

[10] CloudComPy Development Team. (2024). CloudComPy: Python Wrapper for CloudCompare. GitHub. Retrieved from https://github.com/CloudCompare/CloudComPy

Photogrammetry for morphometric analysis of anhydrite-gypsum weathering zones

Adrian Jarzyna, Maciej Bąbel
Faculty of Geology
University of Warsaw
Warsaw, Poland
a.jarzyna@uw.edu.pl, m.babel@uw.edu.pl

Firouz Vladi
Deutsches Gipsmuseum und Karstwanderweg
Düna, Germany
fvladi@t-online.de

Cite as: Jarzyna, A., Babel, M. (2025). Photogrammetry for morphometric analysis of anhydrite-gypsum weathering zones. In: Proceedings of Geomorphometry 2025, 9-13 June, Perugia, Italy. M. Alvioli, L. Melelli, I. Marchesini eds. CNR Edizioni, Rome. ISBN 978-88-8080-765-0. DOI: 10.5281/zenodo.15194704

Abstract - **In anhydrite-gypsum weathering zones, two distinct types of dome-shaped landforms, anhydrite hydration features and gypsum tumuli undergo dynamic morphological changes driven by probable volumetric expansion processes. To capture and quantify these changes, we applied a combined UAV-based and terrestrial photogrammetry approach at sites in Canada and Spain (Fig. 1). High-resolution 3D models and digital datasets allowed us to extract key morphometric parameters, such as landform dimensions, cavity volumes, and fracture patterns. Our results highlight photogrammetry as an effective and precise method for monitoring and analyzing the evolution of landforms in evaporite environments.**

I. Introduction

In the weathering zone of anhydrite-gypsum rock, we documented two distinct types of landforms: anhydrite hydration landforms (Dingwall; Fig. 2A) and gypsum tumuli (Sorbas; Fig. 2B). These features are predominantly dome-like, reaching up to 2 meters in height and extending over 10 meters in length. Some also contain inner cavities. The processes responsible for their formation cause volume expansion and deformation within the rock [1,2].

Hydration landforms form due tothe transformation of anhydrite ($CaSO_4$) into gypsum ($CaSO_4 \cdot 2H_2O$) in the near-surface weathering zone, where meteoric water is available. The displacive crystallization of gypsum replaces anhydrite and generates crystallization pressure, leading to the development of such cavities. Gypsum tumuli are superficial karstic landforms that form in Miocene gypsum through cycles of dissolution and reprecipitation driven by wetting, drying, and evaporation—primarily in semi-arid climates. Rainwater infiltrates selenitic gypsum, dissolves it, and upon drying, crystallization in pores generates pressure that uplifts the surface, creating a convex structure.

Due to their rapid morphological changes over years or decades, we employed an efficient and time-effective approach, photogrammetry, to analyze their morphometric characteristics. Using both aerial and terrestrial photogrammetry, we generated high-resolution models for three study sites in Canada and Spain. The digital datasets allowed us to compute key morphometric parameters, providing valuable insights into the formation and evolution of these landforms.

Figure 1. Study area of the Dingwall abandoned gypsum quarry (Nova Scotia, Canada) and Sorbas gypsum plateau (Andalusia, Spain).

Figure 2. Studied landforms; A - hydration landform at former gypsum quarry in Dingwall (Canada); B – gypsum tumulus recognized at karst zone near Sorbas (Spain; AJ is inside)

II. METHODS

We applied photogrammetry using two models of Unmanned Aerial Vehicles (UAVs: DJI Phantom 4, DJI Air 2s), two models of digital camera, and a GPS receiver with RTK (Topcon Hiper SR) for ground control and checkpoint measurements. Aerial photogrammetry was applied in the Dingwall area twice to analyze rock deformations in time. These works resulted in 2.5D models, orthophotomaps and Digital Surface Models (DSMs) of the quarry bottom, as well as 3D models of anhydrite hydration landforms and gypsum tumuli. For the modeling landforms we included bot outer rock surface and their cavities to describe. Image processing was conducted using Metashape, a Structure from Motion (SfM)-based software [3]. Additionally, digital terrain models (DTMs) and orthophotomaps were analyzed using ArcGIS to extract and interpret morphometric parameters. They include planar dimensions of the outer landforms extent like long and short axis, but also of the inner cavity like true length, true width (Fig. 3). Among these parameters are relative height of the landforms, height of the chamber (cavity), entrance width/height, thickness of detached rock layer and azimuth of elongation of the long axis and true length. For some cavities we computed volume and area. We also documented fracture pattern, computed circularity coefficient, bulge degree.

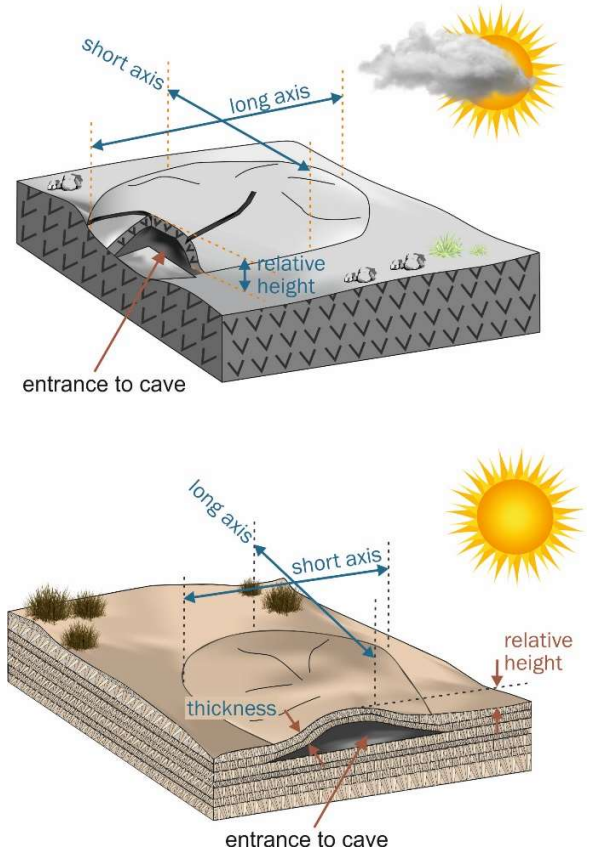

Figure 3. Main morphometric parameters computed and measured for hydration landform (up) and gypsum tumuli (down).

III. RESULTS

We generated high-resolution 3D models of both the broader landscape and individual landforms, achieving a ground resolution of <1 cm/pixel. They represent rock relief created during weathering processes at both sites presenting its dimensions, shape and structural features. In the Dignwall site and the Sorbas site our cartographic works mapped more than a few hundred landforms. The average dimensions of anhydrite hydration landforms were 5.25 m (long axis) × 3.38 m (short axis), while gypsum tumuli averaged 2.37 m × 1.78 m. Generally dimensions of both hydration landforms and gypsum tumuli are similar, but maximum long axis of the first one is larger (Table 1). Described landforms are positive part of the weathering zone characterized by some regularities that was deduced on the basis of linear regression lines and Pearson's correlation coefficient. One of the main relations for hydration landform development is as follows b = 67a (b –short axis, a – long axis), on the other hand for gypsum tumuli is b = 78a. In general, their elongation is described by their coefficient of circularity, C =(a-b)/a, and has an average value of 0.33 for hydration landforms and 0.24 for gypsum tumuli.

Anhydrite hydration landforms	
Name of the parameter	*Minimum-maximum [m]; average value [m]; number of measurements*
Length (long axis)	1.86–23.05; 5.25; 74
Width (short axis)	0.91-9.01; 8.38; 74
Relative height	0.33-2.09; 0.83; 74
Long axis (cavity)	0.70-8.87; 3.15; 52
Short axis (cavity)	0.33-5.10; 2.04; 40
Height of the chamber	0.28-1.35; 0.64; 41
Gypsum tumuli	
Name of the parameter	*Minimum-maximum [m]; average value [m; number of measurements*
Length (Long axis)	0.35-8.40; 2.37; 100
Width (short axis)	0.25-7.95; 1.78; 100
Relative height	0.04-1.30; 0.23; 142
True length	0.60-6.96; 2.27; 66
True width	0.45-5.01; 1.65; 66
Height of the chamber	0.07-1.00; 0.28; 66

Table. 1. Selected morphometric parameters related to anhydrite hydration landforms and gypsum tumuli [1,4,5]

Analyzing part of the anhydrite weathering zone in Dingwall from 2018 to 2023 gave us difficulty specifying elevation differences, only qualitative changes were possible to identify.

IV. CONCLUSIONS

Our results demonstrate that photogrammetry is an efficient and highly accurate tool for analyzing anhydrite-gypsum weathering zones. The combination of UAV-based and terrestrial photogrammetry enables detailed morphometric assessment, aiding in the documentation and monitoring of these rapidly evolving landforms. This approach offers a valuable method for studying dynamic geomorphic processes in karst and evaporite environments.

V. ACKNOWLEGMENTS

This research was funded by Ministry of Higher Education and Science, project within the 'Diamond Grant' programme, grant no. 0002/DIA/2017/46. This research was founded by National Centre of Science, Poland, grant no. DEC-588 2012/05/B/ST10/00918 and by Polish Ministry of Higher Education and Science. We would like to thanks Damian Ługowski for his fieldwork.

REFERENCES

[1] Jarzyna, A.J., Babel, M., Vladi, F., Ługowski, D, 2023. Hydration caves and cavities from the recent weathering zone of anhydrites at Dingwall (Nova Scotia, Canada). Geomorphology 433, 1-21.

[2] Calaforra, J.M., Pulido-Bosch, A., 1999. Genesis and evolution of gypsum tumuli. Earth Surface Processes and Landforms 24, 919-930. https://doi.org/10.1016/j.geomorph.2023.108667

[3] Westoby, M.J., Brasington, J., Glasser, N.F., Hambrey, M.J., Reynolds, J.M., 2012. 'Structure-from Motion' photogrammetry: A low-cost, effective tool for geoscience applications. Geomorphology 179, 300-314 http://dx.doi.org/10.1016/j.geomorph.2012.08.021

[4] Jarzyna, A., Bąbel, M., Ługowski, D., Vladi, F., 2022. Morphology of dome- and tepee-like landforms generated by expansive hydration of weathering anhydrite: a case study at Dingwall, Nova Scotia, Canada. Applied Sciences 12, 7374: 1-34.

[5] Jarzyna, A., Bąbel, M., Czajkowsja, M., Ługowski, D., 2024. Morphometry and morphology of the gypsum tumuli from the Sorbas karst region, SE Spain. Geomorphology 465, 1-18. https://doi.org/10.1016/j.geomorph.2024.109403

Retrieval of Digital Elevation Models from optical sensors data in a Coastal Dune Systems: geomorphometric analysis for environmental monitoring

§ Alfonso Valerio Ragazzo [1,2], Alessandro Mei [1], Giuliano Fontinovo [1], Giorgio Pennazza [2]

[1] Institute on Air Pollution, National Research Council (CNR-IIA), Geomatics and UAS Unit, 00015 Monterotondo, Italy

[2] Department of Engineering, Unit of Electronics for Sensor Systems, University Campus Bio-Medico di Roma, 00128, Rome, Italy

§ alfonsovalerioragazzo@cnr.it

Cite as: Ragazzo, A.V, Mei, A., Fontinovo, G., Pennazza, G. (2025). Retrieval of Digital Elevation Models from optical sensors data in a Coastal Dune Systems: geomorphometric analysis for environmental monitoring.

Abstract - **Beaches and dune belts cover 20% of the world's coastline and represent one of the most vulnerable ecosystem due to their unique environmental, microclimatic, and spatial conditions. The Coastal Dunes System (CDS) is characterized by definite ecosystem and geomorphological features, often threatened by the anthropogenic pressure and specific challenges related to habitat fragmentation and environment vulnerability. The present work focuses on the integration of Unmanned Aerial Vehicle (UAV) RGB and LiDAR data for the environmental analysis of a CDS, located within a high-density vegetation area in the municipality of Lesina (Foggia, Italy). The primary objective is to assess the vegetation distribution, monitoring metrics of psammofile species referred to one Natura 2000 sites in southern Italy, specifically IT9110015 – "Duna e lago di Lesina - Foce del Fortore". In the study area, a major challenge for estimating vegetation volumes is the topographic analysis, as the dense vegetation matrix is too dense to let sensors signal go through. Hence, starting from the Digital Elevation Models (DEMs) and orthophoto obtained from the elaboration of the RGB/LiDAR data, it has been possible to distinguish the contribution of soil and vegetation by using the ExG spectral index. Consequently, by using the Natural Neighbor interpolation technique, it has been possible to reconstruct the Digital Terrain Model (DTM). Hence, the estimation of the total canopy volume was obtained from the Digital Difference Model (DDM), resulting approximately 42098.97 m^3. The following validation process occur comparing UAV-derived DDM with a reference object, analyzed by Terrestrial Laser Scanner (TLS). In summary, this study concerns the following activities: (i) acquisition and elaboration of TLS LiDAR and UAV RGB/LiDAR data; (ii) spectral indices calculation; (iii) spatial analysis and interpolation techniques; (iv) Digital Difference Model (DDM) retrieval; (v) volumes calculation; (vi) DDM-derived volume validation by comparing TLS data.**

I. INTRODUCTION

The study of Coastal Dune Systems (CDS) through remote sensing techniques assumes crucial importance in monitoring ecosystem integrity and resilience [1]. CDS is considered one of the most fragile ecosystems and is compromised, sometimes irreversibly, by both direct and indirect anthropogenic pressure [2]. These ecosystems host a highly specialized flora, constituting a focal point of biodiversity due to the loss of biological diversity and habitat fragmentation [2]. Nowadays, analyzing vegetation through remote sensing techniques has become crucial for the observation of eco-systems' integrity and resilience [3,4]. Accordingly, the data acquisition can involve in the use of sensors applied on Unmanned Aerial Vehicles (UAVs), a high-spatial resolution tool for the environmental monitoring [5,6]. This work features the integration of RGB and Light Detection and Ranging (LiDAR) data derived from UAV survey within a CDS. Furthermore, this work aims to extract and manage point clouds and mesh models, Digital Surface Model (DSM), Digital Terrain Model (DTM), and Digital Difference Model (DDM) for the study of a very dense vegetation environment. As seen in bibliography, the DDM can be an important requirement to compute canopy architecture, monitoring habitat reduction and fragmentation [7]. Currently, UAV technology results fundamental for the geomorphological and ecosystem analysis, representing accurate DEMs useful for land management, soil analysis, and watershed management [8]. Furthermore, several studies have demonstrated that DEM's resolution and scale can significantly influence the interpretation of geomorphic features and ecosystem metrics [9]. Accordingly, the validation of DEMs is essential for identifying uncertainties and ensuring the reliability of spatial data outputs [10]. Hence, in densely vegetated

environments, it can be difficult for positioning and measuring Ground Control Points (GCPs) due to logistical constraints, inaccessibility, and consuming time procedures. Indeed, traditional ground-based vertical accuracy assessments may be insufficient of feasible in such contexts [10]. In this study is shown an alternative approach involving the use of a volume-based validation method, wherein known object geometries, comparing Terrestrial Laser Scanning (TLS) data, used as reference for the accuracy assessment. This strategy shifts the focus from vertical points comparisons to three-dimensional volumetric congruence, which can be particularly advantageous in ecosystems where vegetation structure is complex and spatially heterogeneous.

II. MATERIAL AND METHODS

A. Geographical setting of the study area

The study area is sited in Lesina (Fig. 1), in the province of Foggia (Puglia region, Italy).

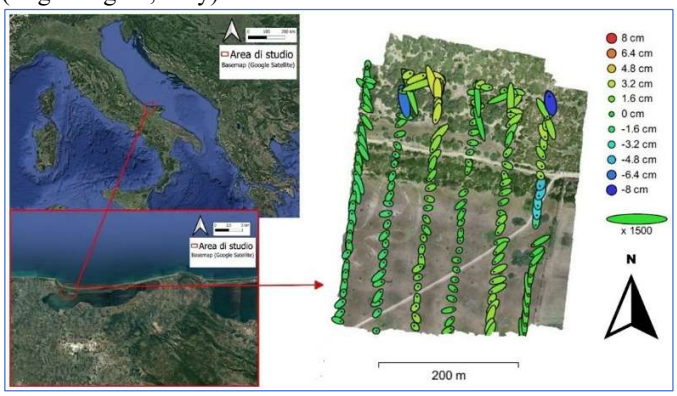

Figure 1. Geographical setting of the study area. Right, orthophoto (Area ~0.11 km^2, ~ 11 ha) where are represented error estimations. Z error is represented by ellipse color. X,Y errors are represented by ellipse shape.

This study focuses on one Natura 2000 sites in southern Italy, specifically IT9110015 – "Duna e lago di Lesina - Foce del Fortore". The area of interest is characterized by an extensive dune systems, presenting an heterogeneous vegetation path, as it encompasses multiple psammophile types of woody vegetation dominated by junipers and other Mediterranean sclerophylls.

B. Unmanned Aerial Vehicle (UAV) and Emesent's Backpack RTK

Surveys were conducted using a MATRICE 300 RTK drone, with an integrated RGB sensor and LIDAR. The mission was conducted with the following flight parameters: (a) flight altitudes (30 m asl); (b) 80% front/side image overlap ratio; (c) flying speed of 5 m/s. Moreover, Emesent's Backpack RTK was used for the validation procedure, ensuring high-precision volume assessment. Emesent's Backpack RTK enables automated georeferencing and drift correction for backpack-based LiDAR surveys, rationalizing the need for GCPs. Hence, by combining real-time RTK positioning with Simultaneous Localization and Mapping (SLAM), it ensures high-precision point cloud retrieval.

C. Data processing

The methodology used in this study means to estimate vegetation parameters (e.g., areas and volumes), starting initially from the generation of a point cloud layer, and, consequently, from the obtainment of orthophoto, DSM, DTM, and DDM, respectively having a spatial resolution of 20, 40, 40 and 40 centimetres. The data are processed through open-source tools, concerning the use of GIS (QGIS Desktop 3.34.13), photogrammetry (OpenDroneMap), 3D modelling (Cloud Compare v. 2.13.1), and data computation software (RStudio and Python). Initially, the workflow provides a dense points cloud integration starting from RGB and LiDAR data. Consequently, the generation of an orthophoto and a DSM occurred, needed for the extraction of a vegetation mask by applying spectral indices such as the Excess Green (ExG). Hence, it has been able to isolate the contribution of the vegetation from the original DSM by choosing pixel thresholds [11]. So, from the DSM has been eliminated the contribution of vegetation, leaving areas characterized by *NoData* values. Thus, to obtain a DTM, the Natural Neighbor interpolation technique is used to fill these areas with significant elevation values of their surroundings. Following, the DTM was subtracted from the DSM for obtaining the DDM. All the previous layers were manually cleaned from noise disturbance by operating directly on the point cloud by using CloudCompare tools. Thus, vegetation areas and volumes are designed from the DDM computation, where canopies' total volume calculation occurred by computing the sum of the product of each elevation value with its corresponding pixel area. In order to not overestimate the total canopy volume value, since it is not the entire volume of the voxel that is filled with canopy, a correction factor was applied to exclude the void gaps typically present within the vegetation structure. Based on a visual estimation conducted on a representative 2x2 meter area, it was observed that approximately 30% of each unit volume of vegetation was composed of air. Therefore, the total calculated canopy volume was adjusted by multiplying it by a coefficient of 0.70, reflecting an estimated 70% actual vegetative material within the total voxel volume. This empirical approximation allowed for a more realistic assessment of the effective canopy volume in the study area.

D. Accuracy metrics

To validate the model, a volume assessment is provided by comparing a known object detected from UAV and TLS investigations. Accuracy of the DDM-derived volume is calculated by comparing reference volumes derived from TLS survey. Data are processed in CloudCompare, using both point

cloud (.las) and mesh (.obj) formats. Hence, V_{LAS} (derived from the TLS point cloud) and V_{OBJ} (derived from the TLS mesh model) volume references are obtained. As follows, the validation occur by estimating DDM-derived volume against the reference volumes (P_{LAS} and P_{OBJ} as volume ratios):

$$P_{LAS} = \frac{V_{DDM}}{V_{LAS}}, P_{OBJ} = \frac{V_{DDM}}{V_{OBJ}}$$

Moreover, the relative errors for point cloud ($E_{REL,LAS}$) and mesh model ($E_{REL,OBJ}$) were calculated, determining the estimation as percentage of the reference.

$$E_{rel,LAS} = \left|\frac{V_{DDM} - V_{LAS}}{V_{LAS}}\right| * 100, E_{rel,OBJ} = \left|\frac{V_{DDM} - V_{TLS}}{V_{TLS}}\right| * 100$$

III. RESULTS

The work starts with the acquisition of UAV RGB and LiDAR data, from which a dense cloud points has been obtained, resulting from the integration of the previous. Firstly, from the orthophoto, the ExG index is obtained, classifying vegetation and soil classes. Hence, the vegetation pixels were deleted, obtaining a raster with only topographical information. Consequently, to fill these areas with significant elevation values of their surroundings, the Natural Neighbor interpolation technique was used (Fig. 2).

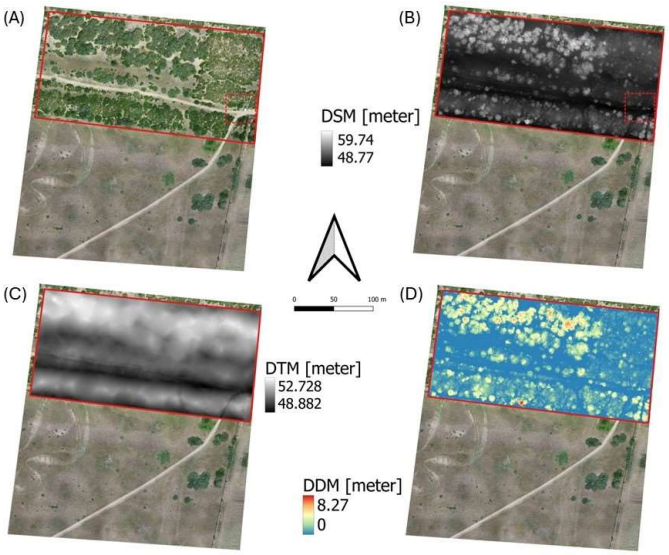

Figure 2. Representation of the main layers used in this study. A) Orthophoto with spatial resolution of 2 cm. B and C) Respectively, DSM and DTM of the study area with spatial resolution of 40 cm. D) DDM representing trees' heights in the study area (spatial resolution: 40 cm). In A and B is shown the AOI used for the validation of the volumes model. All the images are imported into QGIS software (v. 3.28).

Thus, by using the QGIS Raster Calculator, the DTM is subtracted from the DSM to obtain a DDM, concerning trees' heights in the area of interest. The canopy volume values are estimated by measuring the area of each pixel (0.40x0.40m) occupied by vegetation and multiplying the obtained data by the height values relative to the altitude of each selected pixel. Thus, to approximate the volume using the following equation, the canopies are considered as 2.5D geometries.

$$\text{Total canopy volume} = \sum_{i=1}^{n}(area_j * height_j)$$

where *j* is the pixel of interest. The spatial resolution of each pixel is 0.40 m, resulting in an individual pixel area of 0.16m^2.
Hence, from the DDM raster, a topographic dataset is derived to assess spatial distribution of elevation/volume values and their statistical characteristics. Elevation statistics indicate a right-skewed distribution with a long tail toward higher elevation values. The subset of elevation values between 0.5 m and 8 m was analysed separately (Fig. 3).

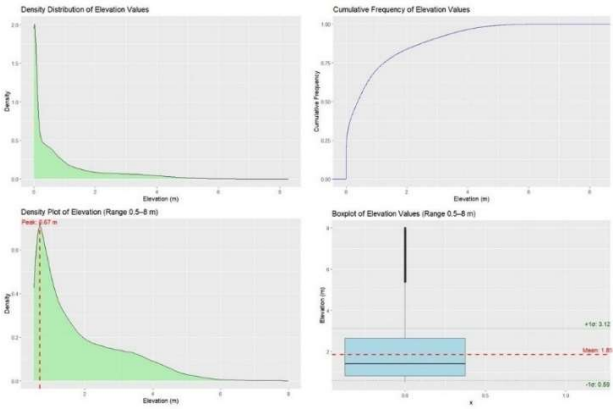

Figure 3. Descriptive statistics, boxplot of elevation values, and density analysis in the range of 0.5-8 m.

From the previous data, the total canopy volume estimation is provided. Statistics indicate a range spanning from 0 to 1,32 m^3, a mean of 0.15 m^3, and a standard deviation of 0.20 m^3. Finally, the estimation of the total canopy volume value results approximately 42098.97 m^3.
The validation process relates the volume error assessment between the UAV RGB/LiDAR and TLS 3D LiDAR RTK-SLAM data. So, topographical analysis, 2.5D and 3D modelling of a known object were gained from the previous data, considering object volume assessment in an AOI within the study area. Below is a summary table (Table 1) and a spatial overview (Fig. 4) for the sample object.

The comparison between DSM-derived volume and TLS reference volume is obtained both from point cloud and mesh model. The volume ratio P_{LAS} and P_{OBJ} result 1.12 and 1.03, respectively. The point cloud-based reference $E_{rel,LAS}$ exhibits a

relative error of 12.10%, suggesting a moderate overestimation. Instead, the mesh-based reference $E_{rel,OBJ}$ presents a relative error of 2.85%, indicating a closer correspondence.

Source	V_{LAS} (m^3)	V_{OBJ} (m^3)	P_{LAS}	P_{OBJ}	$E_{rel,LAS}$ (%)	$E_{rel,OBJ}$ (%)
UAV RGB/LiDAR	18.90	19.10	1.12	1.03	12.10	2.85
TLS	16.86	18.57				

Table 1. Results of the DDM (UAV-derived) validation procedure by using TLS reference volumes. The accuracy metrics P and E_{rel} are based on the volume ratio and the relative error, expressed as non-dimensional and percentage values, respectively.

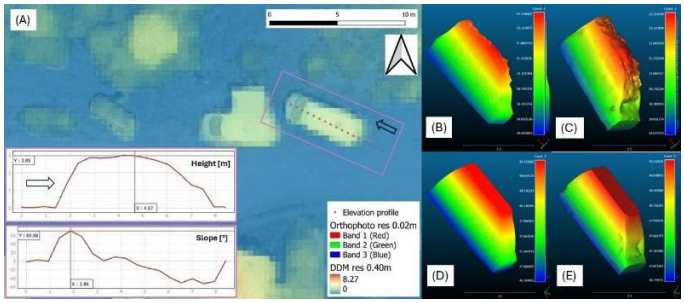

Figure 4. Known object considered for the canopy volume validation. A) DDM, elevation and slope information; B) DDM based point cloud; C) DDM based mesh model; D) TLS-based point cloud; E) TLS-based mesh model.

IV. Discussion and Conclusion

Canopies' areas and volumes estimation set the stage for a biodiversity analysis about habitat reduction and fragmentation within CDSs. Previous findings related to DTMs acquisition from aerial photogrammetric and LiDAR data showed difficulties for the vegetation contribute monitoring [12]. In this study, data extraction has been provided elaborating UAV RGB and LiDAR data. The workflow include the calculation of a DTM, based on a DSM characterized by a high dense vegetation pattern. Geospatial data analysis has permitted the elaboration of data, reducing signal noise in Cloud Compare and determining, through spatial interpolation techniques, topographic values on unknown unsampled points (Natural Neighbor). Consequently, the difference between the DSM and DTM allow to obtain the DDM, representing the height canopy value on each pixel along the area of interest. Accordingly, the total canopy volume estimation is provided, resulting in approximately 42090.97 m^3. Instead, the innovative approach in this study concern the validation process, comprising a known object within the study area for assessing the vertical and volume accurateness. Results have suggested that the DDM-based volume slightly overestimates the measurement, with higher accuracy when validated against mesh-derived volume references. Accordingly, future prospectives will provide information and elaboration of data through an inferential statistical approach, considering the uncertainty of the DTM obtained, fundamental for the DDM extraction. Moreover, future works will plan the measurement of more known object for the accuracy and an optimal volume error estimation. The comparison of these findings underscores the importance of considering the advance on vertical accuracy assessment. In conclusion, this study offers a comprehensive understanding of the spatial distribution of volume's values through raster, point cloud, and mesh model. These insights can be crucial for informed decision-making, particularly in biodiversity, where understanding spatial variability and habitat fragmentation is fundamental.

References

[1] Patrick A. Hesp, Ecological processes and plant adaptations on coastal dunes, Journal of Arid Environments, Volume 21, Issue 2, 1991, Pages 165-191, ISSN 0140-1963,Journal of Arid Environments, Volume 21, Issue 2, 1991, Pages 165-191. https://doi.org/10.1016/S0140-1963(18)30681-5

[2] Debinski, D.M. and Holt, R.D. (2000), A Survey and Overview of Habitat Fragmentation Experiments. Conservation Biology, 14: 342-355. https://doi.org/10.1046/j.1523-1739.2000.98081.x

[3] Adamo, M., Tarantino, C., Tomaselli, V., Veronico, G., Nagendra, H. and Blonda, P. (2016), Habitat mapping of coastal wetlands using expert knowledge and Earth observation data. J Appl Ecol, 53: 1521-1532. https://doi.org/10.1111/1365-2664.12695

[4] Tomaselli, V., Mantino, F., Tarantino, C. et al. Changing landscapes: habitat monitoring and land transformation in a long-time used Mediterranean coastal wetland. Wetlands Ecol Manage 31, 31–58 (2023). https://doi.org/10.1007/s11273-022-09900-5

[5] Laporte-Fauret, Q.; Marieu, V.; Castelle, B.; Michalet, R.; Bujan, S.; Rosebery, D. Low-Cost UAV for High-Resolution and Large-Scale Coastal Dune Change Monitoring Using Photogrammetry. J. Mar. Sci. Eng. 2019, 7, 63. https://doi.org/10.3390/jmse7030063

[6] Mei A, Ragazzo AV, Rantica E, Fontinovo G. Statistics and 3D Modelling on Soil Analysis by Using Unmanned Aircraft Systems and Laboratory Data for a Low-Cost Precision Agriculture Approach. AgriEngineering. 2023; 5(3):1448-1468. https://doi.org/10.3390/agriengineering5030090

[7] Mei, A., Berton, A., Adamo, M., Carruggio, F., Fontinovo, G., Rana, F. B., Ragazzo A. V., Genduso E., Tomaselli, V. (2023), Utilizzo di dati UAS per la caratterizzazione di habitat dunali nella ZSC "Duna e Lago di Lesina e Foce del Fortore" (Parco Nazionale del Gargano). Conference: XVII CONVEGNO NAZIONALE GIT, 13 Settembre 2023, Pietrasanta (Lu). DOI: 10.13140/RG.2.2.13845.09448

[8] Florinsky IV, Kurkov VM, Bliakharskii DP. Geomorphometry from unmanned aerial surveys. Transactions in GIS. 2018; 22: 58–81. https://doi.org/10.1111/tgis.12296

[9] Grieve, S. W. D., Mudd, S. M., Milodowski, D. T., Clubb, F. J., and Furbish, D. J.: How does grid-resolution modulate the topographic expression of geomorphic processes?, Earth Surf. Dynam., 4, 627–653. https://doi.org/10.5194/esurf-4-627-2016, 2016

[10] Szypuła, B. Accuracy of UAV-based DEMs without ground control points. Geoinformatica 28, 1–28 (2024). https://doi.org/10.1007/s10707-023-00498-1

[11] N. Otsu, "A Threshold Selection Method from Gray-Level Histograms," in IEEE Transactions on Systems, Man, and Cybernetics, vol. 9, no. 1, pp. 62-66, Jan. 1979. DOI: 10.1109/TSMC.1979.4310076

[12] Pirotti, F., Guarnieri, A. & Vettore, A. Vegetation filtering of waveform terrestrial laser scanner data for DTM production. Appl Geomat 5, 311–322 (2013). https://doi.org/10.1007/s12518-013-0119-3

The role of elevation in the spatial distribution of sub-daily rainfall extremes

[1]Paola Mazzoglio, Ilaria Butera, Pierluigi Claps

Department of Environment, Land and Infrastructure Engineering (DIATI)
Politecnico di Torino
Torino, Italy

[1] paola.mazzoglio@polito.it

Cite as: Mazzolgio, P., Butera, P., Claps, P. (2025). The role of elevation in the spatial distribution of sub-daily rainfall extremes. In: Proceedings of Geomorphometry 2025, 9-13 June, Perugia, Italy. M. Alvioli, L. Melelli, I. Marchesini eds. CNR Edizioni, Rome. ISBN 978-88-8080-765-0. DOI: 10.5281/zenodo.15212750

Abstract—**In regions with significant elevation variability like Italy, interpolation methods applied to rainfall depths should explicitly account for the elevation effect. This study examines the spatial variability of sub-daily rainfall extremes across Italy, focusing on assessing the role of elevation. Utilizing the Improved Italian - Rainfall Extreme Dataset (I²-RED), we analyzed average annual maxima from approximately 3,800 time series spanning at least 10 years between 1916 and 2020. To assess orographic influences, a local geo-regression approach was employed, aggregating stations located within a certain search radius centered in each 1km size cell used to segment the territory. Various constraints were applied to address challenges posed by low data density in certain regions and elevation-related extrapolation issues, and different criteria for selecting local samples were evaluated. Our findings corroborate previous studies with enhanced detail, revealing a general increase of the 24-hour average annual maxima with elevation (orographic effect), with the exception of few hilly/mountainous areas. Conversely, for 1-hour maxima, negative gradients (reverse orographic effect) were observed in extensive mountainous regions, suggesting decreased short-duration rainfall extremes at higher elevations. These insights contribute to a deeper understanding of rainfall patterns in Italy and can inform the development of improved hydrological models and infrastructure planning.**

I. INTRODUCTION

Large-scale rainfall datasets with high spatial and temporal coverage are often created through spatial interpolation of irregularly spaced rain gauge data onto regular grids. In flat areas, standard interpolation methods like inverse distance weighting and ordinary kriging can provide reliable estimates. In contrast, regions with complex terrain require the application of models that explicitly account for elevation effects, such as regression models, geographically weighted regressions or kriging with an external drift, which incorporate elevation as a predictor.

While the application of a single linear regression model on a wide area is statistically stable with respect to small errors in the observations, it often produces clustered residuals in complex terrains, making localized applications more effective. Geographically weighted regression models like PRISM [1] and Daymet [2] were thus suggested with the aim of improving accuracy by dynamically adjusting station influence based on terrain features and station density. However, their application over new areas remain difficult due to the need of defining a wide set of predictors and related weighting functions. Moreover, most of these models were applied only to ordinary rainfall (daily, monthly or annual totals), while none of them was applied to annual maximum rainfall depths.

In this work, we present a geo-regression approach that optimizes station density and a series of constraints that can be applied to address challenges posed by low data density in certain regions and elevation-related extrapolation issues. This study addresses this gap by using a comprehensive sub-daily rainfall dataset with nationwide coverage. It also allows to analyze elevation impact on rainfall extremes.

II. DATASET

Short-duration (1 to 24h) annual maximum rainfall depths come from the Improved Italian-Rainfall Extreme Dataset (I²-RED) [3]. In this work, we computed average annual maxima from approximately 3,800 time series spanning at least 10 years between 1916 and 2020.

The elevation of the rain gauges and of the surrounding terrain was derived from the Shuttle Radar Topography Mission (STRM) Digital Elevation Model (DEM) at 30 m resolution resampled at 1-km resolution using a cubic interpolation, following the approach suggested in PRISM [1] and adopted also in Daymet [2]. Lower-resolution elevation information was used here since the relationship between precipitation and elevation is more representative if the elevation of the surrounding area is used in place of the actual elevation of the point.

III. METHODOLOGY

A linear geo-regression model was implemented to assess the local relationship between rainfall extremes and elevation in each pixel with coordinates (x, y), by using the equation

$$h_d(x, y) = a(x, y) + b(x, y) \cdot z(x, y) + \varepsilon(x, y)$$

where h_d is the average annual maximum of an assigned duration d (with $d = 1$, 3, 6, 12 and 24 h), a is the intercept, b is the slope (that represents the rainfall gradient), z is the elevation and ε is the residual of the regression. Unlike other models [1], negative rainfall gradients with elevation were considered valid, reflecting previous findings in Italy [4, 5, 6].

To estimate local regression parameters, a circular area around each grid cell was used to select n nearby rain gauges. Two strategies were tested, by using: i) a fixed radius r_{fix} or ii) a variable radius adjusted based on data density to ensure statistical significance. In the first approach we evaluated the regression parameters by using the data of n rain gauges that are located inside a circular area with fixed radius, whatever the statistical significance of the regression model. This approach is in line with the one used in the PRISM and in Daymet models. In the second approach, instead, the search radius increases from r_{min} to r_{max} in each cell, until a statistically-significant regression model (at a 5% level) is found (thus, the "optimal" radius can vary cell by cell). The r_{max} was set to avoid regression models that gather data from areas that are too large, thus leading to the possible presence of high residuals.

To mitigate artifacts from inconsistent rainfall gradients or excessive extrapolation, the study introduced several constraints, such as requiring a minimum elevation range Δz in the local samples of at least 100 m and limiting extrapolation beyond data-supported elevations. Three strategies were explored for handling extrapolation:

i) disallowing it entirely (in grid cells with an elevation z that is higher/lower than those of all the data of the local sample, the regression model is not applied and the predicted value is set as the value obtained by the model in correspondence of the elevation of the highest/lowest rain gauge used);

ii) restricting it within a defined range, while elsewhere the regression limit value is used (in grid cells with an elevation z that is higher/lower than those of the data of the local sample by an amount e_{max}, the model is not applied and the predicted value is set as the value obtained by the model at an elevation that is e_{max} higher/lower than those of the highest/lowest rain gauge of the sample);

iii) restricting it within a defined range, while elsewhere the mean value is used (in grid cells with an elevation z that is e_{max} higher/lower than those of the data of the local sample, the model is not evaluated and the predicted value is computed using the 5 nearest stations).

For a more detailed description of the geo-regression model, the reader can refer to [7].

IV. RESULTS

The geo-regression approach presented in this work, even if simple, involves the selection of different parameters: the number n of rain gauges that forms the local sample, the elevation difference among the rain gauges of the local sample Δz, the search radius (r_{fix}, r_{min}, r_{max}) and the maximum extrapolation allowed e_{max}. Meaningful combinations of the different parameters were applied and several techniques (cross-validation, evaluation of error metrics, comparison of observed vs reconstructed values through boxplots, quantification of the entity of model residual, visual inspection of residual to assess the possible presence of clusters of residuals oh high entity and same sign) were jointly used to select the most accurate model.

The optimal configuration for the Italian case study resulted to be the one that considers a local sample of at least $n = 5$ rain gauges with a minimum difference in elevation Δz of 100 m obtained by pooling data by using a variable search radius that ranges from 1 up to 15 km with no extrapolation allowed. In grid cells with an elevation that is higher/lower than those of all the data of the local sample, the regression model is not applied and the predicted value is set as the value obtained by the model in correspondence of the elevation of the highest/lowest rain gauge used.

For this model configuration it can be worth examining the spatial variability of the slope coefficients emerged by the regression models, that quantify the influence of elevation on the spatial variability of rainfall extremes (Fig. 1).

Across most parts of the Alps, the Liguria region, and sections of the Apennines, there is a noticeable decrease in the 1-hour average annual maxima as elevation increases (Fig. 1a). This observation supports the presence of the "reverse orographic effect," previously identified by [4, 5, 6]. In contrast, in most of the hilly, pre-alpine, and flat regions, the average annual maxima tend to rise with elevation. Fig. 1b, instead, confirms that the 24-hour average annual maxima generally increase with elevation across Italy, with the exception of certain hilly and mountainous areas where this trend does not hold.

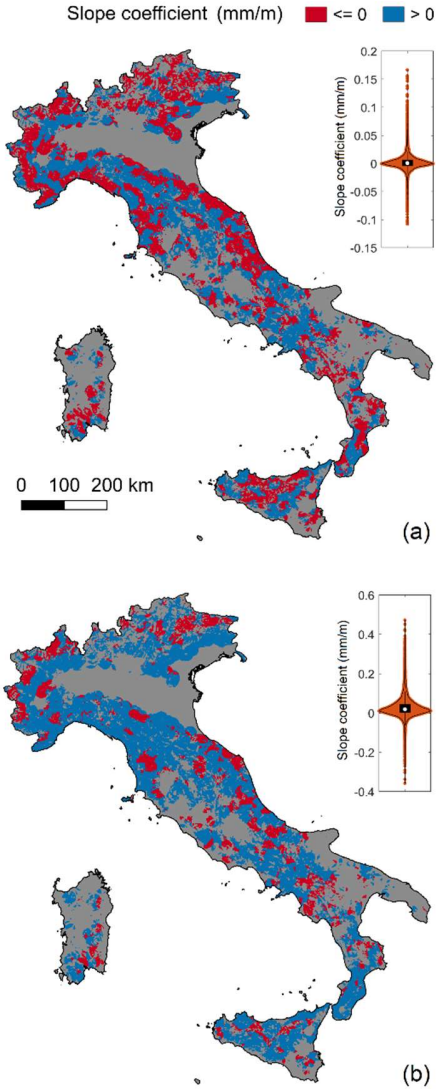

Figure 1. Slope coefficients of the selected regression models for the 1 h (a) and 24 h (b) duration. The grey color is used for the areas where the regression model cannot be applied due to low data density or extrapolation constraints. Source: [7].

V. CONCLUSIONS

This study introduces an enhanced local regression method to analyze the spatial variability of average annual maximum rainfall depths for short durations (1, 3, 6, 12, and 24 hours) across Italy with respect to the elevation. The approach improves interpolation by selecting small, localized samples that leverage areas with high rain gauge density. Special attention was given to mitigating artifacts caused by inconsistent rainfall gradients and extrapolation issues. Unlike other approaches, which treat negative rainfall gradients as errors, this study allows negative values but controls them through constraints on the elevation range of the data.

Results indicate that using a local regression within a 15 km radius best preserves local variability, accommodating the uneven distribution of rain gauges across the country.

This method identifies several regions in Italy with negative orographic gradients, where rainfall decreases with elevation, especially for the 1 h duration. The classical orographic effect instead prevails for longer durations.

VI. ACKNOWLEGMENTS

This research has been supported by the RETURN Extended Partnership and received funding from the European Union NextGenerationEU (National Recovery and Resilience Plan – NRRP, Mission 4, Component 2, Investment 1.3 – D.D. 1243 2/8/2022, PE0000005 – Spoke TS2).

REFERENCES

[1] Daly, C., R.P. Neilson, and D.L. Phillips, 1994. A statistical-topographic model for mapping climatological precipitation over mountainous terrain. Journal of Applied Meteorology and Climatology, 33(2), 140–158. https://doi.org/10.1175/1520-0450(1994)033%3C0140:ASTMFM%3E2.0.CO;2

[2] Thornton, P.E., R. Shrestha, M. Thornton, S.C. Kao, Y. Wei, and B.E. Wilson, 2021. Gridded daily weather data for North America with comprehensive uncertainty quantification. Scientific Data, 8(1), 190. https://doi.org/10.1038/s41597-021-00973-0

[3] Mazzoglio, P., I. Butera, and P. Claps, 2020. I^2-RED: a massive update and quality control of the Italian annual extreme rainfall dataset. Water, 12, 3308. https://doi.org/10.3390/w12123308

[4] Allamano, P., P. Claps, F. Laio, and C. Thea, 2009. A data-based assessment of the dependence of short-duration precipitation on elevation. Physics and Chemistry of the Earth, Parts A/B/C, 34(10-12), 635-641. https://doi.org/10.1016/j.pce.2009.01.001

[5] Avanzi, F., C. De Michele, S. Gabriele, A. Ghezzi, and R. Rosso, 2015. Orographic signature on extreme precipitation of short durations. Journal of Hydrometeorology, 16(1), 278–294. https://doi.org/10.1175/JHM-D-14-0063.1

[6] Mazzoglio, P., I. Butera, M. Alvioli, and P. Claps, 2022. The role of morphology in the spatial distribution of short-duration rainfall extremes in Italy. Hydrology and Earth System Sciences, 26, 1659–1672. https://doi.org/10.5194/hess-26-1659-2022

[7] Mazzoglio, P., I. Butera, and P. Claps, 2023. A local regression approach to analyze the orographic effect on the spatial variability of sub-daily rainfall annual maxima. Geomatics, Natural Hazards and Risk, 14(1). https://doi.org/10.1080/19475705.2023.2205000

3 - GEORESOURCES

Geodiversity and Geomorphometry: Methods and Applications in Landscape Assessment

Zbigniew Zwoliński
Institute of Geoecology and Geoinformation
Adam Mickiewicz University in Poznań
Poznań, Poland
zbzw@amu.edu.pl

Alicja Najwer
Institute of Geoecology and Geoinformation
Adam Mickiewicz University in Poznań
Poznań, Poland
alijas@amu.edu.pl

Cite as: Zwoliński, Z., Najwer, A. (2025). Geodiversity and Geomorphometry: Methods and Applications in Landscape Assessment. In: Proceedings of Geomorphometry 2025, 9-13 June, Perugia, Italy. M. Alvioli, L. Melelli, I. Marchesini eds. CNR Edizioni, Rome. ISBN 978-88-8080-765-0.

Abstract: **Geodiversity – the natural range of Earth's abiotic features – plays a fundamental role in shaping geoecosystems, supporting biodiversity, and guiding conservation planning. This paper examines current methodologies for assessing geodiversity, with a focus on integrating geomorphometric analysis with thematic mapping and Spatial Multi-Criteria Analysis (S-MCA). Through case studies, we illustrate how varying methodologies influence geodiversity mapping outcomes. We highlight the strengths and limitations of qualitative, quantitative, and hybrid approaches, with particular attention to uncertainty and scale of analysis. The study underscores the value of participatory tools, such as geo-questionnaires, and proposes best practices for transparent, repeatable, and policy-relevant geodiversity assessment.**

I. Introduction

Geodiversity – the diversity of Earth's abiotic components – has gained attention in recent decades as a complement to biodiversity (Gray, 2004, Zwoliński, 2004). It encompasses the range of geological, geomorphological, and soil features, along with their assemblages, relationships, and processes. While geodiversity is recognized for underpinning biodiversity and ecosystem functioning, it also possesses intrinsic value independent of its ecological roles. For example, Gray (2004) identifies multiple geodiversity values – intrinsic / existence, cultural, aesthetic, economic, functional, and research / educational – emphasizing how abiotic diversity contributes to landscapes, natural resources, and human understanding. Geodiversity underlies geoheritage, geosites, and geoparks, playing an increasingly important role in geotourism and conservation planning (Najwer & Zwoliński, 2014). Mapping and assessing geodiversity are therefore important for protected and conserved areas (PCAs) management and land-use planning (Jankowski *et al*., 2020, Najwer *et al*., 2016, 2023). The current study aims to synthesize recent developments by exploring the integration of geomorphometry – the quantitative analysis of land surface characteristics – with geodiversity assessment. Geomorphometry provides a powerful toolkit for characterizing topography and modelling spatial patterns of terrain-related factors such as slope, curvature, solar radiation, and moisture indices (Evans, 2012, Minár *et al.*, 2020). When combined with thematic datasets on geology, hydrology, and soils, geomorphometric parameters can support the creation of reproducible, high-resolution geodiversity maps. This fusion holds promise for developing scalable, transferable methods applicable across various landscapes and spatial planning contexts.

II. Definitions and Conceptual Background

Many authors have offered formal definitions of geodiversity. Gray (2004) defined it as "the natural range (diversity) of geological (rocks, minerals, fossils), geomorphological (landforms, processes) and soil features" including their assemblages, interactions, and systems. Zwoliński (2004) similarly emphasizes the natural range of bedrock, landform, and soil deposits, plus associated systems and processes, as constituting geodiversity. More recent definitions expand geodiversity to include hydrological (Gray 2013) and climatic elements (Najwer *et al.*, 2016, Tukiainen *et al.*, 2023). In practice,

these dimensions are often treated as factors in geodiversity assessments (e.g., geology, relief, hydrography, soils, climate).

Outstanding geodiversity landscapes are those that are rare, unique, well-expressed, and of regional significance, whereas representative landscapes serve as exemplars of common abiotic types. Thus, geodiversity mapping often seeks to identify areas with exceptional or representative abiotic diversity. Indeed, geodiversity forms the foundation of many aspects of geoheritage: geo(morpho)sites, fossil sites, and geoparks all derive significance from their underlying abiotic diversity. Effective geodiversity mapping requires integration of datasets on geology, geomorphology, soils, hydrology, and climate at appropriate spatial scales.

III. METHODOLOGY

Assessment approaches. Geodiversity assessment methods vary widely in terms of data sources and procedures. One way to categorize them is into **direct and indirect** approaches (Pellitero *et al.*, 2014). Direct methods quantify specific abiotic components through field surveys or thematic maps (e.g., inventories of rock types or landforms). Indirect methods infer geodiversity from surrogate indicators of environmental conditions that are associated with abiotic diversity: for example, using elevation variability or climate zones as proxies for underlying abiotic variety.

A second classification distinguishes methods by procedure: **qualitative, quantitative, and hybrid** approaches (Zwoliński *et al.*, 2018, 2025). *Qualitative* methods rely on expert-based classification or ranking of abiotic features, often based on experience or interpretation. While such methods are relatively fast and adaptable, they are also subjective and difficult to replicate (results "often not comparable" across studies). *Quantitative* approaches, on the other hand, use numerical data and measurements (digital elevation models, geological maps, field data) to compute indices or spatial metrics. These methods offer high-precision outputs and reproducibility, but they often require extensive data processing and can be costly to acquire. *Hybrid* (qualitative–quantitative) methods aim to combine the strengths of both approaches by integrating expert judgment with numerical data, for example, by applying expert-defined weights to GIS-derived factor maps. This approach leverages both specialist knowledge and the objectivity of measured data, though it still depends on the selection of factors and weighting schemes. The authors argue that hybrid methods "support the collection of quantitative data (i.e., digital) and cause–and–effect data (i.e., relational)", making them particularly useful for geodiversity mapping.

Due to the lack of a single standardized methodology, most studies adopt customized indices or multicriteria analysis frameworks. Among quantitative approaches, the **Geodiversity Index (Gd)** is commonly used. For example, Serrano & RuizFlaño (2007) proposed the following formula:

$$\mathbf{Gd = Eg\ R\ /\ \mathit{ln}\ S}$$

where *Eg* is the number of different abiotic elements in a spatial unit, *R* is a roughness coefficient (terrain variability), *S* is the unit area, and *ln* is the natural logarithm. This formula follows the concept that first linked element richness (*Eg*) with topographic roughness in a geodiversity index (on an area basis). Since then, numerous variants have emerged, modifying or expanding the index by incorporating additional factors, such as lithology counts, curvature measures, moisture indices, etc., depending on the study's objectives and data availability (Pereira *et al.*, 2013, Melelli, 2014, Pellitero *et al.*, 2014, Martinez-Grana *et al.*, 2015, Bétard *et al.*, 2017). Ultimately, the goal of all such approaches is to capture abiotic variety in a single metric.

Another quantitative approach is **GIS-based multi-criteria analysis (MCA)**. Here, a set of thematic layers (geological map, landform fragmentation map, hydrographical map, etc.) is overlaid with assigned importance weights, typically using a Weighted Linear Combination (WLC) method. Each factor layer is first scored; then, for each map cell, the Geodiversity Score = Σ(weight_i $\cdot$ score_i) is computed. Weights are often derived using the Analytical Hierarchy Process (AHP), based on pairwise comparisons following Saaty's (1980) method, which ensures consistency. For example, Najwer *et al.* (2023) assigned weights to streams, lakes, geology, landform fragmentation, and relief energy (0.288, 0.288, 0.174, 0.096, 0.096, and 0.058, respectively) in a study of an Alpine region, achieving a consistency ratio of 0.07. In practice, the final geodiversity map is produced by classifying the combined score, using methods such as natural breaks or expert-defined thresholds.

A recent innovation in this field is the *local WLC* (L-WLC). Unlike standard WLC, i.e., global WLC (G-WLC), where weights are global constants, L-WLC allows weights to vary spatially, capturing local variability (like applying a high-pass filter). Jankowski *et al.* (2020), Zwoliński *et al.* (2021), and Najwer *et al.* (2022) applied L-WLC alongside G-WLC in a crowdsourced study of Karkonosze National Park, Roztocze National Park, and Wolin National Park in Poland. Their findings showed that combining local and global aggregation methods produces a more nuanced geodiversity assessment.

Data sources and factors. Geodiversity mapping draws on a wide range of data sources, including geological maps, soil surveys, DEMs, satellite imagery, etc. Geomorphometric analysis is particularly widespread: researchers compute **DEM-derived indices** such as relief energy (terrain ruggedness), slope, curvature (profile/plan), surface roughness (rugosity), topographic position index (TPI), convergence index, potential/total solar insolation and wetness indices (Topographic Wetness Index - TWI, Topographic Relative Moisture Index - TRMI), among others. For example, Jačková & Romportl (2008)

used relative elevation and landform fragmentation metrics, finding strong links between geodiversity and habitat richness in Czech protected areas. These digital layers are often combined through map algebra to compute geodiversity scores. In some studies, additional static attributes such as lithology, hydrographic density, and climate variables are also incorporated.

Due to methodological diversity, **comparing and integrating** geodiversity maps can be challenging. Outputs can vary significantly depending on spatial resolution and the algorithm used. Scale plays a crucial role: Seijmonsbergen *et al.* (2018) showed that mapping the Hawaiian Islands at a10 km resolution (using global datasets) vs. 500 m (using local datasets) produced markedly different spatial patterns. Similarly, Vregelaar (2015) reported scale sensitivity in the Netherlands. Thus, both the scale classification method (equal-interval vs. natural breaks) and the selection of input factors have a substantial influence on the final results. Moreover, all methods rely on expert decisions (rating scales, weights, and criteria), introducing a degree of subjectivity. Regardless of whether a quantitative or semi-quantitative approach is applied, the final geodiversity classification remains relative to the specific area under investigation. To enable meaningful comparison across regions, a standardized classification system should be developed for each abiotic component, ideally at a global or continental scale. Additionally, the development of classification scales adapted to specific morphoclimatic zones is also worth considering.

IV. Case Studies

Dębnica catchment (Poland). Najwer *et al.* (2016) and Zwoliński *et al.* (2018) illustrate how methodology affects outcomes. They assessed geodiversity in the Postglacial Dębnica River catchment (Western Pomerania) using two approaches applied to the same dataset: (1) a GIS-AHP approach (featuring fine 30×30 m grids and expert weights) and (2) a classical index-based method following Serrano & Ruiz-Flaño (2007) (using coarse 1×1 km grids). The two resulting geodiversity maps were assessed as "diametrically opposed". In the index map, roughness coefficient (R) was the dominant factor, highlighting broad areas of high relief energy. In contrast, the AHP map's highest geodiversity arose in areas with complex geomorphology - characterised by high relative altitudes and varied landform types. In other words, the index method emphasized vertical ruggedness, while the multicriteria method emphasized spatial landform diversity (horizontal ruggedness). The authors conclude that both methods are *equipotential* – each yielding meaningful but not directly comparable results. Interestingly, both approaches identified similar clusters of high- and low-diversity areas despite methodological differences. This case highlights how grid size (spatial assessment unit) and factor prioritization can invert perceived geodiversity.

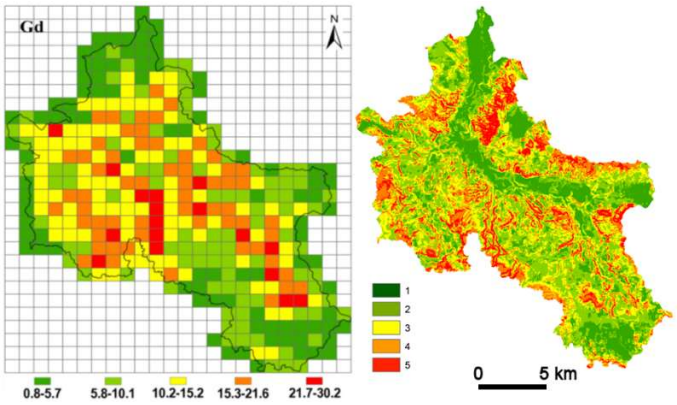

Figure 1. Total geodiversity maps for Dębnica River catchment. On the left, geodiversity is calculated according to geodiversity index (Serrano & Ruiz-Flaño, 2007), and on the right, according to GIS-AHP approach (Najwer *et al.*, 2016). Classes of geodiversity: 1 – very low, 2 – low, 3 – medium, 4 – high, and 5 – very high.

Karkonosze National Park (Poland). In another study, Jankowski *et al.* (2020) conducted a geodiversity assessment of the Karkonosze NP using a novel *crowdsourcing* approach. They gathered ratings from 57 Earth science researchers via a geo-questionnaire (Jankowski *et al.*, 2016) to determine factor scores and weights for variables such as lithology, relief energy, landforms, land cover and land use, soils, solar irradiance, hydrography. The study computed two types of aggregate geodiversity maps: standard WLC (G-WLC) and local WLC (L-WLC, Malczewski, 2011). Key findings were that L-WLC produced more extensive areas of high geodiversity – reflecting localized hotspots – than the G-WLC map. In total, more high geodiversity area was identified by L-WLC (31 km²) than by G-WLC (27.3 km²). Moreover, integrating the two maps with an uncertainty analysis revealed seven areas of high geodiversity with low uncertainty (e.g., Mumlawski Slope, Szrenickie Wetlands, White Gorge, etc.). The authors emphasize that using both local and global weighting in combination provides a more comprehensive picture than using either method individually. This case demonstrates the feasibility of combining crowdsourced expert knowledge with spatial multi-criteria methods to generate detailed geodiversity maps for PCAs.

Mountain catchments (the Alps, Tatra Mts., and Sudetes). Najwer *et al.* (2023) performed a full GIS-WLC analysis with factors like streams, lakes, geology, landform fragmentation, relief energy, and landform preservation in two catchments, i.e., Derborence and Illgraben in the Swiss Alps. Weights were determined using AHP (pairwise comparisons), and the final maps reflected the weighted sum of these layers. In smaller mountain catchments (Wrzosówka Stream in Sudetes, Sucha Woda Stream in Tatra Mts.), and comprehensive DEM-based workflow was used: the researchers derived several factor maps from a DEM, including relief energy, convergence index, general

curvature, topographic openness, topographic position index, topographic wetness index, and total incoming solar radiation. These were then combined using expert-defined weights, into a final geodiversity map (Fig. 2). Across these cases, multi-criteria GIS-based analysis enabled the integration of diverse abiotic data into interpretable geodiversity assessments.

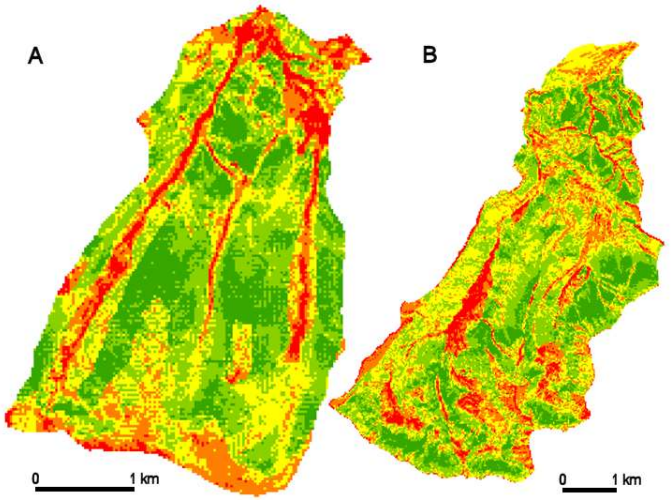

Figure 2. Total geodiversity maps for Wrzosówka Stream (A) and Sucha Woda Stream (B). The colours are explained in Fig. 1.

Scale of geodiversity. A methodological issue of particular importance is the application of the five-point Likert scale (Likert, 1932) for classifying geodiversity across 23 national parks in Poland, based on geomorphometric parameters. A flowchart illustrating the process is shown in Figure 3. A key challenge—relevant to virtually all geodiversity assessments, regardless of the primary evaluation method chosen—is the classification of individual component values and cumulative geodiversity values relative to the value range of the area under investigation. This often leads to a lack of comparability between areas characterized by differing morphometry and morphogenesis. The most commonly applied approach involves calculating geodiversity values separately for each national park (see A in Fig. 4), resulting in an individual range of values for each park. While this method allows for a more detailed characterization of individual areas, it significantly limits the potential for cross-site comparison, making it difficult to identify the park with the highest or lowest level of geodiversity. An alternative approach calculates geodiversity scores using a unified value range for all assessed indices across a broader region (see B in Fig. 4) – in this case, the entirety of Poland. This approach preserves methodological consistency and ensures that the analysed spatial units can be directly compared, facilitating the identification of relative differences in geodiversity levels across the 23 national parks (Fig. 4).

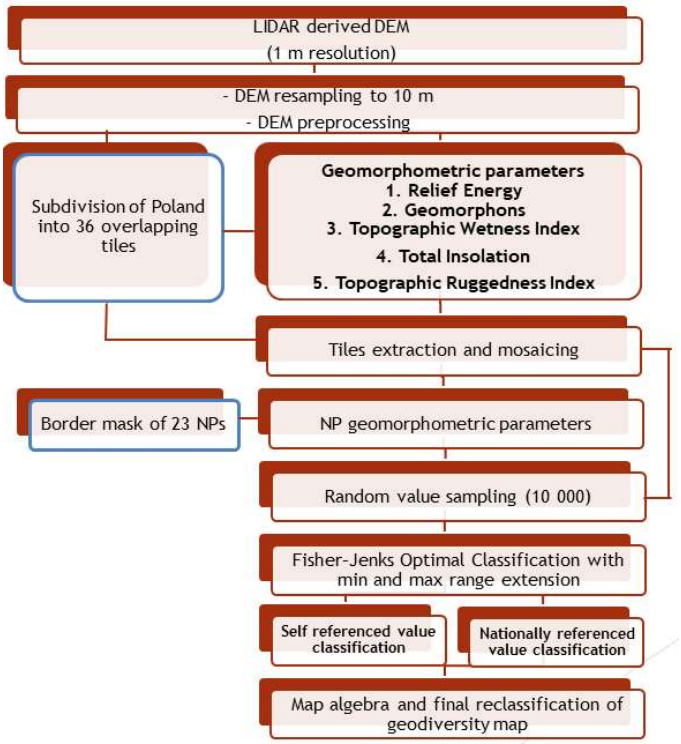

Figure 3. Flowchart for calculating self referenced and nationally referenced values of geodiversity for 23 national parks in Poland.

V. Results and Discussion

These case studies illustrate the **sensitivity** of geodiversity maps to methodological choices. Different approaches can produce markedly different maps even when based on the same raw data. In Dębnica, the coarse-index method compared to the fine-scale AHP method highlighted different features of the landscape, yet both consistently identified key geodiversity clusters. In Karkonosze, allowing weights to vary locally (L-WLC) revealed additional high-diversity zones that a global model might overlook. These findings underscore that geodiversity is not a unique observable quantity but depends on how it is measured (factor selection, weights, resolution) – a point frequently emphasized in the literature (Najwer *et al.*, 2016, Zwoliński *et al.*, 2018). Thus, geodiversity mapping is inherently *relative* and method-dependent; results must be interpreted with care.

At the same time, common patterns emerge: areas with complex geology or rugged relief tend to score high, while uniform plains consistently receive low scores. Geomorphometric factors (roughness, curvature, TPI, etc.) often dominate index-based maps (as seen in Wrzosówka and Sucha Woda streams). Qualitative judgments (through AHP in Dębnica River) tend to

emphasize varied landform types and processes. Both approaches are complementary. Zwoliński *et al.* (2018) suggest using combined outputs (e.g., overlaying multiple methods) to identify robust geodiversity hotspots. In our cases, despite methodological differences, clusters of high geodiversity were found in analogous zones, such as old glacial cirques, tectonic ridges, and similar landforms.

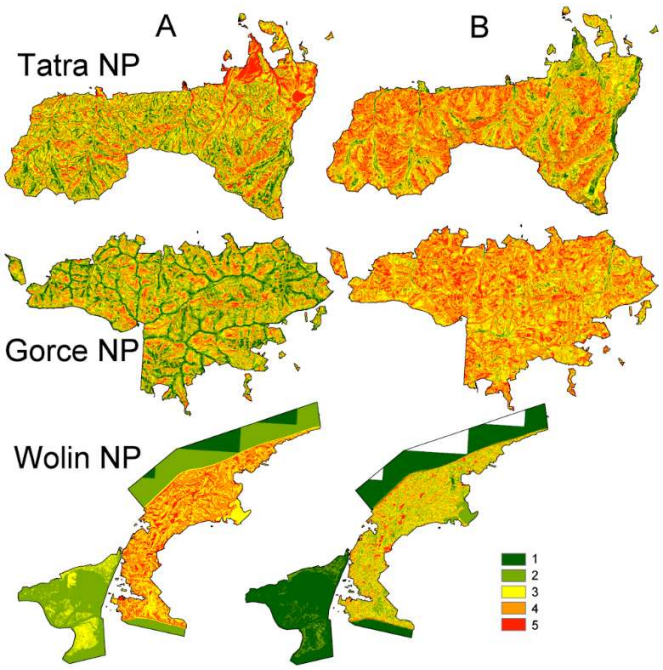

Figure 4. Self referenced (A) and nationally referenced (B) values of geodiversity for Tatra National Park, Gorce National Park, and Wolin National Park. Classes of geodiversity: 1 – very low, 2 – low, 3 – medium, 4 – high, and 5 – very high.

Key challenges remain in geodiversity assessment. The availability of data and the issue of scale are critical: coarse global datasets may miss local detail, while high-resolution local data can be expensive to obtain. Scale effects (global vs. local DEMs) have been clearly demonstrated in places like Hawaii and the Netherlands. Subjectivity is another issue: expert-derived ratings or weights can introduce bias, and different experts may disagree (leading to uncertainty). Even quantitative indices involve choices (e.g., which "elements" to include in *Eg*). As Jankowski *et al.* (2020) note, these ambiguities limit comparability across studies.

Despite these challenges, geodiversity maps provide valuable insights. They can inform management of protected areas by highlighting abiotic diversity patterns that are often invisible in land-cover maps. For example, the Karkonosze NP maps (Jankowski *et al.*, 2020) identified small-scale features of high geodiversity (e.g., rock glaciers, glacial ponds) that warrant conservation attention. The Dębnica map delineated wetland complexes and moraine hills of high geodiversity. Such spatial knowledge can guide zoning, tourism planning, and geo-conservation strategies, enriching the traditional focus on biological diversity with an abiotic perspective.

VI. Conclusion

Geodiversity mapping synthesizes geology, geomorphology, soils, hydrology, and climate into integrated maps that characterize landscape heterogeneity. No single standard method exists; instead, a toolbox of qualitative, quantitative, and hybrid techniques is used to capture the multifaceted nature of the abiotic environment. Quantitative indices (e.g., Serrano & Ruiz-Flaño's formula) and GIS-based multi-criteria models are widely applied to integrate data layers. Case studies (Dębnica, Karkonosze NP) show that methodological choices – grid resolution, factor weighting, index vs AHP – strongly affect the final map outcome. In practice, combining approaches (e.g., global and local weighting) and involving experts helps identify consistent geodiversity hotspots. Geomorphometric analysis (using DEM-derived metrics) underpins most quantitative assessments, offering **objective, reproducible measures** of Earth surface diversity.

Overall, geodiversity mapping is a valuable complement to biodiversity studies, providing a framework to assess, conserve, and utilize Earth's abiotic diversity. The reviewed examples demonstrate how diverse methods can be coherently applied to real landscapes, yielding actionable maps for geoconservation and land management. Moving forward, efforts to standardize methods and to incorporate multi-scale, participatory, and uncertainty-aware approaches will strengthen the rigor of geodiversity research.

References

[1] Betard, F., Hobléa, F., & Portal, C. (2017). Geoheritage as new territorial resource for local development. *Annales de Géographie*, *717*, 523–543. https://doi.org/10.3917/ag.717.0523

[2] Gray, M. (2004). *Geodiversity: Valuing and conserving abiotic nature*. John Wiley & Sons.

[3] Gray, M. (2013). *Geodiversity: Valuing and conserving abiotic nature* (2nd ed.). John Wiley & Sons.

[4] Jačková, K., & Romportl, D. (2008). Relationship between geodiversity and habitat richness in Šumava National Park and Křivoklátsko PLA (Czech Republic): A quantitative analysis approach. *Journal of Landscape Ecology*, *1*(1), 23–38.

[5] Jankowski, P., Czepkiewicz, M., Młodkowski, M., & Zwoliński, Zb. (2016). Geo-questionnaire: A method and tool for public preference elicitation in land use planning. *Transactions in GIS*, *20*(6), 903–924. https://doi.org/10.1111/tgis.12191

[6] Jankowski, P., Najwer, A., Zwoliński, Zb., & Niesterowicz, J. (2020). Geodiversity assessment with crowdsourced data and spatial multicriteria

analysis. *ISPRS International Journal of Geo-Information*, *9*(12), 716. https://doi.org/10.3390/ijgi9120716

[7] Likert, R. (1932). A technique for the measurement of attitudes. *Archives of Psychology*, *140*, 1–55.

[8] Malczewski, J. (2011). Local weighted linear combination. *Transactions in GIS*, *15*, 439–455. https://doi.org/10.1111/j.1467-9671.2011.01275.x

[9] Martinez-Graña, A. M., Goy, J. L., & Cimarra, C. (2015). 2D to 3D geologic mapping transformation using virtual globes and flight simulators and their applications in the analysis of geodiversity in natural areas. *Environmental Earth Sciences*, *73*, 8023–8034. https://doi.org/10.1007/s12665-014-3959-1

[10] Melelli, L. (2014). Geodiversity: A new quantitative index for natural protected areas enhancement. *GeoJournal of Tourism and Geosites*, *1*(13), 27–37.

[11] Najwer, A., Borysiak, J., Gudowicz, J., Mazurek, M., & Zwoliński, Zb. (2016). Geodiversity and biodiversity of the postglacial landscape (Dębnica River catchment, Poland). *Quaestiones Geographicae*, *35*(1), 5–28. https://doi.org/10.1515/quageo-2016-0001

[12] Najwer, A., Reynard, E., & Zwoliński, Zb. (2023). Geodiversity assessment for geomorphosites management: Derborence and Illgraben, Swiss Alps. In L. Kubalíková, P. Coratza, M. Pál, Zb. Zwoliński, P. N. Irapta, & B. van Wyk de Vries (Eds.), *Visages of geodiversity and geoheritage*. Geological Society, London, Special Publications. https://doi.org/10.1144/SP530-2022-122

[13] Najwer, A., & Zwoliński, Zb. (2014). Semantics and geodiversity assessment methods – Review and research proposal. *Landform Analysis*, *26*, 115–127. https://doi.org/10.12657/landfana.026.011

[14] Pellitero, R., Manosso, F. C., & Serrano, E. (2014). Mid- and large-scale geodiversity calculation in Fuentes Carrionas (NW Spain) and Serra do Cadeado (Paraná, Brazil): Methodology and application for land management. *Geografiska Annaler: Series A, Physical Geography*, *97*(2), 219–235. https://doi.org/10.1111/geoa.12057

[15] Pereira, D., Pereira, P., Brilha, J., & Santos, L. (2013). Geodiversity assessment of Paraná State (Brazil): An innovative approach. Environmental Management, 52, 541–552.

[16] Saaty, T. L. (1980). *The analytic hierarchy process*. McGraw-Hill.

[17] Serrano, E., & Ruiz-Flaño, P. (2007). Geodiversity: A theoretical and applied concept. *Geographica Helvetica*, *62*(3), 140–147. https://doi.org/10.5194/gh-62-140-2007

[18] Seijmonsbergen, A. C., Guldenaar, J., & Rijsdijk, K. F. (2018). Exploring Hawaiian long-term insular geodiversity dynamics. *Landform Analysis*, *35*, 31–43. https://doi.org/10.12657/landfana.035.007

[19] Tukiainen, H., Toivanen, M., & Maliniemi, T. (2023). Geodiversity and biodiversity. In L. Kubalíková, P. Coratza, M. Pál, Zb. Zwoliński, P. N. Irapta, & B. van Wyk de Vries (Eds.), *Visages of geodiversity and geoheritage*. Geological Society, London, Special Publications. https://doi.org/10.1144/SP530-2022-107

[20] Zwoliński, Zb. (2004). Geodiversity. In A. S. Goudie (Ed.), *Encyclopedia of geomorphology* (Vol. 1, pp. 417–418). Routledge.

[21] Zwoliński, Zb., Najwer, A., & Giardino, M. (2018, 2025). Methods for assessing geodiversity. In E. Reynard & J. Brilha (Eds.), *Geoheritage: Assessment, protection, and management*. Elsevier.

[22] Zwoliński, Zb., Najwer, A., & Jankowski, P. (2021). Globally and locally weighted linear combination as a methodological approach to geodiversity assessment of geoparks. *Landform Analysis*, *40*, 57–69. https://doi.org/10.12657/landfana-040-003

Geomorphodiversity index of Switzerland for multiscale analysis

Martina Burnelli [1], Massimiliano Alvioli [2]
Istituto di Ricerca per la Protezione Idrogeologica, Consiglio Nazionale delle Ricerche, via Madonna Alta 126, I-06128, Perugia, Italy

Emmanuel Reynard [3]
Institute of Geography and Sustainability, Interdisciplinary Centre for Mountain Research, University of Lausanne, Switzerland

Laura Melelli [4]
Department of Physics and Geology, University of Perugia, Piazza Università, 1, 06100 Perugia, Italy

[1] martinaburnelli@cnr.it, [2] massimiliano.alvioli@irpi.cnr.it, [3] emmanuel.reynard@unil.ch, [4] laura.melelli@unipg.it

Cite as: Burnelli, M., Reynard, E., Melelli, L., Reynard, E. (2025). Geomorphodiversity index of Switzerland for multiscale analysis. In: Proceedings of Geomorphometry 2025, 9-13 June, Perugia, Italy. M. Alvioli, L. Melelli, I. Marchesini eds. CNR Edizioni, Rome. ISBN 978-88-8080-765-0. DOI: 10.5281/zenodo.15274406

Abstract— **Geodiversity refers to the variety of Earth's physical features and processes, and it represents the geosphere counterpart of biodiversity. The abiotic diversity supports natural processes and sustains biotic niches, and it contributes to the human health through a wide range of ecosystem services. Geomorphodiversity, as a part of geodiversity, describes the diversity of landforms, resulting from the lithological and surface processes modelling the landscape. Combining information from a geo-lithological map and quantities derived from a digital elevation model with a simple, multi-scale and reproducible approach, results in discrete geomorphodiversity index (GmI). The raster index has an intuitive content and can be represented at different spatial resolutions, depending on input data and purpose of the study. Here, we implemented the method to obtain the first geomorphodiversity map of Switzerland. The map nicely represents the landscape variability of Switzerland and it can be valuable to identify areas at national scale with a potential hazard for natural phenomena (landslides, flooding, and others). As the index aims at representing the abundance and diversity of landforms in an area, we compared GmI with a field-based geomorphological dataset of the Hérens valley, in Southern Switzerland. The local-scale assessment shows that GmI is an additional tool to understand surface diversity from large- to local-scale, for land use management, and to promote the conservation of natural areas in a broad sense.**

I. Introduction

Geodiversity is "the natural range (diversity) of geological (rocks, minerals, fossils), geomorphological (landforms, processes) and soil features" [1] and is widely recognized as the "silent counterpart" of biodiversity. It supports the natural processes occurring in the ecosystems and human health, through a wide range of ecosystem services [2,3].

Urban sprawl and induced landscape modifications alter the stability of natural ecosystems [4]. The vast majority of the scientific literature and the nature-based solutions focus on biodiversity protection, overlooking the role of the abiotic richness of Earth surface, or geodiversity [5]. Monitoring the heterogeneity and the evolution of the Earth surface and sub-surface abiotic features [6] act as indicators of areas with a high degree of naturalness, enhancing their protection and promoting conservation strategies.

Several different methods exist in the literature to study geodiversity, each with different assumptions and aims [7,8]. Geomorphodiversity specifically considers landforms, their abundance, their diversity, and the morphogenetic processes modelling the landscape. Moreover, geomorphodiversity is a one of the components of ecosystems, and geomorphodiversity mapping may help geo-conservation actions and delimiting Natural Protected Areas [9].

One of the challenges for the assessment and mapping of geomorphodiversity is the definition of proper spatial and temporal scales [10]. Selecting proper spatial scale is essential for including geodiversity as an environmental input if ecological models, to model species distributions, and draw conclusions about conservation strategies [11].

The quantitative index defined by [12] represents geomorphodiversity as the variety of features and the morphogenetic processes modeling the landscape [13], and lithological information [14, 15], combining high resolution elevation data, geology, and digital elevation model (DEM)-derived data, through simple and repeatable steps. [16] improved on the method, including a multi-scale approach. Here, the method is applied to obtain a GmI raster map of Switzerland. Despite its

limited area, Switzerland is characterized by a high variety of geomorphological features [17] resulting from the combination of endogenous and exogenous factors, like the multiple lithotypes, the geological evolution, mainly marked by the Alpine orogeny, and the climatic diversity, due to its peculiar geographical location, at the interface between Northern Europe and the Mediterranean area. These conditions result in diverse landscape types, which are borne out in the proposed GmI. The map provides information about the geomorphological diversity in five classes, which constitutes the abiotic framework and the resources for natural and human development, land management, biodiversity conservation and natural resource management, as well as geoheritage selection and geotourism management.

II. Materials and Methods

Assessment of the GmI for Switzerland, at a national scale, required the following input data.

1. The Copernicus EU–DEM, a raster layer supplied by the European Environmental Agency (EEA, available at https://www.eea.europa.eu/). The horizontal resolution is of 25 m and the vertical accuracy is of 2.9 m. We used this data for the assessment of (i) the slope angle and (ii) the derived terrain forms.

2. A map of the geological complexes of Switzerland at 1:500,000 scale, a vector layer supplied by the Federal Office of Topography swisstopo and describing 25 different lithotypes across Switzerland.

3. The swissTLMRegio dataset, supplied by the Swiss Federal Office of Topography swisstopo, providing river network information. It contains high quality and homogeneous information, with accuracy between 20 m and 60 m.

4. The map of the main geomorphological landscapes at 1:500,000 scale, in a vector format, published in the Atlas of Switzerland in 1975 and providing an overall picture of the four main morphogenetic landscape types of Switzerland: glacial, fluvial, karstic and gravitational. The dataset does not correspond to a field-based geomorphological map, but shows information concerning the most relevant geomorphological agents influencing the landforms variability.

The original approach of [12] adopted a raster resolution of 500 m for the GmI map. In this work, we fully exploited the EU-DEM 25 m resolution and obtained a GmI with the same spatial resolution, and we followed the multi-scale approach by [16, 18]. Moreover, we introduced a more flexible method to combine the partial diversities of each input quantity into the final GmI map. In fact, in previous as well as in this work, we first calculated diversity maps of individual input quantities. With diversity, we mean the number of different classes of each input quantity within a given neighborhood; their combination represents the final GmI result. We considered four raster surface descriptors, namely, DEM-derived slope angle and landforms (terrain patterns), drainage network, and lithological information. Figure 1 outlines the procedure adopted in this work, described in detail in the following.

The slope angle is a relevant factor for the heterogeneity of lands, since it affects the erosion, transport and accumulation processes that determine the denudation of the bedrock. Landforms are an essential feature entering the geomorphological variability in an area. We considered the geomorphons model by [19], which is suitable for large areas and automatically detects up to ten land surface patterns: flat, peak, ridge, shoulder, spur, slope, hollow, foot slope, valley, and pit. We considered such method as a close approximation to landforms existing in the field. The drainage density map allows investigating the

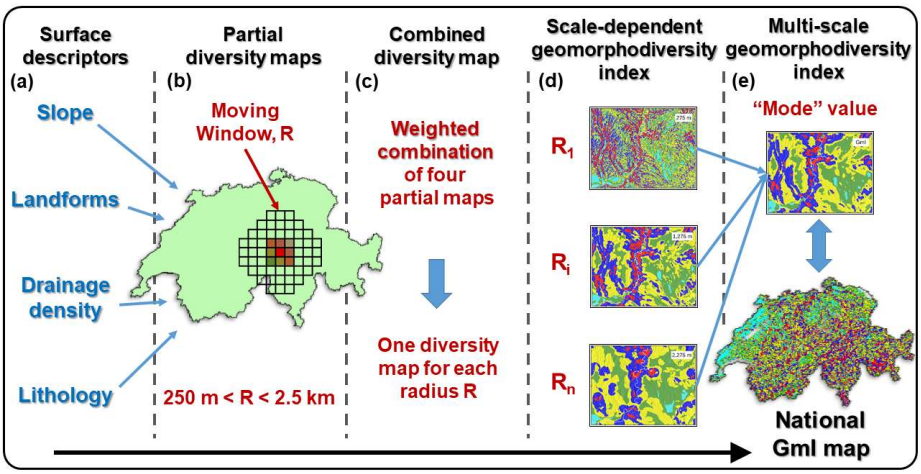

Fig. 1. The workflow leading to the high–resolution geomorphodiversity map (GmI) of Switzerland. From left to right, the different panels illustrate the actions described in Section II. (1) input data, (2) parametric calculation of partial diversity using moving windows, (3) combination of partial maps into as many GmI maps as the values of the parameter R (moving window radius), representing (4) an ensemble, scale–dependent geomorphodiversity assessment, and (5) scale–independent assessment of GmI selecting cell–by–cell most common value of the index across the ensemble. The core of the method is in step (b), corresponding to the assessment of partial diversities, i.e., the calculation of diversity of each input descriptor. Here, by diversity we mean the *number* of different values within the neighborhood singled out by a circular moving window of given size.

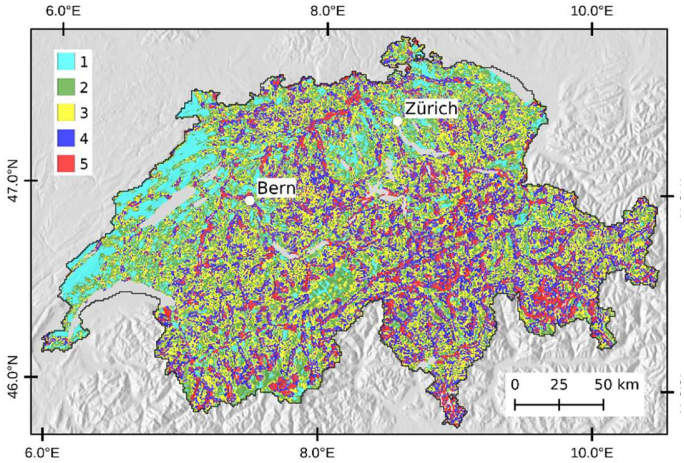

Fig. 2. The land surface diversity index, or geomorphodiversity index (GmI) of Switzerland, obtained in this work. The index is provided in five classes, from 1 (lowest diversity class) to 5 (highest diversity class). In the figure, the raster map is resampled at 500 m resolution, for easy reading; the actual result of this work has 25 m spatial resolution.

morphogenetic processes that occur in fluvial areas and in alluvial plains, where other topographic features, as the slope angle, are mostly uniform and less meaningful using DEMs with a medium horizontal resolution and vertical accuracy. Lastly, we considered the lithological map supplied by the regional Switzerland dataset. The lithological characteristics of a territory are significant information since they affect the response to the exogenous agents and geomorphological evolution of the surface over time.

The first step (Fig. 1(b)) was to calculate four partial diversity grid maps, one for each input raster map (slope, landforms, drainage density and lithology), with a moving window (focal statistic) GIS operator. To get a multi-scale result, we repeated the operation several times, with circular moving windows of radius varying between 11 and 91 grid cells, with grid size 25 m. We ended up with nine different diversity maps for each input quantity and we classified each map in five diversity levels, using Jenks breaks, a data-driven classification method (Fig. 1(c)).

Each group of four partial diversities, calculated with moving windows of the same size, collapses into one preliminary and scale-dependent (moving window radius-dependent) GmI map, by a combination procedure (Fig. 1(d)). In the case of Switzerland, availability of a national geomorphological overview map allowed us to perform an additional customization of the GmI map. We performed combination of partial diversities, followed by final classification, with a weighted sum, using weights to reflect the main morphogenetic landscape units: glacial, fluvial, karstic and gravitational. The geomorphological characteristics of the primary processes in each unit helped selecting meaningful values of the weight. This allowed extra flexibility in reproducing the diversity of landforms in the different geomorphological settings of Switzerland, where specific modeling agents are prevalent. We consider that in karstic landscape morphological unit, fluvial processes have a minor impact as a modelling agent due to the very low values of drainage density. On the contrary, where the fluvial landscape has a crucial role, in particular on wide alluvial plains, the river network represents the most significant modeling agent while the topographic attributes are less meaningful due to the low angle slope values.

Eventually, we obtained a final scale-independent GmI map, out of the nine scale-dependent maps, overlaying them and selecting in each grid cell the most common value across the spectrum of nine different geomorphodiversity values using the option “mode” in GIS raster calculator (Fig. 1(e)). This allowed us to remove GIS processing artifacts, and to obtain a parameter-free approach to GmI assessment.

III. Results

We calculated the GmI map of Switzerland, obtained by weighted combination of the partial diversities of slope angle, drainage density, geomorphons and lithology, classified in five classes; Figure 2 shows the full map.

Areas with GmI = 1, the lowest class, represent 6.68 % of Switzerland and prevails in the karst environment, with sparsely scattered areas. Class 2 covers 28.21 %, which is homogeneously distributed in the four geomorphological environments. The medium geomorphodiversity, class 3, represents 24.67 % and it is prevalent in the glacial (31.33 %), gravitational (33.14 %) and fluvial (32.48 %) environments, whereas the class is less represented in the karst (22.01 %). Class 4 covers 28.07 % of the total surface; the greatest distribution is in the fluvial environments, 30.87 %, followed by the gravitational ones, 28.13 %, the glacial ones, 23.68 %, and the karst, 10.96 %. The GmI 5 class represents 12.39 % of the country. It is slightly prevalent in the fluvial environments (13.88 %), followed by the gravitational (11.76 %) and the glacial (10.69 %) ones. The karst is the landscape with the lowest percentage of the highest class, corresponding to 2.26 %.

IV. Discussions and Conclusions

This work proposes the first geomorphodiversity index map for Switzerland, through a quantitative approach. The basics of the method were inspired by [12] and [16], who described surface diversity of Italy combining raster variability maps of slope, landforms, drainage density and lithology. The final GmI map, in five categories, includes information from these four inputs and represents an intuitive assessment of abiotic diversity in Switzerland.

With respect to previous work, we further exploited an additional data layer that identifies glacial, gravitational, periglacial and karst landscapes, depending on the main geomorphological processes. Hence, we introduced a weighted

approach for partial diversity maps, matching the numerical weights to the geomorphological characteristics of the primary processes in each landscape unit.

In the GmI map, the highest values of diversity are in the fluvial and gravitational environments, followed by glacial contexts. Abundant rivers and channels shape these landscapes, and the lithological complexity represents different endogenous assumptions for the geomorphic agents. Within our approach, the lowest value of GmI is the less represented across the country, and is mostly found in the karstic areas, as expected. In the karst landscapes, altitude resembles that of the fluvial landscapes, and the climatic setting is quite uniform. These parameters affect the processes shaping the landscapes, and their characteristics are compatible with a low surface diversity. The reasons for a lower geomorphodiversity in the karst environment may reside on (i) high permeability and (ii) low drainage density. The karstic landscape, at the scale and in the climatic environment considered in this study, features a gentler topographic surface than areas where glacial and gravitational processes prevail.

The method applied here is versatile, in both the number and type of surface descriptors involved, as well as the resolution of the output GmI map. It includes contributions calculated at different spatial scales, relevant for large areas assessment as well as for local studies. Moreover, it considers different classes of landforms, automatically extracted from the DEM – which gives extra information without the need to resort to manual and subjective terrain classification. Use of specific morphological units (valley, ridges, peaks, and other classes included in this work) was shown to be crucial to add explanatory power in ecological modeling, along with hydrology, soil, and geology information [11].

We acknowledge that an assessment of geomorphodiversity accounting for the spatial distribution of surface descriptors, in addition to the number of different values, would likely change the results presented here. Implementation of the procedure described here into a software module in GRASS GIS is underway.

V. Acknowledgments

L.M. and M.A. were supported by MUR PRIN Project "URGERE: URban Geodiversity for a Resilient Environment" 2022M7EP3M_PE10_PRIN2022 - PNRR M4.C2.1.1 - Funded by the European Union – Next Generation EU - CUP: B53D23007260006. Part of the work was realized during an internship of M.B. at the University of Lausanne.

References

[1] Gray, M., 2008. Geodiversity: developing the paradigm. Proc. Geol. Assoc. 119, 287–298. https://doi.org/10.1016/S0016-7878(08)80307-0

[2] Gordon J.E., Crofts R., Diaz-Martinez E., Sik Woo K., 2018. Enhancing the role of geoconservation in protected area management and nature conservation. Geoheritage 10, 191–203, https://doi.org/10.1007/s12371-017-0240-5

[3] Fox, N., Graham, L.J., Eigenbrod, F., Bullock, J.M., Parks, K.E., 2020. Incorporating geodiversity in ecosystem service decisions. Ecosystems and People 16, 151–159. https://doi.org/10.1080/26395916.2020.1758214

[4] Maimaiti, B., Chen, S., Kasimu, A., Mamat, A., Aierken, N. and Chen, Q., 2022. Coupling and coordination relationships between urban expansion and ecosystem service value in Kashgar City. Remote Sens. 14, 2557. https://doi.org/10.3390/rs14112557

[5] Schrodt, F., Bailey, J., Kissling, W., Rijsdijk, K., Seijmonsbergen, A., van Reed, D., Hjort, J., Lawley, R., Williams, C., Anderson, M., Beier, P., van Beukeringe, P., Boyda, D., Brilha, J., Carcavilla, L., Dahlin, K., Gill, J., Gordon, J., Gray, M., Grundy, M., Hunter, M., Lawler, J., Monge-Ganuzas, M., Royse, K., Stewart, I., Record, S., Turner, W., Zarnetske, P., Field, R., 2019. To advance sustainable stewardship, we must document not only biodiversity but geodiversity. Proc. Natl. Acad. Sci. 116, 16155–16158. https://doi.org/10.1073/pnas.1911799116

[6] Schrodt, F., Vernham, G., Bailey, J., Field, R., Gordon, J.E., Gray, M., Hjort, J., Hoorn, C., Hunter Jr., M.L., Larwood, J., Lausch, A., Monge-Ganuzas, M., Miller, S., van Ree, D., Seijmonsbergen, A.C., Zarnetske, P.L., Daniel Kissling, W., 2024. The status and future of essential geodiversity variables. Phil. Trans. R. Soc. A 382, 20230052. https://doi.org/10.1098/rsta.2023.0052

[7] Zwoliński, Z., Najwer, A., Giardino, M., 2018. Methods for assessing geodiversity. In: Reynard, E., Brilha, J. (Eds.), Geoheritage. Assessment, Protection, and Management. Elsevier, Amsterdam pp. 27–52. https://doi.org/10.1016/B978-0-12-809531-7.00002-2

[8] Kubalíková, L., Coratza, P., 2023. Reflections of geodiversity–culture relationships within the concept of abiotic ecosystem services. Geol. Soc. Lond. Spec. Publ. 530, 49–66. https://doi.org/10.1144/SP530-2022-155

[9] M. Nieto, L., 2024. Geodiversity as a Tool for the Nature Conservation. IntechOpen. https://doi.org/10.5772/intechopen.109010

[10] Stojilković, B., Gray, M., 2024. Geodiversification: The evolution of geodiversity through time. Geoheritage 16, 91. https://doi.org/10.1007/s12371-024-00987-1

[11] Bailey, J., Boyd, D., Field, R., 2018. Models of upland species' distributions are improved by accounting for geodiversity. Landscape Ecology. https://doi.org/10.1007/s10980-018-0723-z

[12] Burnelli, M., Melelli, L., Alvioli, M., 2023. Land surface diversity: a geomorphodiversity index of Italy. Earth Surf. Process. Landf. 48, 3025–3040. https://doi.org/10.1002/esp.5679

[13] Panizza, M., 2009. The geomorphodiversity of the Dolomites (Italy): a key of geoheritage assessment. Geoheritage 1, 33–42. https://doi.org/10.1007/s12371-009-0003-z

[14] Benito-Calvo, A., Pérez-González, A., Magri, O., Meza, P., 2009. Assessing regional geodiversity: the Iberian Peninsula. Earth Surf. Process. Landf. 34, 1433–1445. https://doi.org/10.1002/esp.1840

[15] Melelli, L., Vergari, F., Liucci, L., Del Monte, M., 2017. Geomorphodiversity index: quantifying the diversity of landforms and physical landscape. Sci. Total Environ. 584-585, 701–714. https://doi.org/10.1016/j.scitotenv.2017.01.101

[16] Burnelli, M., Pica, A., Del Monte, M., Delchiaro, M., Melelli, L., Reame, F., Vergari, F., Alvioli, M., 2025. Does anthropogenic morphogenesis contribute to geomorphodiversity in urban environments?. Geomorphology 471, 109582. https://doi.org/10.1016/j.geomorph.2024.109582

[17] Reynard, E. (Ed.), 2021. Landscape and Landforms of Switzerland. Springer Nature, Cham.

[18] Burnelli, M., Melelli, L., Alvioli, M., 2025. Geomorphodiversity and anthropization indices for Italian urban areas. Geomorphology 471, 109532. https://doi.org/10.1016/j.geomorph.2024.109532

[19] Jasiewicz, J., Stepinski, T., 2013. Geomorphons – a pattern recognition approach to classification and mapping of landforms. Geomorphology 182, 147–156. https://doi.org/10.1016/j.geomorph.2012.11.005

Integrating Geosystem Services classifications: a preliminary framework from the piedmont area of the Sesia Val Grande UNESCO Global Geopark

Arianna Negri
Earth Sciences Department
University of Torino
Torino, Italy
arianna.negri@unito.it

Marco Giardino
Earth Sciences Department
University of Torino
Torino, Italy
marco.giardino@unito.it

Cite as: Negri, A., Giardino, M. (2025). Integrating Geosystem Services classifications: a preliminary framework from the piedmont area of the Sesia Val Grande UNESCO Global Geopark. In: Proceedings of Geomorphometry 2025, 9-13 June, Perugia, Italy. M. Alvioli, L. Melelli, I. Marchesini eds. CNR Edizioni, Rome. ISBN 978-88-8080-765-0. DOI: 10.5281/zenodo.15267534

Abstract— **A variety of geological structures, landforms and processes, known as "geodiversity", influences both human society and natural ecosystems. It offers essential services and benefit as Geosystem Services (GS), a concept raised in the last two decades from the better known "Ecosystem Services" (ES). Despite the importance of GS, their classification remains underdeveloped. The present study integrates the two most accepted classification frameworks for ES and GS, to provide an advanced tool for assessing georesources and planning related management in the piedmont sector of the Sesia Val Grande UNESCO Global Geopark, an area rich in geodiversity and potential GS. By combining literature knowledge, remote sensing and field surveys data in a GIS-based environment, main GS services connected to geological and human activities have been mapped. Results suggest that an integrate classification approach provide a more comprehensive overview of GS in the territory. This in turn is fundamental for achieving more conscious management plans in the perspective of sustainable development within Geopark territories.**

I. INTRODUCTION

The Earth we observe today is the product of intricate interactions between long-term geological processes and short-term dynamic processes [1]. The result of these complex interactions is a variety of rocks, minerals, geological structures, landforms and processes that shape geomorphological landscape, resumed with the term "geodiversity" [2].

Due to its double essence, geodiversity exerts influences on both natural world and human societies, creating not only geohazards and risks but also services, such as those shaping and supporting healthy ecosystems, and offering recreational opportunities. Concrete evidence of the positive interaction between abiotic environment and human society is shown by the Geosystem Services (GS) [3].

The concept of GS derives from the definition of Ecosystem Services (ES), that are "the goods and benefits provided by the environment to humans" [4]. Whereas the notion of ES is well established in the scientific community, but also among the general public, it is only recently that the idea of GS has been recognised for its fundamental contribution to human welfare.

Even though the word "ecosystem" includes both abiotic and biotic worlds, the framework used in the Millennium Ecosystem Assessment (MEA) focuses mainly on the living features of the environment. Despite the lack of description of abiotic aspects of the ecosystem, various attempt for GS classification have been made by various authors, but two are the most accepted ones: (i) the classification provided by [2], maintaining the four categories proposed by MEA (regulation, support, provision and cultural) and adding a fifth category (knowledge); and (ii) the Common International Classification of Ecosystem Services (CICES) [5], which, in the last version (V5.1), has expanded its abiotic section of ES, showing three categories (provisioning, regulation and maintenance, and cultural).

GS can play a crucial role in bridging the gap between the knowledge on geodiversity and a comprehensive recognition of its contributions to social, economic and ecological benefits that originate from the natural world. This function is particularly relevant within UNESCO Global Geoparks ("UGGps"; areas of international geological interest "managed with a holistic concept of protection, education and sustainable development" [6]), where GS can contribute to conservation, sustainable development and territorial management.

As for the biotic components of the ecosystem, geodiversity elements are considered as "natural resources" essential for a sustainable development of territories through the achievement of the Sustainable Development Goals (SDGs) from the Agenda 2030 [7]. In this framework, an integrated methodology for the analysis of the geodiversity elements and the related services and benefits to the local society have been applied within the piedmont area of the Sesia Val Grande UGGp (SVUGGp). Within this task, both classification typologies have been used in the study area, first singularly, then integrating the results of the two methodologies with the goal of offering a complete representation of goods and benefits offered by the area.

A solid overview of geological resources and GS is intended as a start for further geodiversity actions to support better and comprehensive management of the geopark, thus avoiding the loss of such fundamental geoenvironmental elements.

II. GEO-ENVIRONMENTAL FRAMEWORK

The SVUGGp is one of the twelve Italian UGGps. It is located in the NW Italian Alps, in an area (2202 km^2) of particular geological interest. It shows rocks deriving from the mantle and the crust at different depth, including the Sesia Magmatic System [8, 9], a Supervolcano collapsed 280 Ma, the Insubric Line and other palaeogeographical and structural evidence of the Alpine Orogeny [10]. Moreover, lithological and geomorphological diversities are among the reasons of the existence of the SVUGGp.

The SVUGGp's motto ("where the stone becomes culture"), highlights the profound link of local geological resources and human culture. To further explore this interplay, a target area (72 km^2) within the piedmont SVUGGp has been selected for the test of the proposed methodology (Fig. 1).

This area represents a precious insight of a piedmont territory with a rich geodiversity, due to the presence of very different types of rocks (Triassic-Jurassic sedimentary succession of Monte Fenera [11], gneiss of the Serie dei Laghi, Porfidi Quarziferi Complex), glacial, fluvio-glacial and fluvial deposits [12] and different geomorphological landscapes (Fig. 1c).

The area shows perfectly traces of a past "stone culture" [10], as for in the territories of the Monte Fenera Natural Park, with the numerous caverns as Palaeolithic human settlements [13], and the important role of the subsurface as a resource, for both mining activities [14] and wine production purposes, such as in the municipalities of the Boca DOC wine.

III. METHODS

The methodology consists of a first part of literature review of environmental and territorial data, followed by remote sensing analysis and a field survey of the study area, in order to create an information system (by means of QGIS software) and to map the geodiversity at different level of details.

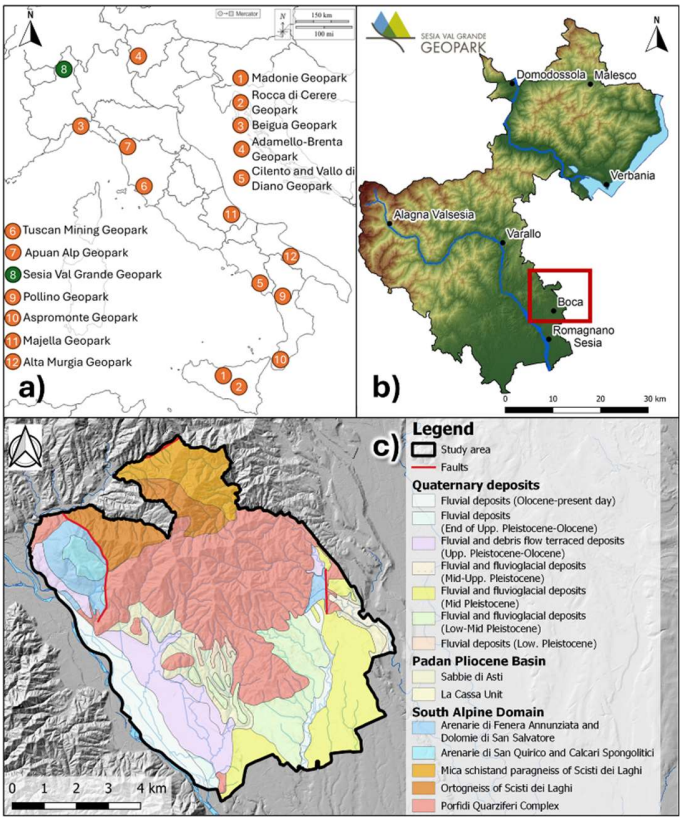

Fig. 1. a) Location of Italian UGGps (orange dots) and SVUGGp (green dot); b) SVUGGp area (red square: study area); c) Geology of the study area (from [12]).

The use of hydrogeological, geomorphological and geological maps, combined with digital elevation models (DEMs), allows the identification of those areas in which benefits and services from the abiotic environment can be potentially found.

Moreover, cultural and socio-economic aspects related to the abiotic environment and the geosphere have been mapped, in order to better individuate the Geosystem Services provided in the area and to integrate them into territorial management plans.

After the collection of the environmental, geological, geomorphological and cultural data, GS have been classified according to [2], followed by a second attempt using the abiotic extension of the CICES method [5]. The two classifications are made comparing the results of the integration of the different maps in the GIS with the lists provided by [2] and [5]. Finally, a combination of the two methods have been performed, in order to implement the knowledge about the study area in terms of resources and services. This step includes an alignment of both frameworks, with the identification of overlapping, and the integration of the two classifications, generating a single thematic map showing the distribution of the integrated Geosystem Services.

IV. Result and Discussion

After the analysis of territorial, cultural and socio-economic data, the main human activities connected with geological and geomorphological contents ("human geoactivities") in the area have been identified and mapped, in order to enrich the geodiversity values of the territory through the GS provided. The human geoactivities are: (i) two geosites under review within the "Piemonte Geosites Inventory List" project in the context of the Piemonte Regional Law n. 23/2023 [15] (the Monte Fenera sedimentary succession and the Caldera of Sesia Supervolcano in Prato Sesia); (ii) caves; (iii) hiking trails, cycling routes, cultural paths, cliffs for climbing (i.e. sites allowing the exploration of the territory and the appraisal of its geological and cultural heritage); (iv) Boca DOC vineyards (grapes growing on soils derived from rocks of the Sesia Supervolcano, with traces of clay, sandstones and dolomitic rocks, contributing to mineral richness of wine); (v) geocultural sites (such as the Boca Sanctuary, built with brick from local clay, and located on a vulcanite outcrop from the Sesia Supervolcano); (vi) schools (as local places for education on the geosciences); (vii) active mining sites (for the ongoing extraction of clays and kaolin, porphyry and feldspar, or inactive sites (important for the environmental restoration of the territory).

A synthesis map of the main geological and geomorphological elements and human geoactivities is shown in Fig. 2.

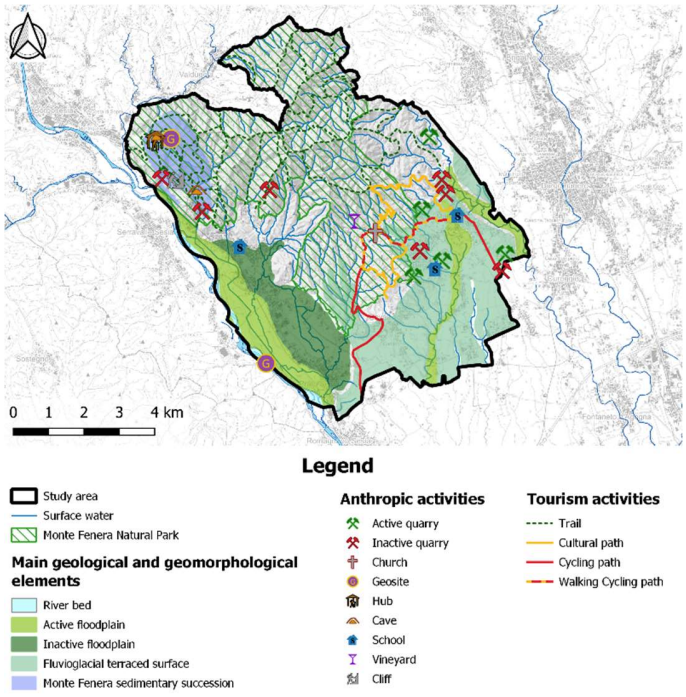

Fig. 2. Synthesis map: geological, geomorphological elements and "human geoactivities" within the piedmont area of SVUGGp.

The interpretation of the map supported a first attempt of classification of the Geosystem Services provided by the territory, according to [2] (Fig. 3a). The analysis revealed each feature could show more than one geosystem service provided, for a total of fifteen types, from the five GS categories: Regulation (2), Supporting (3), Provisioning (4), Cultural (4) and Knowledge (2).

The same area has been assessed according to [5] (Fig. 3b). Even if this method allows very detailed description of biotic ES, results of its application seem not very appropriate for the description of GS: among thirty-one CICES classes, only eight have been found in the study area: Provisioning (3), Regulation and Maintenance (1) and Cultural (4), and each feature shows only one type of GS. Moreover, this method shows a stronger focus on natural aspect, rather than on the interaction of people, geosciences concepts and georesources (e.g. schools, geocultural sites). However, a focus on water resources can be identified, with different classes for each use of the resource and distinguishing surface or groundwater ones. Indeed, the supporting and knowledge functions are not included in the [5] method.

Both [2] and [5] classification methods provide useful territorial, cultural and social information. For this reason, a third attempt of classification has been performed, including both categorisations [2] and [5]. The result is a comprehensive, more complete map (Fig. 4), showing areas where the services provided by the geological resources are directly connected with the natural environment and those where this connection is indirect.

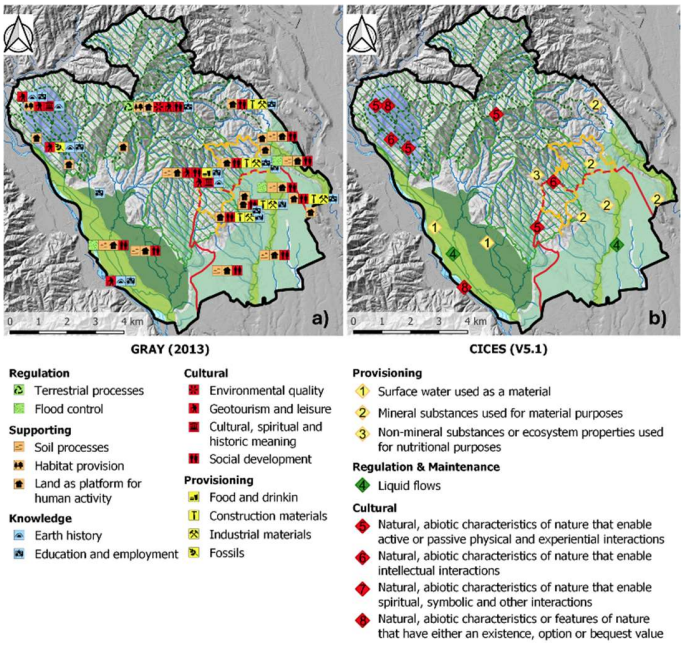

Fig. 3. Comparison of maps from the most accepted classification frameworks for ES and GS within the piedmont area of SVUGGp. a) Results by applying Gray's method [2]; b) Results by applying the CICES method [5].

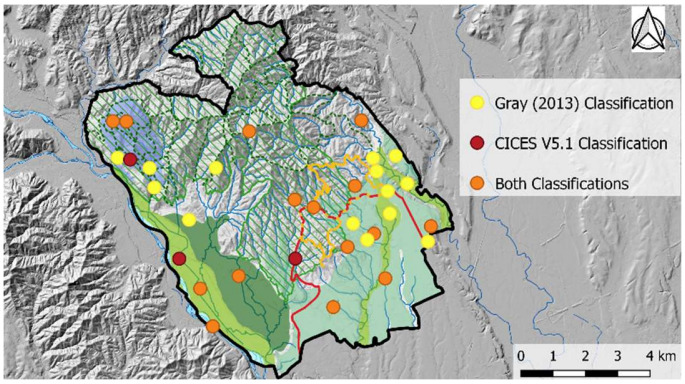

Fig. 4. ES-GS map of the study area from integration of [2] and [5].

V. Conclusions

The UGGps are territories rich in geodiversity, hence they have a high potential for offering geosystem services (GS). Even though various attempts for comprehensive classification of ecosystem services have been made [2, 5], these methodologies do not entirely represent the goods and benefits provided by the abiotic environment to human society. The present study illustrated a comparative classification of GS within a piedmont sector in the Sesia Val Grande UGGp, with the aim of highlighting the most important GS for further territorial management plan development. After separate classification of GS by using first [2] then [5] methods, a final integration of the two methodologies has been performed. The reason of this choice is connected to need of including all the environmental aspects assessed in each methodology. In fact, [5] focuses mainly on the good and benefits provided only by the abiotic components of the environment, while [2] propose a more inclusive classification, in which, next to regulation, provision and cultural services, it includes also the supporting services and the knowledge ones, such as places where it is possible to learn about geology and Earth Sciences. The combined use of the two methodologies allowed advanced understanding of the georesources of the piedmont area of the SVUGGp territory, highlighting areas with a predominance of environmental aspects, and other areas where the human have a central role.

This research prepares the ground for new analysis of both non-living and living components of the SVUGGp ecosystems. Comprehensive multiscale assessments will allow to highlight the areas with stronger biodiversity-geodiversity interactions, in order to implement the management policies to preserve the environment. Further application of the methodology will be addressed both to small sites such as the “Bocciole” clay quarry, (Mineraria di Boca S.p.A. company), to emphasise the richness of GS provided by mining sites, and to the whole area of SVUGGp, to implement environmental knowledge on a Geopark territory.

VI. Acknowledgments

Project funded by the European Union - NextGenerationEU, Mission 4 Component 2 - ECS00000036 – CUP D17G22000150001 (NODES), Mineraria di Boca S.p.A. and UniTO-DST Industrial PhD (CUP B63B22000010001). Thanks to Sesia Val Grande UGGp, Associazione SVGGp and Ente di Gestione delle Aree Protette della Valsesia for supporting the research and helping in field-based activities.

References

[1] Prosser, C., M. Murphy, and J. Larwood, 2006. Geological conservation: A guide to good practice. English Nature, Peterborough, 145.

[2] Gray, M., 2013. Geodiversity: Valuing and conserving abiotic nature. John Wiley & Sons.

[3] Gray, M., 2011. Other nature: Geodiversity and geosystem services. Environmental Conservation. 38. 271 - 274. https://doi.org/10.1017/S0376892911000117

[4] Millennium Ecosystem Assessment (MEA), 2005. Ecosystems and Human Well-Being: Synthesis; Island Press: Washington, DC, USA, 2005; ISBN 978-1-59726-040-4.

[5] Haines-Young, R. and M.B. Potschin, 2018. Common International Classification of Ecosystem Services (CICES) V5.1 and Guidance on the Application of the Revised Structure. Available from www.cices.eu

[6] UNESCO, 2021. UNESCO Global Geoparks. Retrieved from https://www.unesco.org/en/iggp/geoparks/about

[7] Gill, J.C., 2017. Geology and the Sustainable Development Goals. Episodes, 40, 70-76. https://doi.org/10.18814/epiiugs/2017/v40i1/017010

[8] Quick, J.E., S. Sinigoi, G. Peressini, G. Demarchi, J.L. Wooden and A. Sbisà, 2009. Magmatic plumbing of a large Permian caldera exposed to a depth of 25 km. Geology, 37, 7, 603–606. https://doi.org/10.1130/G30003A.1

[9] Sinigoi, S., J.E. Quick, G. Demarchi, G. Peressini, 2010. The Sesia Magmatic System. J. Virtual Explor. 36, 1–33. DOI 10.3809/jvirtex.2009.00218

[10] Perotti, L., I.M. Bollati, C. Viani, E. Zanoletti, V. Caironi, M. Pelfini, M. Giardino, 2020. Fieldtrips and Virtual Tours as Geotourism Resources: Examples from the Sesia Val Grande UNESCO Global Geopark (NW Italy). Resources. 9, 6, 63. https://doi.org/10.3390/resources9060063

[11] Fantoni, R., A. Decarlis, and E. Fantoni, 2005. Geologia del Monte Fenera. In R. Fantoni, R. Cerri, & E. Dellarole (Eds.), D’acqua e di pietra. Il Monte Fenera e le sue collezioni museali (pp. 86–91). Associazione Culturale ZEISCIU Centro Studi.

[12] Piana, F., G. Fioraso, A. Irace, P. Mosca, A. d’Atri, L. Barale, … G.B. Vigna, 2017. Geology of Piemonte region (NW Italy, Alps–Apennines interference zone). Journal of Maps, 13(2), 395–405. https://doi.org/10.1080/17445647.2017.1316218

[13] Angelucci, D.E., M. Zambaldi, U. Tessari, C. Vaccaro, J. Arnaud, G.L.F. Berruti, S. Daffara, M. Arzarello, 2019. New insights on the Monte Fenera Palaeolithic, Italy: Geoarchaeology of the Ciota Ciara cave. Geoarchaeology 34, 413–429. https://doi.org/10.1007/s41982-024-00173-3

[14] Bertolani, M., A.G. Loschi Ghittoni, 1986. La serie sedimentaria caolinizzata della miniera Bocciole (Boca–Novara): caratteristiche e impieghi nel settore ceramico. Ceramica 39 (4), 1–10.

[15] Piemonte Regional Law, n. 23. 6 October 2023. Available online: http://arianna.cr.piemonte.it/iterlegcoordweb/dettaglioLegge.do?urnLegge=urn:nir:regione.piemonte:legge:2023;23@2024-05-14&tornaIndietro=true (accessed on 15th Dec 2024).

Modeling Pre-Anthropogenic Topography: A Reconstruction in the Perugia Center Using Subsoil Data

Laura Paola Calderon Cucunuba, Laura Melelli, Fabio Silvani
Department of Physics and Geology, University of Perugia, Piazza Università, 1, 06100 Perugia, Italy
{laurapaola.calderoncucunuba, laura.melelli, fabio.silvani}@unipg.it

Luca Domenico Venanti
S.G.A. Studio Geologi Associati
Via XX Settembre, 76 – 06124 Perugia (PG), Italy
ldvenanti@studiogeologiassociati.eu

Massimiliano Alvioli
Istituto di Ricerca per la Protezione Idrogeologica, Consiglio Nazionale delle Ricerche, Via Madonna Alta 126, I - 06128 Perugia (PG), Italy - massimiliano.alvioli@irpi.cnr.it

Cite as: Calderon Cucunuba, L. P., Melelli, L., Silvani, F., Venanti, D., Alvioli, M. (2025). Modeling Pre-Anthropogenic Topography: A Reconstruction in the Perugia Center Using Subsoil Data. In: Proceedings of Geomorphometry 2025, 9-13 June, Perugia, Italy. M. Alvioli, L. Melelli, I. Marchesini eds. CNR Edizioni, Rome. ISBN 978-88-8080-765-0. DOI: 10.5281/zenodo.15223183

Abstract— **This study aimed at developing a digital elevation model of the city center of Perugia, the capital city of Umbria region (Central Italy), to approximate the terrain as it existed prior to human settlement, and study the anthropogenic deposits identified in different locations of the study area. In fact, the foundation of the city dates back 3000 years, and human modifications played a key role in shaping the area. Main modifications exist in the city center area, located on a series of hilltops. Data about the thickness of anthropogenic deposits, from approximately 200 boreholes, allowed us to reconstruct the pre-settlement topography. Numerical interpolation of data about thickness of deposits revealed key areas with significant modifications, mostly located close the watersheds' drainage divide, where the fluvial and gravitational erosional processes acted in the past. In contrast, other areas close to the top of the hill displayed evidence of artificial leveling. This research enhances the geomorphological mapping of Perugia by precisely delineating the extent and thickness of anthropogenic deposits and allows to recognize and perimeter inactive landforms, currently invisible on the topographic surface. Knowledge of the pre-settlement topography provides critical insights into the historical evolution of the landscape and offers valuable support for urban planning and stability assessments. The methodology holds promise for application in similar urban contexts across Umbria and beyond.**

I. Introduction

The understanding of geological elements, such as the type and distribution of rocks, along with the past and present geomorphological evolution, is essential for understanding the development of cities. In this context, urban geology plays a key role in identifying natural hazards and preserving geological heritage, especially in cities with high cultural value, whose historic centers experienced significant transformations of the original morphology over time. This makes the application of urban geology in the assessment of risks and available resources even more relevant, thus contributing to more sustainable and resilient territorial planning [1].

Over the centuries, urban settlements have been transforming the original topography, particularly in areas with hilly or irregular morphology. In Perugia, Central Italy, such transformations were necessary to prevent landslides and enable urban development. In this work, we developed a digital elevation model (DEM), with anthropogenic deposits removed, providing an approximation of the pre-settlement topography [2].

This analysis allows determining the thickness of anthropogenic deposits in the area, and studying the modifications introduced over time. The results support the geomorphological assessment in urban areas where the anthropogenic process modify, even drastically, the original topographic settlement [3]. Identifying the filling and leveling areas supports the creation of a geomorphological map, allowing identifying and delineating anthropic landforms and natural features modified by human activities [4].

Accurate knowledge of human modifications may help in planning sustainable cities, where the geological and

geomorphological arrangement are the first step for the assessment of natural hazards, conservation of the value of geodiversity, and study the link with the biosphere [5-7].

II. Materials and Methods

A. Materials

For the creation of a pre-settlement DEM, we used data on the thickness of anthropogenic fill, obtained through boreholes drilled in the urban area of Perugia, specifically within the historic center, including areas both inside and near the boundaries of the Etruscan and Medieval walls. This information was sourced from the 'Geognostic and Geophysical Investigations Database' provided open access by Open Data Umbria (accessible at https://dati.regione.umbria.it/dataset/banca-dati-indagini-geognostiche-geofisiche). The data, available in KMZ format for visualization in Google Earth, includes reports on 265 areas corresponding to regional technical maps. Reviewing the Google Earth reports of individual investigations in their original PDF format, we focused on boreholes or surveys containing stratigraphic information, both in the presence and in absence of anthropogenic deposits.

B. Method

We used a database to store information about the wells, each assigned a unique ID along with thickness of the anthropogenic deposit, data acquisition year, location details, borehole identifier, responsible company, and X-Y coordinates. Projecting the database onto the map ensured consistency between the recorded locations and their descriptions, making it easier to identify and remove duplicates. Only 5% of the 300 entries were duplicate, leaving 285 different boreholes for the study. These boreholes correspond to drilling conducted between 1969 and 2024.

The borehole database was imported into ArcGIS Pro software for the interpolation process, using the LiDAR DEM as the current terrain baseline. In ArcGIS Pro, the "Extract Values to Points" tool helped associating each well's location with the corresponding pixel in the LiDAR DEM, generating a new shapefile. This shapefile contains both the anthropogenic deposit thickness and a data column with the current surface elevation at each well location. Using these two datasets and the "Field Calculator" tool, a new column was created to represent the original terrain elevation by subtracting the deposit thickness.

The 285 well points were distributed across the historic center of Perugia. Considering the city's morphology, characterized by hills and valleys, the points were grouped into clusters based on proximity. This approach enabled the independent analysis of each area and allowed for a more refined selection of wells by excluding clusters that extended beyond the study area or points that did not associate with any cluster. Using these clusters and local knowledge, nine regions were defined for interpolating the morphology of the anthropogenic deposits, ultimately utilizing data from 221 wells (Table 1).

The terrain elevation data, obtained by subtracting the deposit thickness, was interpolated using a simplified approach based on deterministic 'Topo to Raster' tool in ArcGIS Pro, also known as ANUDEM [8-9]. This method was chosen because it was specifically developed to produce hydrologically correct digital elevation models (DEMs) capable of capturing abrupt variations and providing accurate representations of ridges and streams [8-10]. Such capabilities align with our objective of identifying possible paleo-channels that may have been overlain by anthropogenic deposits.

The use of kriging was considered less appropriate in this context, as the low density of data points within each cluster did not support the construction of a reliable variogram model. Furthermore, the data do not represent a natural, undisturbed phenomenon, but rather terrain altered by human activity, which reduces the applicability of standard geostatistical assumptions [11].

To refine the model, random points were extracted from the LiDAR-derived DEM. A buffer zone was applied around each borehole to ensure that random points were not placed too close to, or directly on, these measured locations. The random LiDAR points were then combined with the borehole data for interpolation. The resulting terrain model—representing the pre-settlement surface—was compared to the current LiDAR topography using the *Raster Calculator*. Areas where current elevation exceeds pre-settlement elevation were identified as anthropogenic deposits and highlighted as polygonal features.

Table I. Number of wells for each interpolation area in Figure 1.

Area ID	Name	No. wells
A	Elce	4
B	Cupa & San Francesco	103
C	Bulagaio	14
D	Arconi	34
E	Santa Margherita 1	5
F	Santa Margherita 2	10
G	Sant'Anna	31
H	Rocca Paolina	13
I	Bucaccio	7
-	Non included	64
Total		285

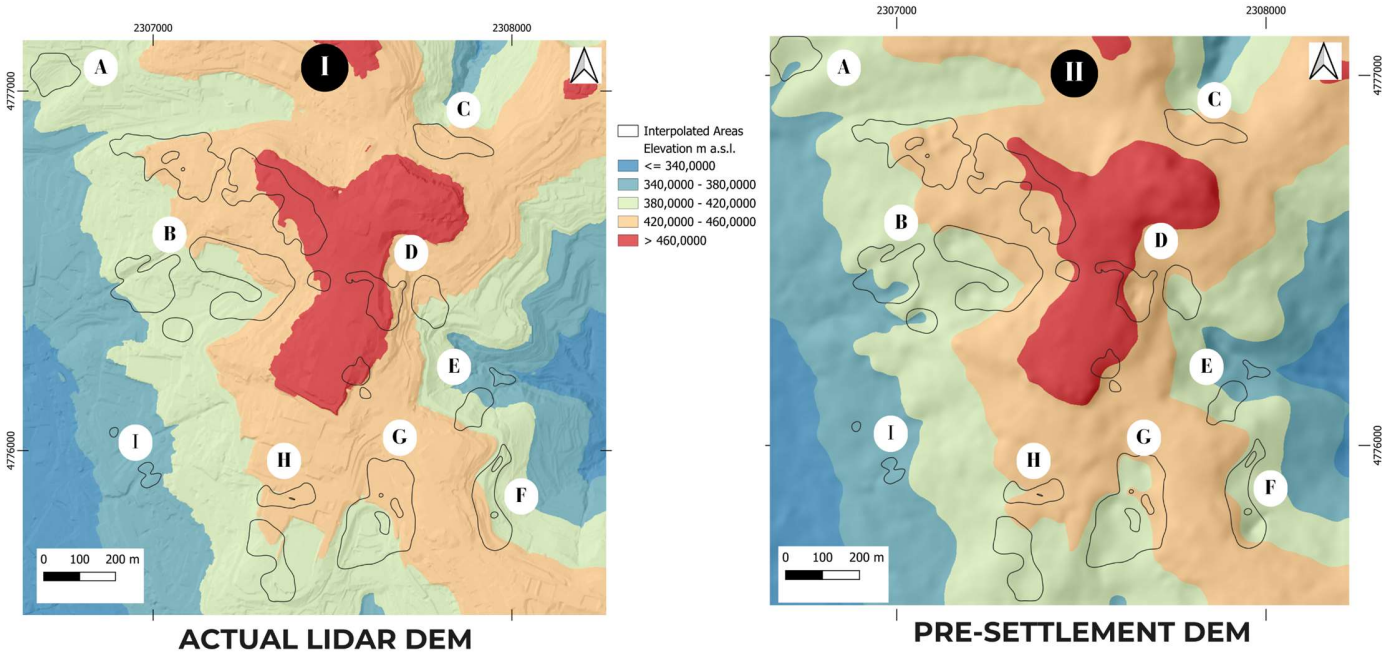

Figure 1. (I) Current digital elevation of Perugia based on LiDAR-derived DEM. (II) Interpolated pre-anthropogenic digital elevation of Perugia. Interpolated areas: **A.** Elce, **B.** Cupa and San Francesco, **C.** Bulagaio, **D.** Arconi, **E.** Santa Margherita 2, **F.** Santa Margherita 1, **G.** Sant'Anna, **H.** Rocca Paolina, I. Bucaccio.

Deposits thinner than one meter were excluded from analysis, as such minor changes are commonly found in urban environments due to structural modifications and do not necessarily indicate significant anthropogenic fill. Figure 1 shows the DEM generated through interpolation and compares it with the current topography, highlighting with polygons the areas of anthropogenic deposits.

To evaluate the interpolation robustness, five repetitions were performed using different sets of random points. The variability among these five interpolated models was assessed by calculating the standard deviation at each pixel. To determine the model with the lowest relative variability, the coefficient of variation (CV)—defined as the ratio of the standard deviation to the mean elevation—was computed for each pixel across models.

III. Results

The interpolated areas, derived from borehole data, were primarily located in the headwater streams, including zones denoted in Figure 1 and Table I as Elce (A), Cupa (B), Bulagaio (C), Arconi (D), Santa Margherita 1 and 2 (E, F), and Sant'Anna (G). Notably, the last three belong to the same hydrographic basin of Santa Margherita. Conversely, areas like San Francesco (B), Bucaccio (I), and Rocca Paolina (H) revealed fills in summit zones, suggesting processes of terrain leveling.

The interpolation performed using the *Topo to Raster* tool produced a topographic surface consistent with the area's natural relief. Among the five evaluated models, the maximum standard deviation was 8.18 meters, indicating a relatively stable interpolation. The resulting DEM clearly reflects the topographic pattern of Perugia, where the city center is situated at a higher elevation that gradually decreases toward the surrounding valleys (Figure 1). This elevation gradient is especially evident in areas such as Cupa (B), Bulagaio (C), Arconi (D), Santa Margherita (E, F), and Sant'Anna (G).

A comparison between the most recent LiDAR-based and the interpolated (representing topography without anthropogenic deposits) DEMs allowed identifying deposit depths, based on point data. Thickness ranged from 2 to 20 m, with the largest values concentrated in areas like Cupa-San Francesco, Arconi, Sant'Anna, and Santa Margherita, corresponding to the headwaters of watercourses.

Areas with fewer than 10 boreholes for interpolation, such as Santa Margherita 1 and 2, Bucaccio, and Elce, had limited coverage. On the other hand, zones like Rocca Paolina, Bulagaio, Sant'Anna, and Arconi contained an intermediate number of data points, ranging from 13 to 34. This facilitated broader coverage in some cases, such as in Sant'Anna, or the confirmation of highly excavated zones like Arconi, thanks to the availability of nearby

points. Cupa and San Francesco emerged as the areas with the highest borehole density, with 103 points.

IV. Discussion and conclusions

In an ideal spatial interpolation procedure, a large and evenly distributed set of borehole data would be preferable. However, in Perugia, most boreholes were drilled in specific areas for infrastructural purposes, resulting in a high data density in limited zones, such as near the churches of San Filippo Neri and San Francesco al Prato. Conversely, there are examples of isolated boreholes with significant fill information, complicating the understanding of surrounding morphology due to the lack of additional control points. For instance, one borehole in Santa Margherita recorded a thickness of 25.8 meters, and one borehole in Cupa recorded 20 meters. To ensure analytical reliability, the study included only areas with thicknesses equal to or greater than 2 meters of anthropogenic fill.

The spatial interpolation of measured deposit thickness proven very useful. In fact, although information on anthropogenic fills was available, their spatial distribution in the terrain was not well understood. Additionally, the results shed light on morphological changes in the headwater streams, such as Santa Margherita, Sant'Anna, and Cupa, highlighting how these areas were modified by human settlements and by natural erosion. Furthermore, the interpolation allowed for the identification of artificially leveled zones, such as Rocca Paolina and San Francesco al Prato.

Although it was not a statistical interpolation but a deterministic one using the ANUDEM method, the results could be evaluated by calculating the standard deviation among them, reaching a maximum difference of 8 meters between the interpolations.

This research contributes significantly to the ongoing geomorphological cartography project in central Perugia. The data enable the accurate identification of anthropogenic fill areas and provide detailed information on the thickness and depth of these deposits.

A few key areas, including via Pascoli and Corso Vannucci (not shown in the figure), contained a limited number of boreholes (fewer than two), preventing a meaningful interpolation.

It was also essential to include boreholes with null fill values or with thickness less than 2 meters, in the interpolation process, as this ensured a proper delineation of areas with deposits and enhanced confidence in identifying zones likely unaffected by anthropogenic fills.

Finally, this methodology is recommended for similar urban areas, both in Umbria and in other Italian regions with available fill data. It offers valuable insights into the evolution of relief in these zones and supports assessments of urban stability.

V. Acknowledgments

L. Melelli, M. Alvioli, and L.P. Calderon Cucunuba were supported by the MUR PRIN Project 'URGERE: URban Geodiversity for a Resilient Environment' (2022M7EP3M_PE10_PRIN2022 - PNRR M4.C2.1.1), funded by the European Union – Next Generation EU (CUP: B53D23007260006).

References

[1] Melelli, L., Silvani, F., Ercoli, M. Pauselli, C. Todi, G., Radicioni, F., 2021. Urban geology for the enhancement of the hypogean geosites: The Perugia underground (Central Italy). Geoheritage, 13(1), 18. DOI: 10.1007/s12371-021-00545-z

[2] Luberti, G.M., Vergari, F., Pica, A., Del Monte, M., 2019. Estimation of the thickness of anthropogenic deposits in historical urban centers: An interdisciplinary methodology applied to Rome (Italy). The Holocene Vol 29 (1), DOI: 10.1177/0959683618804630

[3] Vergari, F., Pica, A., Brandolini, P., Melelli, L., Del Monte, M., 2022. Geomorphological classification of the landscape in urban areas. Hints from some study cases in Italy. 848 Rendiconti Online Della Società Geologica Italiana 57, 33-39. DOI: 10.3301/ROL.2022.09

[4] Vergari, F., Luberti, G.M., Pica, A., Del Monte, M., 2021. Geomorphology of the historic centre of the Urbs (Rome, Italy). Journal of Maps 17(4), 6-17. DOI: 10.1080/17445647.2020.1761465

[5] Burnelli M., Melelli L., Alvioli M., 2025. Geomorphodiversity and anthropization indices for Italian urban areas. Geomorphology, Article number 109532 vol. 471, 15 February 2024, DOI: DOI: 10.1016/j.geomorph.2024.109532

[6] Burnelli, M., Pica, A., Del Monte, M., Delchiaro, M., Melelli, L., Reame, F., Vergari, F., Alvioli, M., 2025. Does anthropogenic morphogenesis contribute to geomorphodiversity in urban environments? Geomorphology, Article number 109582 vol. 471. DOI: DOI: 10.1016/j.geomorph.2024.109582

[7] Pereira Balaguer, L., da Glória Motta Garcia, M., de Almeida Leite Ribeiro, M.L., 2022. Combined assessment of geodiversity as a tool to territorial management: application to southeastern coast of state of São Paulo, Brazil. Geoheritage, 14(2), 60. DOI: 10.1007/s12371-022-00696-7

[8] Hutchinson, M. F., Xu, T., & Stein, J. A. (2011). Recent progress in the ANUDEM elevation gridding procedure. *Geomorphometry*, *2011*, 19-22.

[9] Habib, M., Alzubi, Y., Malkawi, A., & Awwad, M., 2020. Impact of interpolation techniques on the accuracy of large-scale digital elevation model. *Open Geosciences*, *12*(1), 190-202. DOI: 10.1515/geo-2020-0012

[10] Bergonse, R., & Reis, E., 2015. Reconstructing pre-erosion topography using spatial interpolation techniques: A validation-based approach. *Journal of Geographical Sciences*, *25*, 196-210. DOI: 10.1007/s11442-015-1162-2

[11] Burrough, P. A. (1998). *Principles of geographical information systems*. Oxford University Press. (pp. 98–140)

Global Assessment of Mining Activities Using TanDEM-X Digital Elevation Change Maps

Vitezslav Moudry
Faculty of Environmental Sciences
Czech University of Life Sciences
Prague - Suchdol, 16500, Czechia
moudry@fzp.czu.cz

Katerina Gdulova
Faculty of Environmental Sciences
Czech University of Life Sciences
Prague - Suchdol, 16500, Czechia
gdulova@fzp.czu.cz

Kamila Svobodova
Faculty of Environmental Sciences
Czech University of Life Sciences
Prague - Suchdol, 16500, Czechia
ksvobodova@fzp.czu.cz

Cite as: Moudry, V., Gdulova, K., Svobodova, K. (2025). Global Assessment of Mining Activities Using TanDEM-X Digital Elevation Change Maps. In: Proceedings of Geomorphometry 2025, 9-13 June, Perugia, Italy. M. Alvioli, L. Melelli, I. Marchesini eds. CNR Edizioni, Rome. ISBN 978-88-8080-765-0. DOI: 10.5281/zenodo.15383600

Abstract—**The growing global demand for raw materials has led to a significant expansion in mineral extraction, resulting in widespread social and environmental impacts. However, the world's mining areas and the volumes of extracted and deposited materials remain poorly documented, limiting our ability to assess their full impact and implement effective mitigation measures to reduce environmental and social damage. To address these challenges, we use global remote sensing products to estimate the volumes of excavated and deposited materials from opencast mining activities worldwide. Using the recently produced TanDEM-X 30m Change Maps, which provide global elevation change information, and the global-scale mining polygons dataset designating mining areas, we assess the contribution of each continent and country to the volume of excavated and deposited material. Our results show that, globally, the total volume of material excavated between the periods of 2011–2015 and 2016–2022 was 180,989 million cubic meters, while the volume of deposited material was 186,347 million cubic meters. During this period, the depth of the mines (and height of heaps) has increased on average by approximately 2–5 meters per square meter, depending on the continent. In North America, for example, the total excavated volume was equivalent to digging a hole of roughly 10x10x10 meters in size per every square kilometer of the continent, while in Australia, such a hole would be more than twice the size. The majority of opencast mining occurred in China, Indonesia, Australia, Russia, and the U.S. However, when normalized by country area, the data revealed a higher intensity of mining activities in smaller countries such as Suriname and Czechia. The calculated volumes of excavated and deposited material provide a more accurate representation of mining intensity than site area alone and enable cross-site comparisons for global monitoring.**

I. Introduction

In recent decades, the growing global demand for raw materials has fueled a significant expansion of mineral extraction, leading to a wide range of social and environmental consequences worldwide. However, despite the sector's global importance, the impacts of the world's mining areas remain poorly documented [1]. This knowledge gap is particularly concerning given the growing push for digitalization and the sector's rapid transformation, driven by the increasing demand for critical materials such as cobalt and lithium while reducing our reliance on fossil fuels [2].

To address these challenges and bridge the knowledge gap, remote sensing data are increasingly being utilized as a valuable resource for mapping mining areas. For instance, Maus et al. [3] used satellite imagery to develop a global dataset representing the extent of land used for mining. This and other existing datasets, such as the S&P Global Market Intelligence database, typically represent mines as points or polygons and lack complete and site-specific information on mining intensity, including the volumes of extracted and disposed materials, which neglects the differences in the scale of impacts among mining locations [1].

Digital Elevation Models (DEMs) of Difference (DoD) are remote sensing products that can be useful in detecting and quantifying changes in surface elevation over time. By comparing elevation data from different time periods, DoD allows researchers to monitor various earth surface processes, including anthropogenic activities such as mining. In 2023, the German Aerospace Center released the TanDEM-X DEM Change Maps, representing global surface elevation changes yielded by

comparing the first global TanDEM-X DEM (acquired between 2011 and 2015) with the newly acquired DEM scenes (2016 to 2022) [4]. This dataset offers an excellent resource for assessing volumes of extracted and disposed materials in opencast mines.

This study aimed to estimate the volumes of excavated and deposited materials resulting from opencast mining activities worldwide and the differences among continents and countries in this respect.

II. Materials and Methods

The presented study used two global datasets: The TanDEM-X 30m Change Maps [4], which provide global elevation change information, and the global-scale mining polygons dataset (version 1), which represents mining areas [3].

TanDEM-X satellite mission is a joint effort by the German Aerospace Center and Airbus Defence and Space to map the Earth's surface. It is a constellation of two satellites, flying in close orbit formation and acquiring radar images of the Earth surface [5]. The data acquired during the mission were used for the development of several global digital elevation models. The TanDEM-X 30m DEM Change Maps at a 1 arc-second spatial resolution represent the most recent addition to the family of the mission products. TanDEM-X 30m DEM Change Maps are available in two versions [4] [6]. Here, we used the last DEM change, which represents elevation changes between the TanDEM-X 30m Edited DEM – produced using data acquired over a four-year period between December 2010 and January 2015 – and most recent data acquired between 2016 and 2022 (hereafter DCM). DCM is available from https://geoservice.dlr.de/web/maps/tdm:dcm30.

The Global-scale mining polygons dataset (version 1) consists of 21,060 polygons covering 57,277 km^2 of mining areas. Mining areas were identified using coordinates from the S&P Global Market Intelligence database and manually delineated through visual inspection of several satellite-based, cloudless images (Google Satellite, Microsoft Bing Imagery, and Sentinel-2). The polygons cover various land uses related to mining activities such as open cuts, waste dumps, and processing facilities but they do not distinguish between them [3]. This dataset provides comprehensive information on global mining, though it is still far from covering all existing mines worldwide [1]. The reported omission and commission errors of mines were 21% and 3%, respectively [3]. The global-scale mining polygons dataset (v1) is available from https://doi.org/10.1594/PANGAEA.910894.

We assessed the volume of excavated and deposited material (i.e., the overall volumetric terrain change) for all mining polygons worldwide. To calculate the volumetric change, we summed up the elevation differences of all cells in the DCM within each mining polygon and multiplied the result by the area of a single cell. To differentiate between positive and negative elevation changes (i.e., to distinguish between mining and dumping areas), we treated cells with positive and negative values in the DCM separately. This approach provided three values for each mining polygon: the volume of excavated material, the volume of deposited material, and the overall volumetric change (i.e., the sum of excavated and deposited material). Subsequently, we calculated the contribution of individual countries and continents to global mining activities and their associated volumetric changes.

III. Results

Worldwide, the total volume of excavated material during the period 2011–2015 and 2016–2022 was 180,989 million m^3 while the volume of deposited material was 186,347 million m^3. Figure 1 illustrates the contribution of each continent to the volume of deposited and excavated material.

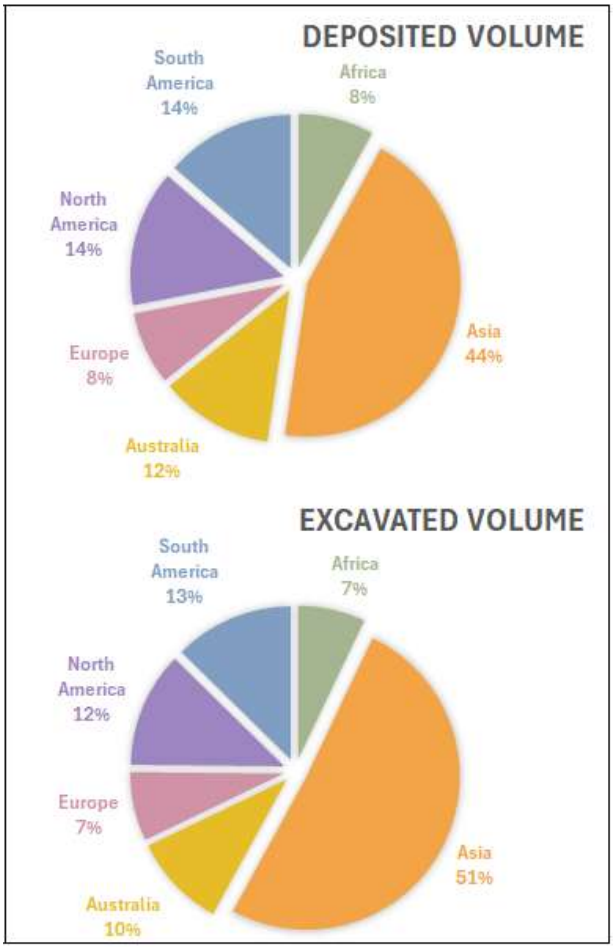

Figure 1. Contribution of each continent to the total volume of deposited and excavated material from opencast mining activities.

During the studied period, the depth of the mines (and the height of the heaps) has increased on average by approximately 2-

5 meters per square meter of mining areas, depending on the continent. Figure 2 compares the excavated (negative values) and deposited (positive values) material across each continent relative to the area of mining sites and the continent's total area. For example, in North America, the total excavated volume was equivalent to digging a hole of approximately 10x10x10 meters in size per square kilometer (Fig. 2).

A summary of the total volume of deposited and excavated material classified by country showed that the majority of opencast mining activities were concentrated in five countries: China, Indonesia, Australia, Russian Federation, and the United States (Fig. 3). This ranking slightly differed from the ranking based solely on the area of mining sites (Fig. 4). When normalized by a country area, however, the data revealed a higher intensity of mining activities in smaller countries such as Suriname, New Caledonia, Germany, and Czechia (Fig. 3). Only Indonesia was included among the top 5 countries according to both above-mentioned assessment criteria.

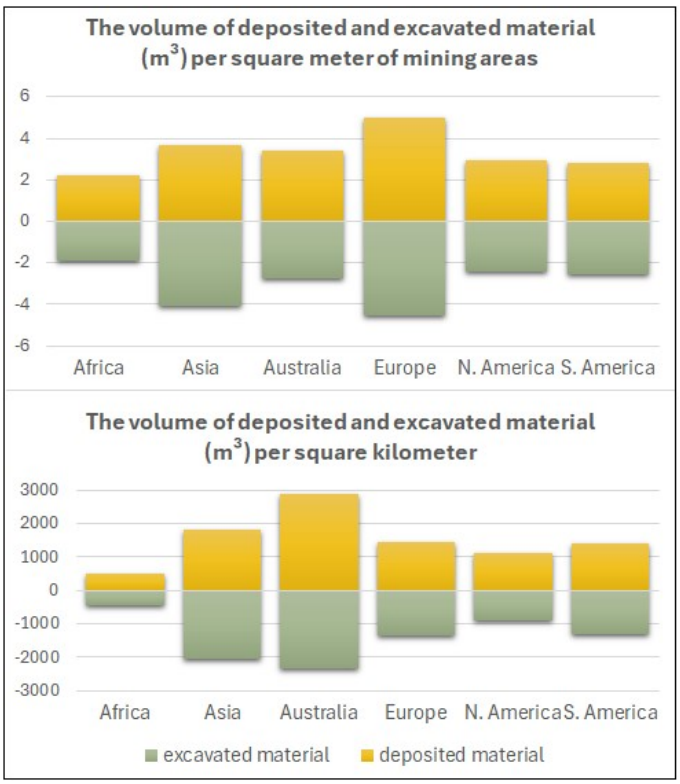

Figure 2. Comparison of excavated material (negative values) and deposited material (positive values) across each continent, shown relative to the area of mining sites (top) and the continent's total area (bottom)

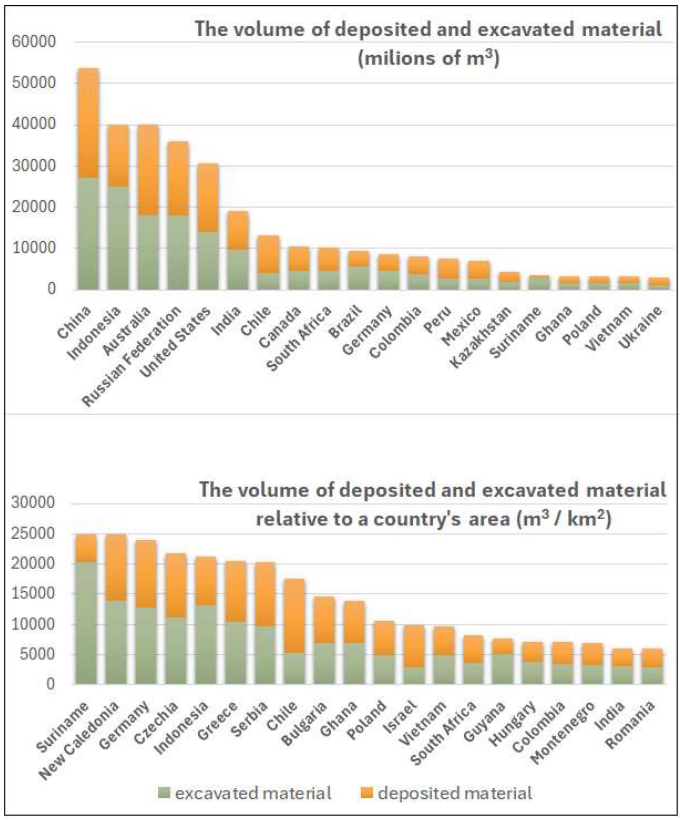

Figure 3. Ranking of countries according to the total volumes of deposited and excavated material (top) and according to the volumes relative to each country's area (bottom).

IV. Discussion and Conclusions

We demonstrated the usability of TanDEM-X 30m Change Maps for analyzing global mining activities. The calculated volumes of excavated and deposited material provide a quantitative indicator of mining intensity and its impact on Earth's surface topography. The calculated volumes account for differences in the magnitude of impacts between mining sites and provide a more accurate representation of the effects of mining activities on the surrounding areas compared to the simple use of mining site area [1]. The volumes of excavated and deposited material offer a standardized way to evaluate mining impacts globally and enable cross-site and cross-country comparisons of mining activities, providing a tool for global monitoring and enhancing transparency in the mining sector. Moreover, the volumes can aid in assessing the long-term risks of mining activities to local ecosystems and communities, facilitating early intervention strategies for mitigating damage.

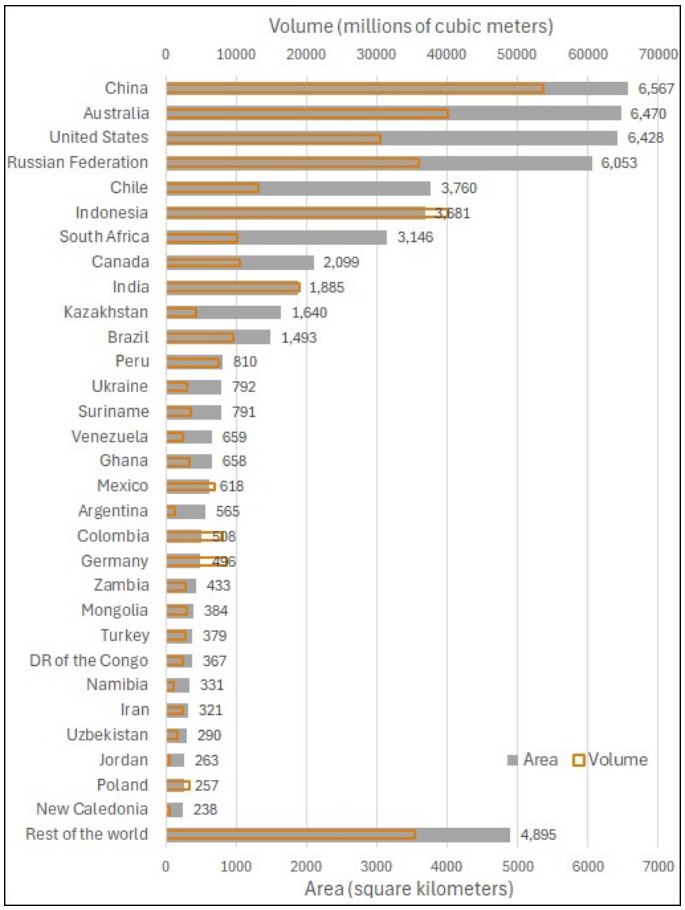

Figure 4. Ranking of countries by mining area and volume. In this case, the volume is calculated as the sum of the excavated and deposited materials.

The results of this exploratory analysis show terrain changes caused by mining activities over a relatively short period. Future studies should, therefore, incorporate near-global topographic data from the Shuttle Radar Topography Mission (SRTM), acquired in 2000, to provide a more comprehensive assessment of mining activities in this century. Additionally, a newer version of the Global-scale mining polygons dataset is available now, including 44,929 polygon features covering 101,583 km² [7].

V. Acknowledgments

This work was funded by the Horizon Europe project EarthBridge (grant agreement No. 101079310). Funded by the European Union. Views and opinions expressed are, however, those of the author(s) only and do not necessarily reflect those of the European Union or the European Research Council Executive Agency. Neither the European Union nor the granting authority can be held responsible for them.

References

[1] Maus, V., and T. T. Werner, 2024. Impacts for half of the world's mining areas are undocumented. Nature, 625, 26–29. https://doi.org/10.1038/d41586-023-04090-3

[2] Svobodova, K., 2023. Navigating community transitions away from mining. Nature Energy, 8, 1054-1057. https://doi.org/10.1038/s41560-023-01359-9

[3] Maus, V., S. Giljum, J. Gutschlhofer, D.M. da Silva, M. Probst, S.L.B. Gass, S. Luckeneder, M. Lieber, and I. McCallum, 2020. A global-scale data set of mining areas. Scientific data, 7, 289. https://doi.org/10.1038/s41597-020-00624-w

[4] Lachaise, M., and B. Schweisshelm, 2023. TD-GS-PS-0216 TanDEM-X 30m DEM Change Maps Product Description, Oct 2023 1.0.

[5] Rizzoli, P., M. Martone, C. Gonzalez, C. Wecklich, D.B. Tridon, B. Bräutigam, ... and A. Moreira, 2017. Generation and performance assessment of the global TanDEM-X digital elevation model. ISPRS Journal of Photogrammetry and Remote Sensing, 132, 119-139. https://doi.org/10.1016/j.isprsjprs.2017.08.008

[6] Lachaise, M., C. González, P. Rizzoli, B. Schweißhelm and M. Zink, "The New Tandem-X DEM Change Maps Product", IGARSS 2022 - 2022 IEEE International Geoscience and Remote Sensing Symposium, Kuala Lumpur, Malaysia, 2022, pp. 5432-5435, doi: 10.1109/IGARSS46834.2022.9883612

[7] Maus, V., S. Giljum, D.M. da Silva, J. Gutschlhofer, R.P. da Rosa, S. Luckeneder, S.L.B. Gass, M. Lieber, and I. McCallum, 2022. An update on global mining land use. Scientific data, 9, 433. https://doi.org/10.1038/s41597-022-01547-4

The use of historical cartographic materials and contemporary lidar models to determine changes in terrain relief in hard coal mining area (Bytomka Catchment, Southern Poland)

Maksymilian Solarski
Institute of Social and Economic Geography and Spatial Management
Faculty of Natural Sciences, University of Silesia
Sosnowiec, Poland
maksymilian.solarski@us.edu.pl

Mariusz Rzętała
Institute of Earth Sciences
Faculty of Natural Sciences, University of Silesia
Sosnowiec, Poland
mariusz.rzetala@us.edu.pl

Robert Machowski
Institute of Earth Sciences
Faculty of Natural Sciences, University of Silesia
Sosnowiec, Poland
robert.machowski@us.edu.pl

Martyna A. Rzętała
Institute of Earth Sciences Faculty of Natural Sciences,
University of Silesia
Sosnowiec, Poland
martyna.rzetala@us.edu.pl

Cite as: Solarski, M., Rzętała, M., Machowski, R., Rzętała, M. A. (2025). The use of historical cartographic materials and contemporary lidar models to determine changes in terrain relief in hard coal mining area (Bytomka Catchment, Southern Poland). In: Proceedings of Geomorphometry 2025, 9-13 June, Perugia, Italy. M. Alvioli, L. Melelli, I. Marchesini eds. CNR Edizioni, Rome. ISBN 978-88-8080-765-0. DOI: 10.5281/zenodo.15110492

Abstract— **The subject of the research was to determine the changes in the terrain that occurred in the Bytomka catchment area under the influence of mining anthropopressure. The research used various source materials. These were archival cartographic materials - Prussian topographic maps from the 19th century and Polish topographic maps from the end of the 20th century. Terrain models for two periods were created on the basis of these maps. The model from the end of the 19th century presented an almost natural terrain (pre-industrial) in the study area, while the model from the end of the 20th century presented the terrain after more than 100 years of mining activity. Additionally, in order to illustrate contemporary changes in the terrain, lidar models from 2011 and 2021 were used. Mining activities, carried out using the deep methods, led to a number of changes on the surface of the terrain, such as: a decrease in the average absolute height, the formation of no-drain depressions (sedimentary basins), changes in the course of the watershed, or an increase in denivelation range.**

I. INTRODUCTION

The Bytomka catchment area is located in the southern part of Poland in the Silesian Upland. In geological terms, it is the area of the Upper Silesian Coal Basin (USCB). The Upper Silesian Coal Basin is one of the largest mining areas in Europe. Its area is approximately 7,000 km^2 and stretches across southern Poland (Silesia Mountains, Lesser Poland) and northeastern Bohemia (Czech Silesia). The history of hard coal mining here dates back to the 16th century, but its dynamic development began in the mid-19th century [1]. For over 150 years, mining was one of the main factors determining the economic development of this area, contributing to the influx of people and the development of settlement units. It was also a factor that had a very strong impact on the natural relief of the USCB. The dynamic development of coal mining, especially in the 20th century, contributed to the formation of some of the largest subsidence basins in Europe

[2,3]. These forms are characteristic of mining areas where mining is carried out using the roof collapse method (without the use of backfill filling the post-mining voids). The lowering of the land surface leads not only to the formation of new forms of relief, which are sedimentation depressions or local depressions of the terrain changing the longitudinal profiles of river valleys, but also to the formation of so-called mining damage, i.e. damage to buildings, communication infrastructure, or the development of floodlands and wetlands in agricultural areas [4,5]. The Bytomka catchment is located in an area where intensive mining activity has been carried out since the end of the 19th century. The peak of mining exploitation occurred in the second half of the 20th century, and since the turn of the 20th and 21st centuries, due to the decreasing profitability of extraction, subsequent mines have been closed. Currently, there is one active coal mine within the boundaries of the study area. The aim of this study was to determine the extent to which long-term mining activity has influenced changes in the terrain in the area of the catchment selected for research.

II. STUDY AREA AND RESEARCH METHODS

The Bytomka is a small river draining the western part of the Silesian Upland. Its length is only 19.2 km, and the contemporary catchment area is 142.9 km^2. It is one of the tributaries of the Kłodnica, which then flows into the Oder.

Several source materials were used in the research. The oldest materials were historical Prussian topographic maps on a scale of 1:25,000 (Messtischblätter) made in the late 19th century. The terrain shown on these maps reflects the natural (pre-industrial) state - at the time they were made, mining activities (hard coal mining) were in the early stages of development, and therefore the area occupied by landforms related to mining activities was limited to small areas. These maps were made by qualified military cartographers. They can be used for measurements and show relatively small errors compared to contemporary materials - the vertical accuracy of the terrain representation on the maps is up to several meters [6].

In order to determine the absolute height of the research area at the end of the 20th century, Polish topographic maps at a scale of 1:10,000 were used. Historical Prussian maps were rectified to the contemporary coordinate system using the affine method, using several dozen reference points (churches, crossroads). Based on the contour intervals on both sets of maps, two digital terrain models were created, which aimed to recreate the relief from the end of the 19th century (pre-industrial period) and the end of the 20th century, with the contour intervals adjusted to the maximum accuracy of the Prussian maps (accuracy of 1.5 meters). Using simple raster map algebra, changes in the relief that occurred from 1883 to 1994 were determined. The maximum vertical error in this case was determined at the level of ±1.5 m. The research used measurement data of terrain configuration reconnaissance using lasers (Light Detection and Ranging, LIDAR) [7] conducted as part of airborne laser scanning (ALS) [8]. Data from remote sensing reconnaissance were used to create a digital terrain model (DTM), which is a representation of the shape of the topographic surface after filtering out other cover elements. Two LIDAR models showing relief in 2011 and 2021 were used to trace the changes in relief taking place until 2021. Similarly, as with maps, relief at both points in time was compared using simple raster map algebra. The lidar models used in work are very accurate terrain imaging made using laser scanning. In the case of the juxtaposition of the two LIDAR models, the maximum vertical error was ±0.3 m (with horizontal errors not exceeding 1 m). In addition, after the LIDAR models had been adjusted, they were compared with the models produced on the basis of both sets of maps, which provided information on how relief changed throughout the study period from 1883 to 2021, as well as from 1994 to 2011 and from 1994 to 2021. Modern terrain models have been generalized to an accuracy comparable to that achieved through the digitization of historical maps, with results presented using contour lines depicting subsidence.

III. RESULTS AND DISCUSSION

According to topographic maps from the end of the 19th century, the maximum absolute height in the Bytomka catchment area was 328 meters above sea level, and the minimum was 220 meters above sea level. The average elevation was 269.7 meters above sea level, and the height difference was 108 meters. However, at the end of the 20th century, both the maximum, average and minimum height of the terrain in the study area decreased. The maximum height was then 327.1 meters above sea level, the minimum height was 217.4 meters above sea level, and the average was 265.9 meters above sea level. However, the height difference increased to 109.7 meters. The reason for the changes in height were land subsidence occurring in the eastern part of the study area (Fig.1). In this part of the catchment area, hard coal mining was developed by underground methods at the end of the 19th century. Its dynamic development, especially from the end of the 19th century to the end of the 20th century, led to the creation of a number of landforms such as: extensive subsidence basins, sinkholes (concave forms) and spoil heaps and mounds (convex forms). Extraction of hard coal using roof collapse methods (without the use of backfill filling the post-mining voids) led to the creation of extensive subsidence basins and, consequently, to changes in altitude relations in the Bytomka catchment area. The analysis of terrain models made on the basis of topographic maps from the end of the 19th and 20th centuries

shows that the surface of the catchment area in the period from 1883 to 1994 decreased by an average of 3.8 meters, which gives an average anthropogenic denudation index of about 3.4 cm/ year. The consequence of the impact of mining activities was not only the decrease in the surface of the area in the eastern part of the catchment area, but also changes in the course of the watershed (Fig.1). During this period, the catchment area decreased by 7.1 km^2. Due to the development of a vast undrained area in the northeastern part of the study area. Extensive and deep subsidence basins also developed in the catchment area itself, leading to the development of undrained areas.

According to the analysis of the lidar model performed in 2011, the maximum absolute height in the catchment area was 327.3 meters, and the minimum 215.7 meters above sea level, with an average of 265.8. Compared to the situation at the end of the 20th century, there was a slight decrease in the average height of the terrain (0.1 meters) and an increase in the denivelation to 111.6 meters. The slight changes in the average absolute height of the terrain resulted primarily from a much shorter period and from the fact that at the end of the 20th century, the mining plants operating in this area began to be gradually liquidated. Waste rock mounds, which were used to level subsidence basins or, for example, as material for road construction, also began to disappear from the landscape. It should be emphasized, however, that the model based on the 1994 topographic map is much less accurate than the 2011 lidar model and does not include many smaller landforms (such as road or railway embankments, etc.).

The analysis of the model performed in 2021 shows that in the decade 2011-2021 the altitude relations changed very little. The maximum height was then 327.5 meters above sea level (an increase of 0.2 m), the minimum 214.7 meters above sea level (a decrease of 1.0 meter), and the average height 265.8 meters (no change in the period 2011-2021).

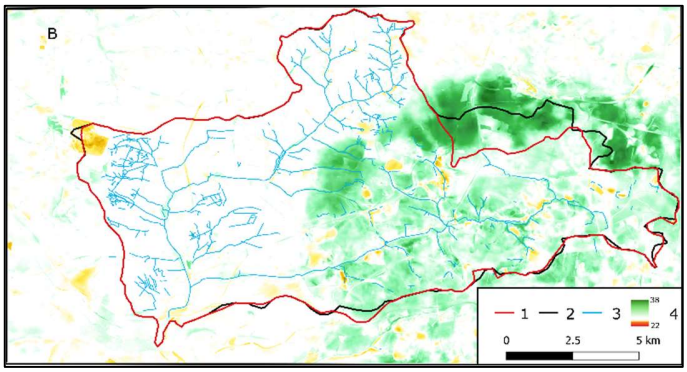

Figure 1. Changes in terrain elevation in the study area from 1883 to 2021: 1 - watershed in 2021, 2 – watershed in 1883, 3 – streams, 4 – changes in ground height in meters.

IV. CONCLUSIONS

By using various source materials, historical topographic maps and lidar models, it was possible to reconstruct absolute height changes in the area subject to long-term mining anthropopressure. As a result of long-term activities related to hard coal mining using deep methods (without filling post-mining voids), extensive land subsidence occurred, which covered a total surface of about 76 km^2, including the eastern part of the study area. This led to the formation of deep subsidence basins, the maximum depths of which exceeded 35 meters, thus causing a decrease in the average absolute height in the area of the studied catchment, as well as a change in the course of watersheds and the formation of no-drain areas. The volume of subsidence calculated on the basis of changes in the average absolute elevation of the terrain for the period 1883-2021 amounted to 567.0 million cubic meters.

REFERENCES

[1] Jaros, J. 1984. “Historical Dictionary of Coal Mines in Poland”, “Śląsk” Publishing House, 198p .

[2] Solarski, M. 2013. “Anthropogenic transformations of the Bytom area relief in the period of 1883–1994", Environ. Socio-Econ. Stud. 1, 1–8.

[3] Dulias, R. 2106: “Changes in Morphometric Parameters of Terrain Caused by Mining. In The Impact of Mining on the Landscape; Environmental Science and Engineering”, Springer: Berlin/Heidelberg, Germany, 83–93.

[4] Machowski, R., Rzetala, M.A., Rzetala, M., Solarski, M. 2016. „Geomorphological and Hydrological Effects of Subsidence and Land use Change in Industrial and Urban Areas”, Land Degrad. Dev. 2016, 27, 1740–1752.

[5] Solarski, M., Machowski, R., Rzetala, M., Rzetala, M.A. 2022. „Hypsometric changes in urban areas resulting from multiple years of mining activity”, Sci. Rep., 12, 2982.

[6] Konias, A. 2010. “Topographic Cartography of the State and the Prussian Partition from the Second Half of the 18th Century to the Middle of the 20th Century”, Pomeranian Academy in Słupsk Publishing House: Słupsk, Poland, 232 p.

[7] Geoportal. Available online: https://www.geoportal.gov.pl/pl/dane/dane-pomiarowe-lidar-lidar/ (accessed on 20 November 2024).

[8] Affek, A. 2014. “Airborne laser scanning (ALS) in terrain modelling—New opportunities and pitfalls”, Probl. Landsc. Ecol. 38, 217–236.

edizioni
Consiglio Nazionale delle Ricerche